Cranfield University

College of Aeronautics

PhD Thesis

Academic Year 1998-1999

Scott Thomas Shaw

Numerical Study of the Unsteady Aerodynamics of Helicopter Rotor Aerofoils

Supervisor: Dr N. Qin

March 1999

Abstract

A two-dimensional model of the aerodynamics of rotor blades in forward flight is proposed in which the motion of the blade is represented by periodical variations of the freestream velocity and incidence. A novel implicit methodology for the solution of the compressible Reynolds averaged Navier-Stokes equations and a two-equation model of turbulence is developed. The spatial discretisation is based upon Osher's approximate Riemann solver, while time integration is performed using a Newton-Krylov method.

The method is employed to calculate the steady transonic aerodynamics of two supercritical aerofoils and the unsteady aerodynamics of pitching aerofoils. Comparison with experiment and independent calculations for these test cases is satisfactory. Further calculations are performed for the self-excited periodic flow around a bi-convex aerofoil. Comparison of quasi-steady and unsteady calculations suggests that the flow instability responsible for the self-excited flow is due to the presence of a shock induced separation bubble in the corresponding steady flow.

Finally the method is used to predict the aerodynamics of aerofoils performing inplane and combined inplane-pitching motions. Results show that quasi-steady aerodynamic models are unsuitable at conditions representative of high-speed forward flight. For shock free flows, the unsteady effects of freestream oscillations can be represented by a simple phase lag. For transonic flows the influence of unsteadiness on shock wave dynamics is shown to be complex. Calculations for indicial motion show that the unsteady behaviour of the flow is related to the finite time taken by disturbance waves to travel to the shock wave from the leading and trailing edges of the aerofoil.

'The purpose of computing is
insight, not numbers'

Hamming

Acknowledgements

I wish to express my sincere gratitude to my supervisor, Dr Ning Qin, for his patience, enthusiasm and expert guidance throughout the course of my PhD studies.

A great debt is also owed to Dr K. Badcock and Professor B.E. Richards of Glasgow University who provided a copy of their Navier-Stokes solver AFCGS which greatly eased my transition into the field of computational fluid dynamics and has provided a useful reference for my own work. The assistance and interest of Dr K. Kokkalis (CFD Specialist), Mr R. Harrison (Assistant Chief Aerodynamicist) and Mr J. Perry (Chief Aerodynamicist) all of GKN Westland Helicopters Ltd has also been invaluable.

As somebody once said 'Time wasted in the company of great men is time well spent', with this in mind I would like to thank my friends and colleagues David Ludlow, Simon Prince, Yon Han Chong, Yuping Zhu, Aeghis Barberopoulos and all the past residents of 9 The Crescent for the time which we wasted together.

During the course of my studies I have had the good fortune to work on a number of research projects for the Defence Evaluation and Research Agency (DERA) which have helped to broaden my understanding of both aerodynamics and computational fluid dynamics. I would like to thank both Professor J. Edwards (DERA Fort Halstead) and Trevor Birch (DERA Bedford) for these opportunities.

The help and assistance of Dr Kevin Garry (head of department), Pauline Foreshaw and Marie Breen (department secretaries) and Dr Les Oswald (computer manager) is also gratefully acknowledged. Finally I would like to thank and dedicate this thesis to my family for their support during my studies.

This work was supported by EPSRC under grant number GR/K31664.

Contents

1

Introduction

1.1 Motivation

Despite considerable experimental and theoretical work over the last century the accurate simulation of the flowfield around helicopter rotors in forward flight continues to present a significant problem for the helicopter engineer. The flow is highly unsteady and contains regions in which quite different physical mechanisms dominate the flow development. The advancing blade tips operates at high, typically transonic, Mach numbers and low lift coefficient while conversely on the retreating side the blade experiences high lift coefficients at more modest Mach numbers. In addition there are local regions of high loading due to strong interactions of the blade with the wake system and tip vortices of preceding blades. The situation is further complicated because of the strong coupling between the blade aerodynamics and blade motion.

In principal the Navier-Stokes equations contain all of the physics that are required to accurately represent the complex nature of these phenomena and can be coupled with models of the rotor structural dynamics [(2)]. However, such a direct approach has the disadvantage that it is very computer intensive especially considering the complex nature of the phenomena which must be resolved. Instead, reduced physical models that illustrate and quantify the behaviour of the individual aspects of the flow problem are required.

If the helicopter rotor is conceived as a very high aspect ratio wing (typical aspect ratio's for a single blade are in excess of 15) then it is possible to justify the use of a two-dimensional approximation [3]. The blade loads can then be calculated by the use of a strip theory in which the local aerodynamic loading is obtained for a number of blade elements across the span. The local loads are obtained using steady data at the appropriate Mach number and incidence, the blade loading is then obtained by integrating the section data across the span. This approach has been widely adopted within the helicopter community as a basis for the prediction of helicopter performance and vibratory loading, see for example Johnson [4].

Recently Hansford and Vorwald [5] compared load predictions computed using a number of industrial tools (all of which employ strip theory) with vibratory loads measured in flight tests [6] of the Lynx helicopter. Their report highlights deficiencies in the use of quasi-steady aerodynamics to obtain the blade element loads. Furthermore it was demonstrated that the use of 'improved technology models' which account for unsteady effects associated with blade pitching and plunging significantly improved comparisons between computation and measurement. It was also shown that the major deficiency in vibratory load calculations was at high forward flight speeds.

For a two-dimensional blade section the variation of Mach number and incidence during one revolution may be illustrated by a 'figure-of-eight' diagram, upon which the locus of Mach number and angle of attack is plotted for a given forward flight velocity. A typical example of such a plot is given in Figure (1.1) which shows the variation of Mach number and incidence at r/R = 0.93 for the Wessex helicopter main blade in forward flight with an advance ratio of 0.33 [7]. It is readily apparent from such figures that in high-speed forward flight both the variation of incidence and the variation of Mach number may be responsible for significant unsteady effects.

Today we understand well the qualitative and quantitative behaviour of the aerodynamics of aerofoils that are oscillated about the pitch axis. This has largely been due to careful observation and measurement of wind tunnel experiments. In contrast we have only a rudimentary understanding of the behaviour of the unsteady shock waves

which characterise the advancing blade in high-speed forward flight, largely because of difficulties in representing such motion in the wind tunnel.

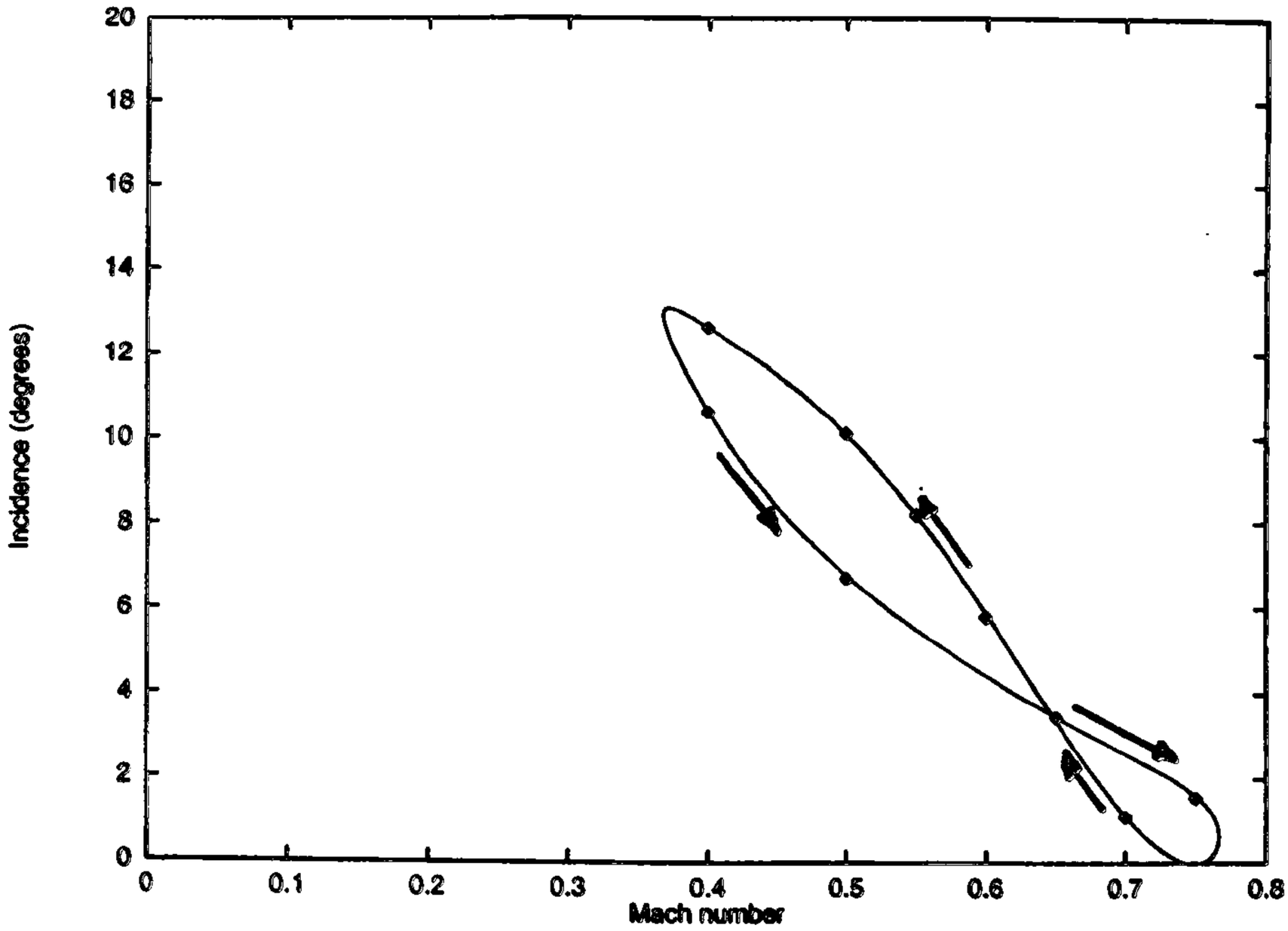

Figure (1.1) Locus of Mach number and incidence

1.2 Aims and objectives

This work aims to develop an improved understanding of the aerodynamics of the advancing rotor blade in forward flight. In order to make the problem more tractable a two-dimensional approximation is adopted in which the complex flow around the rotor blade is represented by an aerofoil performing representative inplane and pitching motions. The absence of a suitable wind tunnel facility precludes experimental measurement and so instead a study based upon numerical solutions of the Navier-Stokes equations is proposed.

In order to meet the aims of this sudy a number of clear objectives can be identifdied

- The development of a numerical framework within which problems related to the forward flight aerodynamics of the helicopter main rotor can be explored.

- Validation and verification of the numerical method by comparison of the computed results with suitable experimental measurements.
- Detailed investigation of the flow around aerofoils performing representative inplane and pitching motions.aerodynamics of aerofoils subjected to secondly to provide some insight into the dynamics of the advancing blade shock wave.

1.3 Outline of Thesis

The study can be naturally subdivided into three major parts. The first concerns the development of an accurate and efficient two-dimensional flow solver for the unsteady Navier-Stokes equations together with a two-equation model of turbulence. The second part of the study concerns the validation of the methodology by comparison of computed solutions with experiments for which the flow physics are well understood. In the final part of the study an investigation of the effects of Mach number oscillations on the processes of shock formation and motion for helicopter rotor aerofoils at conditions representative of high-speed forward flight is performed.

In the next chapter the aerodynamic environment of the helicopter main rotor is described. Progress in the application of numerical methods to the problem of determining rotor loads is then reviewed. The consequences of a two dimensional approximation of the blade aerodynamics are then considered in full. In the following chapter's a novel unfactored implicit method is presented for the solution of the Navier-Stokes equations on a moving grid together with a strongly coupled turbulence model. The performance of the method is considered in detail. In chapter 6 calculations of the steady flow around the RAE 2822 and NACA 0012 aerofoils are presented. In chapters 7 and 8 results for pitching aerofoils and transonic self-excited oscillations are considered. Qualitative and quantitative comparison is made between computations performed using the method described in Chapters 3-5, independent calculations and experiment. Finally in Chapter 9 the aerodynamics of in-plane oscillations and combined translation-pitch oscillations respectively are investigated. The thesis concludes with a discussion of the main findings of the study and some suggestions for future work.

2

Aerodynamics of the Helicopter Main Rotor

In this chapter the aerodynamic environment of the helicopter main rotor is introduced. The role of computational fluid dynamics in predicting the three-dimensional flowfield around rotor blades is discussed. A two-dimensional approximation is then described which reduces computational expense while retaining a reasonable physical representation of the rotor aerodynamics.

2.1 The aerodynamic environment of the main rotor

The aerodynamics of the rotating wing has been investigated comprehensively over the past fifty years. In hover and axial flight the flow around the rotor is largely independent of azimuth angle and each of the blade elements experiences essentially constant flow conditions. The aerodynamic problems in these flight regimes are similar to those that occur for a propeller in axial motion with two major exceptions. Firstly the helicopter has a relatively low disc loading (for gas turbine powered rotorcraft the disc loading is typically [8] around 40kG/m^2) unlike the propeller which generally has a very high disc loading. Secondly the helicopter rotor blade interacts with its own wake. Such interactions can have a major influence on the rotor performance particularly in hover and descent.

In forward flight the flow behaviour is less straightforward as the rotor blades experience a component of the forward flight velocity in addition to that due to their

own rotation. In a plane parallel to the flight direction, see Figure (2.1), the effective velocity experienced by a chordwise section of the rotor blade can be determined from,

$$U = r\Omega + U_f \sin(\Omega t) \tag{2.1}$$

in which r is the spanwise distance measured from the rotor hub, Ω is the angular velocity of the blade and U_f is the forward flight velocity.

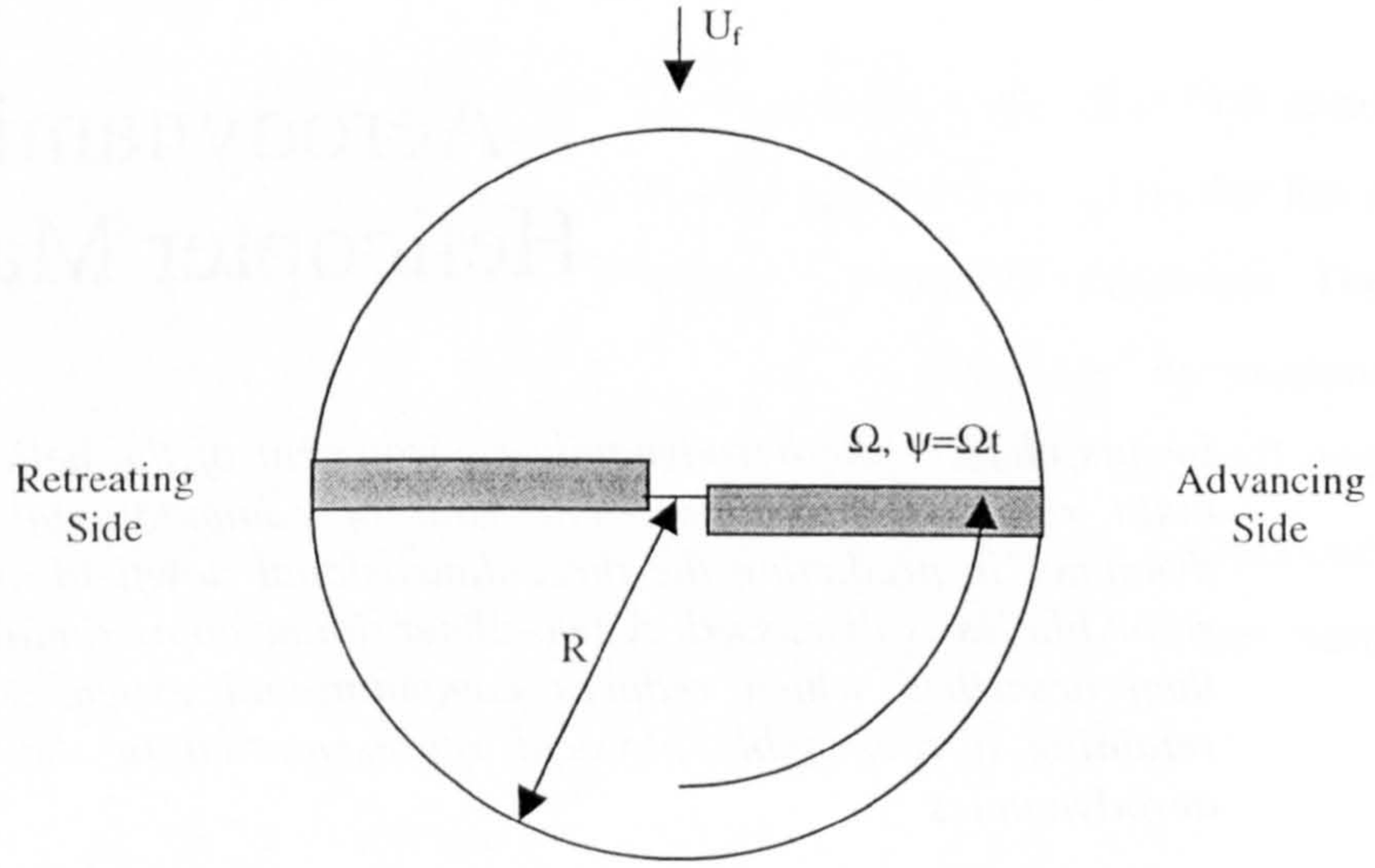

Figure (2.1) Planform view of rotor in forward flight

The two main effects of the forward flight velocity can be deduced from Equation (2.1);

(1) The flow field is no longer independent of time

(2) The flow field no longer enjoys the rotational symmetry which existed for the hovering rotor

For a rigid rotor the effects of such asymmetry can be catastrophic; on the advancing side the increased dynamic pressure produces increased lift while on the retreating side less lift is generated. This imbalance produces large oscillatory bending stresses at the blade root together with a large rolling moment. The incorporation of flapping and lead-lag hinges close to the hub effectively overcomes such problems by allowing the

blades to adjust their effective angle of attack to ensure that the air-loads across the rotor disc are in balance. The additional degrees of freedom offered by such a system have the drawback that they introduce a strong coupling between the blade aerodynamics and structural dynamics. Thus the advancing blade operates in a high speed flow at small angles of attack while the retreating blade must operate in a low speed flow at angles of attack close to that at which stall occurs. The resulting flowfield is highly complex as evinced by Figure (2.2) below (after Caradonna [9]) which illustrates the flow phenomena that are of principal interest in forward flight.

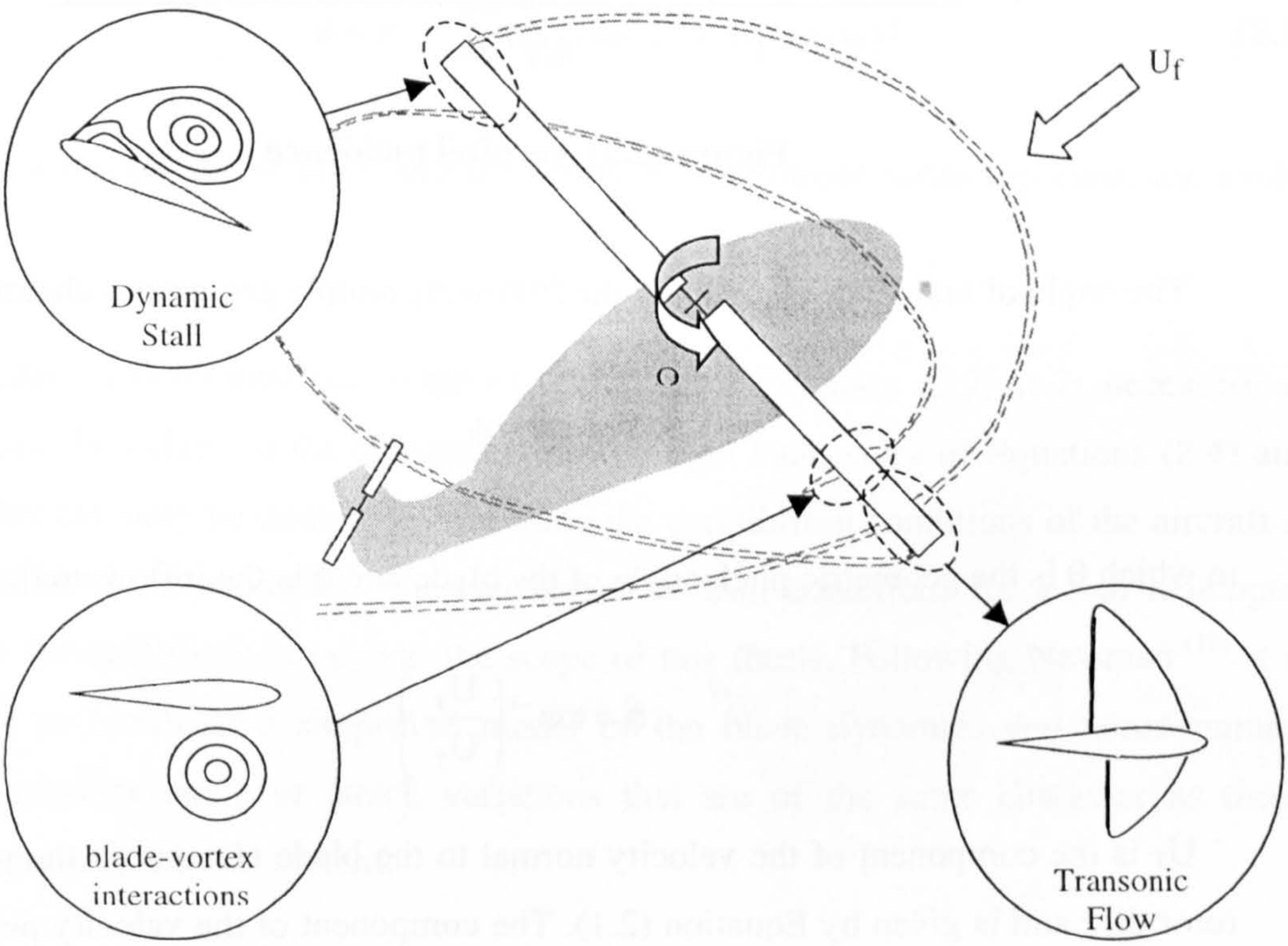

Figure (2.2) Rotor Flow Problems

For convenience we shall consider the individual flow phenomena shown in Figure (2.2) in isolation, whilst this will provide a clear understanding of the physical problems which must solved it is important to realise that the phenomena are inter-related and it is difficult to make such distinctions in practice.

2.1.1 Pitching oscillations

In forward flight the angle of incidence of the rotor becomes a complex function of the forward flight speed, induced velocity, blade flapping and blade pitch angle. This is shown schematically in Figure (2.3) below for a typical blade element.

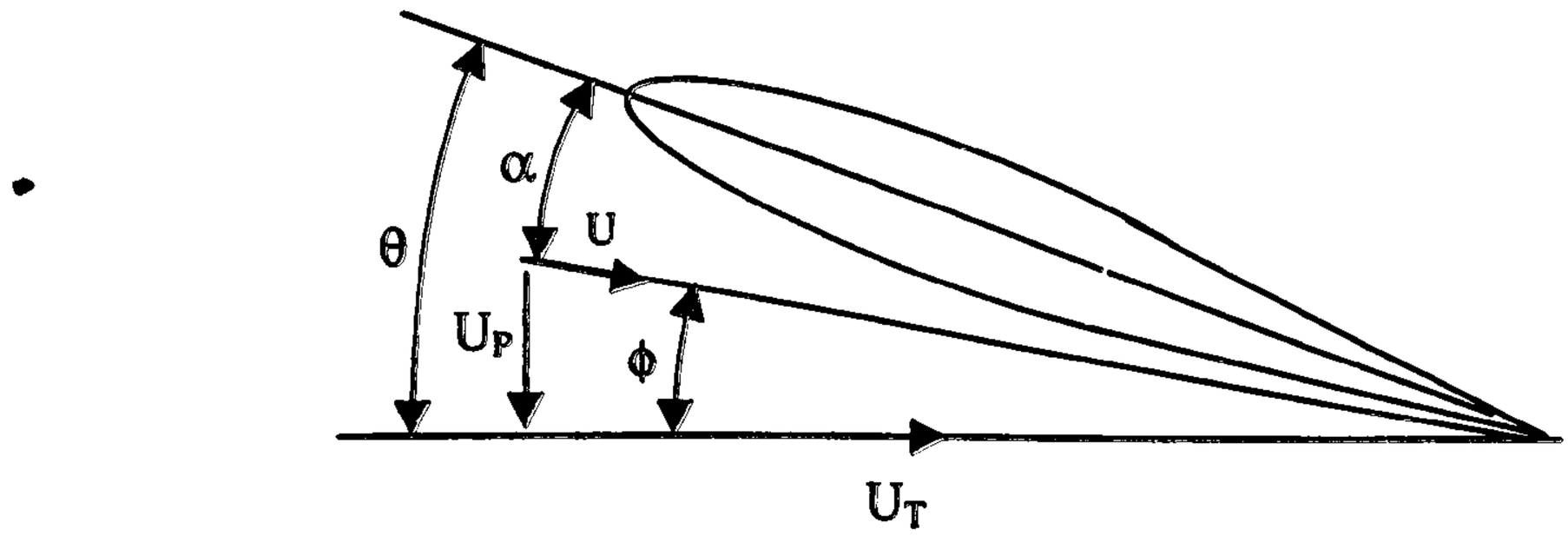

Figure (2.3) Aerofoil incidence

The angle of incidence is given by the following simple geometric relationship,

$$\alpha = \theta - \phi \tag{2.2}$$

in which θ is the geometric pitch angle of the blade and ϕ is the inflow angle,

$$\phi = \tan^{-1}\left(\frac{U_P}{U_T}\right) \tag{2.3}$$

U_T is the component of the velocity normal to the blade element in the plane of the rotor disc and is given by Equation (2.1). The component of the velocity perpendicular to the plane of the rotor disc, U_P is made up of contributions from the flow induced by the blades through the rotor disc, λ, and components of the spanwise velocity and angular velocity due to blade flapping. Thus the component of velocity perpendicular to the blade is,

$$U_P = \lambda + \beta\mu\cos(\Omega t) + r\dot{\beta} \tag{2.4}$$

where the symbol β denotes the blade flapping angle. Unlike fixed wing aircraft, the helicopter employs a single aerodynamic system (the main rotor) to obtain the forces and moments that are required for lift, control and propulsion. By varying the magnitude of the thrust and its direction of application through changes in the pitch of the rotor blades the pilot is able to control completely the speed and direction of the flight. The magnitude of the rotor thrust is controlled by a uniform change of blade pitch around the rotor (collective pitch), while the attitude of the rotor disc is controlled by a periodic variation of the pitch angle, the pitch angle is therefore of the general form,

$$\theta = \theta_o - \sum \left(A_n \cos(\psi) + B_n \sin(\psi) \right) \tag{2.5}$$

here θ_o is the collective pitch and the terms of the Fourier series represent the cyclic pitch.

In order to determine the angle of attack from Equation (2.2) it is necessary to determine the values of the parameters on the right hand sides of Equations (2.4) and (2.5), this can only be done by establishing the equilibrium conditions of the aircraft at a particular flight condition. The calculation of trim conditions for a real helicopter rotor in forward flight is beyond the scope of this thesis. Following Newman [10] it is possible to construct a simplified model of the blade dynamics and aerodynamics which provides angle of attack variations that are of the same character as those experienced by the real system.

In Figure (2.4a) the variation of blade incidence over the rotor is shown for Case 1 of Table (9.1) in Reference (10) at a forward flight velocity of 50 m/s ($\mu = 0.25$). In Figure (2.4b) the angle of incidence is plotted against azimuth angle for a single blade element located at the rotor tip. The variation of incidence can be represented using a Fourier series containing relatively few terms. However, as the principle variation is first harmonic in character, motion of the form,

$$\alpha = \alpha_o + \Delta\alpha \sin(\Omega t) \tag{2.6}$$

has generally been studied.

Experimental studies of pitching aerofoils have shown that under attached subsonic flow conditions some hysteresis is produced in both the forces and moments. However, the measured normal force and pitching moment do not differ significantly from static measurements (the hysteresis loops are relatively narrow). The occurrence of flow hysteresis can be explained using classical aerofoil theory [11,12]. When the aerofoil changes incidence the aerodynamic loads change, this implies a change in the bound circulation of the aerofoil. This change in bound circulation is accompanied by the shedding of vorticity into the wake, consequently an oscillating wake is generated behind the aerofoil. The near wake will produce fluctuations in the aerofoil loads about their mean values. From this analysis it is clear that the ratio of the semi-chord length to the wavelength of the wake will govern the importance of unsteady effects. This parameter is the reduced frequency,

$$k = \frac{\frac{c}{2}}{U} = \frac{\omega c}{2U} \qquad (2.7)$$
$$\overline{\omega}$$

Here ω is the frequency of the motion, which for the helicopter rotor is simply $\omega = \Omega/2\pi$. From (2.7) we can see that as the frequency of the forcing motion is reduced unsteady effects will diminish.

For inviscid, incompressible flows analytical solutions of the linearised potential equation have been obtained by Theodorsen [13] as a function of the reduced frequency and have been extended to include the influence of the rotor wake, see Johnson [4]. Beddoes [14] employed indicial functions to obtain lift response to arbitrary forcing in compressible flow.

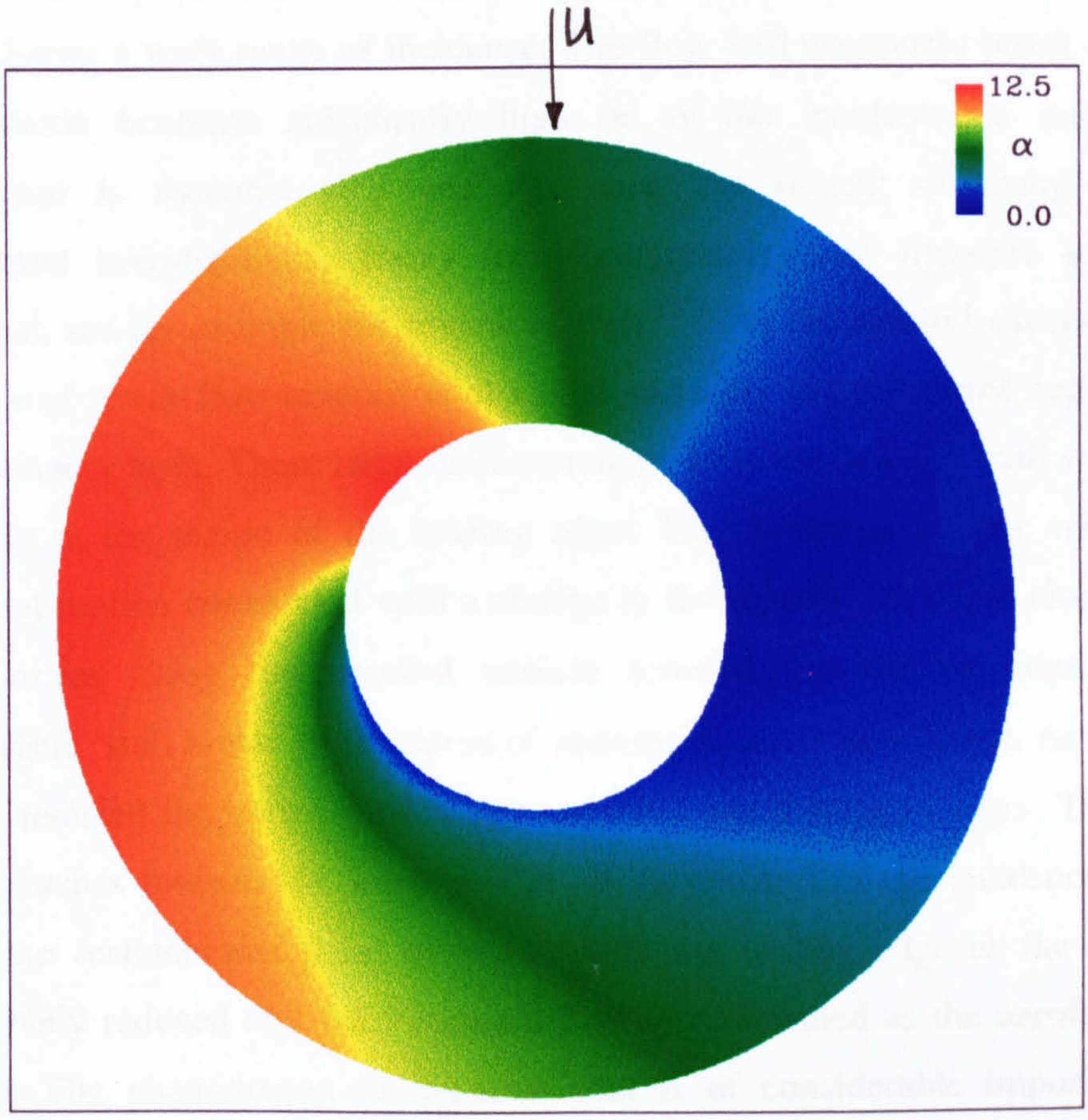

(a) On the rotor disc

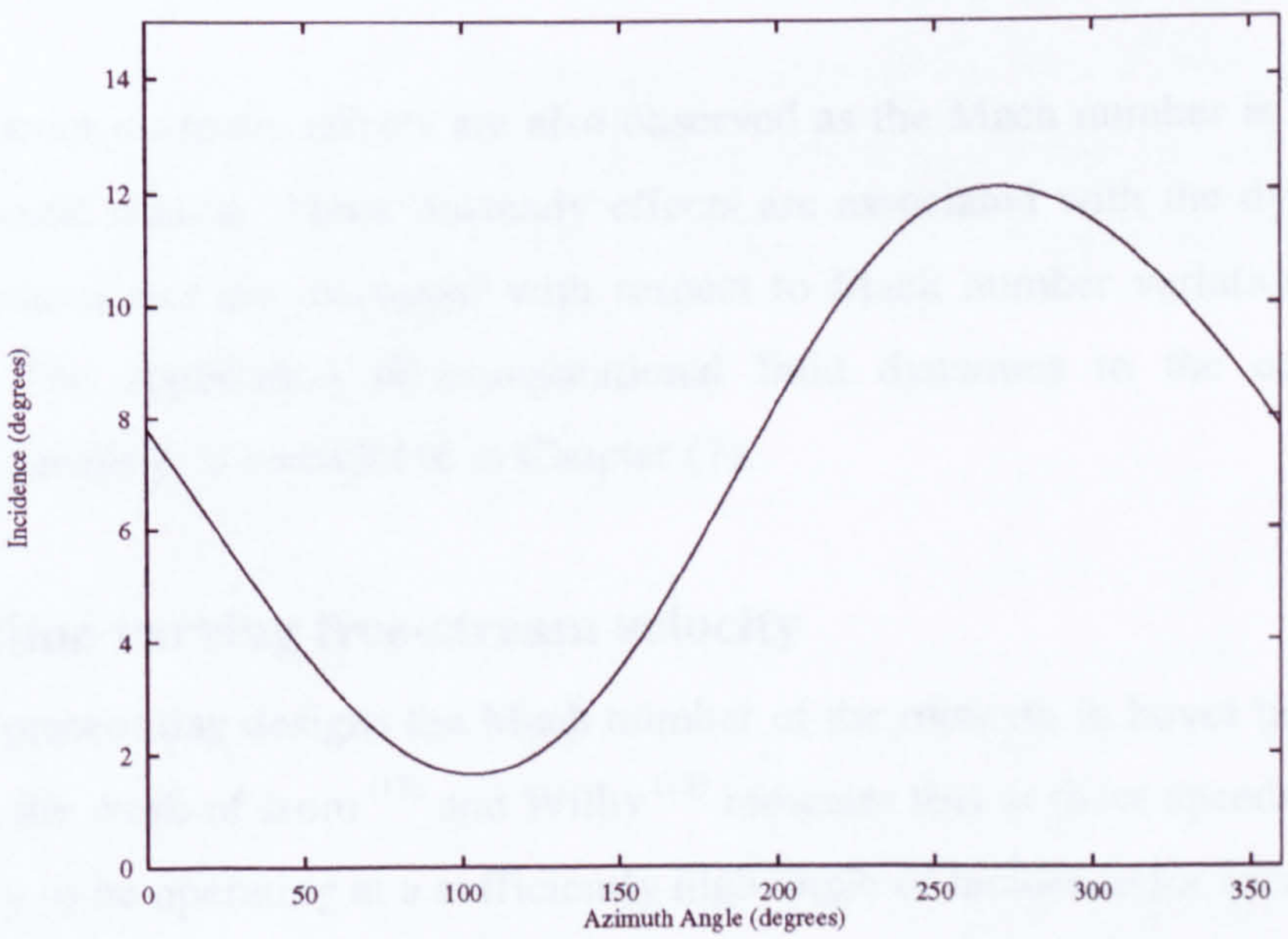

(b) At r/R = 1.0

Figure (2.4) Variation of incidence

It was noted by Carta [15] that as the incidence of the pitching aerofoil is increased progressively beyond that at which static stall occurs useful lift continues to be generated over a wide range of incidence. The flow will eventually break down when the incidence becomes sufficiently high or as the incidence is reduced. This phenomenon is dynamic stall and has been the subject of many subsequent experimental investigations. Today the phenomenology of dynamic stall is well understood, see for example the review of Carr [16]. As the aerofoil exceeds the static stall angle of attack flow reversal is observed and eddy like structures begin to appear in the boundary layer. These large-scale structures form the dynamic stall vortex, which is initially in the region of the leading edge. The formation of this vortex and its subsequent motion correspond with a change in the aerofoil lift curve slope. The stall vortex moves along the aerofoil surface towards the trailing edge causing a characteristic 'stall break' in the curve of pitching moment coefficient. As the angle of attack is reduced the vortex moves into the wake and lift stall occurs. The boundary layer reattaches towards the leading edge of the aerofoil as the incidence is reduced further, the reattachment point moves towards the trailing edge as the incidence is progressively reduced and fully attached flow is established as the aerofoil begins to pitch up. The phenomenon of dynamic stall is of considerable importance as the breakdown of flow on the retreating blade establishes the operating limits of the helicopter rotor.

Significant unsteady effects are also observed as the Mach number is increased into the transonic regime. These unsteady effects are associated with the dynamics of the shock system and are discussed with respect to Mach number variations in the next section. The application of computational fluid dynamics to the computation of pitching aerofoils is considered in Chapter (7).

2.1.2 Time varying free-stream velocity

With present day designs the Mach number of the rotor tip in hover lies between 0.6 and 0.7, the work of Isom [17] and Wilby [18] indicates that at these speeds the blade tips are likely to be operating at a sufficiently high angle of incidence for locally supersonic flow to be encountered. Further, in forward flight individual blade elements experience

an unsteady component of the forward flight speed, the effective free-stream velocity is given by Equation (2.1).

Significant losses due to compressibility are encountered when the advancing blade tip Mach number exceeds 0.85-0.90, see Fradenburgh[19], however by careful aerofoil selection the effects of compressibility can be delayed. More importantly the advancing blade flow is highly unsteady due to the formation, movement and disappearance of the shock wave. Lerat and Sides [20] have shown the importance of shock-wave dynamics on the development of the unsteady flow. Numerical solutions of the Euler equations for a rotor aerofoil in an oscillating free-stream indicate that there is a significant delay between the formation and motion of the shock-wave and the unsteady Mach number variations.

The development of the steady transonic flow-field for a RAE 102 aerofoil as Mach number and incidence are increased is described by Lock [21]. For completeness a brief description of the development of the flow with increasing Mach number is presented here. Initially the flow around the aerofoil is shock free, but as Mach number is increased beyond the Mach number at which the flow becomes locally sonic, a shock wave develops close to the point of maximum thickness. This shock wave becomes progressively stronger as the Mach number is increased further and moves towards the trailing edge. The measured shock strength is consistently below that predicted using the Rankine-Hugonoit relationship (this is attributed to viscous effects) but generally follows the trend of the curve until the local Mach number immediately upstream of the shock-wave is above 1.3.

Beyond this Mach number the boundary layer is unable to negotiate the steep pressure drop and boundary layer separation occurs at the foot of the shock wave. Initially the boundary layer reattaches downstream to form a separation bubble. As the free-stream Mach number is increased further the shock location becomes 'frozen' and the separation bubble increases in size. Eventually the reattachment point moves beyond the trailing edge and the boundary layer becomes fully separated. Further

increases in Mach number produce a rearward motion of the shock wave (and a smaller separated region) until eventually the trailing edge is reached

The optimum blade geometry for a given helicopter can be derived only if its transonic characteristics are well understood. That this is the case has been amply demonstrated by the contributions of Wilby and Pearcey [3,7,18] to the British experimental rotor program (BERP). However, the development of aerofoil sections for the BERP rotor was primarily performed on the basis of a clear understanding of steady transonic aerodynamics. It is to be expected that a proper understanding and control of unsteady transonic flow on the advancing blade may yield further performance improvements.

Most of the experimental and theoretical studies of unsteady transonic flow to date have been aimed at providing information that is relevant to the aeroelastic stability of fixed wing aircraft. Among those studies the work of Tidjeman [22] is of particular importance. Tidjeman studied the dynamics of shock motion on a conventional aerofoil section with an oscillating trailing edge flap. From an analysis of the time history of the shock motion three classes of unsteady shock motion, Types A, B and C, were observed:

Type A: Sinusoidal shock-wave motion

For large free-stream Mach numbers (M_∞ =0.9) the shock wave was observed to move in a sinusoidal manner about the steady location. Phase lags were observed between the motion of the driving flap, the shock strength and shock location.

Type B: Interrupted shock-wave motion

At lower free-stream Mach numbers (M_∞ = 0.875) the shock-wave motion is again almost sinusoidal, but the shock wave disappears during part of its downstream motion.

Type C: Upstream propagated shock wave

For free-stream Mach numbers that are close to the critical Mach number of the aerofoil a third class of shock motion was observed. As the flap begins its upward

motion a shock wave is formed on the aerofoil upper surface, this shock wave moves upstream and increases in strength. This continues until the flap angle reaches its maximum value, as the flap deflection reduces the shock-wave diminishes in strength but continues to move upstream eventually passing over the leading edge of the aerofoil to form a free shock wave. The free shock wave then propagates upstream of the aerofoil. This behaviour is periodic with a frequency half that of the forcing motion.

Tidjeman [22] has derived a simple physical model, Equation (2.8), from the Rankine-Hugoinot relationship that is able to describe the different classes of periodical shock-wave motion. The model provides a qualitative understanding of the effects of the main parameters of interest: shock strength, Mach number distribution ahead of the shock, magnitude and frequency of the pressure disturbances.

$$\frac{\overline{P}_2}{\overline{P}_1} = \left(\frac{P_2}{P_1}\right)_{x,steady} + \frac{4\gamma}{\gamma+1} M_1 \left[\frac{\partial M_1}{\partial x} - \frac{i\omega}{a_1}\right] x_o e^{i\omega t} \qquad (2.8)$$

The model is limited to cases involving thin aerofoils (the influence of pressure gradients normal to the aerofoil surface is neglected) and low frequencies (the pressure distributions are assumed to change in a quasi-steady manner). It should be noted that the model allows all three classes of shock motion to be present for flows of the same Mach number, but different forcing frequencies.

Tidjeman also studied the unsteady behaviour of shock waves on aerofoils pitched sinusoidally about their quarter-chord point. It was shown that the phase lag between the shock wave and forcing motions varied almost linearly with the forcing frequency. This observation is in close agreement with the experimental results of Erickson and Stephenson [23], who showed a strong correspondence between the time it takes pressure disturbances (Kutta waves) to travel upstream from the trailing edge to the shock-wave and the phase lag between shock-motion and the aerodynamic forcing.

A more detailed understanding of the role of Kutta waves in oscillatory shock motion has recently been presented by Lee, Murty and Jiang [24] who studied the propagation of pressure disturbances generated at the trailing edge of an aerofoil using numerical

solutions of the transonic small disturbance equations. Preliminary results from this study show that the propagation time,

$$T = -\int_{l}^{x_s} \frac{dx}{(1 - M_l)a_l} \tag{2.9}$$

matches closely the results obtained using a simple empirical model [22] for the local Mach number, M_l,

$$M_l = R\{M_{l,surface} - M_\infty\} + M_\infty \tag{2.10}$$

when the value R=0.7 is used.

Much of our understanding of shock wave dynamics has come through careful experimentation at fixed Mach numbers using flap deflections or pitching oscillations to generate the required unsteadiness. It is not however clear from such studies the role that variations in free-stream Mach number will play in the development of the unsteady flow. Few experiments have been carried out to clarify this issue. To the author's knowledge only the experiments recently performed by Krause [25] have sufficiently high free-stream Mach numbers and variations to be of direct relevance to the understanding of the advancing blade shock dynamics. Unfortunately the experimental arrangement adopted by Krause is unsatisfactory, the rotating plate used to generate variations in the free-stream Mach number was placed downstream of the aerofoil and consequently significant upstream influence is expected. A small number of computational investigations have been performed which employ numerical solutions of the full potential and Euler equations. These studies are discussed in Chapter (9).

2.1.3 The rotor wake and blade-vortex interaction

In hover, each of the rotor blades produces an extensive wake system. In addition to the strong tip vortex the wake contains trailed vortex filaments due to the spanwise variation in bound vorticity. The strength of these filaments varies along the span, with the strongest elements in the tip region. Close to the tip the vortex filaments 'roll up'

into the tip vortex so that beyond about 45° of vortex age the wake is dominated by the tip vortex. In forward-flight the situation is complicated further by the variations in both incidence and effective Mach number discussed previously. Each change in Mach number and incidence produces a change in the aerodynamic loads experienced by the blade together with a corresponding variation in the bound circulation. Each of these changes is accompanied by the shedding of a counter rotating vortex into the wake. The resulting rotor wake therefore contains a complicated mixture of vortical structures due to both shed and trailed vorticity. The detailed structure of such wakes and their interactions with the helicopter rotor is not currently well understood. McCroskey [26] has produced a comprehensive review of the vortex wakes of rotorcraft.

In high-speed forward flight the wake is convected rapidly downstream from the rotor and its influence on the blade loading is significantly reduced, however there are still high local loads associated with the passage of the tip vortex over the tail rotor. Such interactions are known as blade-vortex interactions (BVI) and have a significant effect on the vibratory and acoustic loading of the rotor. The problem of BVI has been documented comprehensively in the literature, see for example the introductory remarks of Leishman, Baker and Coyne [27]. The main aim of early experiments was to isolate the fundamental behaviour of the problem by studying a single interaction, see for example Kokkalis[28], Such studies have provided important information on the basic fluid dynamical aspects of the problem and have identified the group of parameters which govern the severity of the BVI problem. More recently there has been considerable interest in the computation of BVI, see for example the work of Ng[29]

2.2 Aerodynamic prediction for rotorcraft

The availability of high-speed digital computers and the development of accurate and efficient numerical techniques for the solution of the equations of gas dynamics have changed the way in which aerodynamics is done. Computational fluid dynamics is now widely accepted as an equal complement to both experimental and analytical approaches. The complexity of the equations that must be solved depends upon the flow phenomena that are in question and the information that is required from the analysis. We have seen in the opening sections of this chapter that in order to be able to

predict the aerodynamic performance of the rotor system with confidence it is necessary to account for a wide range of complex time dependent flow physics.

In principle the unsteady Navier-Stokes equations contain all of the relevant physics to describe these phenomena, however until very recently the computational resources required by such analyses were not widely available. Instead a variety of techniques were developed based upon a hierarchy of computationally tractable reduced physical models. In this respect the development of computational approaches for the calculation of rotor aerodynamics has closely paralleled that for fixed wing aerodynamics. Indeed many of the methods used within the rotorcraft industry have been developed from existing fixed wing analyses[9].

2.2.1 Classical methods

(a) The actuator disc

The basic characteristics of the helicopter rotor can be determined by application of the fundamental laws of fluid to an idealised model of the rotor and its associated flowfield. The simplest model is the actuator disc model in which the hovering rotor is conceived as a disc across which there is a uniform pressure difference and the surrounding flow is divided into two distinct regions, a stream tube above and below the disc that contains all of the fluid disturbed by the rotor and the remaining undisturbed mass of air. Application of Newton's laws to the stream tube allows the determination of a relationship between the static thrust, T, and the velocity induced across the rotor disc, v_i

$$T = 2\rho A v_i^2 \tag{2.11}$$

From Equation (2.11) we can obtain the ideal induced power P_i,

$$P_i = T v_i \tag{2.12}$$

Equation (2.11) shows that a given thrust can be obtained in two ways: by a large acceleration of a small mass (high disc loading) or a small acceleration of a large air

mass (low disc loading). It is clear however from Equation (2.12) that a high disc loading is less efficient. Although the actuator disc model was originally conceived for propellers in axial motion it has since been extended for rotors in forward flight [30].

The application of momentum theory to helicopter rotor aerodynamics is rather limited. While it provides some basic insights, in particular highlighting the importance of disc loading and explaining the basic geometry of the helicopter rotor it does not provide any understanding of the aerodynamics of the individual blades.

(b) Blade element theory

If the helicopter rotor blade is conceived as a rigid beam that is hinged at, or close to, the hub then it is possible to derive equations for the dynamics of the rotor in terms of the blade section aerodynamic data. Iteration between the equations of motion of the blade and the blade section data will then allow the computation of the detailed motion of the blade and the unsteady behaviour of the forces and moments. A typical process for calculating rotor characteristics then takes the following basic form[31],

- For the given input calculate an approximate set of flapping coefficients
- Calculate the blade section velocities and angle of incidence (using Equations (2.1)-(2.5))
- Calculate the blade section Mach number from the section velocities
- Obtain the blade section aerodynamic characteristics corresponding to the section Mach number and incidence
- Using the blade section data calculate new values for the flapping coefficients
- Repeat until the flapping coefficients are converged and then calculate the required performance data

While it is possible to use three-dimensional unsteady data to obtain the section characteristics this does not usually happen. More typically the aerodynamic characteristics of the blade sections are determined from tables of forces and moments

measured on two-dimensional aerofoils over a range of Mach numbers, Reynolds numbers and incidences.

A number of limitations of the methodology, in particular the inability of the method to include unsteady effects, were identified in the review paper of Yaggy[32]. However, in the intervening years the methodology has been extended so that it has now largely overcome such difficulties. The blade element concept is an extremely powerful tool and has proven to be successful in predicting rotor characteristics under normal operating conditions. The blade element approach forms the basis of all of the comprehensive analysis tools which are in current use by the rotorcraft industry. Hansford[5] compares the predictions a number of these codes against flight measurements.

2.2.2 Full Potential Equations

A considerable simplification of the equations that govern the motion of an inviscid fluid can be obtained by assuming that the flow is irrotational. The three components of velocity can then be replaced by the gradients of a single scalar potential field, this allows the four equations describing the conservation of momentum and energy to be replaced by a single algebraic equation (Bernoulli's equation). This equation together with the continuity equation form a closed system of equations from which the velocity potential can be determined, see Caradonna[9]. If disturbances to the flowfield are assumed to be small further simplification of the full potential equations can be obtained. The transonic small disturbance (TSD) equation represents the simplest approximation capable of representing unsteady transonic flow. Caradonna and Isom [33] solved the TSD equations in a rotating frame of reference to obtain the steady flow around helicopter rotors in hover. Subsequently Caradonna et al [34,35] presented solutions for the unsteady flow around rotor blades in forward flight. Following this initial work Tauber [36-38] employed the conservative full potential equations to obtain steady and unsteady aerodynamic characteristics of thick section rotor blades in hover and advancing flight.

A major drawback of the full potential equations as a flow model for rotorcraft is that they contain no mechanisms for the production, convection and dissipation of vorticity. As there is no possibility of 'capturing' the wake directly as part of the solution of the governing equations the only alternative is to specify it, this task preoccupied many of the early investigators. In fixed wing calculations the effect of the wake is typically modelled by a surface along which the potential is discontinuous, the magnitude of the discontinuity being chosen to satisfy the Kutta condition. Early attempts to include the influence of a rotor wake advanced this concept by introducing a sheet of potential discontinuities into the domain. The geometry of the near wake was either specified (prescribed wake model) or allowed to develop (free wake model) as part of the solution, while the far wake was included through an effective angle of attack modification[9] computed using the Biot-Savart law. A principal drawback of such an approach is that coding logic dictates [39] that the vortices defining the edges of the circulation sheet must be constrained to a plane which corresponds to one of the three grid directions. However, as we have already seen in (2.1.3) the rotor wake is a complex three-dimensional surface that is aligned in an arbitrary direction to the grid. A more satisfactory approach is that of velocity decomposition[40], in which the velocity field is expressed as the sum of irrotational and rotational fields.

2.2.3 Euler Equations

The Euler equations accurately model the strength, position and wave drag of shock waves of any strength. While this is of practical importance in many fields of aerospace engineering for helicopter aerodynamics, where shock waves are typically weak, it is a secondary consideration. The main attraction of the Euler equations to the helicopter aerodynamicist lies in their ability to accurately model the dynamics of the vortex wake and its interaction with the main lifting surfaces. The vortex wake is sufficiently thin that it can be considered as an inviscid feature of the flow (although the mechanism by which it is generated is inherently viscous in nature).

The earliest application of the Euler equations to rotorcraft problems appears to be the work of Roberts and Murmann[41] who solved for the steady flow around a two-bladed rotor in hover using a non-inertial co-ordinate system attached to a single blade.

The influence of the remaining blades was modelled using a periodical boundary condition. Subsequently solutions for hovering rotors were obtained by a number of authors[42-6]. Generally good agreement is obtained between computation and experiment, the most significant discrepancies arise in the tip region where shock waves are present.

More recently Euler calculations for the flow around helicopter rotors in forward flight have been presented[43,47,52]. Calculations performed using the Euler and full potential equations are compared with experimental measurements by Wake[47]. In general good agreement is obtained between computations and experimental measurements. Surprisingly, solutions of the Euler equations offer little improvement in accuracy when compared to solutions obtained using the full potential equations.

The need to accurately resolve the vortex wake has preoccupied much recent research. A number of approaches have been developed of which the most promising appear to be the use of adaptive meshing and overset gridding. An adaptive unstructured finite volume scheme for helicopter rotors in forward flight was reported by Strawn and Barth[53]. An alternative approach is the use of overset grid techniques[55]. This technique was succesfully employed by Pahlke and Raddatz[54] and Boniface et al[56-7]. Prelimanary calculations demonstrate the ability of the chimera technique to resolve and conserve vortical flows. However, the most promising feature of the technique is the natural manner in which components in relative motion may be treated.

While the Euler equations provide useful information for flow features which are largely influenced by the main inviscid flow, for example high speed impulsive noise[58], they require almost an order higher computational time to obtain solutions and do not appear to provide significantly improved results when compared to solutions of the full potential equations. However, the Euler equations provide a convenient framework in which to develop methods for the unsteady Navier-Stokes equations. For this reason, the studies discussed above should be recognised as important steps towards this goal.

2.2.4 Navier-Stokes Equations

The Navier-Stokes equations offer several potential benefits over the inviscid models described in the preceding sections. While numerical solutions of the Euler equations may contain vortical wakes such features are a numerical artefact caused by the presence of artificial dissipation. The Navier-Stokes equations contain the necessary physics to describe the generation of vorticity accurately (and therefore reliably). In addition the growth of the boundary layer on helicopter rotor blades will have a significant influence on the location and strength of shock waves in the inviscid outer flow. Finally the ability to predict boundary layer separation is a prerequisite for accurate modelling of the flow on the retreating side of rotor blades. The principle drawback of the Navier-Stokes equations is that the need to resolve gradients across the boundary layer imposes a stringent requirement on the length and time scales that must be represented by the discretised equations. Consequently the use of Navier-Stokes equations has been limited in the past primarily due to the large computational resource that is required.

The earliest Navier-Stokes calculations were presented for the steady flow of helicopter rotors in hover. Wake and Sankar[59] reported results obtained using the Navier-Stokes equations for non-lifting and lifting rotor blades. The computational domain was limited to the near field region of a single blade and the influence of the far wake was modelled through a correction to the geometric angle of attack. Fair agreement was observed between computed and measured pressure distributions. Subsequently Srinivasan[60] attempted to capture the wake structure directly by refining the grid close to the blade tip. The governing equations were solved in an inertial co-ordinate system using a time-accurate solution procedure. In general very good agreement was obtained with experiment. However, for high tip Mach numbers the method performs poorly in the presence of shock waves. This problem was largely overcome in subsequent work[61-3] by replacing the original algorithm with a shock capturing scheme.

All of the methods mentioned above used a single block body conforming grid to discretise the flowfield. Such an arrangement is unsuitable for flows containing features that are not aligned with a particular grid direction because they are unable to resolve such features without inefficient recourse to a large number of additional grid points. In response to these problems Duque and Srinivasan[64-5] modified an existing methodology[63] using the Chimera technique. Results for hover were presented using both structured[64] and unstructured[65] background meshes. Duque concludes that unstructured tetrahedral cells are unsuitable for rotor flowfields. Despite this the method shows great promise and is readily adaptable to flows in which components move relative to one another.

The first Navier-Stokes calculations for a rotor in forward flight were presented by Wake[66-7]. In general, the computed results compare favourably with experimental measurements. However, for lifting rotors the wake is poorly represented and Wake suggests that techniques developed for Euler solvers in which correction terms are applied to the geometric angle of attack should be employed.

In an attempt to reduce the computational cost of Navier-Stokes calculations of rotors in forward flight Berezin[68] proposes the use of a coupled analysis involving solution of the Navier-Stokes equations and the full potential equations. The method is based upon the decomposition of the domain into two regions a near-field domain that wraps around the blade and a farfield domain that extends from the outer boundary of the near field to the farfield. The Navier-Stokes equations are solved on the near field domain in which viscous effects are important, while in the farfield domain the flow is essentially inviscid and can therefore be treated with the full potential equations. The accuracy of this approach is comparable with that obtained when the Navier-Stokes equations are applied over the full computational domain and gives good agreement with experiment. CPU time savings of 42% are reported when compared with the stand alone Navier-Stokes solver.

In addition to the calculation of rotor flows in hover and forward flight Navier-Stokes methods have also been widely used to study the 'fixed wing' aerodynamics of

helicopter rotor blades. Duque[69] studied the aerodynamics of different blade planforms in order to understand the physical mechanisms that have contributed to the success of the unconventional geometry employed in the British Experimental Rotor Program (BERP). Scott and Narramore[70] investigated the formation of tip vortices in the flowfield of the Bell Helicopters 'hyperbolic tip' geometry at various sweep angles.

While the main concentration of this thesis is on aerodynamic prediction for the helicopter main rotor it should be noted that CFD has proven to be a valuable tool in other areas of rotorcraft aerodynamics. Indeed its use as an engineering tool in the design of components such as the fuselage, tail boom and air-intakes is much more advanced than is currently the case for the main rotor.

Rajagopalan and Keys[71] investigated the performance of the RAH-66 TailFan™ using solutions of the incompressible Navier-Stokes equations. In their calculations the influence of the fan on the external flow was represented using time averaged source terms. This technique has since been used to obtain a detailed understanding of the momentum 'fountain' effect produced by the interaction between the two side-by-side rotors of the V22-Osprey tilt-rotor in hover[72]. Chaffin and Berry[73] have employed a similar approach to model the helicopter main rotor in their study of fuselage-rotor interference effects.

Serr and Cantillon[74] used solutions of the Navier-Stokes equations understand the global characteristics of the flow around helicopter air-intakes in dry air and to identify possible flow problems. Based upon the two-dimensional calculations they obtained a reduced design space in which optimisation studies were performed using three-dimensional flow calculations. The benefits in terms of both time and computational cost of such a design philosophy are clear.

2.3 A two dimensional approximation

The complex nature of the flow phenomena and their interactions, the wide range of physical length and time scales, the strong coupling of the aerodynamics and structural dynamics and the need to represent the rigid body motion and elastic deformation of

bodies in relative motion places solution techniques for the computation of rotorcraft flowfields at the very cutting edge of Computational Fluid Dynamics. Unfortunately, the computational resources required to solve such problems are beyond the reach of the design engineer. Lower order methods, which are more amenable to solution on modern digital computer workstations are required that contain sufficient detail to provide a reasonable physical representation of the flow around rotors.

The helicopter rotor can be conceived as a very high aspect ratio wing and this gives rise to a common approximation to the real flow in which the blade is represented by a series of two-dimensional blade elements. For a large extent of the rotor radius, to within one or two chord lengths of the tip, a two-dimensional approximation is relatively accurate. Despite this simplification the model still approaches the complexity of the physical system which it represents. The model can be simplified further by assuming that unsteady effects have a minimal effect on the flow development, the airloads can then be determined using the instantaneous velocity and angle of attack. Such an approach has been widely adopted by industry for use in analysis methods based upon blade element theory. However, for flight conditions close to the edges of the flight envelope the effects of flow unsteadiness are substantial and a quasi-static model can no longer be justified.

Following Sections (2.1.1) and (2.1.2) the rigid body motion of a blade section can be represented by the following equations,

$$M_r(\tau) = \frac{r}{R} M_{tip}\left(1 + \mu_r \sin(2\pi k_r \tau)\right) \tag{2.13}$$

$$\alpha(\tau) = \sum_{n=0} \left(A_n \cos(2\pi n k_r \tau) + B_n \sin(2\pi n k_r \tau)\right) \tag{2.14}$$

which describe respectively the variation of Mach number and angle of attack with non-dimensional time for a blade section located a distance r from the rotor hub. Here

μ_r is the ratio of forward flight speed to the rotational velocity at the spanwise station which may be related to the advance ratio of the rotor using the following expression,

$$\mu_r = \frac{U_f}{\frac{r}{R}U_{tip}} = \frac{R}{r}\mu \tag{2.15}$$

The distribution of reduced frequency, k_r, over the span of the blade depends only upon the blade planform,

$$k_r = \frac{\Omega c_r}{U_r} = \frac{\Omega c_r}{\Omega r} = \frac{c_r}{r} \tag{2.16}$$

which for rectangular blade sections is inversely proportional to the aspect ratio of a blade that has its tip at the spanwise station of interest.

In order to understand the assumptions that are inherent in a two-dimensional approach it is useful to compare the governing equations of two-dimensional flow with a reduced form of the equations that govern the flow around a rotating blade. The following form of the Navier-Stokes equations is obtained for a helicopter rotor in forward flight using a non-inertial co-ordinate system attached to the rotor blade,

$$\frac{\partial}{\partial t}\iiint_V Q dV + \iint_S \vec{n}\cdot F dS - \Omega\iint_S zQ(\vec{e}_x\vec{n})dS + \Omega\iint_S xQ(\vec{e}_z\vec{n})dS = \iiint_V H dV \tag{2.17}$$

where Q is the vector of conserved variables, F is the flux and H is a momentum source term which contains the effects of the Coriolis and centrifugal forces. Equation (2.17) should be compared with the equations for two-dimensional unsteady flow,

$$\frac{\partial}{\partial t}\iiint_V Q dV + \iint_S \vec{n}.F dS = 0 \tag{2.18}$$

For a wing of infinite aspect ratio we may set the spanwise derivatives equal to zero. When this is done, we can obtain the two-dimensional result by neglecting the additional terms on the right hand side of (2.17) which arise from Coriolis, centrifugal

force and crossflow momentum considerations. The effects of this approximation on the boundary layer of a rotating blade have been widely investigated. Following the analysis of McCroskey[76] we can transform the boundary layer equations to a blade fixed rotating co-ordinate system the equations are then,

$$\frac{\partial u}{\partial x}+\frac{\partial v}{\partial y}+\frac{\partial w}{\partial z}=0$$

$$\frac{\partial u}{\partial t}+u\frac{\partial u}{\partial x}+v\frac{\partial u}{\partial y}+w\frac{\partial u}{\partial z}-2\Omega w=\frac{\partial \tau_x}{\partial y}-\Omega^2 x-\frac{1}{\rho}\frac{\partial P}{\partial x} \qquad (2.19)$$

$$\frac{\partial w}{\partial t}+u\frac{\partial w}{\partial x}+v\frac{\partial w}{\partial y}+w\frac{\partial w}{\partial z}+2\Omega u=\frac{\partial \tau_z}{\partial y}-\Omega^2 z-\frac{1}{\rho}\frac{\partial P}{\partial z}$$

and the chordwise pressure gradient is given by,

$$-\frac{1}{\rho}\frac{\partial P}{\partial x}=\frac{\partial U_e}{\partial t}+U_e\frac{\partial U_e}{\partial x}+W_e\frac{\partial U_e'}{\partial z}-2\Omega W_e\cos(\gamma)+\Omega^2 x \qquad (2.20)$$

The chordwise momentum equation can be rearranged so that the dominant terms are collected together on the on the left hand side while terms of secondary importance appear on the right hand side.

$$u\frac{\partial u}{\partial x}+v\frac{\partial u}{\partial y}-U_e\frac{\partial \tau_x}{\partial x}-U_e\frac{\partial U_e}{\partial x}= \qquad (2.21)$$

$$\frac{\partial(U_e-u)}{\partial t}-2\Omega(W_e-w)+\left(W_e-\frac{wu}{U_e}\right)\frac{\partial U_e}{\partial z}-wU_e\frac{\partial u/U_e}{\partial z}$$

The classical result for the thin boundary layer on a two-dimensional body[77] can be rearranged in a similar manner to obtain,

$$u\frac{\partial u}{\partial x}+v\frac{\partial u}{\partial y}-U_e\frac{\partial \tau_x}{\partial x}-U_e\frac{\partial U_e}{\partial x}=\frac{\partial(U_e-u)}{\partial t} \qquad (2.22)$$

To a first approximation the additional terms that appear on the right hand side of Equation (2.21) may be viewed as acting as an additional chordwise pressure gradient. The magnitude and influence of the crossflow momentum on the viscous flow (so

called centrifugal pumping) has been studied extensively. Analysis of laminar flow in hover by Fogarty[78] suggests that radial flow is relatively unimportant, subsequent experimental studies[79] largely support Fogarty's analysis.

Philippe and Chattot[80] have studied the differences between two- and three-dimensional calculations of the flow around a rotor blade in forward flight using the quasi-steady TSD equation. In a non-inertial blade fixed co-ordinate system the quasi-steady TSD equation is of the form,

$$\frac{\partial}{\partial x}\left[B\frac{\partial \phi}{\partial x}+B\left(\frac{\partial \phi}{\partial x}\right)^2\right]+C\frac{\partial^2 \phi}{\partial x \partial y}+D\frac{\partial^2 \phi}{\partial y^2}+E\frac{\partial^2 \phi}{\partial z^2}=0 \qquad (2.23)$$

In (2.23) B, D and E are symmetric functions of azimuth angle while the coefficient of the cross derivative term is anti-symmetric. Results presented by Philippe and Chattot indicate significant crossflow momentum effects. The shock wave at $\psi = 60°$ is significantly stronger than that at $\psi = 120°$, see Figure (9) of Reference (80). However, this result contradicts three-dimensional experimental measurements which show the opposite behaviour. As expected the crossflow momentum term becomes increasingly important as the blade tip is approached, Figure (10) of Reference (80). The value of the coefficient C can be obtained from the following equation,

$$C = 2M^2 \frac{\frac{c}{R}}{\left(\frac{t}{c}\right)^{\frac{2}{3}}}\mu\cos(\psi)\{r+\mu\sin(\psi)\} \qquad (2.24)$$

in which t is the relative thickness of the blade profile. This coefficient is proportional to the product of the blade normal and spanwise components of velocity the freestream velocity in the plane of the rotor disc. The blade normal component of velocity (the term in braces) is symmetric about $\psi = 90°$ while the spanwise component of velocity is anti-symmetric. The behaviour of the crossflow momentum term is therefore dominated by the influence of the spanwise component of the freestream velocity and consequently for azimuth angles close to $\psi = 90°$ and $\psi = 270°$ the effect of this term will be relatively small.

Brotherhood and James[81] performed in-flight measurements of the pressure distribution on the XH51N helicopter rotor blade in both hover and forward flight. Correlation of the data that was obtained with static wind tunnel measurements of wings having the same cross section was considered to be very good.

Based upon the studies outlined above it seems that two-dimensional aerofoil characteristics can be applied with confidence to within one or two chord lengths of the blade tip to determine the aerodynamics of helicopter rotors for blade sections. Indeed it is of note that the success of the British Experimental Rotor Program in developing a blade which allowed Westland Helicopters to establish a new world speed record for pure helicopters in 1986 has largely been attributed to the detailed understanding of the aerodynamics of aerofoils at high Mach number and high lift in both steady and unsteady flow[3] .

2.4 Concluding remarks

In this Chapter, the complex nature of the flow around helicopter rotors in forward flight was introduced. It was shown that the flow is dominated by the effects of changes in both the Mach number and angle of incidence experienced by the individual blade sections. A hierarchy of prediction techniques was described which ranged from simple momentum considerations to the numerical solution of the Navier-Stokes equations. Lower order methods provide insight into the aerodynamics of the rotor blade, but ignore important physical effects. Higher order methods provide greater physical realism at the expense of increased computing time. Furthermore, prediction methodologies based upon the three-dimensional Navier-Stokes equations lack sufficient maturity for general use in the helicopter design process. An alternative technique based upon the solution of a two-dimensional flow problem was suggested. This approximation was shown to ignore the importance of cross-flow, Coriolis and centrifugal effects. However, previous studies show that the performance of large aspect ratio rotor blades can be represented to a good approximation by the aerodynamics of aerofoil sections.

Governing Equations

In the previous chapter, the basis for a two-dimensional unsteady model for rotor blade aerodynamics in forward flight was described. In this chapter, the concept is advanced further and a detailed mathematical description of the model is developed. The unsteady Navier-Stokes equations are introduced and methods for reformulating the equations to obtain a more convenient description of the flow around moving bodies are considered. The need for turbulence modelling is addressed, and the models used in the present study are described.

3.1 The Navier-Stokes Equations

The physical principles that govern the continuum flow of a fluid or gas can be expressed as,

(a) mass must be conserved

(b) momentum must be conserved (Newton's second law)

(c) energy must be conserved (first law of thermodynamics)

From these three basic statements (and by making a number of simplifying assumptions) it is possible to obtain a hierarchy of mathematical models that describe the physical system fully. The most complete mathematical description, the Navier-Stokes equations, has been known for more than 100 years[82]. The two-dimensional unsteady Navier-Stokes equations may be expressed in the following compact form,

$$\frac{\partial}{\partial t}\iiint_{v} \mathbf{Q}\,dV + \iint_{s} \left(\mathbf{F}^{i} - \mathbf{F}^{v}\right) dS = 0 \tag{3.1}$$

here the vector of conserved variables **Q** is given by,

$$\begin{bmatrix} \rho & \rho u & \rho v & \rho E \end{bmatrix}^{T} \tag{3.2}$$

here ρ is the density of the fluid, u and v are the components of velocity in a Cartesian co-ordinate system and E is the energy of the fluid particle element,

$$E = e + \tfrac{1}{2}\rho\left(u^{2} + v^{2}\right) \tag{3.2a}$$

F represents the flux vector, and is made up from contributions that may be conveniently grouped together as convection and diffusion terms, denoted by the superscripts i and v respectively. The fluxes due to the convection terms may be written in the following form,

$$\mathbf{F}_{x}^{i} = \begin{bmatrix} \rho u \\ \rho u^{2} + P \\ \rho uv \\ u(\rho E + P) \end{bmatrix}, \quad \mathbf{F}_{y}^{i} = \begin{bmatrix} \rho v \\ \rho uv \\ \rho v^{2} + P \\ v(\rho E + P) \end{bmatrix} \tag{3.3}$$

here the subscripts x and y refer to the components of the flux vector in the Cartesian co-ordinate directions and P is the static pressure. The corresponding components of the viscous flux vector are,

$$\mathbf{F}_{x}^{v} = \begin{bmatrix} 0 \\ \tau_{xx} \\ \tau_{xy} \\ u\tau_{xx} + v\tau_{xy} - q_{x} \end{bmatrix}, \quad \mathbf{F}_{y}^{v} = \begin{bmatrix} 0 \\ \tau_{xy} \\ \tau_{yy} \\ u\tau_{xy} + v\tau_{yy} - q_{y} \end{bmatrix} \tag{3.4}$$

here τ is the shear stress tensor and q is the heat flux vector. For a Newtonian fluid the constitutive relationship between stress and strain rate is,

$$\tau_{ij} = 2\mu S_{ij} + \lambda \frac{\partial u_k}{\partial x_k} \delta_{ij} \tag{3.5}$$

where S_{ij} is the strain-rate,

$$S_{ij} = \frac{1}{2}\left(\frac{\partial u_i}{\partial x_j} + \frac{\partial u_j}{\partial x_i} \right) \tag{3.6}$$

μ is the molecular viscosity determined from Sutherland's law, λ is a second coefficient of viscosity[83] and δ_{ij} is the Kronecker delta. Stokes proposes a further simplification of (3.5) using,

$$\lambda = -\frac{2}{3}\mu \tag{3.7}$$

In order to obtain a closed mathematical system a number of auxiliary relations describing the interdependence of the thermodynamic variables are introduced. For a perfect gas the pressure, density and temperature are then related to one another using Boyle's thermal equation of state,

$$P = \rho R T \tag{3.8}$$

in which R is the universal gas constant and T is the temperature. Density and pressure are related to one another through the internal energy e,

$$e = \frac{1}{(\gamma - 1)} \frac{P}{\rho} \tag{3.9}$$

in this equation γ is the ratio of specific heats.

3.2 The Navier-Stokes equations for moving bodies

In the previous section, the unsteady Navier-Stokes equations were described for a stationary (inertial) frame of reference. In such a system, the motion of a particle relative to the stationary co-ordinate axes can be described by Newton's laws of

motion. For the vast majority of flow problems an inertial treatment of the governing equations is adequate, however for problems which involve a well defined time dependent motion it is advantageous to consider an alternate non-inertial co-ordinate system.

The governing equations can be transformed directly from an inertial frame to the non-inertial co-ordinate system using the ideas of vector calculus. However, many flow problems involve physical domains that change over time, in such situations the rigid grid system inherent in such transformations is no longer ideal. Instead a system must be devised in which the governing equations can be obtained for a grid that is allowed to deform with the moving boundary. A more general technique, the moving grid approach, has been developed for deforming geometries. In this approach the grid consists of a number of points that are fixed in the computational domain. These points are fixed in time, i.e. they do not move with respect to the computational space. The governing equations are solved in the computational space with appropriate transformations to account for the movement of the grid points in the physical domain.

Consider the time rate of change of the quantity Q in the domain $[V_1(t), V_2(t)]$,

$$\text{rate of change of Q in the domain } [V_1(t), V_2(t)] = \frac{d}{dt}\int_{V_1(t)}^{V_2(t)} Q\,dV \tag{3.10}$$

integrating in space from $V_1(t)$ to $V_2(t)$ the time rate of change of Q in the domain is obtained as,

$$\frac{d}{dt}\int_{V_1(t)}^{V_2(t)} Q\,dV = \frac{d}{dt}\left[\phi(V_2(t),t) - \phi(V_1(t),t)\right] \tag{3.11}$$

where $\phi = \int Q\,dV$. Expanding the total derivative in terms of the partial derivatives with respect to both space and time the following equation is obtained,

$$\frac{d}{dt}[\phi(V_2(t),t)-\phi(V_1(t),t)]=\frac{\partial\phi(V_2(t),t)}{\partial V_2(t)}\frac{dV_2(t)}{dt}-\frac{\partial\phi(V_1(t),t)}{\partial V_1(t)}\frac{dV_1(t)}{dt}+\frac{\partial\phi(V_2(t),t)}{\partial t}-\frac{\partial\phi(V_1(t),t)}{\partial t} \quad (3.12)$$

Rewriting Equation (3.12) in the integral form of (3.10) an equation relating the conserved variable to the time rate of change in the volume and the numerical flux due to the deformation of the cell boundary is obtained thus,

$$\int_{V_1(t)}^{V_2(t)}\frac{\partial Q}{\partial t}dV=\frac{d}{dt}\int_{V_1(t)}^{V_2(t)}QdV-\int_{V_1(t)}^{V_2(t)}\frac{dV}{dt}\frac{\partial Q}{\partial V}dV \quad (3.13)$$

Making the appropriate substitutions in Equation (3.1) the moving grid formulation of the Navier-Stokes equations is obtained.

$$\frac{d}{dt}\iiint_V QdV+\iint_S\hat{F}.\vec{n}dS=0 \quad (3.14)$$

Here,

$$\hat{F}_x=\begin{bmatrix}\rho\bar{U}\\ \rho u\bar{U}+P\\ \rho v\bar{U}\\ \bar{U}(\rho E+P)+u_T P\end{bmatrix} \text{ and } \hat{F}_y=\begin{bmatrix}\rho\bar{V}\\ \rho u\bar{V}\\ \rho v\bar{V}+P\\ \bar{V}(\rho E+P)+v_T P\end{bmatrix} \quad (3.15)$$

and the contravariant velocities are,

$$\bar{U}=u-u_T \text{ and } \bar{V}=v-v_T$$

The term's u_T and v_T represent the velocities, $\frac{dx}{dt}$ and $\frac{dy}{dt}$, with which the integration boundaries move, often referred to as the grid velocities.

The co-ordinate system that is used to perform the integration in (3.14) can be used regardless of whether it is fixed or variable. However, since the components of velocity

in the x and y directions appear within the integral the co-ordinate system to which they are referenced must be fixed. The two co-ordinate systems may be the same, although this is not necessary. In practice it is most convenient to fix the co-ordinate system of the integration to the moving body, whilst the co-ordinate system to which the velocity is referenced is fixed in the physical space, thus removing the need for an additional source term. The moving grid approach can be combined with the non-inertial co-ordinate system described in the previous section, see for example Pahlke[84].

3.3 Turbulence modelling

The majority of flows of practical interest are turbulent, it is therefore of great importance to be able to understand and predict the effects of turbulence. In principle it is possible to integrate the Navier-Stokes equations numerically to obtain a direct simulation of the turbulent (DNS). In concept it is perhaps the simplest approach in that it resolves all of the motion contained within the flow without introducing any further simplification. However, in practice the realisation of the full motion requires that a wide range of length and time scales must be considered. The need to resolve all of the relevant time and length scales to provide a valid simulation results in a significant computational burden which makes the computation of high Reynolds number flows impractical.

It has been suggested that the motion of larger scale turbulent structures is more important than that of the smaller scale turbulent structures, which are typically much less energetic, in the transport process. These notions have given rise to the concept of large eddy simulation (LES) in which only the large scale structure of the flow is simulated directly using the Navier-Stokes equations while smaller 'sub-grid' scale structures are modelled. While this approach still requires large computational resources it presents a more realistic approach than DNS for the simulation of high Reynolds number flows around aircraft components.

While there is little doubt that DNS and LES will play an increasingly important role in the understanding of complex flow phenomena an alternative, computationally more tractable, approach is required for engineering applications. Experimental studies of

turbulent flows have shown that turbulence, while random in nature, does exhibit a macroscopic structure which can be characterised by random fluctuations of the density, pressure and velocity fields about mean values. Based upon this characterisation Reynolds[82], and later Favre[85], proposed that rather than treating this process in a deterministic manner it would be acceptable for most purposes to treat the random fluctuations using statistical techniques. Reynolds suggested that the Navier-Stokes equations should be time-averaged to obtain equations for the mean flow variables. The time averaged value of a flow variable F(x) is obtained from the instantaneous value f(x,t) using the following integral,

$$F(x) = \lim_{T \to \infty} \frac{1}{T} \int_{t}^{t+T} f(x,t)dt \qquad (3.16)$$

it is clear that this process is appropriate only for stationary turbulence, that is turbulent flows that on average do not change over time. Other forms of averaging appropriate for homogeneous turbulence (spatial), unsteady flow (ensemble) and periodic flow (phase) have been described in the literature[86].

Ensemble averaging is clearly required for flows in which the time scales of the mean flow unsteadiness are comparable with those of the large-scale turbulent structures. However, for flows in which there is a clear distinction between the time scales of the mean flow and the turbulence a modified form of Reynolds time averaging may be possible. This is of particular importance because a significant amount of effort has been expended developing turbulence models for stationary turbulence. Provided that sufficient separation can be shown between the time scales of the mean flow and turbulence for the problems that are of interest in this study existing turbulence models can be employed without further modification.

For non-stationary turbulence the instantaneous value of the flow variable f(x,t), may be written in the form,

$$f(x,t) = F(x) + F'(x,t_1) + f'(x,t_2) \qquad (3.17)$$

in which F(x) is the mean component of the flow variable, $F'(x,t_1)$ is the unsteady component of the mean flow and $f'(x,t_2)$ is the turbulent fluctuation. Clearly if we take the limit $T \rightarrow \infty$, then the effects of both the unsteady component of the mean flow and the turbulent fluctuations will be lost. Instead Equation (3.16) is modified thus,

$$F(x,t) = F(x) + \lim_{T\to 0} \frac{1}{T} \int_{t}^{t+T} F'(x,t_1)dt = \lim_{T\to \infty} \frac{1}{T} \int_{t}^{t+T} f(x,t_2)dt \qquad (3.16a)$$

in which t_1 is the time scale of the turbulent fluctuations and t_2 is the time scale of the flow unsteadiness that we do not wish to regard as belonging to the turbulence. The time averaging process is performed using a time scale, T, which is long compared to that of the turbulence but short compared to that of the mean flow, that is,

$$t_2 << T << t_1 \qquad (3.18)$$

As T approaches ∞ the second term on the right hand side of (3.16a) will be equal to the time average of the turbulent fluctuations which vanishes for sufficiently large T. Finally, if we take the limit T approaches 0 for the first term then (3.16a) becomes simply,

$$F(x,t) = F(x) + F'(x,t) \qquad (3.19)$$

Such an unusual averaging process can be fully justified, see for example Wilcox[86].

In order to justify this averaging process for problems related to the current study the dominant time scale of the helicopter rotor (i.e. the first harmonic) must be compared with typical time scales of the large scale turbulent eddies. In Chapter (2) it was shown that the reduced frequency based upon the blade tip speed was a function of the blade planform only. For individual blade elements the following equation was obtained,

$$k_r = \frac{c_r}{r} \qquad (3.20)$$

Taking a typical blade with c/D=1/30 and a root cut out at r/R=0.2 the range of reduced frequencies which is of principal interest varies from 0.167 at the root cut out to 0.033 at the blade tip.

Chapman[87] measured the mean reduced frequency of the largest turbulent eddies formed in a fully developed flat plate boundary layer. The mean reduced frequency of the turbulent eddies increases with Reynolds number, but for the Reynolds number range considered the reduced frequencies are of the order k = 10. There is therefore significant separation (about two orders of magnitude) between the time scales of the mean flow and those of the turbulence and consequently the Reynolds averaged Navier-Stokes equations together with a stationary model of turbulence may be employed with confidence.

For compressible flow it is necessary to account for the influence of density and temperature fluctuations in addition to that of the pressure and velocity fluctuations. Direct application of Reynolds averaging is undesirable because it increases the complexity of the correlated terms. In order to overcome this problem Favre introduced the concept of mass averaging in which density and velocity fluctuations are represented by the fluctuation of a single dependent variable, momentum. The Favre averaged Navier-Stokes equations are,

$$\frac{\partial}{\partial t}\iiint_V \mathbf{Q}_r dV + \iint_S \left(\mathbf{F}^i - \mathbf{F}^v - \mathbf{F}'\right) dS = \rho \mathbf{H} \tag{3.21}$$

the vector of conserved variables, $\mathbf{Q}$, the convective flux, $\mathbf{F}^i$, and the diffusive flux, $\mathbf{F}^v$, are of the same general form given in Equations (3.3) and (3.4) the additional terms, $\mathbf{F}'$, due to the averaging process are,

$$\mathbf{F}'_x = \begin{bmatrix} 0 \\ \bar{\tau}_{xx} \\ \bar{\tau}_{xy} \\ -\bar{q}_x - \overline{\rho u'_x \tfrac{1}{2} u'^2} + \\ \tau_{xx} u'_x + \tau_{xy} u'_y \end{bmatrix}, \mathbf{F}'_y = \begin{bmatrix} 0 \\ \bar{\tau}_{xy} \\ \bar{\tau}_{yy} \\ -\bar{q}_y - \overline{\rho u'_y \tfrac{1}{2} u'^2} + \\ \tau_{xy} u'_x + \tau_{yy} u'_y \end{bmatrix} \tag{3.22}$$

The presence of these terms, the Reynold's stresses and the turbulent scalar heat flux, gives rise to the problem of turbulence closure as the system of equations is under prescribed. It is impossible to close the system of equations directly, indeed taking moments of the Favre averaged Navier-Stokes equations to obtain differential equations for the correlated terms introduces additional correlation's. The correlated terms must therefore be modelled giving rise to the concept of turbulence modelling. Today efforts to model turbulence preoccupies the CFD community and continues to represent the greatest hurdle to the acceptance of CFD by the aerodynamics community.

By analogy with the molecular transport of momentum Boussinesq[88] suggests that the turbulent stresses should be modelled as the product of an eddy viscosity,μ_T, and the velocity gradient. The total molecular and Reynolds stresses are then,

$$\begin{aligned} \tau_{ij} &= \tau^l_{ij} + \tau^T_{ij} \\ \tau^l_{ij} &= 2\mu \left(S_{ij} + \tfrac{1}{3} S_{nn} \delta_{ij} \right) \\ \tau^T_{ij} &= 2\mu_T \left(S_{ij} + \tfrac{1}{3} S_{nn} \delta_{ij} \right) - \tfrac{2}{3} \rho k \delta_{ij} \end{aligned} \tag{3.23}$$

The arguments leading to Equation (3.23) are based upon a number of simplifying assumptions. The most important is that the principal axes of the shear stress tensor are co-incident with those of the mean strain-rate tensor for all points in the flow, that is the constitutive relationship between stress and strain is linear. Close to a solid boundary the Knudsen number is about Kn=0.4 which casts some doubt on the use of such relationships in the near wall region. Furthermore, the analogy between turbulent motion and random motion is not complete as can be seen from the coefficients of molecular and turbulent viscosity in Equation (3.23). The coefficient of molecular viscosity, μ, is a property of the fluid while the corresponding coefficient, μ_T, in the

expression for the Reynolds stresses depends upon both the fluid properties and the flow itself.

One approach to achieving a more appropriate description of the stress tensor is to introduce a non-linear constitutive relationship[89] which assume that the Boussinesq approximation is the leading term of a Taylor series expansion. Non-linear constitutive relationships for unsteady turbulent flows remain an area of active research, while turbulence models based upon this approach provide improved predictions of turbulent flow they retain many of the deficiencies of more conventional linear models. For this reason they are not considered in the present study.

Accepting the Boussinesq approximation the problem of modelling the Reynolds stresses is reduced to finding a suitable model for the eddy viscosity, μ_T. The earliest turbulence models relied heavily on dimensional arguments, Prandtl[90] developed a simple algebraic expression for the eddy viscosity in which the turbulent viscosity is related to a mixing length thus,

$$\mu_T = \rho l_{mix}^2 \left| \frac{du}{dy} \right| \tag{3.24}$$

The principal drawback of such an approach is that it cannot be applied universally, but instead requires a detailed prior knowledge of the flow that we wish to compute. For model problems the mixing length hypothesis performs very well, however this is unsurprising as the model is normally calibrated to provide good agreement for such flows. Despite its deficiencies the underlying approach has proven fruitful and a wide variety of models based upon this formulation have been proposed.

Most current algebraic turbulence models are based upon the observation that there are three distinct regions within the developing boundary layer, the viscous sub-layer, the log layer and the defect layer. In the Baldwin-Lomax model[91] the viscous sub-layer and log layer are usually considered together and the eddy viscosity is given by,

$$\mu_T = \begin{cases} \mu_T^i, & y \le y_m \\ \mu_T^o, & y > y_m \end{cases} \tag{3.25}$$

where y_m is the point at which the eddy viscosities of the inner and outer layers are identical. In the inner layer,

$$\mu_T = \rho l_{mix}^2 \left(\left(\frac{\partial u}{\partial y} \right)^2 + \left(\frac{\partial v}{\partial x} \right)^2 \right)^{1/2} \qquad (3.26)$$

$$l_{mix} = \kappa y \left(1 - e^{-y^+/A^+} \right)$$

where κ=0.41, A^+=26. While in the outer layer the eddy viscosity is given by the following expression,

$$\mu_T^o = \alpha \rho u_{y=\delta} \delta_v^* F_{Kleb}$$

$$\delta_v^* = \int_0^\delta \left(1 - u/u_{y=\delta} \right) dy \qquad (3.27)$$

$$F_{wake} = \min \left[y_{max} F_{max}, \frac{C_{wake} y_{max} \left(u - u_{y=0} \right)^2}{F_{max}} \right] \qquad (3.28)$$

$$F_{max} = \frac{1}{\kappa} \max \left(l_{mix} \varpi \right)$$

where the closure coefficients have the values α=0.0168, C_{CP}=1.6, C_{Kleb}=0.3 and C_{wake}=1.0. The Baldwin-Lomax model has been widely used to model attached boundary layers with weak pressure gradients. For stronger pressure gradients and separated flows the model performs relatively poorly. Due to the nature of the model the expression for μ_T is non-differentiable. This poses some difficulty when implementing an implicit scheme such as that described in Chapter (5), for this reason the Jacobian terms related to the Baldwin-Lomax turbulence model are set equal to zero in the remainder of this study.

Algebraic models such as those discussed in the preceding paragraphs are described as incomplete[86] because they do not calculate the turbulent length scale directly but instead relate it to some characteristic length scale of the mean flow. In order to obtain

the length scale of the turbulence we must develop additional differential equations that describe the transport of quantities from which it may be determined. Returning to Prandtl's mixing length hypothesis we see that on dimensional grounds the turbulent viscosity is related to the product of a turbulent length scale and a turbulent velocity scale. For the turbulent velocity it is natural to introduce a transport equation for the turbulent kinetic energy, k. The choice of an equation for the turbulence length scale is more troublesome. On dimensional grounds the eddy viscosity is given by,

$$\mu_T \sim \frac{\rho k}{\omega} \quad \text{or} \quad \mu_T = \frac{\rho k^2}{\varepsilon} \tag{3.29}$$

where ε and ω are the dissipation and rate of dissipation of turbulent kinetic energy respectively.

A number of two equation models have been proposed, notable examples are Coakley's[92] q-ω model, the Jones-Launder[93] k-ε model and its development, the k-τ model of Rizzi[94] and the k-g model of Kalitzin[95]. However, for the external compressible flow around aircraft, formulations based upon k and ω appear to provide the best results. The first two equation k-ω model was introduced by Kolmogorov[96]. Saffmann[97] and later Spalding[98] both offered improved models, which have subsequently been further developed by Wilcox[86]. The standard Wilcox k-ω model is given by,

$$\begin{aligned}
\frac{\partial \rho k}{\partial t} + \frac{\partial \rho u_j k}{\partial x_j} &= \tau_{ij}\frac{\partial u_i}{\partial x_j} - \beta^* \rho k \omega + \frac{\partial}{\partial x_j}\left((\mu + \sigma^* \mu_T)\frac{\partial k}{\partial x_j}\right) \\
\frac{\partial \rho \omega}{\partial t} + \frac{\partial \rho u_j \omega}{\partial x_j} &= \alpha\frac{\omega}{k}\tau_{ij}\frac{\partial u_i}{\partial x_j} - \beta \rho \omega^2 + \frac{\partial}{\partial x_j}\left((\mu + \sigma \mu_T)\frac{\partial \omega}{\partial x_j}\right) \qquad (3.30) \\
\mu_T &= \frac{\rho k}{\omega}
\end{aligned}$$

where the closure coefficients are,

$$\alpha = 5/9, \quad \beta = 3/40, \quad \beta^* = 3/100, \quad \sigma = 1/2, \quad \sigma^* = 1/2$$

This model has been widely adopted by the CFD community and has several desirable features. It is wall distance free, does not require damping functions in the viscous sub-layer and performs satisfactorily in the presence of strong adverse pressure gradients. However, a number of problems have been identified by Menter[99]. Mathematical analysis reveals that the basic model is sensitive to the value specified for the freestream specific dissipation (ω_∞). This has been investigated in detail by Menter who shows that while such behaviour is undesirable it is not significant for wall bounded flows. Menter[100] proposes a modified model, which incorporates aspects of the k-ω and k-ε models. Furthermore, Menter also includes terms that model the transport of the turbulent shear stress. While Menter's model improves the solution for steady and unsteady flows in non-trivial ways the use of complex wall distance dependent blending functions introduces considerable difficulties for implicit schemes as the source term is not continuously differentiable. For this reason the standard k-ω model has been selected for the present study. However, it should be noted that the general methodology outlined in subsequent chapters is applicable to all two-equation turbulence models that are of similar mathematical form to the k-ω model.

3.4 Concluding remarks

In this chapter the equations which govern the physical processes that are of direct importance to the current study were described. The equations were reformulated to obtain a convenient description for the flow around moving bodies. In an accelerating system, time independent transformations to a non-inertial co-ordinate system cannot generally be found and therefore the use of such a co-ordinate system offers no practical advantage. The moving grid approach provides greater flexibility when dealing with complex motion without the need for additional source terms. While the current study does not require such flexibility, it is believed that the latter approach offers scope for future improvements. It was shown that for the cases of interest in the present study the governing equations could be time averaged in such a way that a stationary model of turbulence could be applied without modification. The turbulence models used in the present study, the Baldwin-Lomax and standard Wilcox k-ω models, were then introduced.

4

Spatial Discretisation

In the previous chapter, a mathematical model for the unsteady flow around rotor blade sections was described. The discretisation process can be conveniently divided into two parts, spatial discretisation and temporal discretisation. The latter is considered in the next chapter, while the former is described below. The spatial discretisation of the governing equations is based upon a strongly coupled finite volume procedure in which the convective contributions to the governing equations are discretised using a novel extension to an existing approximate Riemann solver.

The Navier-Stokes equations are a system of non-linear partial differential equations for which there is no known general analytical solution. Closed form solutions can be obtained for a few idealised cases, but only after considerable physical simplification (for example the assumption of incompressible and irrotational flow). For the class of problems that are of principal interest to the aerospace community, turbulent compressible flow, such assumptions and simplifications are of limited value. While much work was done at the beginning of the 20th century to develop a theoretical basis for the numerical solution of ordinary and partial differential equations, it was not until the advent of high performance computing in the late 1960's that the necessary tools to pursue problems of engineering complexity became available.

4.1 Numerical Solution of the Navier-Stokes Equations

The earliest application of numerical techniques to the equations that govern fluid motion is generally attributed to Richardson[101] who presented a numerical technique for use in the solution of elliptic partial differential equations. Following Richardson's

work Courant, Friedrichs and Levy[102] developed theory for the discretisation of hyperbolic systems of partial differential equations (such as the Euler equations) upon which modern computational techniques for compressible flow have subsequently been built. The discretisation of the governing equations may be classified as finite difference, finite element or finite volume depending upon the form of the governing equations and the manner in which the solution is represented upon the computational mesh. In the present study a finite volume approach is adopted.

Finite volume formulations for solution of the equations of fluid dynamics were introduced independently by McDonald[103] and MacCormack and Paullay[104]. In this approach, the domain is divided into a number of smaller sub-domains. The integral form of the governing equations is then applied to each of the sub-domains in turn. Thus the system of conservation laws,

$$\int_v \frac{\partial \mathbf{Q}}{\partial t} dV + \int_s \mathbf{F} \cdot \vec{\mathbf{n}} ds = 0 \tag{4.1}$$

is replaced by,

$$\frac{\partial \mathbf{Q}_i \mathbf{V}_i}{\partial t} + \sum_{\text{sides}} \mathbf{E}(\mathbf{Q}_i) \vec{\mathbf{n}} \cdot \mathbf{S} = 0 \tag{4.2}$$

for each of the i sub-domains. This discretisation ensures the conservation of mass, momentum and energy. This property is desirable and ensures that if the solution of the discretised equations converges boundedly to a function Q(x,t) then that function is a weak solution of the governing PDE[105]. Furthermore, as the method is based upon an integral formulation of the governing equations discontinuous solutions for the conserved variables are possible and consequently shock waves can be calculated without special treatment.

Early applications of the finite volume method used central approaches in which the flux was taken as a simple average of the fluxes in adjacent cells. More recently, efforts

have focused on the development of discretisation schemes that attempt to incorporate the general character of the physical phenomena that are to be modelled. For high-speed flows, this may be most readily achieved by upwinding. Two main approaches to the problem of identifying the upwind directions can be identified in the literature; flux vector splitting and flux difference splitting.

(a) Flux vector splitting

For a non-linear hyperbolic system the simplest approach to identifying the upwind directions is to decompose the Jacobian matrix in the following manner,

$$\mathbf{A} = \mathbf{A}^{+} + \mathbf{A}^{-} \tag{4.3}$$

so that the matrix $\mathbf{A}^{+}$ has only positive Eigenvalues while conversely the matrix $\mathbf{A}^{-}$ has only negative Eigenvalues. If the system of equations is homogenous then such decomposition results in a natural splitting of the flux vector f(Q),

$$\mathbf{f}(\mathbf{Q}) = \mathbf{f}^{+}(\mathbf{Q}_L) + \mathbf{f}^{-}(\mathbf{Q}_R) \tag{4.4}$$

where the superscript refers to the direction of the Eigenvalue, Q is the vector of the conserved variables and the subscripts L and R refer to the conditions immediately downstream and upstream of the point at which the flux is calculated. The splitting (4.4) is not unique and a number of different methods have been suggested[106-9].

One of the major drawbacks with the flux vector splitting approach is a relatively poor resolution of discontinuities. This deficiency was highlighted by Qin[110] who considered the axi-symmetric laminar flow around a cone set at zero degrees of incidence to an oncoming flow of M=7.95. Grid converged solutions obtained using Van Leers flux vector splitting scheme[107-8] and Osher's flux difference splitting[115] scheme show that boundary layer resolution is sensitive to the discretisation scheme employed. Moreover, it was shown that calculations obtained using the FDS method with as few as 17 grid points in the wall normal direction produced results of comparable accuracy to those obtained with the FVS scheme using 33 grid points in the wall normal direction.

(b) Flux Difference Splitting

The second group of upwind schemes have their basis in the numerical scheme devised by Godunov[111]. Godunov's method contains two stages. In the first stage, the initial data are modified to obtain a piecewise constant distribution. The modified data set consists of a series of constant states which generate local Riemann problems at the intercell boundaries. The second stage of the method is then to evaluate the intercell fluxes using an exact solution of the local Riemann problems, once the intercell fluxes are known the solution can be advanced in time to the next time step.

Godunov's method requires the solution of the exact Riemann problem for all of the cell boundaries at each time step, thus it is unsuitable for problems of engineering complexity due to the computational effort required. Further, information regarding the structure of the exact solution to the local Riemann problem is not employed directly but is instead averaged over the cell volume reducing the overall accuracy of the scheme. These observations have led to the development of so called 'Approximate Riemann solvers' in which the local Riemann problems are solved approximately using computationally efficient algorithms. Harten, Lax and Van Leer[112] present general theory regarding the application of approximate Riemann solvers to problems in fluid mechanics. A wide variety of methods have been described in the literature, see for example Chapters 9-12 of Toro[113]. In the present study a modified form of Osher's FDS is employed.

4.2 A Strongly Coupled Approach

Before discussing the approximate Riemann solver employed in the current work it is helpful to consider how the mean flow and turbulence equations should be coupled. Two approaches can be adopted, termed the loosely and strongly coupled approaches. In conventional numerical schemes the mean flow equations and turbulence equations are generally solved in a loosely coupled manner. In a typical iteration of such a scheme the mean flow equations are first solved with a fixed eddy viscosity. Once this step has been completed the turbulence equations are then solved with fixed values of the mean flow variables. An alternate approach that appears less often in the open

literature is to solve the mean flow and turbulence equations simultaneously, this is the so-called closely coupled approach.

The loosely coupled approach has a number of desirable properties. Chief amongst these is the convenient manner in which additional turbulence models may be implemented. Only minor changes to the computer code, very often only the addition of an extra subroutine, are required. The strongly coupled method does not share this property for all turbulence models, but by careful construction closely coupled numerical methods can be generalised for a particular class of turbulence models having the same mathematical form. The explicit solver CRANS2e[116] developed at Cranfield University employs a closely coupled approach to solve the Navier-Stokes equations together with a choice of six two-equation turbulence models. In most cases the only modifications required to the computer program were the addition of subroutines associated with the new source terms.

Further it is suggested that by decoupling the governing equations it is possible to choose numerical algorithms that are best suited to the individual systems of equations. This property has been extensively used in the design of numerical methods for two-equation turbulence models where semi-implicit discretisations of the source term are generally employed to enhance the convergence properties of the scheme. Unfortunately in many cases the differing numerical methods may have different stability criteria. This poses considerable problems in the framework of unsteady flow calculations in ensuring that the time step meets the conflicting stability criteria.

For fully converged steady flow calculations the coupled and uncoupled methods are equivalent. This is not true for unsteady flows where the turbulence quantities calculated using the uncoupled approach lag behind those of the mean flow. For unsteady flow a loosely coupled approach will therefore require sub-iteration during each physical time step to remedy the situation. Alternatively, the time step can be restricted to ensure that the additional error introduced by the time lag is small.

Closely coupled numerical schemes have been presented by Gorski[117-119], Takakura[120] and Lin and Chieng[121] who solved the Navier-Stokes equations and a k-ε turbulence model using upwind TVD schemes for a range of physical problems in external high speed aerodynamics. Subsequently Liu and Ji[122] developed a strongly coupled multi-grid method for use with the k-ω model of turbulence. More recently methods have been proposed based upon Roe's flux difference splitting[114]. Siikonen[123] implements Roe's scheme with a strongly coupled k-ε turbulence model for two- and three-dimensional transonic flows while Yegorov et al[124] developed a closely coupled algorithm for the q-ω turbulence model based upon Roe's FDS.

In the current work a closely coupled implicit algorithm has been developed for the Navier-Stokes equations and a k-ω model of turbulence based upon Osher's flux difference splitting. The basic algorithm together with its linearisation are discussed in the remaining sections of this chapter.

4.3 Mathematical Properties of the Convective Terms

Retaining only the convective terms of Equation (3.1) we can obtain the following one dimensional system of equations,

$$\frac{\partial \mathbf{Q}}{\partial t}+\frac{\partial \mathbf{E}(\mathbf{Q})}{\partial x}=0 \tag{4.5}$$

in which Q is the vector of conserved variables $[\rho \quad m \quad e \quad \rho k \quad \rho\omega]^T$ and E(Q) is the flux vector in the x co-ordinate direction,

$$\mathbf{E}(\mathbf{Q})=\begin{bmatrix} \rho u \\ \rho u^2+(\gamma-1)\left(e-\frac{1}{2}\rho u^2-\rho k\right) \\ u\left(e+(\gamma-1)\left(e-\frac{1}{2}\rho u^2-\rho k\right)\right) \\ \rho u k \\ \rho u \omega \end{bmatrix} \tag{4.6}$$

Equation (4.5) is written in strong conservation form. In order to determine the mathematical properties of the system of Equations represented by (4.5) the following quasi-linear form is introduced,

$$\frac{\partial \mathbf{Q}}{\partial t} + \mathbf{A}(\mathbf{Q})\frac{\partial \mathbf{Q}}{\partial x} = 0 \tag{4.7}$$

in which the matrix $\mathbf{A}(\mathbf{Q})$ is the Jacobian of the flux vector E with respect to the conserved variables Q. The individual elements of the Jacobian matrix, $\mathbf{A}(\mathbf{Q})$ are obtained from the following expression.

$$\mathbf{A}(\mathbf{Q})_{ij} = \frac{\partial \mathbf{E}(\mathbf{Q})_i}{\partial \mathbf{Q}_j} \tag{4.8}$$

For the system of equations represented by (4.5) the following Jacobian matrix is obtained,

$$\mathbf{A}(\mathbf{Q}) = \begin{bmatrix} 0 & 1 & 0 & 0 & 0 \\ \frac{(\gamma-3)}{2}u^2 & (3-\gamma)u & (\gamma-1) & -(\gamma-1) & 0 \\ -\frac{\gamma u E}{\rho} + u(\gamma-1)(u^2+k) & \frac{\gamma E}{\rho} - (\gamma-1)\left(\frac{3}{2}u^2+k\right) & \gamma u & -(\gamma-1)u & 0 \\ -uk & k & 0 & u & 0 \\ -u\omega & \omega & 0 & 0 & u \end{bmatrix} \tag{4.9}$$

The Eigenvalues associated with Equation (4.5) are,

$$\begin{aligned} \lambda_1 &= u - c \\ \lambda_2 = \lambda_3 &= \lambda_4 = u \\ \lambda_5 &= u + c \end{aligned} \tag{4.10}$$

and the right Eigenvectors r_i corresponding with the Eigenvalues λ_i are,

$$r_1 = \left[1 \quad u-c \quad \frac{\gamma e}{\rho} - (\gamma-1)\left(\frac{u^2}{\rho}+k\right) - uc \quad \frac{\phi_1}{\rho} \quad \frac{\phi_2}{\rho}\right]^T$$

$$r_2 = \left[1 \quad u \quad \frac{u^2}{2} \quad 0 \quad 0\right]^T$$

$$r_3 = \left[0 \quad 0 \quad 1 \quad 1 \quad 0\right]^T \tag{4.11}$$

$$r_4 = \left[0 \quad 0 \quad 0 \quad 0 \quad 1\right]^T$$

$$r_5 = \left[1 \quad u+c \quad \frac{\gamma e}{\rho} - (\gamma-1)\left(\frac{u^2}{\rho}+k\right) + uc \quad \frac{\phi_1}{\rho} \quad \frac{\phi_2}{\rho}\right]^T$$

The system of equations (4.5) therefore has five real, linearly independent Eigenvectors and the Jacobian matrix can be written in the following form,

$$\mathbf{A(Q) = R\Lambda R^{-1}} \tag{4.12}$$

where Λ is the diagonal matrix of the Eigenvalues (4.10) and R is the matrix whose columns are constructed from the five right Eigenvectors (r1 r2 r3 r4 r5). Equation (4.5) is therefore hyperbolic with respect to time.

The Eigenvectors r_1 and r_5 satisfy the following inequality,

$$\nabla\lambda_i \cdot \mathbf{R}_k \neq 0 \tag{4.13}$$

and are therefore genuinely non-linear. The remaining Eigenvectors are linearly degenerate. If we consider the solution of the local Riemann problem associated with Equation (4.5) then we can deduce that there will be two simple wave solutions (a compression wave and a rarefaction fan) associated with the two genuinely non-linear right Eigenvectors and a contact discontinuity associated with the remaining linearly degenerate fields.

The Riemann invariants, ψ, of this system are obtained from the solution of the differential equation,

$$\nabla_w \psi_k(w) \cdot r_k(w) = 0 \tag{4.14}$$

Comparing (4.13) and (4.14) we immediately deduce that for the genuinely non-linear fields the associated Eigenvalue is also a Riemann invariant. It may be easily verified that the Riemann invariants ψ^i corresponding to the Eigenvectors r_i are,

$$\begin{aligned}
\psi_2^1 = \frac{P}{\rho^\gamma}, \psi_3^1 = u + \frac{2}{(\gamma-1)}c, \psi_4^1 = k, \psi_5^1 = \omega \\
\psi_1^2 = u, \psi_3^2 = P, \\
\psi_1^3 = u, \psi_3^3 = P, \\
\psi_1^4 = u, \psi_3^4 = P, \\
\psi_1^5 = \frac{P}{\rho^\gamma}, \psi_2^5 = u - \frac{2}{(\gamma-1)}c, \psi_4^5 = k, \psi_5^5 = \omega
\end{aligned} \tag{4.15}$$

In the solution of the Navier-Stokes equations with a two-equation model of turbulence the convective and diffusive terms are coupled by the presence of the term $(2\rho k/3)$. In the analysis presented above this term has not been included in the convective flux on physical grounds (the term arises in the diffusive flux and not the convective flux). Siikonen[123] has presented an alternative analysis of the quasi-linear form of Equation (4.5) in which this term is included in the convective flux. For perfect gases the analysis is relatively straight forward and the influence of the additional term can be included by expressing the speed of sound in the following form,

$$c^2 = \frac{\tilde{a}}{\tilde{n}}\left[P + \tfrac{2}{3}\tilde{n}k\right] \tag{4.16}$$

Unpublished numerical experiments by Ludlow[125] indicate that the influence of this term on both the convergence history and the computed solution is small for steady two dimensional transonic flow calculations performed using an explicit time marching methodology.

4.4 The approximate Riemann solver of Osher

The Osher scheme described in the next section is an upwind, shock-capturing algorithm. Although the algorithm has been developed for application to problems in gas dynamics the underlying philosophy may be applied directly to any system of hyperbolic conservation laws. The algorithm is patterned after Godunov's method, but instead of computing the intercell flux exactly an approximate splitting is introduced. The method was first introduced by Enquist and Osher[126-7] for solution of the TSD equation. Subsequently Osher generalised the scheme for arbitrary systems of non-linear hyperbolic equations. Applications of the method to the for one-dimensional equations of gas dynamics were presented by Osher and Solomon[115], while Osher and Chakravarthy[128] applied the method to the two-dimensional Euler equations in order to obtain the steady transonic flow around an aerofoil.

The starting point of Osher's scheme is the supposition that there exists a unique flux splitting,

$$\mathbf{f}(\mathbf{Q}) = \mathbf{f}^{+}(\mathbf{Q}) - \mathbf{f}^{-}(\mathbf{Q}) \tag{4.17}$$

Following from Equation (4.17) it is natural to propose that the numerical flux should be calculated using the following Riemann solver,

$$\mathbf{f}(\mathbf{Q}_i, \mathbf{Q}_{i+1}) = \mathbf{f}^{+}(\mathbf{Q}_i) - \mathbf{f}^{-}(\mathbf{Q}_{i+1}) \tag{4.18}$$

Osher recognised that the flux splitting (4.18) could be rewritten in the following mathematically equivalent form,

$$\tilde{\mathbf{f}}_{i+\frac{1}{2}} = \frac{1}{2}\left[\mathbf{f}_i + \mathbf{f}_{i+1} - \int_{\mathbf{Q}_i}^{\mathbf{Q}_{i+1}} |\mathbf{A}(\mathbf{Q})| d\mathbf{Q}\right] \tag{4.19}$$

where the integration is performed in the phase (or state) space. Which replaces the problem of defining the splitting (4.18) with the problem of performing the integration in (4.19). It should be noted that as the integrals,

$$\int_{Q_i}^{Q_{i+1}} \mathbf{A}^{-}(\mathbf{Q})d\mathbf{Q} \text{ and } \int_{Q_i}^{Q_{i+1}} \mathbf{A}^{+}(\mathbf{Q})d\mathbf{Q} \tag{4.20}$$

depend upon the choice of integration path the splitting (4.17) is not generally unique and for this reason Osher's method is approximate.

The key feature of Osher's scheme is the use of the solution of the local Riemann problem to provide guidance when constructing the integration path between the states $\mathbf{Q}_i$ and $\mathbf{Q}_{i+1}$ in phase space. The integration is performed along paths that are tangential to the Eigenvectors, Equation (4.17), of the system. In Osher's original scheme the integration was performed with a reversed ordering of the sub-curves (known as the O-variant) in order to prove some analytical properties of the scheme. A more natural ordering is in the direction associated with the physical ordering of the Riemann invariants (P-variant) which ensures that the flux is exact in the absence of shock waves. As the Eigenvectors associated with λ_2, λ_3 and λ_4 are linearly degenerate we can omit the intersection points connecting their associated sub-paths in phase space. The integration path corresponding with the physical ordering is illustrated in Figure (4.1).

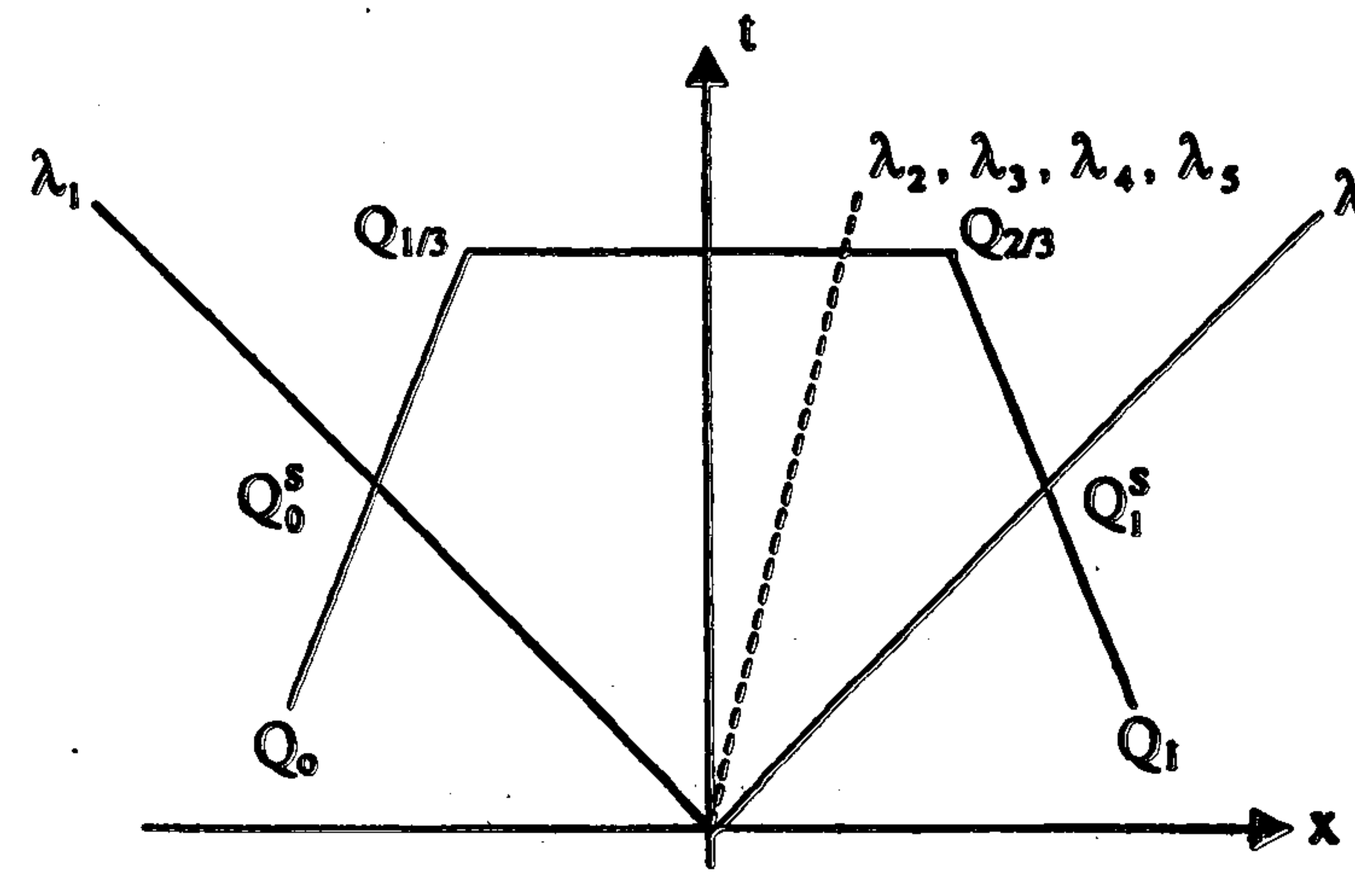

Figure (4.1) Integration paths for Osher's scheme with P-ordering

The data at the end points, Q_o and Q_1, are known and therefore by equating the Riemann invariants at the end points of the sub-paths we can obtain a system of 10 algebraic equations for the 10 unknown values $Q_{1/3}$ and $Q_{2/3}$. Furthermore, it can be shown that the Eigenvalues associated with the Eigenvectors r_1 and r_5 can change sign along their respective sub-paths and consequently it is necessary to determine values for the state variables at the sonic points. Conditions at the sonic points can be obtained using the Riemann invariants ψ_1 or ψ_5 and the sonic condition $\lambda_1=0$ or $\lambda_5=0$. The integration paths of the approximate Riemann solver for the closely coupled system are identical to those of the original scheme and the evaluation of the integral is therefore given by[129],

$$\int_{Q_{i-1}}^{Q_i} \mathbf{A}^+ dQ + \int_{Q_i}^{Q_{i+1}} \mathbf{A}^- dQ = \tilde{\mathbf{E}}(Q_{i+1}) + \int_{i-1}^{i-\frac{2}{3}} \mathbf{A}^- \left(\frac{\partial Q}{\partial S}\right)_1 ds + \int_{i-\frac{2}{3}}^{i-\frac{1}{3}} \mathbf{A}^- \left(\frac{\partial Q}{\partial S}\right)_2 ds + \int_{i-\frac{1}{3}}^{i} \mathbf{A}^- \left(\frac{\partial Q}{\partial S}\right)_3 ds$$
$$- \tilde{\mathbf{E}}(Q_i) - \int_{i}^{i+\frac{1}{3}} \mathbf{A}^+ \left(\frac{\partial Q}{\partial S}\right)_4 ds - \int_{i+\frac{1}{3}}^{i+\frac{2}{3}} \mathbf{A}^+ \left(\frac{\partial Q}{\partial S}\right)_5 ds - \int_{i+\frac{2}{3}}^{i+1} \mathbf{A}^+ \left(\frac{\partial Q}{\partial S}\right)_6 ds \qquad (4.21)$$

The evaluation of the integrals along the sub-paths is relatively straight forward, the final form of the intercell flux is presented in Table (4.1) below.

	$U_o<C_o$, $U_1>-C_1$	$U_o>C_o$, $U_1>-C_1$	$U_o<C_o$, $U_1<-C_1$	$U_o>C_o$, $U_1<-C_1$
$U_b \geq 0$ $U_b \geq C_{1/3}$	$f(Q_o^s)$	$f(Q_o)$	$f(Q_1)-f(Q_1^s)+f(Q_o^s)$	$f(Q_o)-f(Q_1^s)+f(Q_1)$
$U_b \geq 0$ $U_b \leq C_{1/3}$	$f(Q_{1/3})$	$f(Q_o)-f(Q_o^s)+f(Q_{1/3})$	$f(Q_1)-f(Q_1^s)+f(Q_{1/3})$	$f(Q_o)-f(Q_o^s)+f(Q_{1/3})-f(Q_1^s)+f(Q_1)$
$U_b \leq 0$ $U_b \geq -C_{2/3}$	$f(Q_{2/3})$	$f(Q_o)-f(Q_o^s)+f(Q_{2/3})$	$f(Q_1)-f(Q_1^s)+f(Q_{2/3})$	$f(Q_o)-f(Q_o^s)+f(Q_{2/3})-f(Q_1^s)+f(Q_1)$
$U_b \leq 0$ $U_b \leq -C_{2/3}$	$f(Q_1^s)$	$f(Q_o)-f(Q_o^s)+f(Q_1^s)$	$f(Q_1)$	$f(Q_o)-f(Q_o^s)+f(Q_1)$

Table 4.1 Calculation of the intercell flux using Osher's scheme.

4.5 Spatial discretisation of the diffusion terms

The discretisation of the diffusive terms requires a knowledge of the velocity gradients at the intercell boundaries so that the stress tensor can be evaluated. The auxiliary cell contains nodes at which no data is stored. However, the required data can be obtained from the surrounding cell centres using simple spatial averages. The average value of the velocity derivative over the auxiliary cell is then related to the nodal values using Gauss' theorem,

$$\int_V \nabla \cdot \mathbf{u} dV = \oint_S \mathbf{u} \cdot \vec{\mathbf{n}} dS \tag{4.22}$$

The discrete form of Equation (4.22) is,

$$\nabla \mathbf{u} = \frac{1}{V} \sum \mathbf{u} \cdot \vec{\mathbf{n}} S \tag{4.23}$$

where the summation is performed over the faces of the cell. Here S is the area of the cell face. The resulting discretisation is second order accurate on a smoothly varying mesh.

4.6 Higher order spatial discretisations

As described above Osher's method is at most first order accurate giving poor accuracy in smooth regions of the flow. Van Leer[130-132] proposed modifications to the initial data used in the solution of the approximate Riemann problem to obtain higher order spatial accuracy. This idea is the basis of MUSCL scheme in which the constant initial data are replaced by linear functions of the conserved variables, thus the data at the point x are reconstructed using expressions of the form,

$$Q_i(x) = Q_i^n + (x - x_i)\Delta \tag{4.24}$$

in which Δ is the slope of the data in the cell defined by x_{i+1} and x_i. The choice of slope function determines both the spatial accuracy and the computational stencil of the

numerical scheme. In the current work the slope is determined using the following function,

$$\Delta = \tfrac{1}{2}(1+\kappa)(Q_i^n - Q_{i-1}^n) + \tfrac{1}{2}(1-\kappa)(Q_{i+1}^n - Q_i^n) \tag{4.25}$$

which results in the following expressions for the states Q_L and Q_R,

$$\begin{aligned} Q_L &= \{Q_i + \tfrac{1}{4}[(1-\kappa)(Q_i - Q_{i-1}) + (1+\kappa)(Q_{i+1} - Q_i)]\} \\ Q_R &= \{Q_{i+1} - \tfrac{1}{4}[(1+\kappa)(Q_i - Q_{i+1}) + (1-\kappa)(Q_{i+1} - Q_{i+2})]\} \end{aligned} \tag{4.26}$$

here the parameter κ is a free parameter in the range $-1 \le \kappa \le 1$ that controls the properties of the resultant scheme. For $\kappa=1/3$ we obtain a nominally third order upwind biased scheme. Numerical experiments with higher order schemes indicate that improved accuracy is obtained in smooth regions of the flow, however in the vicinity of flow discontinuities spurious oscillations are observed that eventually cause the calculation to fail. This behaviour is expected as Godunov's theorem[113] states that here are no monotone, linear schemes of second or higher order'. In order to overcome this problem it is necessary to modify (4.25) in a manner that retains the high order form of (4.26) when the flow is smooth, but ensures that the scheme reverts to first order accuracy in the presence of strong flow gradients. This can be achieved by introducing the concept of slope limiting, in which the slope function Δ is modified to ensure that the numerical scheme remains TVD. Equation (4.26) is rewritten thus,

$$\begin{aligned} Q_L &= \left\{Q_i + \frac{\phi}{4}[(1-\phi\kappa)(Q_i - Q_{i-1}) + (1+\phi\kappa)(Q_{i+1} - Q_i)]\right\} \\ Q_R &= \left\{Q_{i+1} - \frac{\phi}{4}[(1+\phi\kappa)(Q_i - Q_{i+1}) + (1-\phi\kappa)(Q_{i+1} - Q_{i+2})]\right\} \end{aligned} \tag{4.26a}$$

where ϕ is the slope limiter, when the slope limiter function is $\phi=0$ the scheme reverts to first order accuracy, while for $\phi=1$ the scheme is in its original form. The conditions required to ensure that (4.26a) is TVD have been examined in some depth by Spekreijse[129]. The following limiter was used in the current study,

$$\phi = \frac{2(Q_{i+1} - Q_i)(Q_i - Q_{i-1})}{(Q_{i+1} - Q_i)^2 + (Q_i - Q_{i-1})^2} \tag{4.27}$$

A small number, ε, is usually introduced in both the numerator and the denominator to prevent division by zero in regions of null gradient. In the present work, the MUSCL scheme is applied to the primitive variables.

4.7 Calculation of the flux Jacobian

The time marching scheme described in the next Chapter employs an implicit approach that requires knowledge of the flux Jacobians associated with the spatial discretisation. Use of a finite difference approximation for the flux Jacobian has gained favour among many authors because of the ease with which such an approach can be implemented. However, the use of finite differences is computationally expensive, a first order spatial discretisation of the governing equations requires 54 evaluations of the right hand side terms in Equation (4.5) while second order accuracy requires 150 evaluations. Qin and Richards[133,134] compared a sparse finite difference Newton method for the solution of the Navier-Stokes equations with a sparse quasi-Newton method and concluded that while the former can demonstrate a quadratic convergence the latter can be more efficient as the approximate Jacobian is updated rather than calculated. Instead of calculating the Jacobian using finite differences, Badcock and Richards[135] followed an alternate approach in which the chain-rule was first used to obtain the following expression,

$$\frac{\partial \mathbf{F}}{\partial \mathbf{Q}_i} = \frac{\partial \mathbf{F}}{\partial \mathbf{Q}_0}\frac{\partial \mathbf{Q}_0}{\partial \mathbf{Q}_i} + \frac{\partial \mathbf{F}}{\partial \mathbf{Q}_1}\frac{\partial \mathbf{Q}_1}{\partial \mathbf{Q}_i} \tag{4.28}$$

Here $\frac{\partial \mathbf{F}}{\partial \mathbf{Q}_0}$ and $\frac{\partial \mathbf{F}}{\partial \mathbf{Q}_1}$ are the Jacobians of the flux vector with respect to the left and right states used in the approximate Riemann solver. The remaining terms $\frac{\partial \mathbf{Q}_0}{\partial \mathbf{Q}_i}$ and

$\frac{\partial Q_1}{\partial Q_i}$ arise from the MUSCL interpolation of the primitive variables and were obtained using a symbolic manipulation package. By recasting the problem in this manner the computational work is reduced dramatically as compare with a direct application of the finite difference method. 48 flux evaluations are required (this is equivalent to 24 right hand side calculations) for second order accuracy of the Jacobian terms together with a small overhead for the calculation of the terms arising from the interpolation procedure. Further improvements in computational efficiency can be obtained by using analytical expressions to evaluate all of the terms on the right hand side of (4.28). The complicated nature of the numerical fluxes arising from Osher's scheme has dissuaded most authors from deriving analytical expressions for the flux Jacobians directly. Instead analytical expressions have been derived for simplified forms of Osher's scheme[136] or symbolic manipulation packages have been employed to generate the required information, see Badcock[137]. Orkwis and Vanden[138] have highlighted some weaknesses of using symbolic manipulation packages, which tend to produce long pieces of code that are inefficient and difficult to check for coding errors.

By careful use of the chain rule it is possible to reduce the difficult problem of deriving an analytical Jacobian to a series of more tractable problems, the use of the chain rule is also a key component in the process used to obtain compact expressions when using symbolic manipulation packages. Equation (4.28) forms the basis of the analytical expressions used in the current work. Expressions for the Jacobian terms can be deduced very easily for Osher's approximate Riemann solver from Table (4.1) and are summarised in Table (4.2) below. The terms in Table (4.2) can be obtained with relative ease and are given by Spekreijse[129] for the two-dimensional Euler equations in a Cartesian co-ordinate system. The determination of the additional terms arising from the closely coupled turbulence model and the transformation to body fitted co-ordinates are trivial.

Derivation of analytical expressions for the contribution of the viscous terms to the Jacobian matrix is a relatively straightforward procedure. Again the chain rule is used, the viscous Jacobian is first obtained using the auxiliary cell variables. The auxiliary

variables are the values of the primitive variables at the faces of the cell used to evaluate the derivatives required for the viscous terms. These variables are obtained from the primitive variables using a simple arithmetic averaging technique involving the values of the variable at the surrounding cell centres. Once the Jacobian is known in terms of these variables a simple transformation is required to obtain the Jacobian based upon the cell centred variables.

Finally the calculation of the Jacobian terms corresponding to the source term is considered. The numerical stability of the inviscid one-dimensional wave equation with a source term is considered by Wilcox[86]. For first order time accuracy it can be shown that implicit discretisations are unconditionally unstable when production exceeds dissipation, it is therefore not possible to employ the exact Jacobian for the source term. Instead it is necessary to make some approximation of the implicit operator, in the current work only the dissipation terms are treated implicitly, while the remaining production terms are treated explicitly. This simplification leads to a simple block diagonal implicit operator for the source term.

	$U_0 < C_0$	$U_0 > C_0$
$C_{1/3} < U_H$	$\frac{\partial E}{\partial Q_{1/6}} \frac{\partial Q_{1/6}}{\partial Q_0}$	$\frac{\partial E}{\partial Q_0}$
$0 < U_H < C_{1/3}$	$\frac{\partial E}{\partial Q_{1/3}} \frac{\partial Q_{1/3}}{\partial Q_0}$	$\frac{\partial E}{\partial Q_0} - \frac{\partial E}{\partial Q_{1/6}} \frac{\partial Q_{1/6}}{\partial Q_0} + \frac{\partial E}{\partial Q_{1/3}} \frac{\partial Q_{1/3}}{\partial Q_0}$
$-C_{2/3} < U_H < 0$	$\frac{\partial E}{\partial Q_{2/3}} \frac{\partial Q_{2/3}}{\partial Q_0}$	$\frac{\partial E}{\partial Q_0} - \frac{\partial E}{\partial Q_{1/6}} \frac{\partial Q_{1/6}}{\partial Q_0} + \frac{\partial E}{\partial Q_{2/3}} \frac{\partial Q_{2/3}}{\partial Q_0}$
$U_H < -C_{2/3}$	0	$\frac{\partial E}{\partial Q_0} - \frac{\partial E}{\partial Q_{1/6}} \frac{\partial Q_{1/6}}{\partial Q_0}$

Table 4.2(a) Calculation of $\partial E/\partial Q_0$.

	$U_1 > -C_1$	$U_1 < -C_1$
$C_{1/3} < U_H$	0	$-\frac{\partial E}{\partial Q_{5/6}}\frac{\partial Q_{5/6}}{\partial Q_1}+\frac{\partial E}{\partial Q_1}$
$0 < U_H < C_{1/3}$	$\frac{\partial E}{\partial Q_{1/3}}\frac{\partial Q_{1/3}}{\partial Q_1}$	$\frac{\partial E}{\partial Q_1}-\frac{\partial E}{\partial Q_{5/6}}\frac{\partial Q_{5/6}}{\partial Q_1}+\frac{\partial E}{\partial Q_{1/3}}\frac{\partial Q_{1/3}}{\partial Q_1}$
$-C_{2/3} < U_H < 0$	$\frac{\partial E}{\partial Q_{2/3}}\frac{\partial Q_{2/3}}{\partial Q_1}$	$\frac{\partial E}{\partial Q_1}-\frac{\partial E}{\partial Q_{5/6}}\frac{\partial Q_{5/6}}{\partial Q_1}+\frac{\partial E}{\partial Q_{2/3}}\frac{\partial Q_{2/3}}{\partial Q_1}$
$U_H < -C_{2/3}$	$\frac{\partial E}{\partial Q_{5/6}}\frac{\partial Q_{5/6}}{\partial Q_1}$	$\frac{\partial E}{\partial Q_1}$

Table 4.2(b) Calculation of $\partial E/\partial Q_1$

4.8 Concluding Remarks

In this chapter the spatial discretisation of the governing equations was considered. A finite volume scheme was developed for the Reynolds averaged Navier-Stokes equations and a closely coupled equation of turbulence. The spatial discretisation is based upon a novel extension of Osher and Solomon's flux difference splitting scheme which includes the additional equations arising from the turbulence model. The approximate Riemann solver was extended to third order accuracy using MUSCL interpolation of the primitive variables. The viscous terms were then discretised using a second order finite volume scheme based upon Gauss' theorem. Using the chain rule the difficult problem of analytically determining the flux Jacobian for the extended scheme was reduced to a sequence of more tractable problems.

5

Temporal Discretisation

The spatial discretisation adopted for the convective and diffusive terms of the Navier-Stokes equations was described in the previous chapter. In order to complete the development of a discrete form of the governing equations it is neccesary to consider the integration of the resulting system of ordinary differential equations. The choice of a suitable integration scheme is the focus of this chapter. A number of existing strategies are considered, and their relative performance is measured. The main contributions of this chapter include the first known application of the linear solver GMRESR to a non-model problem and an investigation of the utility of a Newton type approach for the soultion of unsteady problems.

The computation of unsteady flows requires the discretisation of time in addition to space. While the PDE's that govern unsteady compressible viscous flow are hyperbolic-parabolic in character, there are considerable differences in the behaviour of the space and time terms. Generally a disturbance at a point, P, in space will influence the development of the flow at all other points in space in the domain (important exceptions are attached boundary layers and regions in which the flow is locally supersonic). In contrast disturbances in the flow at an instant in time t_o only influence the flow in the future, i.e. $t > t_o$. Given the differing behaviour of the space and time terms it is convenient to adopt a numerical scheme that allows the spatial and temporal discretisations to be performed independently of one another, such an approach offers enormous flexibility in the choice of numerical methods for the individual problems.

Performing the spatial discretisation first we obtain a system of ODE's that is continuos in time,

$$\frac{dQ}{dt} = -R(Q) \tag{5.1}$$

here R represents the spatial discretisation at time t. Equation (5.1) is an initial value problem (IVP) subject to the initial condition,

$$Q_{t=0} = Q_o \tag{5.2}$$

Using such an approach the solution can be marched in time, that is a sequence of IVP's are solved each advancing the solution by a time step Δt. Furthermore the solution obtained for each IVP provides the initial condition for the next IVP. A range of numerical techniques are available for the solution of ODE's. Explicit methods are generally simplest to construct because they only require information about the solution at the current time level. However, such methods generally require that the time step be restricted in order to ensure the numerical stability of the solution process. Implicit methods are typically free of such restrictions but are more difficult to implement as the right hand side calculation involves the unknown solution at time levels in the future.

5.1 Explicit Methods

Equation (5.1) may be integrated wih respect to time to obtain,

$$\int_{t_n}^{t_{n+1}} \frac{dQ}{dt} dt = Q^{n+1} - Q^n = -\int_{t_n}^{t_{n+1}} R(t, Q(t)) dt \tag{5.3}$$

The integral on the right hand side of Equation (5.3) is then evaluated using numerical quadrature. The simplest approach is to consider R(t,Q(t)) constant over the time interval, we then obtain the update,

$$Q^{n+1} - Q^n = -\Delta t R(Q^n) \tag{5.4}$$

subject to the stability restriction,

$$\Delta t = MIN\left(\frac{\Delta x \Delta y}{\left\{ (|u| + a) + \left(\frac{2\gamma}{\rho Re Pr} \frac{\mu}{\Delta x \Delta y} \right) \right\} \Delta y + \left\{ (|v| + a) + \left(\frac{2\gamma}{\rho Re Pr} \frac{\mu}{\Delta x \Delta y} \right) \right\} \Delta x} \right) \quad (5.5)$$

here Re and Pr are the Reynolds number and Prandtl number respectively.

For flows that vary slowly in time, the minimum time step required for time accuracy may be much larger than that imposed by stability considerations. In order to demonstrate this we consider a simple example, the viscous flow around an aerofoil of unit chord that is oscillating in pitch with a reduced frequency k=0.1. The spatial discretisation is performed on a mesh having a near wall spacing of 0.00001c in the normal direction and 0.02c around the aerofoil. The time period corresponding to the reduced frequency k is given by,

$$\Delta t = \left(\frac{kU_\infty}{\pi c} \right)^{-1} \quad (5.6)$$

Furthermore it is assumed that each period of the motion may be accurately resolved using just N integration steps. The time step required too ensure accuracy is therefore,

$$\Delta t = \left(\frac{NkU_\infty}{\pi c} \right)^{-1} \quad (5.6a)$$

while a conservative estimate due to stability restrictions (ignoring the influence of the viscous term) requires that the time step be limited to,

$$\Delta t = CFL \frac{\Delta y}{(|v| + a)} \quad (5.7)$$

if we assume that the minimum time step will occur near the wall and that the speed of sound in the boundary layer is of the order of the freestream velocity then an explicit scheme with CFL = 1.0 requires,

$$\left(\frac{\pi c}{NkU_\infty}\right)\left(\frac{1}{CFL}\right)\left(\frac{U_\infty}{\Delta y}\right)=\left(\frac{\pi c}{k\Delta y}\right)\left(\frac{1}{NCFL}\right)\approx\frac{\pi}{2N}10^6 \qquad (5.8)$$

time steps to advance the solution by a time step equivalent to that required for the numerical scheme to be time accurate. For pitching aerofoils N can be as small as 36 for a scheme that is second order accurate in time, see Gaitonde and Fiddes[139]. Therefore, for a given flow problem and spatial discretisation the efficiency of the solution process depends only upon two factors, the maximum CFL number that can be employed and the computational cost of the method. For an unconditionally stable numerical scheme the time step can be chosen to match that required by accuracy, provided that the associated increase in operation count is relatively modest (2-3 orders of magnitude) then the overall scheme will be substantially more efficient than any of the explicit schemes described above. For this reason we turn our attention to implicit methods.

5.2 Implicit Methods

If $R(Q)$ has a constant value $R(Q^{n+1})$ over the time interval Δt we obtain the first order update,

$$Q^{n+1}-Q^n=-R(Q^{n+1}) \qquad (5.9)$$

which is the basis of the implicit scheme employed in the current work. For linear problems the right hands side of Equation (5.9) may be linearised exactly as,

$$R(Q^{n+1})=R(Q^n)+\frac{\partial R(Q^n)}{\partial Q}(Q^{n+1}-Q^n) \qquad (5.10)$$

In order to treat the non-linear terms involved in the spatial discretisation of the Navier-Stokes equations Briley[140] proposed a local linearisation of the right hand side of (5.9). This involves a Taylor series expansion of the right hand side operator about the time level $t=t_n$, truncating the higher order terms we obtain,

$$\mathbf{R}(\mathbf{Q}^{n+1}) = \mathbf{R}(\mathbf{Q}^{n}) + \frac{\partial \mathbf{R}(\mathbf{Q}^{n})}{\partial \mathbf{Q}}\left(\mathbf{Q}^{n+1} - \mathbf{Q}^{n}\right) + O\left(\Delta t^{2}\right) \tag{5.11}$$

Note that the linearisation error, $O(\Delta t^2)$, is comparable in magnitude to the temporal discretisation error, therefore Equation (5.11) may be substituted into (5.9) with no loss of accuracy to obtain the following first order scheme,

$$\left[\mathbf{I} + \Delta t \frac{\partial \mathbf{R}(\mathbf{Q}^{n})}{\partial \mathbf{Q}^{n}}\right]\left(\mathbf{Q}^{n+1} - \mathbf{Q}^{n}\right) = -\mathbf{R}(\mathbf{Q}^{n}) \tag{5.12}$$

Beam and Warming[141] propose a more general method,

$$\left[(\mathbf{I}+\xi) + \theta\Delta t \frac{\partial \mathbf{R}(\mathbf{Q}^{n})}{\partial \mathbf{Q}^{n}}\right]\left(\mathbf{Q}^{n+1} - \mathbf{Q}^{n}\right) = -\mathbf{R}(\mathbf{Q}^{n}) - \xi\left(\mathbf{Q}^{n} - \mathbf{Q}^{n-1}\right) \tag{5.13}$$

in which the constants ξ and θ may be selected to improve the accuracy of the temporal discretisation. There are two major difficulties associated with implicit schemes. The first concerns the construction of the matrix on the left hand side of (5.13). For simple discretisations, such as central schemes, the construction of the Jacobian is relatively straightforward and has a simple banded structure. In the current work the spatial discretisation is less straightforward and consequently the Jacobian matrix is more complex. The calculation of the Jacobian terms was considered in Chapter (4) and will not be repeated here. The matrix that results from the application of (5.14) to Osher's scheme is sparse, unsymmetric and generally ill conditioned.

Equation (5.13) may be rewritten in the following form,

$$\mathbf{Ax=b} \tag{5.14}$$

The solution of (5.14) provides the second major obstacle to the efficient implementation of implicit methods. A full review of methods for the solution of (5.14) is beyond the scope of this thesis, see Golub[142] for an introduction to the solution of algebraic systems of equations.

5.2.1 Factored methods

The right hand side of (5.10) may be rewritten in the following form,

$$\mathbf{R}^{n+1} = \left(\mathbf{R}_x^i + \mathbf{R}_x^v\right)^{n+1} + \left(\mathbf{R}_y^i + \mathbf{R}_y^v\right)^{n+1} \tag{5.15}$$

in which terms sharing a common direction have been collected together. It is relatively straightforward to factorise the implicit operator that results when (5.15) is used to rewrite the left-hand side of (5.13). The alternating direction implicit methods are a particular class of this method. The principal of the ADI technique is to separate the implicit operators into one-dimensional components involving operations originating from a single co-ordinate direction, in this way we obtain,

$$\left[\mathbf{I} + \Delta t\left(\mathbf{S}_x \cdot + \mathbf{S}_y \cdot\right)\right]\mathbf{Q}^{n+1} = -\Delta t\mathbf{R} + \mathbf{Q}^n \tag{5.16}$$

which can be factorised into the product of two one-dimensional implicit operators $\mathbf{S}_x$ and $\mathbf{S}_y$,

$$\left[\mathbf{I} + \Delta t\mathbf{S}_x \cdot\right]\left[\mathbf{I} + \Delta t\mathbf{S}_y \cdot\right]\mathbf{Q}^{n+1} = -\Delta t\mathbf{R} + \mathbf{Q}^n \tag{5.17}$$

multiplying the terms on the left of Equation (5.17) we find that the leading term of the factorisation error is second order, the overall accuracy of the discretisation is therefore unchanged. The factored equations are solved in two stages using a direct solver to invert the matrices in turn. Pulliam and Chausee[143] propose a further approximation to

(5.15) that reduces the matrix operations required to resolve the resulting system of equations to a sequence of scalar tri-diagonal inversions.

During the course of the current work the directional factorisation,

$$\left[\mathbf{I}+\Delta t\frac{\partial \mathbf{R}_x(\mathbf{Q}^n)}{\partial \mathbf{Q}^n}\right]\left[\mathbf{I}+\Delta t\frac{\partial \mathbf{R}_y(\mathbf{Q}^n)}{\partial \mathbf{Q}^n}\right]\left(\mathbf{Q}^{n+1}-\mathbf{Q}^n\right)=-\Delta t\mathbf{R}(\mathbf{Q}^n) \qquad (5.18)$$

was investigated. The presence of cross diffusion terms in the full Reynolds averaged Navier-Stokes equations prevents a direct factorisation of the form indicated in (5.18), however if those terms are neglected the equations are decoupled and the factorisation is easily obtained. Each of the factors then consists of a block diagonal matrix and each of the blocks is in turn block penta-diagonal. This system can be solved efficiently using LU decomposition. The resulting numerical scheme requires about a factor of 10 more computation than the basic explicit scheme. Comparisons of the convergence behaviour of an explicit scheme and (5.18) obtained by Shaw[144] for steady laminar flow around a tangent ogive forebody using the PINK-PNS solver indicate that for CFL numbers above 10 the method does not converge, Figure (5.1). This behaviour is attributed to the increasing importance of the factorisation error as CFL number is increased. For CFL numbers below 10 the implicit scheme converges rapidly to the steady state solution, Figure (5.2), however when the computational costs of the methods are considered, Figure (5.3), the implicit method is found to be only around 3 times quicker than the explicit scheme.

5.2.2 Iterative methods

Iterative methods provide an alternative method for solving the system **Ax=b** arising at each step of the implicit procedure. Iterative methods begin with an approximate solution and improve it using a recurrence formula. In this manner, a sequence of improved solutions is obtained that under certain conditions converges to the exact solution. Most iterative schemes can be written in the following form,

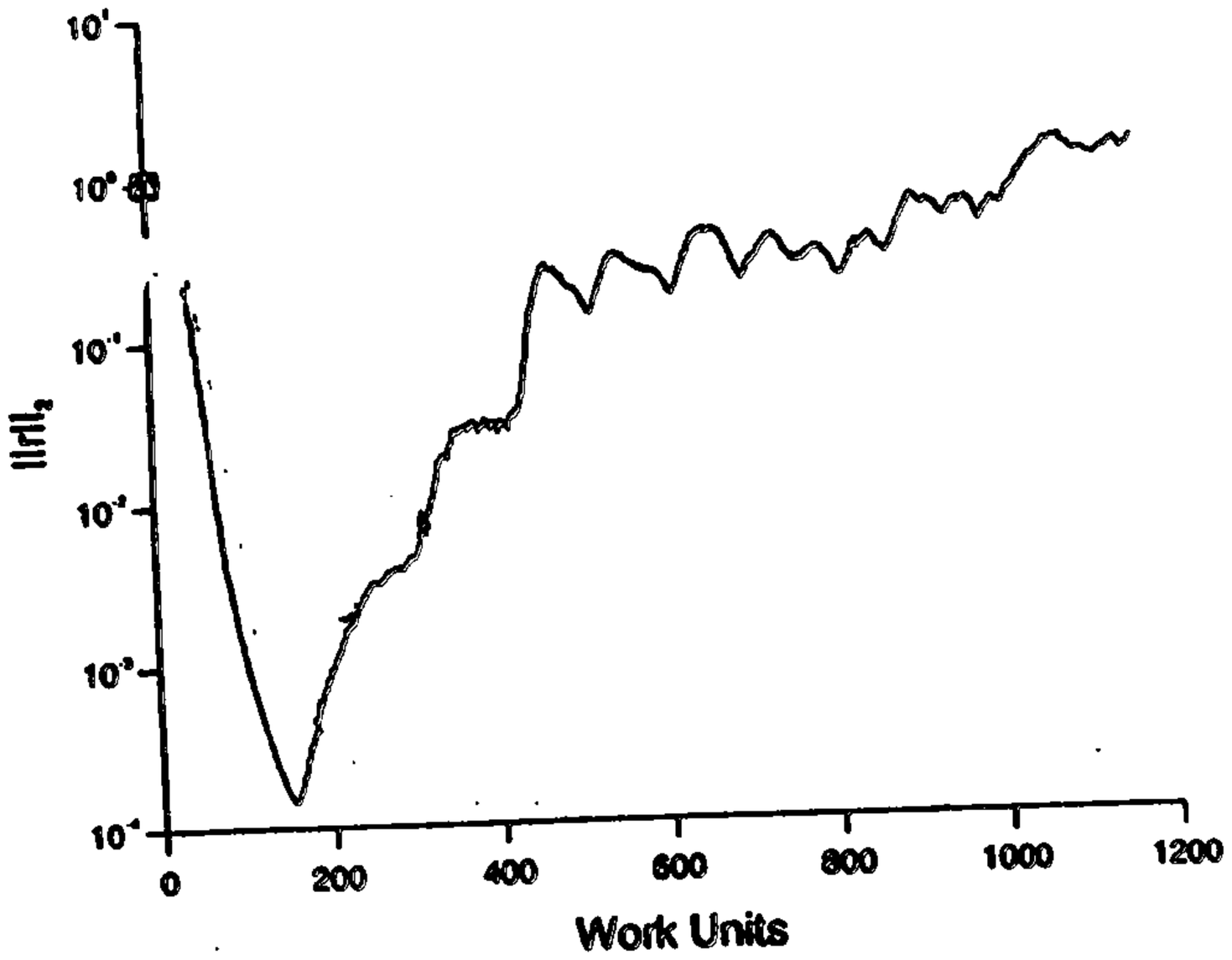

Figure (5.1) Convergence history of factored scheme, CFL = 15.

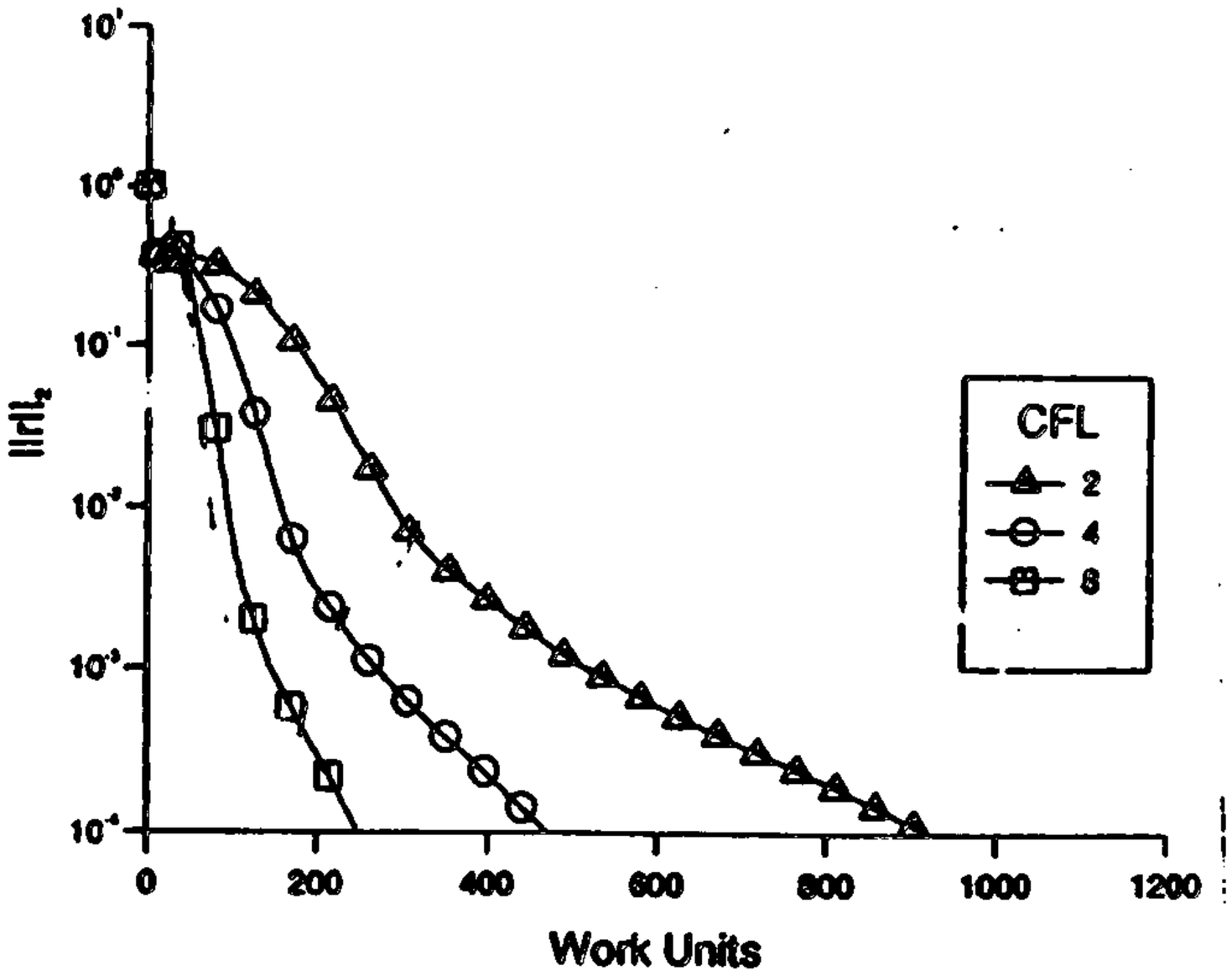

Figure (5.2) Convergence history of factored scheme, CFL < 10.

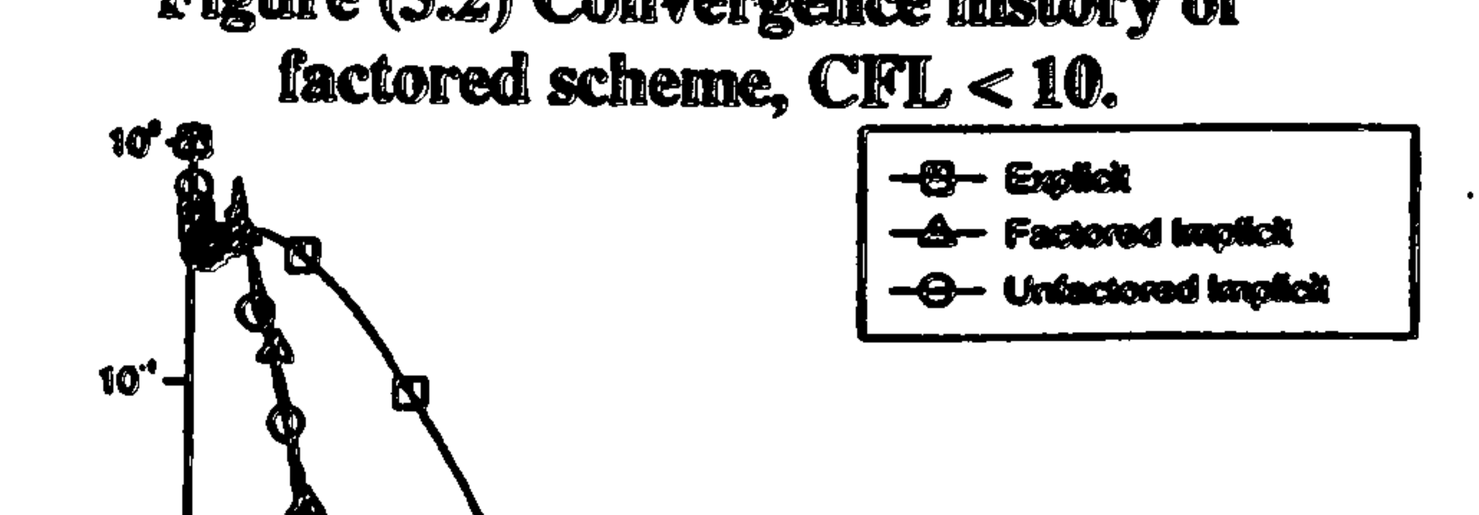

Figure (5.3) Computational cost of factored scheme.

$$\mathbf{M}\mathbf{Q}^{n+1} = \mathbf{N}\mathbf{Q}^{n} - \mathbf{R}(\mathbf{Q}) \tag{5.19}$$

where **M** and **N** are matrices that represent the operation of the iterative scheme. The matrices **M** and **N** are related to the system matrix by,

$$\mathbf{A} = \mathbf{M} - \mathbf{N} \tag{5.20}$$

For an iterative scheme to be effective the matrices **M** and **N** must be easily constructed, furthermore the matrix **M** must be easily invertible. Simple methods such as Jacobi iteration (**M** is the diagonal block of **A**), Gauss-Seidel (**M** is the lower triangular part of **A**) can be used, however the convergence of these methods is slow.

(a) Krylov-subspace methods

More recently a class of iterative methods based upon the construction of a Krylov subspace have been employed to accelerate the convergence of implicit methods. Such methods are based upon an iterative improvement of an approximate solution $\mathbf{x}_0$ using steps of the form,

$$\mathbf{x}_n = \mathbf{x}_0 + \mathbf{K}_n(\mathbf{r}_0, \mathbf{A}) \tag{5.21}$$

where $\mathbf{r}_0 = \mathbf{b} - \mathbf{A}\mathbf{x}_0$ and $\mathbf{K}(\mathbf{r}_0, \mathbf{A})$ is a Krylov subspace of the solution vector space. The simplest such approach is the method of steepest descent. Given an initial approximation $\mathbf{x}_0$ the function that we wish to minimise decreases most rapidly in the direction of the residual. This method is globally convergent but the rate of convergence may be unacceptably small when the gradient directions are too close. To avoid this problem a set of search directions that are unrelated to the residual are chosen. In the conjugate gradient approach, the next search direction is chosen to be the closest vector to the current. The conjugate gradient method is only suitable for the solution of problems involving symmetric system matrices but can be extended for non-symmetric matrices with suitable modification. Sonneveld[145] proposes CGS in which the transpose of **A** is employed. CGS is guaranteed to converge to the exact solution in at most N iterations, but the convergence behaviour can be highly irregular.

The CGS method has been used by Badcock et al[135,137] to accelerate the convergence of solvers for the Euler and Navier-Stokes equations.

In the GMRES[146] method it is assumed that the solution lies within a subspace span$\{r_o, Ar_o, A^2r_o.....\}$. The subspace is constructed using a modified Gram-Schmidt[142] process in which the next vector is orthogonal to the previous vector in the sequence. Once a vector subspace of dimension k has been defined we have the factorisation,

$$AQ_k = Q_{k+1}H_k \tag{5.22}$$

where the columns of Q_{k+1} are the orthonormal vectors and H_k is an upper Hessenberg matrix. The approximate solution is then found by minimising the residual $|b-Ax_k|_2$ subject to the constraint that the solution has the form $x_k = x_o + Q_k y_k$. The minimisation process can be solved efficiently using QR factorisation[142]. The principal disadvantage of GMRES over CGS is the need to store the subspace, memory requirements for the three schemes considered in this section are shown in Table (5.1) below.

$$r_o = b - Ax_o$$

DO $k = 1,2,\ldots$

$$\rho_1 = (r_o, r_{k-1})$$

$$\beta = \frac{\rho_1}{\rho_o}$$

$$u_k = r_{k-1} + \beta p_{k-1}$$

$$p_k = u_k + \beta(q_{k-1} + \beta p_{k-1})$$

$$v_k = Ap_k$$

$$\alpha = \frac{\rho_1}{(r_o, v_k)}$$

$$q_k = u_k - \alpha v_k$$

$$r_k = r_{k-1} - \alpha A(u_k + q_k)$$

$$x_k = x_{k-1} - \alpha(u_k + q_k)$$

ENDDO

Sketch of CGS[145]

GMRES[146] has the desirable property that it minimises the residual over the current Krylov subspace. If the Krylov subspace has the same dimension as that of the system matrix then GMRES obtains the exact solution. However, a full implementation of GMRES is undesirable because the computational work associated with the orthogonalisation process increases quadratically with respect to the system size while the memory requirements increase linearly. In order to avoid this problem Saad and Shultz[146] advocate truncation of the subspace, this is the so called restarted GMRES(m) method in which GMRES with a subspace size of m is applied in an iterative manner until the required tolerance on the solution is obtained. Numerical schemes based upon restarted GMRES has been widely adopted in the CFD community[147-149]. Van der Vorst[150] notes that the convergence of restarted GMRES

$$\mathbf{r}_o = \mathbf{b} - \mathbf{A}\mathbf{x}_o$$
$$\mathbf{v}_1 = \mathbf{r}_o$$
$$\mathrm{DO}\, j = 1,2,\ldots,m$$
$$\mathbf{w} = \mathbf{A}\mathbf{v}_j$$
$$\mathrm{DO}\;\; i = 1,\ldots,j$$
$$h_{i,j} = (\mathbf{w}, \mathbf{v}_i)$$
$$\mathbf{w} = \mathbf{w} - h_{i,j}\mathbf{v}_i$$
$$\mathrm{ENDDO}$$
$$h_{j+1,j} = \|\mathbf{w}\|_2$$
$$\mathbf{v}_{j+1} = \frac{\mathbf{w}}{h_{j+1,j}}$$
$$\mathrm{ENDDO}$$
$$\mathrm{Solve}\, \mathbf{H}_m \mathbf{y}_m = \|\mathbf{r}_o\| \mathbf{e}_1$$
$$\mathbf{x} = \mathbf{x}_o + [\mathbf{v}_1, \ldots\ldots, \mathbf{v}_m]\mathbf{y}_m$$

Sketch of GMRES[146]

depends critically upon the value of m, this behaviour has been observed in numerical studies performed as part of the current work. Furthermore, convergence of the restarted variant of GMRES is often sub-optimal because no use is made of information

available from previous steps of the method. In order to overcome this problem Van der Vorst[150] suggests that combining GMRES with other methods will restrict the number of GMRES steps required to obtain convergence to the desired tolerance. A family of nested methods is proposed in which Krylov-subspace methods are used to precondition the inner steps of GMRES. Selecting GMRES for this purpose a recursive scheme known as GMRESR is obtained. It is shown that for problems that would usually require relatively large subspaces GMRESR converges more quickly than GMRES.

The application of GMRESR presented at the end of this section is the first published use of the method to solve practical problems in CFD.

In the remaining parts of this section the three methods detailed above are applied to a representative problem. The problem considered is the solution of the Euler equations for the flow around an aerofoil performing periodic inplane motions, more details can be found in Shaw[151]. In Figure (5.4) the convergence behaviour of CGS, GMRES(10) and GMRESR(5,2) on a relatively coarse grid (153x48) is compared for the first time step of the unsteady calculation. As expected both GMRES and GMRESR converge monotonically while the behaviour of CGS is highly erratic. The convergence histories shown in Figure (5.4) suggest that GMRES (10) is optimal for the current problem. Experience has shown however, that over the course of a full cycle of the aerofoil motion the number of iterations required to meet a given tolerance reduces as the solution converges to the periodic solution, thus it is necessary to consider computational cost over a full cycle of the motion. This is done in Figure (5.5) which presents the computational cost of the GMRES (10) and CGS methods for various time steps. We observe that for a smaller number of time steps/cycle (corresponding to larger time steps) GMRES is more efficient than CGS, indeed for large enough time steps CGS does not converge to the relatively modest tolerance chosen and the solution process 'blows up'. For smaller time steps CGS appears to out perform GMRES, but subsequent tests suggest that this is not true when a stricter convergence tolerance is employed.

Solver	Memory (vectors)
CGS	11
GMRES(m)	5 + m
GMRES(m,n)	9 + 2n + m

Table (5.1) Memory requirement of Krylov subspace methods.

$r_o = b - Ax_o$

DO $j = 1,2,\ldots$

Solve $Az_m = r_j$

using GMRES

$c = Az_m$

DO $i = 1,\ldots,j$

$\alpha = (c_i, c)$

$c = c - \alpha c_i$

$z = z - \alpha u_i$

ENDDO

$$c_j = \frac{c}{\|c\|_2}$$

$$u_j = \frac{z_m}{\|c\|_2}$$

$x_{j+1} = x_j + (c_i, r_i)u_i$

$r_{j+1} = r_j - (c_i, r_i)c_i$

ENDDO

Sketch of GMRESR(150)

The sensitivity of the convergence behaviour of GMRESR to the number of inner and outer iterations performed was investigated and results are compared with GMRES(10) in Figures (5.6) and (5.7) respectively, here a finer grid containing 259x96 nodes was used. As the number of inner iterations is increased the effectiveness of GMRES as a preconditioner to the system matrix increases leading to improved efficiency of the outer iterations. This is illustrated in Figure (5.7) which indicates that a modest increase in the number of inner iterations from 2 to 5 has a dramatic impact on the CPU time required to converge the system to the required tolerance. The results presented in Figure (5.7) show that increasing the number of outer iterations performed by GMRESR can lead to some small gains in performance. These gains in computational efficiency are however at the expense of increased memory. The performance of GMRESR is disappointing for the problems considered. It appears that the method offers little real benefit when compared with GMRES. Indeed the additional memory costs associated with GMRESR mitigate against its use in preference to GMRES. This conclusion is broadly in line with Van der Vorst's suggestion that the method may only be suitable for systems that require the construction of large subspaces.

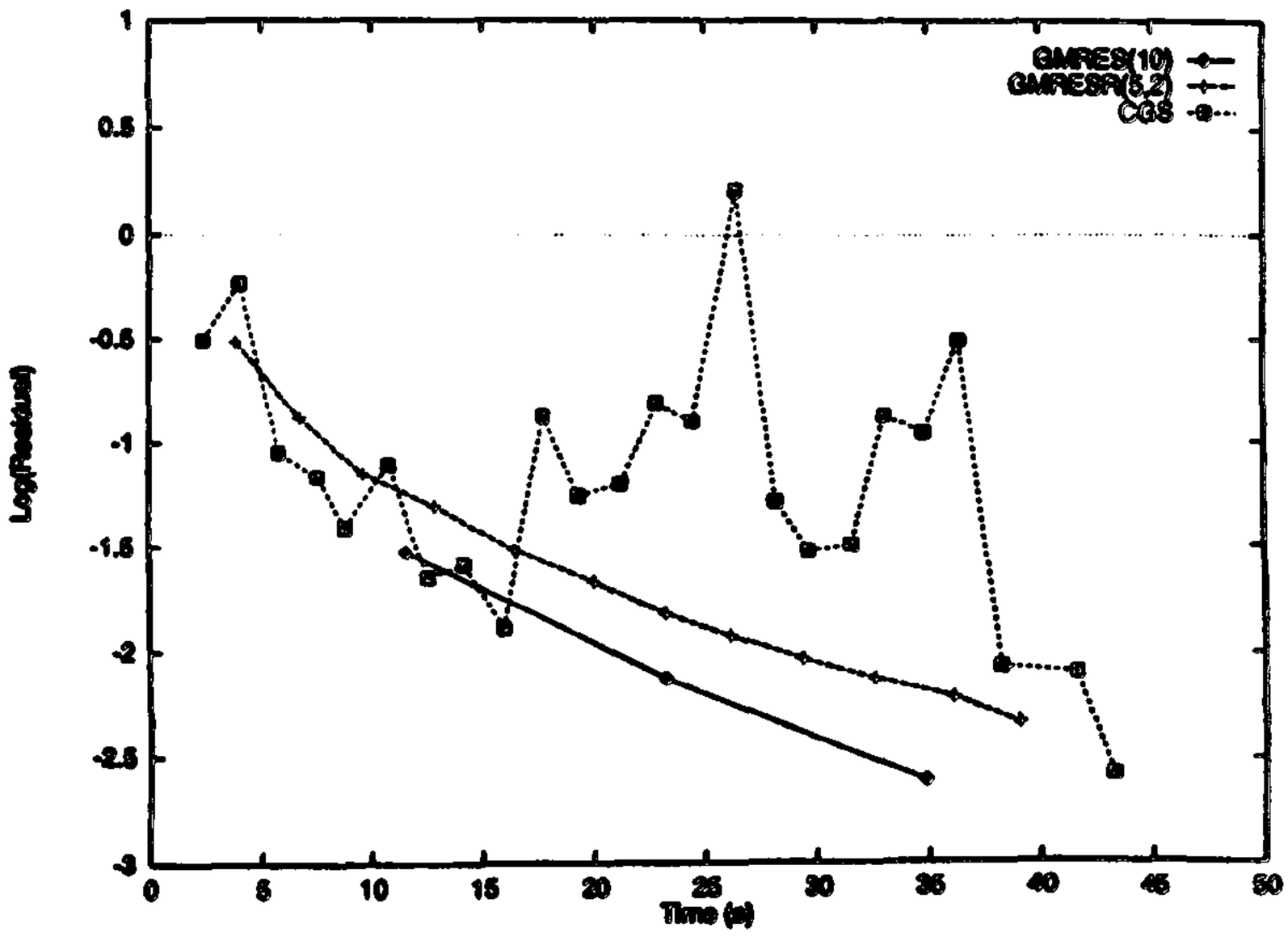

Figure (5.4) Convergence of Krylov schemes

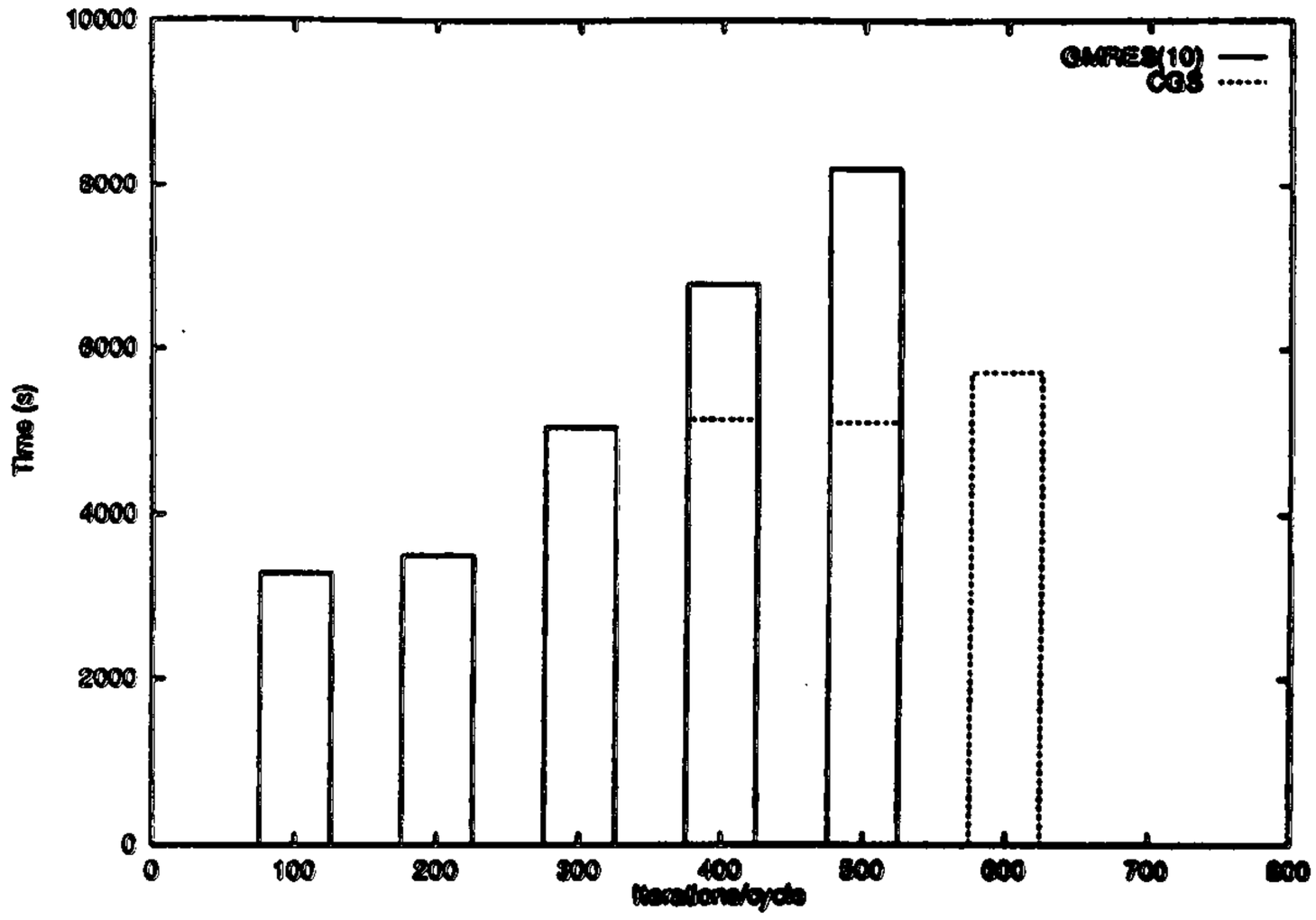

Figure (5.5) Cost of Krylov subspace schemes

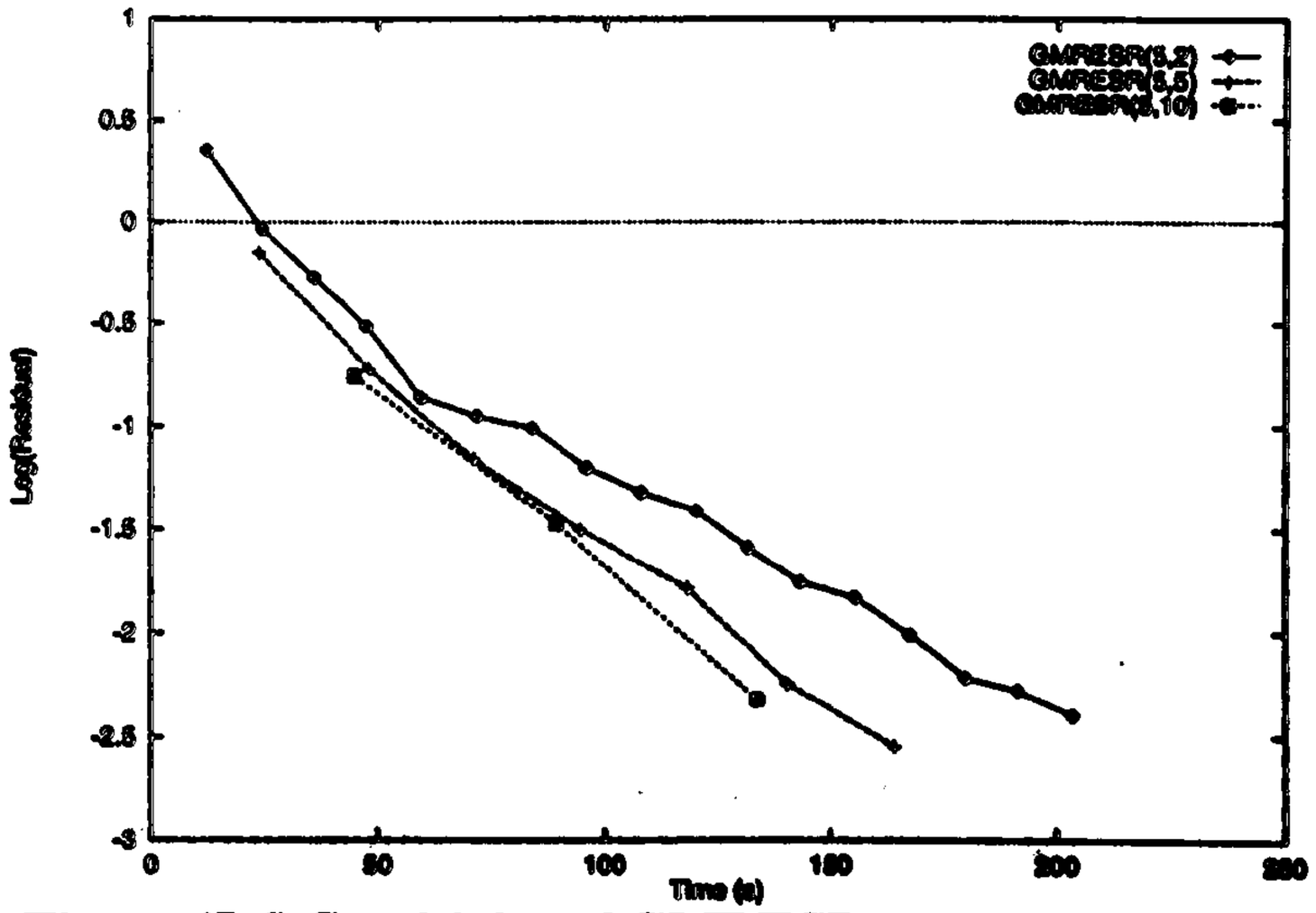

Figure (5.6) Sensitivity of GMRESR to inner iterations

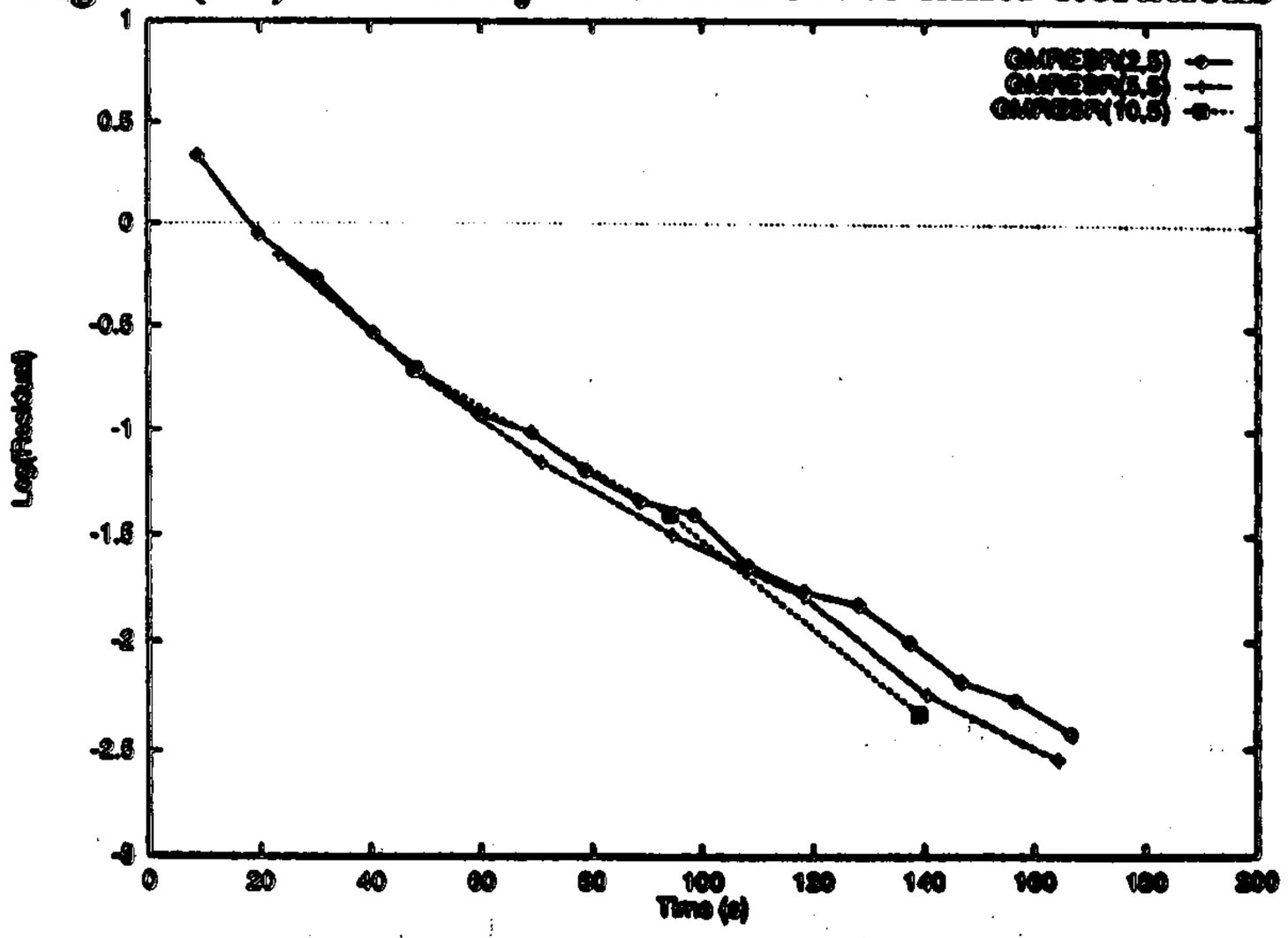

Figure (5.7) Sensitivity of GMRESR to outer iterations.

Finally we note that for this class of solvers the system matrix is only required in the evaluation of matrix vector products. Based upon this observation we can construct Krylov subspace methods that do not require explicit evaluation of the Jacobian matrix. Consider the matrix vector product Ay with,

$$\mathbf{A} = \frac{\partial \mathbf{R}}{\partial \mathbf{Q}} \tag{5.23}$$

recalling the Taylor series expansion,

$$f(x + \varepsilon h) = f(x) + \varepsilon h \frac{\partial f}{\partial x} + O(\varepsilon^2 h^2) \tag{5.24}$$

then making the appropriate substitutions and setting the parameter ε using,

$$\varepsilon = \frac{\sqrt{\text{machinezero}}}{\|y\|_2} \tag{5.25}$$

we obtain,

$$\mathbf{A}y = \frac{\mathbf{R}(\mathbf{Q}_o + \varepsilon y) - \mathbf{R}(\mathbf{Q}_o)}{\varepsilon} + O(\text{machine zero}) \tag{5.26}$$

Equation (5.26) is an approximation to the matrix vector product that requires two evaluations of the right hand side and is accurate to machine precision. This property has been used extensively[152-4] to reduce the memory overheads of implicit methods. While a matrix-free method was developed by Qin, Ludlow and Shaw[155] it was not used in the current work due to stability problems that arise from a fully implicit discretisation of the turbulent source term.

(b) Preconditioning techniques

Iterative methods for the solution of ill-conditioned problems generally perform poorly. Instead, we seek to modify the original problem in a manner that improves the

condition of the matrix, this is known as preconditioning. The basis of preconditioned Krylov subspace methods is that given a suitable approximation $\mathbf{P}^{-1}$ to the inverse of the system matrix then a preconditioned system,

$$\begin{aligned}\mathbf{P}^{-1}\mathbf{A}\mathbf{x} &= \mathbf{P}^{-1}\mathbf{b} \\ \mathbf{A}\mathbf{P}^{-1}(\mathbf{P}\mathbf{x}) &= \mathbf{b}\end{aligned} \tag{5.27}$$

is obtained that is better conditioned and easier to solve than the original system. The preconditioning can be applied in two forms termed left and right preconditioning respectively. The first part of (5.27) is an example of the former while the second expression is an example of the latter.

Venkatakrishnan[156] investigated the use of a lower order preconditioning based upon the block Jacobi method and a lower order approximation to the spatial discretisation. It was shown that for stiff problems the use of lower order approximations may lead to a scheme that does not converge. The use of an implicit operator that is consistent with the right hand side evaluation is therefore desirable. Block Jacobi provides a relatively simple preconditioner which when combined with a matrix free approach produces a numerical scheme with low memory overheads that is easily parallelised. Unfortunately block diagonal preconditioning is generally ineffectual, see for example the discussion in Qin[157]. In order to overcome these problems Qin and Richards[158] propose a variant of block diagonal preconditioning in which a damping factor, α, is introduced,

$$(\alpha + \mathbf{D}^{-1}\mathbf{A})\mathbf{Q}^{k+1} = \mathbf{D}^{-1}\mathbf{b} + \alpha\mathbf{Q}^{k} \tag{5.28}$$

The resulting multilevel iterative solver, α-GMRES, retains the desirable properties of the underlying block diagonal scheme and was found to be efficient for a wide range of problems.

The approximately factored schemes discussed earlier are good candidates for the preconditioning matrix. Schemes based upon approximate factorisation and incomplete

LU decomposition have found widespread application in the solution of the implicit system arising from CFD problems. Badcock et al[135,137] have shown that approximate factorisation provides a fast and efficient means of preconditioning the unsteady Navier-Stokes equations. Replacing the right hand side of Equation (5.18) with the matrix vector product **Ax** we obtain,

$$\left[\mathbf{I}+\Delta t\frac{\partial \mathbf{R}_x(\mathbf{Q}^n)}{\partial \mathbf{Q}^n}\right]\left[\mathbf{I}+\Delta t\frac{\partial \mathbf{R}_y(\mathbf{Q}^n)}{\partial \mathbf{Q}^n}\right](\mathbf{S})=\mathbf{Ax} \qquad (5.29)$$

then the preconditioned matrix-vector product can be obtained by solving (5.29) for **S**. Furthermore the solution of (5.29) provides a good initial solution for the Krylov subspace method.

In order to reduce computational cost the system of linear equation that is generated at each step of the time marching method is not solved exactly. Instead an initial solution is first obtained by factorisation and the Krylov subspace method is then applied in an iterative manner to increase the accuracy of the solution. Once the ratio of the current residual to the initial residual has been reduced below a prescribed tolerance the linear system is considered to have been solved and the solution is updated. The tolerance placed upon the solution of the linear system can therefore be considered as a measure of the factorisation error associated with the calculation and the iterative method can be viewed as a means of removing the factorisation error associated with (5.29). A major drawback of approximate factorisation is that as time step is increased the factorisation becomes an increasingly poor approximation to the system matrix. The use of approximate factorisation as a preconditioner therefore limits the maximum time step that may be used in the implicit method. Saad[159] discusses higher order preconditioning techniques based upon increasingly sophisticated representations of the system matrix **A**. Of these methods incomplete LU preconditioning appears to be the most promising and has been widely used to compute both steady and unsteady flow problems[160-1]

5.3 Newton methods

Finally, we consider Newton's method. For a system of non-linear equations of the general form,

$$\mathbf{F}(\mathbf{u}) = 0 \tag{5.30}$$

Newton's method can be derived by approximating $\mathbf{F}(\mathbf{u})$ by the affine portion of a Taylor series centred around the current estimate $\mathbf{u}^n$ thus,

$$\left(\frac{\partial \mathbf{F}(\mathbf{u})}{\partial \mathbf{u}}\right)^n \Delta^n \mathbf{u} = -\mathbf{F}^n(\mathbf{u})$$
$$\mathbf{u}^{n+1} = \mathbf{u}^n + \Delta^n \mathbf{u} \tag{5.31}$$

A solution is obtained by evaluating the function, $\mathbf{F}(\mathbf{u})$, and the Jacobian , $\frac{\partial \mathbf{F}(\mathbf{u})}{\partial \mathbf{u}}$, at the current iteration n. The solution at the new iteration level, n+1, is obtained by solving the resulting system of linear algebraic equations. The function at $\mathbf{u}^n$ is approximated by,

$$\mathbf{f}(\mathbf{u}) = \mathbf{F}(\mathbf{u}^n) + \frac{\partial \mathbf{F}(\mathbf{u}^n)}{\partial \mathbf{u}}(\mathbf{u} - \mathbf{u}^n) \tag{5.32}$$

which describes the straight line which is tangent to $\mathbf{F}$ at $\mathbf{u}^k$. The next iterate, $\mathbf{u}^{n+1}$, is formed from the intersection of $\mathbf{f}(\mathbf{u})$ with $\mathbf{u} = 0$.

A general requirement for any iterative method should be that it is convergent in the sense that for a typical iteration,

$$\|\mathbf{F}(\mathbf{u}^{n+1})\| \leq \|\mathbf{F}(\mathbf{u}^n)\| \tag{5.33}$$

Newton's method does not necessarily satisfy this requirement for a typical iteration unless the initial solution is already a sufficiently good approximation to $\mathbf{u}^n$. Despite

these difficulties Newton iteration remains of great interest because of the fact that, in exact arithmetic, the error can be shown to follow the form,

$$\left\|\mathbf{u}^{n+1}-\mathbf{u}^{*}\right\| \leq c\left\|\mathbf{u}^{n}-\mathbf{u}^{*}\right\|^{2} \qquad (5.33a)$$

that is the method converges quadratically provided that the starting solution, $\mathbf{u}^0$, is a sufficiently close approximation to $\mathbf{u}^*$. In order to improve the robustness of Newton iteration a number of hybrid methods have been suggested (see for example Dennis and Schnabel[162]) which incorporate globally convergent schemes with the locally quadratic convergence of Newton's method. One such simple modification is the damped Newton method,

$$\left(\frac{\partial \mathbf{F}(\mathbf{u})}{\partial \mathbf{u}}+\lambda \mathbf{I}\right)^{n} \Delta^{n}\mathbf{u} = -\mathbf{F}^{n}(\mathbf{u}) \qquad (5.34)$$

here $\mathbf{I}$ is the identity matrix and λ is a damping parameter chosen to ensure the global convergence of the method. The importance of Equation (5.34) is immediately apparent when it is compared with the discretised Navier-Stokes equations obtained earlier,

$$\left(\left(\frac{\partial \mathbf{R}(\mathbf{Q})}{\partial \mathbf{Q}}\right)+\frac{1}{\Delta t}\mathbf{I}\right)\Delta^{n}\mathbf{Q} = -\mathbf{R}(\mathbf{Q}) \qquad (5.35)$$

In Equation (5.35) the damping parameter, λ, is replaced by $1/\Delta t$. For smaller time steps the scheme reduces to the standard implicit method discussed in the proceeding sections, while in the limit $\Delta t \rightarrow \infty$ an exact Newton's method is obtained for the steady Navier-Stokes equations. Much of the computational effort of the Newton method arises from the need to evaluate the Jacobian and inverse Jacobian matrices at each iteration, it is therefore reasonable to expect that some performance benefits may arise from methods which avoid the need to recalculate these matrices. A simplified Newton method can be obtained by 'freezing' the Jacobian matrix after the first Newton iteration (Kim and Orkwis[163]),

$$\Delta^n \mathbf{u} = -\left(\frac{\partial \mathbf{F}(\mathbf{u}^1)}{\partial \mathbf{u}^1}\right)^{-1} \mathbf{F}(\mathbf{u}^n) \tag{5.36}$$

While the first iteration has the same computational cost as that of the standard Newton method subsequent iterations require only $O(n)$ operations for the evaluation of the matrix-vector product compared to the $O(n^2)$ operations required for the inversion of the matrix. Despite significant reductions in the operation cost for each iteration this algorithm performs poorly because the convergence rate becomes linear. More successful algorithms can be constructed by combining the exact Newton and simplified Newton iterations. The hybrid scheme then becomes,

$$\Delta^n \mathbf{u} = -\left(\frac{\partial \mathbf{F}(\mathbf{u}^k)}{\partial \mathbf{u}^k}\right)^{-1} \mathbf{F}(\mathbf{u}^n) \tag{5.37}$$

in which k is some integer less than or equal to n, for the case k=n the standard Newton method is obtained. If the Jacobian matrix is evaluated every m iterations then a single step of the modified method may be written as,

$$\begin{gathered} \mathbf{u}^{n+1} = \mathbf{u}^{n,m} \\ \mathbf{u}^{n,i} = \mathbf{u}^{n,i-1} - \left(\frac{\partial \mathbf{F}(\mathbf{u}^n)}{\partial \mathbf{u}^n}\right)^{-1} \mathbf{F}(\mathbf{u}^{n,i-1}), i = 1, \ldots, m \\ \mathbf{u}^{n,0} = \mathbf{u}^n \end{gathered} \tag{5.38}$$

Each iteration of the modified Newton method therefore combines a single exact Newton step together with $(m-1)$ simplified steps. Modified schemes of this form have been demonstrated to exhibit super-convergence, that is convergence which is greater than quadratic. In general a modified Newton method in which the Jacobian is evaluated once every m steps has a rate of convergence of order m+1 (a detailed proof is provided by Ortega and Rheinboldt[164]).

Qin[165-167] developed Newton-like methods, i.e. the sparse finite difference Newton method and the sparse quasi-Newton method, to solve problems in supersonic and hypersonic aerodynamics. In Reference (165) the sparse quasi-Newton (SQN) and sparse finite difference Newton (SFDN) methods were employed to accelerate convergence to a steady state for an inviscid nozzle problem. The method was subsequently extended for multi-dimensional problems[167] and shown to be more efficient than conventional time marching approaches. Making use of the sparsity pattern of the Jacobian matrix the SFDN method provides an efficient means to calculate the Jacobian of the linear system. In the method, the conserved variables are perturbed and the Jacobian terms calculated using the difference of the fluxes for the perturbed and unperturbed variables. By careful selection of the magnitude of the perturbation, it is possible to obtain an approximation to the Jacobian that is sufficiently accurate to ensure quadratic convergence (indeed, in exact arithmetic the 'approximate' Jacobian is exact). In the sparse quasi-Newton method the Jacobian matrix is updated using the sparsity structure of the matrix and the current evaluation of the numerical flux. This method is approximate and consequently the convergence is degraded. Qin showed that the method has super-linear convergence for the problems considered. A Newton-Krylov method employing α-GMRES was proposed in Reference (166) and applied to the solution of the locally conical Navier-Stokes equations. The methods developed by Qin are of particular interest because they seek derivative information from the numerical fluxes, rather than from analytical expressions, allowing the system to be treated as a black box. This has several advantages; Firstly, it is relatively straightforward to extend the method to arbitrary spatial discretisations and secondly the underlying algorithm (which requires repeated calculation of the numerical fluxes) is a good candidate for parallelisation.

Orkwis and McRae have applied Newton's method to the calculation of supersonic viscous flowfields[168-70]. They found that solutions could not be obtained with the exact Newton method when calculations were started from freestream conditions. In order to overcome these problems the damped Newton method was adopted. In subsequent calculations the time step was chosen based on the residual,

$$\text{e.g. } \Delta t = \frac{\Delta t_o}{\|R^n\|_2 / \|R^o\|_2} \tag{5.39}$$

here $\|R^n\|_2$ is the L_2 norm of the residual at the n^{th} iteration and Δt_o is the initial time step. The computational costs associated with each Newton iteration are such that it is imperative that quadratic convergence be obtained as quickly as possible. This point is clearly demonstrated by the results of Orkwis and McCrae which exhibit large regions in which there is little convergence, therefore the initial solution remains an important consideration.

Finally, we consider the application of Newton's method to unsteady problems. A backward Euler time discretisation of the governing equations gives,

$$\frac{Q^{n+1} - Q^n}{\Delta t} + R(Q^{n+1}) = 0 \tag{5.40}$$

where R(Q) is the spatial discretisation. This is of the general form,

$$\tilde{R}(Q^{n+1}) = 0 \tag{5.41}$$

and a straightforward application of Newton's method to (5.41) gives,

$$\frac{\partial \tilde{R}}{\partial Q^{n+1}} (\Delta Q^{n+1})^l = -\tilde{R}(Q^{n+1})^l \tag{5.42}$$

Newton iterations are performed until the system is converged. Application of Newton's method to unsteady problems has two key advantages. Firstly, the matrix on the right handside of (5.42) is generally better conditioned than the corresponding steady problem due to the presence of the timestep on the denominator of the diagonal. Secondly, a good initial solution is typically available in the form of the solution from the previous time step. Equation (5.42) is the basis of the unsteady solver developed in

the current work. Qin, Ludlow and Shaw[171] used a matrix-free Newton method to calculate the unsteady flow around a NACA 0012 aerofoil performing combined inplane and pitching motions. It was shown that provided the right and left hand sides of (5.42) are consistent quadratic convergence can be obtained, see Figure (5.8) which presents a typical convergence history for solution of the laminar flow. In Reference (171) the Baldwin-Lomax turbulence model was employed for turbulent calculations and consequently the operators on the left and right hand sides of (5.42) are inconsistent. This has clear adverse effects on the convergence of the scheme at each physical time step, see Figure (5.0) which should be contrasted with Figure (5.10). For the time step sizes considered in the study described in Reference (171) the use of a Newton method provided little improvement in accuracy at enormous additional expense. The main limitation on time step is believed to be the AF preconditioning employed, and it is expected that the Newton method will be more competitive when time step is increased.

5.4 Concluding Remarks

In this Chapter the temporal discretisation of the governing equations was considered. It was shown that for slowly varying unsteady flows the use of explicit methods was undesirable. Implicit methods were investigated and example calculations were presented which demonstrate the relative merits of approximate factorisation, preconditioned Krylov subspace methods and Newton methods for a range of problems. Considering these investigations a Newton-Krylov methodology employing GMRES with an AF preconditioner was selected for the remainder of this study. For unsteady problems a full Newton method approach is employed, although typically only a single step of the method was utilised. For steady problems a damped Newton-like method was employed to obtain accelerated convergence to the steady state.

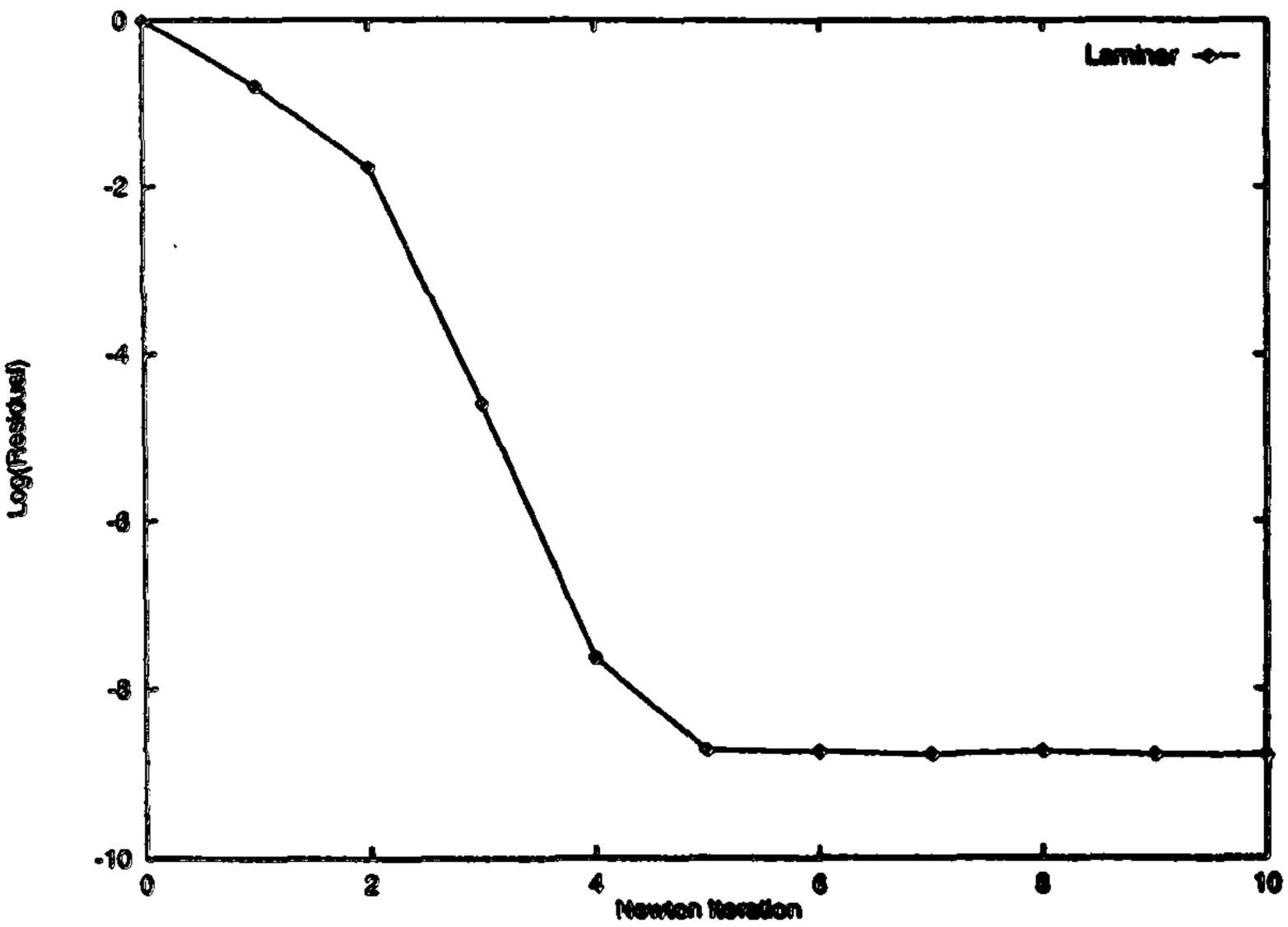

Figure (5.8) Convergence of unsteady Newton method (laminar)

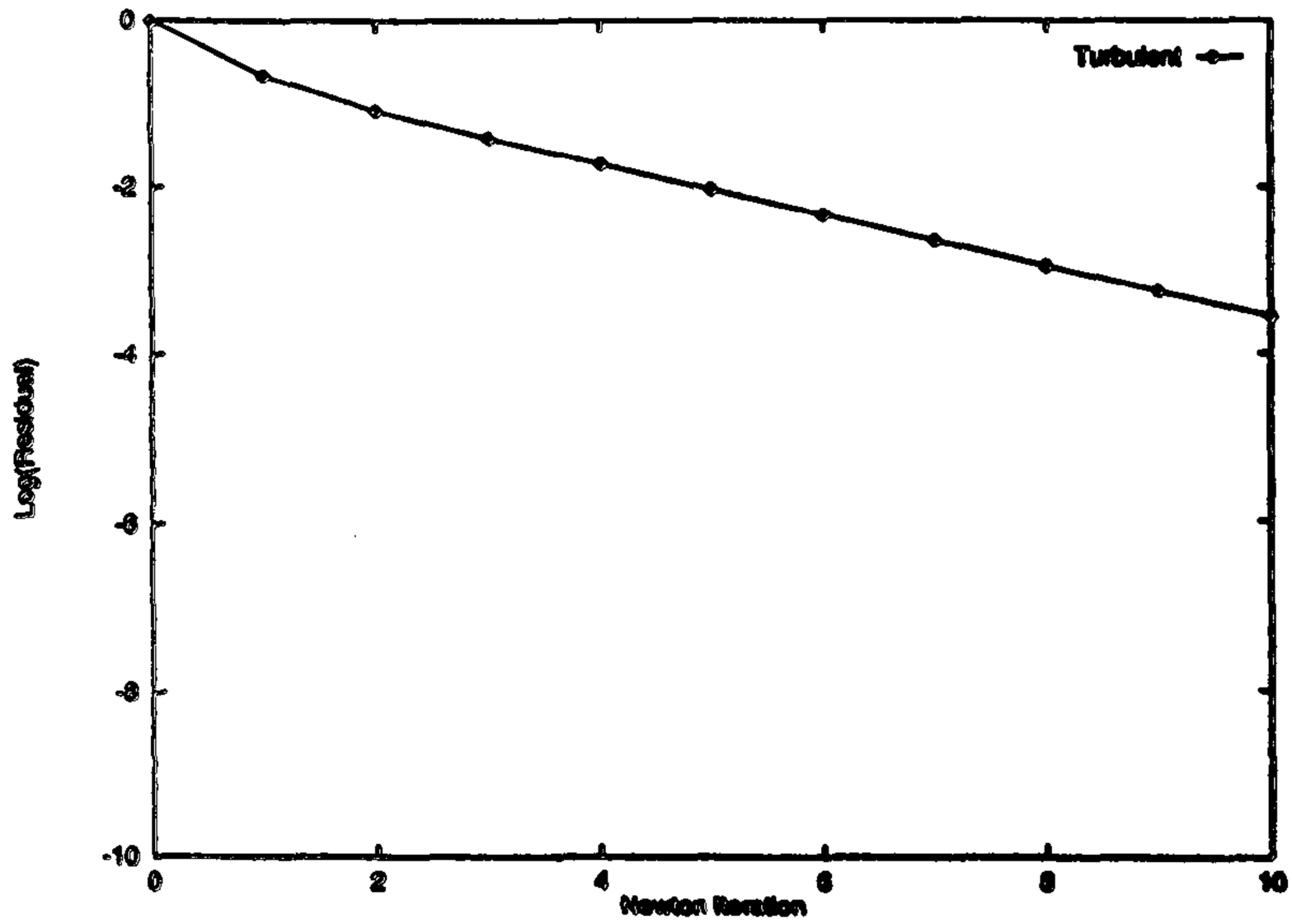

Figure (5.9) Convergence of unsteady Newton method (turbulent)

6

Steady Flow Calculations

In the previous chapters a two-dimensional unsteady model of the aerodynamics of helicopter rotors was developed. In order to demonstrate the validity of the model comparison must be made between computations and experimental measurements. In Chapters 7 and 8 comparison is made for unsteady flows. However, before such comparisons are made it is important to demonstrate that the numerical method performs adequately for steady flows. In order to meet this objective calculations of the steady flow around the RAE 2822 and NACA 0012 aerofoils are presented. Comparison of the computed pressure distributions, skin friction distributions and forces and moments are made with both experiment and independent computations, which demonstrate the range of applicability of the method.

The ability to accurately predict the aerodynamics of steady flows is an important prerequisite for the prediction of unsteady flow. In this chapter we consider the steady aerodynamics of two aerofoils, the RAE 2822 and NACA 0012 at subsonic and transonic flow conditions. For each aerofoil three combinations of Mach number, Reynolds number and angle of incidence are selected which cover a range of flow conditions including both attached and mildly separated transonic flow

6.1 NACA 0012 aerofoil

The thickness distribution of the NACA four digit series family of aerofoils is described by the following equation[11],

$$y_t = \frac{t}{0.20}\left(0.2969\sqrt{x} - 0.1260x - 0.3516x^2 + 0.2843x^3 - 0.1015x^4\right) \qquad (6.1)$$

in which t is the maximum thickness expressed as a fraction of the chord. A close inspection of Equation (6.1) reveals that the aerofoil has a blunt trailing edge. The current computational methods have been developed for single block grids with a C-type topology and are unsuitable for this aerofoil. In order to remedy this situation the chord of the aerofoil is extended in the chordwise direction until zero thickness is obtained. The aerofoil ordinates in the x-direction are then non-dimensionalised with respect to the new chord length while the ordinates in the y-direction are unchanged. This has the effect of producing an aerofoil geometry that has a sharp trailing edge and the correct thickness, however the chordwise distribution of thickness is slightly altered, a similar procedure was adopted by Holst[172]. The original and modified thickness distributions are compared in Figure (6.1). For the remainder of this thesis references to the NACA four digit series of aerofoils will refer to aerofoils having this modified thickness form.

Case	M_∞	$Re_C \times 10^{-6}$	Measured α	Corrected α[172]
1	0.700	9.0	1.86	1.49
2	0.550	9.0	9.86	8.34
3	0.799	9.0	2.86	2.26

Table (6.1) NACA 0012 aerofoil test conditions

For this aerofoil the three cases computed previously by Rumsey[173] are considered, see Table (6.1). The three cases selected correspond to experiments reported by Harris[174]. Computations were performed upon two algebraic grids to assess the sensitivity of the solution to mesh density. The finest grid was generated using an algebraic grid generation technique that ensures the grid is normal to the aerofoil in the near wall region and has 379 grid points around the aerofoil and 129 points in the aerofoil normal direction, see Figure (6.2). While the second coarser grid (having 189x65 points) was generated by removing every second point from the finer grid in

each of the co-ordinate directions, see Figure (6.3). The computations were started impulsively from freestream conditions. 500 iterations of the explicit method were performed using a CFL number of 0.2, followed by 2000 iterations of the implicit damped Newton method with a CFL number that increased from 0.2 to 100.0 as the solution progressed. Typically convergence of the residual to machine zero could be obtained with the Baldwin-Lomax model, Figure (6.4a) while the convergence of the k-ω model stalls after about a four order reduction of the residual from its initial value, Figure (6.4b).

In order to assess the sensitivity of the current computations to grid size, calculations were performed on the coarse and fine meshes for Case 1 of Table (6.1). The calculated values of lift and drag obtained using the fine grid were 0.2404 and 0.00878 respectively compared to the corresponding values of 0.2355 and 0.01059 obtained on the coarser mesh. The results show significant sensitivity to the grid. Closer examination of the calculated drag coefficient, Table (6.2), suggests that the discrepancy is related to the integration of the pressure distribution, this is demonstrated by Figure (6.5) in which the calculated pressure distributions obtained on both the coarse and fine grids are compared with experiment. Subsequent calculations were performed on the fine grid.

Model	C_l	$C_{d,p}$	C_f	$C_d = C_{d,p} + C_f$
(Experiment)	0.241	-	-	0.0079
Baldwin-Lomax[173]	0.253	0.00250	0.00547	0.0080
Johnson-King[173]	0.240	0.00263	0.00526	0.0079
Baldwin-Lomax (fine)	0.244	0.00277	0.00561	0.0083
Wilcox k-ω (fine)	0.241	0.00280	0.00599	0.0088
Wilcox k-ω (coarse)	0.236	0.00469	0.00593	0.0106

Table (6.2) Comparison of computed and measured force coefficients, Case 1.

In Figure (6.6) the calculated pressure distributions are compared with the experimental measurements of Harris[174]. The pressure distributions obtained using the

two turbulence models are almost identical. Comparison with experiment is generally good except in the region of the aerofoil maximum thickness where the current calculations (and those reported by Rumsey[173] and Holst[172]) indicate the presence of a weak shockwave on the upper surface of the aerofoil. Computed lift and drag are compared with experimental values and the computations of Rumsey in Table (6.2). The computed lift coefficients obtained using both the k-ω and Baldwin-Lomax models are in excellent agreement with the measured values. The computed drag coefficient is disappointing, both the pressure and viscous contributions are over estimated when compared with Rumseys Johnson-King computation and consequently Rumseys good overall agreement with experiment is not reflected in the current results. However, the predicted levels of drag compare favourably with the computations reported by Holst[172].

The flow corresponding to the second case is dominated by the presence of a strong shock wave, in the region of the leading edge. This shock wave is sufficiently strong to provoke a mild separation. The boundary layer reattaches a short distance downstream of the shock wave to form a short separation bubble, the presence of which is reflected in the measured pressure, see Figure (6.7). The extent of the separation bubble in the current calculations is presented in Figure (6.8) which shows the distribution of skin friction along the upper surface of the aerofoil. The computed pressure distributions, Figure (6.7), are in good agreement with the experimental data over much of the aerofoil. However, the changes observed in the computed pressure distributions downstream of the shock due to the presence of the separation bubble are not observed in the computations. The two turbulence models are in good agreement with the exception of the shock location, which is further forward in the solution obtained with the k-ω model. Calculated lift and drag are compared with independent computations and the experimental values in Table (6.3) below. The computed lift coefficients are in fair agreement with the experimental measurements, differences are attributed to the under prediction of the pressure plateau upstream of the shock wave. Surprisingly the Baldwin-Lomax calculation provides a better estimation of the lift coefficient than the two-equation model, but this is fortuitous and is associated with the respective shock locations in the two computations. The better overall agreement of the current k-ω

model calculation with experiment is reflected in the comparison of measured and computed drag coefficients.

Finally, we consider Case 3 of Table (6.1). In this case there is a strong shock wave and significant shock induced separation. The flow reattaches downstream to form a large separation bubble. Chord-wise distributions of calculated pressure coefficient are compared with experimental measurements in Figure (6.9) and the corresponding skin friction distributions are shown in Figure (6.10). The agreement between experiment and compuatation is generally poor. This is largely due to the inability of the current methodology to correctly predicit the location and extent of boundary layer separation. The delays in separation observed in the current calculations are consistent with the work reported by Holst[172] (see for example Figure (3) of (172)). Unsurprisingly the computed force coefficients are also in poor agreement with the corresponding experimental measurements, see Table (6.4).

Model	C_l	$C_{d,p}$	C_f	$C_d = C_{d,p} + C_f$
(Experiment)	0.983	-	-	0.0353
Baldwin-Lomax[173]	0.990	0.03251	0.00376	0.03327
Johnson-King[173]	0.917	0.03023	0.00395	0.03418
Baldwin-Lomax (fine)	0.971	0.03273	0.00353	0.03626
Wilcox k-ω (fine)	0.941	0.03083	0.00430	0.03513

Table (6.3) Comparison of computed and measured force coefficients, Case 2.

(Experiment)	0.390	-	-	0.0331
Baldwin-Lomax[173]	0.492	0.04024	0.00493	0.04517
Johnson-King[173]	0.300	0.02979	0.00393	0.03372
Baldwin-Lomax (fine)	0.446	0.03805	0.00487	0.04293
Wilcox k-ω (fine)	0.419	0.03657	0.00534	0.04191

Table (6.4) Comparison of computed and measured force coefficients, Case 3.

6.2 RAE 2822

The RAE 2822 aerofoil is a supercritcial aerofoil designed to have a lift coefficient of 0.56 at the design Mach number of 0.66. This is achieved using a rooftop pressure distribution and significant rear loading. The aerofoil has been the subject of extensive numerical and physical study. The experimental database reported by Cook et al[175] contains measurements of surface pressure, skin friction and boundary layer profiles at a wide range of flow conditions.

In this work three cases corresponding to Cases 6, 9 and 10 of Cook et al[175] are considered (see Table 6.5 below). The calculations were performed at the corrected angles of incidence suggested by Rumsey[173].

Case	M_∞	$Re_C \times 10^{-6}$	Measured α°	Corrected α°[173]
6	0.725	6.5	2.92	2.54
9	0.730	6.5	3.19	2.79
10	0.750	6.2	3.19	2.81

Table (6.5) RAE 2822 aerofoil test conditions

Computed pressure and skin friction obtained using the k-ω model of turbulence are compared with experimental measurements in Figure (6.12) for Case 6 of Reference (175). The computed results are in excellent overall agreement with the experimental data. There are small discrepancies close to the leading edge which are attributed to transition effects. In the current calculations the flow is assumed fully turbulent, while in the experiment transition was fixed at x/c = 0.03. The shock location and strength are well predicted. Skin friction data are available at five chordwise locations (four on the upper surface and one on the lower). It should be noted that for the purposes of presentation the lower surface skin friction coefficients are presented as negative values. Predicted skin friction is in good overall agreement with experiment.

In Figure (6.13) calculated distributions of surface pressure and skin friction coefficients are compared with the measured data for Case 9. This case features a

stronger shock-boundary layer interaction, which is sufficient to bring the boundary layer close to separation, as indicated in Figure (6.13b). Comparison with experiment is good. Once again there are small discrepancies close to the leading edge suction peak associated with transition. However, in this case the pressure coefficient is consistently over predicted over the full extent of the rooftop. This may be improved by small adjustments to the corrected incidence. As a consequence the shock wave is slightly aft of the measured position and a little stronger. Comparison of computed and measured skin friction is once again good, the only significant discrepancies are immediately aft of the shock wave and correspond with the over prediction of pressure within that region.

In the final case (Case 10) the shock-boundary layer is sufficiently strong to provoke boundary layer separation over a significant portion of the aerofoil chord. Computed results using both the Baldwin-Lomax and k-ω turbulence models are compared with experimental measurements in Figure (6.14). For this case the results are disappointing. In both calculations separation is delayed well aft of the point recorded in the experiments. This results in a computed shockwave that is significantly stronger and much further aft. Surprisingly, the computed skin friction, Figure (6.14b), is in good agreement with experimental measurements, however the chord-wise stations for which data are available are upstream of the shock wave and downstream of the reattachment point respectively. No comparison is available within the separated region.

Cases (6) and (10) were also considered by Holst[172] and Rumsey[173]. For Case (6) all of the turbulence models considered provided similar results to those reported here. For Case (10) all of the methods based upon the Navier-Stokes equations performed poorly with the exception of methods based upon the Johnson-King[176] turbulence model.

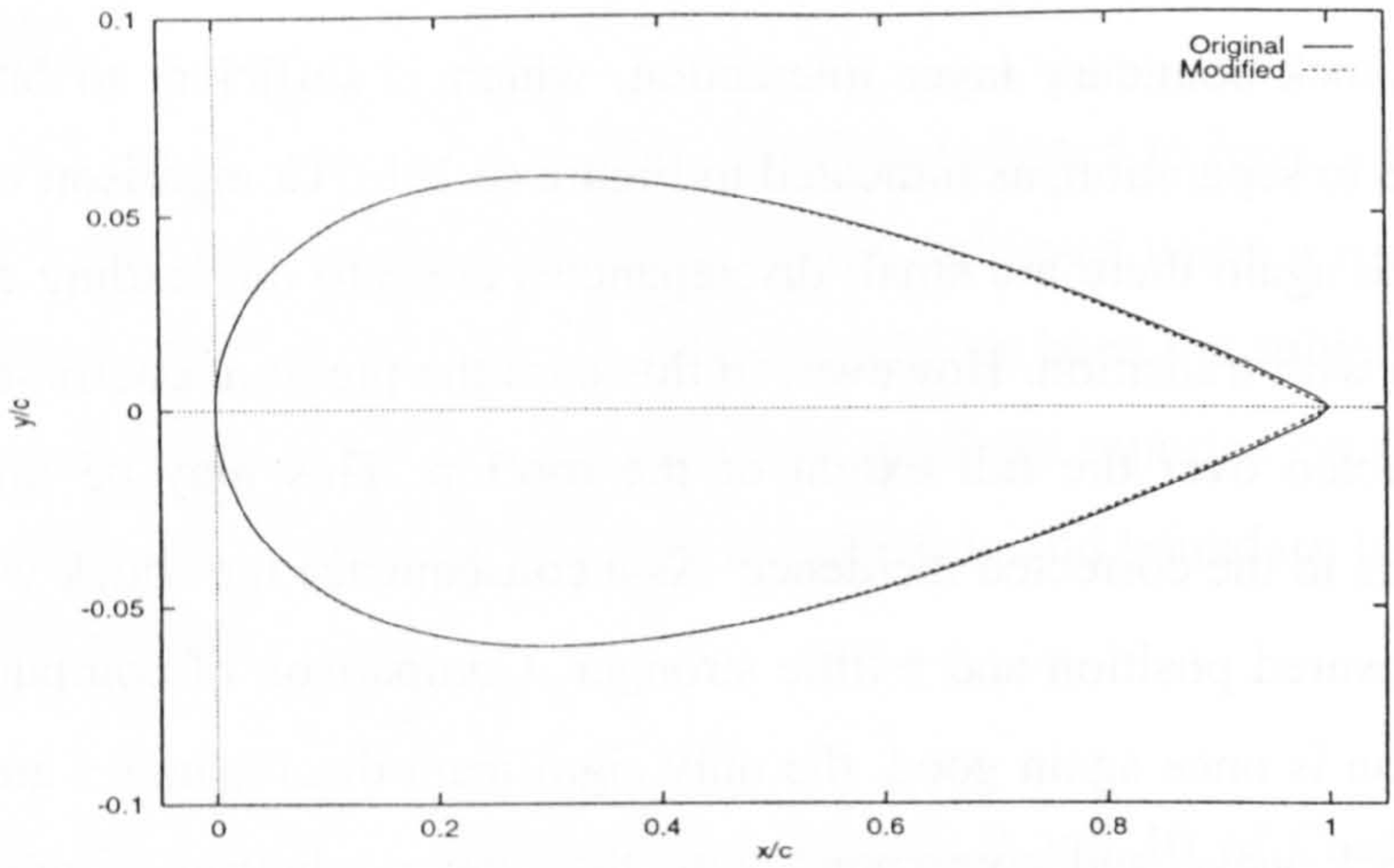

Figure (6.1) Comparison of the computational and experimental geometries

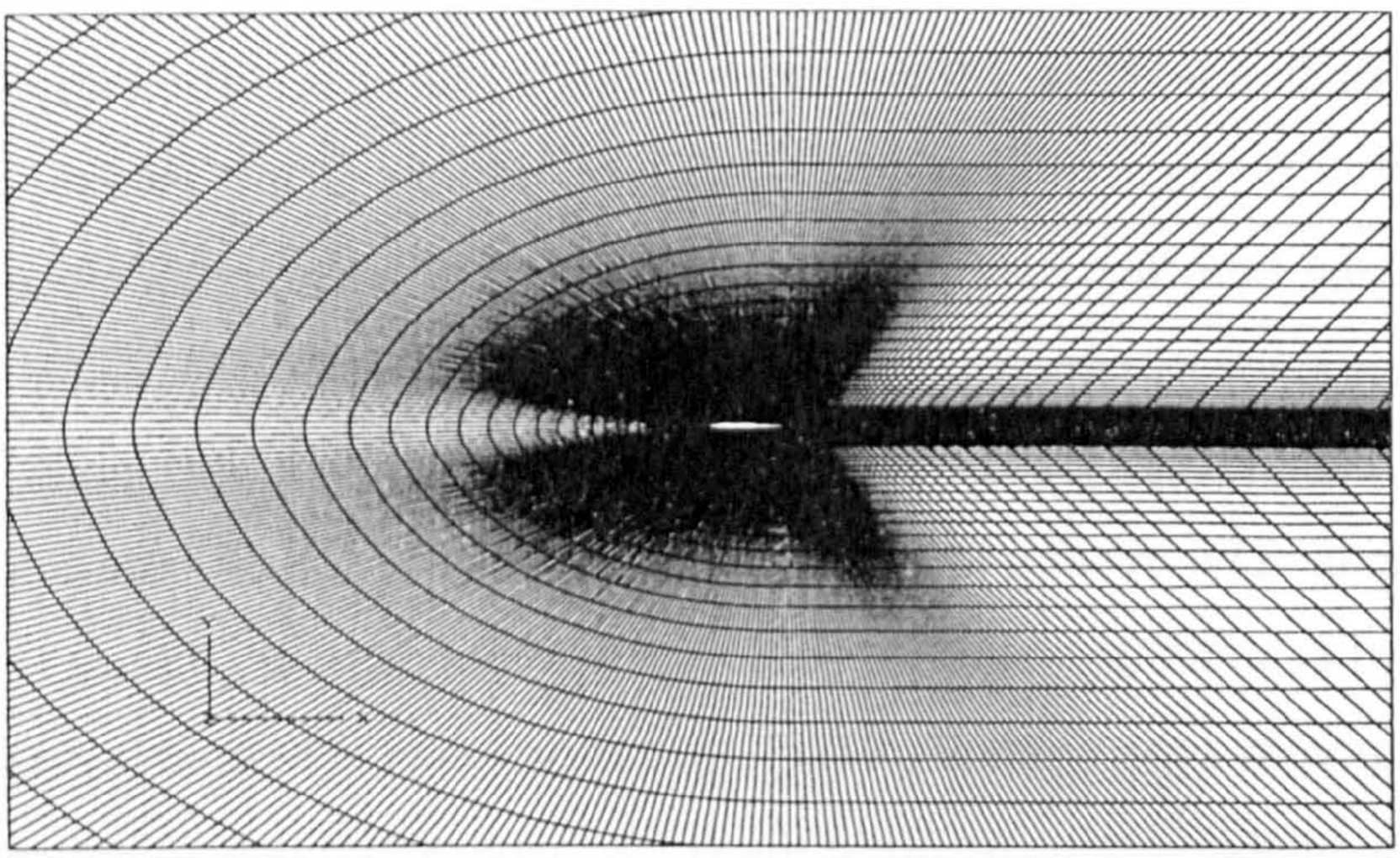

Figure (6.2) Fine grid around the NACA 0012 geometry

Figure (6.3) Medium grid around the NACA0012 geometry

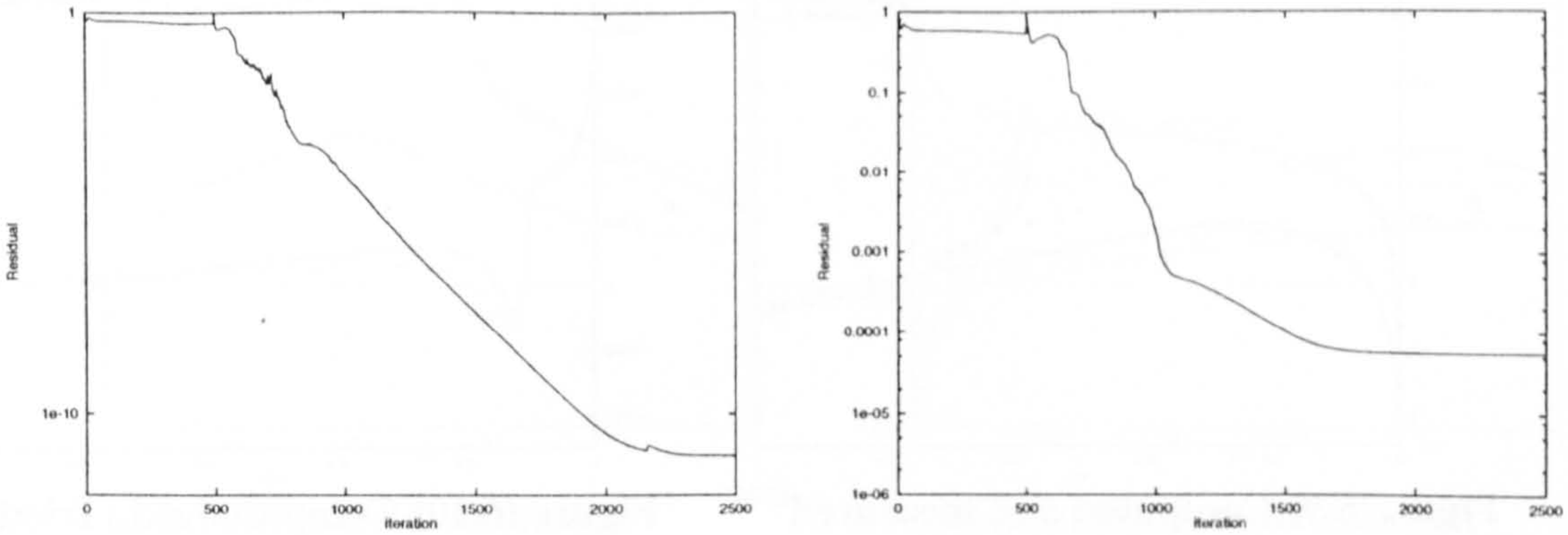

(a) Baldwin-Lomax **(b) Wilcox k-ω**

Figure (6.4) Convergence history for NACA 0012 aerofoil (Case 1)

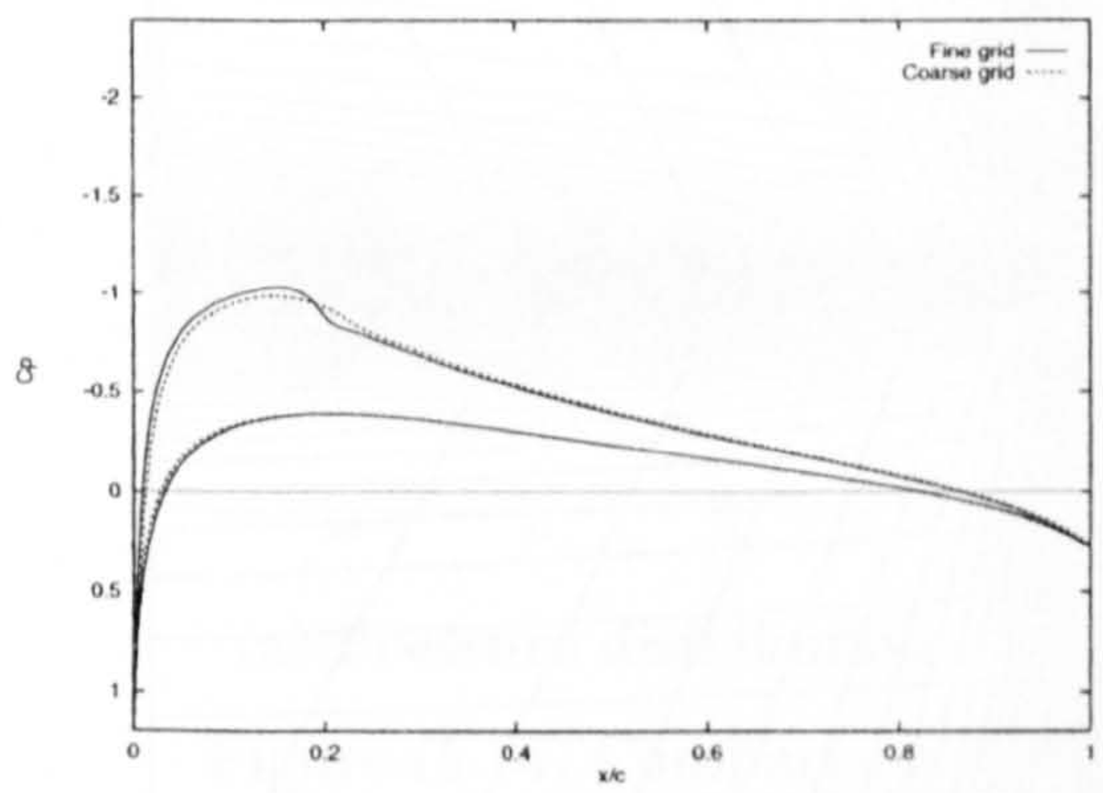

Figure (6.5) Sensitivity of solution to grid density (Case 1)

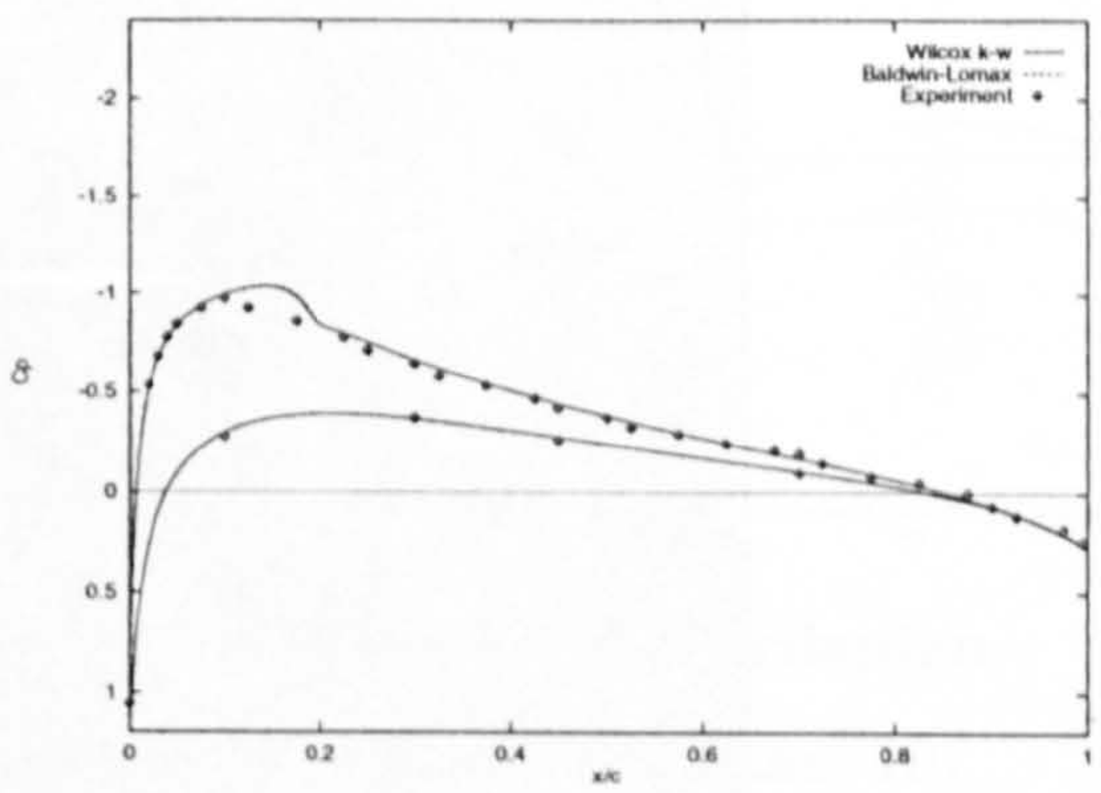

Figure(6.6) Computed and measured[174] pressure distributions (Case 1)

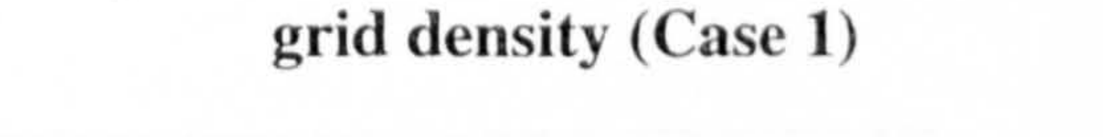

Figure(6.7) Computed and measured[174] pressure distributions (Case 2)

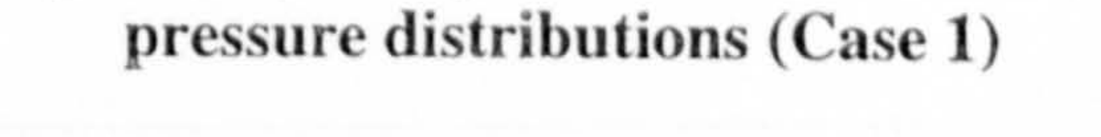

Figure (6.8) Computed skin friction distribution (Case 2)

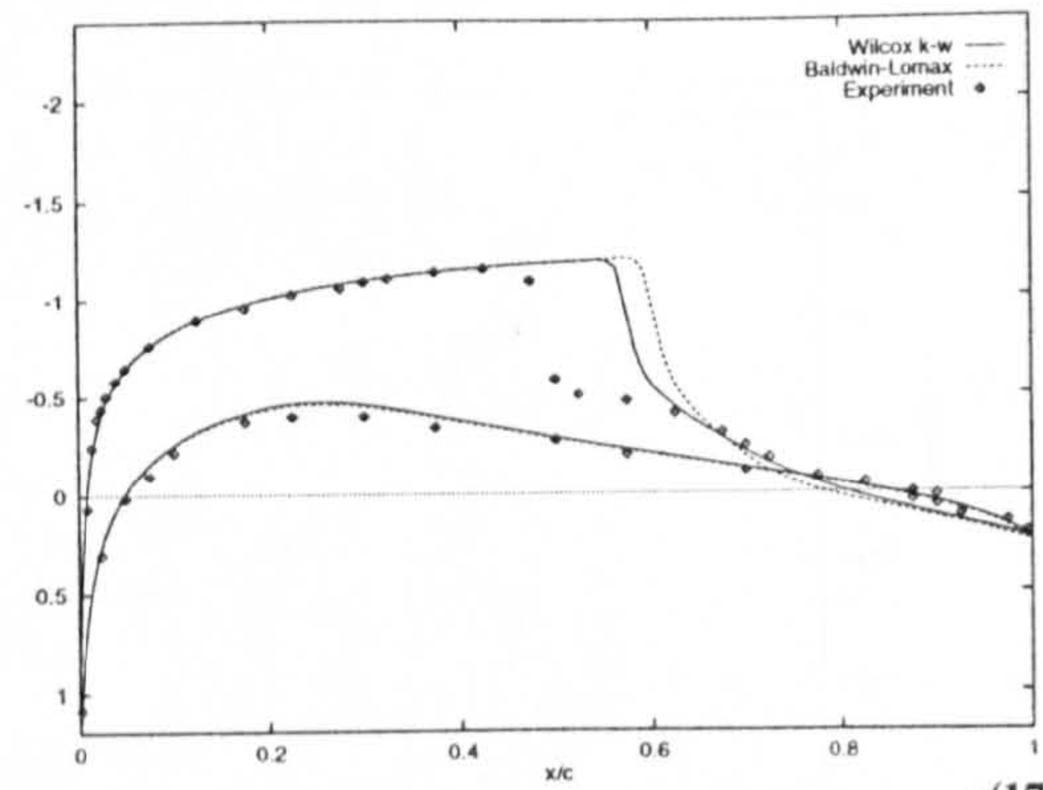

gure(6.9) Computed and measured[174] pressure distributions (Case 3)

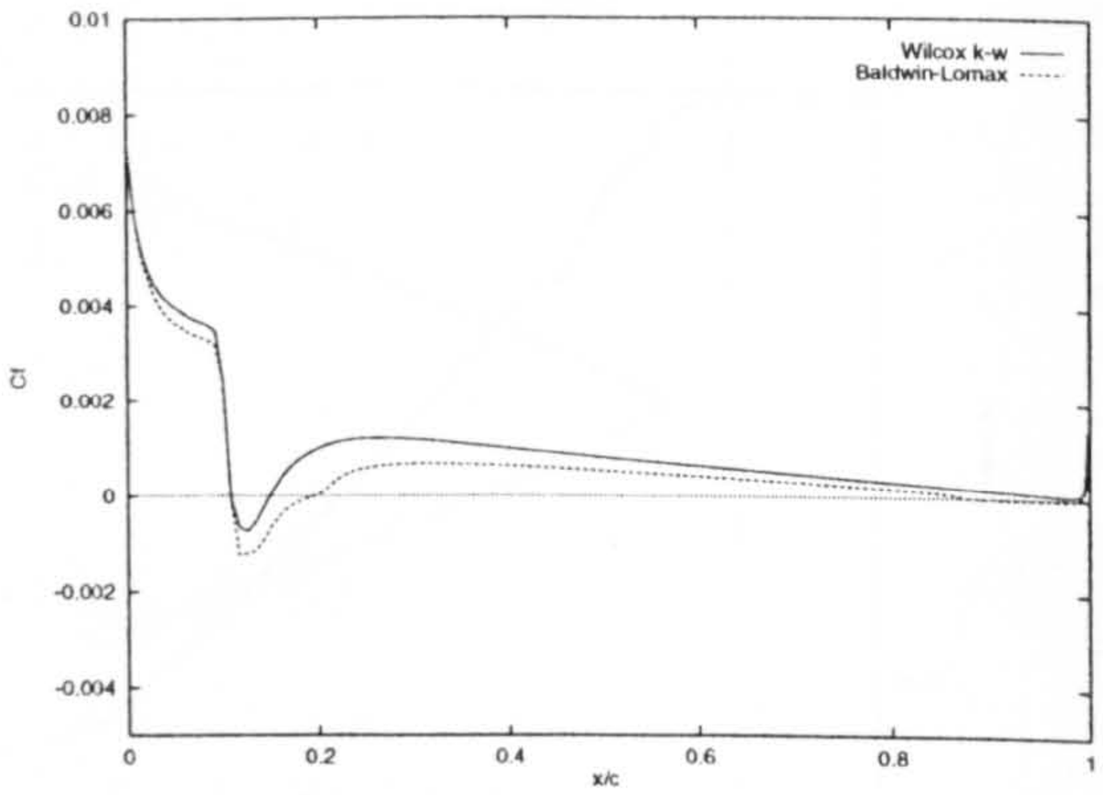

Figure (6.10) Computed skin friction distribution (Case 3)

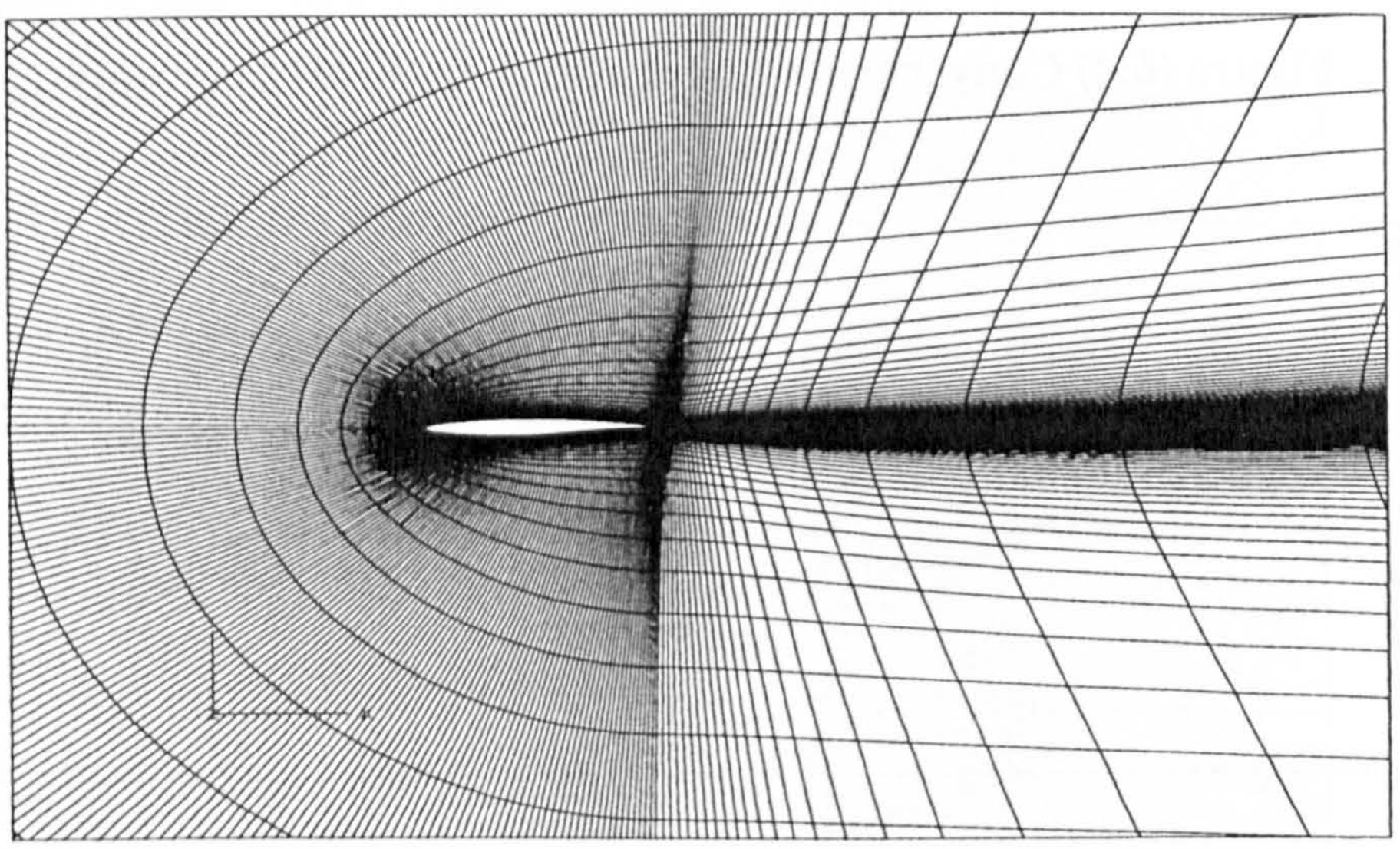

Figure (6.11) Computational grid for the RAE 2822 aerofoil

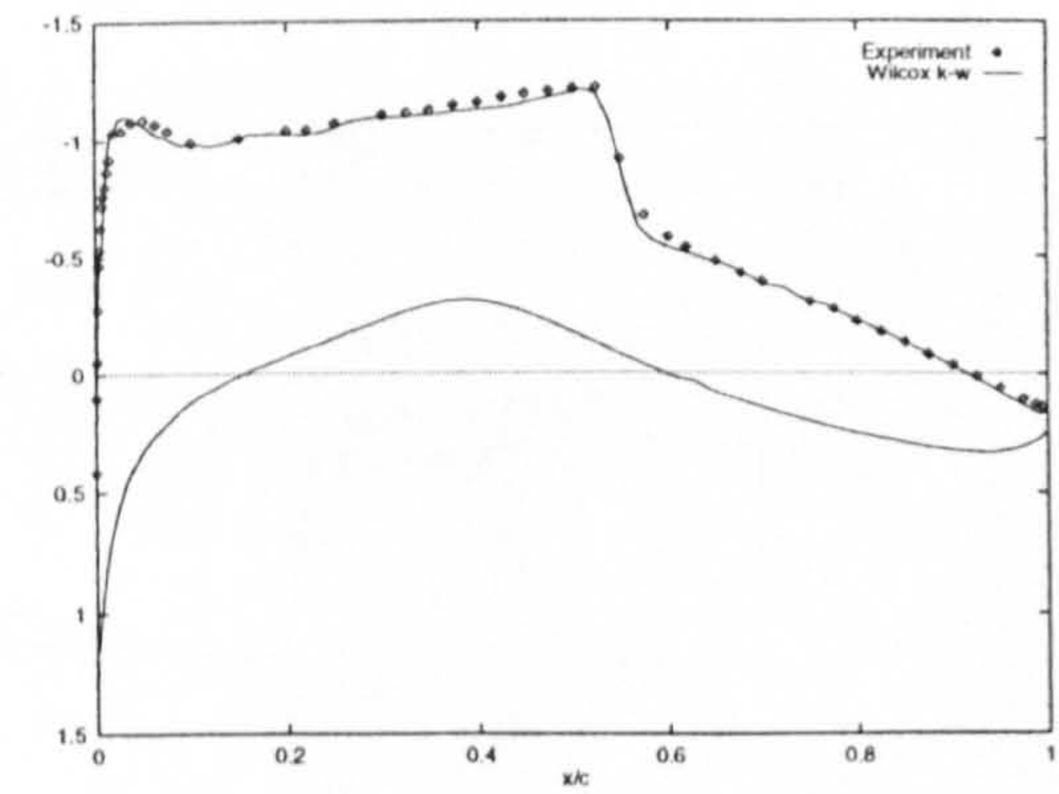

(a) Pressure distribution

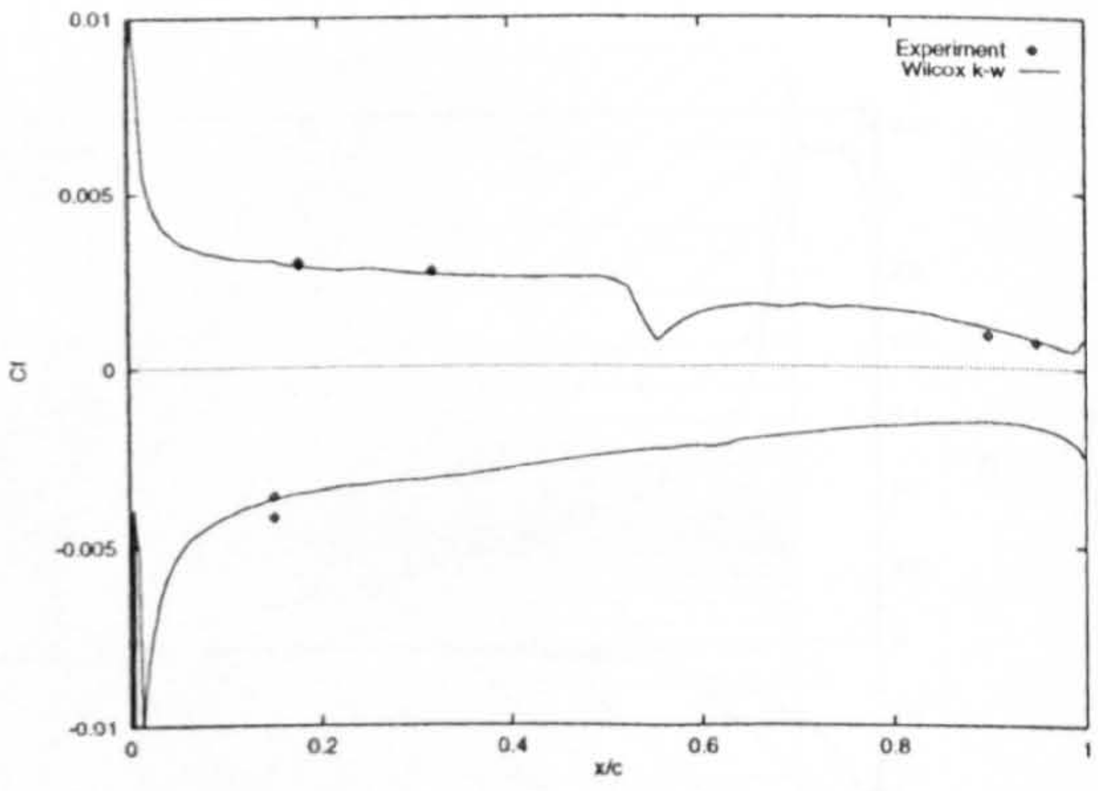

(b) Skin friction distribution

Figure (6.12) Comparison with experiment[175] – RAE 2822 (Case 6)

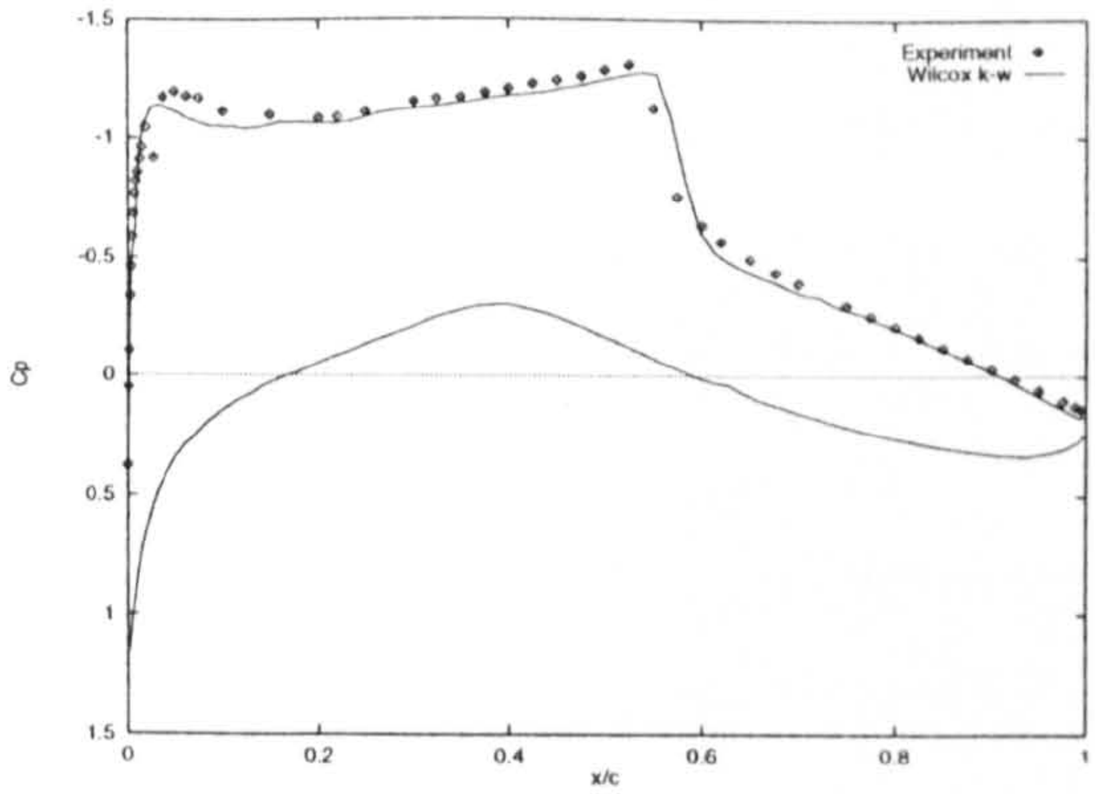

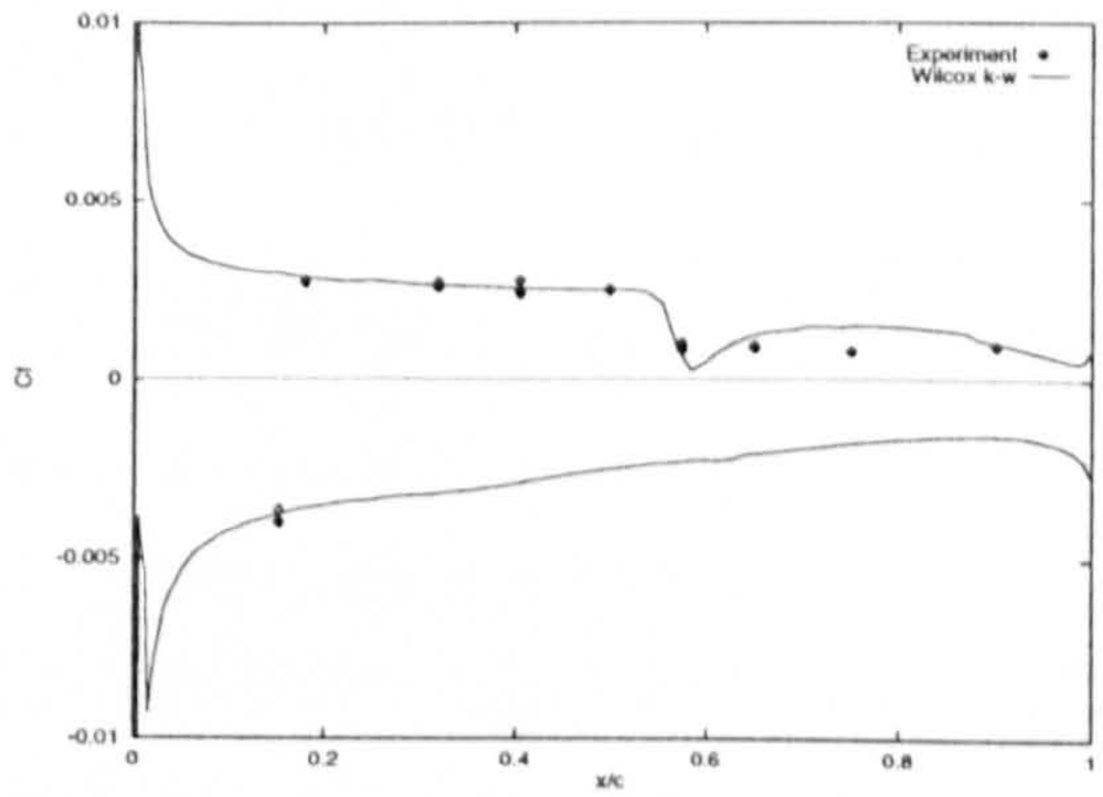

(a) Pressure distribution **(b) Skin friction distribution**

Figure (6.13) Comparison with experiment[175] – RAE 2822 (Case 9)

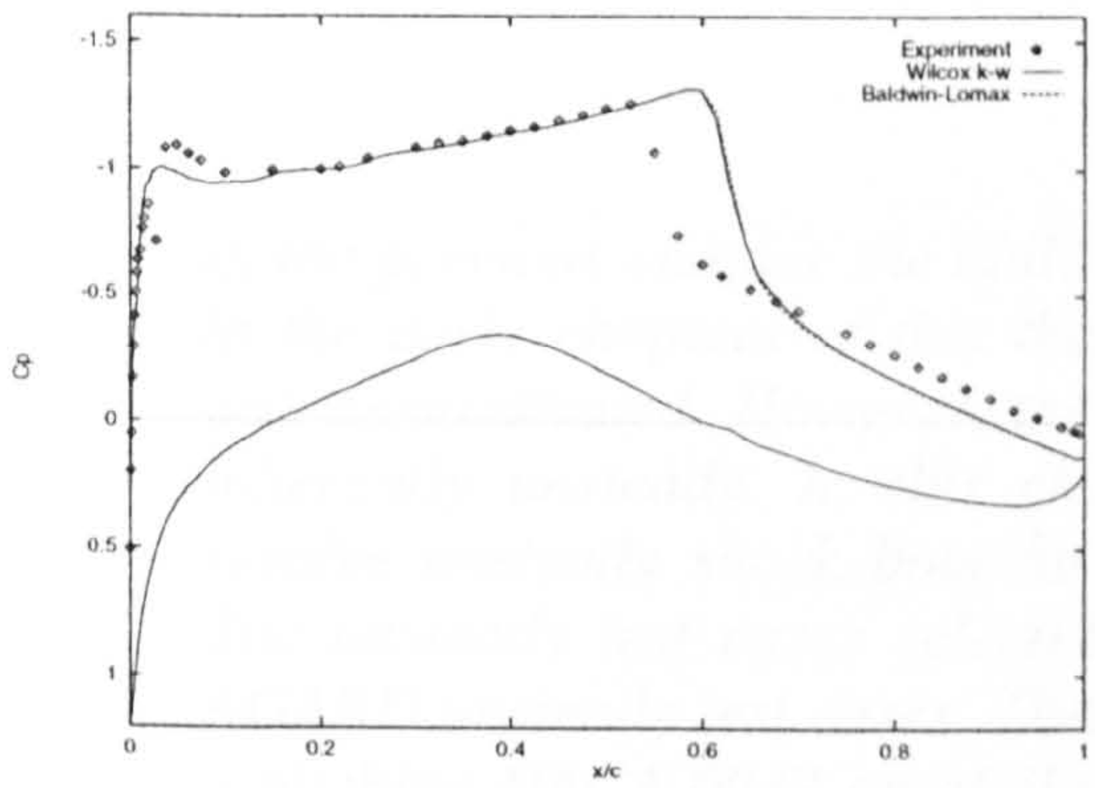

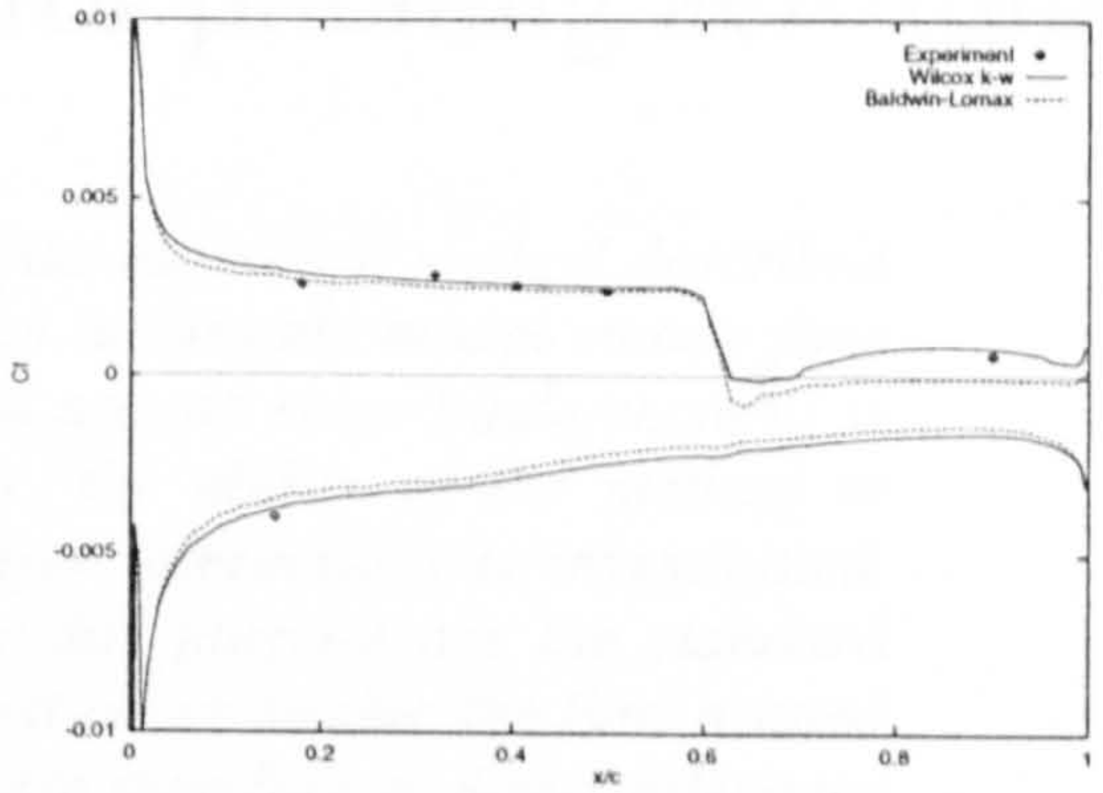

(a) Pressure distribution **(b) Skin friction distribution**

Figure (6.14) Comparison with experiment[175] – RAE 2822 (Case 10)

7

Numerical results for pitching aerofoils

In the previous chapter the ability of the numerical method described in the early chapters of this thesis to accurately model steady flow was demonstrated. However, the flow around rotor blade sections is inherently unsteady. In this chapter, the ability of the method to resolve unsteady shock boundary layer interactions is investigated. The unsteady test cases selected for this purpose are the standard AGARD unsteady test cases. These test cases involve the flow around a pitching NACA 0012 aerofoil and are therefore of direct relevance to a proper understanding of the advancing blade aerodynamics.. Computations performed for this class of motion demonstrate the ability of the proposed method to accurately resolve unsteady shock-boundary layer interactions.

In order to establish confidence in the ability of the numerical to accurately resolve unsteady shock-boundary layer interactions, calculations have been performed for the unsteady flow around pitching aerofoils. The aerodynamics of pitching aerofoils has been studied extensively, both numerically and experimentally, because of the importance of this motion in helicopter aerodynamics and aircraft aero-elasticity. In the following Chapter unsteady oscillatory pitching of the aerofoil about the quarter chord point is considered. For this motion the instantaneous angle of attack can be determined from,

$$\alpha(\tau) = \alpha_o + \Delta\alpha\sin(k\tau) \tag{7.1}$$

in which α_o , k and $\Delta\alpha$ are the mean angle of attack, frequency and amplitude of the unsteady motion respectively. Motions of this type have direct relevance to the understanding of the aerodynamics of the retreating blade, see for example the discussion of Chapter (2). By careful selection of the main physical parameters it is possible to construct test cases that highlight two important flow regimes. With a relatively high free-stream velocity, close to or beyond the critical Mach number, the flowfield is dominated by the effect of an unsteady shock system and its interaction with the boundary layer. This class of flow problems is therefore useful in demonstrating the ability of the numerical method to capture aerodynamic phenomena associated with the advancing side of the helicopter rotor. With a more modest free-stream velocity but large pitch amplitude dynamic stall is obtained. Within this regime the flow is characterised by the effect of leading edge separation and the formation of a strong dynamic stall vortex. The subsequent motion of this vortex dominates the development of the unsteady flowfield and the resultant forces and moments. While dynamic stall is three-dimensional in nature the ability to correctly predict the phenomenology of two-dimensional dynamic stall is a prerequisite for the successful understanding of the aerodynamic problems of retreating blade stall.

7.1 AGARD Two-dimensional Aeroelastic Configurations

AGARD have established a number of standard configurations for use in the development and validation of theoretical methods for the prediction of aeroelastic responses and their associated unsteady aerodynamics[177]. Lambourne[178] has collated experimental measurements for the standard configurations. For the purposes of the present comparisons the experimental data set of Landon[179] is employed. The data presented by Landon have been extracted from a larger scale experimental program[180] whose main purpose was to examine the conditions of dynamic stall at reduced frequencies and pitch rates similar to those experienced by helicopter rotors.

The experimental data were obtained for a NACA 0012 aerofoil in the ARA two-dimensional wind tunnel using the pitch-heave rig described by Landon[181]. Experimental conditions are summarised in Table (7.1) below. In Landon's experiments the model Reynolds number closely matched that of the application for

which the measurements were gathered and consequently no external devices were employed to promote transition. Data are presented for instantaneous values of the pressure, normal force and pitching moment coefficients. The forces and moments were evaluated from the measured differential pressures using the following integrals,

$$C_n' = \int_0^1 \Delta C_p \, d\left(\frac{x}{c}\right) \tag{7.2}$$

$$C_m' = \int_0^1 \Delta C_p \left(0.25 - \left(\frac{x}{c}\right)\right) d\left(\frac{x}{c}\right) \tag{7.3}$$

where the use of a prime indicates the uncorrected wind tunnel measurements. Corrections to the instantaneous angle of incidence, integrated forces and moments and Mach number for wind tunnel constraint effects were then applied based upon quasi-steady considerations.

Case	M_o	$\alpha°_o$	$\Delta\alpha°$	Re_c	K
CT 1	0.6	2.89	2.41	4,800,000	0.0808
CT 2	0.6	3.16	4.59	4,800,000	0.0811
CT 3	0.6	4.86	2.44	4,800,000	0.0810
CT 5	0.755	0.016	2.51	5,500,000	0.0814

Table (7.1) Experimental conditions[179]

A range of physical models have been used to compute the unsteady flow around the NACA 0012 aerofoil at conditions corresponding to the experiments of Landon[179]. Edwards[182] employed the TSD equation to successfully compute the unsteady forces and moments for a NACA 0012 aerofoil oscillating in pitch. Subsequently Sankar[183] solved the conservative full potential equation using approximate factorisation. Calculated normal force coefficient is in good agreement with experiment. For case CT5 comparisons of calculated pressure and pitching moment coefficients were also presented. Generally the shock wave was predicted upstream of the measured location

and the pressure immediately downstream of the shock wave was over-predicted. Despite this comparison of computed pitching moment coefficient with experiment is good, the general character of the curve is well predicted, although the level of pitching moment is over predicted for most of the upstroke.

Venkatakrishnan[184] solved the Euler equations for CT1 using a three stage Runge-Kutta scheme. The technique of residual smoothing was extended in a form which allowed the use of modest Courant numbers (CFL=5) while retaining time accuracy. Good agreement was observed between computed and measured normal force and pressure coefficients over the full incidence range. Further solutions of the Euler equations were presented by Kandil[185] and Borel[186]. The former employed the Beam-Warming implicit scheme while Borel computed the unsteady flow by means of a time discretisation based upon a combination of the one step Lax-Wendroff scheme and residual smoothing.

Gaitonde and Fiddes[139,187-90] have presented an extensive study of two-dimensional pitching aerofoils. The Euler equations were solved using a dual time stepping procedure for periodical motions of the aerofoil. More recently the methodology has been extended for viscous flows and solutions of the turbulent Reynolds averaged Navier-Stokes equations have been published[189-90]. In their work some confusion seems to have arisen over the correct axis for use in the determination of pitching moment coefficient. Gaitonde[187] found that a movement of the moment centre from the quarter chord point to a point slightly downstream (27.3% of chord) produced better agreement between calculated and measured pitching moment coefficients for case CT1. This can be most readily seen in Figure (6) of Reference (187). However, as is clear from the discussion of the experimental data reduction[179] the pitching moment is not measured directly using a balance (as is implicitly assumed by Gaitonde) but is deduced from the measured pressure distribution. The location about which pitching moment should be determined is therefore unambiguous.

Badcock[191] has offered a plausible explanation for the general improvement observed when the pitch centre is moved aft. Typically the shock wave predicted using

solutions of the Euler equations is aft of that observed in the corresponding viscous flow. When the shock wave lies behind the pitching centre this will have the effect of increasing the nose down contribution to pitching moment. If the position about which the pitching moment is moved aft then the moment arm corresponding to the nose down pitching moment is reduced while at the same time the nose up moment arm is increased. Consequently, the overall effect will be to reduce pitching moment. By careful selection of the pitch centre it is possible to balance the contributions from the nose up and nose down pitching moments in such a way that the 'correct' viscous result can be obtained using an inviscid method.

Badcock[135,137,191-194] has published a series of papers in which an unfactored implicit method based upon a preconditioned CGS solver is developed for solution of the unsteady thin layer Navier-Stokes equations with a turbulent contribution to viscosity calculated using the Baldwin-Lomax model. More recently[191] the implicit solver has been used within a dual time stepping framework to obtain solutions with of the full Navier-Stokes equations and a loosely coupled k-ω turbulence model. Solutions obtained using the two methods compare favourably with both experiment and other published solutions.

Rumsey[173] compares the capabilities of two upwind schemes, the FDS scheme of Roe and the FVS method of van Leer for the unsteady flow around pitching aerofoils. In the limit of infinite mesh size, Rumsey concludes that the FVS and FDS schemes produce identical results, but the FDS scheme is generally found to be more accurate for a given mesh size. However, the improved accuracy of the FDS scheme must be offset against a reduction in the maximum CFL number which can be employed. It is not clear why the CFL number of the FDS should be restricted in this manner. Rumsey also considered the influence of turbulence modelling on the computed forces and moments. Calculated normal force coefficients obtained using the Baldwin-Lomax turbulence model compare favourably with those measured in the experiments of Landon[179], while the pitching moment coefficient was under predicted over the full incidence range. Application of the one-equation Johnson-King model significantly improves the prediction of pitching moment coefficient over the lower incidence range,

however the behaviour of the predicted normal force is markedly different from that observed experimentally and computed using the Baldwin-Lomax model. These discrepancies appear to arise as a consequence of the computed shock location. In the Baldwin-Lomax calculations the strength and location of the shock wave are in good overall agreement with experiment, however corresponding calculations using the Johnson-King model predict the shock wave to be much further forward than is observed in the experiments, this observation is consistent with earlier steady flow calculations presented by Rumsey[173].

Thomadakis[195-6] solved the full Navier-Stokes equations to obtain the unsteady flow around the NACA 0012 aerofoil at conditions corresponding to the AGARD CT5 test case. For turbulent flows the algebraic model proposed by Baldwin and Lomax was employed. The mean incidence of the CT5 test case is 0.016° which is sufficiently close to zero that a near symmetric solution should be expected. Thomadakis' calculations appear to confirm that this is indeed the case. However, the experimental data is clearly not symmetric.

7.2 Unsteady calculations

Before examining in detail the results that have been obtained using the present methodology it is helpful to make a few general remarks regarding the manner in which the current calculations have been performed. The first stage of the numerical procedure was to obtain converged steady solutions at the mean flow conditions. Initially a small number of explicit iterations were performed (between 500 and 1000) at a CFL number of 0.2. The explicit iterations were followed by 500 steps of the damped Newton method described in Chapter (5) with a CFL number that increased linearly with reductions in the non-dimensional residual up to a maximum value of 100.

The unsteady solution was then started impulsively from the flowfield obtained for the mean flow conditions. This choice of initial conditions was to a large extent arbitrary, however it was found that while the initial behaviour of the solution was dependent upon the initial flow conditions the periodic solution was not. The initial behaviour of the solution is dominated by 'spurious' transients generated due to the

impulsively started flow. These transients are rapidly damped and the solution can be considered to have converged to the periodic solution within about one half of the first cycle. This behaviour is typical of the flow development in all of the cases considered subsequently, for this reason the data discussed below are taken from the third cycle of the unsteady motion.

The grids described in Chapter (6) for the NACA 0012 aerofoil were used in the current computations. The computational grids are shown in Figures (6.2) and (6.3) for the coarse and fine meshes respectively. Computations performed with a Krylov subspace size of 20 on the fine grid require approximately 500Mb of main memory on the Silicon Graphics Origin 200 system installed at Cranfield University, while the coarser grid requires approximately 125Mb of main memory.

Calculations were performed on the two grids to determine the sensitivity of the solution to mesh spacing. Results obtained for the CT1 test case are shown in Figure (7.1) which shows the computed normal force and pitching moment obtained with the k-ω turbulence model. The results cannot be considered to be fully grid converged, but further refinement of the grid was not possible due to computational constraints. The differences that are observed in the computed forces and moments arise as a consequence of relatively small changes in the shock location and shock strength. It is believed that further refinement of the grid is unlikely to lead too significant further changes in the resolution of the shock wave.

Extensive numerical tests were performed to determine the sensitivity of the computed solutions to the remaining numerical parameters. These parameters can be subdivided into two main groups, those associated with the spatial discretisation, such as mesh size, order of accuracy and limiter strength, and those concerning the temporal discretisation, time step, subspace size and GMRES tolerance. The main details of these tests are summarised in Table (7.2)

The solutions can be considered to be converged with respect to time step. However the use of the largest time step is not optimal. This is because there is a trade off

between reduced number of time steps and the convergence of the implicit scheme at each time step. As time step is increased the matrix appearing on the left hand side of (5.12) becomes less diagonally dominant and at the same time the factorisation becomes a poorer approximation to the flux Jacobian. These changes are reflected in an increase in the number of GMRES iterations required to meet the specified tolerance and a general reduction in the robustness of the scheme. This latter point is reflected in the larger subspace size required to ensure convergence on the fine grid. Further, in the case of the Baldwin-Lomax calculations it was found that converged solutions could not be obtained without a reduction in the time step size.

Case	Time Step, $\Delta\psi°$	Order	Limiter, ε	GMRES Tolerance
CT1	0.25	3	10^{-5}	0.005
CT1	0.25	3	10^{-7}	0.005
CT1	0.25	3	10^{-9}	0.005
CT1	1.0	3	10^{-7}	0.005
CT1	0.5	3	10^{-7}	0.005
CT1	0.33	3	10^{-7}	0.005
CT1	0.25	3	10^{-7}	0.050
CT1	0.25	3	10^{-7}	0.500

Table (7.2) Numerical experiments

In order to reduce computational cost the system of linear equations that is generated at each time step is not solved exactly. Instead an initial solution is first obtained by factorisation, restarted GMRES is then applied in an iterative manner to increase the accuracy of the solution. Once the ratio of the current residual to the initial residual has been reduced below a prescribed tolerance the linear system is considered to have been solved and the solution is updated. The tolerance placed upon the solution of the linear system can therefore be considered as a measure of the factorisation error associated with the calculation and for this reason must be considered in conjunction with the time step size. It is expected that for a given overall accuracy larger time steps (which imply

larger factorisation errors) will require that a much smaller tolerance be imposed. However, for the values of this parameter considered no differences could be observed between the calculations.

Unless otherwise stated the calculations described in the remainder of this chapter were performed on the fine grid using the third order scheme, a limiter value of $\varepsilon=10^{-7}$, a GMRES tolerance of 0.005 and a subspace of 10.

(a) AGARD CT 1

In this example a NACA 0012 aerofoil set at an incidence of $\alpha = 2.89°$ in a flow with a freestream Mach number of $M_\infty = 0.60$ and a Reynolds number of $Re_c = 4.80$ million is pitched about its quarter chord with an amplitude of $\Delta\alpha = 2.41°$ and a reduced frequency of $k = 0.0808$. Unsteady calculations on the fine grid employed 1080 and 2160 time steps per cycle respectively for the two-equation and Baldwin-Lomax model calculations.

Figure (7.2) shows the variation of computed pressure with time. By observing the variation between consecutive time steps it is possible to catalogue the shock motion according to the classification scheme developed by Tidjeman. In this case the flowfield is initially subsonic, as the angle of attack is increased the flow is accelerated around the leading edge of the aerofoil, this is reflected in a gradual reduction in the leading edge pressure coefficient, eventually becoming locally supersonic. The supersonic pocket extends a short distance along the aerofoil chord and is terminated by a shock wave. As incidence is increased further the shock wave increases in strength. Significant hysterisis effects are observed as the incidence reaches its peak value and begins to fall. As incidence is reduced the shock wave weakens and the flow becomes subsonic once more. From Figure (7.2) it can be seen that the shock wave disappears over a significant proportion of the period and the unsteady flow should therefore be classified as Type B. This is in agreement with the flow classification obtained from Landon's experimental measurements[179].

Figure (7.3a) compares the calculated normal force with experimental measurements. The unsteady computations are generally in good agreement, however there are relatively large differences between the two models during the final stages of the upstroke and the initial stages of the down stroke. The Baldwin-Lomax calculation predicts increased loading over that obtained with the k-ω model. Comparison of the unsteady computations with the measured data is encouraging, the k-ω calculations appear to be in close agreement with the experimental data except for the latter stages of the down stroke. A similar comparison of the computed pitching moment with experiment, Figure (7.3b), is less promising. There are significant differences between the results obtained using the algebraic and two-equation turbulence models over the whole cycle. The data obtained using the k-ω model consistently over predict the pitching moment coefficient when compared with similar data obtained from the Baldwin-Lomax calculation. Comparison with experiment is relatively poor over much of the cycle, the Baldwin-Lomax calculation appears to agree closely with the experimental data during the upstroke while the k-ω model computation can only be considered to be good over the latter stages of the upstroke. The current predictions of computed normal force and pitching moment are in broad agreement with previous calculations performed using the Euler equations, Gaitonde[187-190], and the thin-layer Navier-Stokes equations, Badcock [193].

Also presented in Figure (7.2) are the measured pressure coefficients. A number of general observations can be made concerning the comparison of the computed and experimental data. Firstly, the computed value of trailing edge pressure is consistently over predicted when compared with experiment, this is most likely due to differences in geometry between the aerofoil employed in the experiments and computations. Modifications required to the basic NACA 0012 aerofoil trailing edge geometry to allow the use of a C-type grid have been discussed in Chapter (6), furthermore the aerofoil used in the experiments was manufactured with a blunter trailing edge than employed in the basic NACA 0012 thickness distribution. The second key difference between the computed and measured pressure distributions concerns the peak in pressure coefficient close to the leading edge which is under predicted when compared with the experimental data. Such behaviour is often related to poor leading edge grid

resolution, but a comparison of the fine grid and coarse grid calculations does not provide firm evidence that this is the case for the current calculations. Finally, the development of the shock wave seems to lag that of the experiment, during the upward motion of the aerofoil the computed shock is further forward and much weaker than observed in the experiments. The computed shock wave agrees more closely with experiment as the aerofoil approaches the extremes of its motion and the incidence begins to fall. During the down stroke, the computed shock is again weaker and further forward than measured in the experiment. The latter observations are consistent with a mismatch of the instantaneous flow conditions at the respective points in the experiments and computations. Comparisons of the calculated data with experiment have been performed for a prescribed angle of attack, unfortunately this makes it impossible to compare the experimental and computed data at corresponding instants in time. This is because the experimental data are presented at an angle of attack that has been corrected for wind tunnel constraint effects, while the parameters describing the motion have not. The effects of this can best be demonstrated by example. Selecting the data at the 18th experimental data point we obtain azimuth angles of $\psi = 114.1°$ and $\psi = 90.03°$ respectively based upon the given (corrected) incidence and the measured time, the corresponding incidences are $\alpha = 5.09°$ and $\alpha = 5.3°$.

(b) AGARD CT 2

In the second example, the amplitude of the unsteady motion is increased to $\Delta\alpha$=4.59° while the mean flow conditions are similar to those used in the first test case, M_∞=0.60, $\alpha_0 = 3.16$, $k = 0.0811$ and $Re_c = 4.8$ million. The Baldwin-Lomax calculation employed 2160 time steps per cycle, while the k-ω calculation used 1080 time steps per cycle. Figure (7.4) presents comparison of the present computed forces and moments with experimental measurements[179]. Comparison between the experimental data and the computed normal force and pitching moment coefficients is favourable over the lower incidence range but deteriorates as the aerofoil pitches up to the maximum incidence. While the peak normal force coefficient is in line with that obtained experimentally, the normal force coefficient appears to be under predicted over the latter stages of the upstroke. Much larger discrepancies exist between the computed and measured pitching moment over a similar incidence range. The computations are in

good overall qualitative agreement with the measured data and the shape of the experimental curve is well captured, this can be seen more clearly when the data are compared with Figure (18c) of Wood[180].

As before the normal force coefficient obtained using the algebraic and two-equation turbulence models are in excellent agreement over much of the incidence range. The only significant differences that can be observed occur over the initial stages of the down stroke. While this is encouraging, comparisons of the calculated pitching moment obtained with the two models reveal significant differences between the model predictions. The discrepancy between the models is relatively small over much of the motion, however during the early part of the down stroke the k-ω model predicts much higher levels of pitching moment than observed in both the Baldwin-Lomax models and experiment. Differences between the calculations are attributed to lags between the corresponding shock motions. Calculations using the Baldwin-Lomax model predict the instantaneous shock-wave location slightly aft of that obtained using the k-ω model, this can be clearly seen in Figure (7.5).

The present results are in good agreement with those reported by Badcock[193] and Gaitonde[190]. Gaitonde[190] compares results obtained using the Baldwin-Lomax turbulence model and the one-equation model due to Johnson and King[176]. A direct comparison of the pitching moment calculated using the two turbulence models reveals a similar trend to that noted above, that is the higher order model produces predictions of pitching moment that are much greater than those obtained with the algebraic model, and hence in much poorer agreement with the experimental measurements. However, some care must be exercised in comparing the data sets in this manner as the pitching moment data presented by Gaitonde in Figure (8) of Reference (190) are calculated with the pitch centre at x=0.273c rather than x=0.250c as used in the current computations.

In Figure (7.5) the calculated instantaneous surface pressure is compared with experiment. As before the flow is initially subsonic, as incidence is increased the flow becomes locally supersonic around the aerofoil leading edge and a shock wave forms.

The shock wave moves downstream as incidence is increased and increases in strength, the maximum shock strength being achieved as the aerofoil begins its down stroke. The shock strength diminishes with further reductions in incidence until eventually the flow becomes subsonic once more. From Figure (7.5) the shock motion is identified as Type B.

Comparison with experiment is satisfactory. During the upstroke the strength of the shock wave and its location are predicted well. Similar agreement is observed during the early stages of the down stroke. However at an azimuth angle of 171° the shock location and strength are in poor agreement with experimental measurement, this discrepancy was also observed by Gaitonde[190] and Badcock[193] suggesting that the experimental data may be in error. Agreement between computed and measured pressure distributions for the remaining azimuth angles is generally good.

A close examination of the experimental data presented by Landon[179] again reveals large differences between the azimuth angles obtained using the indicated incidence and the measured time. For this case t=0 does not correspond with $\alpha = \alpha_0$, however we can identify three data points from Table (3.12) of Reference (179) that are separated by the same phase angle when the azimuth angles are calculated using both measured time and incidence. Using these three points it is possible to obtain angles of incidence corresponding to the measured time for each of the remaining data points. The calculations were repeated to obtain the instantaneous flowfield data at the new azimuth angles. Using this information the correspondence between the measured and computed normal force and pitching moment coefficients is dramatically improved, Figures (7.6a) and (7.6b) respectively. However, some caution must be exercised as the choice of data points upon which to base the transformation may be flawed. However, the comparisons obtained in Figure (7.6) serve to illustrate the problems that exist with the experimental data.

(c) AGARD CT 3

In this test case the mean angle of incidence is increased to $\alpha = 4.86°$ and the aerofoil is pitched about the quarter chord with a reduced frequency of k = 0.0810 and an

amplitude of $\Delta\alpha = 2.44°$. The remaining mean flow parameters are identical to those experienced in the first (CT1) test case. The relatively high mean angle of incidence is sufficient to ensure that a shock wave will be present over most of the cycle. Furthermore, the shock wave will generally be much stronger than in either of the previous test cases. Flow calculations were made with a time step corresponding to 0.17° of azimuth (2160 steps per cycle).

A clearly established Type B shock wave motion is evident from the instantaneous surface pressure distributions, see Figure (7.7). The corresponding experimental measurements are also shown. It is clear from this Figure that the shock wave is substantially stronger than observed in the previous test case. Despite this the computed and measured pressure distributions are in excellent agreement. The pressure plateau ahead of the shock wave is well predicted, as is the shock position and strength. During the latter stages of the upwards motion of the aerofoil the shock wave is predicted slightly upstream of the measured location while conversely during the early part of the down stroke the shock is slightly downstream of the measured location. There is evidence of a separation bubble in the experimental data that does not appear to be reflected in the computed pressure distributions. Visualisation of computed Mach contours seems to support the presence of a separation bubble. Following the disappearance of the separation bubble agreement with experiment becomes progressively worse, the calculations appear to lead the experimental measurements. Generally the peak pressures are substantially below the measured values and consequently the shock wave is further forward and much weaker.

In Figure (7.8) time histories of the computed normal force and pitching moment coefficients are compared with those measured in the experiment of Landon[179]. The computed data are in good qualitative agreement with the experiment, in particular the narrow loop in normal force coefficient shown by Wood[180] is resolved in the computation. Quantitative agreement between the computed and measured forces and moments is fair. The computed normal force is larger than the measured value over most of the incidence range, except for the loop at the extremes of the motion, in this region the normal force is generally lower than observed in experiment.

Agreement between the two turbulence models is good, as in the previous calculations the k-ω model predicts slightly lower levels of normal force than are computed with the Baldwin-Lomax model. More substantial differences are observed between the two calculations over the higher incidence range, this is most evident in the general form of the normal force loop. The narrower loop predicted in the Baldwin-Lomax calculation is more consistent with the full experimental data set presented by Wood[180] than the fuller loop obtained using the two-equation model. In contrast to the previous calculations pitching moment coefficients obtained using the two models disagree over substantial ranges of incidence.

A closer examination of the pressure distributions presented in Figure (7.7) provide the key to understanding this discrepancy. It is observed that for those azimuth angles corresponding to locally supersonic flow the location of the shock wave predicted using the k-ω model is generally further forward than that obtained in the computation performed with the algebraic model. The increase in aerodynamic loading provided by such small differences in shock location is almost negligible and consequently relatively small reductions in normal force coefficient are observed between the two-equation and Baldwin-Lomax model calculations. In contrast, pitching moment coefficient is sensitive to small changes in the pressure distribution. Ahead of the pitch centre reductions in aerodynamic loading produce a net increase in the nose down pitching moment, thus the large increase in pitching moment coefficient observed between the algebraic and two equation turbulence models is consistent with the respective shock positions shown in Figure (7.7). In the absence of a shock wave comparison between the two turbulence models improves substantially. Furthermore, when examined in this context the results obtained using the two turbulence models are seen to be consistent for all three of the test cases considered so far. In the previous two cases the shock wave was observed over a narrower incidence range and was generally weaker than in the current case, consequently differences between the pitching moment coefficients obtained using the two turbulence models were small and confined to the higher incidence range. In the present case the discrepancies are more apparent because the shock wave is present over a much larger incidence range and is stronger.

(d) AGARD CT 5

The final periodic motion considered is the AGARD CT 5 test case in which the aerofoil is pitched about α=0.016° with an amplitude of $\Delta\alpha$=2.51° at a reduced frequency of k=0.0814. The freestream Mach number has been increased to M_∞=0.755 which is close to the critical Mach number at the mean incidence. The Reynolds number is taken as Re_c=5.5 million. The increase in freestream velocity is sufficient to ensure that shock waves are present over the full range of azimuth angles. This is clear from the instantaneous surface pressure coefficients presented in Figure (7.9) which show a well-developed Type A shock motion.

In Figure (7.10) the computed normal and pitching moment coefficients are compared with experimental measurements. Poor agreement is observed over the whole incidence range, computed normal force shows reasonable qualitative comparison but consistently under predicts the measured values. The behaviour of pitching moment coefficient observed in the experiment is not reproduced by either the k-ω or Baldwin-Lomax calculation. Of concern is the fact that the computations appear to show the opposite trend to the measured data. When the absolute value of incidence is high the calculated pitching moments are of the same sign as the incidence while the pitching moment is of opposite sign to the incidence in the experimental data.

Thomadakis[195-6] observed similar behaviour when the Navier-Stokes equations were solved on a coarse grid. When the grid was refined in the streamwise direction the computational trend was reversed and the calculated pitching coefficients were in good qualitative and quantitative agreement with the experiment. However, this result is misleading, in order to reduce computational cost Thomadakis coarsened the grid in the aerofoil normal direction to maintain the same time step for a given CFL number. Computations of normal force and pitching moment coefficient performed on the current coarse and fine grids show some small differences, they are not sufficiently large to suggest that further refinement of the grid will produce substantially different results.

The mean angle of incidence of α=0.016° is sufficiently close to zero that a near symmetric solution should be expected from the computational method. Provided that the solver calculates the flow symmetrically there is in practice no need to perform a second calculation. Instead the computed data can be manipulated to provide the symmetric solution, in this case we need only multiply the incidence, normal force and pitching moment by -1. This is done in Figure (7.11) in which the k-ω solution is compared with its corresponding symmetric solution. Both calculated normal force and pitching moment coefficients show a high degree of symmetry. Also shown in Figure (7.9) are the corresponding experimental data. There are large discrepancies between the measured data and the corresponding symmetric data that go some way to explaining the discrepancies observed in Figures (7.10).

7.3 Concluding Remarks

This chapter has focused on demonstrating the validity of the present approach for unsteady flow problems related to the aerodynamics of the helicopter main rotor. The numerical results have generally shown good agreement when compared with experimental measurements made for pitching aerofoils over a wide range of flow conditions. For the periodic motions small differences were observed between the computations obtained using the two turbulence models. These differences are attributed to the respective shock locations predicted by the models. Typically the k-ω calculations predict the shock wave slightly forward of the location obtained using the Baldwin-Lomax model, this has a relatively small influence on the calculated forces but can have a substantial impact on the nose-down pitching moment contribution. In the absence of shock waves, the pitching moments calculated by the two models are in much closer agreement. For flows in which there is flow separation (case CT 3) the models perform less well.

A number of problems have been identified in the experimental data that are of some concern. While the instantaneous data have been corrected for (steady) wind tunnel constraints the unsteady motion has not. This raises some questions concerning the manner in which the data should be used when comparisons between computed and experimental data are required. It has been shown for AGARD CT2 that agreement

between the computational methods and experiment is much improved when the comparison is performed at the same instant in time.

For fully attached flows there appears to be little difference between the prediction's made by the two turbulence models. Given the uncertainties in the experimental data it is difficult to judge which of the turbulence models provides the best prediction of the unsteady flow. It is clear however that neither model is capable of providing a good prediction of the flow development following boundary layer separation. This is attributed in the most part to weaknesses in the turbulence modelling approaches. Furthermore, it should be noted that in the absence of experimental guidance the present calculations have been performed with the turbulence model applied over the full chord of the aerofoil. Clearly, in the experiment there will be regions of laminar and transitional flow in the proximity of the aerofoil leading edge. The extent of these regions is unknown, but it can be assumed that they will play an important part in the flow development when the shock wave and separation point are close to the transition region.

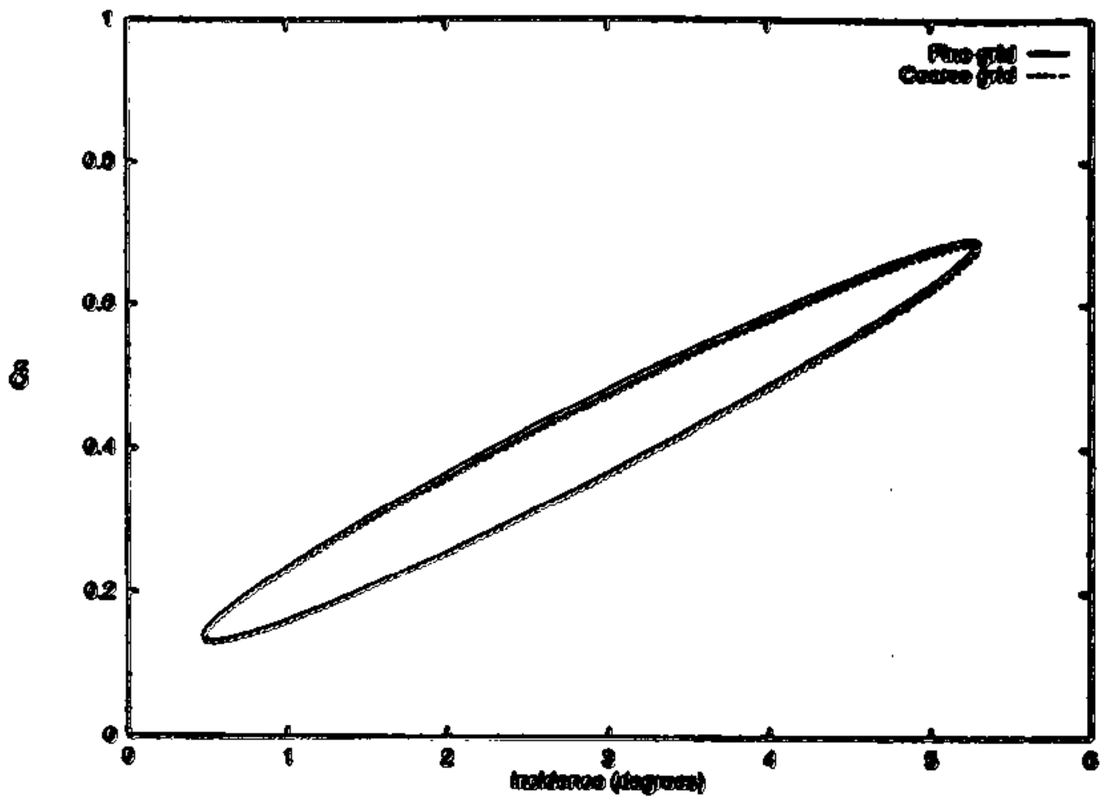

(a) Normal Force

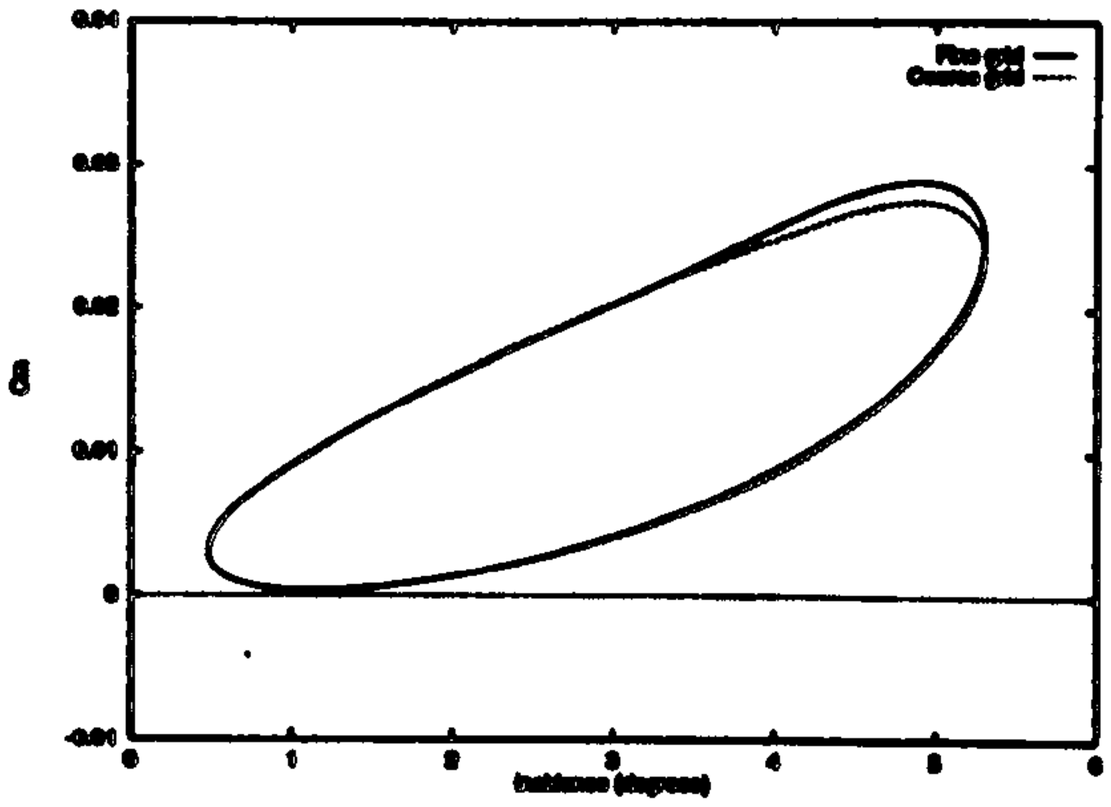

(b) Pitching Moment

Figure (7.1)Sensitivity of calculated forces and moments to grid density

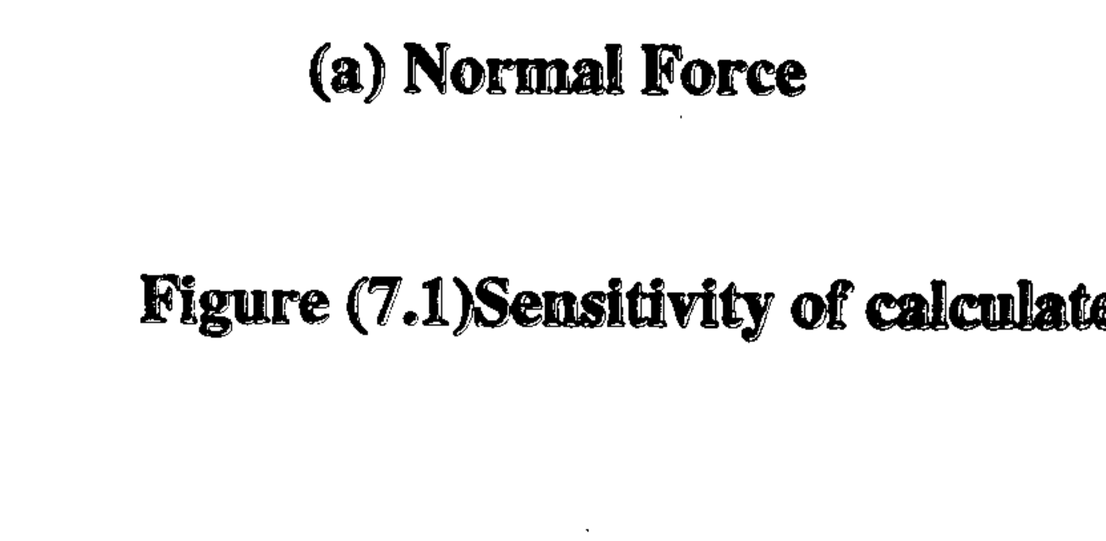

(a) $\psi = 1.90°$

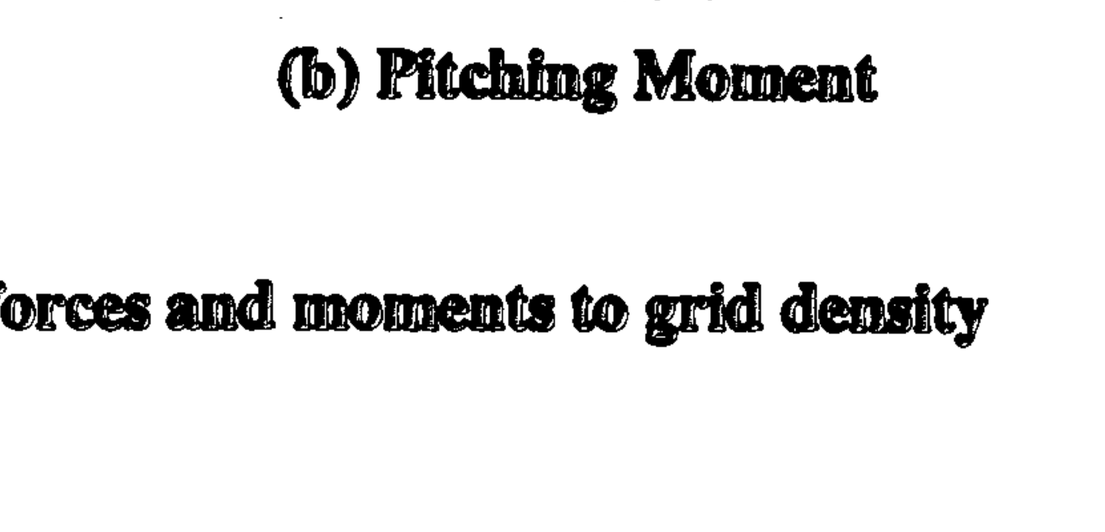

(c) $\psi = 53.60°$

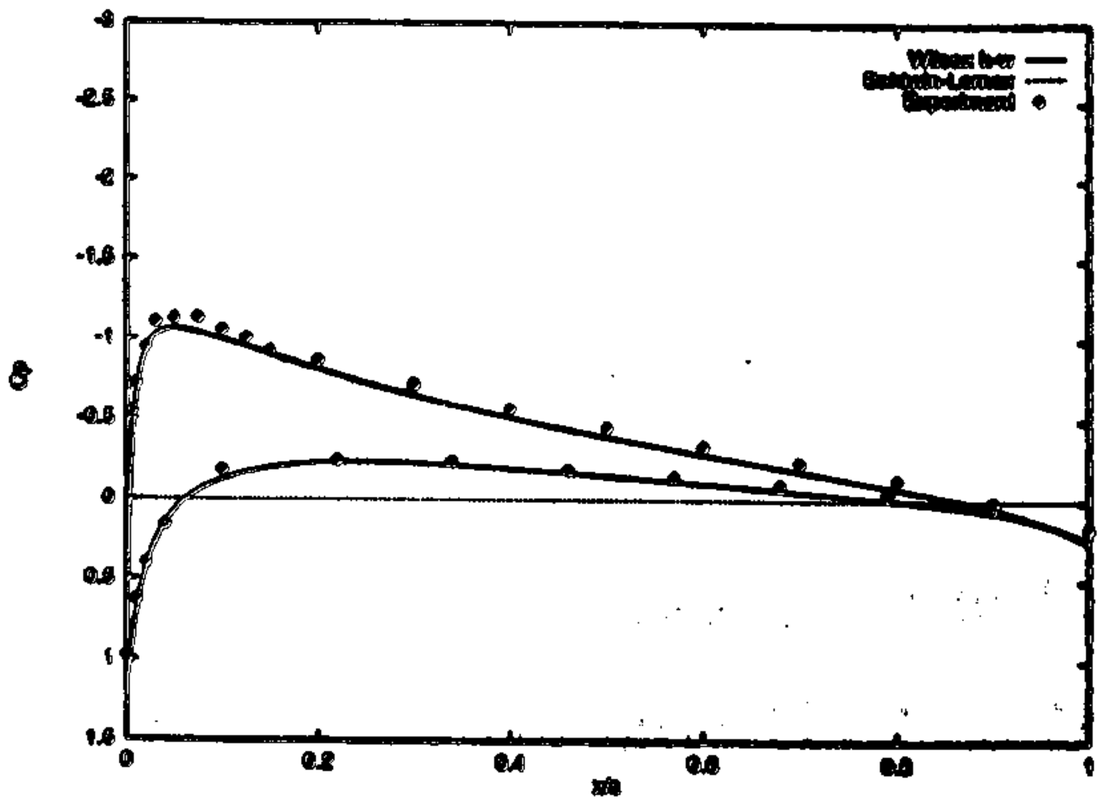

(b) $\psi = 22.46°$

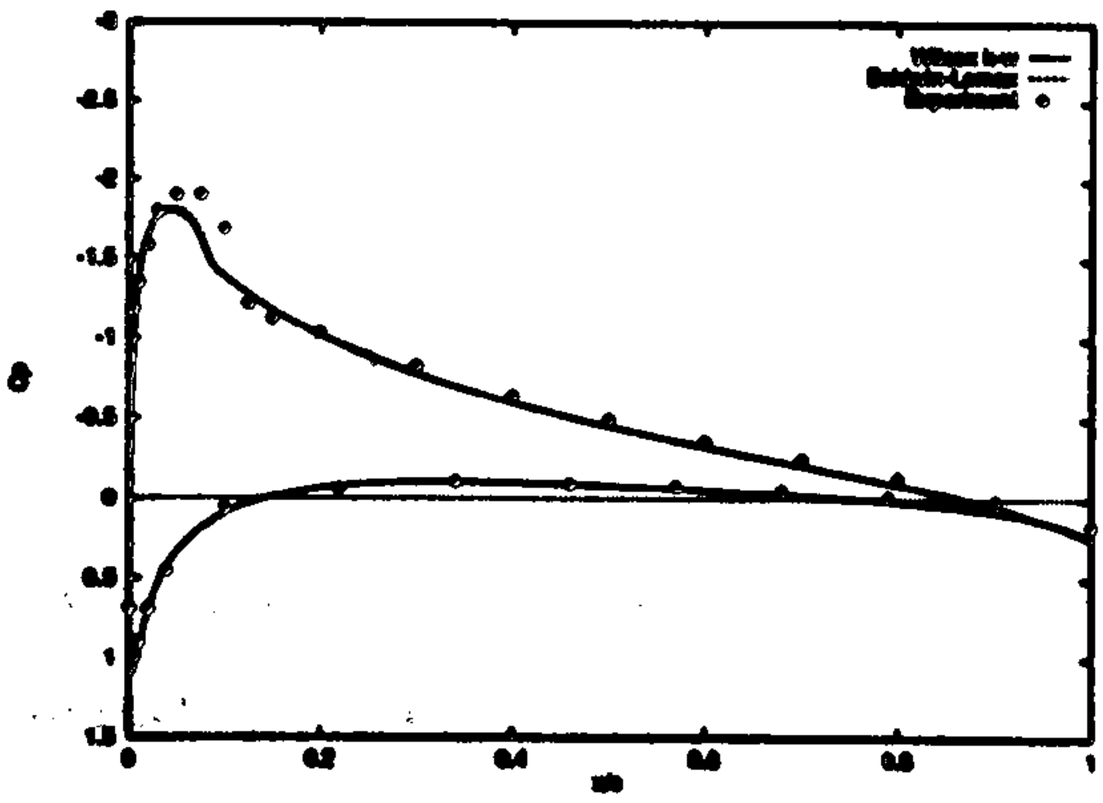

(d) $\psi = 90.03°$

Figure (7.2) Comparison of calculated pressure distributions with experiment[179] (Case CT1)

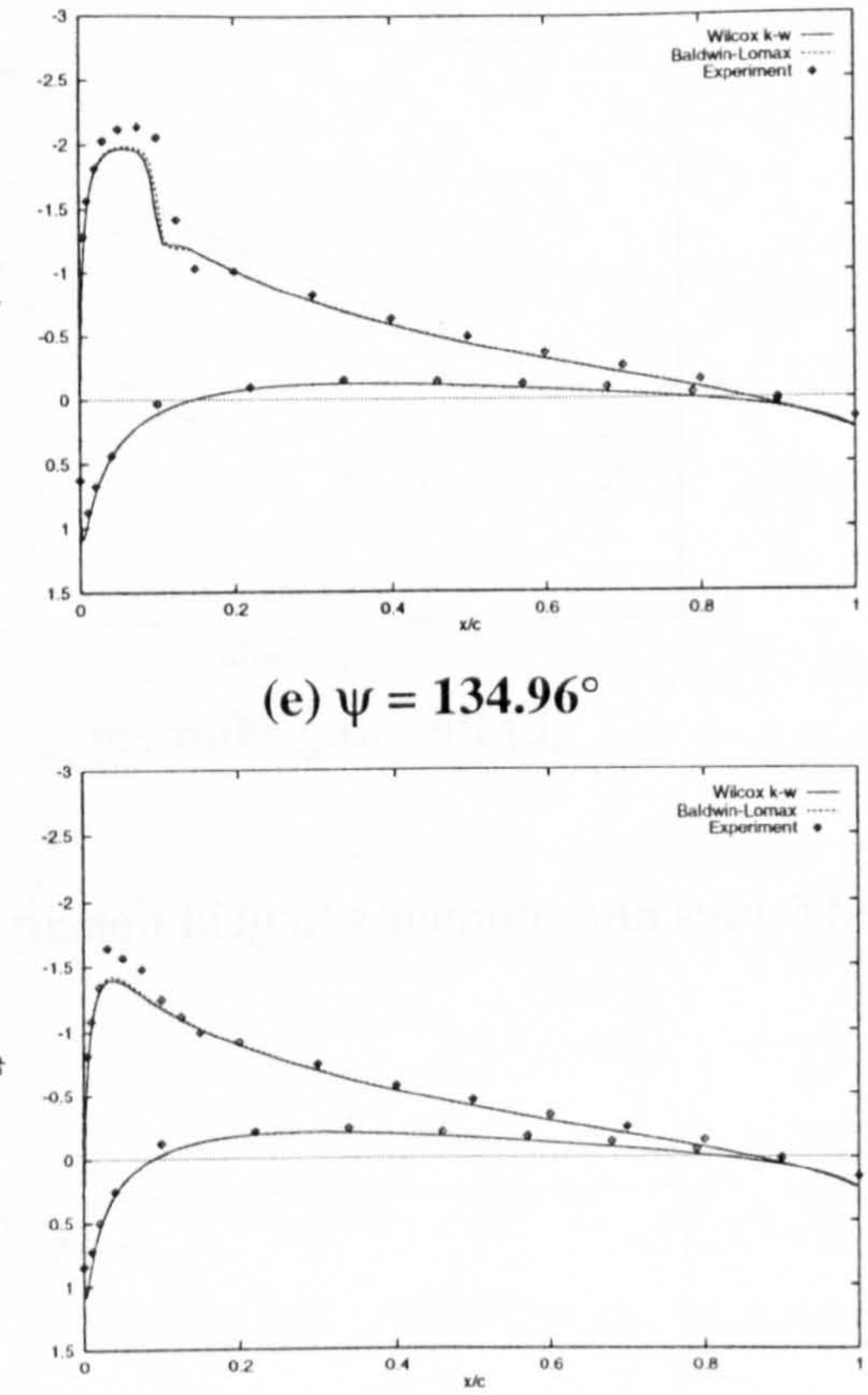

(e) $\psi = 134.96°$

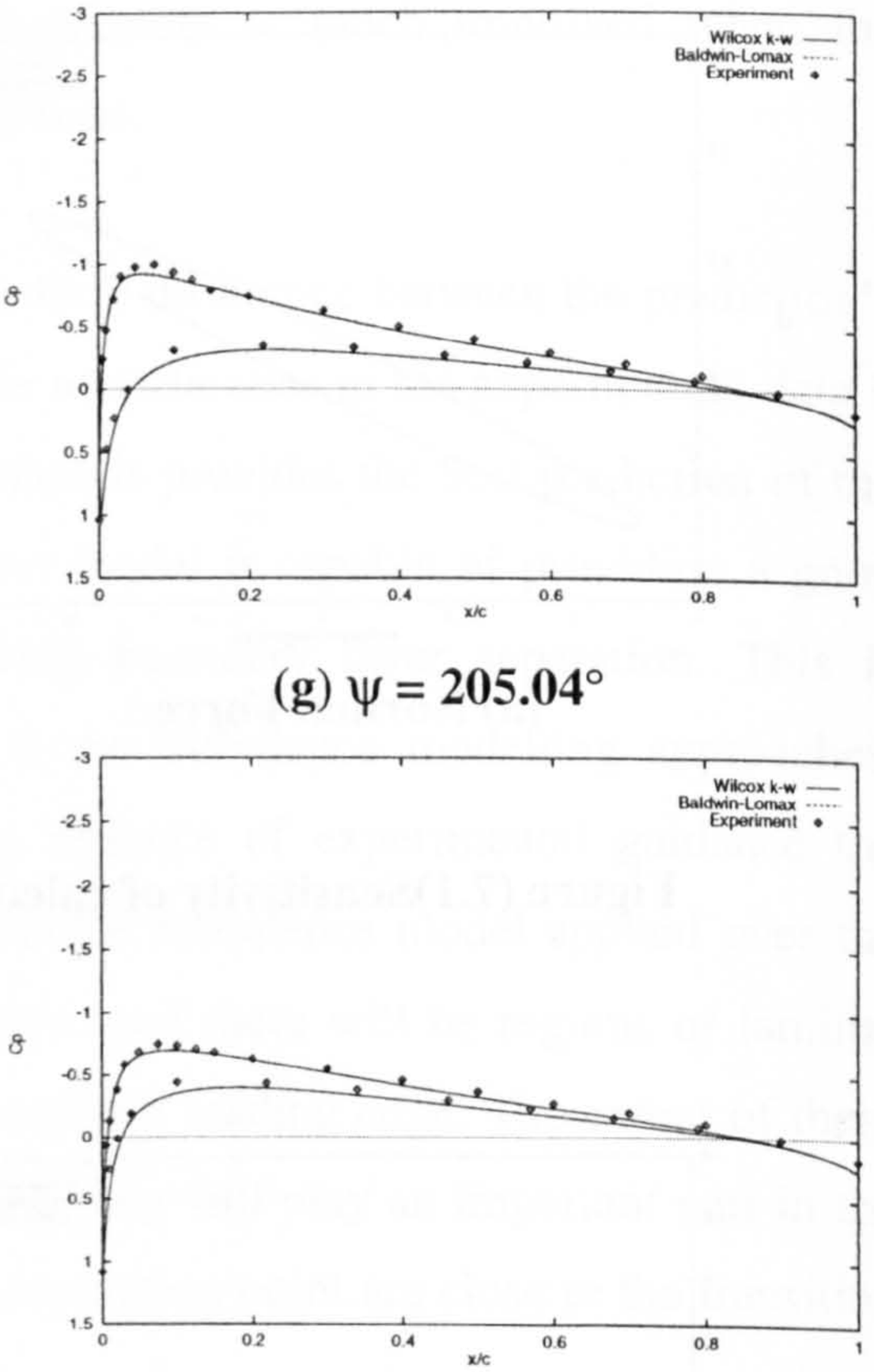

(g) $\psi = 205.04°$

(f) $\psi = 186.43°$

(h) $\psi = 270.0°$

Figure (7.2) Comparison of calculated pressure distributions with experiment[179] (Case CT1) – concluded

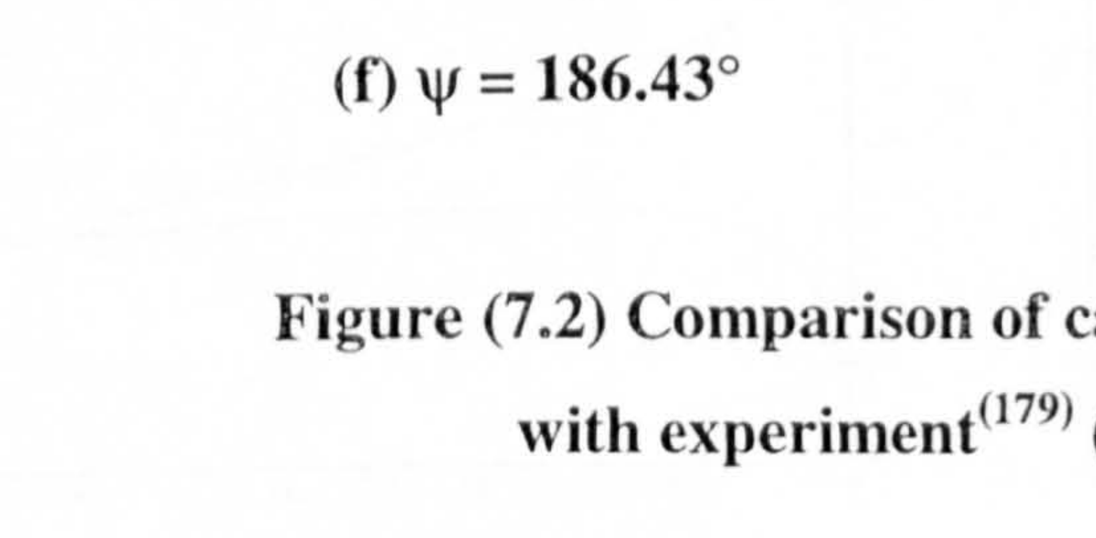

(a) Normal Force

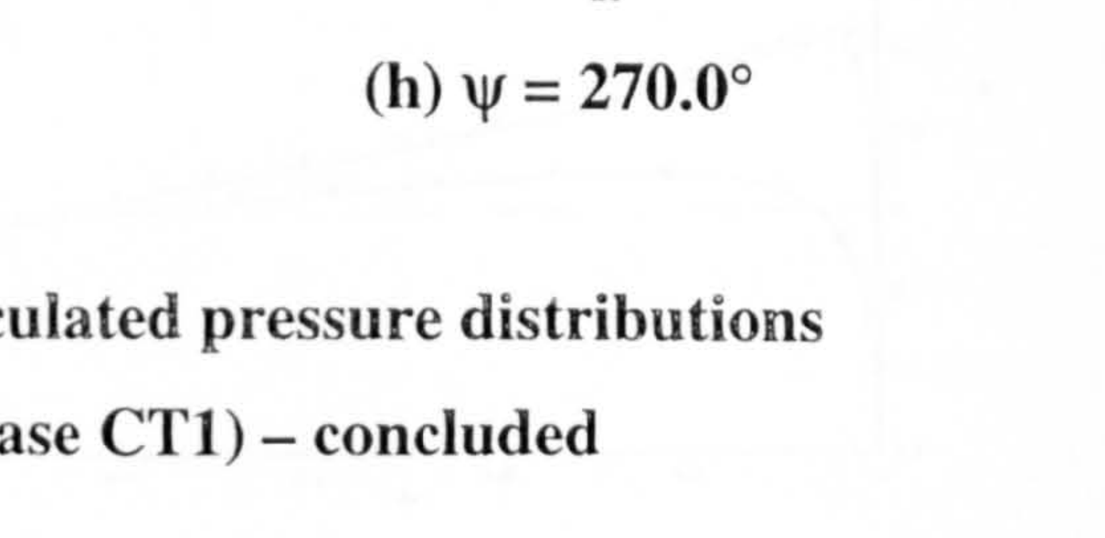

(b) Pitching Moment

Figure (7.3) Comparison of computed and Measured[179] forces and moments (Case CT1)

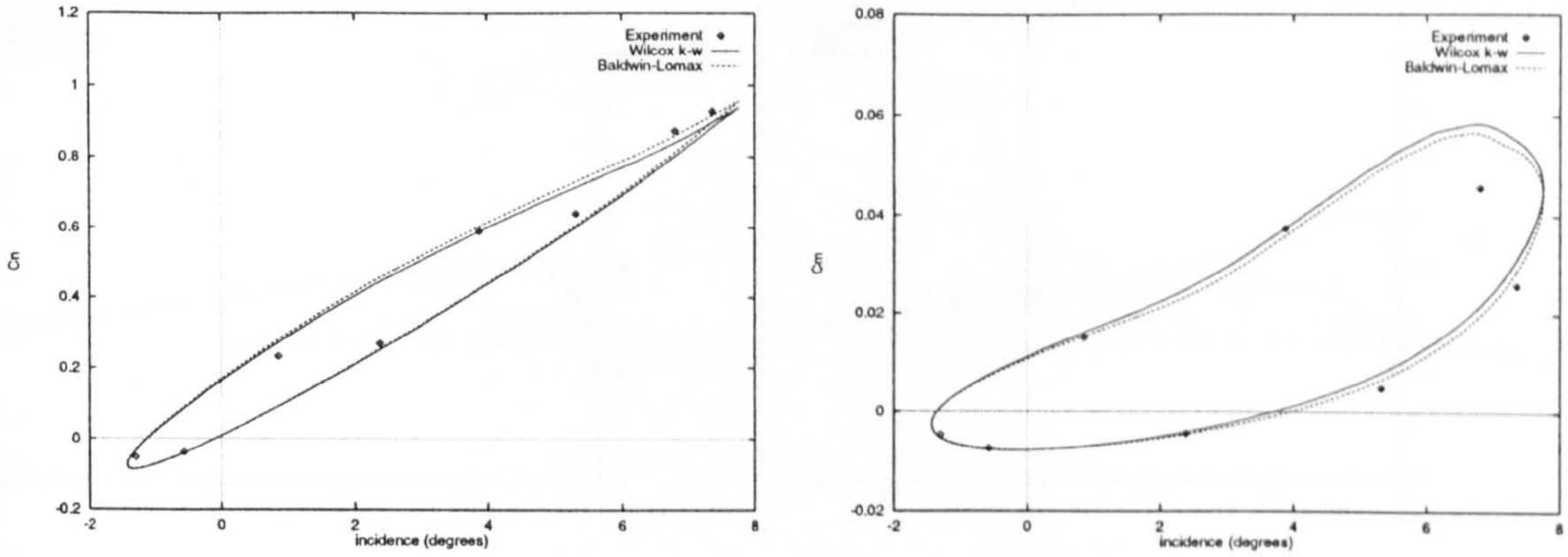

(a) Normal Force **(b)Pitching Moment**

Figure (7.4) Comparison of computed and Measured[179] forces and moments (Case CT2)

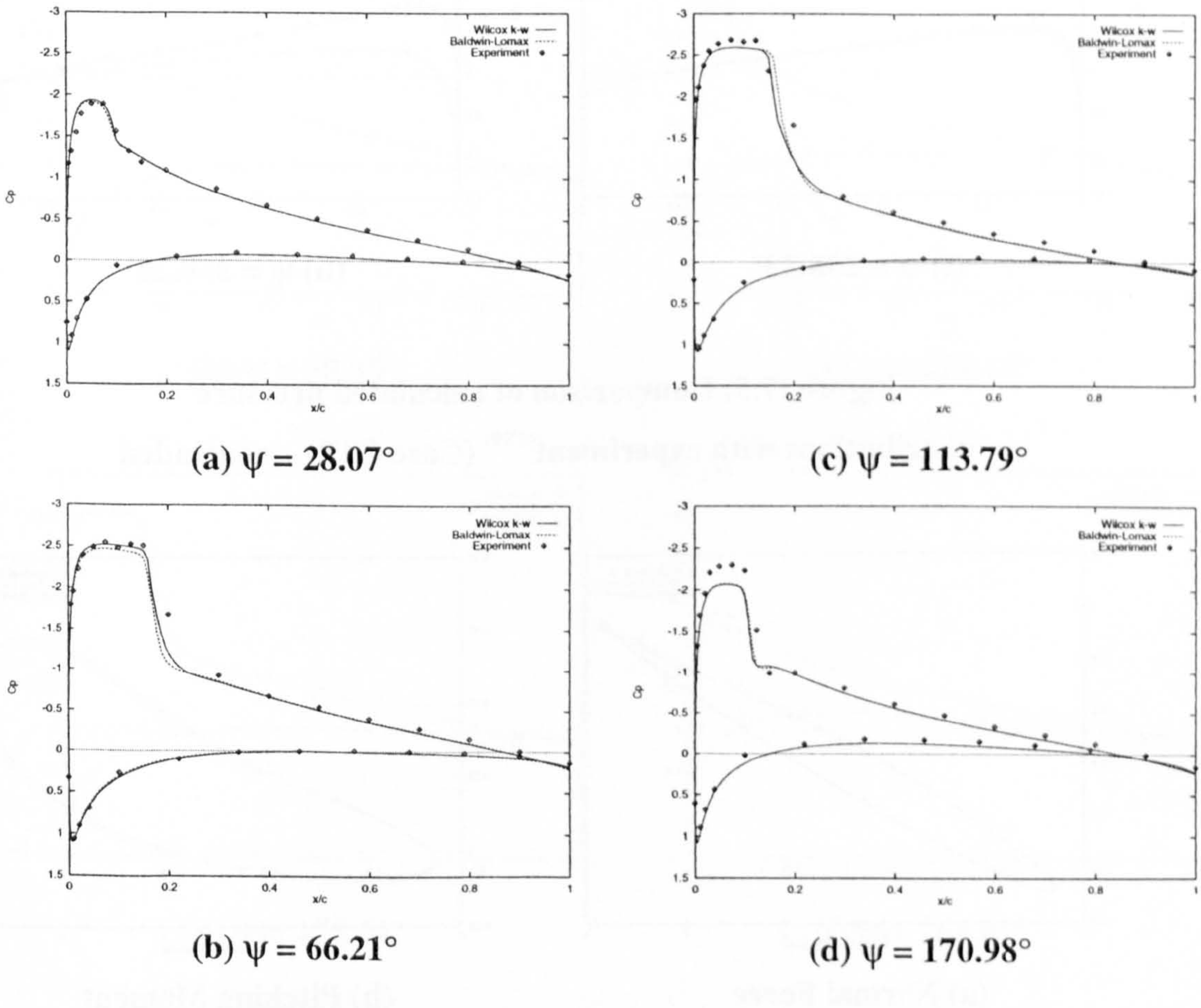

(a) ψ = 28.07° **(c) ψ = 113.79°**

(b) ψ = 66.21° **(d) ψ = 170.98°**

Figure (7.5) Comparison of calculated pressure distributions with experiment[179] (Case CT2)

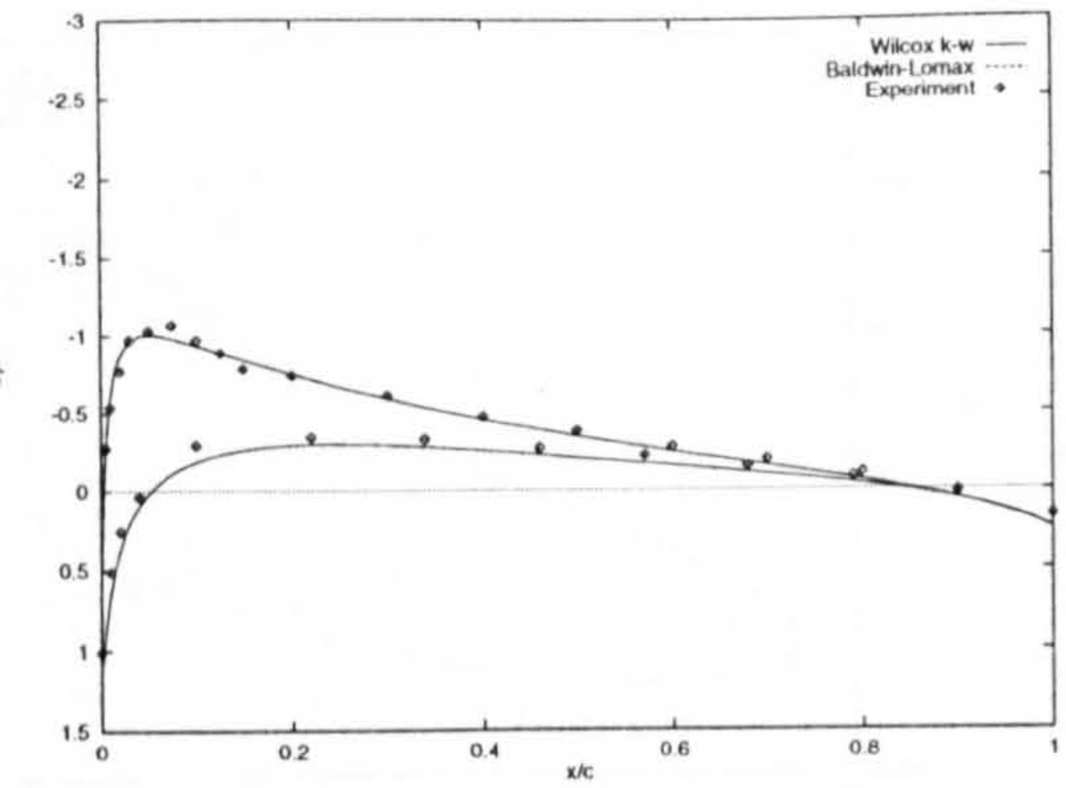

(e) ψ = 210.07°

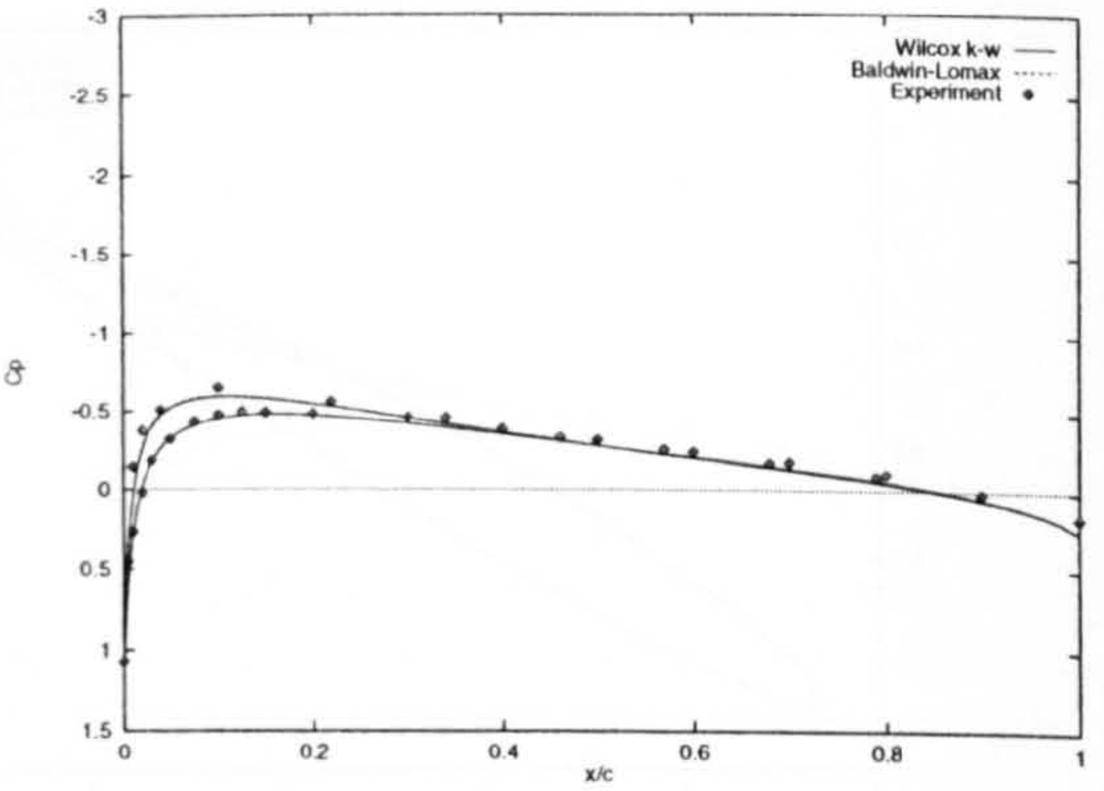

(g) ψ = 305.65°

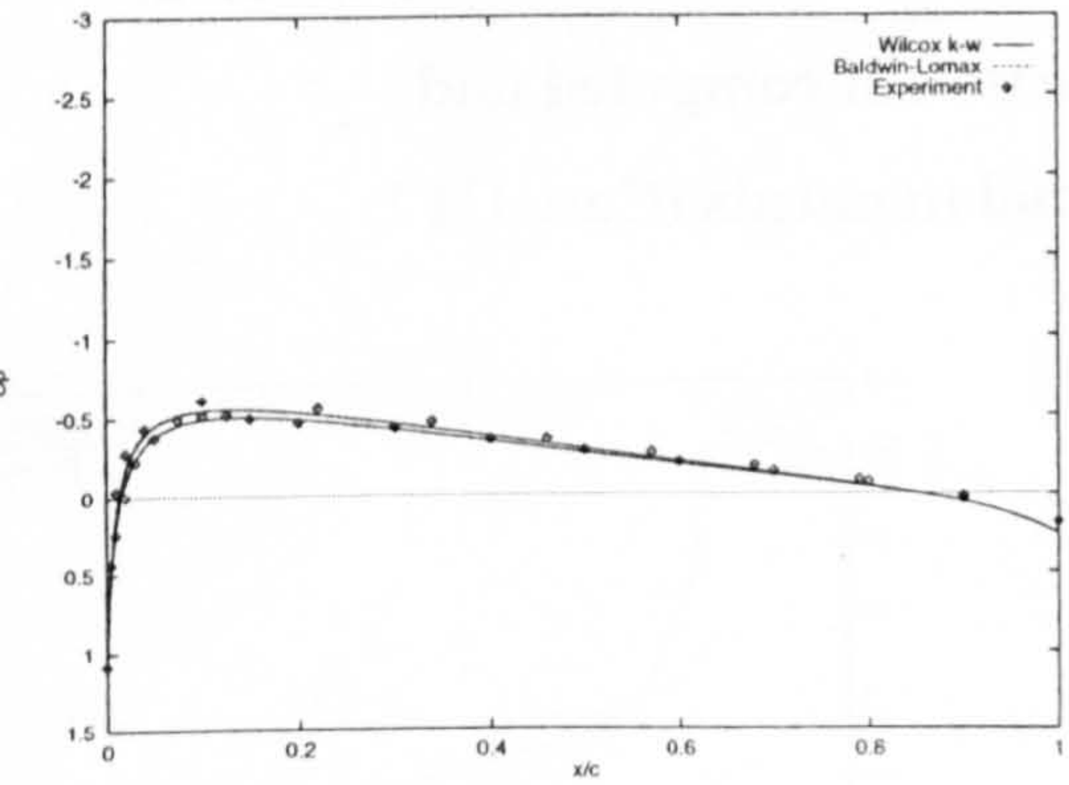

(f) ψ = 256.33°

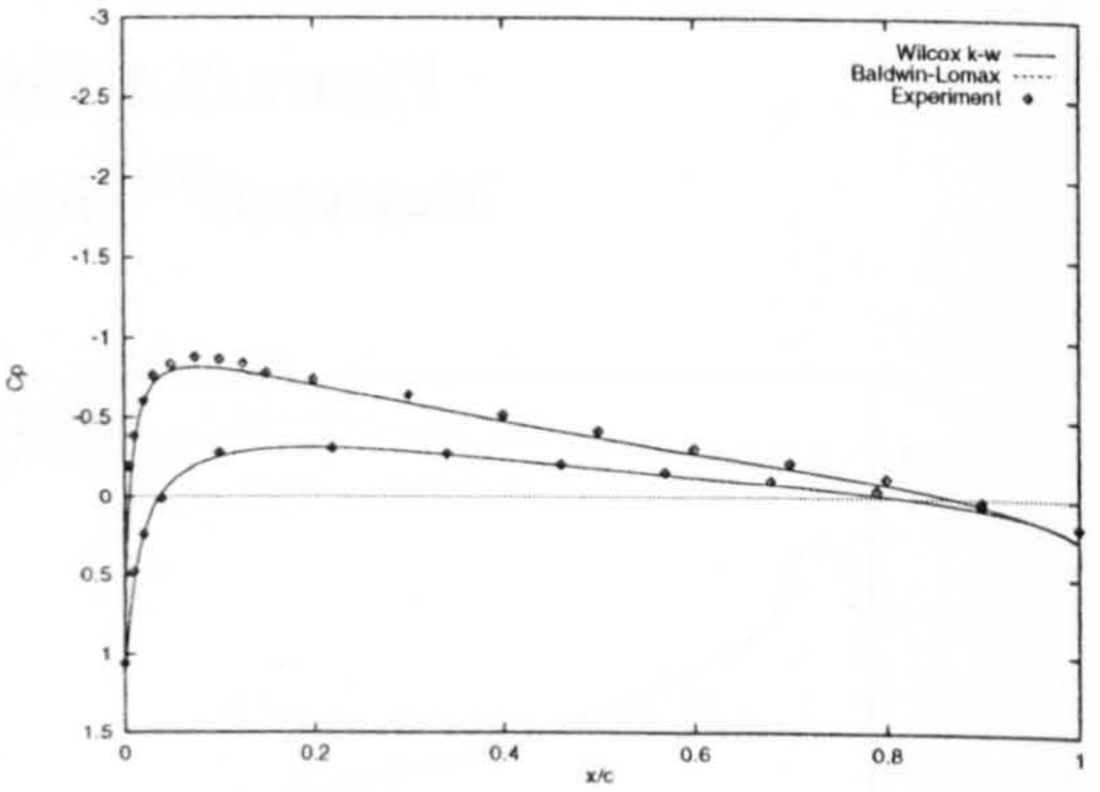

(h) ψ = 350.22°

Figure (7.5) Comparison of calculated pressure distributions with experiment[179] (Case CT2) – concluded

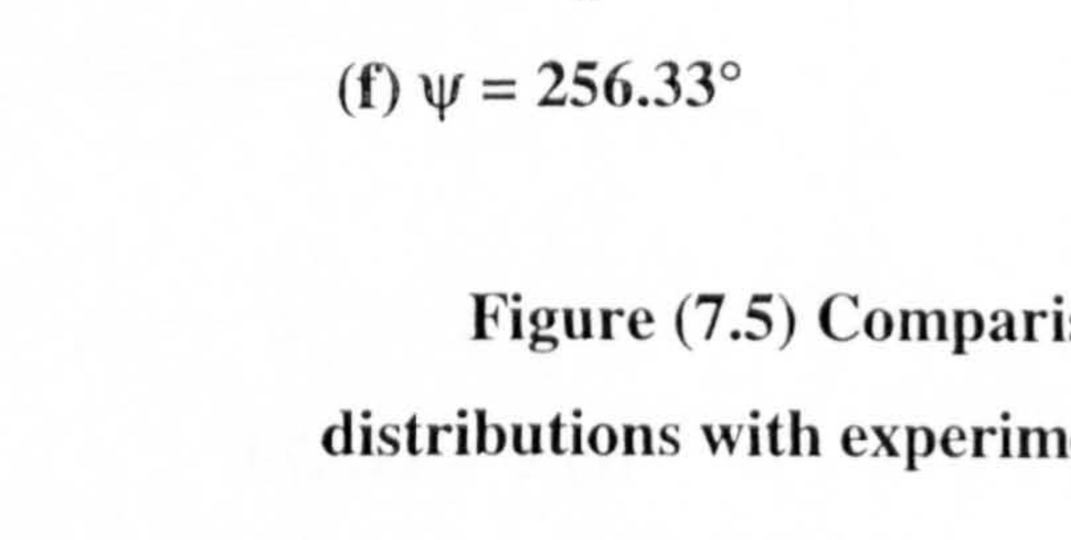

(a) Normal Force

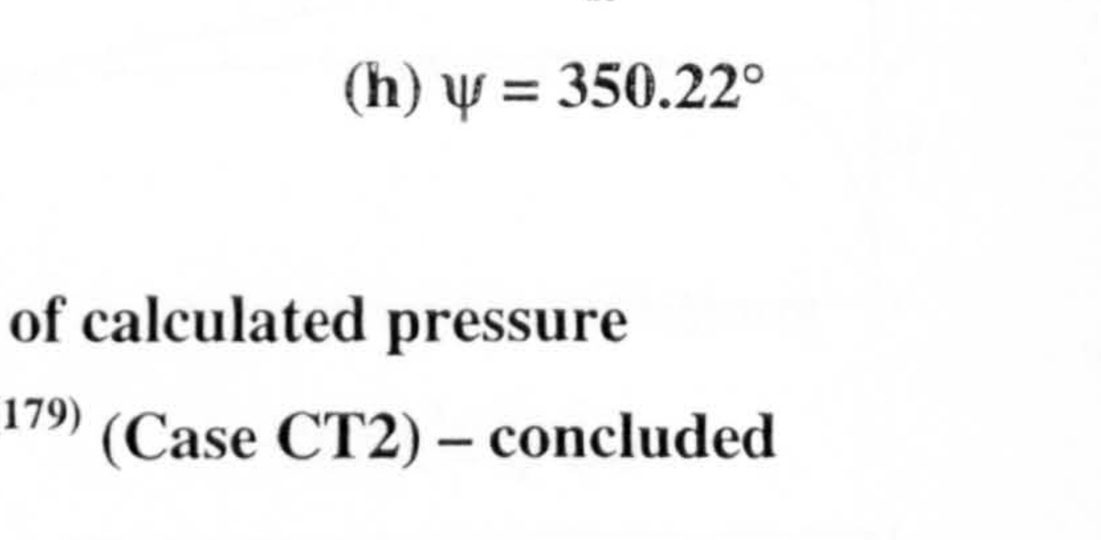

(b) Pitching Moment

Figure (7.6) Comparison of computed forces and moments with modified experimental data (Case CT2)

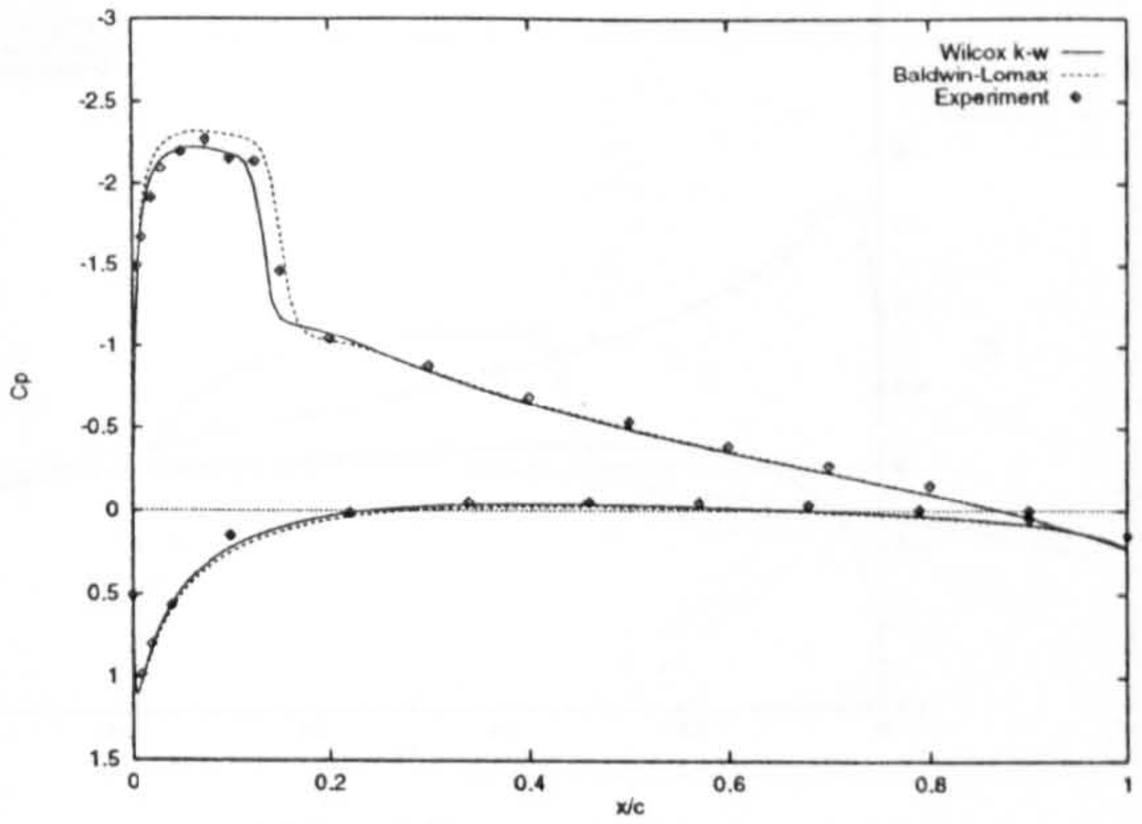

(a) $\psi = 26.53°$

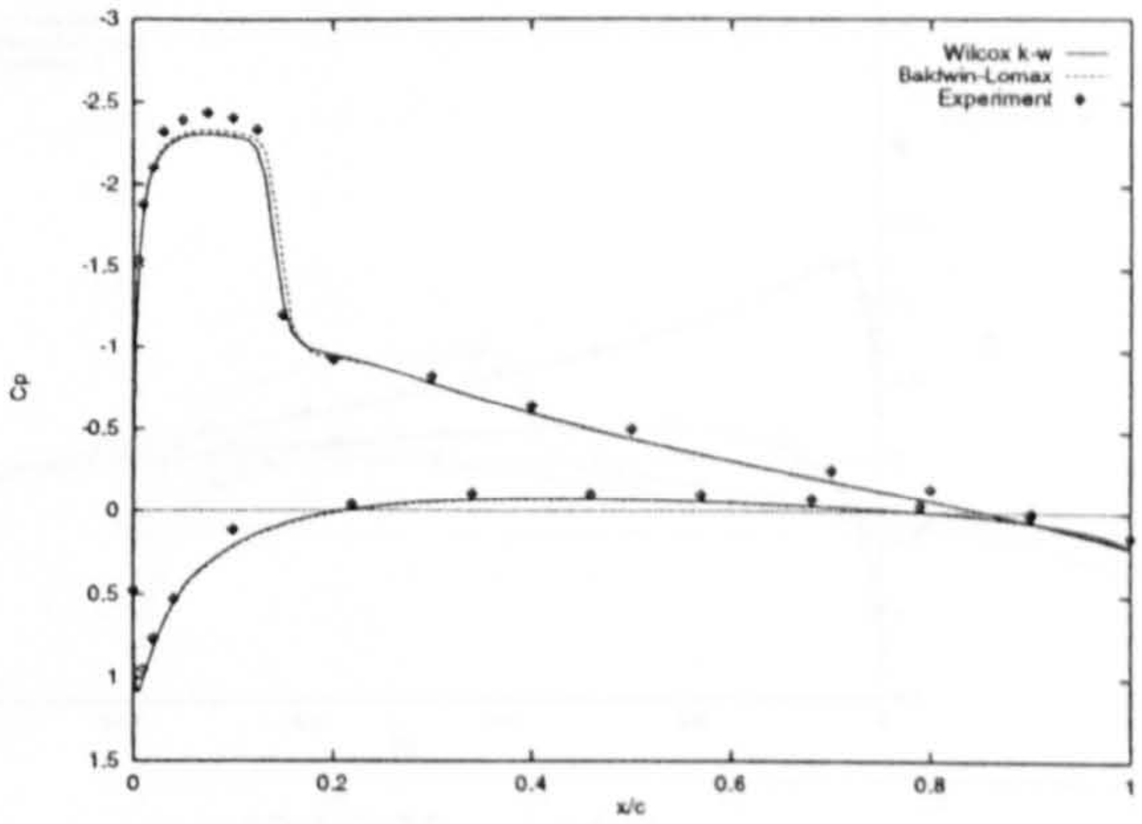

(d) $\psi = 174.12°$

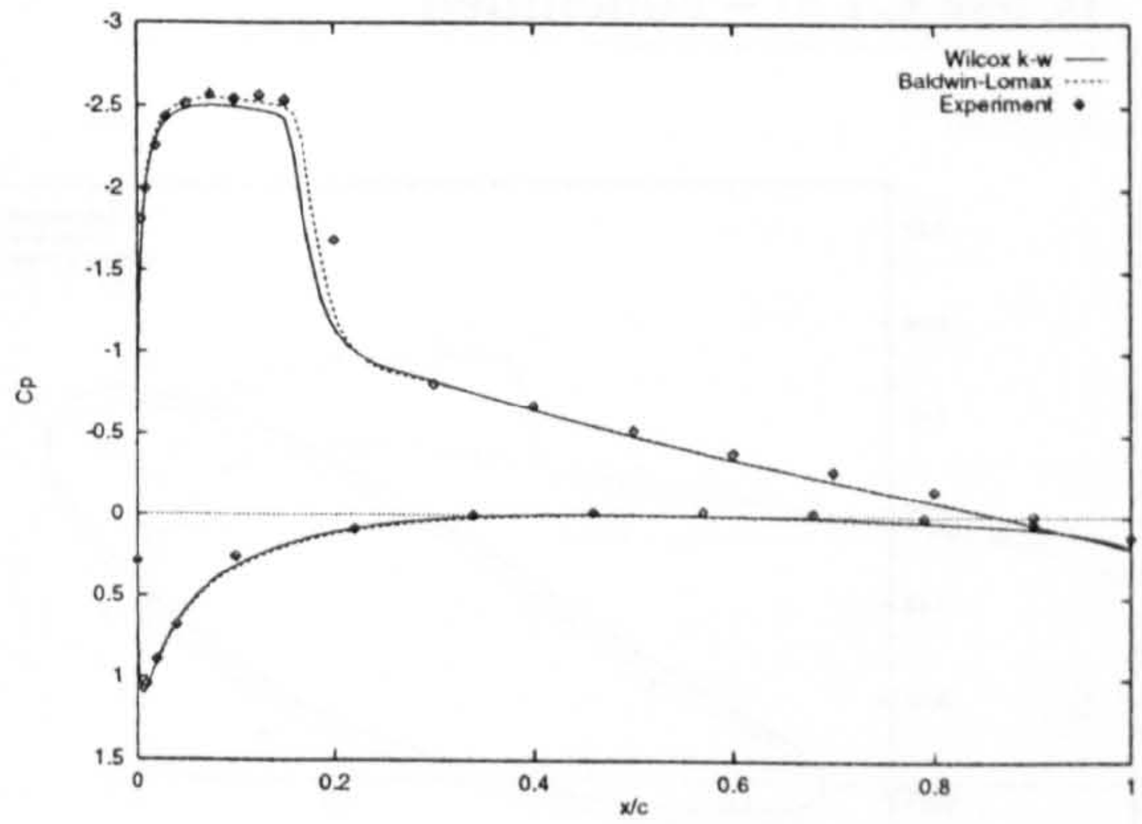

(b) $\psi = 59.85°$

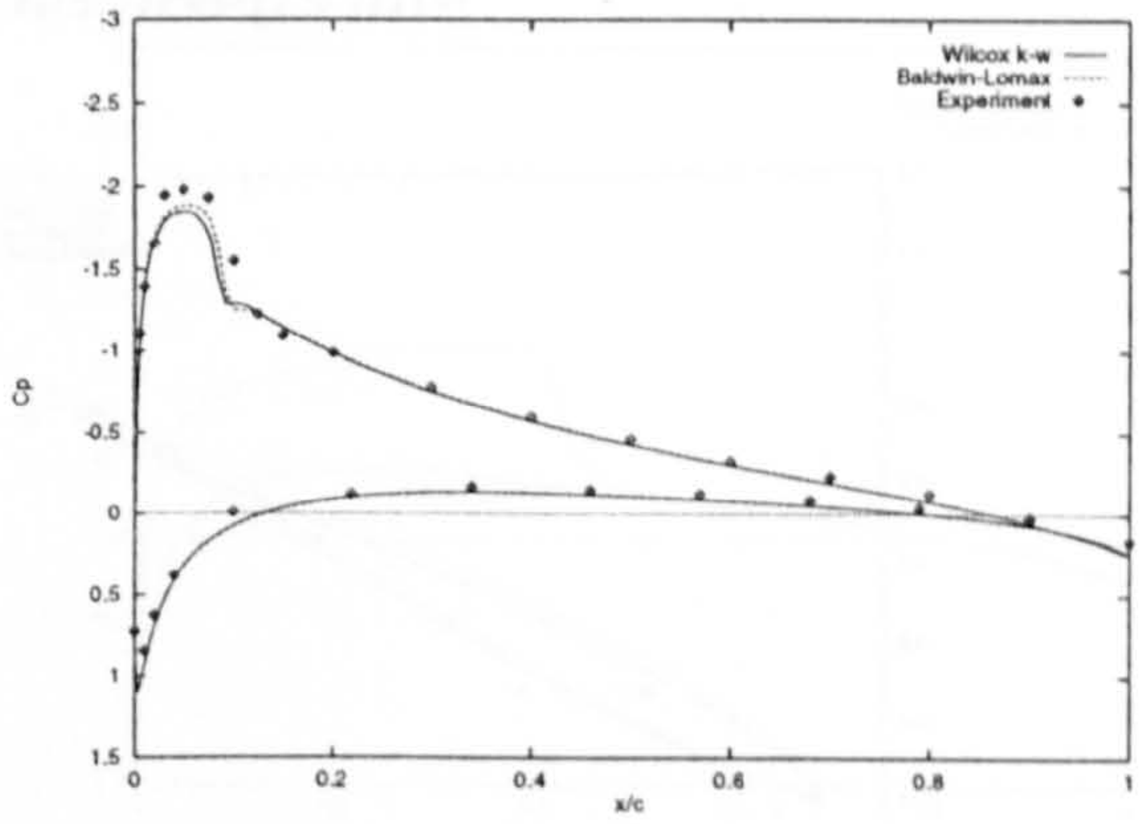

(e) $\psi = 214.16°$

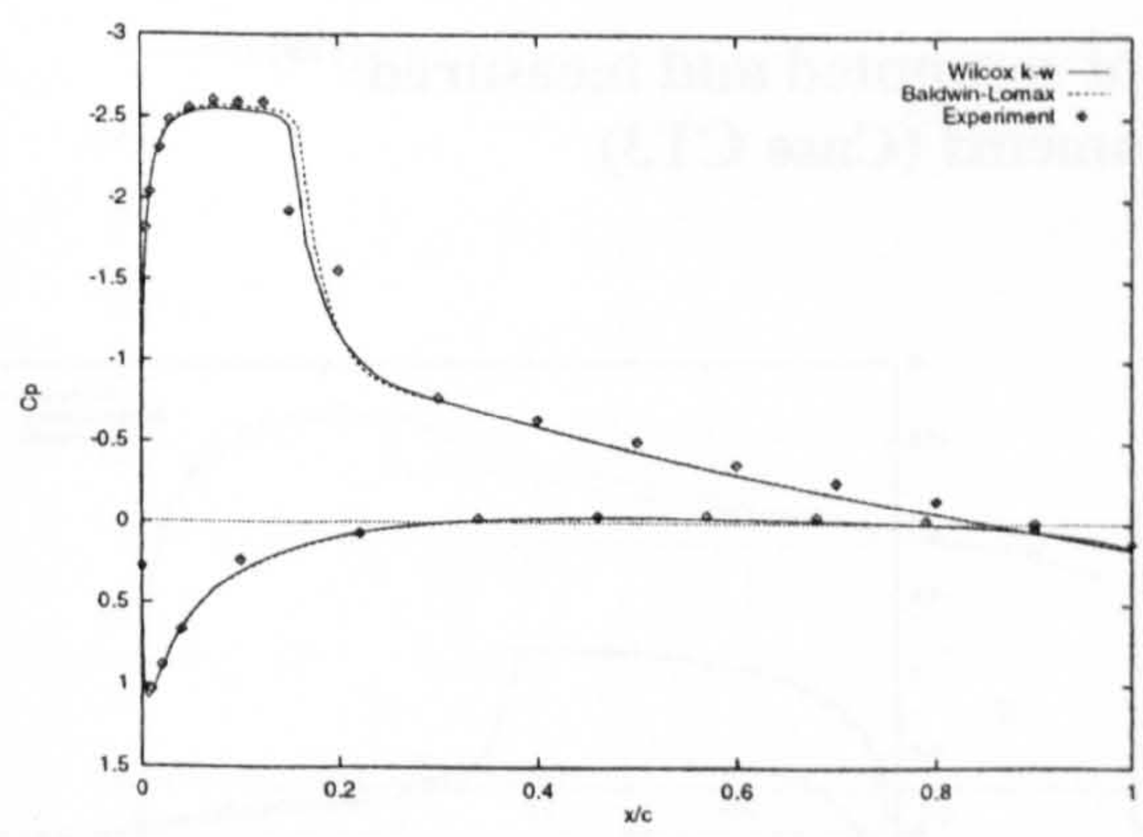

(c) $\psi = 135.51°$

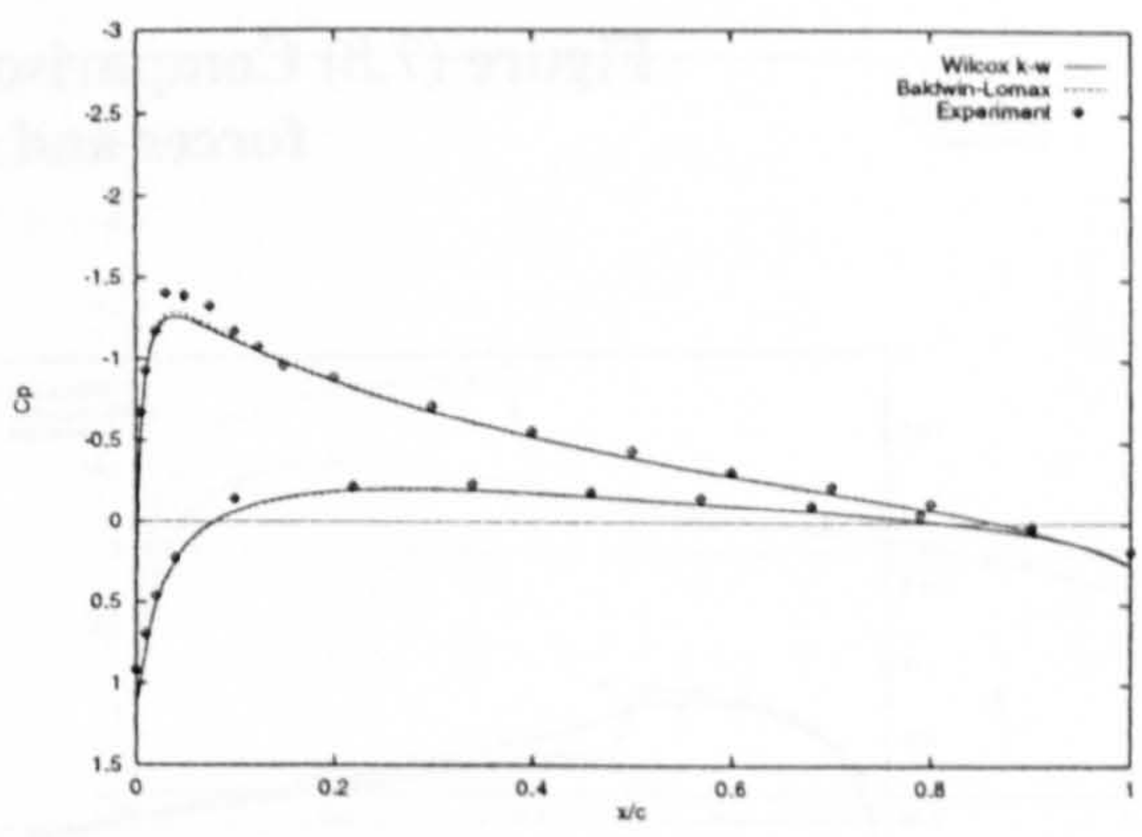

(f) $\psi = 264.81°$

Figure (7.7) Comparison of calculated pressure distributions with experiment[179] (Case CT3)

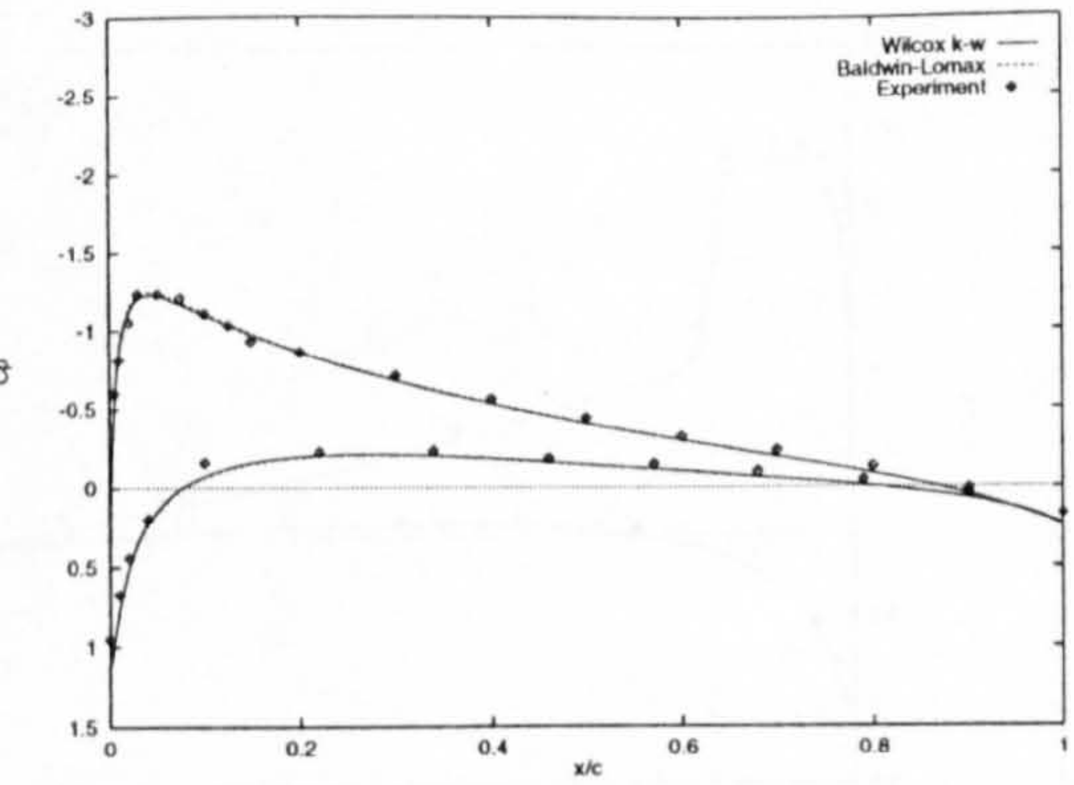

(g) $\psi = 296.16°$

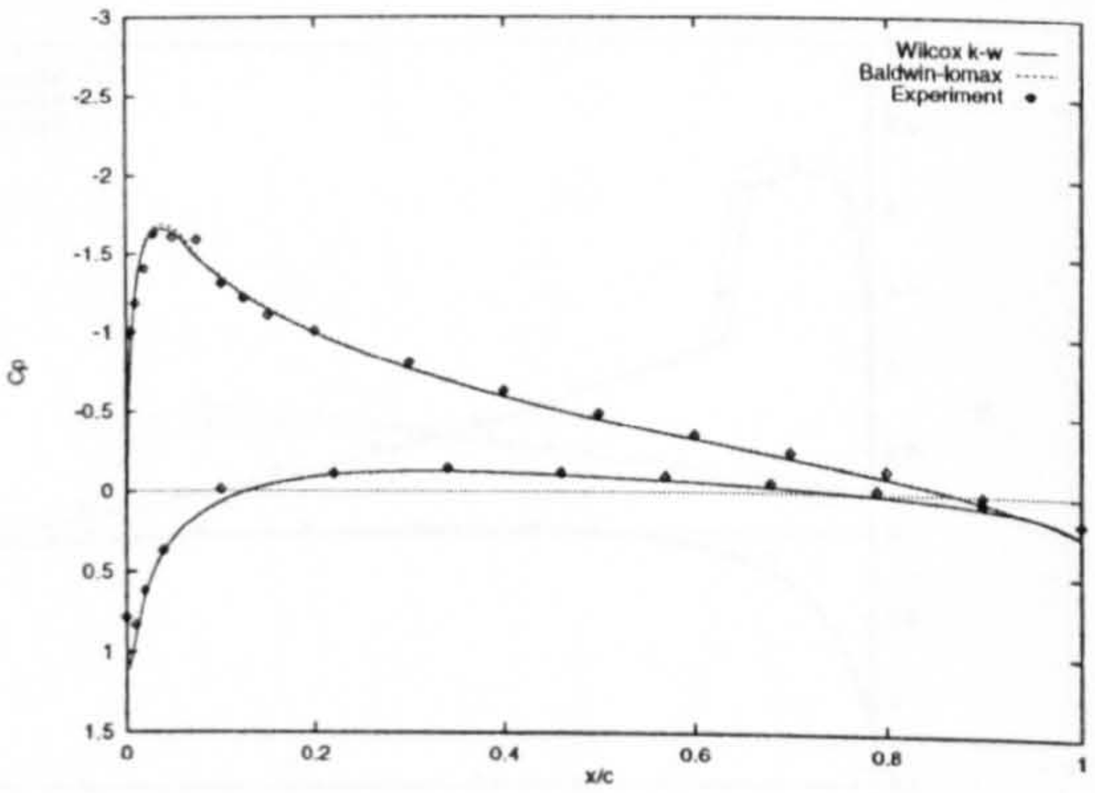

(h) $\psi = 346.25°$

Figure (7.7) Comparison of calculated pressure distributions with experiment[179] (Case CT3) – concluded

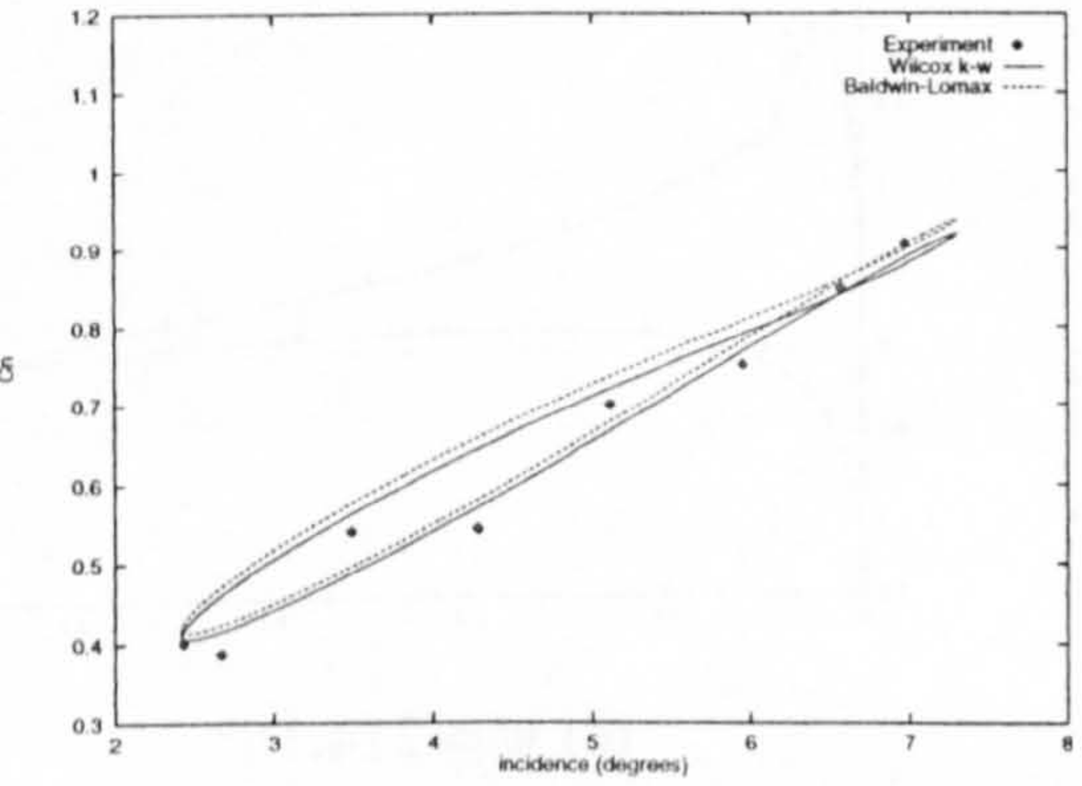

(a) Normal Force

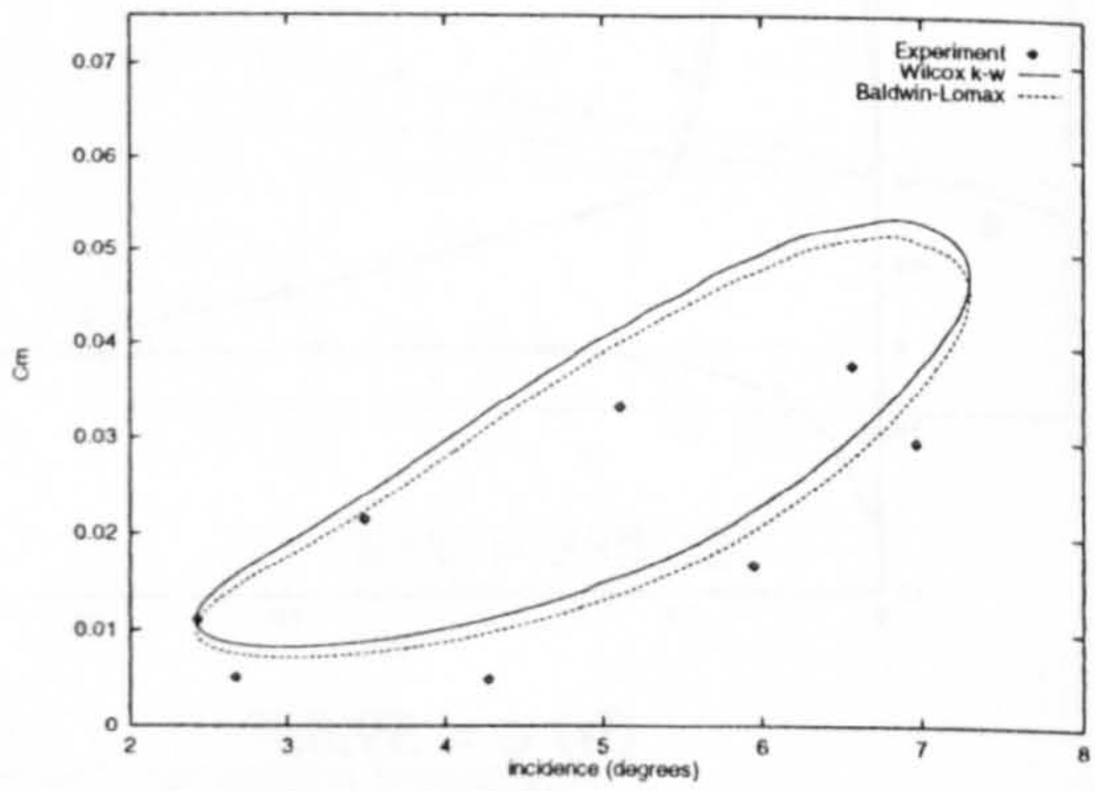

(b) Pitching Moment

Figure (7.8) Comparison of computed and measured[179] forces and moments (Case CT3)

(a) $\psi = 25.33°$

(b) $\psi = 113.20°$

Figure (7.9) Comparison of calculated pressure distributions with experiment[179] (Case CT5)

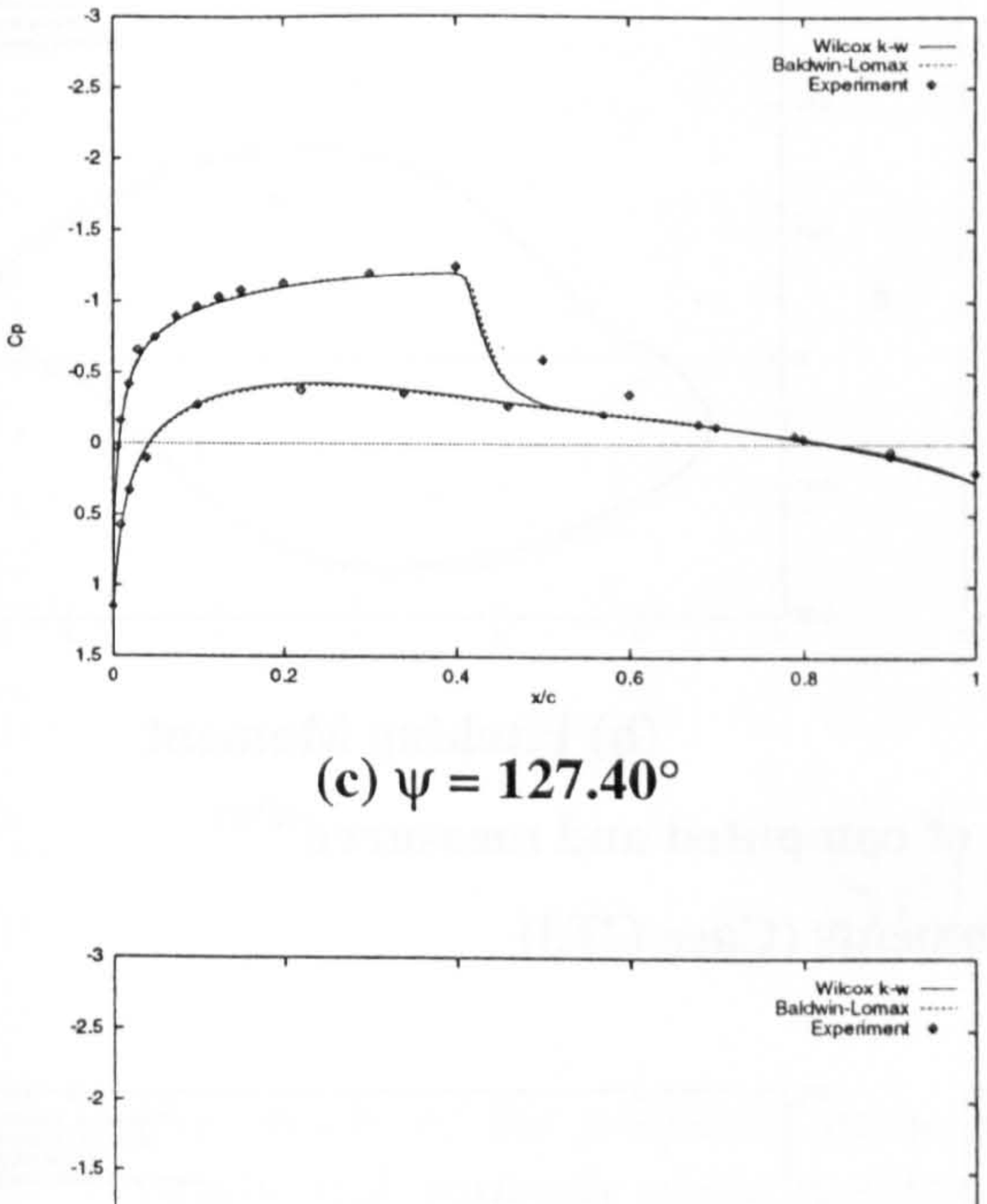

(c) $\psi = 127.40°$

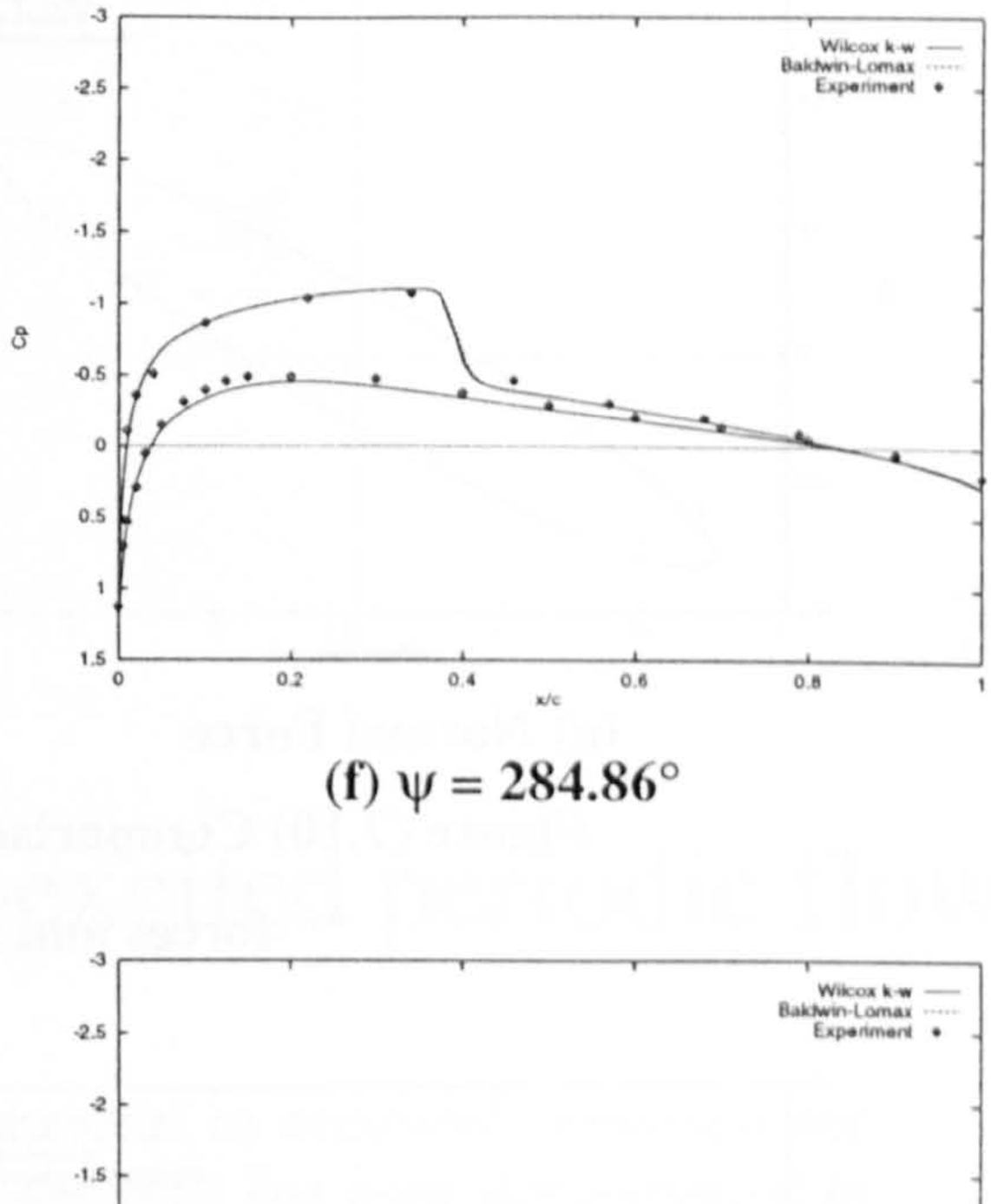

(f) $\psi = 284.86°$

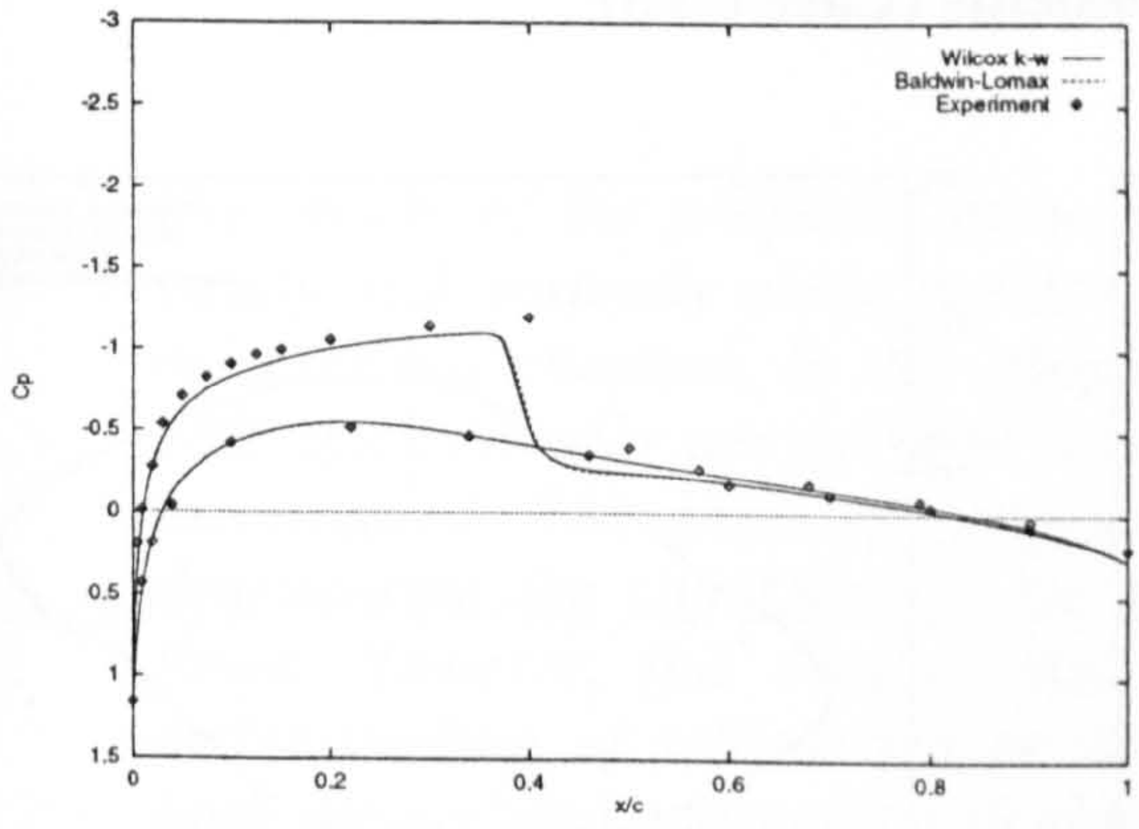

(d) $\psi = 168.42°$

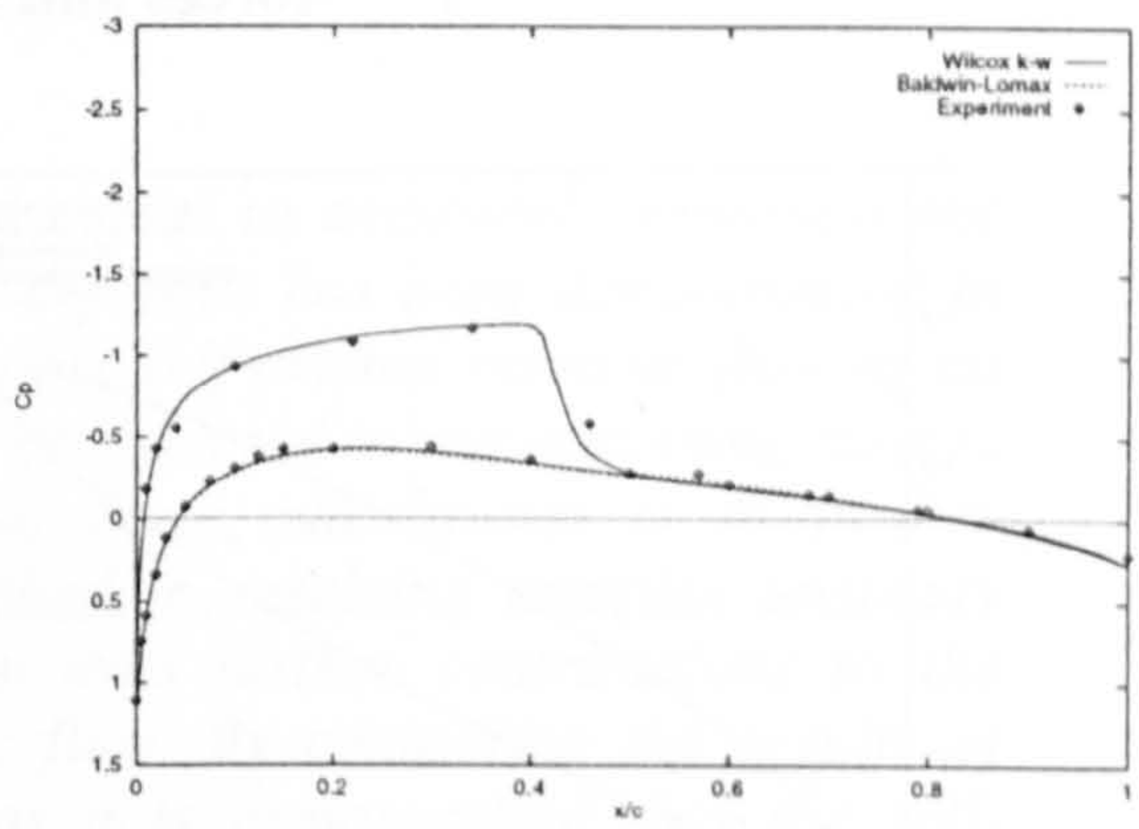

(g) $\psi = 306.56°$

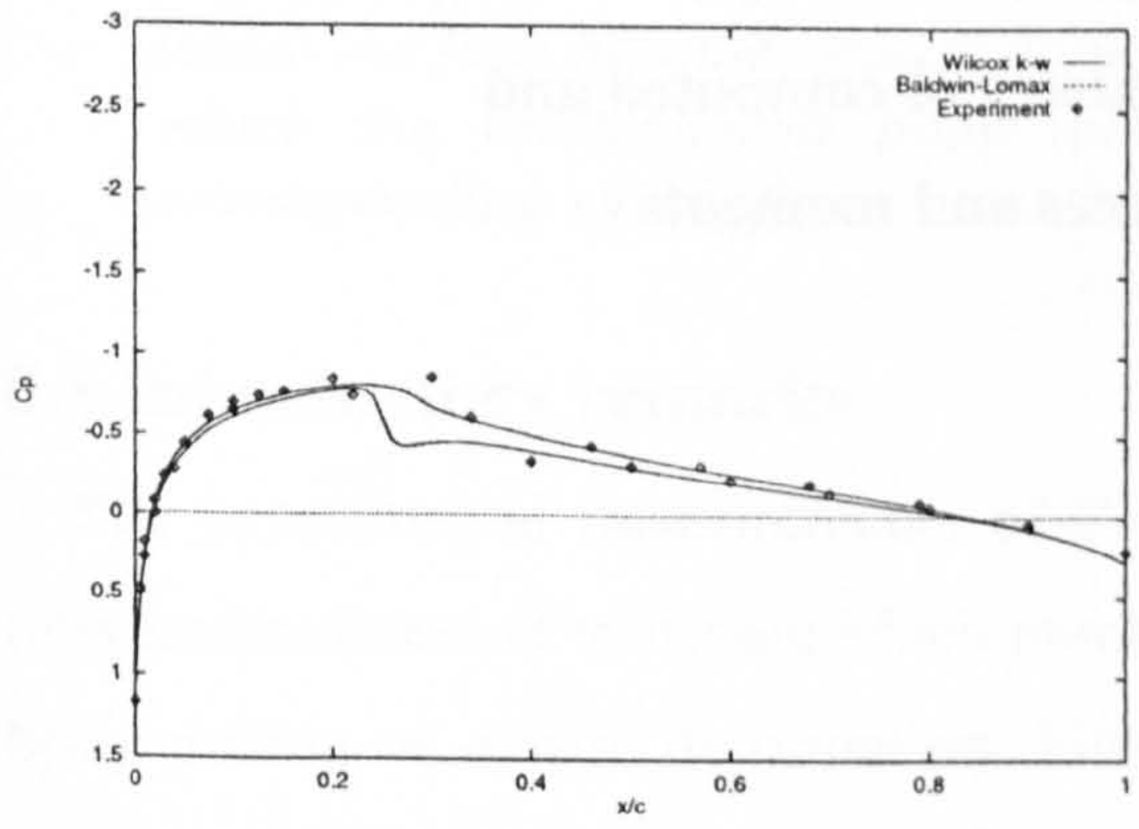

(e) $\psi = 210.29°$

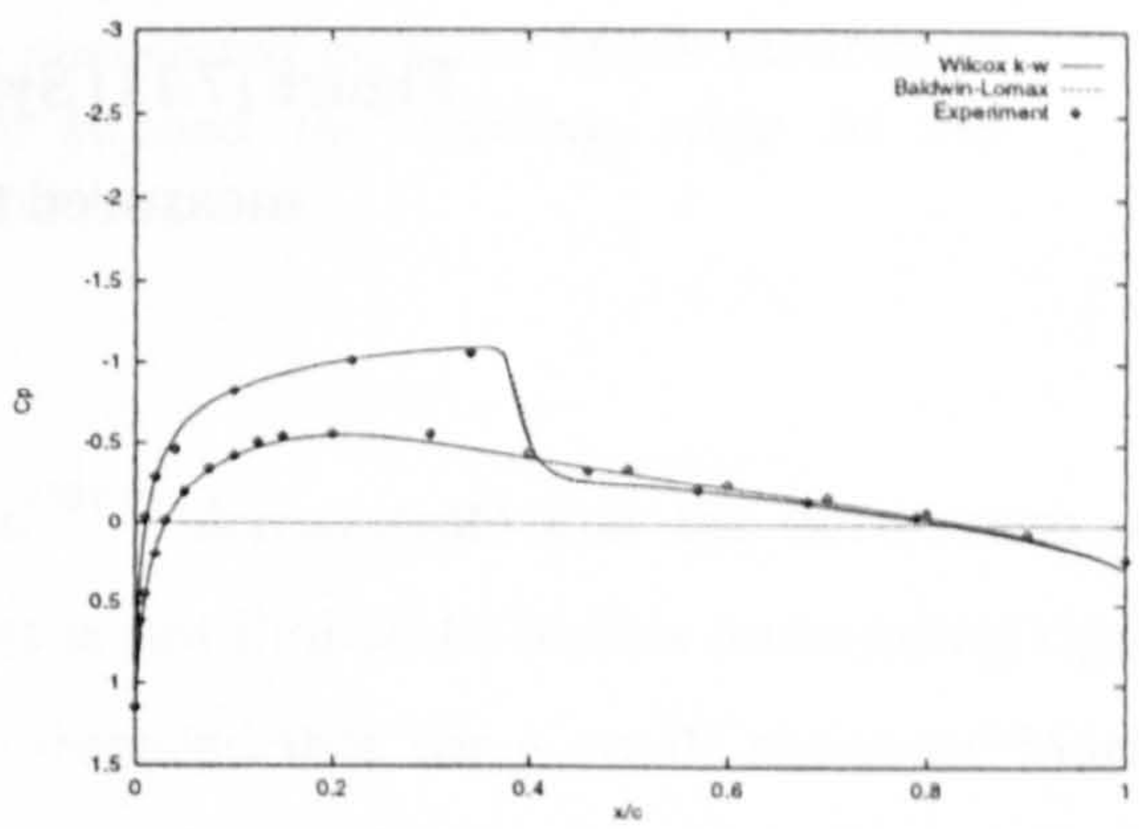

(h) $\psi = 347.20°$

Figure (7.9) Comparison of calculated pressure distributions with experiment[179] (Case CT5) - concluded

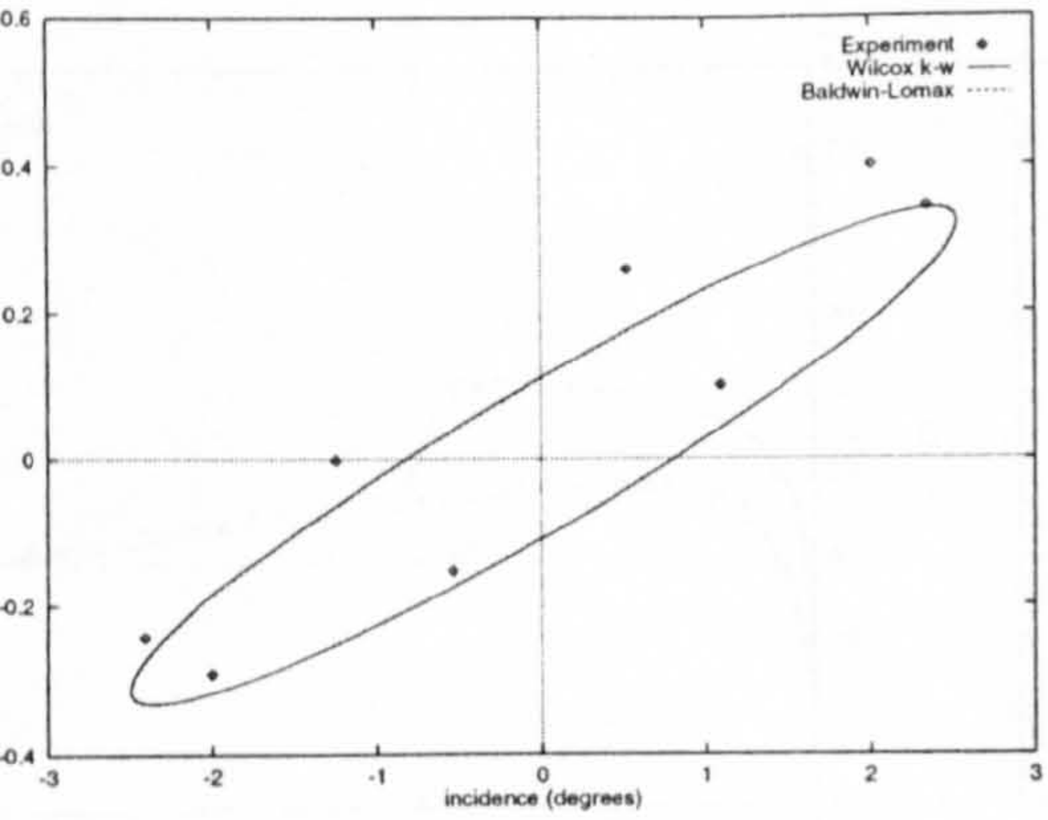

(a) Normal Force

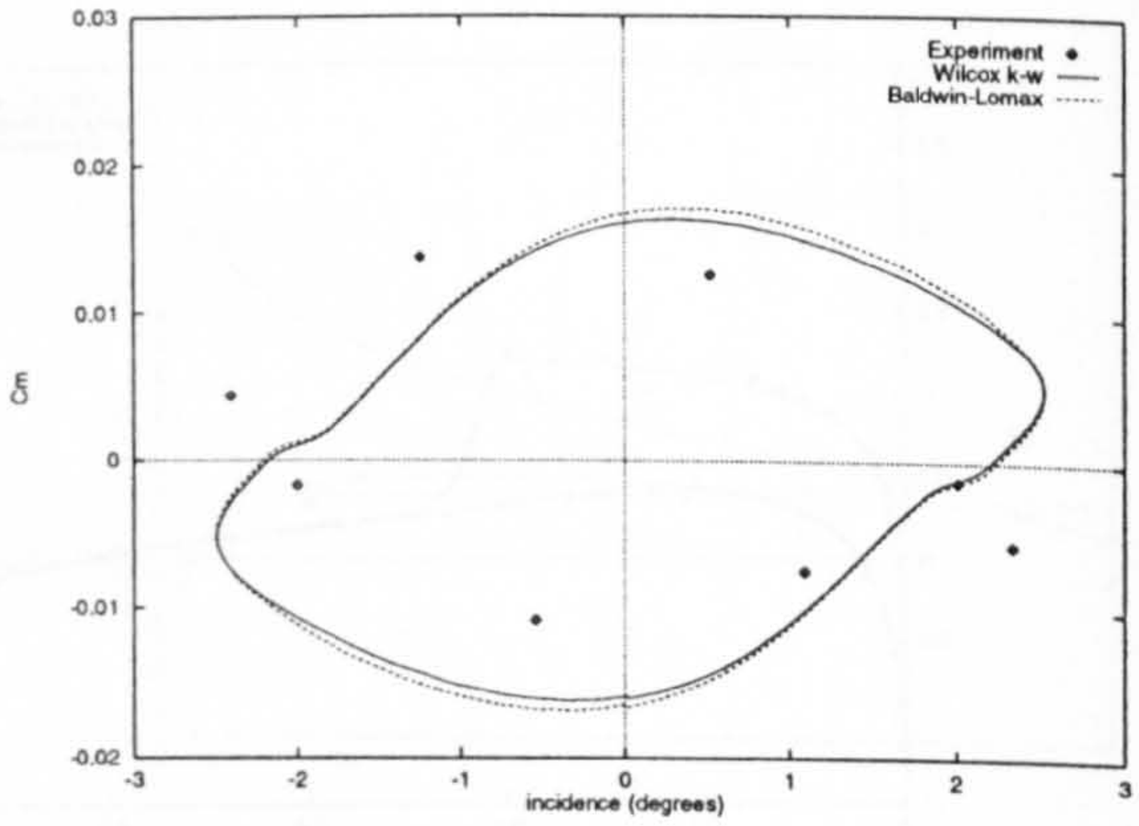

(b) Pitching Moment

Figure (7.10) Comparison of computed and measured[179] forces and moments (Case CT3)

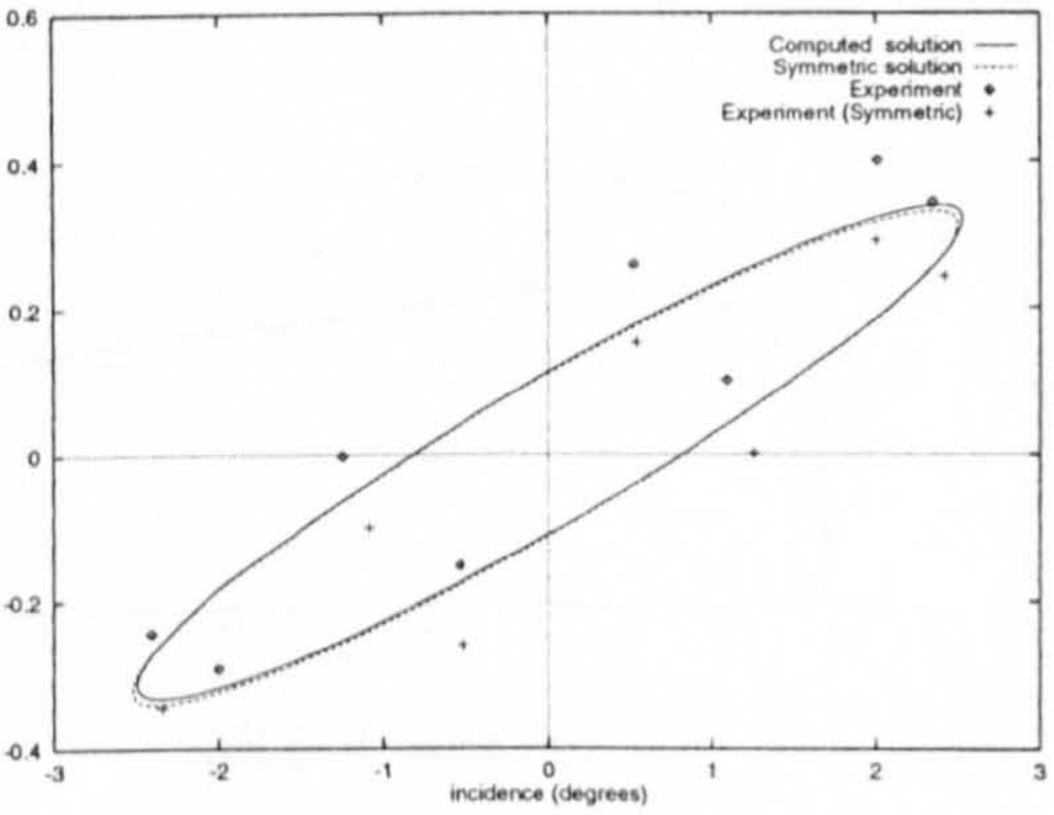

(a) Normal Force

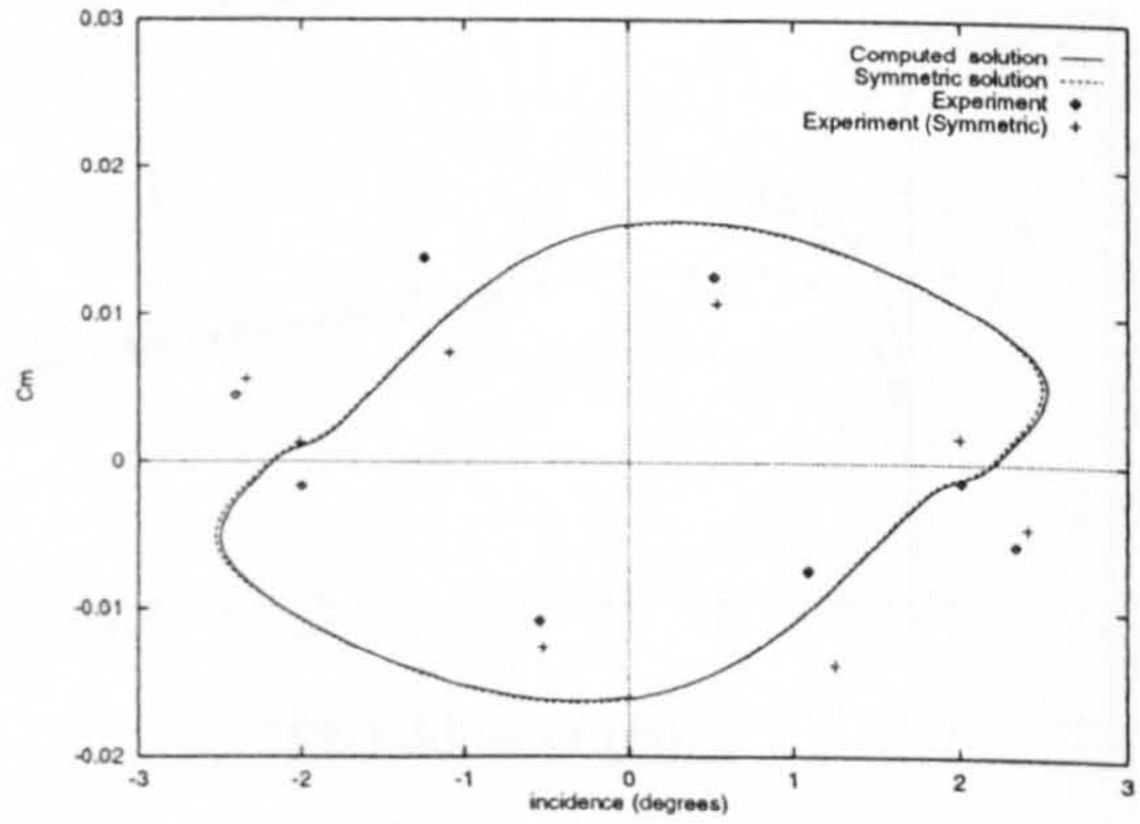

(b) Pitching Moment

Figure (7.11) Symmetry of computed and measured forces and moments

8

Self-excited periodic flow

The ability of the proposed numerical model to accurately represent the steady and unsteady aerodynamics of aerofoils has been demonstrated in the previous chapters. In this chapter, the self-excited periodic flow of an 18% thick circular arc aerofoil set at zero degree to the oncoming flow is investigated. The primary purpose of these calculations is to further demonstrate the capability of the method in resolving complex unsteady flows. However, this chapter also presents further contributions to the understanding of self-excited periodic flow. By comparing the results of both steady and unsteady calculations it is demonstrated that the self-excited flow is related to the instability of the shock induced separation bubble. Onset of periodic flow is shown to occur at a Mach number corresponding to incipient shock induced separation. The Mach number at which the flow becomes steady, can be correlated with the Mach number at which the reattachment point moves beyond the trailing edge in the corresponding steady flow.

8.1 Introductory remarks

The experimental measurements of Finke[197-8] demonstrate that the occurrence of flow unsteadiness at transonic Mach numbers is not limited to bodies undergoing rigid body motion or elastic deformation. Finke observed that for a small range of Mach numbers an unsteady asymmetric flow was established for a symmetric circular arc aerofoil set at zero degree incidence to the oncoming flow. McDevitt[199-200] also detected oscillatory flow separation over a narrow range of Mach numbers, $0.73 < M_{\infty} < 0.78$, at zero incidence for an 18% thick bi-convex aerofoil. Mabey[201-2] showed that periodic oscillations occur for circular arc aerofoils with thickness to chord ratios ranging from 10% to 20%. Subsequently, a comprehensive study of the periodic flow

around a number of symmetric aerofoils with a thickness in the range 6-14% of chord was performed at Cranfield University[203-6]. Gibb [206] also observed the phenomenon for non-symmetric aerofoils with little or no aft camber.

Figure (8.1), after Mabey [207], shows the important features of the flow development as the freestream Mach number is increased. Below the onset of periodic flow the transonic flow develops in a conventional manner, just below the onset Mach number small regions of separated flow appear close to the trailing edge. With a further small increase in Mach number large scale flow separation occurs and a periodic asymmetric flow is established. Large pressure fluctuations develop over the aft region of the aerofoil due to large chordwise displacements of the shock waves on both the upper and lower surfaces. The shock-waves move in anti-phase to one another and both shock-induced and trailing edge separation are observed. The periodic flow persists over a narrow range of Mach numbers beyond which the flow is again steady. At this point shock-induced separation is observed on both the upper and lower surfaces of the aerofoil.

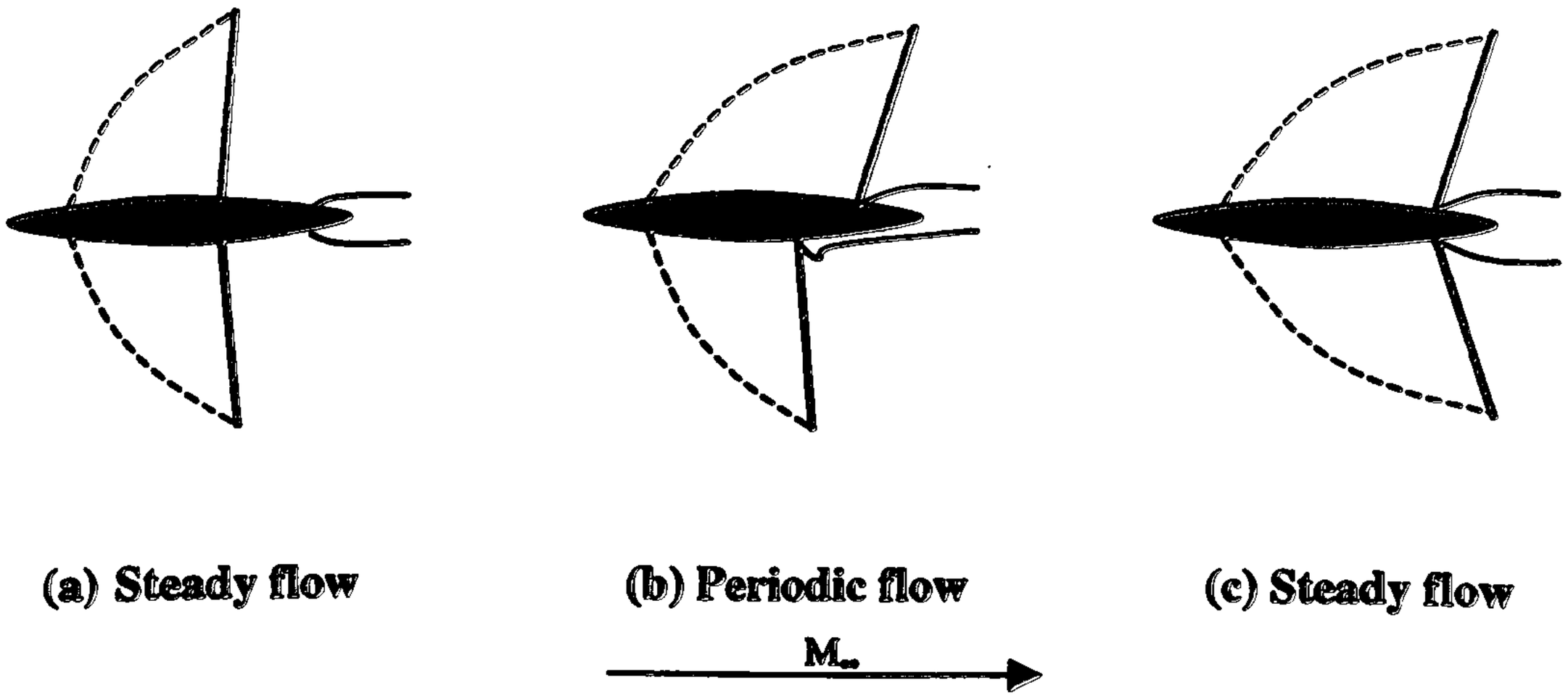

Figure (8.1) Flow development with increasing Mach number

From experimental measurements a number of criteria have been developed that must be satisfied for the flow to be periodic:

(a) The local Mach number upstream of the shock-wave must be in the range $1.14 < M_1 < 1.24$[201]

(b) The thickness to chord ratio must be greater than 10%[206]

(c) The aerofoil must have a large trailing edge angle[204]

(d) The aerofoil must have little or no aft camber[204]

While such criteria provide useful guidance for the aircraft designer they do not provide a clear understanding of the physical mechanisms responsible for the unsteady excitation. By plotting the transonic similarity parameter corresponding to the boundaries of the periodic flow Mabey[201] deduced that the flow instability was unlikely to be an inherent feature of the inviscid outer flow. Subsequent numerical studies, see for example Levy[208], employing solutions of the Euler equations demonstrate conclusively that the phenomenon is viscous in nature.

It was shown by Mabey that the measured data can be correlated with the time taken for pressure disturbances to travel from the trailing edge to the shock wave using the simple empirical relationship established by Erickson and Stephenson[23],

$$A = \frac{\omega L}{U} = \frac{\pi(1 - M_\infty)}{2M_\infty} \qquad (8.1)$$

This correlation provides firm evidence that the excitation of the shock wave is strongly related to the behaviour at the trailing edge of the aerofoil, which is dominated by the oscillation of the wake.

Based upon such observations Yamamoto and Tanida[209] have suggested a simple physical model, Figure (8.2), of the phenomena for aerofoils in a two-dimensional channel. The model relates the unsteady shock wave to the displacement effect of the oscillating wake. The physical process consists of the upstream propagation of pressure disturbances in the main flow, amplification of the pressure disturbances by the flow around the trailing edge and the downstream convection of disturbances due to the boundary layer separation.

The model is based upon the one-dimensional linearised wave equation with an assumed solution for the pressure perturbation of the form,

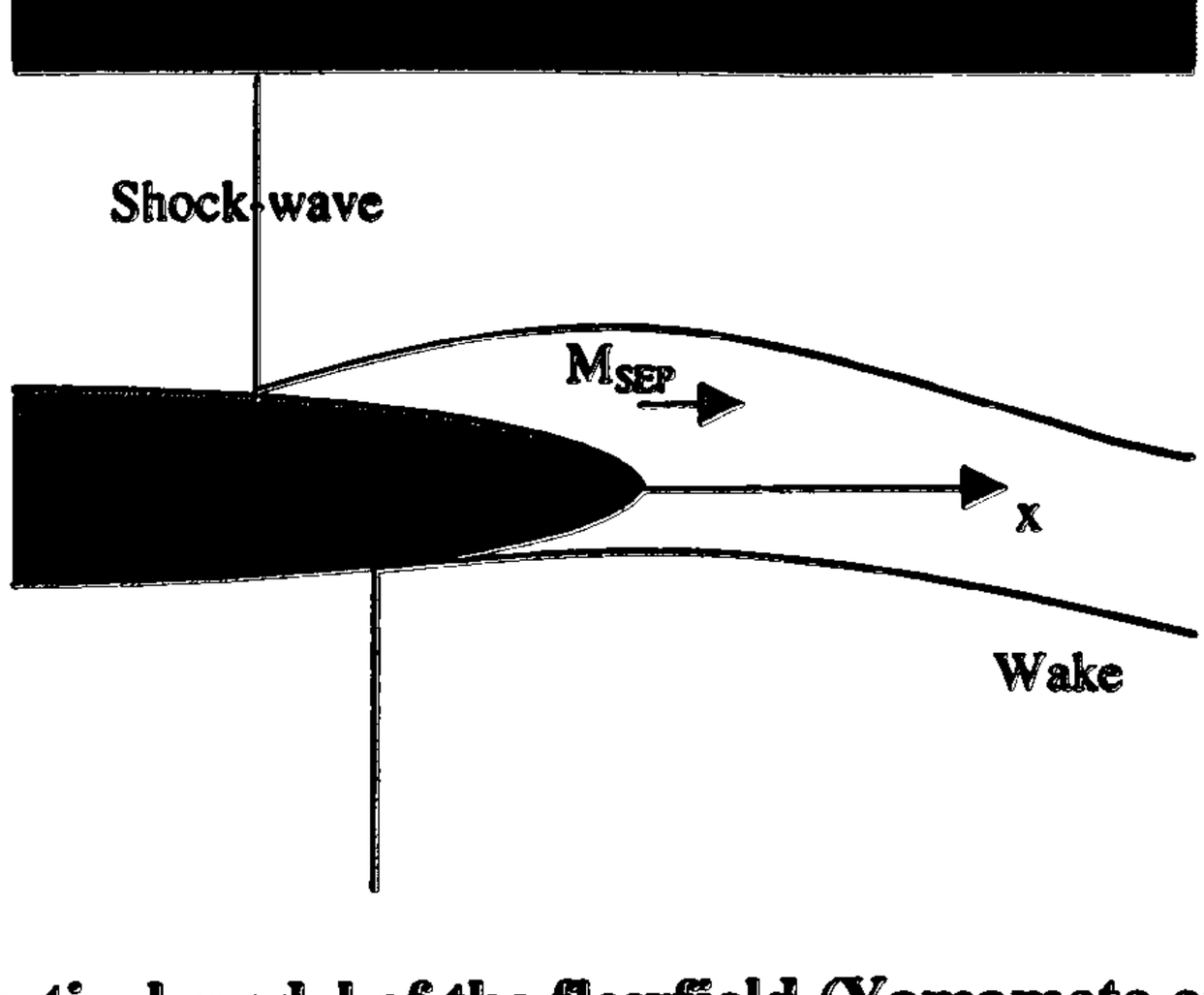

Figure (8.2) Theoretical model of the flowfield (Yamamoto and Tanida[209])

$$p = \left[p_{+} e^{\frac{i\omega x}{1+M_2}} + p_{-} e^{\frac{i\omega x}{1-M_2}} + p_{sep} e^{\frac{i\omega(x-x_{sh})}{M_{SEP}}} \right] e^{i\omega t} \qquad (8.2)$$

here the first two terms represent the downstream and upstream propagating pressure waves, while the final term is the pressure wave caused by the oscillation of the wake.

In Equation (8.2) ω is the Eigenvalue of the flow oscillation. When the imaginary component of ω is positive the flow is unstable with respect to small perturbations and a self-sustaining unsteady flow is predicted, conversely when the imaginary component of ω is negative the flow is stable to small pressure perturbations and no flow unsteadiness is predicted. Yamamoto and Tanida have solved (8.2) for the flow around a ten-percent thick aerofoil in a narrow channel. The predicted frequency parameter is in good agreement with experimental measurements when the mean shock position is located close to the centre of the aerofoil chord. However, as the shock-wave approaches the aerofoil trailing edge the frequency parameter predicted by the model tends towards an infinite value and consequently agreement with experiment becomes progressively worse.

Despite the inability of the model to predict the frequency parameter accurately over the full chord of the aerofoil it is still of great practical interest because it provides a clear understanding of how interactions between an unsteady shock-wave and an unsteady separation can produce a self-sustaining periodic flow. Furthermore, the

model provides an explanation for the narrow range of Mach numbers over which the phenomenon is observed. As the mean shock position moves downstream (i.e. as Mach number is increased) the amplitude of the pressure disturbance required to excite the shock wave increases eventually exceeding that of the disturbance produced by the unsteady separation.

While Yamamoto's model explains how small disturbances can be amplified and sustained to produce large-scale flow asymmetry it does not provide an explanation for the origin of the initial disturbances. In his study of the phenomena Gibb's[206] suggests that small scale disturbances, caused for example by turbulent fluctuations in the boundary layer, may be sufficient to cause premature shock induced separation on one side of the aerofoil. As a result of the separation, the shock wave on the upper surface will weaken and move upstream. The flow on the lower side of the aerofoil is unable to adjust immediately to the changes on the upper surface because of the finite time that is required for pressure disturbances to be communicated via the trailing edge and an asymmetric flow is established. The flow asymmetry induces flow around the trailing edge which in turn causes the wake to be deflected upwards toward the separated boundary layer. Thus, the initial small asymmetric disturbance has produced a flow that closely resembles the conditions required for the generation of self-sustained periodic flow using Yamamoto's model.

The problem can therefore be viewed as one in which the stability of the mean flow to small disturbances is of critical importance. That this is the case has been amply demonstrated by McDevit[199-200]. In McDevit's experiments type B oscillatory flow was observed over a narrow range of Mach numbers, $0.76 < M_\infty < 0.78$ when the Mach number was increased. However, when the Mach number was later reduced the extent of the observed boundaries increased, significant flow unsteadiness now being observed over the Mach number range $0.73 < M_\infty < 0.78$. Sensitivity to the initial flow conditions provides a reasonable physical explanation for the flow hysterisis that is observed. When the Mach number is increased from steady attached flow conditions the excitation mechanism is provided by freestream turbulence, in well designed experiments the freestream turbulence level is typically small and consequently

provides only small perturbations to the system. Conversely, when the Mach number is decreased the initial conditions are already highly unsteady providing significant levels of aerodynamic excitation.

Mabey[201] suggests that the clear boundary between oscillatory and non-oscillatory flow makes the computation of such flows a good candidate for the validation of CFD methods. However, in principle it should not be possible to predict such flows by solution of the Navier-Stokes equation's as time averaging removes the background turbulence fluctuations that are believed to be the primary mechanism for excitation of the unsteady response. While it is possible to introduce an artificial disturbance, for example an instantaneous perturbation of the incidence, no guidance has been provided on the scale of disturbance that is required to simulate the experimental arrangement correctly. Despite this apparent problem oscillatory solutions have been reported by a number of authors, see the review of Edwards[210] and the discussion below.

In the absence of a physical mechanism with which to excite the flow unsteadiness our ability to successfully simulate this flow must be attributed to the presence of numerical errors within the calculation. It is well known that numerical methods are subject to rounding errors associated with the finite arithmetic precision of digital computers. While such errors are not random in nature (they are reproducible) it is believed that these errors can provide the required fluctuations necessary to establish self-excited periodic oscillations. Some scatter in the predicted onset Mach number is therefore expected between different numerical methodologies.

The accurate prediction of self-excited periodic oscillations presents a significant challenge for computational methods because of the need to predict large-scale separation and strong viscous-inviscid interactions. The earliest attempts to compute this flow are attributed to Levy[211-2] and Diewert[213-4] who were able to reproduce qualitatively the essential flow physics from solutions of the thin-layer Navier-Stokes equations. In their studies the sharp aerofoil leading edge was rounded to avoid numerical instabilities. Heavy buffet was predicted at a Mach number of 0.754 with a reduced frequency of 0.4. The calculated frequency compares favourably with the

experimentally determined value of 0.47. In a later study Steger[215] was unable to reproduce these results, instead buffet was predicted at M=0.783 with a reduced frequency of 0.41. This apparent disparity may be attributed to Steger's use of freestream boundary conditions in the far-field while Levy and Deiwert chose to model the contoured walls of the wind tunnel in which the experiments were performed. Further computations have been performed by Seegmiller[216], La Balleur[217], Gillan[218] and Edwards[219] using a number of different methodologies.

In all of these numerical studies reduced frequencies for the self-excited flow around an 18% thick bi-convex aerofoil significantly lower (20-30%) than those observed in the experiments were reported for isolated Mach numbers within the experimentally observed buffet range. The large disparity between experimental measurements and computation has been attributed to a wide range of causes, of which the absence of tunnel walls in the computational model and inadequate turbulence modelling are most common.

It is significant that the thin-layer Navier-Stokes equations were employed in all of the above studies (with the exception of that due to La Balleur[217] who solved the TSD equations using a viscous-inviscid interactive approach). Edwards[219] abandoned the Navier-Stokes equations in favour of the TSD equations and an interactive lag-entrainment boundary layer method. The calculated reduced frequency obtained using this method, k = 0.47 at a Mach number of 0.76, is in excellent agreement with experimental measurements and Edwards produced the first successful computations of the hysterisis observed by McDevit. Furthermore, Edwards showed that the maximum value of boundary layer shape factor, H, was between 20 and 40 indicating that the free shear-layer is well off the aerofoil surface. This suggests that the use of a thin-layer approximation may be inappropriate for this class of flows.

Subsequently Gillan et al[220] compared results obtained using the thin-layer and full Reynolds averaged Navier-Stokes equations, reduced frequencies of k=0.396 and k=0.46 were obtained. Despite the use of an algebraic turbulence model the results

obtained using the full form of the governing equations are in good agreement with experimental measurements.

The influence of more advanced turbulence models has been explored in recent papers by Rumsey[221], Ji[222] and Badcock[223]. Rumsey[221] presents a detailed investigation of the flow around an 18% thick circular arc aerofoil using the thin-layer Navier-Stokes equations together with the algebraic Balwin-Lomax and the one-equation Spalart-Allmaras turbulence models. A reduced frequency of about 0.39 is obtained using the Baldwin-Lomax model. The Spalart-Allmasras model produces a reduced frequency of about 0.49, which is in excellent agreement with that determined in the experiments of Levy[211]. The Mach number at which asymmetric flow first appears is in close agreement with experiment and the hysterisis observed by Levy is also reproduced numerically.

Ji and Liu[222] solved the full Navier-Stokes equations for a 10% thick circular arc aerofoil in a channel using the Baldwin-Lomax turbulence model and the standard, baseline and SST k-ω turbulence models. The Baldwin-Lomax calculations reproduce qualitatively the experiments of Yamomoto[209] but the calculated amplitude and frequency are in poor agreement with measurements. Surprisingly, calculations performed using the three two-equation turbulence models yielded steady state solutions, the reasons for this are not clear.

Badcock[223] employed the Navier-Stokes equations together with the k-ω turbulence model to simulate the flow around an 18% thick circular arc aerofoil at a Reynolds number based on chord of 2 million. Results are presented for three discrete Mach numbers 0.74, 0.77 and 0.82 which lie below, within and above the experimental range observed by McDevit. While oscillatory flow is predicted at $M_\infty = 0.77$ no qualitative information on the reduced frequency is provided.

In the following section results obtained using the methodology outlined in Chapters (3)-(5) obtained for the flow around an 18% thick circular arc aerofoil are described. The calculations were performed at a Reynolds number of $Re_c = 11$ million over a

Mach number range $0.70 < M_\infty < 0.80$ which corresponds with the experiments of McDevitt[199-200]. An algebraic C-grid containing 369x129 grid points (260 points on the aerofoil surface) was generated about the aerofoil with the freestream boundaries located 20 chord lengths from the aerofoil surface. Care was taken to ensure that grid lines were normal to the aerofoil surface, although in the region of the leading edge this was not possible because of the grid topology that had been adopted. In contrast to the studies mentioned above no numerical difficulties were encountered due to the sharp leading edge of the aerofoil and consequently there was no need for it to be rounded. The grid is shown in Figure (8.3). A coarser grid containing 185x65 grid points (130 points on the aerofoil surface) was then obtained by deleting every second point of the original grid. The maximum distance between the wall and the adjacent cell centre was $1.27 \times 10^{-6}c$ and $6.0 \times 10^{-7}c$ for the coarse and fine grids respectively.

8.2 Steady flow calculations

In order to obtain numerical solutions for the steady flow around the 18% thick circular arc aerofoil the governing equations were integrated in time using a time step that was consistent with the local CFL condition. While this procedure destroys time accuracy it allows steady solutions to be obtained with considerably reduced computational effort. Computations were performed for Mach numbers in the range $0.70 < M_\infty < 0.80$ with steps of $\Delta M=0.01$ using the grids discussed above. Initially 500 explicit iterations at a CFL number of 0.2 were performed followed by 2000 implicit iterations with a CFL number which varies linearly with the residual to a maximum value of 80.

In Figure (8.4) the convergence of normal force with iteration number is shown for Mach numbers in the range $0.70 < M_\infty < 0.80$ using the k-ω turbulence model. From Figure (8.4) we can identify two distinct classes of behaviour. Firstly, for freestream Mach numbers below $M_\infty = 0.76$ the normal force has an initial value that is zero within machine accuracy (typical values are around 1×10^{-11}). Shortly after application of the implicit methodology a non-zero value of normal force is developed. The occurrence of this non-zero value corresponds with the rapid initial convergence of the system

associated with the initiation of the implicit steps. With further implicit iterations the normal force tends to zero.

For Mach numbers above $M_\infty = 0.76$ non-zero values of normal force are again developed shortly after application of the implicit methodology. However, for these cases the non-zero value develops into a periodic oscillation, initially the oscillation grows exponentially until it eventually reaches a limiting value. For the cases considered the oscillatory flow has a large reduced frequency and relatively small magnitude, such limit cycle oscillations are generally indicative of unsteadiness in the corresponding physical flow, although they do not simulate the real unsteady flow due to the local time stepping used.

While the calculations for Mach numbers above $M_\infty = 0.76$ are not strictly steady it is still of interest to consider the development of the 'steady' flowfield for the Mach number range over which we expect to observe large scale asymmetric periodic flow. In Figure (8.5) the steady pressure distributions obtained in the present k-ω and Baldwin-Lomax calculations for $M_\infty = 0.72$ are compared with the measurements reported by McDevitt[199]. Significant differences are observed between the computed and measured pressure coefficient, there is evidence of a shock wave in both the calculations but none in the experiment. Similar behaviour was observed by Levy[211] and is attributed to the influence of the tunnel walls (see Figure (6a) of Reference (199) in which computations performed with and without the influence of tunnel walls are compared).

The flow development with increasing Mach number is shown in Figure (8.6) in which curves of pressure ratio P/H_∞ are plotted. The flow develops in a conventional manner, as Mach number increases from 0.70 to 0.76 the shock-wave forms and moves aft in a smooth fashion gradually increasing in strength. The boundary layer remains fully attached (this can be deduced from Figure (8.7a) which shows contours of local Mach number for a freestream Mach number 0.73) although there is significant thickening as it traverses the shock wave.

At $M_\infty = 0.76$ the boundary layer separates at the foot of the shock reattaching a short distance downstream to form a separation bubble, see Figure (8.7b). In addition a further separated region is observed in close proximity to the aerofoil trailing edge. As Mach number is increased further the extent of the separation bubble and the trailing edge separation increase until eventually at M_∞=0.78 they merge to produce a separated region which begins at the foot of the shock-wave and extends over the remaining chord, this is shown in Figure (8.7c). The breakdown of the flow with increasing Mach number corresponds to type B1 (rear separation provoked by bubble) using the classification scheme developed by Pearcey[224].

8.3 Unsteady flow calculations

Time histories of the computed normal force obtained using Wilcox's k-ω turbulence model are presented in Figure (8.8) for freestream Mach numbers in the range $0.74 \leq M_\infty \leq 0.81$. For $M_\infty = 0.74$ and $M_\infty = 0.75$ no significant unsteady effects are observed. While there are fluctuations in both the normal force and pitching moment they are random in nature and have magnitudes close to the rounding error ($C_N \sim 10^{-9}$) of the machine upon which the calculations were performed. When the freestream Mach number was increased to $M_\infty = 0.76$ unsteady flow was observed. Initially small regular fluctuations were observed, the scale of the fluctuations growing exponentially with increasing time. The latter stages of this can be clearly seen in Figure (8.8c) for non-dimensional times between 4 and 8. Subsequently, fully developed flow is obtained with a magnitude of around C_N=0.26 and a reduced frequency of k=0.465. This corresponds closely with experimental measurements of around k=0.48. As Mach number is increased further (M_∞=0.77 and M_∞=0.78) flow unsteadiness persists. The magnitude of the peak normal force coefficient increases with increasing Mach number up to a value of about C_N=0.30 while the reduced frequency remains constant, in addition the development of the periodic flow is accelerated. Computations at a freestream Mach number of $M_\infty = 0.79$ indicate a sudden collapse in the peak loading and a sharp rise in reduced frequency. The amplitudes of the fluctuations are small about C_N=0.05. Furthermore, the flow does not appear to be fully developed - a clear periodic flow is not observed. Further computations at M_∞=0.80 and M_∞=0.81 indicate

that the flow is steady once again. In Figure (8.8g) results for M_∞=0.80 are presented. We observe that initially the flow development closely parallels that at M_∞=0.79, the flow is unsteady and as before the scale of the fluctuations grows exponentially. A limit cycle oscillation is obtained, but the scale and frequency of the unsteadiness are quite different from those obtained in previous calculations. This limit cycle oscillation is not self-sustaining and diminishes in the later stages of the calculation and the subsequently steady flow is re-established. As has been noted small disturbances were observed in the steady solutions that were used to initiate the current unsteady calculations. It seems that these disturbances are sufficiently large to excite unsteady flow but as Mach number is increased the flow becomes insensitive to the disturbances and steady flow is re-established.

In Figure (8.9) instantaneous contours of local Mach number are plotted around the aerofoil for M_∞=0.77. During the initial stage of the flow oscillation, the shock waves on the upper and lower surfaces are symmetric and the flow is attached. As the flow develops separation is observed on the upper surface of the aerofoil while on the lower surface the flow remains attached. The shock wave on the upper surface moves towards the leading edge while that on the lower surface travels towards the leading edge. The shock wave on the upper surface diminishes in strength and eventually disappears. As a consequence the flow on the upper surface reattaches, the shockwave on the lower surface now begins to move towards the leading edge. The shockwave on the upper surface reappears and begins its movement towards the trailing edge growing in strength as it does so. Eventually the initial symmetric flow is attained once more. The flow development described for the first half of the motion is repeated, with the upper and lower surfaces transposed. The flow oscillation is classified as Tidjemann Type B.

In Figure (8.10) the computed data are compared with experimental measurements. Mach numbers for which unsteady flow was obtained are represented by a cross while calculations in which steady flow was observed are represented by open symbols. The measured range of flow unsteadiness is indicated by solid and dashed lines representing the boundaries for $dM_\infty/dt > 0$ and $dM_\infty/dt < 0$ respectively. While no attempt has been made to resolve the exact location of the flow boundaries in the present work the

correspondence between the computations and experiments is satisfactory. In Figure (8.11) the calculated reduced frequency is compared with experimental measurements. The computed values of k=0.465 are in excellent agreement with measured values which range from k=0.48 at M_∞=0.76 to k=0.47 at M_∞=0.78.

It is useful to contrast the present unsteady results with the quasi-steady calculations obtained in the previous section. The onset of large scale flow unsteadiness at M_∞=0.76 corresponds closely with the incipient shock induced separation. For modest increases in freestream Mach number to M_∞=0.77 and M_∞=0.78 a separation bubble is observed in the steady flow and unsteady flow persists in the corresponding unsteady flows. Furthermore, shock-freeze is observed in the steady flow. This observation goes some way to explaining the constant reduced frequency calculated in the unsteady flows. The Mach number at which the reattchment point moves beyond the aerofoil trailing edge correlates closely with that at which the large-scale unsteady separation disappears.

Similar calculations were performed using the Baldwin-Lomax turbulence model. As before the onset of flow unsteadiness is again predicted at M_∞=0.76. Small differences are observed in both the magnitude and reduced frequency of the fully developed periodic flow when compared with the previous two-equation model calculations. The fluctuations have a magnitude of C_N=0.30 and the frequency is around k=0.51. As before increases in the freestream Mach number lead to larger scale fluctuations, C_N=0.35 at M_∞=0.77, while the reduced frequency remains almost constant. Small discrepancies become apparent in the initial behaviour of the normal force coefficient history. These discrepancies become increasingly evident as freestream Mach number is increased.

Unsteady flow persists too much later Mach numbers in the algebraic model computations than in the previous two-equation model computations. At M_∞=0.80 the initial flow development is highly irregular, furthermore we see an increase in the reduced frequency. At M_∞=0.81 the magnitude of the unsteady flow collapses and there is a considerable increase in reduced frequency. Calculations for higher freestream Mach numbers indicate the presence of small-scale periodic oscillations. These

fluctuations are 1-2 orders of magnitude less than the unsteadiness observed between M_∞=0.76 and M_∞=0.80 and are typical of the quasi-steady flow observed experimentally for Mach numbers above which large scale shock induced separation occurs. In Figure (8.12) and (8.13) the occurrence and frequency of the unsteady fluctuations are compared with experimental measurements. As noted previously the onset of periodic flow corresponds closely with that observed in the k-ω calculations and is consistent with the experimental measurements. The periodic flow persists too much higher freestream Mach numbers than in either the experiments or two-equation model calculations. The calculated reduced frequency of around k=0.45 agrees satisfactorily with the experimental measurements and is consistent with predictions made by other authors[221].

8.4 Concluding remarks

In this chapter the flow around an 18% thick circular arc aerofoil was computed over a wide range of Mach numbers. From the flow calculations a range of Mach numbers was identified for which the flow was unsteady. The onset of flow unsteadiness was observed at M_∞=0.76 in both the algebraic and two-equation model calculations. This is consistent with the wind tunnel measurements of Reference (199). Unsteady flow with a reduced frequency of about k=0.465 and k=0.45 were obtained with the two and zero equation models respectively. The former is in excellent agreement with experimental observations, while the latter is satisfactory. The unsteady flow calculated using the k-ω model persists until M_∞=0.79 which is consistent with experiment. The unsteady shock motion persists much later in the Baldwin-Lomax calculations than in the experiment. The unsteady flow development was also compared with the quasi-steady flow obtained using local time stepping. It was shown that the point at which flow unsteadiness is observed corresponds closely with the point at which incipient shock induced separation occurs. There is also a strong correlation between the growth of the separation bubble and the range of Mach numbers for which unsteadiness is observed. In the unsteady calculations flow unsteadiness persists while there is a clearly defined separation bubble in the steady flow. Once the separation bubble 'bursts' and the shock induced separation extends over the trailing edge the flow reverts to a (quasi-) steady state.

Comparison of the computed results with experiment suggest that both turbulence models are capable of resolving unsteady shock boundary layer interactions. However, the predictions obtained using the two-equation model show better qualitative and quantitative agreement with experimental data than the Baldwin-Lomax model. For this reason, results obtained using the two-equation model will form the focus of the calculations presented in subsequent chapters.

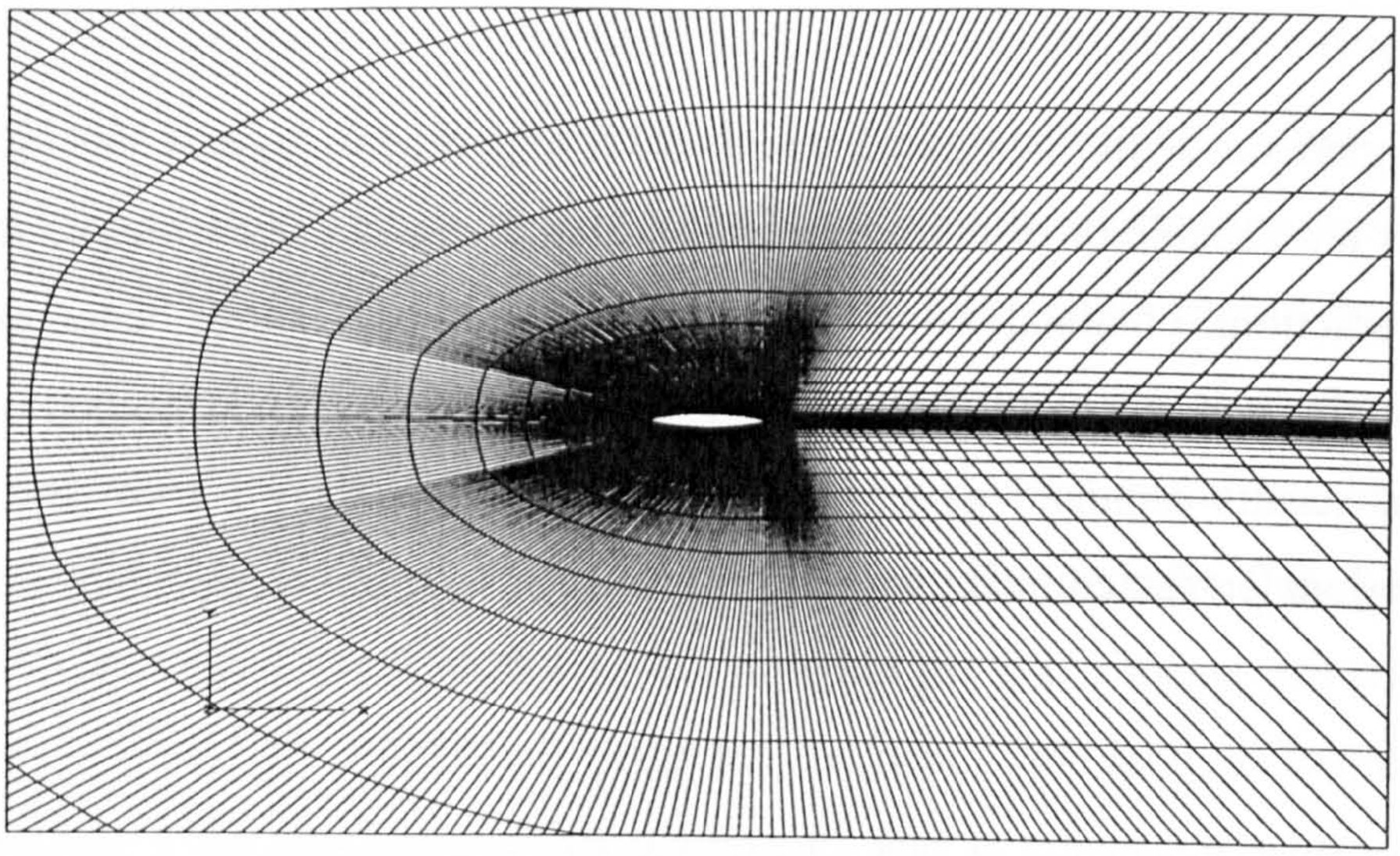

Figure (8.3) Computational grid

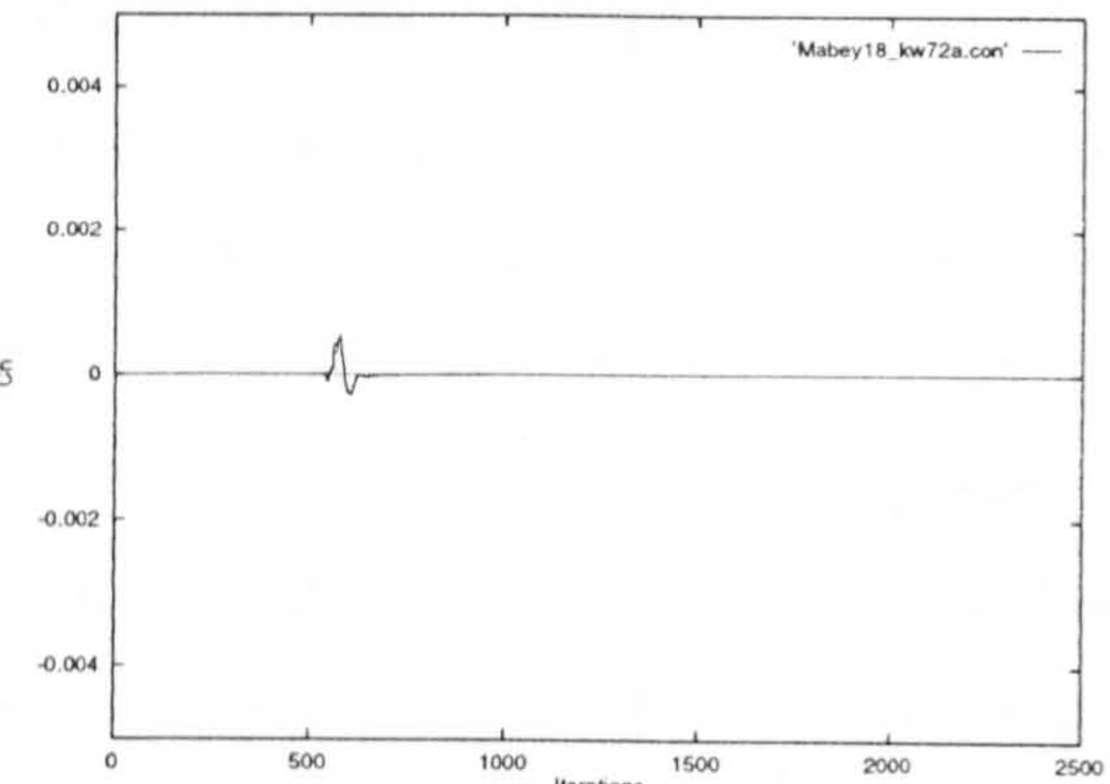

(a) $M_\infty = 0.72$

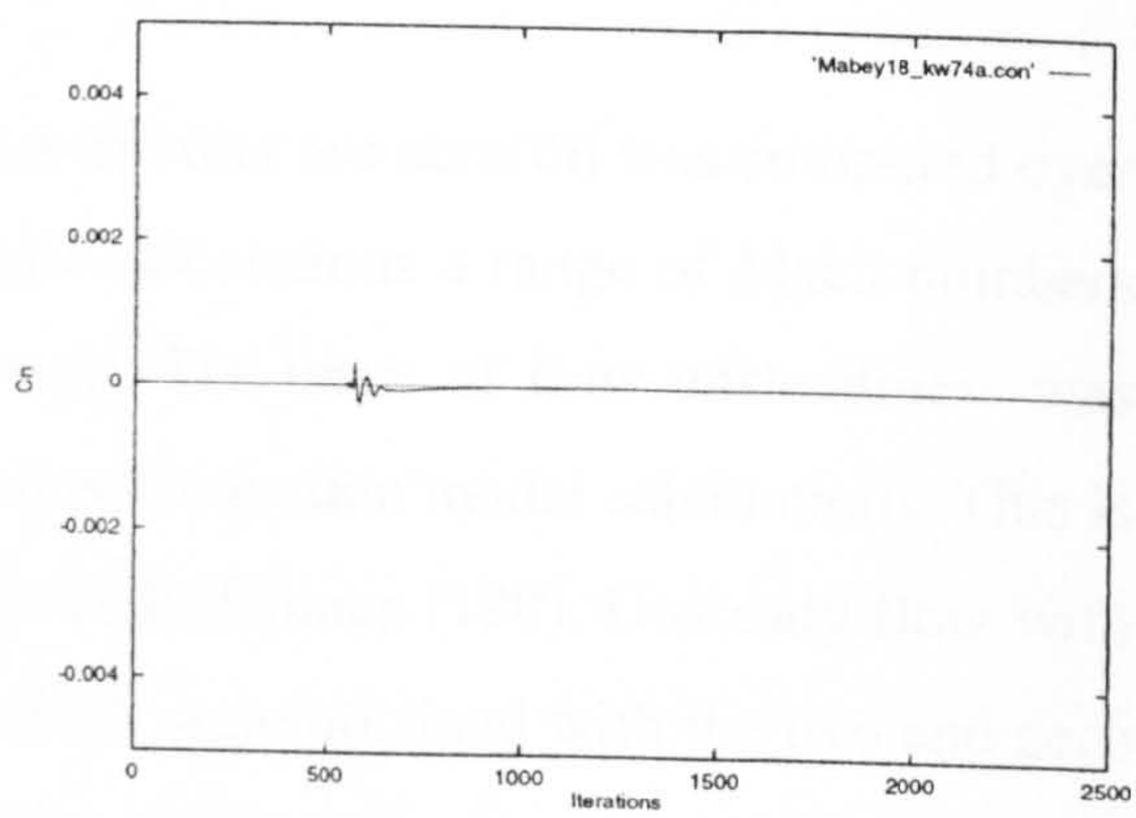

(b) $M_\infty = 0.74$

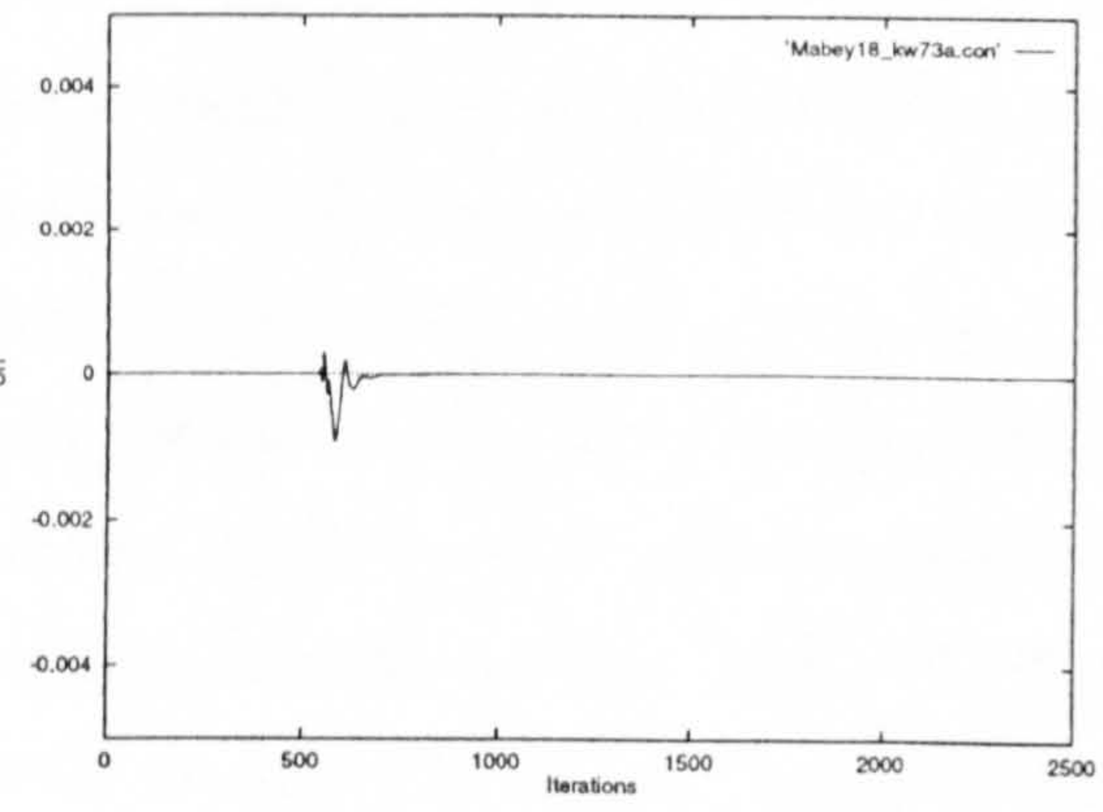

(b) $M_\infty = 0.73$

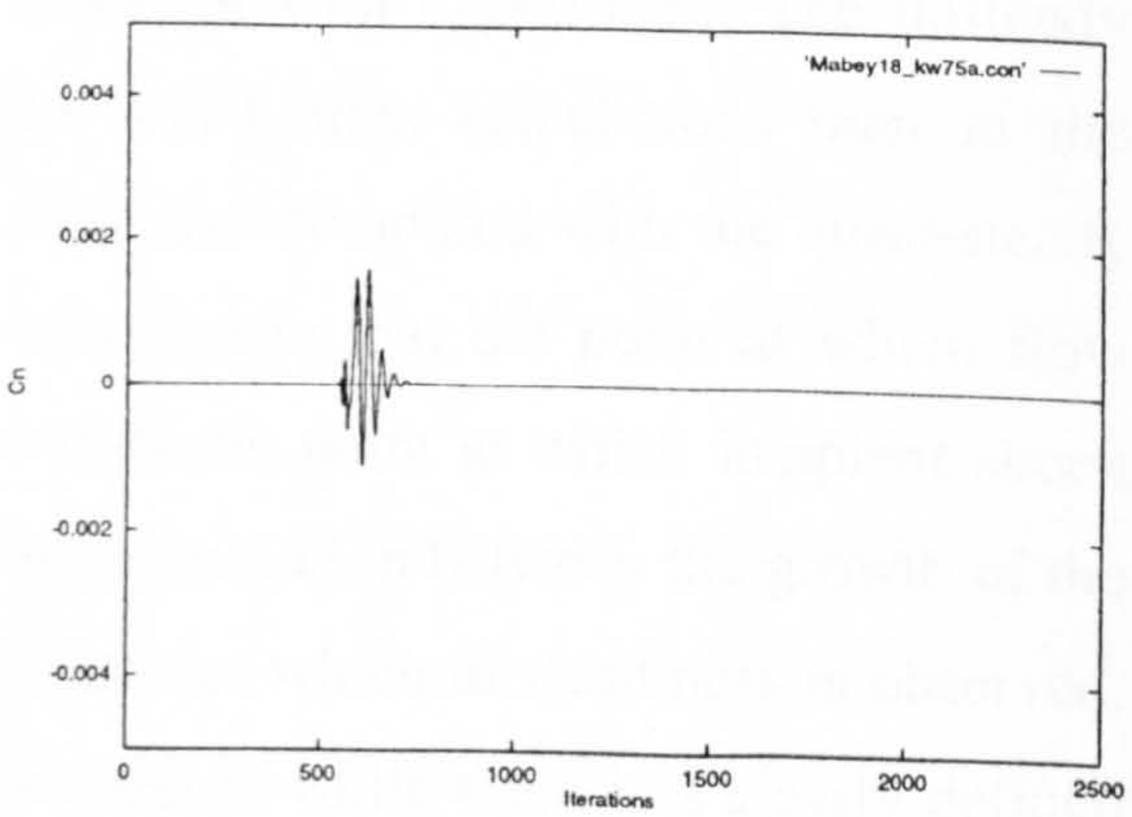

(c) $M_\infty = 0.75$

Figure (8.4) Normal force history (Steady calculations)

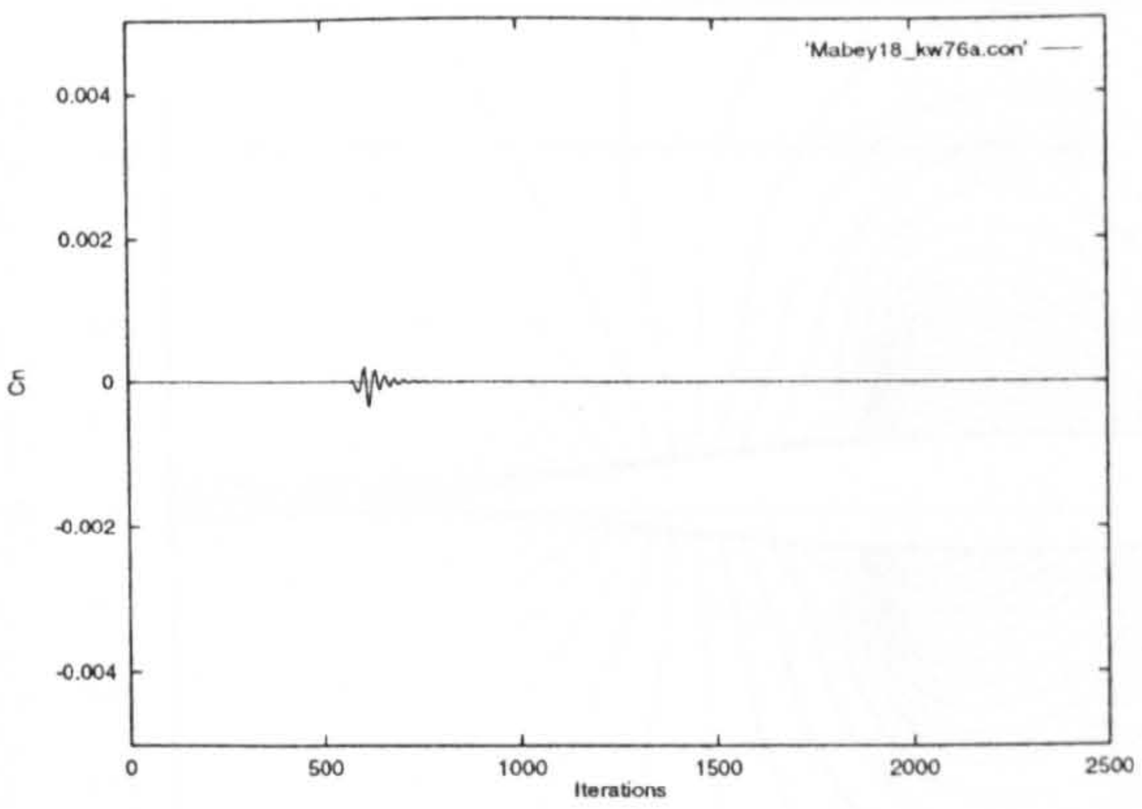

(e) $M_\infty = 0.76$

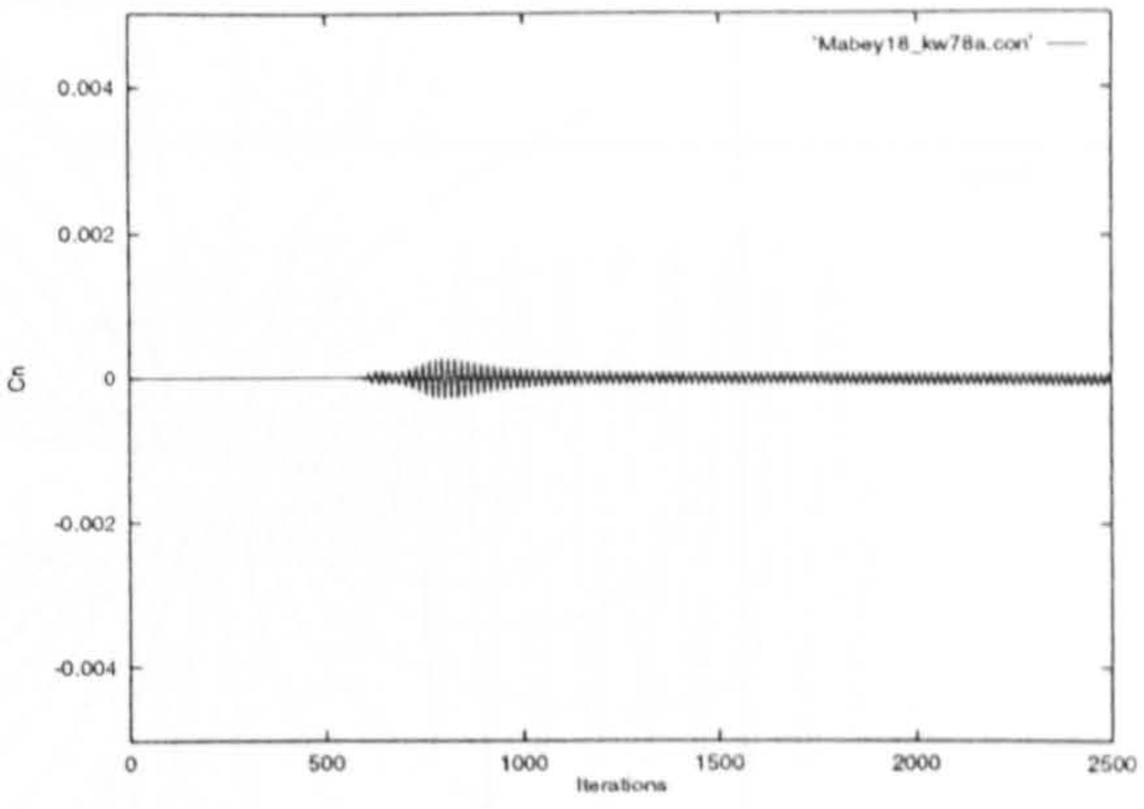

(g) $M_\infty = 0.78$

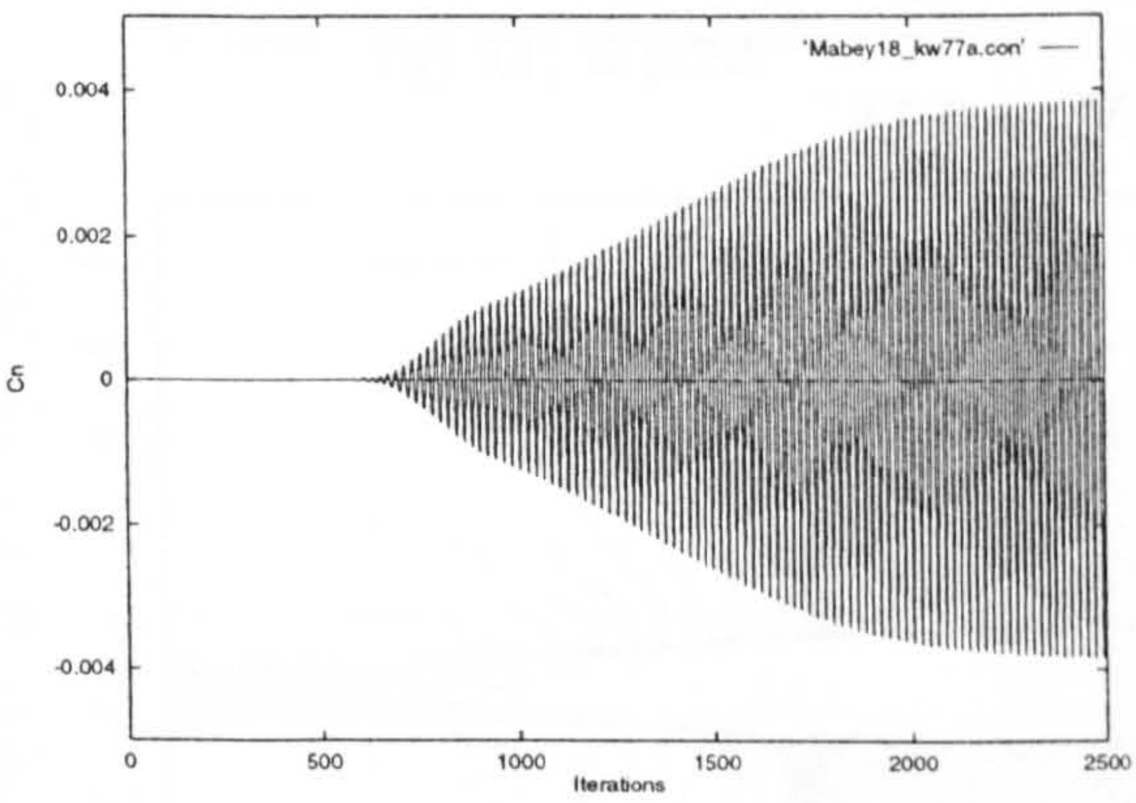

(f) $M_\infty = 0.77$

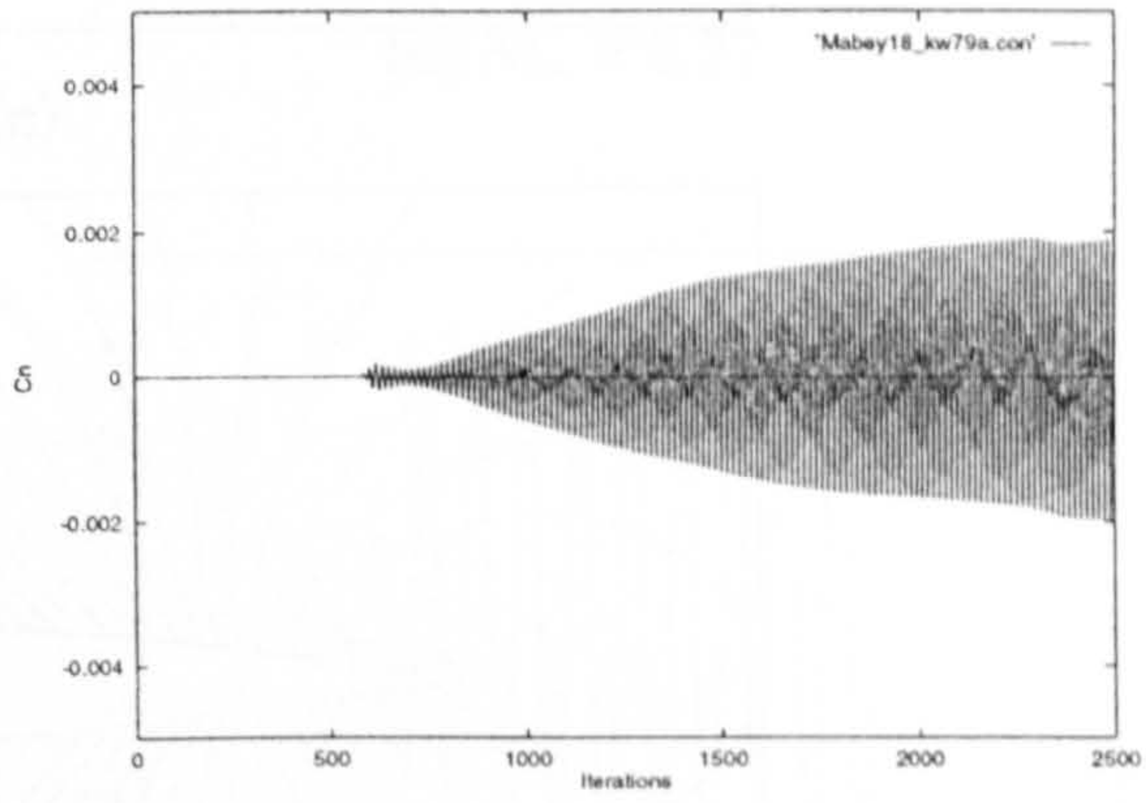

(h) $M_\infty = 0.79$

Figure (8.4) Normal force history (Steady calculations)

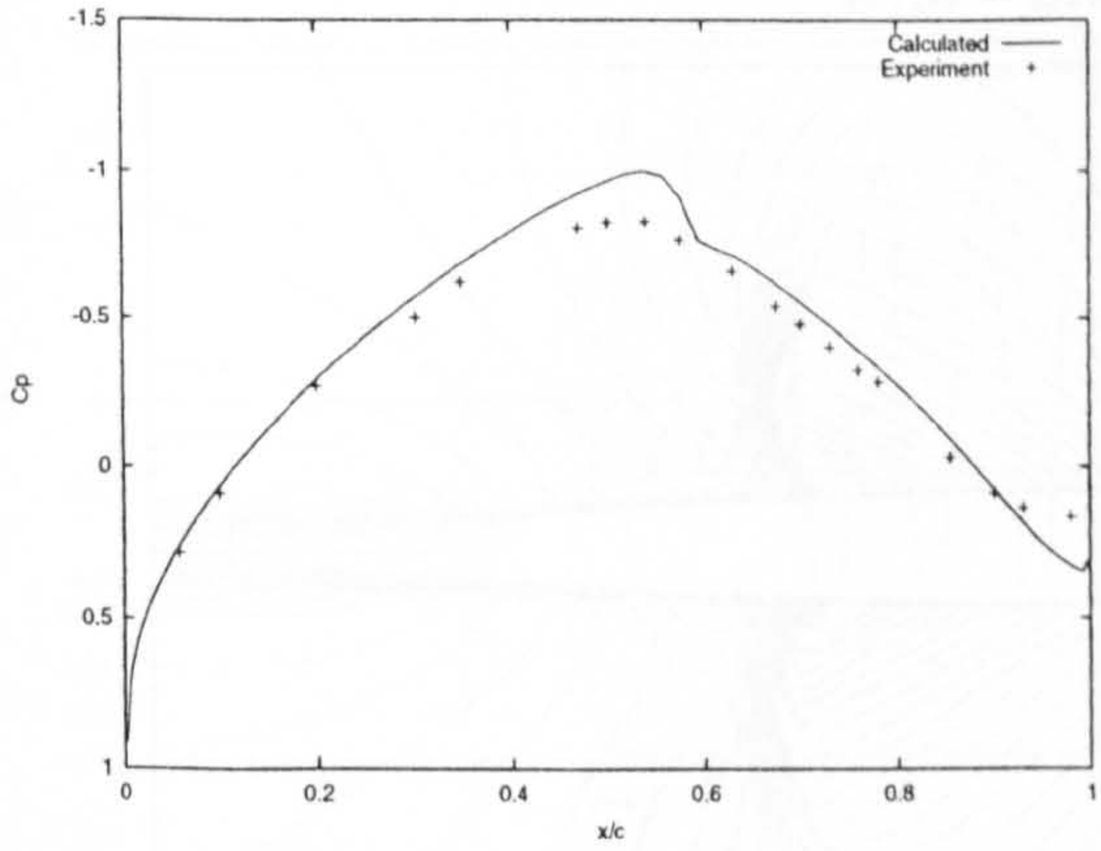

Figure(8.5) Computed and measured[200] pressure distributions ($M_\infty = 0.72$)

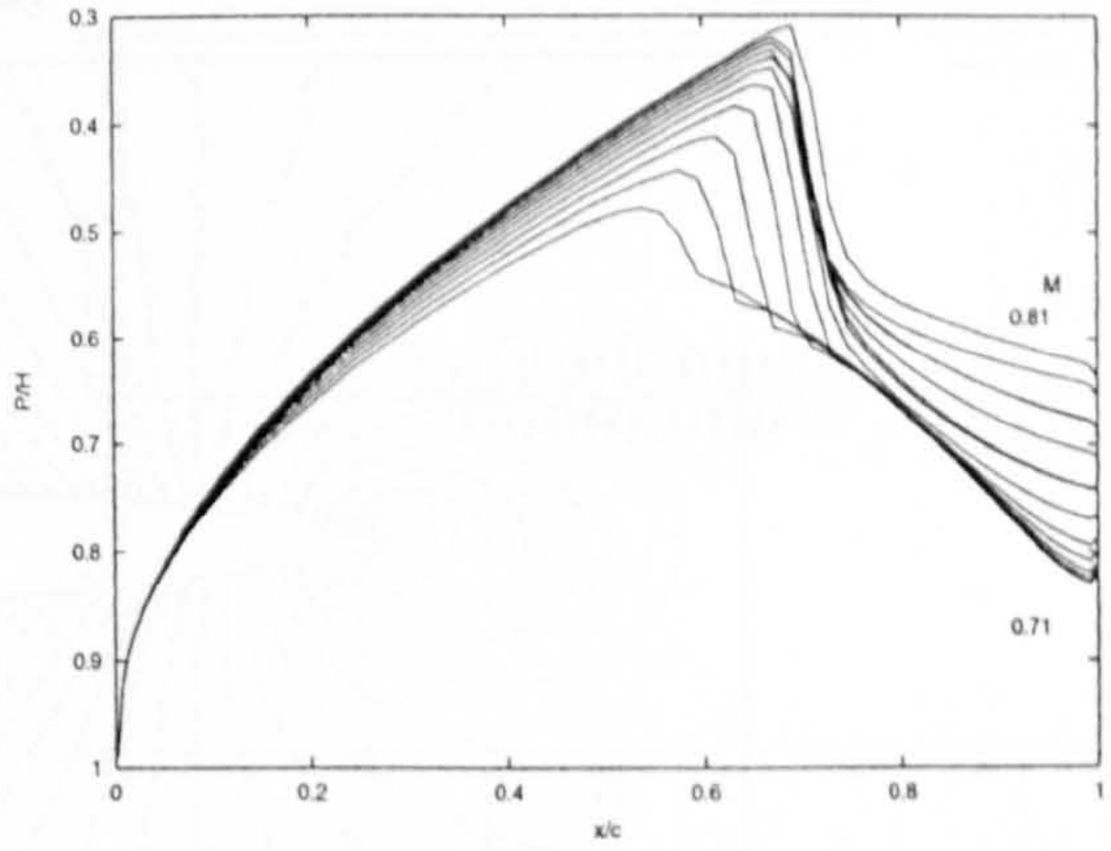

Figure (8.6) Variation of pressure coefficient with Mach number

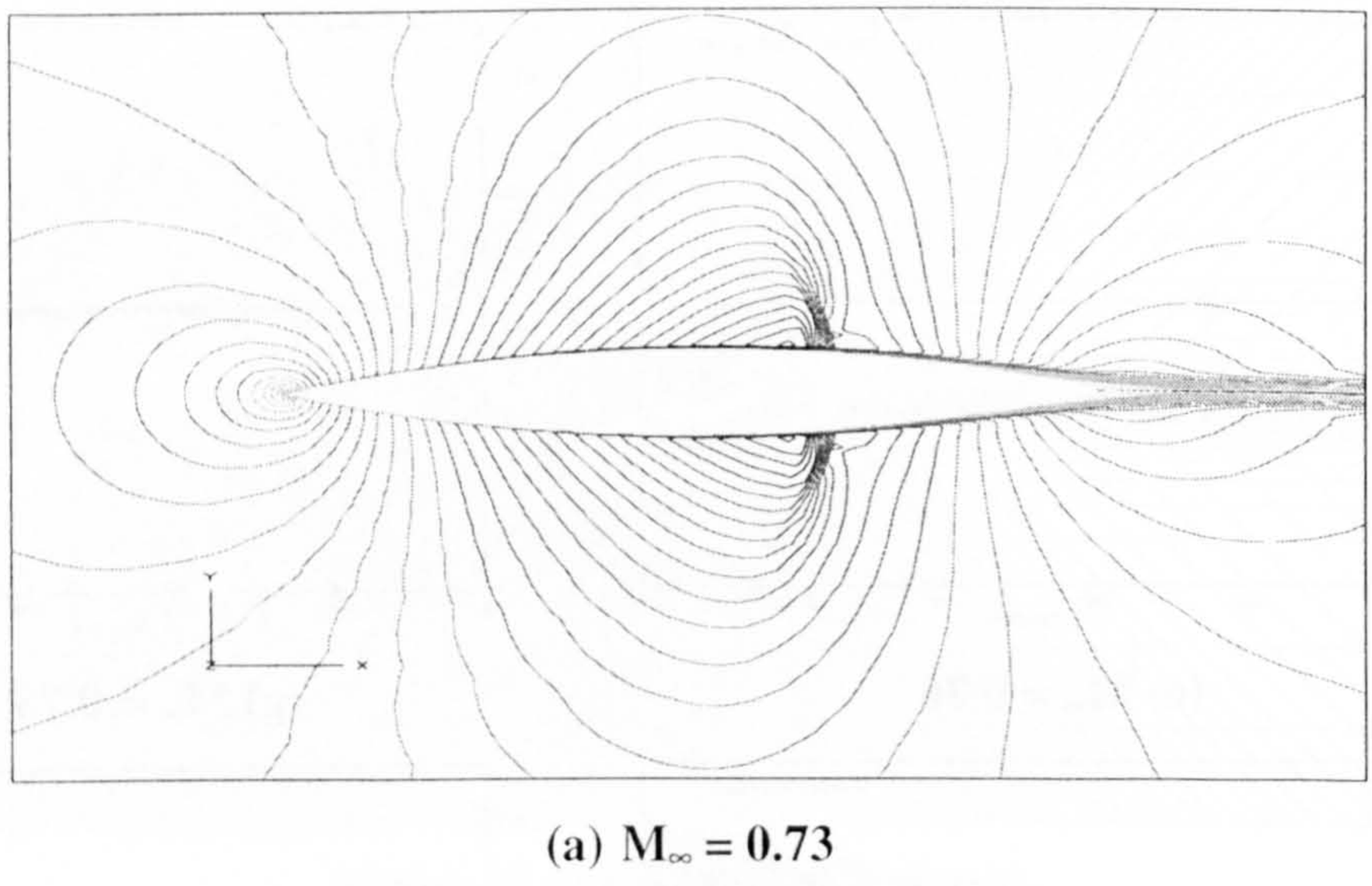

(a) $M_\infty = 0.73$

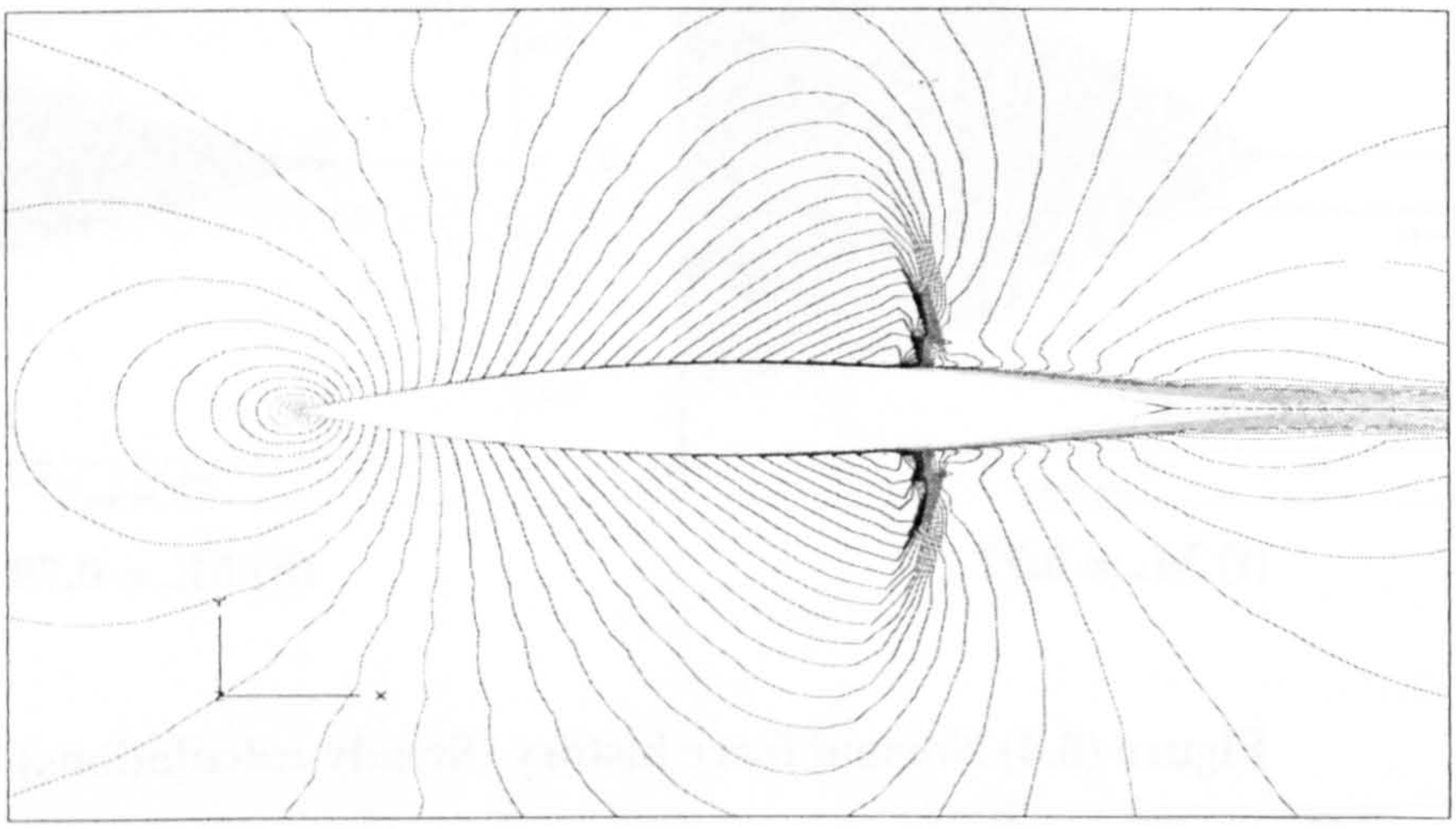

(b) $M_\infty = 0.76$

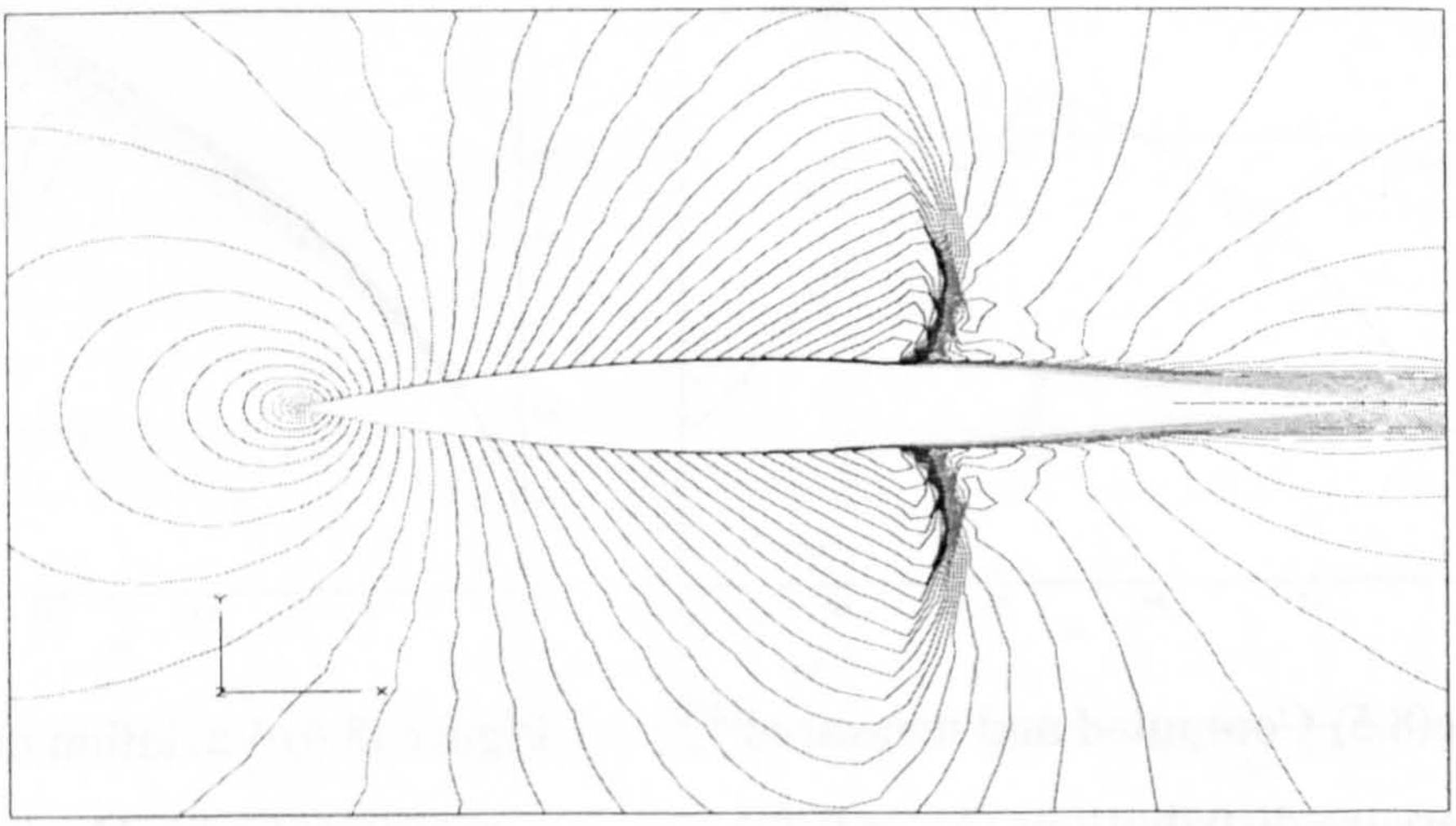

(c) $M_\infty = 0.78$

Figure (8.7) Computed Mach contours

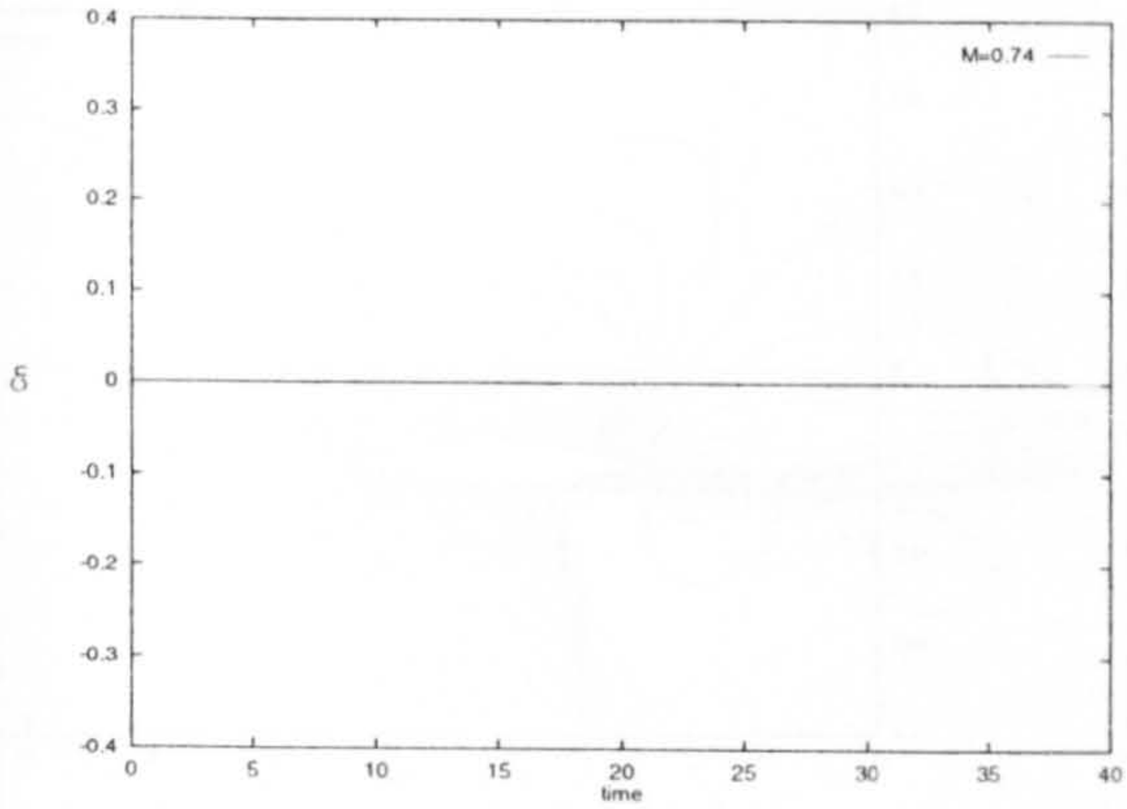

(a) $M_\infty = 0.74$

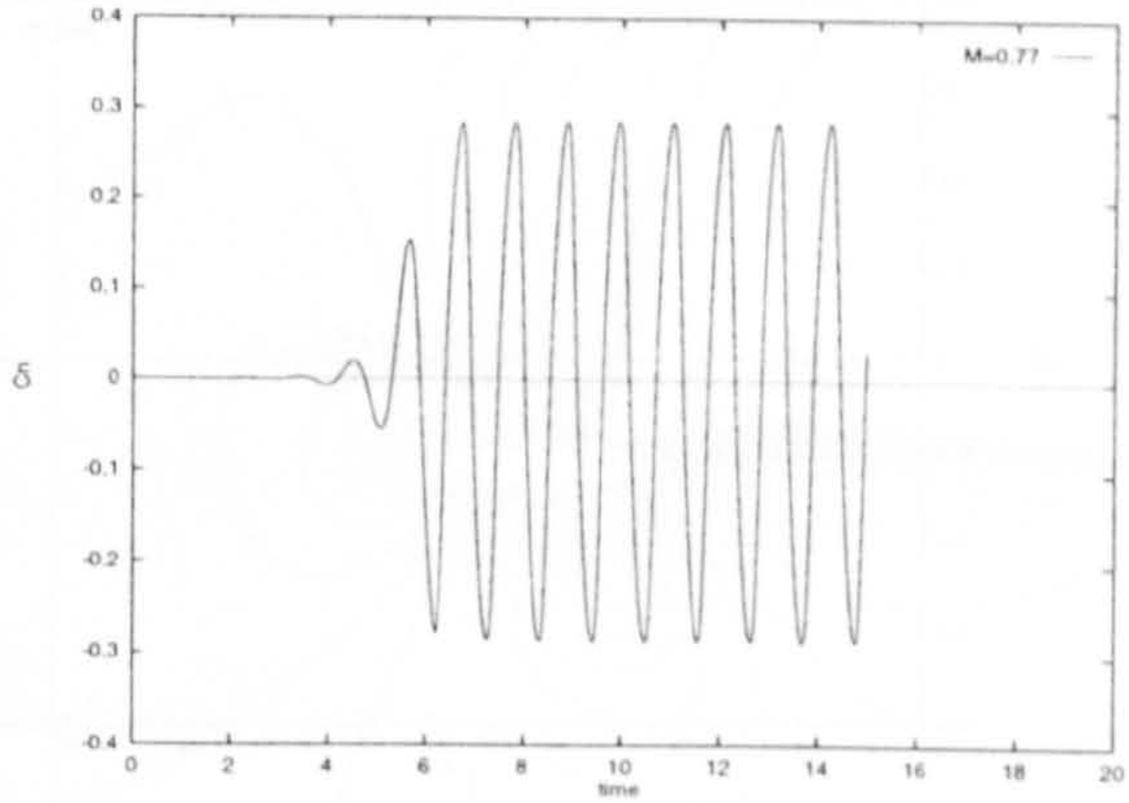

(d) $M_\infty = 0.77$

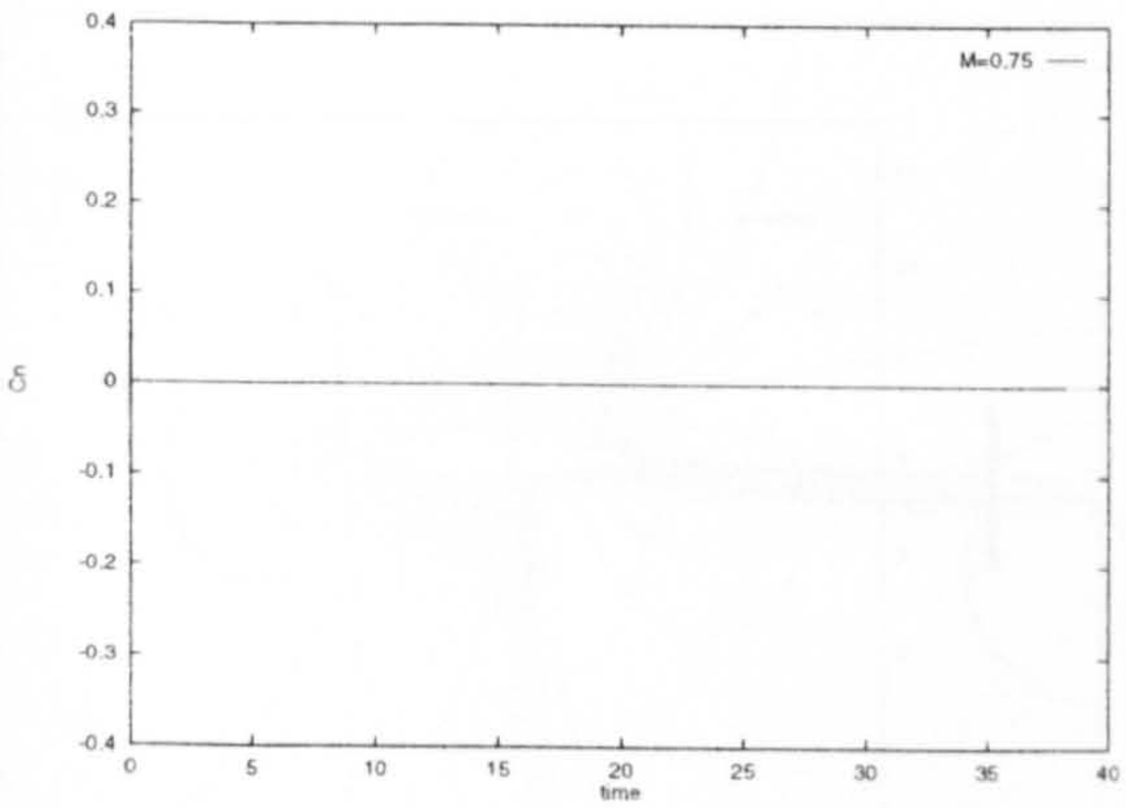

(b) $M_\infty = 0.75$

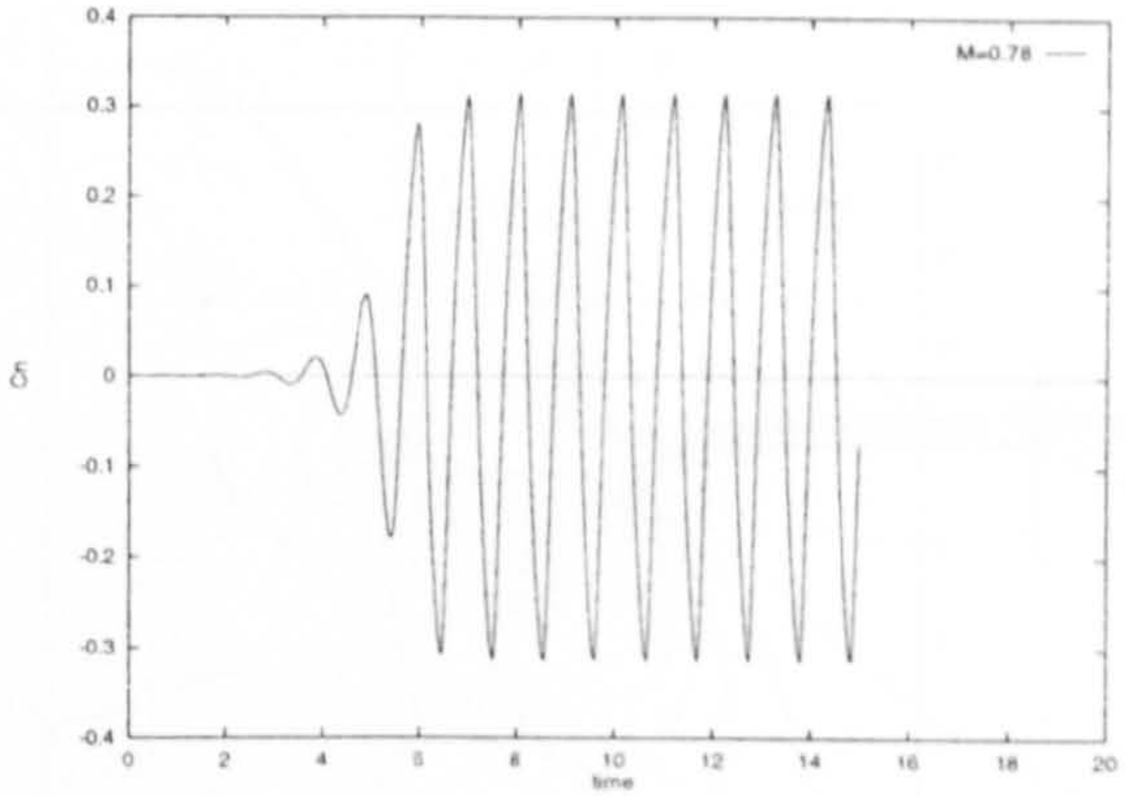

(e) $M_\infty = 0.78$

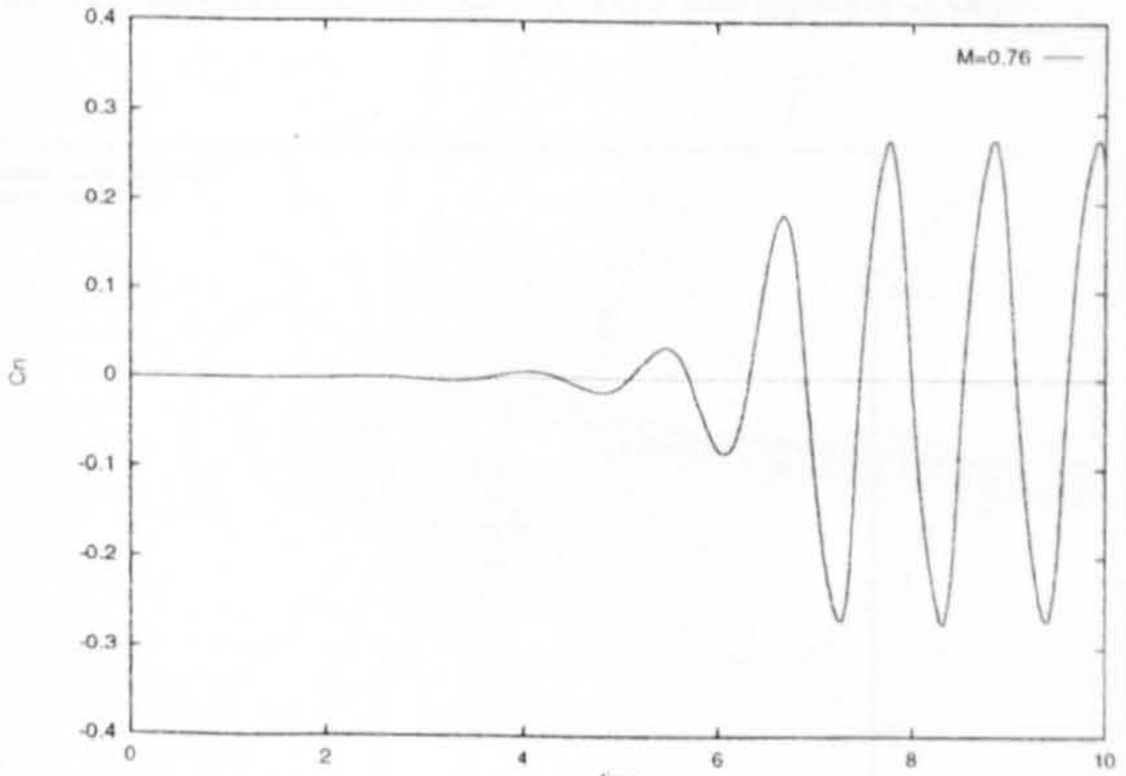

(c) $M_\infty = 0.76$

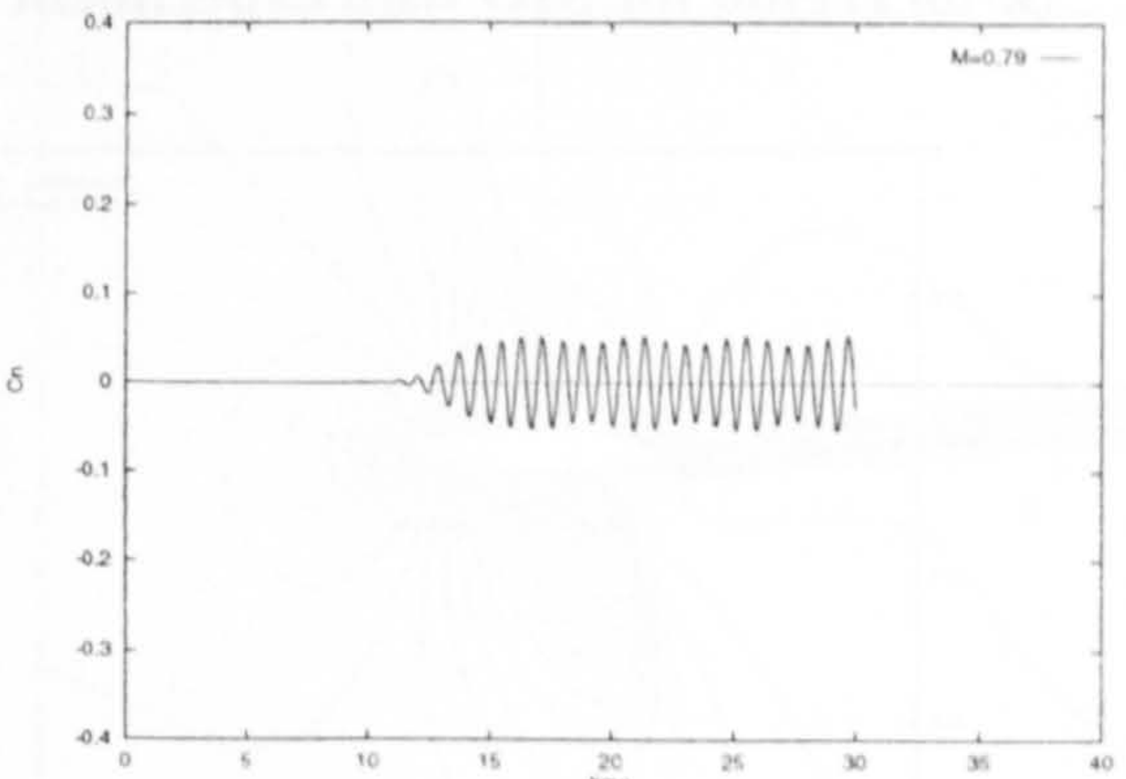

(f) $M_\infty = 0.79$

Figure (8.8) Computed variation of Normal force coefficient

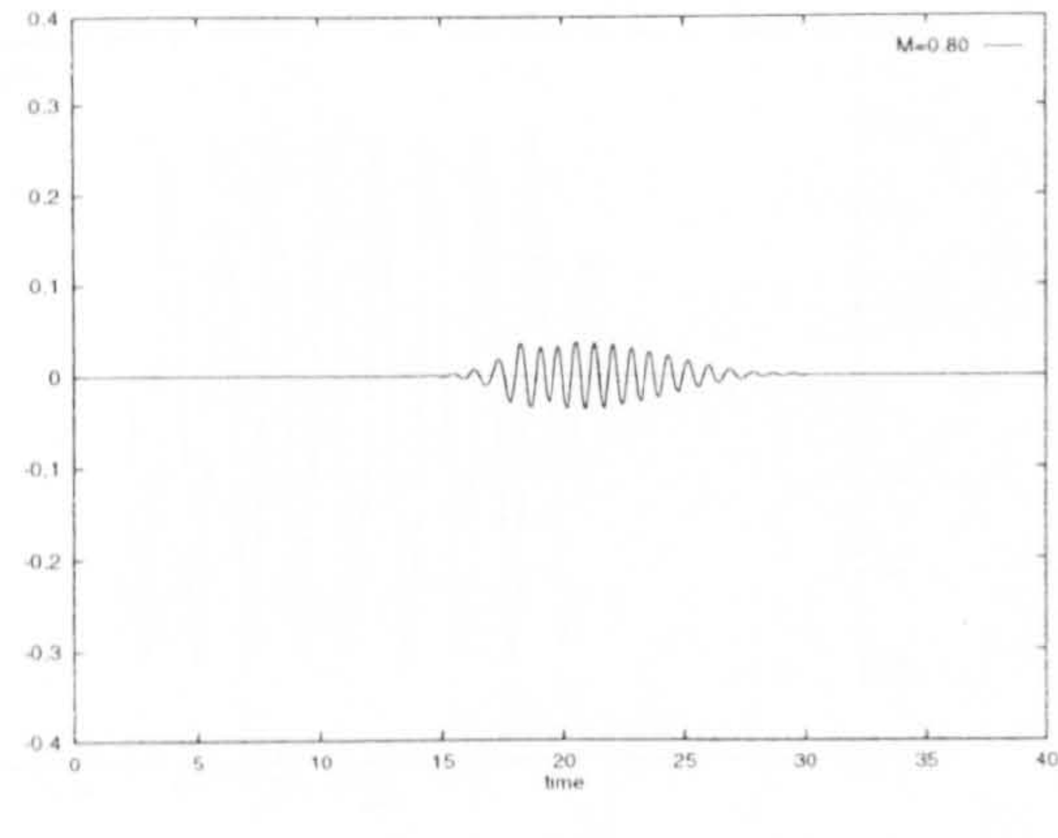

(g) $M_\infty = 0.80$

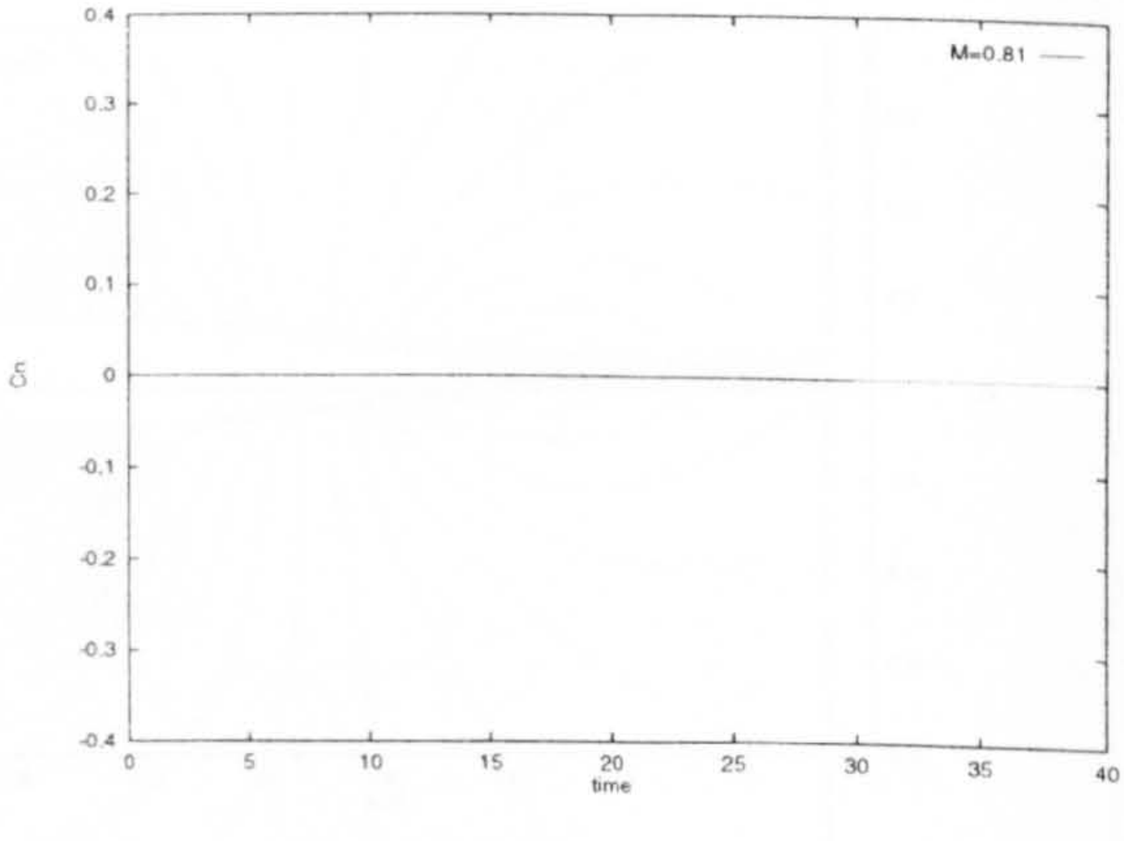

(h) $M_\infty = 0.81$

Figure (8.8) Computed variation of Normal force coefficient – concluded

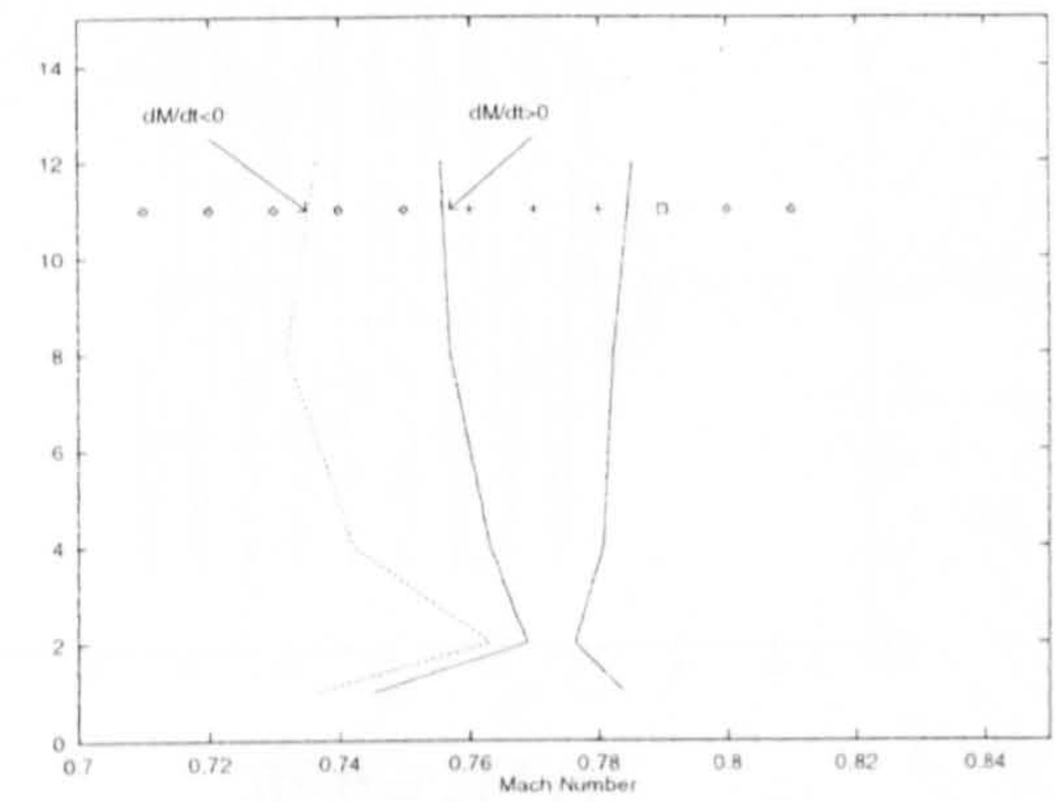

Figure (8.10) Comparison of computed (k-ω) region for SIO with experiment[200]

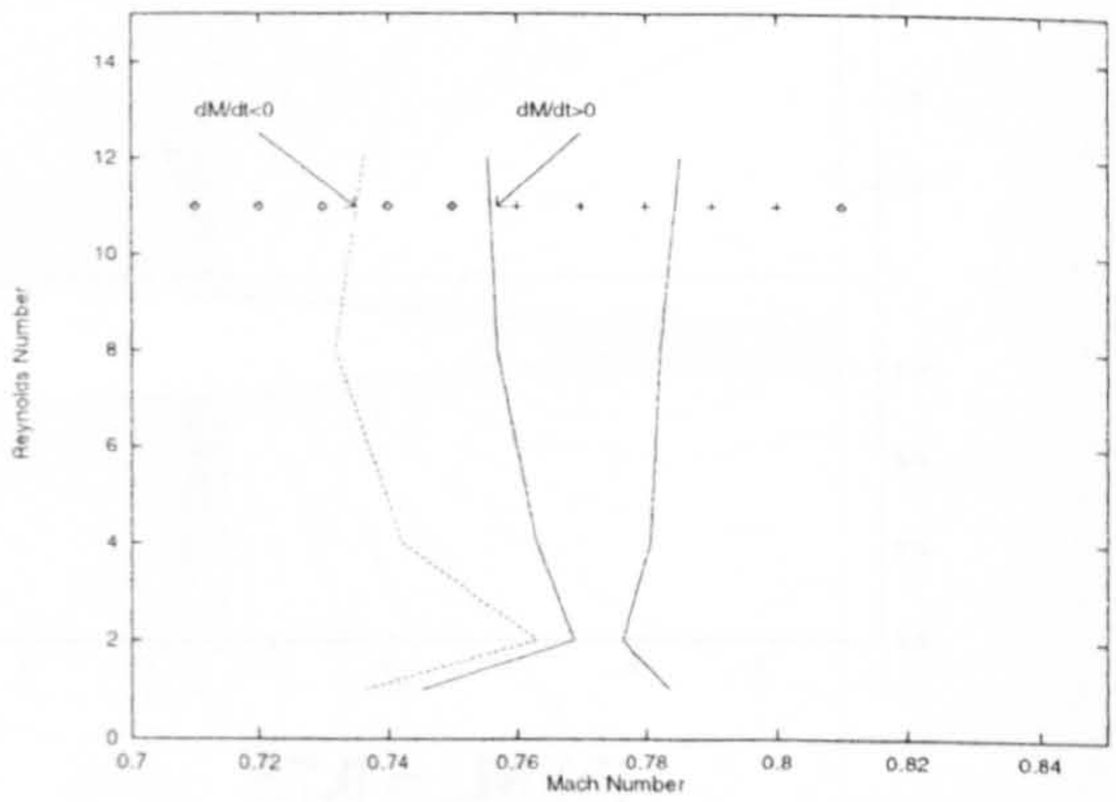

Figure (8.12) Comparison of computed (BL) region for SIO with experiment[200]

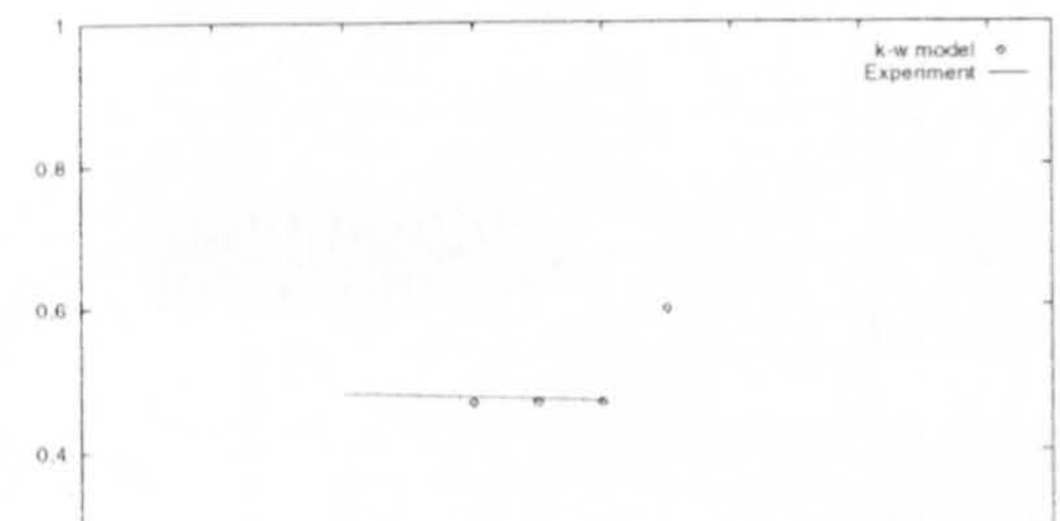

Figure (8.11) Comparison of computed (k-ω) frequency with experiment[200]

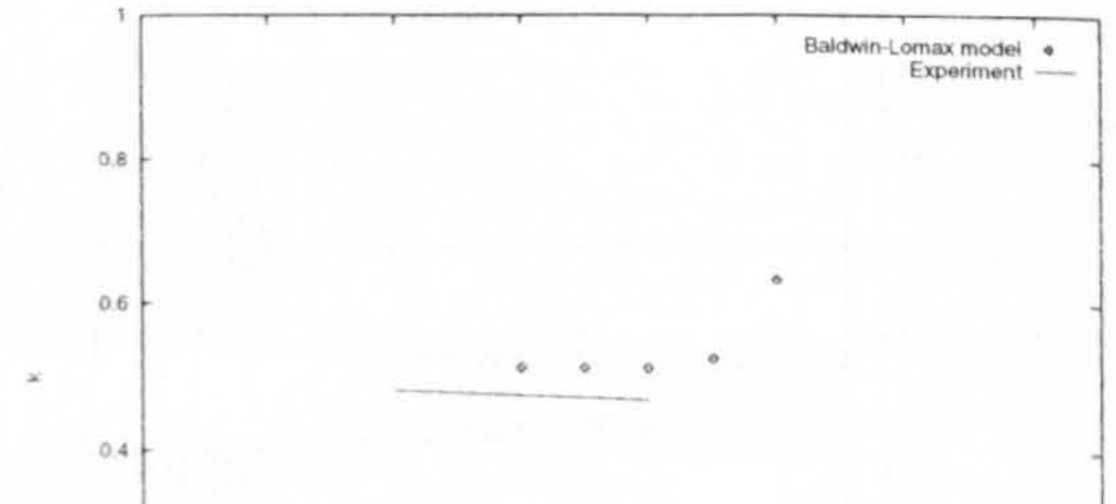

Figure(8.13) Comparison of computed (BL) frequency with experiment[200]

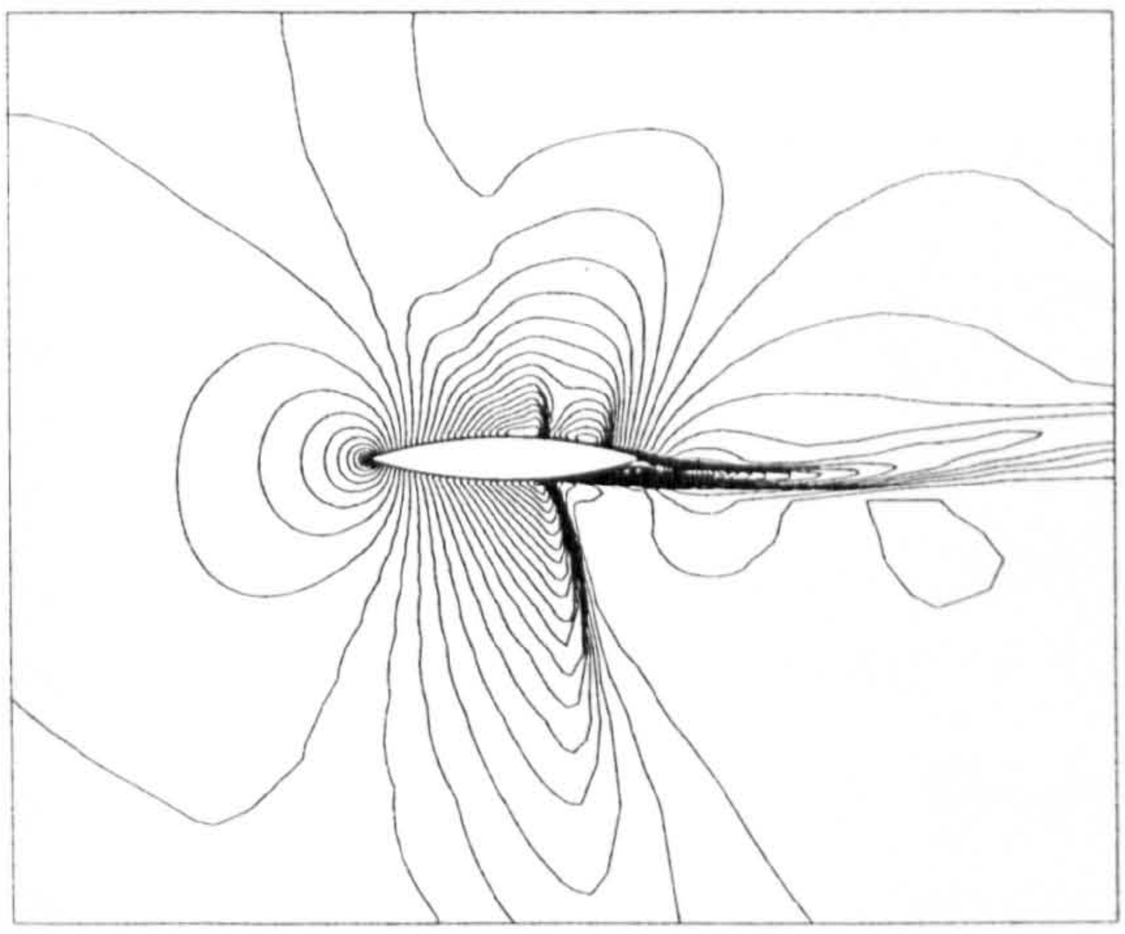

(a) t = 0.262

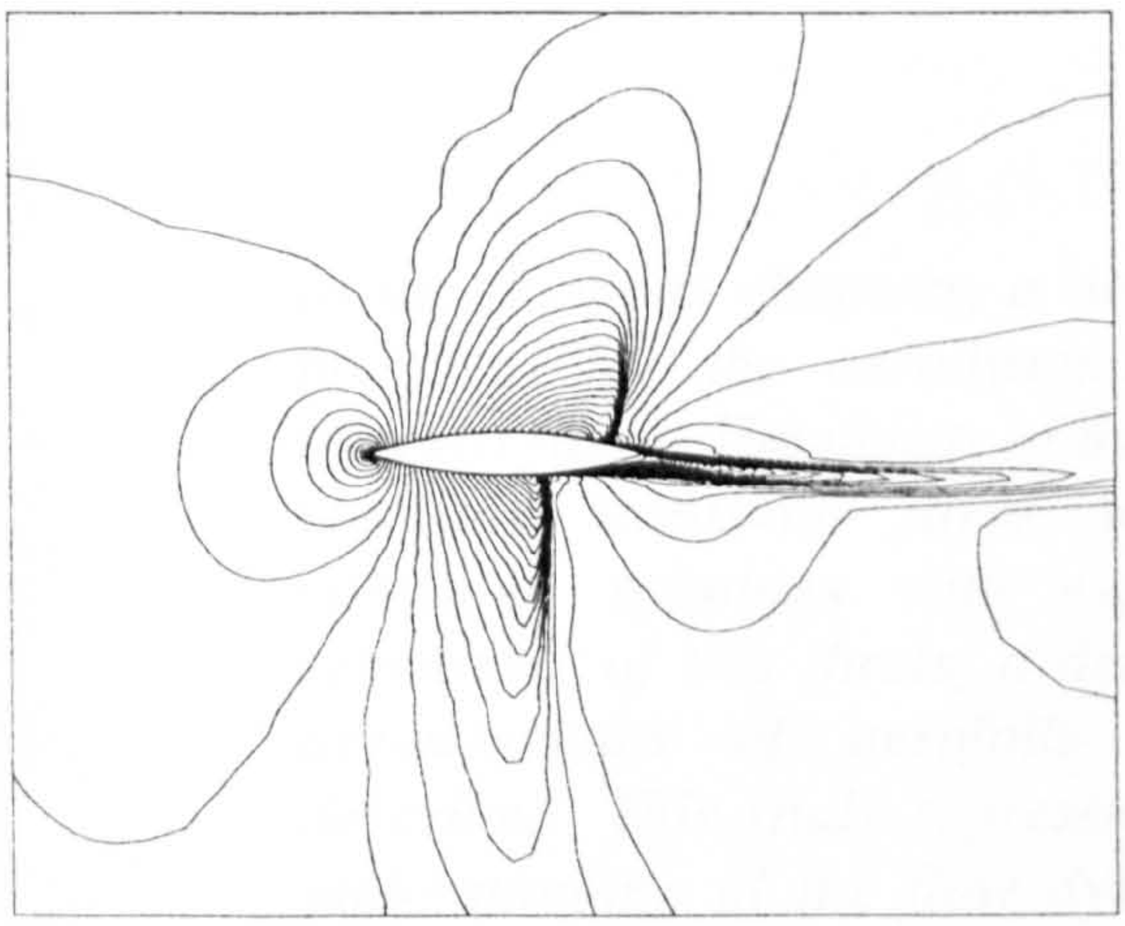

(b) t=1.309

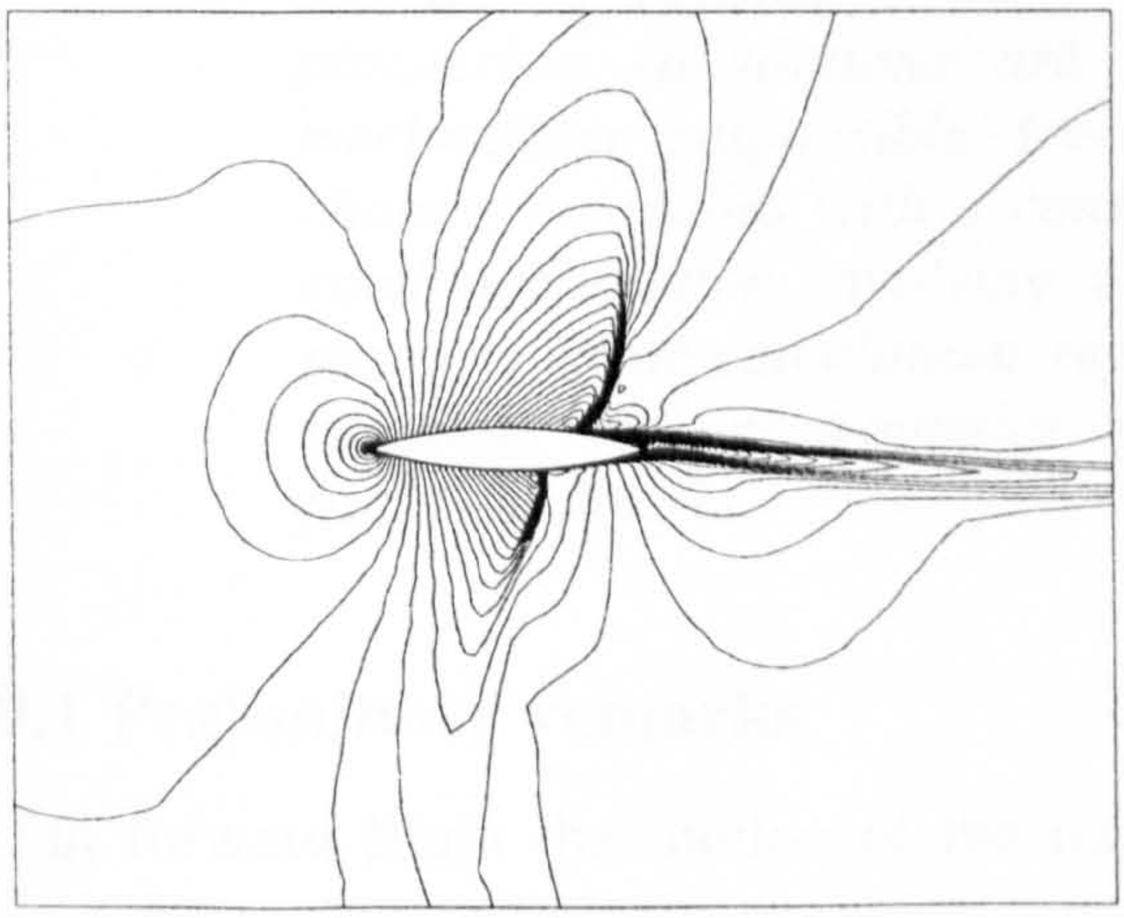

(c) t=2.356

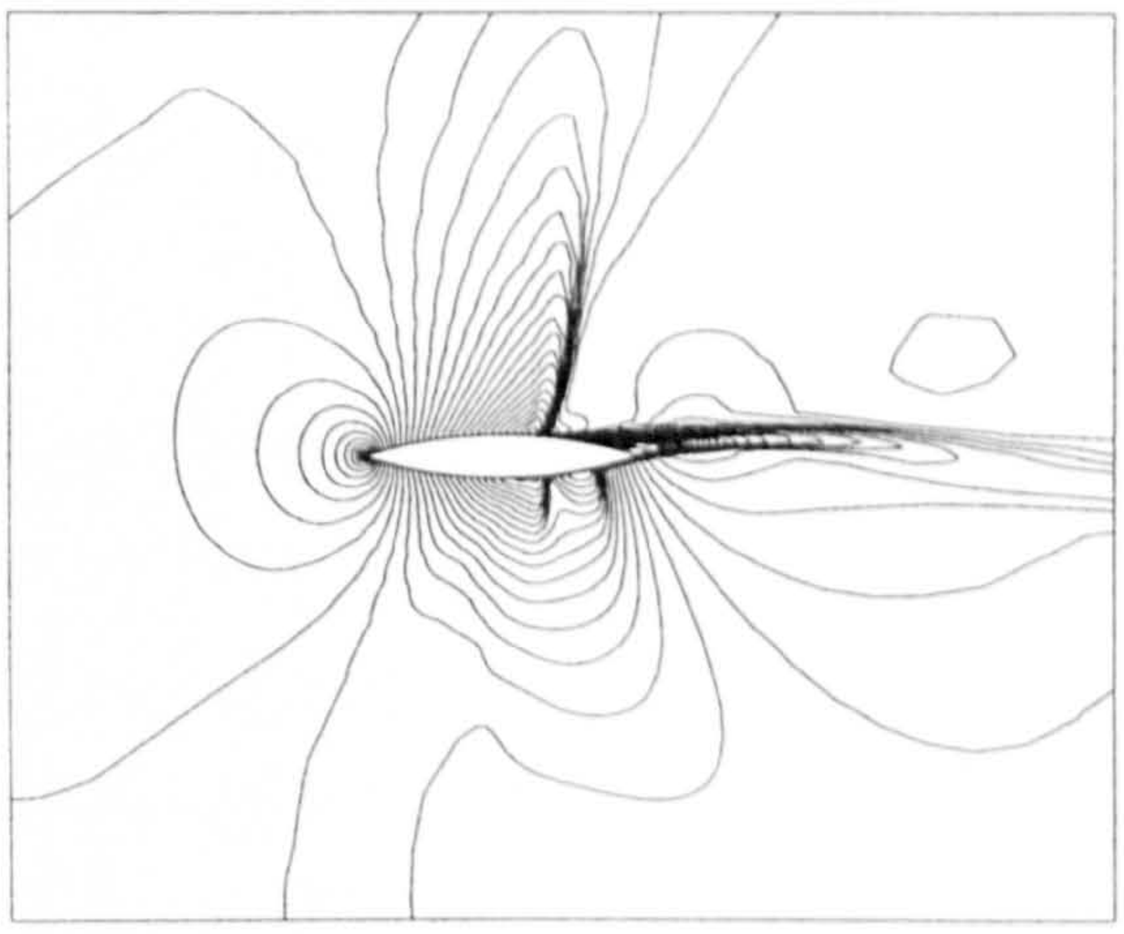

(d) t=3.665

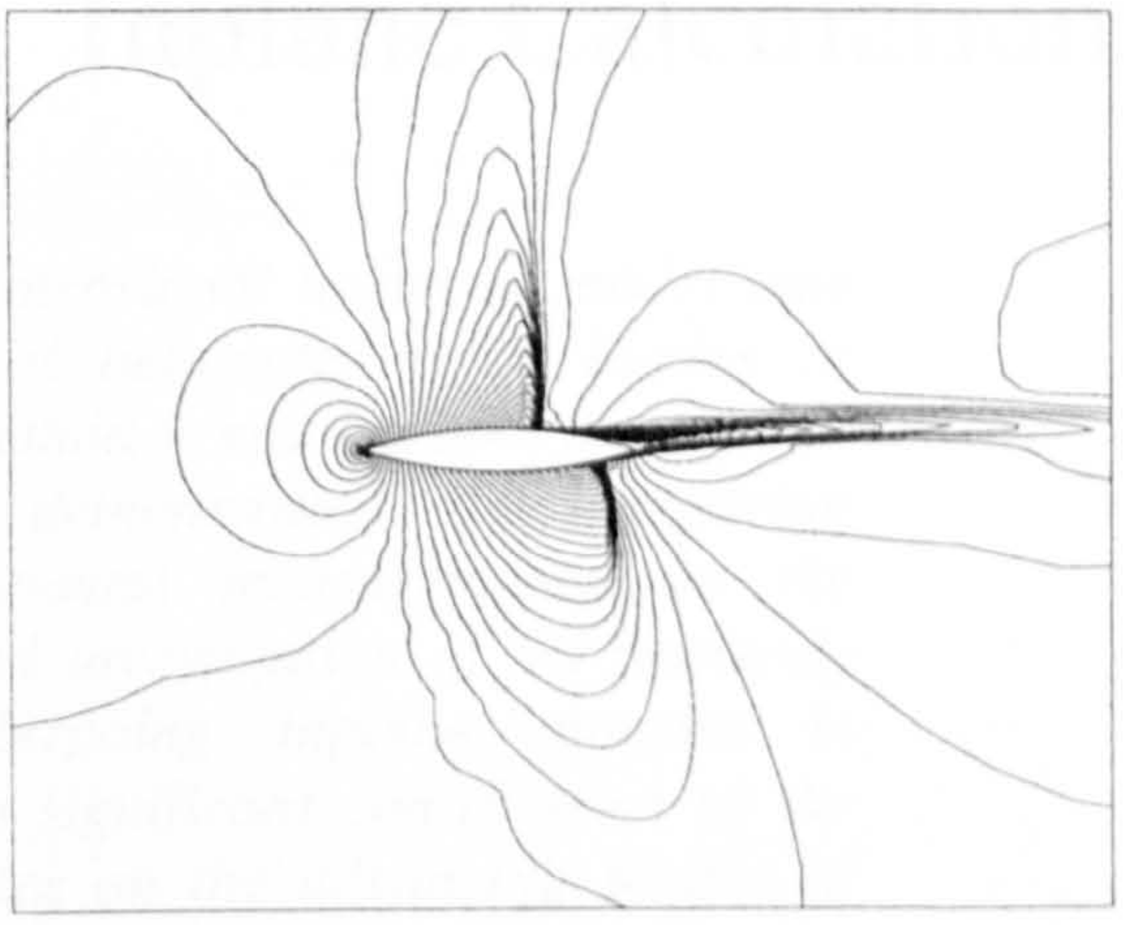

(e) t=4.712

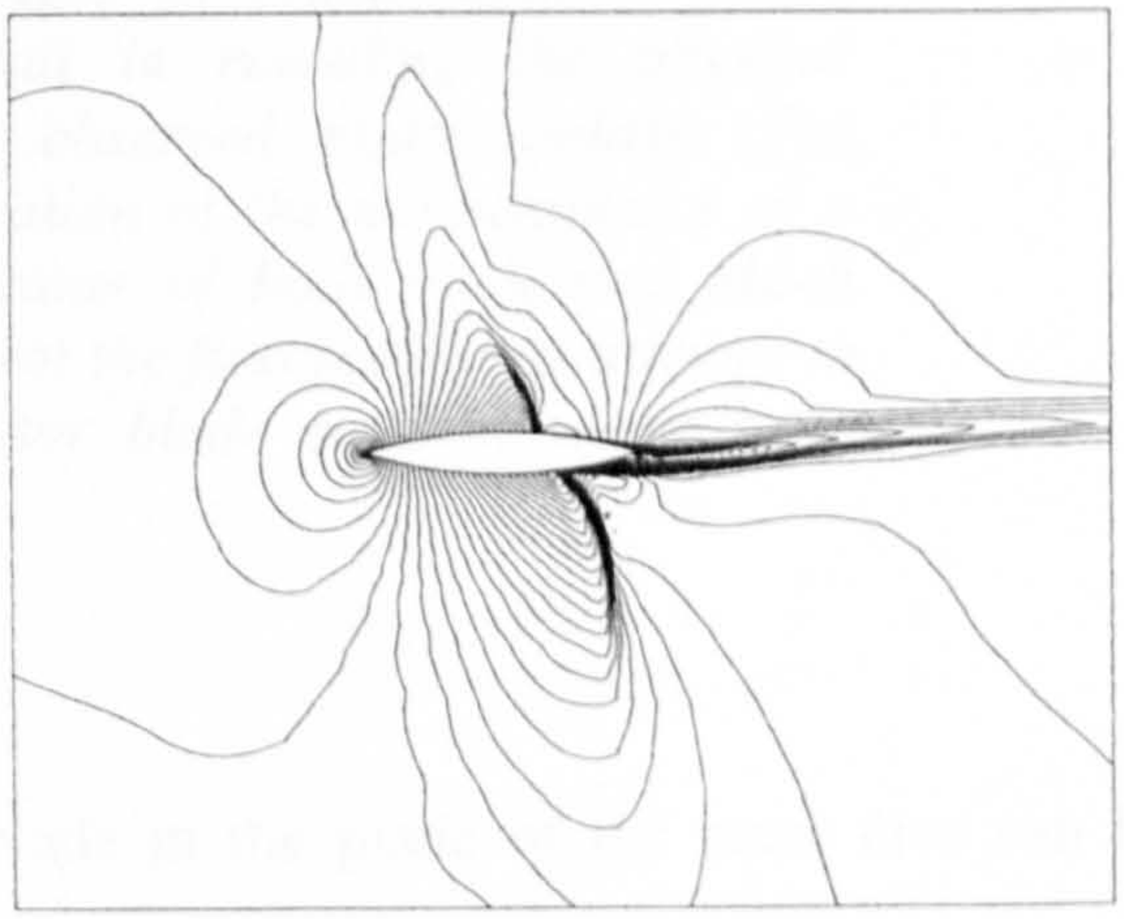

(f) t=6.021

Figure (8.9) Computed instantaneous Mach contours

9

Inplane Calculations

In the previous chapters, a two-dimensional unsteady model was proposed for the aerodynamics of helicopter rotor blades in forward flight. The ability of the method to resolve both steady and unsteady transonic flows was demonstrated by comparing computed solutions with experimental measurements. In the remainder of this thesis, a detailed investigation of the unsteady aerodynamics of aerofoils undergoing inplane motions is described. This study represents a significant contribution to the understanding of the flow dynamics on the advancing blades of helicopter rotors. In addition to the inplane calculations, results are also presented for step changes in Mach number. These pioneering calculations are usefull in revealing the physical mechanisms responsible for the observed phase delays. The chapter concludes with a consideration of the aerodynamics of a combined motion involving variations of both pitch and Mach number. These calculations represent the first published attempt to calculate the aerodynamics of rotor blade sections at realistic flight conditions.

9.1 Preliminary remarks

In forward flight the motion of the rotor blade in the plane of the rotor disc can be approximately represented by longitudinal oscillations of the form,

$$M_\infty(\tau) = \frac{r}{R} M_{tip}\left(1 + \mu_r \sin\left(2\pi k_r \tau\right)\right) \qquad (9.1)$$

where M_{tip} is the tip Mach number in hover. The influence of such oscillations on the low speed aerodynamics of aerofoils has been investigated by Maresca[226], Krause[25] and Ho[227,229-231]. Maresca[226] considered the aerodynamics of a NACA 0012 aerofoil set at incidence to an oncoming flow of 2.5 - 20 m/s. It was shown that for incidences below the static stall unsteady effects were weak. Furthermore, the flow was largely insensitive to variations in both amplitude and reduced frequency. For incidences above that of static stall a separation bubble was observed at the leading edge. The subsequent development and bursting of the separation bubble produced large unsteady effects which were strongly dependent upon the amplitude and frequency of the aerofoil motion. Subsequently Krause demonstrated that for larger amplitude oscillations, inplane motions can play an important role in the development of the flowfield for angles of attack below static stall.

Ho[227] analysed water tunnel data obtained for a NACA 0012 aerofoil performing low amplitude inplane oscillations at the static stall angle of attack. He was able to show that the evolution of the attached flow was governed not by the reduced frequency, but by the time-period of the freestream variation. For freestream amplitudes sufficiently high to promote separation the characteristic time scale is strongly related to the convection speed of the stall vortex and can be correlated with reduced frequency. Similar observations were reported for the flow around delta-wings[229]. Further parametric studies[230-1] of unsteady separated flows due to inplane oscillations of aerofoils and wings close to stall indicate that the lift force is a strong function of reduced frequency. Furthermore, the frequency at which the ratio of the unsteady to quasi-steady lift is greatest was shown to be independent of the frequency with which the stall vortex is shed into the aerofoil wake. Morinishi[232] presented numerical solutions of the incompressible Navier-Stokes equations for this problem.

Such investigations have mainly served to demonstrate the influence of inplane motion at very low Mach numbers and high angles of attack. While this provides insight into the dynamic stall process on the retreating blade, the flow conditions studied provide no information about the influence of dynamic effects on the advancing blade. Szumowski[233] investigated the effect of background flow oscillations at transonic conditions. The oscillations were generated by means of a rotating plate placed downstream of the aerofoil. While the rotation of the plate produces a sinusoidal freestream, the flow over the aerofoil is also influenced by upstream propagating disturbances caused by the plate. It was shown that the transonic aerodynamics of aerofoils is sensitive to external excitation of the flow. For low amplitude oscillations the observed behaviour was characterised as Tidjeman Type B, however as the amplitude was increased the nature of the shock dynamics changed. For sufficiently high amplitudes a free shock wave was observed to propagate upstream of the aerofoil leading edge (Tidjeman Type C). No further experimental studies related to the transonic aerodynamics of aerofoils performing inplane motions have been published in the open literature.

Numerous authors have presented analytical approaches to the problem of aerofoils in an incompressible oscillating stream. Van der Wall[234] comprehensively reviewed aerodynamic theories for the prediction of the unsteady aerodynamic forces and moments of an aerofoil in an oscillating freestream. The approach outlined is based upon analytical studies for an inviscid, incompressible and irrotational fluid and consequently the solutions obtained cannot be applied directly to the current problem. Two modes of motion were discussed, in the first mode (fore-aft) the aerofoil is subject to a uniform velocity variation across the chord while in the second (axial gust) mode the aerofoil experiences a chordwise velocity gradient. For small reduced frequencies the two modes can be considered equivalent.

The earliest calculations of the flow around an aerofoil in a time varying freestream appear to be those of Lerat[20] who solved the Euler equations for the flow at conditions representative of high-speed forward flight. The calculations show satisfactory agreement

with experimental data and illustrate the complex unsteady flow on the advancing blade of a helicopter rotor. Habibie[235] investigated the aerodynamics of aerofoils subject to variations in Mach number, in his work both harmonic oscillations and ramping motions were studied. For freestream variations around a mean velocity close to the speed of sound little hysterisis was observed in the computed forces and moments, although there were differences between the unsteady and quasi-steady calculations Subsequently Pahlke[236-7] presented solutions of the Euler equations at conditions representative of helicopter rotors at various forward flight speeds. By comparison with three-dimensional solutions at the same flow conditions it was demonstrated that three-dimensional effects were significant for the rotor considered. Solutions of the Navier-Stokes equations for this problem were first presented by Shaw and Qin[238-40] who used the thin layer Navier-Stokes equations together with the Baldwin-Lomax turbulence model. In that work the development of an asymmetric flow with a period twice that of the forcing motion was identified for conditions corresponding to Lerat's [20] Euler calculations.

9.2 Comparison with experiment

The objective of the calculations presented in this section was to assess the ability of the proposed model to simulate the advancing blade aerodynamics of helicopter rotors in high-speed forward flight. Three non-lifting test cases were selected for consideration. The simulated conditions correspond to experimental measurements of a two-bladed rotor[241-3]. Details of the tip Mach number, advance ratio, angle of attack and Reynolds number can be found in Table (9.1) below. In addition to the experimental data the three test cases have been the subject of extensive numerical study. The first test case corresponds to that studied by Wake[67] using a three-dimensional Navier-Stokes methodology. The second test case is that investigated by Lerat and Sides[20] using a two-dimensional inviscid solver. While the final test case was the subject of recent attempts by Pahlke[244] to assess the accuracy of existing Euler solvers and is included because it provides a means to assess the influence of three-dimensional effects in the region of the blade tip.

Case	r/R	M_{hover}	μ	$\alpha°$	Re (million)
1	0.855	0.598	0.45	0	1.75
2	0.892	0.600	0.55	0	1.75
3	0.855, 0.892, 0.946	0.625	0.50	0	1.75

Table (9.1) Inplane calculations

9.2.1 Experimental Data

In the experimental study[241-3] a rigid twin bladed rotor was investigated. The model blades were identical to those of the Alouette tail rotor and had removable tip sections at 80% span. For the purposes of the present investigation comparison is made with data measured for blades having a trapezoidal planform, the chord varies linearly from 0.115 metres at the tip to 0.127 metres at 80% span. The blades have a diameter of 1.5 metres giving a maximum aspect ratio (R/c_{max}) of 4.7. The blade section consists of a series of symmetric NACA four digit series aerofoils that have a thickness to chord ratio decreasing from root to tip. The blade was instrumented with pressure transducers located at three spanwise locations, r = 0.946R, r = 0.892R and r = 0.855R. The aerofoil sections at these stations are 10.5%, 12% and 13% thick respectively.

9.2.2 Unsteady Computations

Unless otherwise stated the unsteady fully turbulent calculations discussed below were performed on a medium mesh similar to that described in Chapter (6), see Figure (6.3). Grids for the 10.5% and 13% thick aerofoils were obtained by scaling of the grid by the appropriate factors. The calculations were started impulsively from steady state solutions with a time step size equivalent to 1/4° of azimuth. A Krylov subspace size of 20 was employed throughout the calculations and the implicit system arising at each time step was considered to be solved when the non-dimensional residual fell below 0.005. This was typically achieved with a single step of the GMRES method once the initial solution

transients had been damped. Data are presented for the third cycle of the unsteady motion only.

(a) <u>Case 1</u>

In the first test case the effective velocity experienced by the aerofoil at the 0.855R spanwise station is,

$$M(\psi) = 0.5113\left(1 + 0.5263\sin(\psi)\right)$$

Figure (9.1) shows the unsteady pressure coefficient on the aerofoil at azimuth angles of 30°, 60°, 90°, 120° and 150° calculated using the k-ω turbulence model. Agreement is generally good for cases in which there is no shock wave, the expansion of the flow around the leading edge is weaker than observed in the experiments and the peak pressure is further aft. At 90° azimuth the suction peak is over predicted. Furthermore the shock wave appears to be further aft and moderately weaker than observed in the experimental measurements. As azimuth is increased beyond 90° the computed shock wave is much stronger and further aft than indicated by the surface pressure measurements. However, the pressure recovery at the foot of the shock is comparable with that observed in the experiments. At 150° azimuth the flow is shock free and there is good overall agreement with the experimental measurements. The computed shock motion is Tidjeman type B. For this case the overall agreement between experiment and computation can be considered satisfactory.

(b) <u>Case 2</u>

The second test case corresponds to that investigated numerically by Lerat[20]. In this case comparison is made with data measured closer to the tip, r = 0.892R. The unsteady Mach number experienced by the aerofoil is now,

$$M(\psi) = 0.536\left(1 + 0.61\sin(\psi)\right)$$

In Figure (9.2) the variation of the instantaneous pressure coefficient on the aerofoil upper surface at x/c=0.5 calculated using the Euler equations is presented. Also shown are the inviscid computations performed by Lerat. The present Euler computations are in excellent overall agreement with those of Lerat and provide confidence in the ability of the basic numerical scheme to resolve the inviscid shock dynamics.

The computations shown in Figure (9.2) were repeated using the Navier-Stokes equations together with the k-ω turbulence model. The resulting unsteady data are compared with the experimental measurements reported by Philippe[242] in Figure (9.3). While the qualitative and quantitative behaviour of the flow at x/c = 0.2 is generally acceptable over much of the azimuth range, the development of the shock wave clearly lags that measured in the experiments. Of particular concern is the observation that the upstream propagation of the shock wave lags approximately 15° of azimuth behind that indicated by the experiments. The inability of the two-dimensional model to accurately represent the quantitative behaviour of the flow is clearly illustrated at x/c = 0.5. The downstream travelling shock wave appears much earlier in the flow development, while conversely the upstream travelling shock appears much later.

In Lerat[20] poor agreement between the two-dimensional Euler computations and experimental measurements is attributed to the inviscid model used to perform the computations. This would seem to be supported by the contours of local Mach number plotted in Figure (9.4) for azimuth angles of 60°, 90° and 120° which provide clear evidence of periodic symmetric shock induced separation. Philippe[242] does not report the occurrence of flow separation during the experiments. However, as can be seen from Figure (9.5), when the pressure data are presented in the form of Figure (9.1) it is difficult to note any substantial differences between the solutions obtained using the inviscid and viscous models.

Finally the results obtained using the Baldwin-Lomax turbulence model are presented. For this case Shaw and Qin[245] previously presented solutions which exhibit an unsteady non-symmetric flow with a period twice that of the aerofoil motion. In the course of the present investigation the Baldwin-Lomax calculations were repeated using the full Reynolds averaged Navier-Stokes equations. The computed variation of unsteady pressure coefficient with azimuth angle at x/c = 0.2 and x/c = 0.5 is shown in Figure (9.6), also shown are the corresponding data obtained using the two-equation model of turbulence. As in the previous thin-layer calculations the computed flow exhibits a strong asymmetry and is periodic with a time period twice that of the forcing motion, see Figure (9.7) in which the unsteady normal force coefficient and instantaneous freestream Mach number are plotted against time. A comparison of the upper and lower surface pressure coefficients with the symmetric k-ω model solution is revealing. The pressure coefficients on the lower surface of the aerofoil obtained with the Baldwin-Lomax model are in good agreement with the corresponding two-equation model calculation, while the calculated upper surface pressure coefficient appears to be in closer agreement with the experimental data. In order to understand this behaviour further it is helpful to consider the development of the unsteady flowfield in more detail.

The development of the calculated flowfield with increasing azimuth is illustrated in Figure (9.8) which shows computed instantaneous Mach contours for azimuth angles of 30°, 60°, 90°, 120° and 150°. The flow is initially symmetric and subsonic, Figure (9.9a); as the Mach number is increased a region of high-pressure gradient develops over the mid-chord region. At 90° azimuth, Figure (9.8b), there is clear evidence of a shock wave, the boundary layer remains attached and the flow is symmetric (as evinced by both the Mach contours and also the zero value of normal force). Between 90° and 120° azimuth flow separation occurs from the foot of the shock wave, Figure (9.8c). The shock induced separation is limited to the upper surface, while the boundary layer on the lower surface remains attached and as a consequence the subsequent flow development, Figures (9.8d) and (9.8e), is asymmetric. As the azimuth angle approaches 180° the boundary layer reattaches, a small upward deflection of the wake is apparent and the subsequent flow

development is near symmetric. As a consequence of this initial behaviour subsequent periods of the aerofoil motion also exhibit strong asymmetry during the latter stages of shock wave development. The maximum Mach number attained by the aerofoil is close to that at which incipient shock induced separation occurs in the corresponding steady flow. Consequently the slight upward deflection of the wake during the previous cycle, which has an effect similar to that of a deflected flap, is sufficiently large to promote flow separation on the lower side of the aerofoil. This periodic separation and wake deflection provides a self-sustaining mechanism for periodic asymmetric flow in much the same way as observed previously for the bi-convex aerofoil. However, in this case detailed parametric studies[245] of the solutions obtained with the thin-layer Navier-Stokes equations indicate that there is some sensitivity of the computed flow development to numerical parameters, in particular the chosen time step. This, together with the absence of the phenomenon from the results obtained using a two-equation model of turbulence suggests that the observed behaviour is non-physical. Despite careful investigation of the algorithms used to model the unsteady flow it was not possible to explain this behaviour further.

(c) <u>Case 3</u>

In order to assess the influence of three-dimensional effects due to the low aspect ratio of the model rotor blade computations were performed for each of the three instrumented blade sections. Calculated pressure coefficients are compared with the measured values in Figures (9.9), (9.10) and (9.11) for y/R=0.85, y/R=0.90 and y/R=0.95 respectively. The local advance ratio, mean Mach number and reduced frequency are given in Table (9.2) below. The agreement between computation and experiment for the outboard station is poor. For 0° azimuth the pressure is significantly under predicted over the full extent of the chord. At 60° azimuth a weak shock is apparent in both the computational and experimental results, however the computation again predicts much lower values of pressure coefficient than were measured. The development of the shock wave shown in Figures (9.9c)-(9.9d) is qualitatively correct, however the peak suction pressure is substantially over predicted leading to significant discrepancies between the calculated

shock strength and shock position. Indeed at 150° azimuth the pressure recovery across the computed shockwave is about twice that observed in the experiment.

Case	r/R	M_o	μ'	k'
3a	0.85	0.53125	0.5882	0.0965
3b	0.90	0.5625	0.5556	0.0910
3c	0.95	0.59375	0.5263	0.0840

Table (9.2) Section conditions for Case 3

For y/R = 0.90 comparison with experiment is much improved. At 30° azimuth the computations and experiments are in good agreement. The development of the shockwave, Figures (9.10b)-(9.10d) is qualitatively correct. Furthermore, for this range of azimuth angles the pressure recovery across the shock is in good agreement with the measured value. However, the shockwave is consistently predicted to be downstream of the measured location. At 150° azimuth the computed shock location is in good agreement with the measured location but the pressure ahead of the shock is much lower than recorded in the experiment and consequently the shock is much stronger than observed in the experiment. At 180° azimuth the measured and computed pressure distributions are in excellent agreement.

At 0° azimuth the computed and measured data for the inboard station, y/R = 0.85, are in excellent agreement. The computed shock development leads that of the experiment as the Mach number increases. At 90° azimuth the shock wave is stronger than that measured in the experiment and much further aft. The measured and computed pressure distributions at 120° azimuth, Figure (9.11d) show remarkable similarity with those at 90°, Figure (9.11c). The computed shock motion now appears to lag that observed in the experiments. At 150° there is excellent agreement with the measured data over the first 20% of the chord. However, the measured shock wave is just aft of x/c = 0.2 while the computed shock wave

is close to x/c = 0.6. The behaviour of the measured pressure distribution aft of the shock wave indicates the possibility of boundary layer separation, although the occurrence of flow separation was not reported in References (241-3). The computed data do not indicate the occurrence of flow separation.

9.2.3 Classification of three-dimensional effects

By comparison of the computed two-dimensional results with the reported experimental data and three-dimensional Euler and Navier-Stokes calculations presented by other authors it is apparent that for the present test cases three-dimensional effects are of some importance. Based upon physical reasoning and careful comparison of the computed two-dimensional data with sources of three-dimensional data the effects of spanwise flow mechanisms can be identified and categorised.

(a) <u>Tip relief</u>

For Case (3) the correlation between the computed and measured data at r/R = 0.95 is significantly different from that observed at the two inboard stations. Similar comparisons presented by Pahlke[244] using three-dimensional solutions of the Euler equations do not exhibit such dramatic changes in behaviour. This suggests that there are important effects close to the rotor tip, that cannot be properly accounted for using the present two-dimensional model. From elementary aerodynamic considerations it is clear that the blade tip cannot support a pressure difference, as the airstreams above and below the blade surface are free to travel around the tip. Consequently the spanwise loading must reduce to zero over a finite distance at the blade tip. This requires the existence of strong three-dimensional effects. Some indication of the spanwise extent of region over which such effects are likely to be significant can be obtained from the simplified models employed in momentum theory to account for the tip losses. In momentum theory the aerodynamic influence of the blade tip on the integrated forces and moments is accounted for using the concept of an effective radius. Numerous theoretical and empirical formulae have been presented for this parameter, see for example the discussion of Johnson[1], but for the purposes of the present discussion a simple approximation is,

$$R_{effective} = R\left(1 - 0.5\frac{c}{R}\right) \tag{9.1}$$

where c is the average value of the blade chord. From this we can conclude that the aerodynamic phenomena responsible for tip losses have a significant influence only in close proximity of the rotor tip and are otherwise negligible.

(b) Effective sweep

The discrepancies observed between computations and experiment for the inner blade sections can be explained in part by the effects of sweep on the chordwise pressure distribution. For an infinitely swept wing the independence theorem applies and the effects of sweep can be accounted for using only the component of the flow that is normal to the leading edge of the wing. Thus the effects of forward and backward sweep on the chordwise pressure distribution are identical. In the present work the rotation of the blade provides an effective time dependent sweep angle with respect to the forward flight velocity vector. The independence theorem is therefore implicit in the current two-dimensional model. For wings of finite aspect ratio the behaviour of the flow at both the root and tip introduces important spanwise effects over the planform. Furthermore, the component of the freestream velocity vector in the spanwise direction will play a role in the development of the chordwise flow. As a direct consequence of the three-dimensional nature of the flow on finite wings the independence theorem no longer applies. On the advancing side of the rotor disc the blade corresponds to a swept backward wing for azimuth angles $\psi < 90°$. In this case the effect of finite aspect ratio is to cause isobars to become concentrated towards the leading edge producing an additional adverse pressure gradient. For advancing side azimuth angles beyond 90° the rotor blade behaves as a swept forwards wing, the isobars become less concentrated and the effect of sweep is to produce an additional favourable pressure gradient.

In light of the expected influence of additional pressure gradient terms on the chordwise distribution the discrepancies observed between the numerical model and the experimental data for the cases presented above are not unexpected. The solutions of the two- and three-dimensional Euler equations presented in Figure (10) of Pahlke et al[237] appear to confirm this view. Favourable comparison is observed between three-dimensional computations using the Euler equations and experimental measurements over much of the azimuth range, while the comparison between the computed three-dimensional shock dynamics and those obtained for the corresponding two-dimensional flow show similar behaviour to those predicted by the present method. The current comparison is therefore encouraging and it is believed that more favourable results would be obtained if results obtained using the two-dimensional model were to be compared with experimental measurements for a higher aspect ratio blade.

In addition to the gross effects of sweep on the blade loading it is almost certain that there will be a component of the airloads which is dependent upon the unsteady effect of changing sweep angle. The magnitude of this term cannot be inferred from the present comparisons although it is suggested that it will be of secondary importance.

(c) <u>Crossflow</u>

In Chapter (2) it was shown that to a first approximation the additional terms that appear in the chordwise momentum equation for a rotating blade, Equation (2.21), can be viewed as acting as an additional chordwise pressure gradient.

$$u\frac{\partial u}{\partial x}+v\frac{\partial u}{\partial y}-U_e\frac{\partial \tau_x}{\partial x}-U_e\frac{\partial U_e}{\partial x}-\frac{\partial(U_e-u)}{\partial t}=$$

$$\underbrace{-2\Omega(W_e-w)+\left(W_e-\frac{wu}{U_e}\right)\frac{\partial U_e}{\partial z}-wU_e\frac{\partial u/U_e}{\partial z}}_{\text{Additional terms}} \qquad (2.21)$$

Experimental investigations of the laminar flow about rotating plates and analysis of the Navier-Stokes equations has shown that under most circumstances these terms are relatively unimportant. The forward flight case is more difficult to analyse due to the effects of unsteady flow. However, it has been established that in the main the influence of cross flow velocity is dominated by the spanwise component of the forward flight velocity component,

$$V(t) = M_{tip}\mu\cos(\omega t) \tag{9.2}$$

This term will be small for azimuth angles close to $\psi = 90°$. While the additional terms in Equation (2.21) are generally only of secondary importance they will play an important role in determining the conditions under which boundary layer separation is experienced. This can be demonstrated by considering the results obtained for Case (2). While the predictions of the Baldwin-Lomax turbulence model are clearly erroneous they provide some useful insight into the probable state of the boundary layer during the experimental investigation. It was previously remarked that the calculated upper surface behaviour was in closer agreement with the experimental measurements than that of the lower surface, Figure (9.6). Examination of the Mach contours presented in Figure (9.8) show that as the flow decelerates there is significant flow separation on the aerofoil upper surface, while on the lower surface the boundary layer remains attached until later in the flow development. The subsequent boundary layer separation is less severe. Based upon these observations it is suggested that there may be significant separation in the experiment. The inability of the present model to predict this behaviour can be explained by the presence of additional terms arising from radial inflow in the chordwise momentum equation. When the sign of these terms is positive the main flow is accelerated and skin friction is increased – separation is then delayed - conversely when the sign of these terms is negative the main flow is decelerated and skin friction is reduced – boundary layer separation is promoted.

McCroskey[76] has outlined a number of circumstances under which separation is delayed on the helicopter rotor. For the present discussion the following are important,

- Cross flow radially outwards – positive net spanwise momentum flux
- Cross flow radially inwards – positive net Coriolis acceleration

On the advancing blade the cross flow is radially outwards for $\psi < 90°$ and radially inwards for $\psi > 90°$. There is a complex interaction between the competing secondary terms on the advancing side of the rotor blade. It has been shown however that the former effect dominates close to the leading edge, while the latter is more important at the trailing edge. It is therefore expected that the net effects of the spanwise momentum flux and Coriolis acceleration will be to promote separation for $\psi < 90°$ and delay it for $\psi > 90°$. Thus, the results obtained using a two-dimensional model of the flow will tend to under-predict the effects of separation as the flow decelerates.

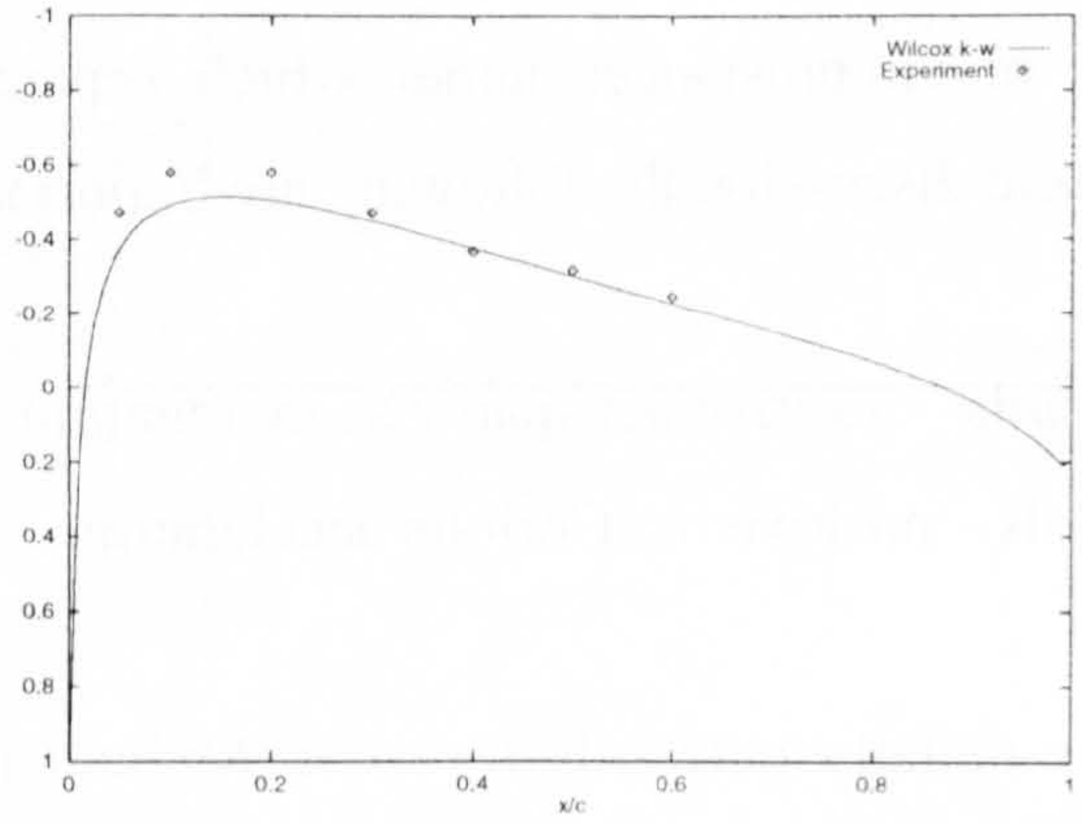

(a) $\psi = 30°$

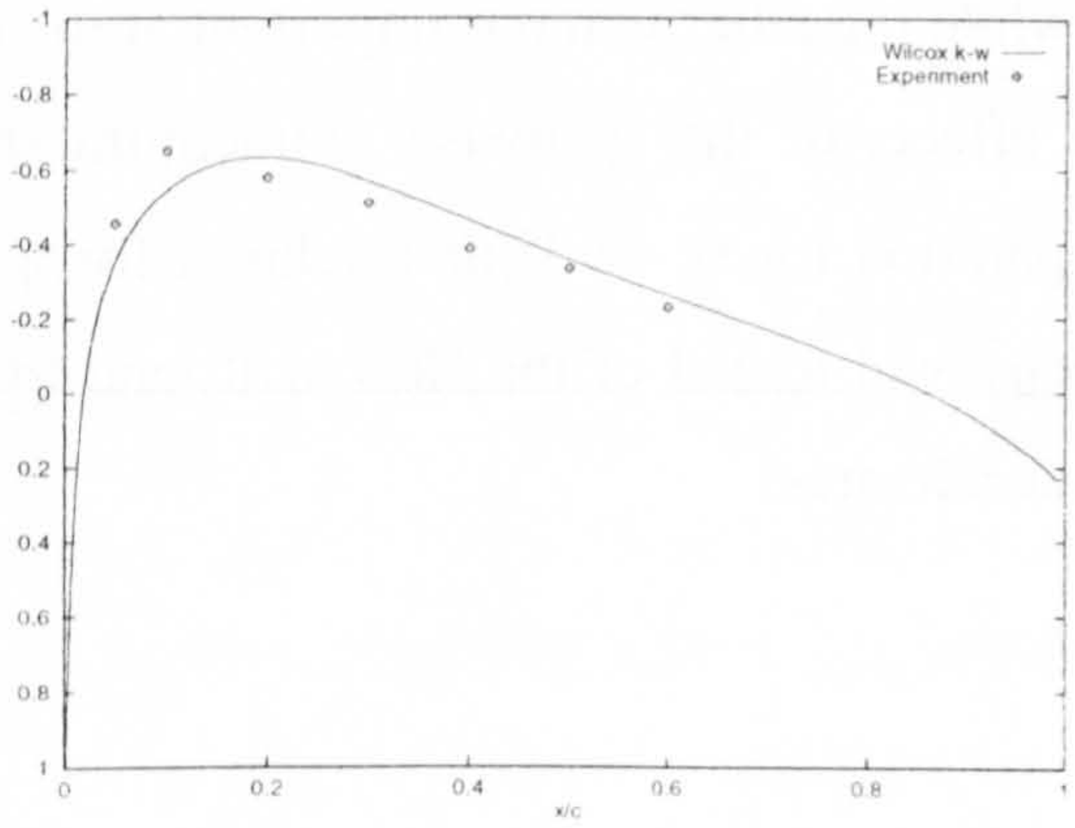

(b) $\psi = 60°$

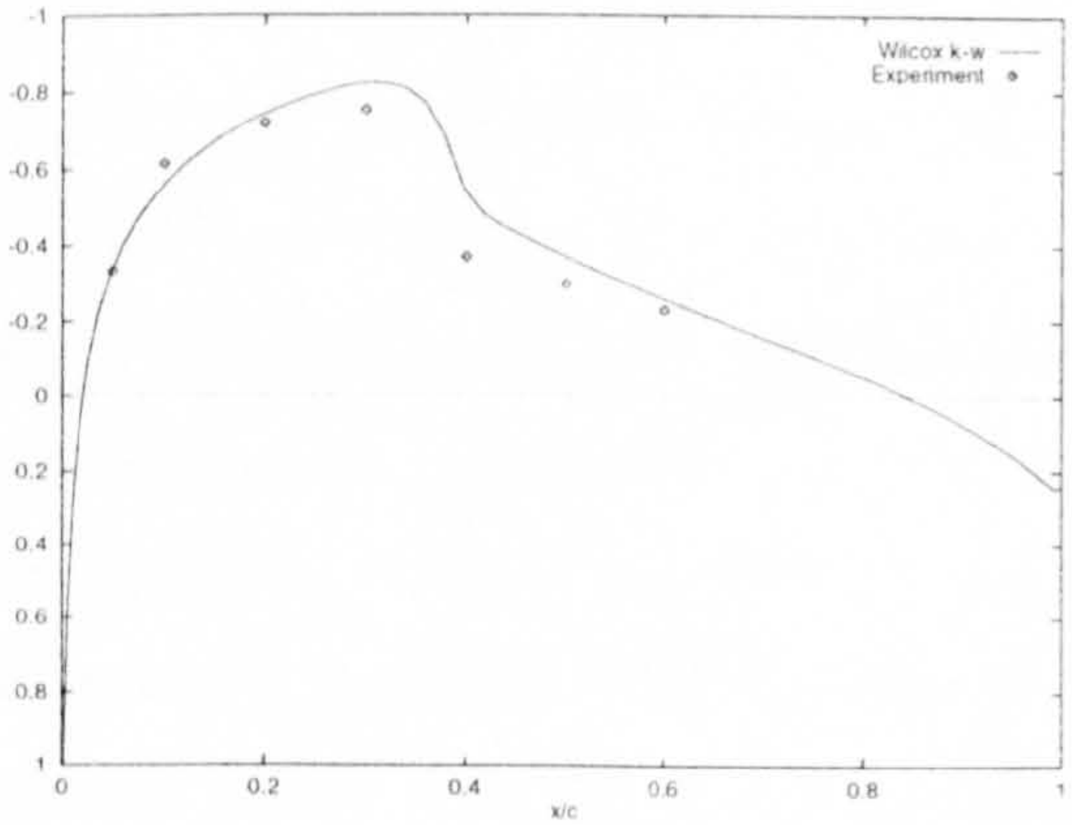

(c) $\psi = 90°$

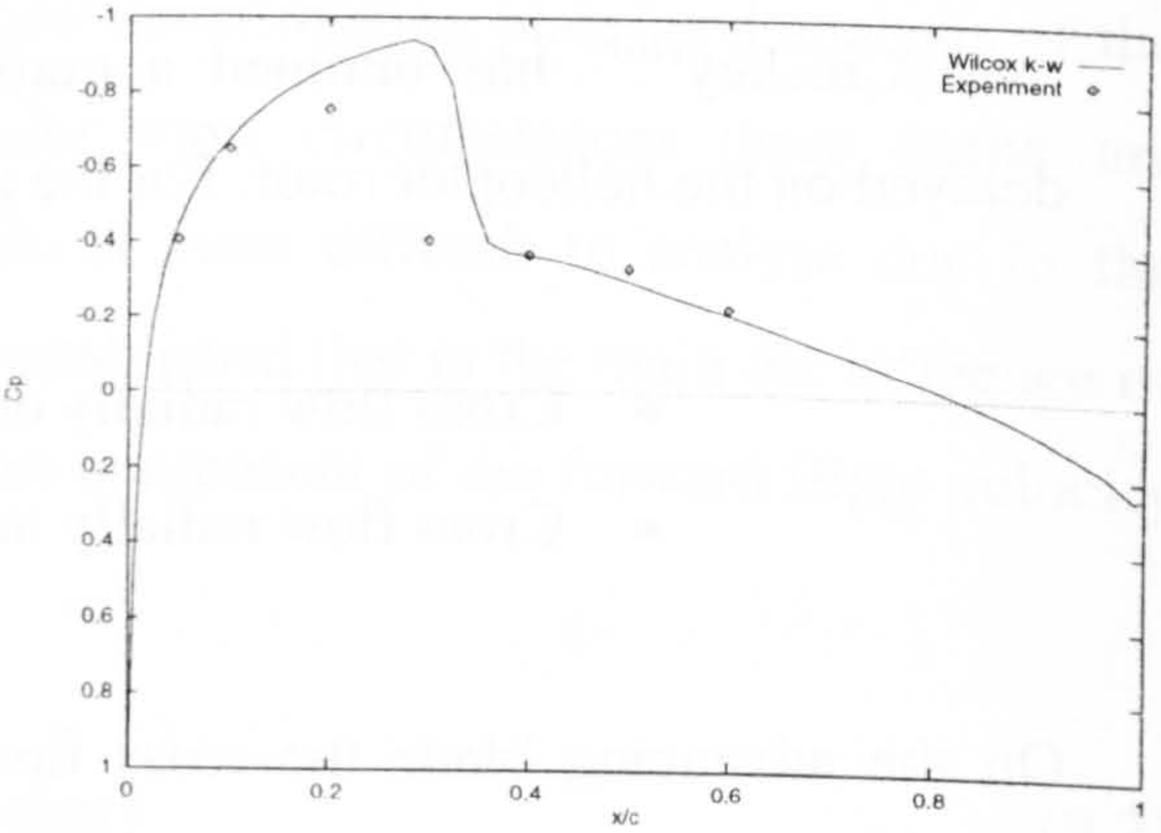

(d) $\psi = 120°$

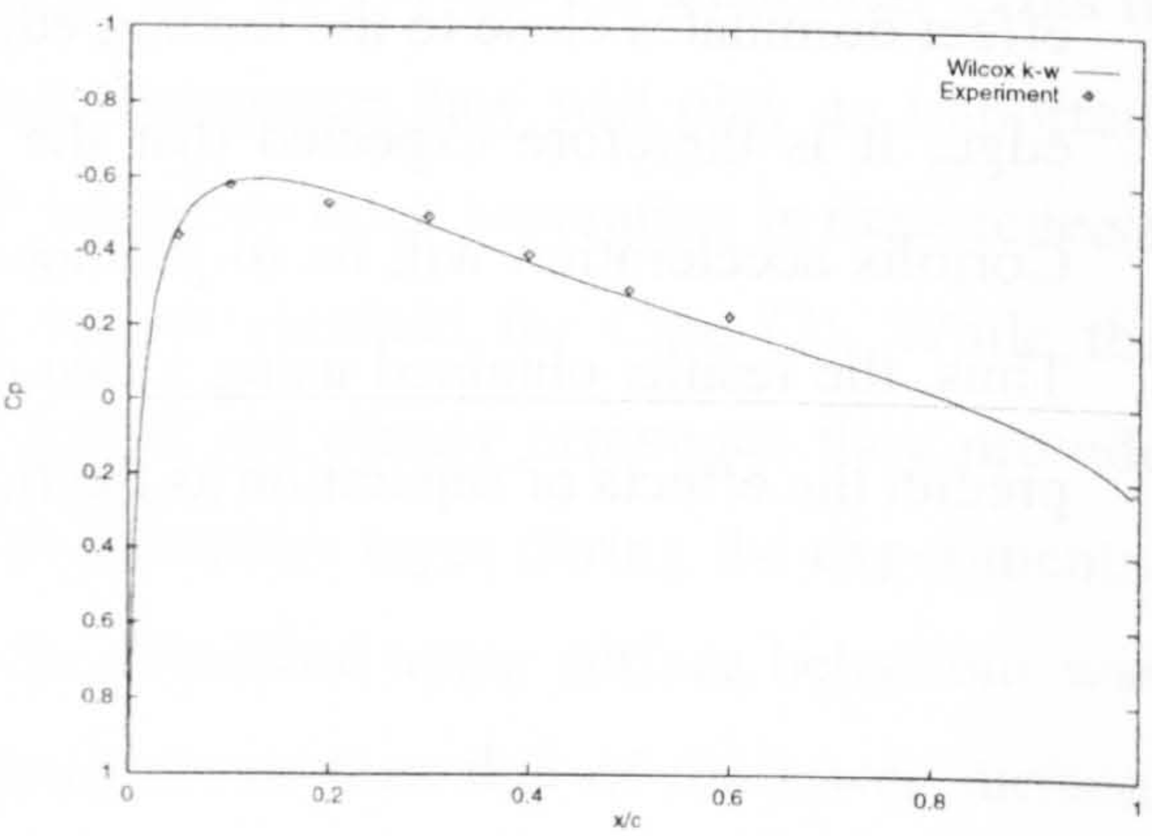

(e) $\psi = 150°$

Figure (9.1) Comparison of two-dimensional calculated pressure coefficients with three-dimensional experimental data[241-3]

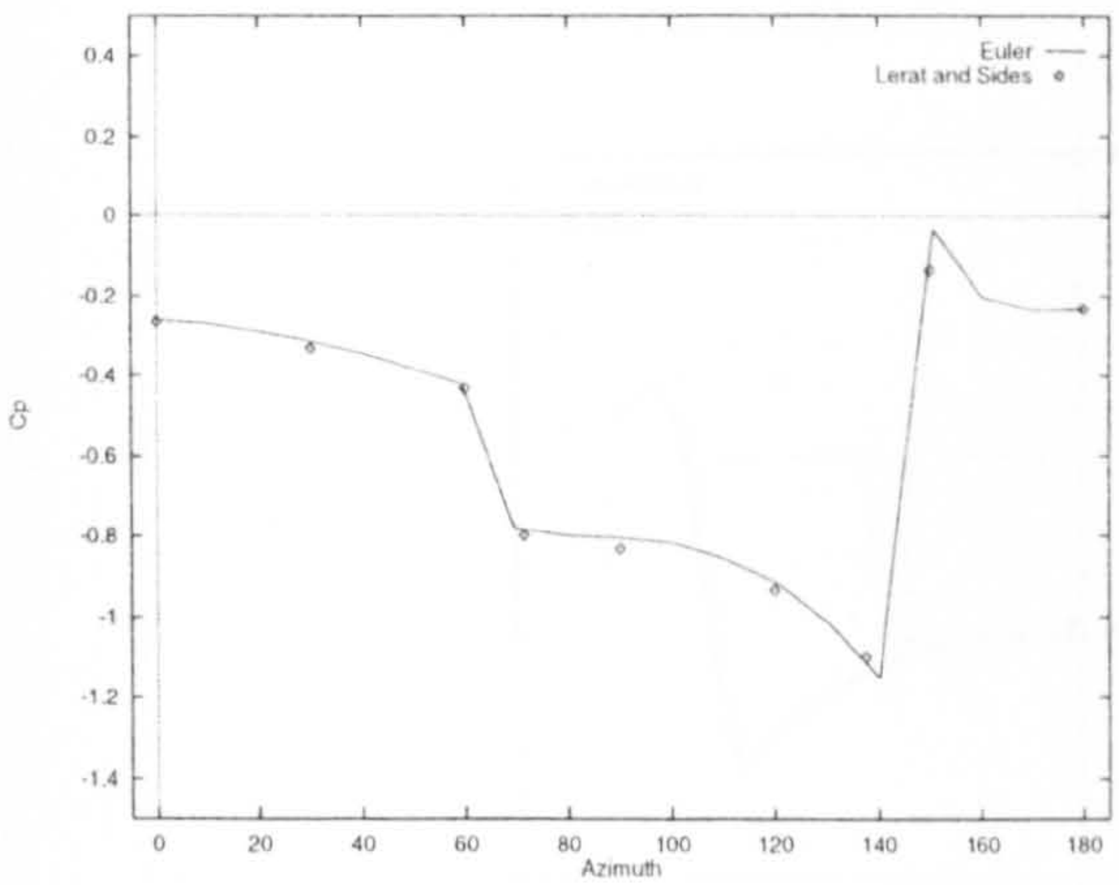

Figure (9.2) Inviscid computation of the unsteady pressure coefficient at x/c = 0.5

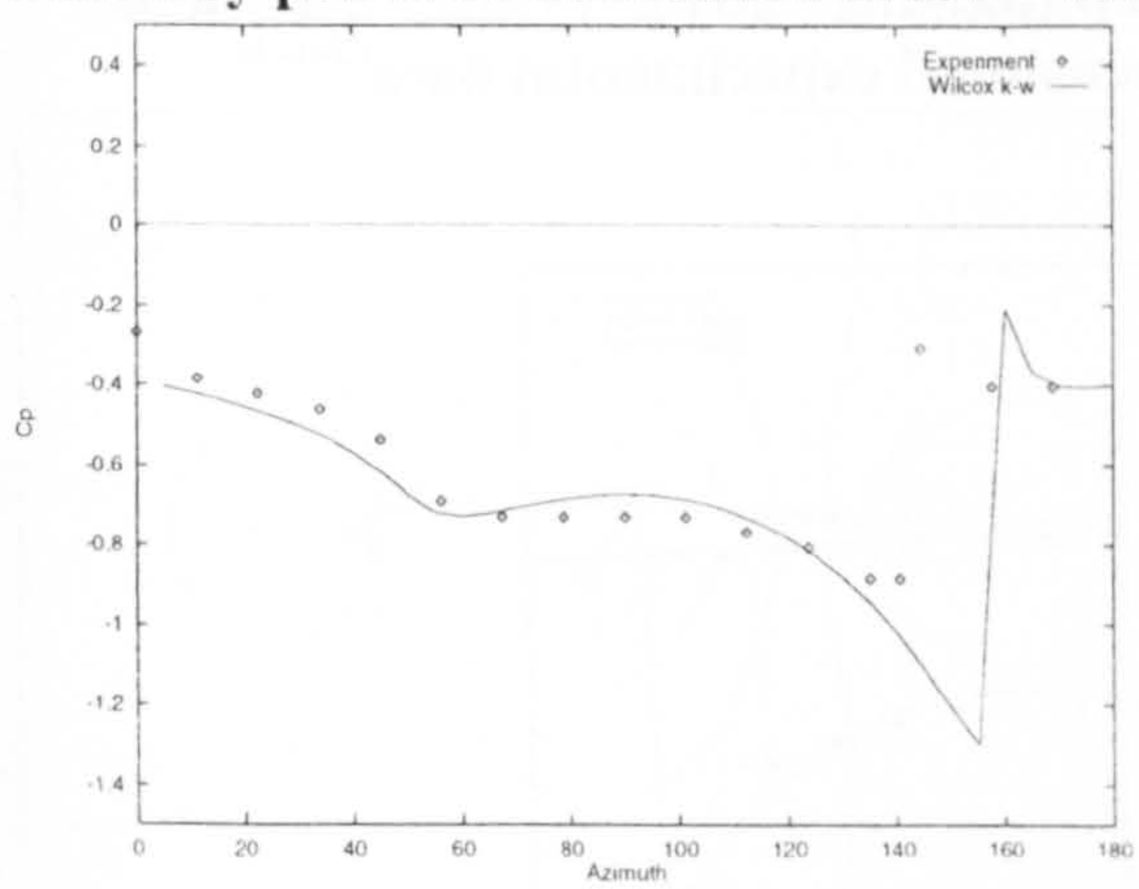

(a) x/c = 0.2

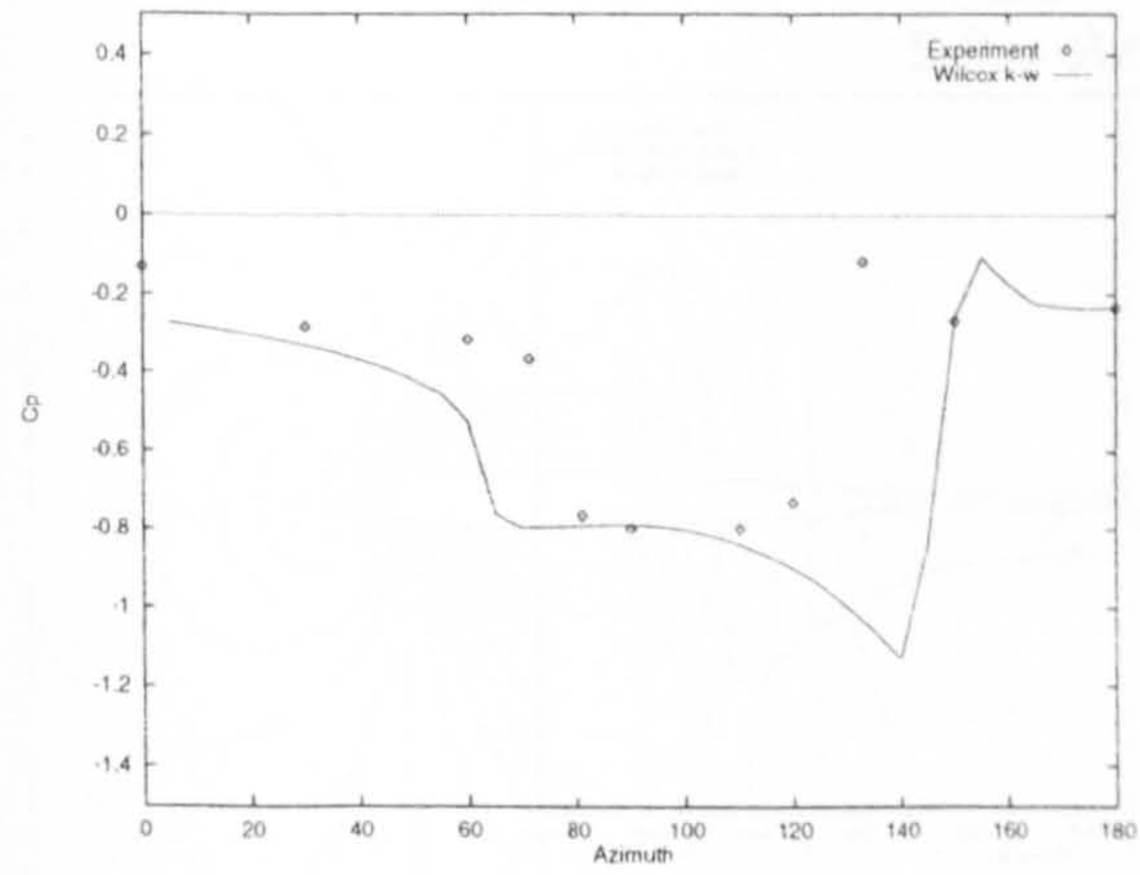

(b) x/c = 0.5

Figure (9.3) Comparison of computed pressure coeffcient distribution with three-dimensional experimental data[241-3]

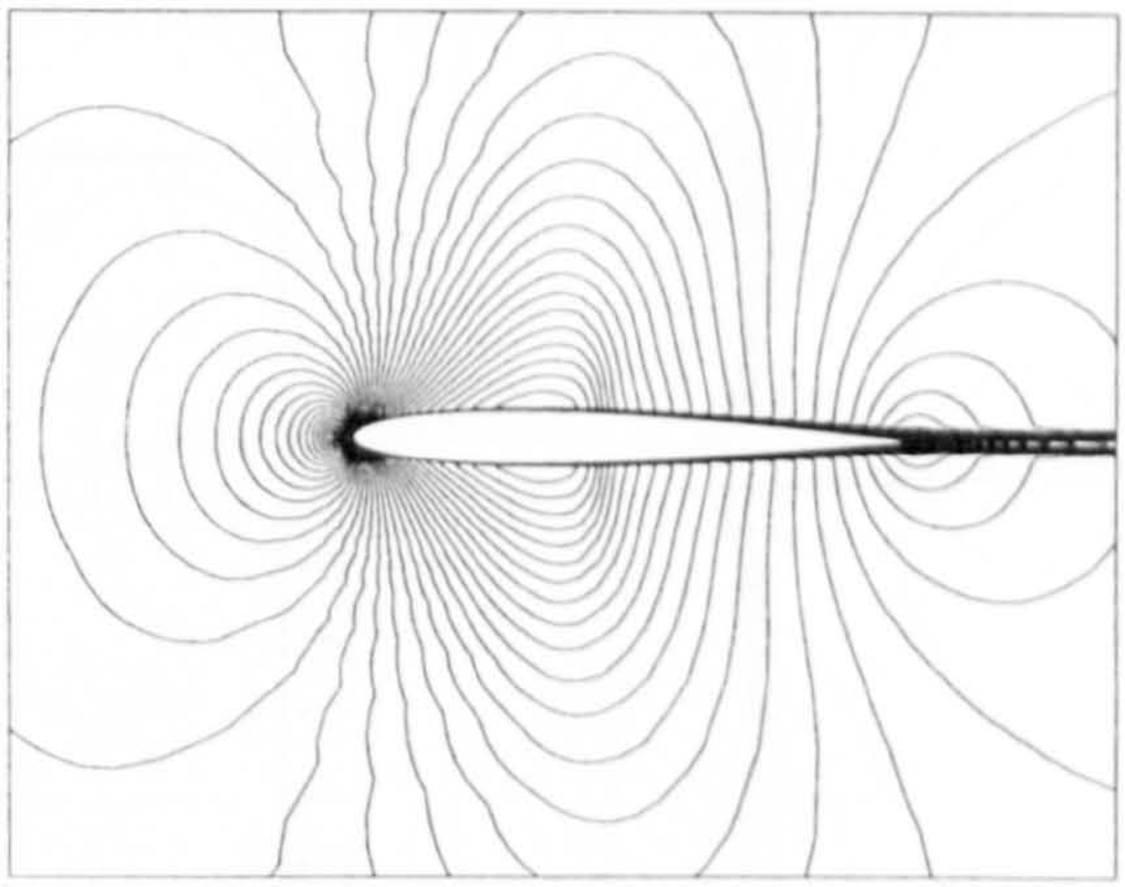

(a) 60°

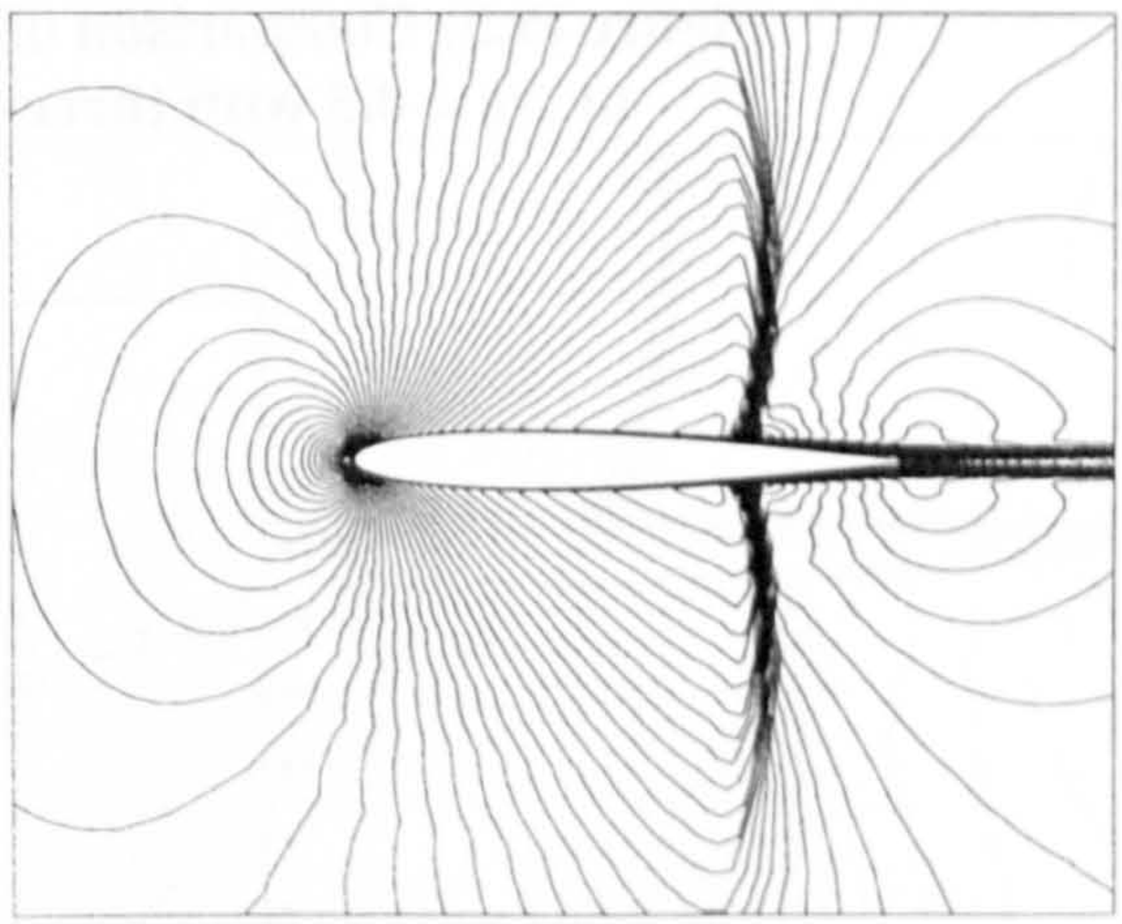

(b) 90°

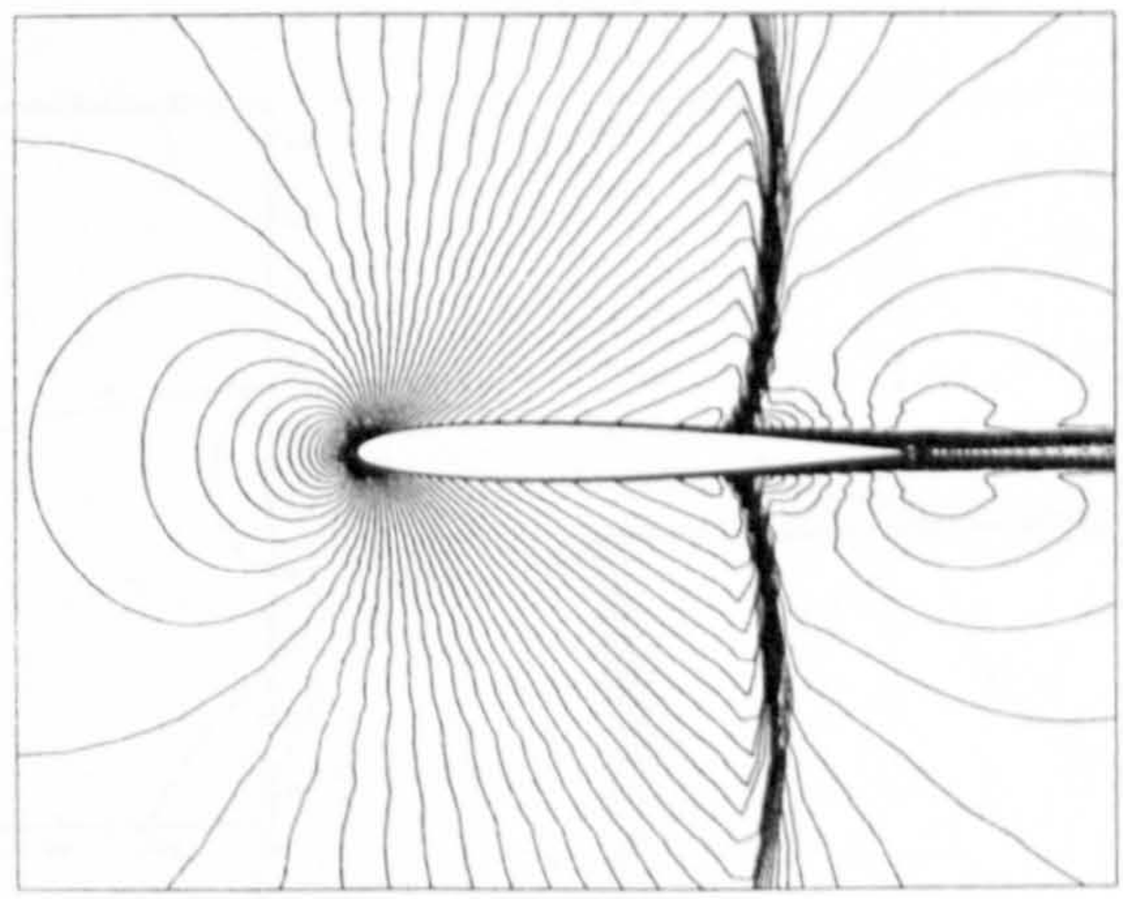

(c) 120°

Figure (9.4) Computed contours of local Mach number (Wilcox k-ω model)

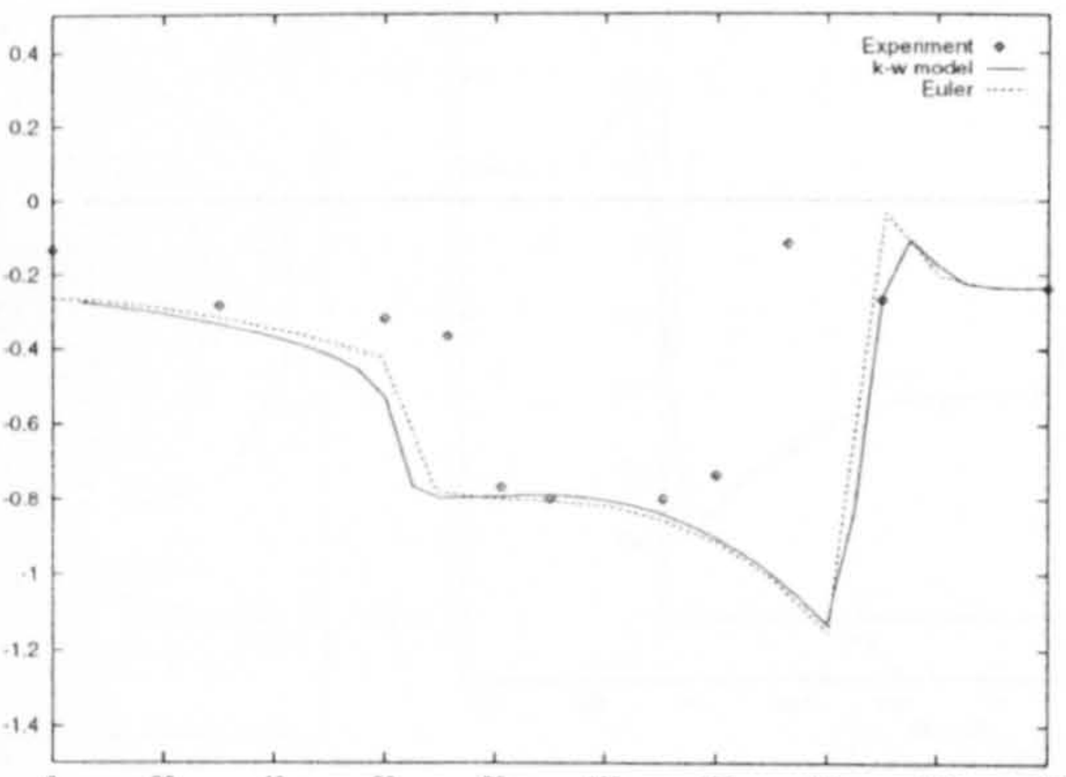

Figure (9.5) Comparison of computed unsteady pressure coefficient at x/c = 0.5 with three-dimensional experimental data[241-3]

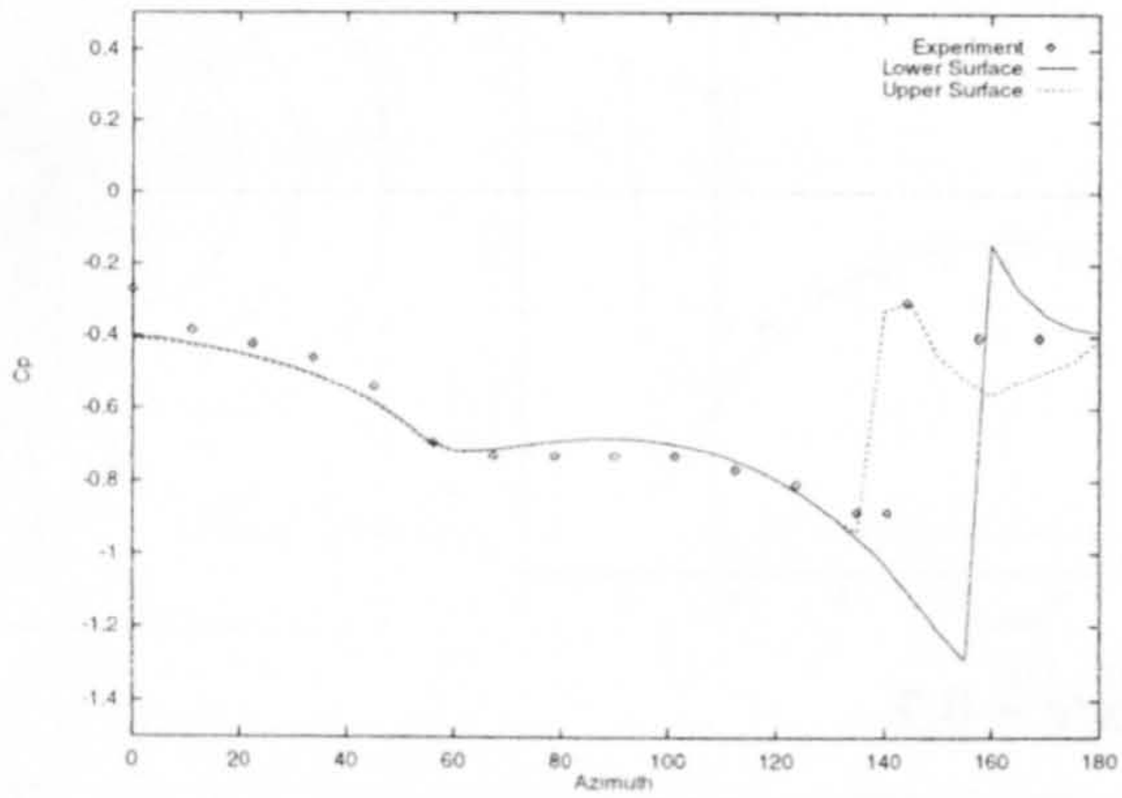

(a) x/c = 0.2

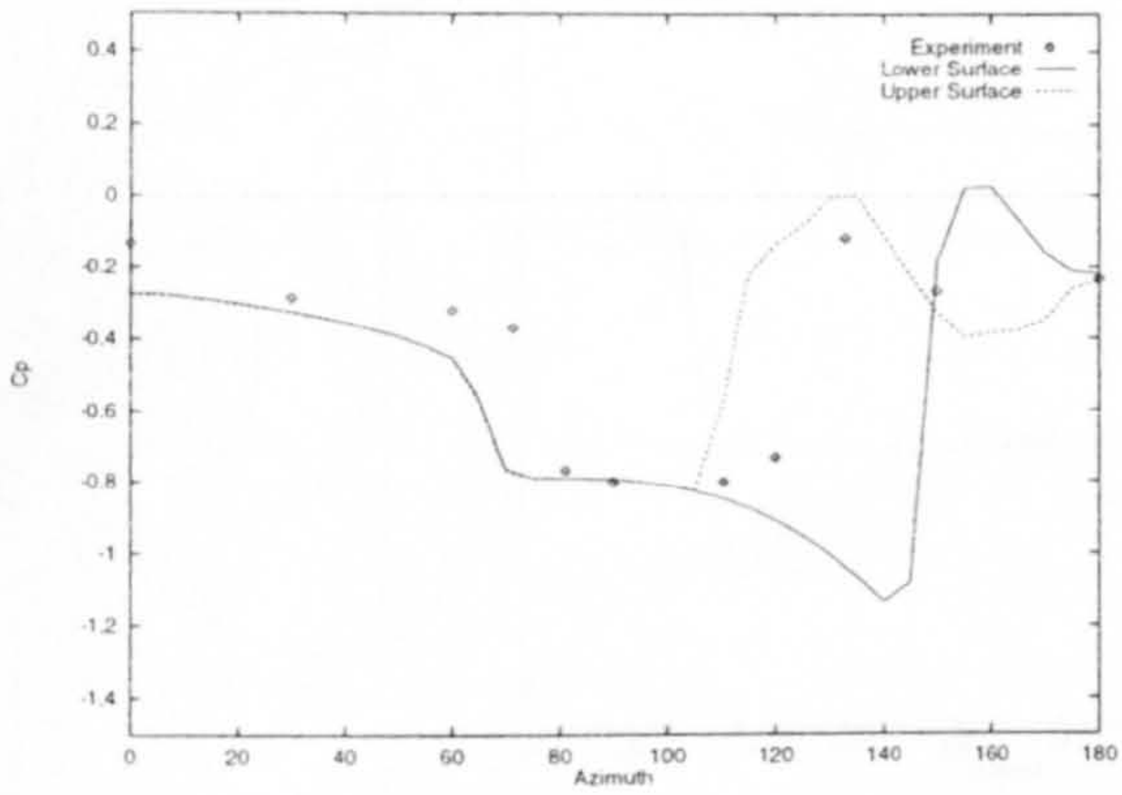

(b) x/c = 0.5

Figure (9.6) Comparison of computed pressure coefficient with three-dimensional experimental data[241-3]

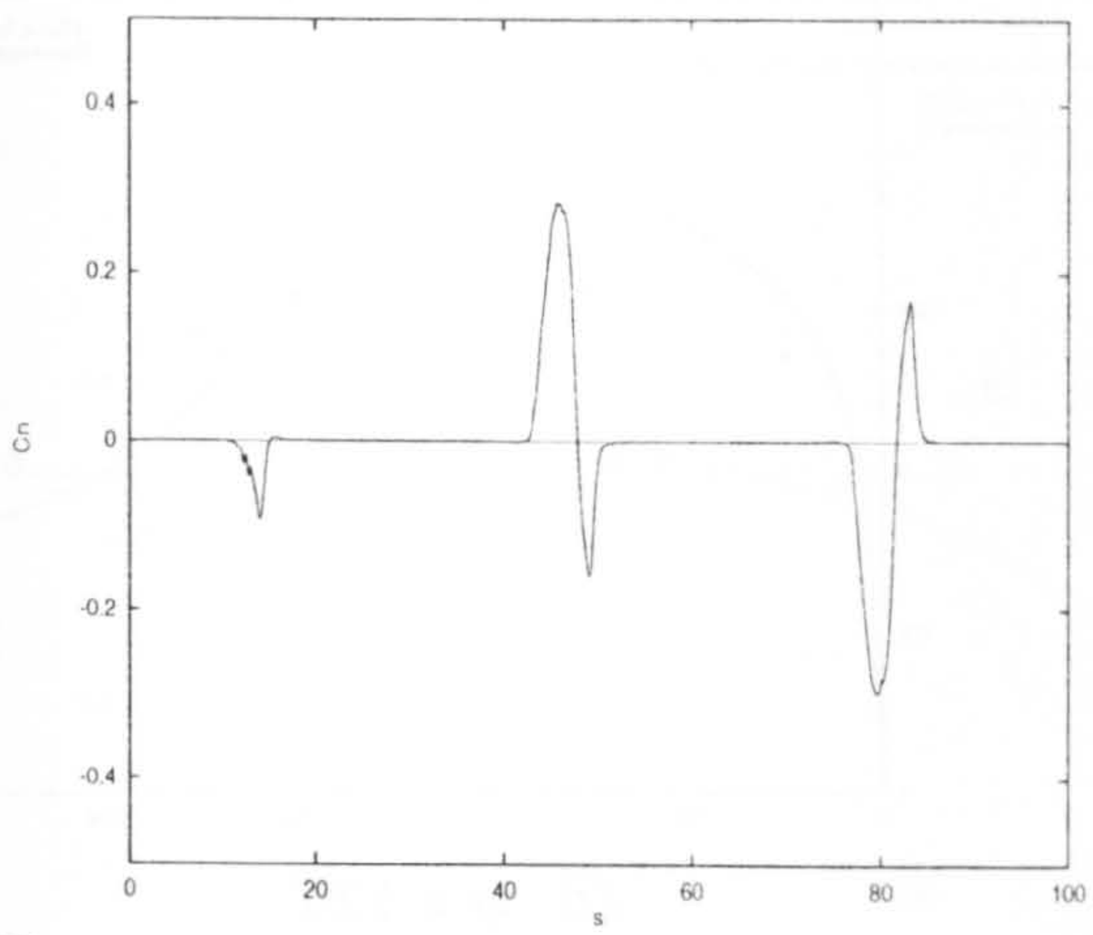

Figure (9.7) Calculated unsteady normal force coefficient (Baldwin-Lomax)

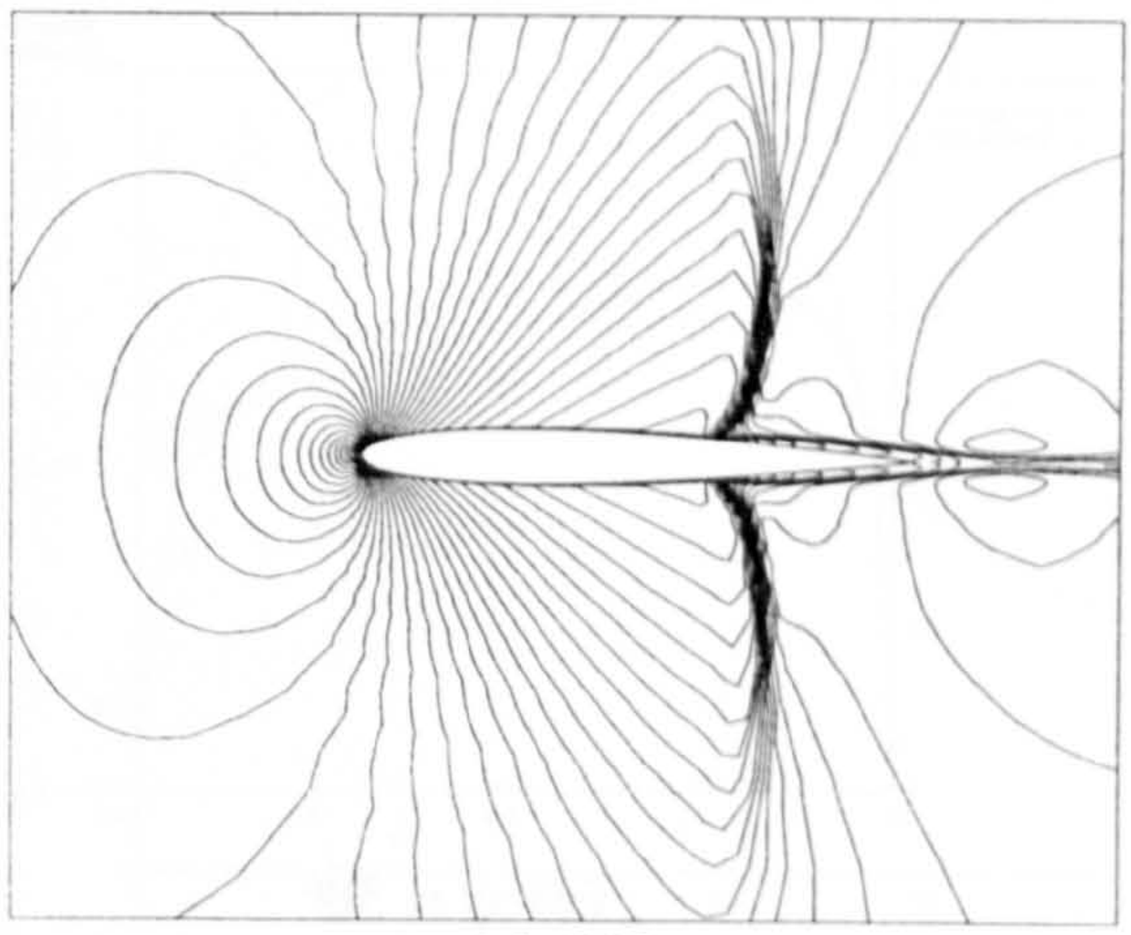

(c) 90°

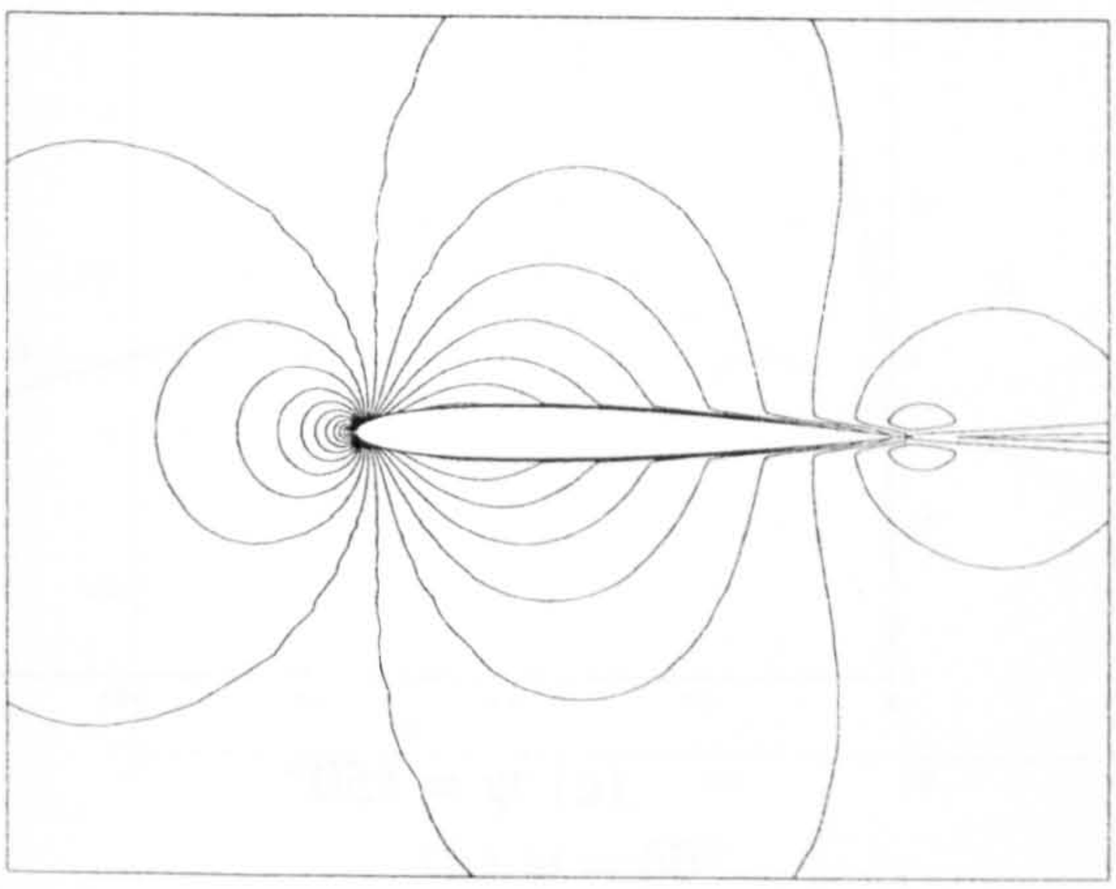

(a) 30°

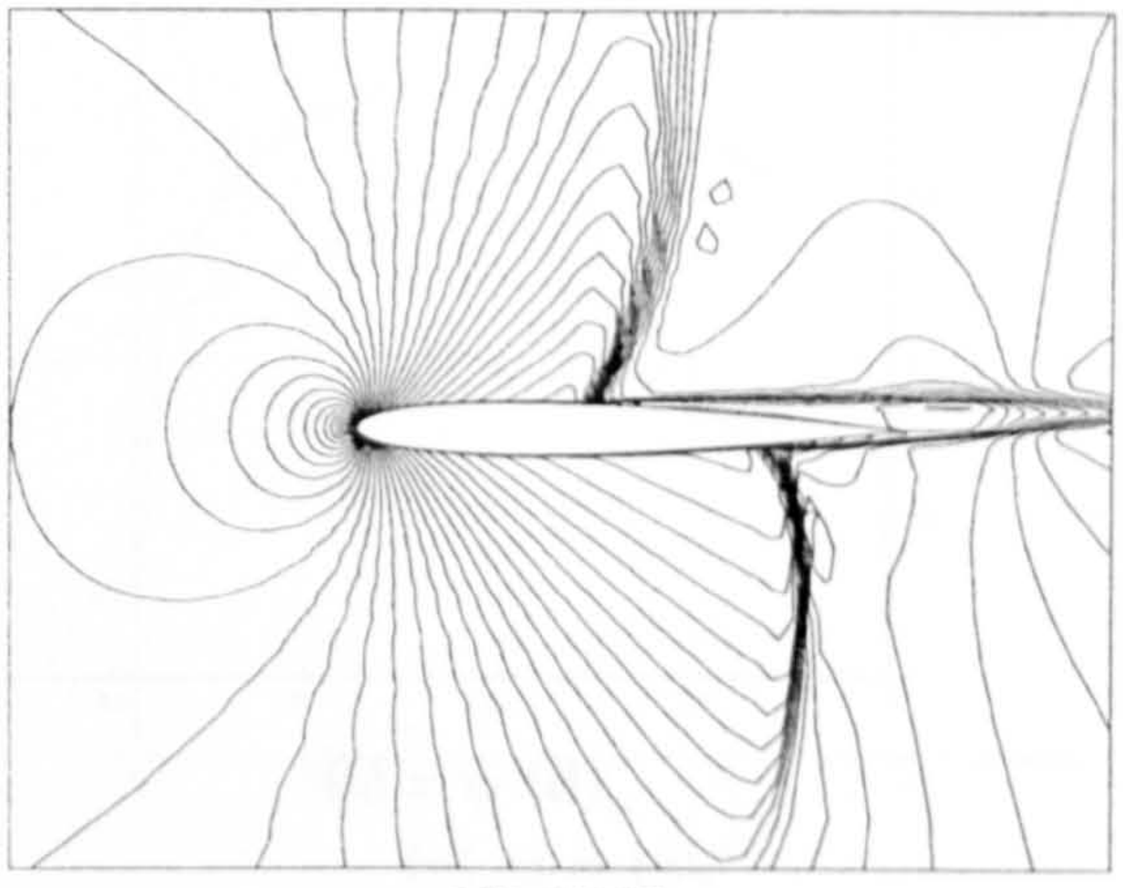

(d) 120°

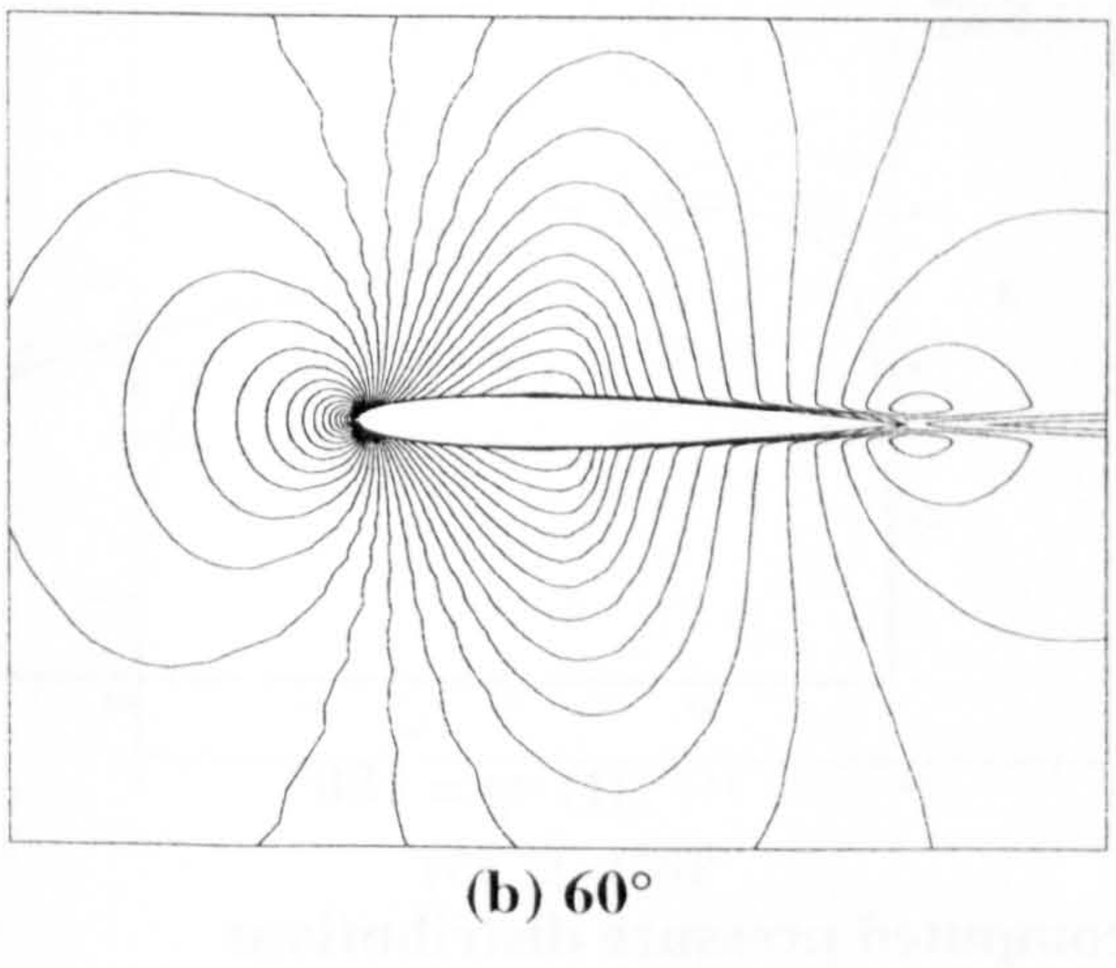

(b) 60°

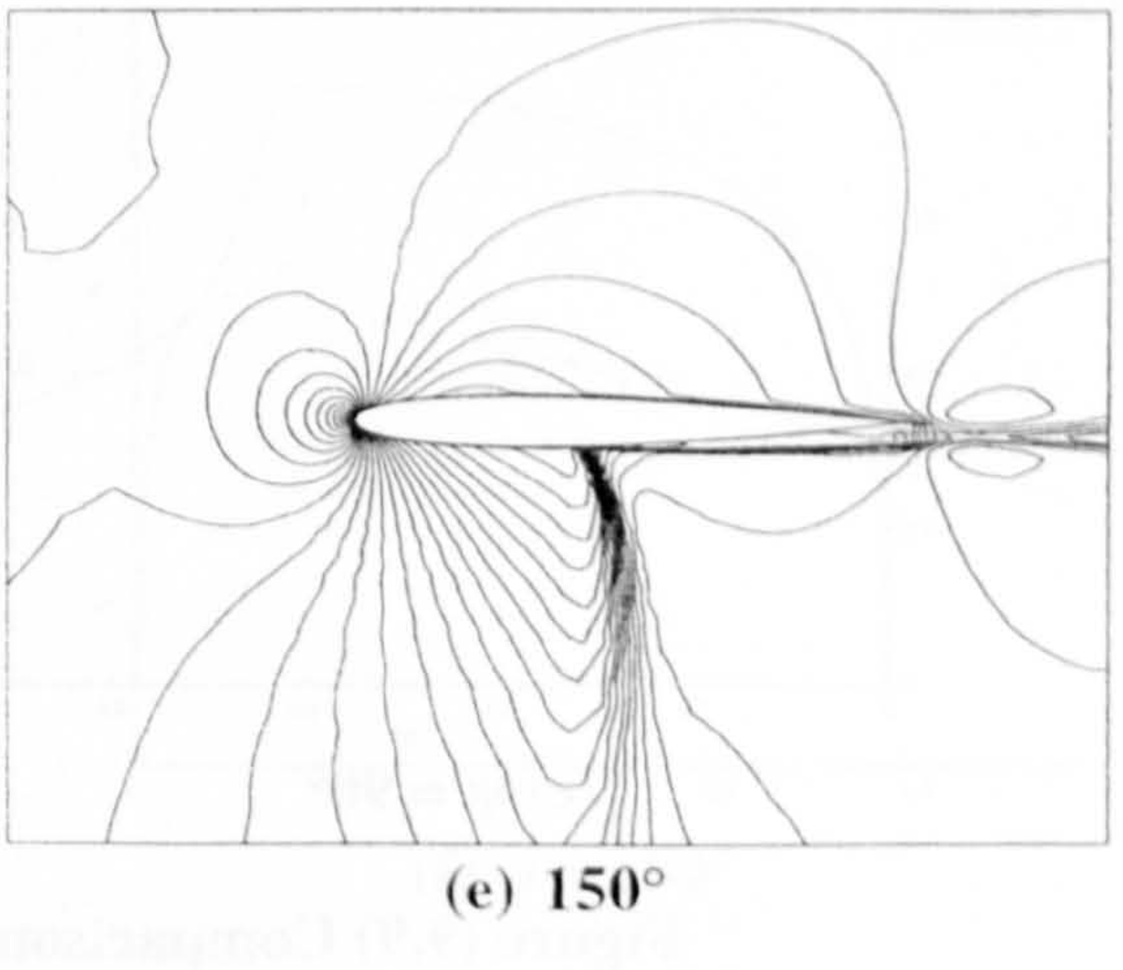

(e) 150°

Figure (9.8) Calculated instantaneous Mach number contours (Baldwin-Lomax)

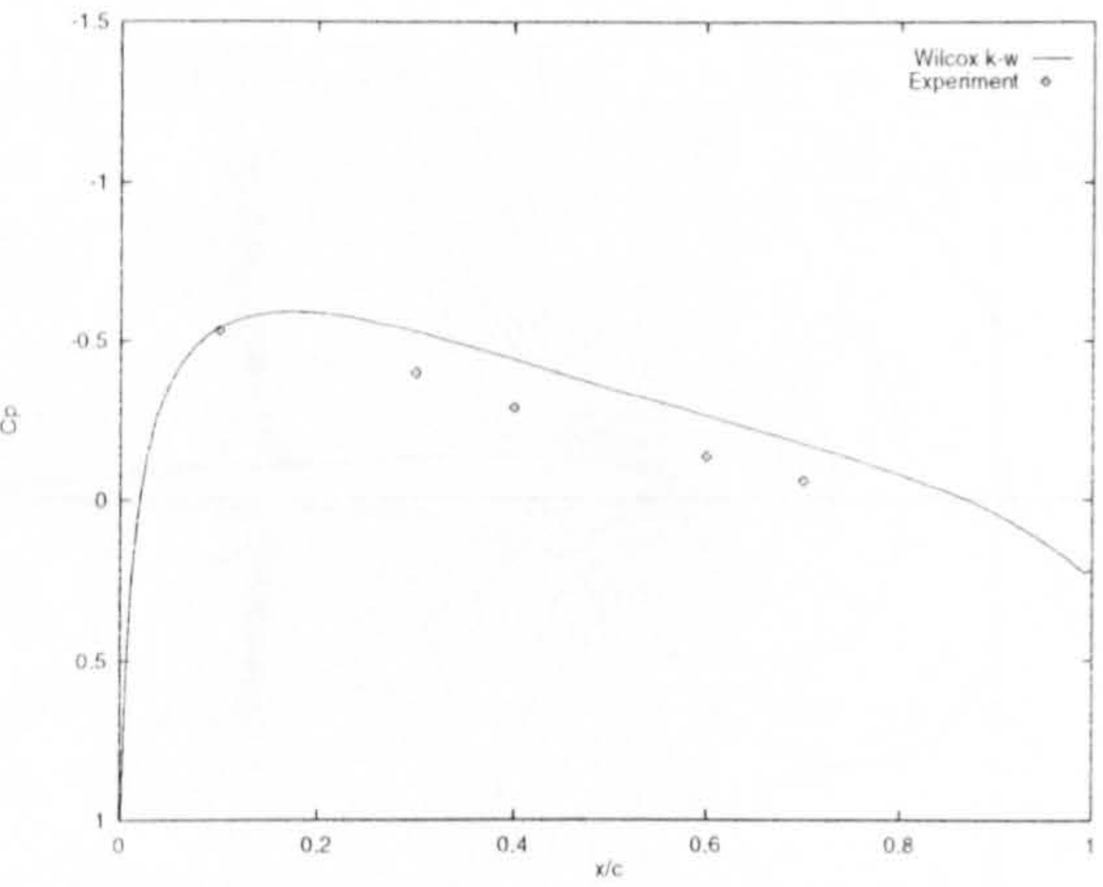

(a) $\psi = 30°$

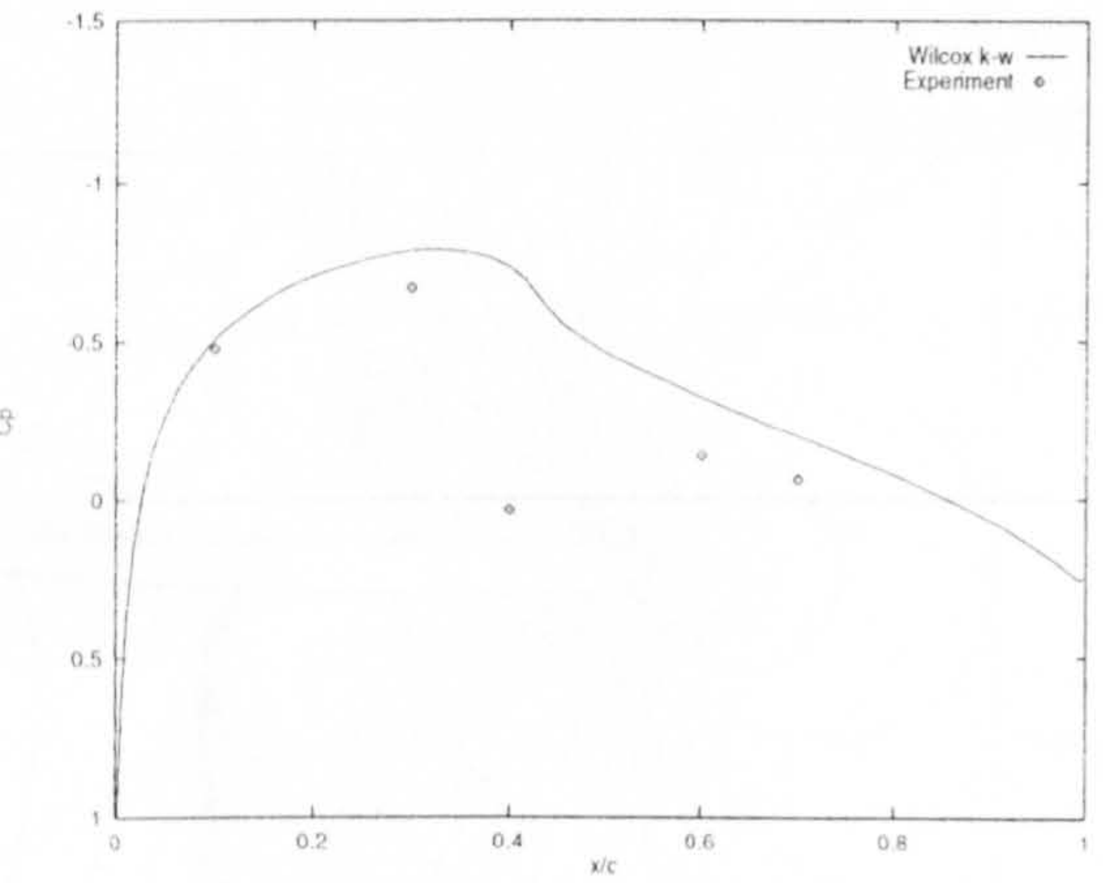

(b) $\psi = 60°$

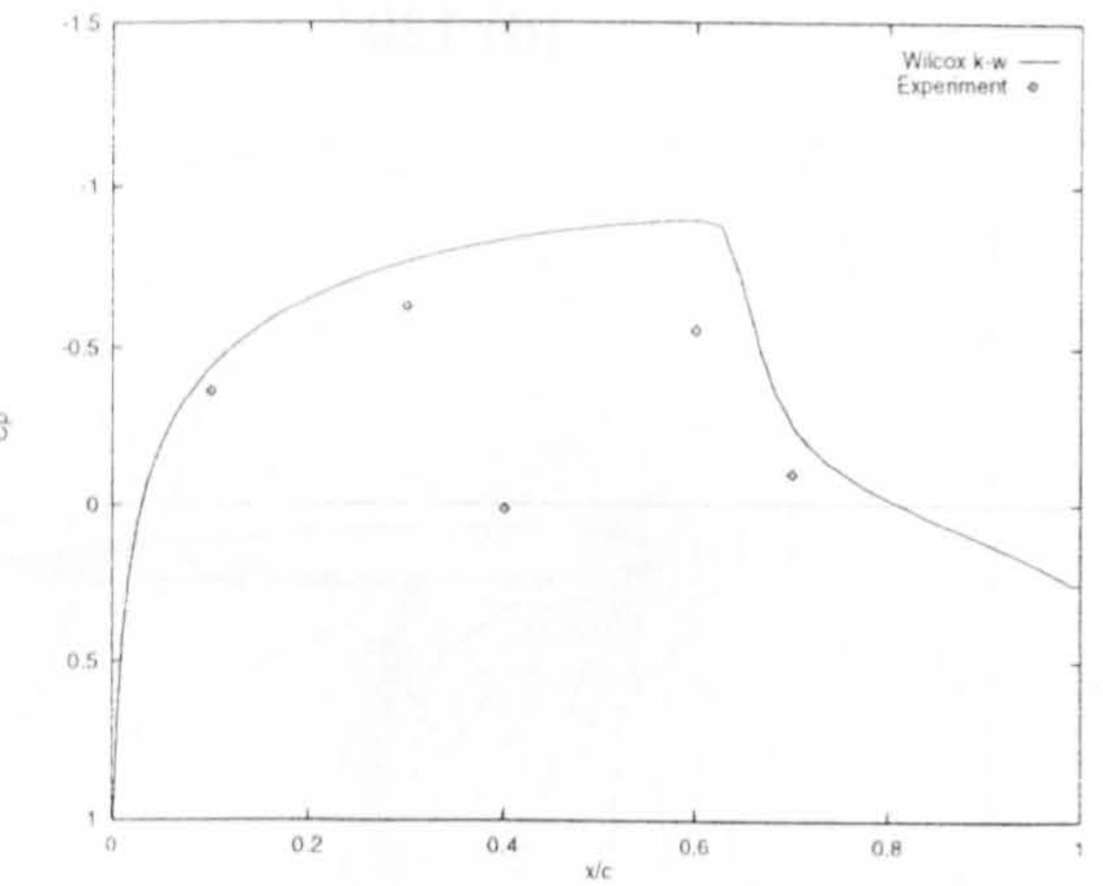

(c) $\psi = 90°$

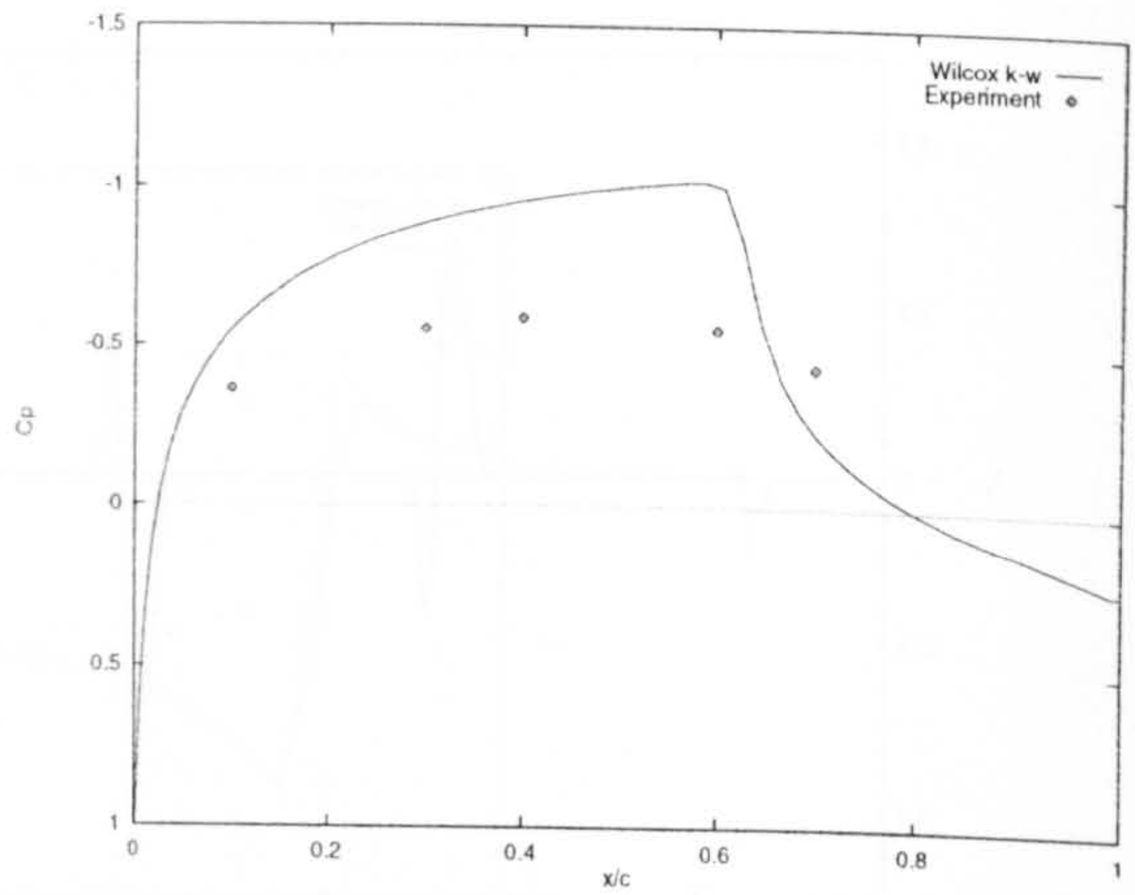

(d) $\psi = 120°$

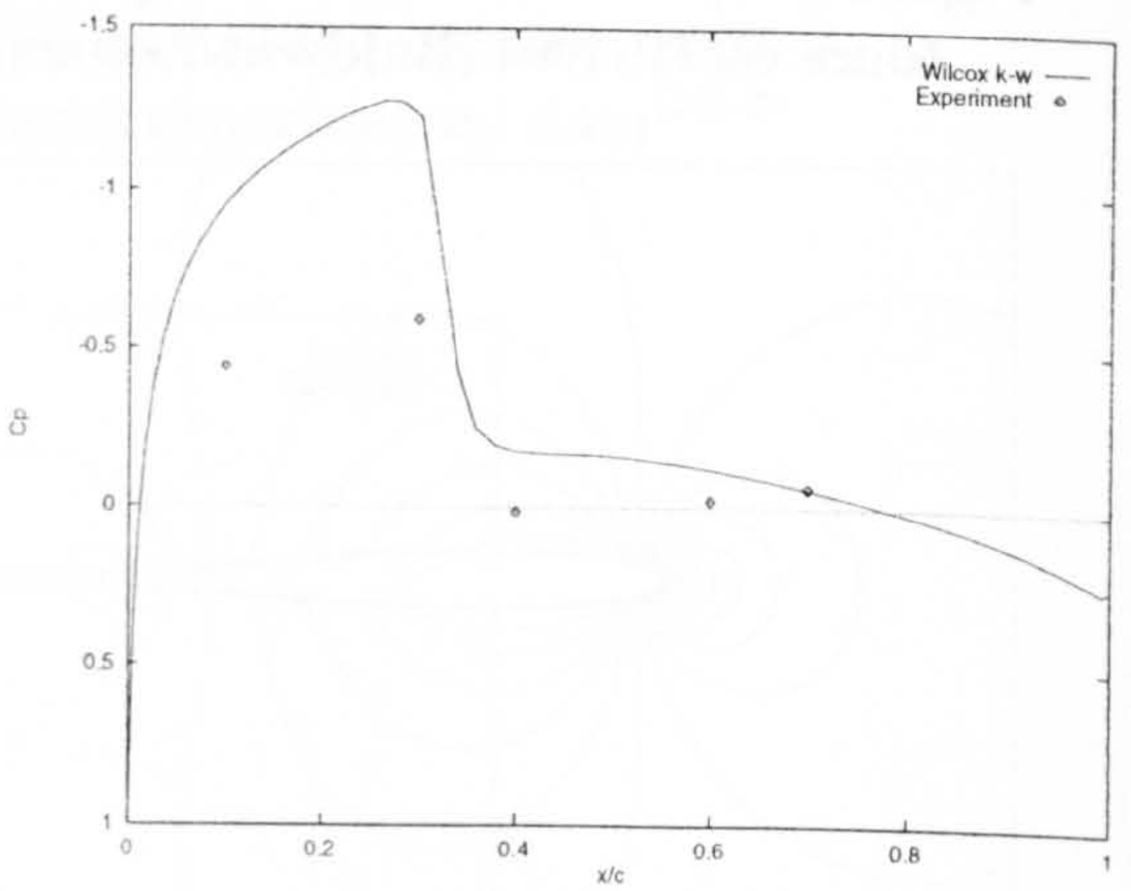

(e) $\psi = 150°$

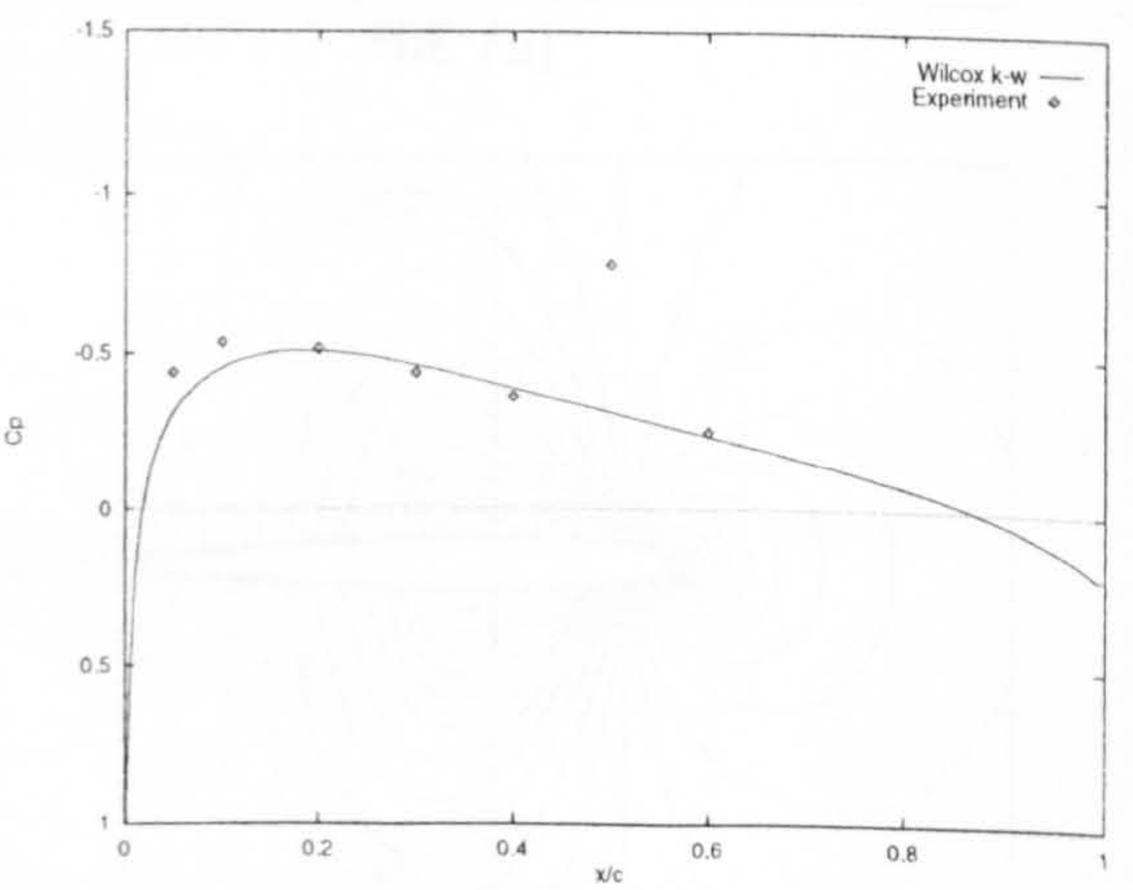

(f) $\psi = 180°$

Figure (9.9) Comparison of computed pressure distributions with three-dimensional experimental data[241-3] y/R = 0.85 (Case 3)

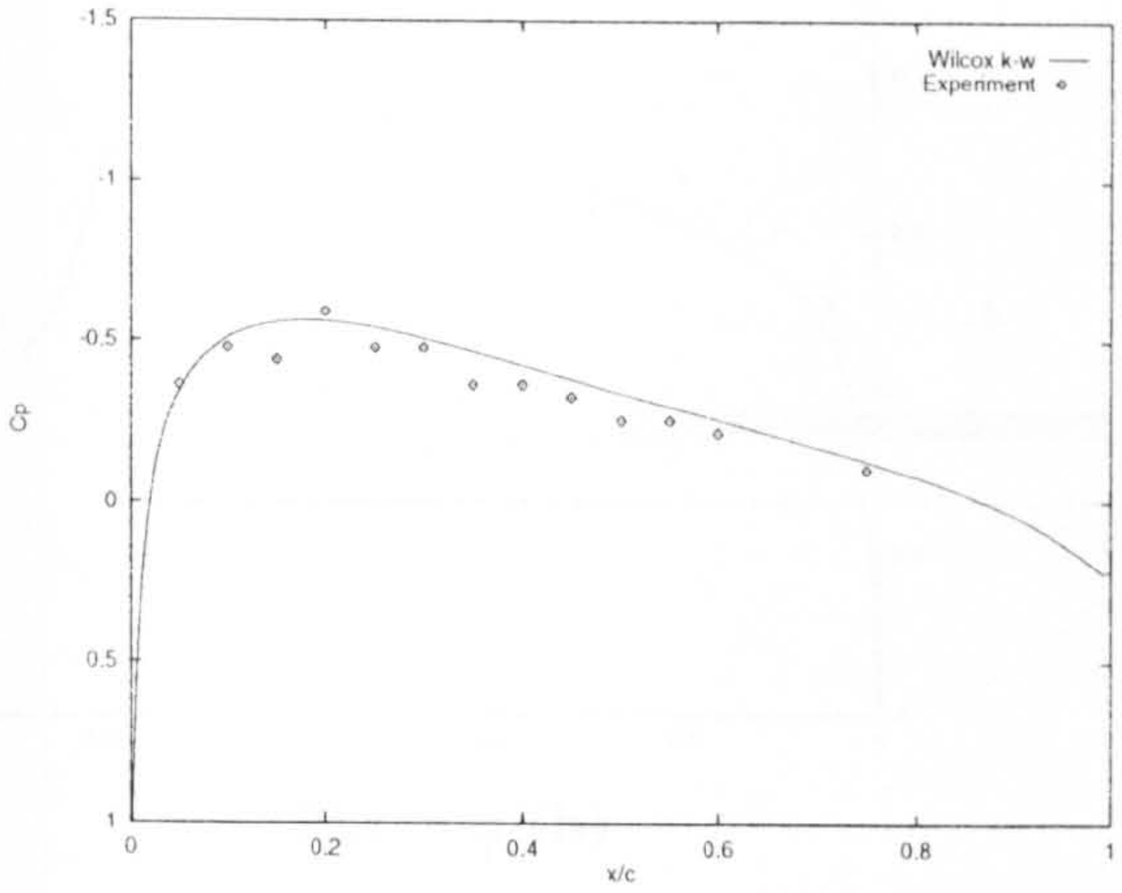

(a) $\psi = 30°$

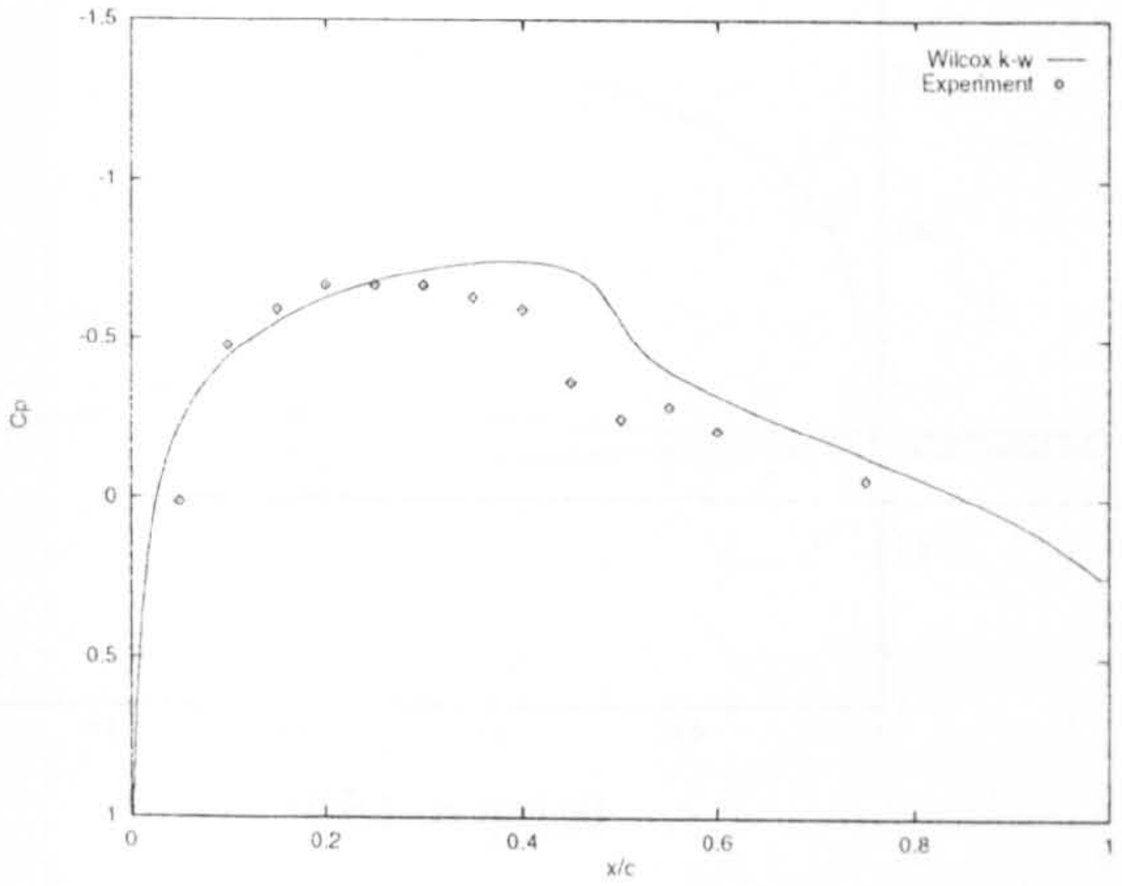

(b) $\psi = 60°$

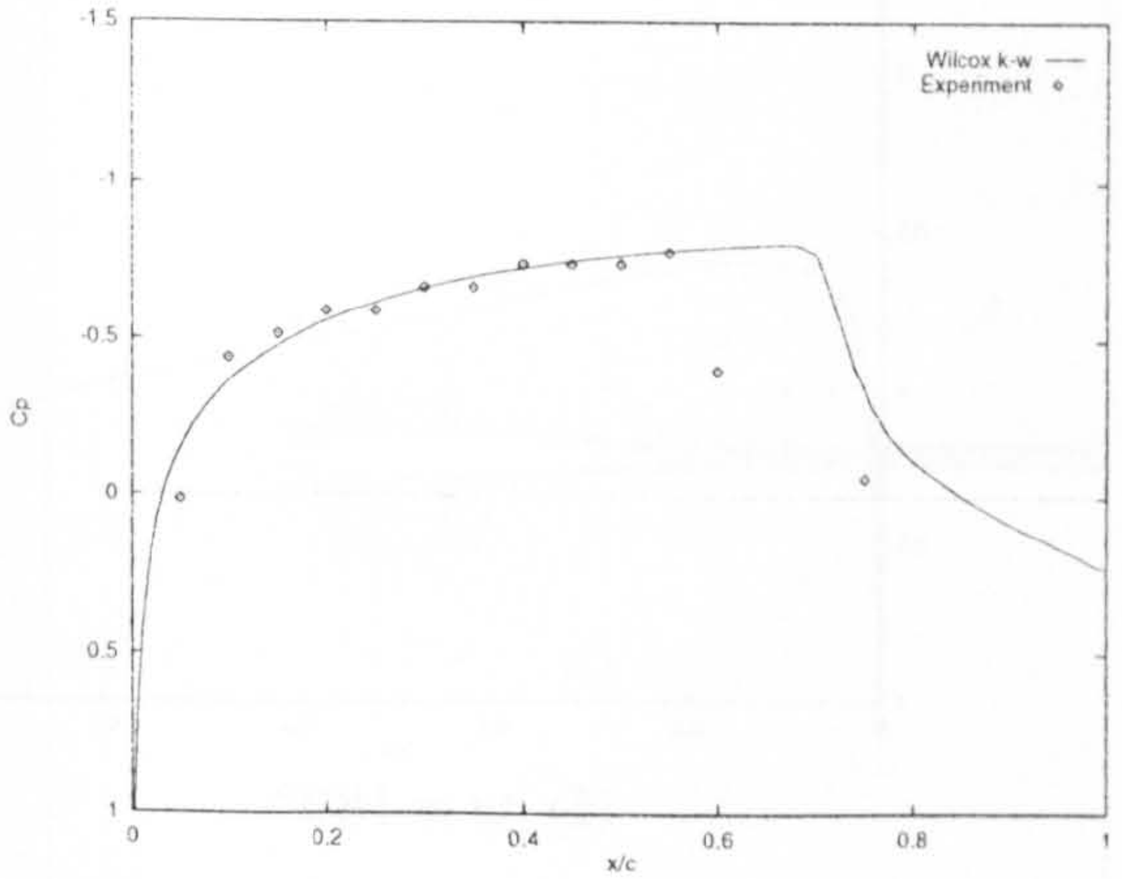

(c) $\psi = 90°$

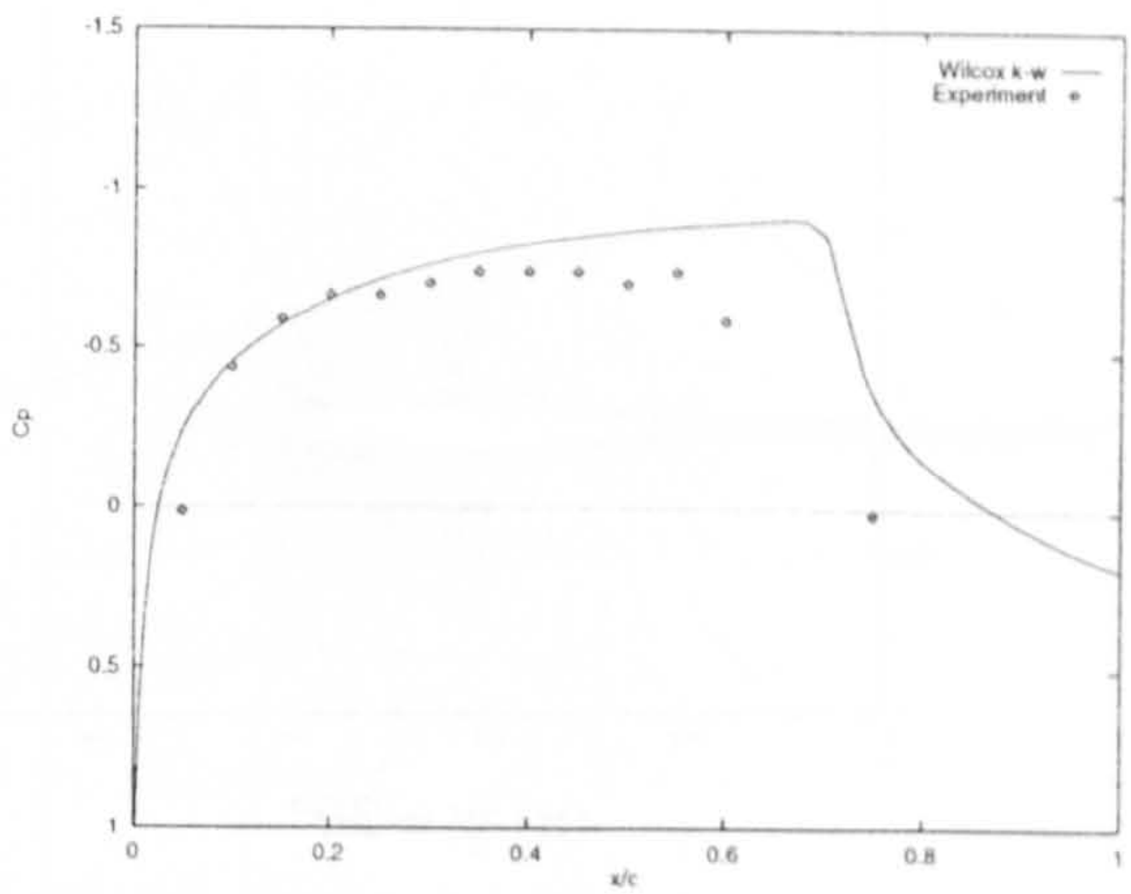

(d) $\psi = 120°$

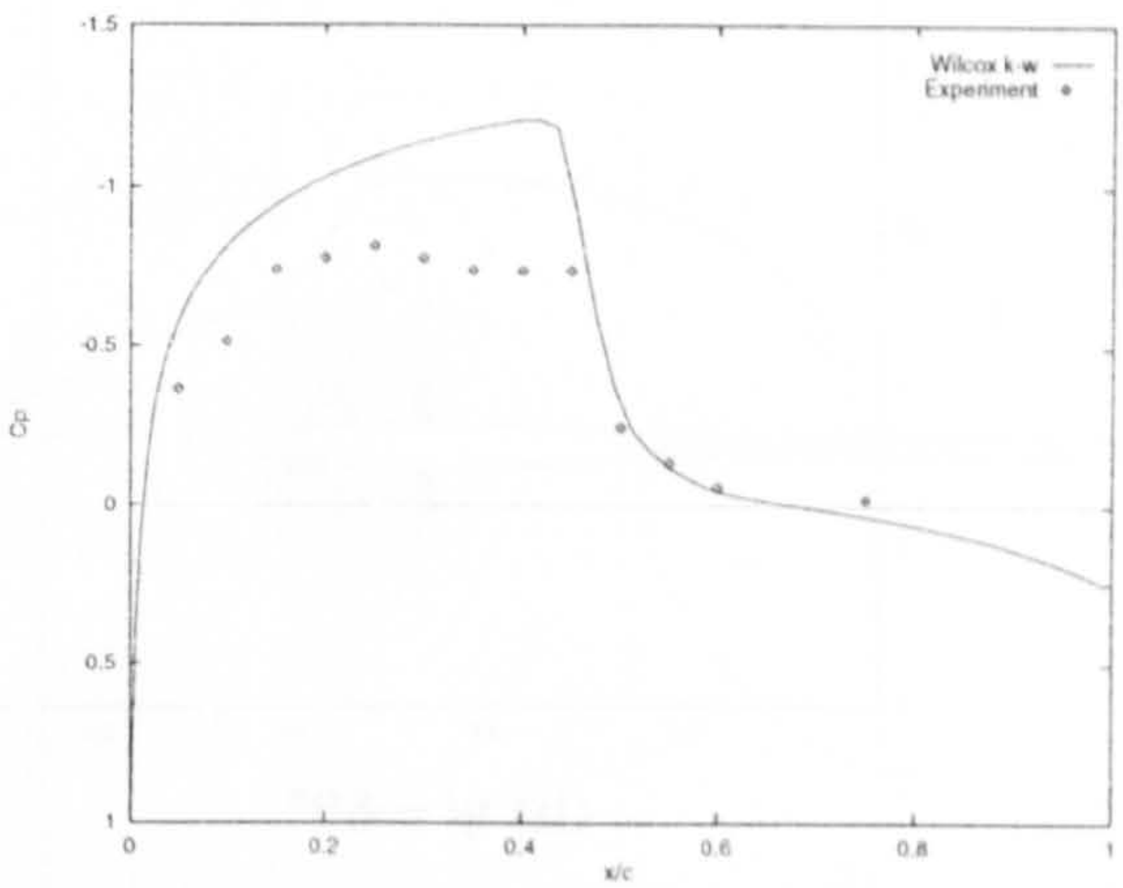

(e) $\psi = 150°$

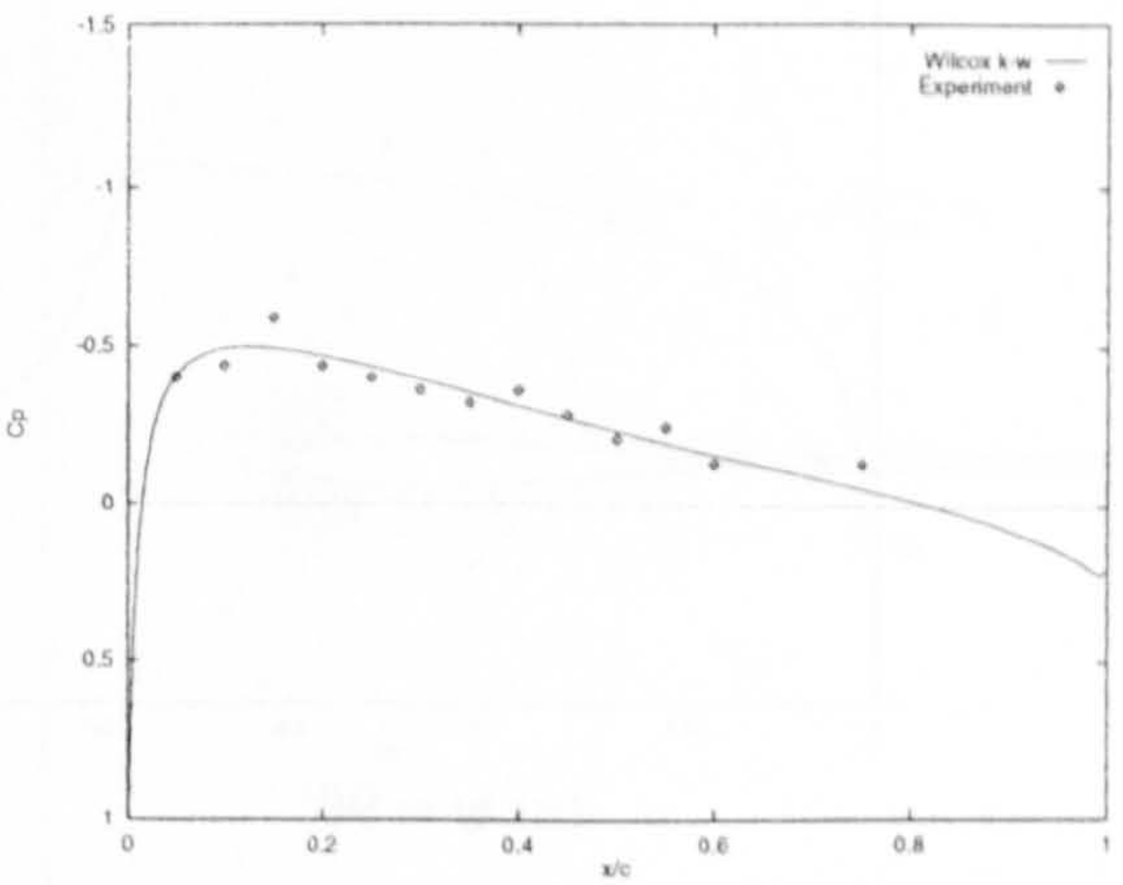

(f) $\psi = 180°$

Figure (9.10) Comparison of computed pressure distributions with three-dimensional experimental data[241-3] y/R = 0.90 (Case 3)

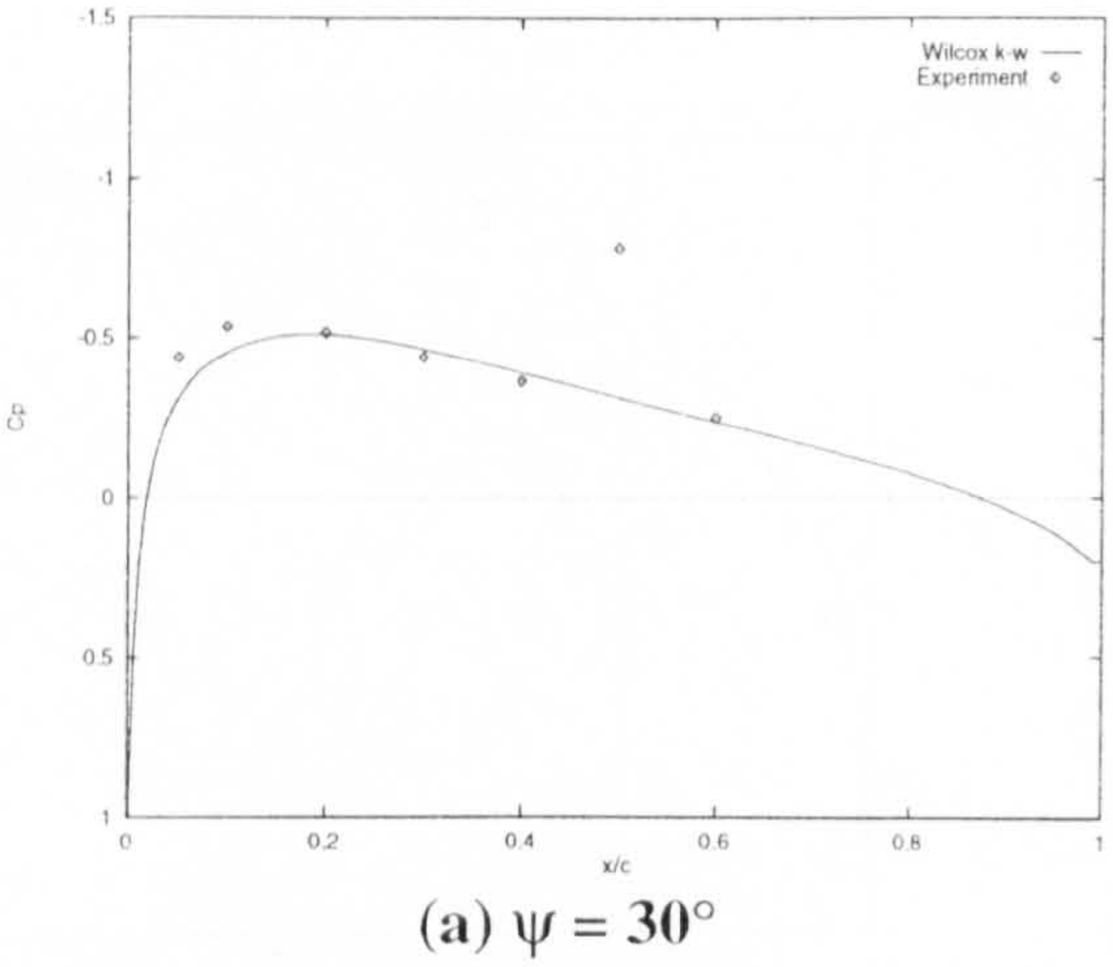

(a) $\psi = 30°$

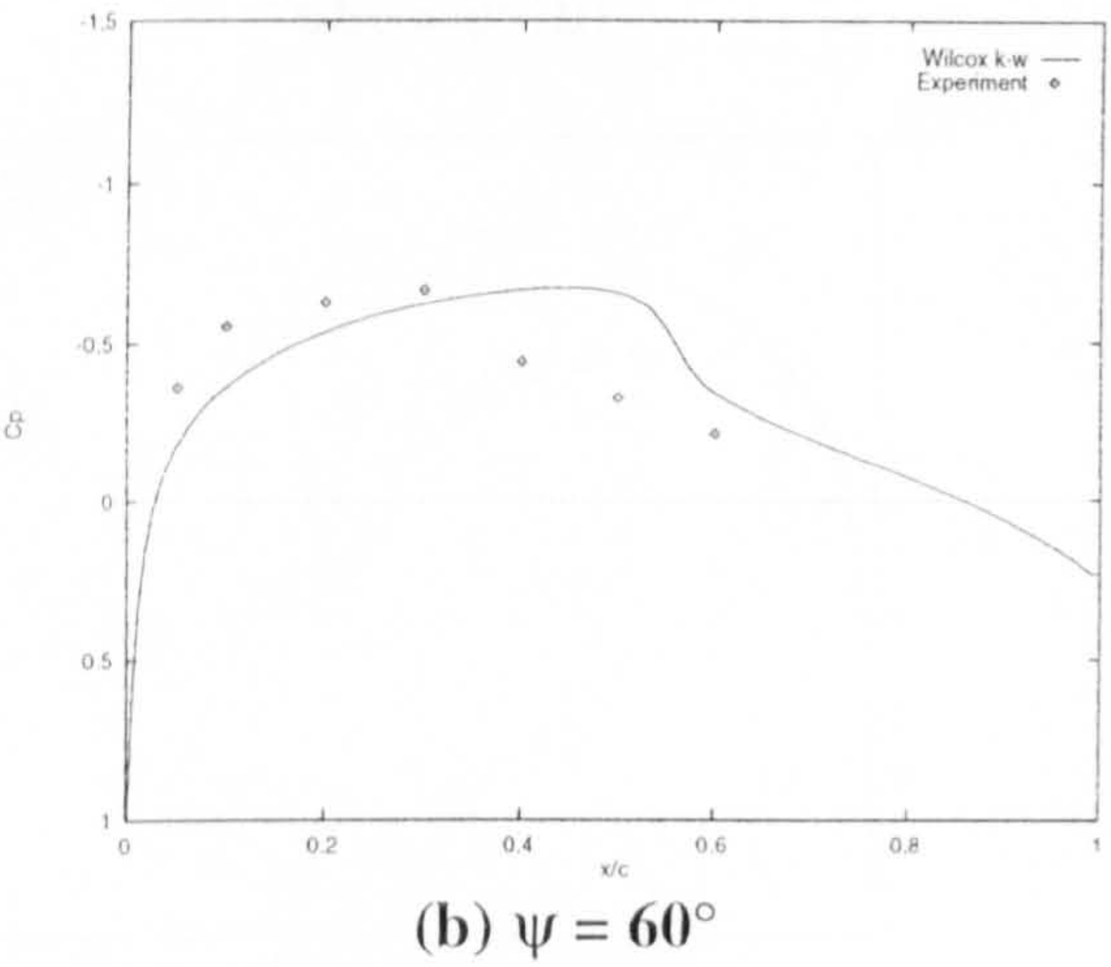

(b) $\psi = 60°$

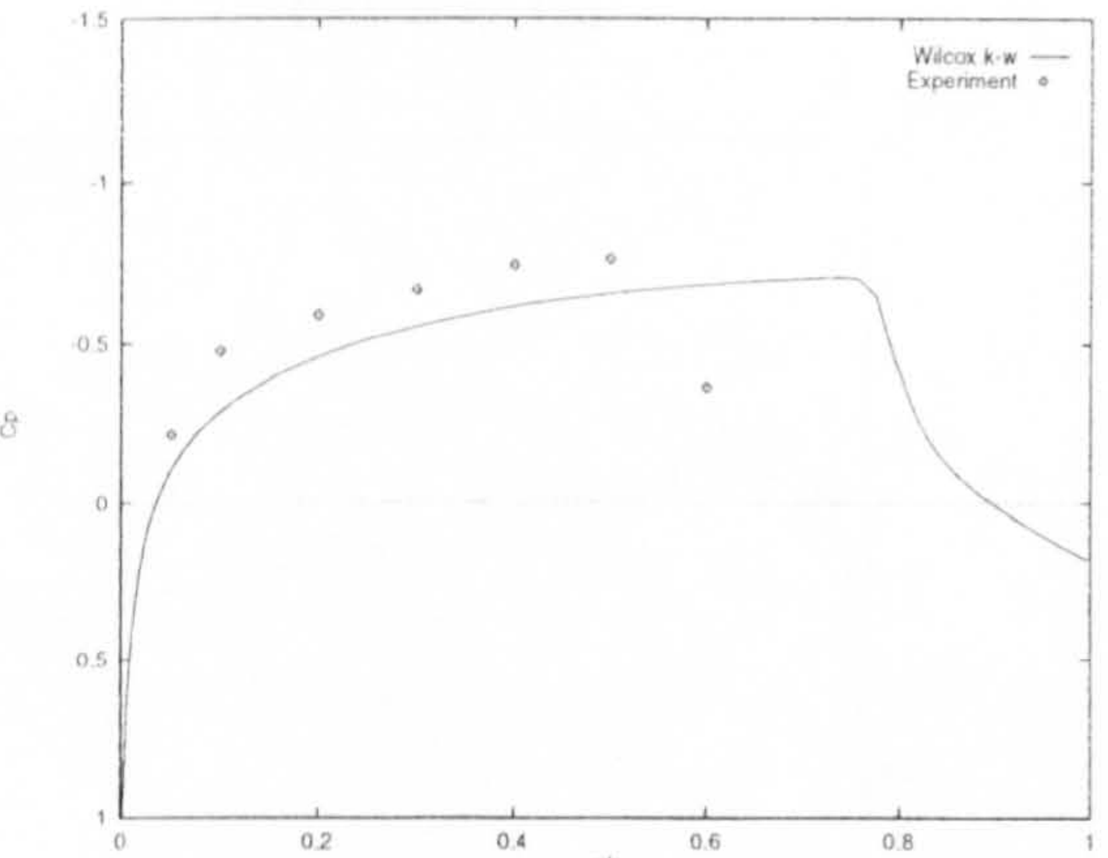

(c) $\psi = 90°$

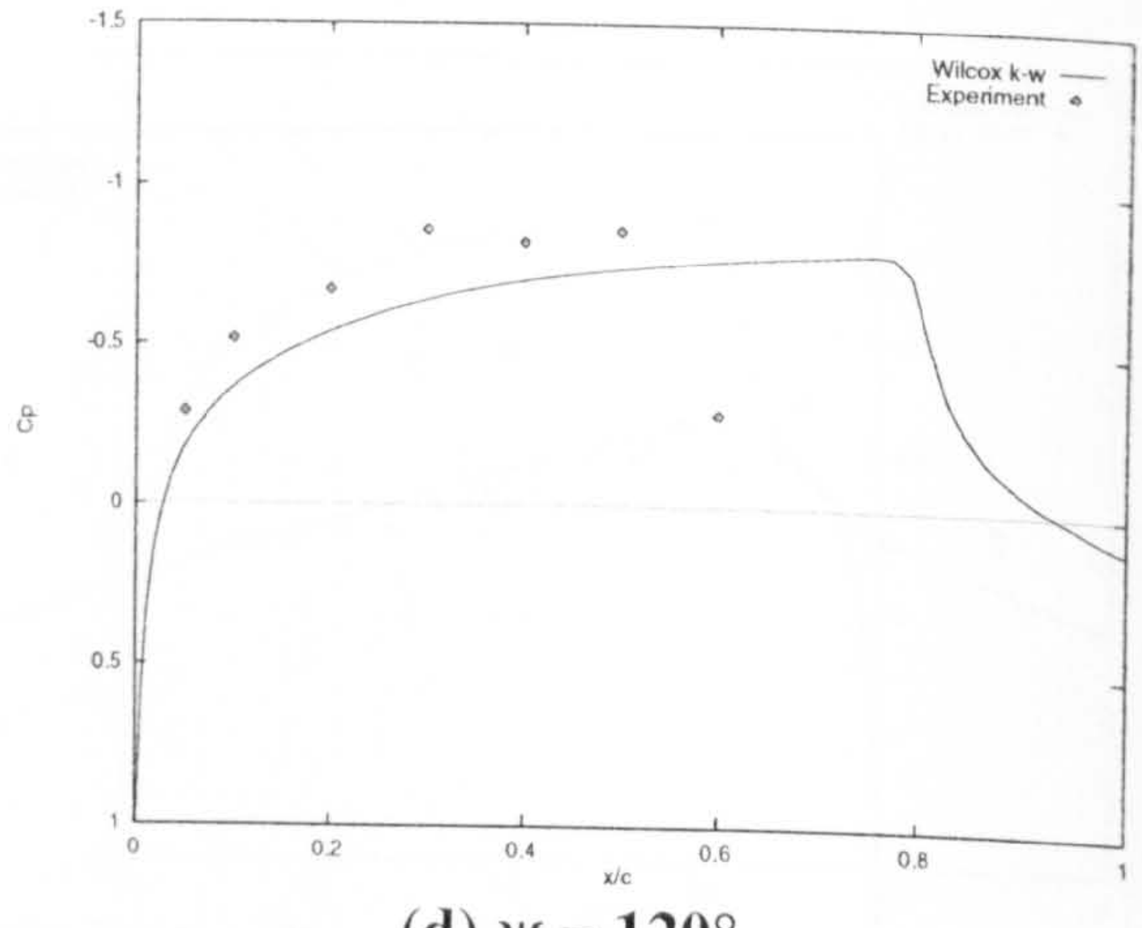

(d) $\psi = 120°$

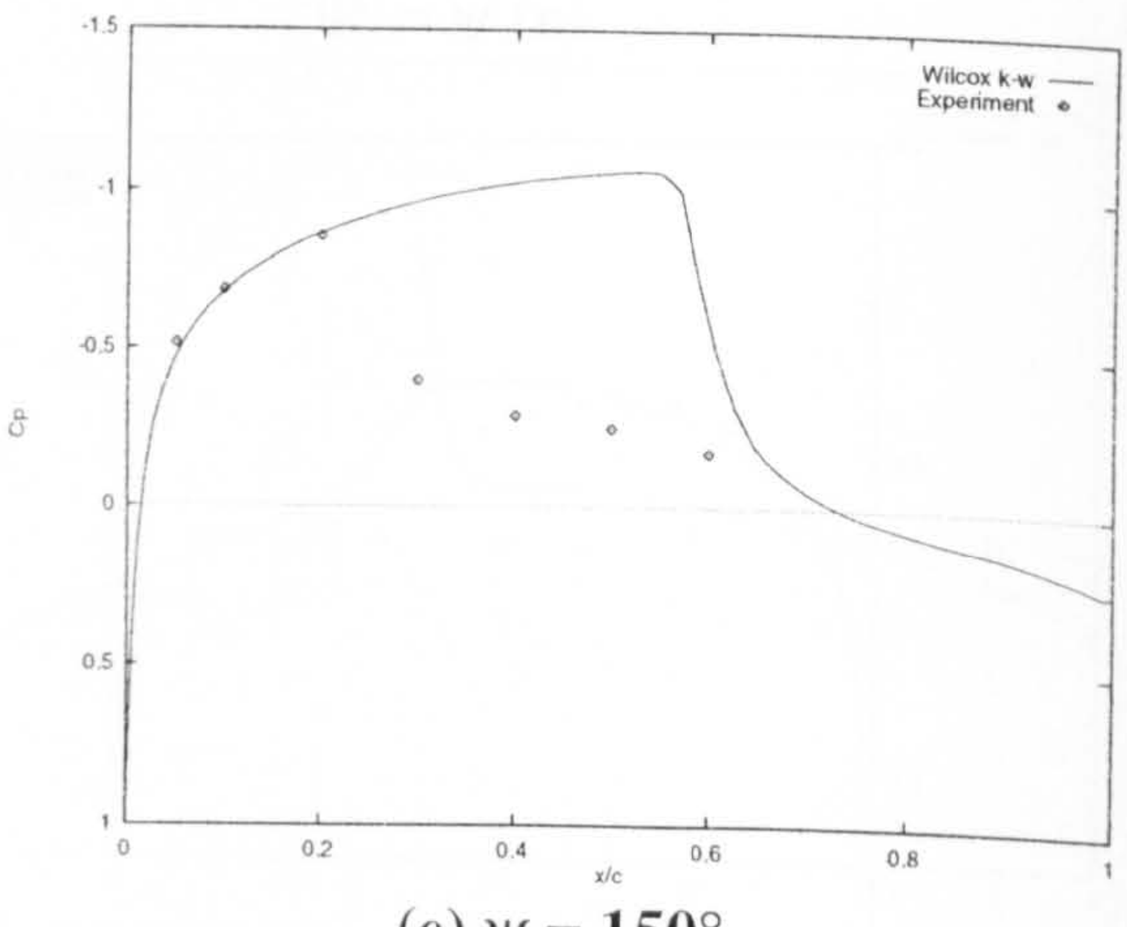

(e) $\psi = 150°$

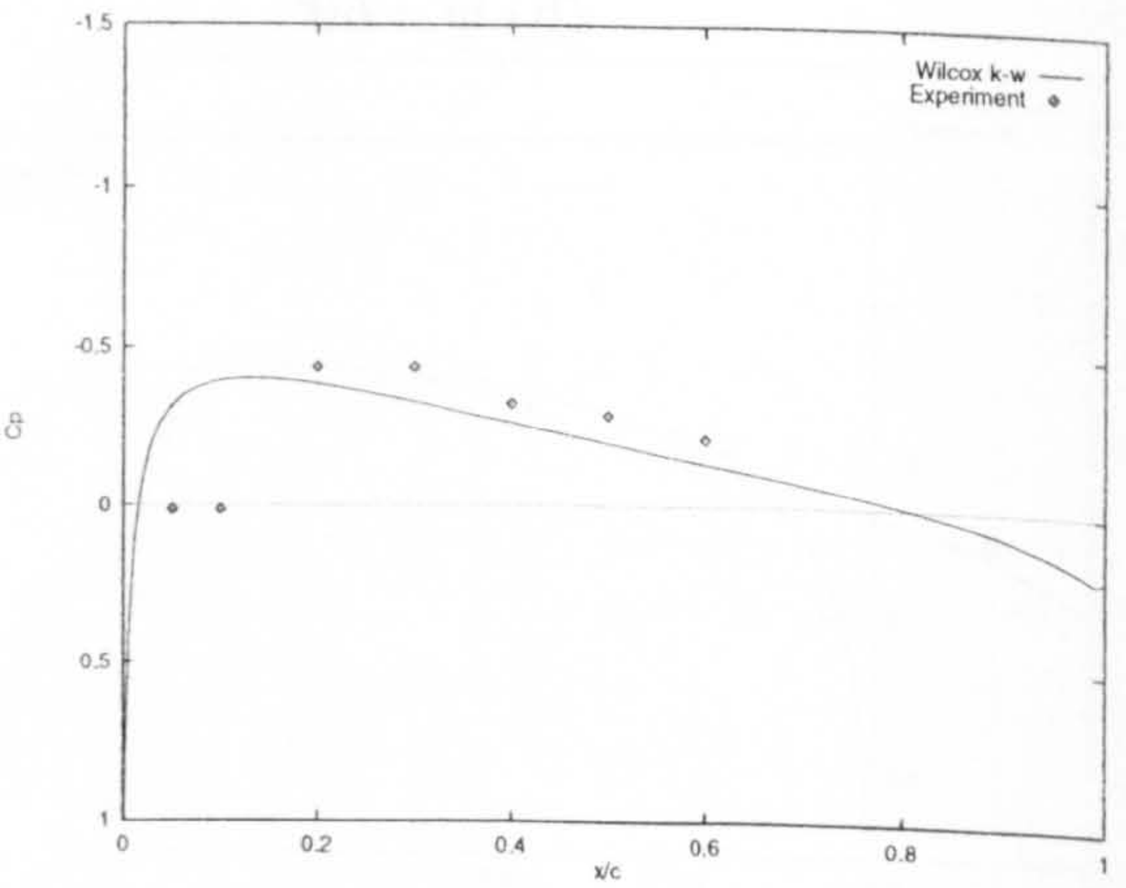

(f) $\psi = 180°$

Figure (9.11) Comparison of computed pressure distributions with three-dimensional experimental data[241-3] y/R = 0.95 (Case 3)

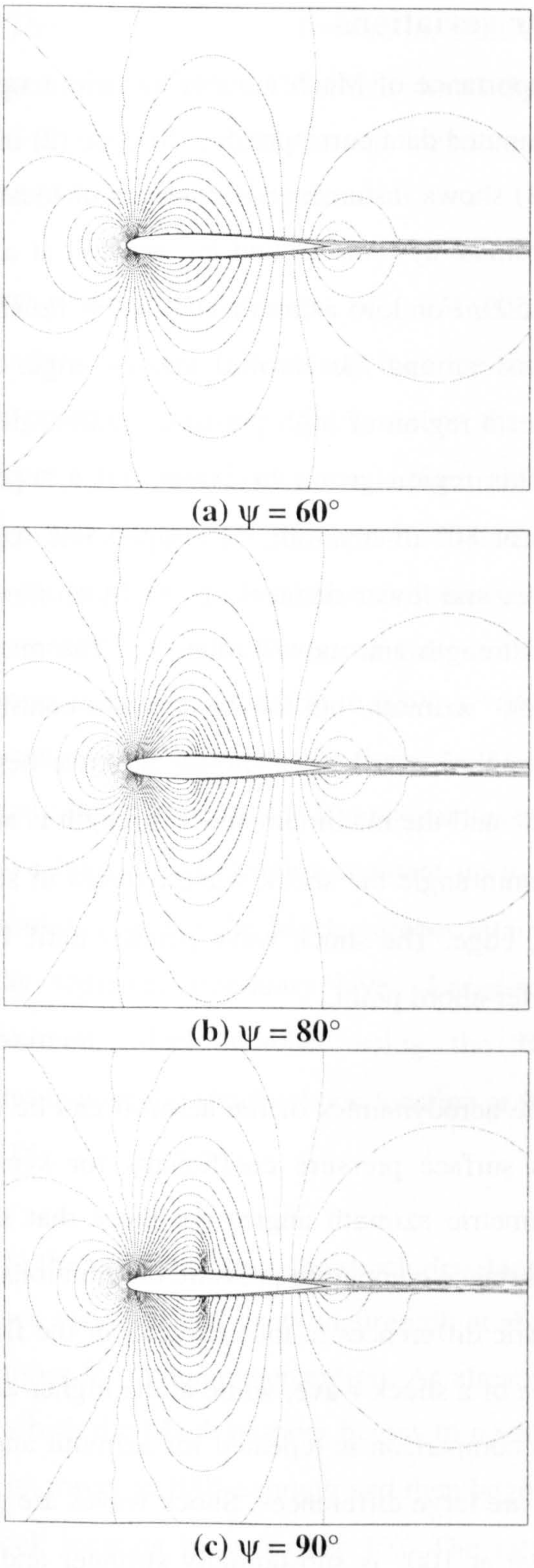

(a) $\psi = 60°$

(b) $\psi = 80°$

(c) $\psi = 90°$

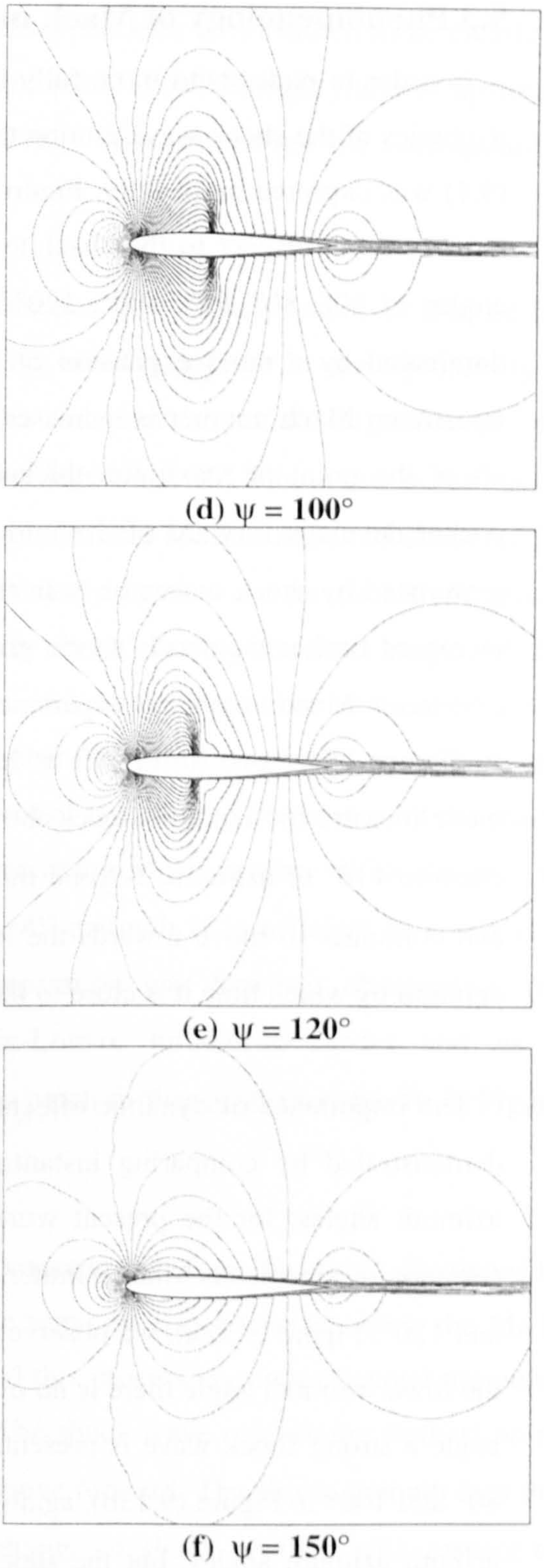

(d) $\psi = 100°$

(e) $\psi = 120°$

(f) $\psi = 150°$

Figure (9.12) Development of unsteady flow (Case 1)

9.3 Phenomenology of Mach number variations

In order to understand more fully the importance of Mach number variations upon the dynamics of the shock wave motion the computed data corresponding to Case (2) of Table (9.1) was explored more fully. Figure (9.12) shows instantaneous contours of local Mach number (with respect to the absolute co-ordinate system) around the aerofoil at azimuth angles of 60°, 80°, 90°, 100°, 120° and 150°. For low azimuth angles the flowfield is dominated by a rapid expansion of the flow around the aerofoil leading edge. As the freestream Mach number is increased further a region of high pressure gradient develops aft of the point of maximum thickness. This region grows in extent and a supersonic pocket develops forward of the mid-chord at 80° of azimuth. The supersonic region is terminated by shock waves on both the upper and lower surfaces, as the Mach number is increased further the shock waves grow in strength and move further aft. The maximum freestream Mach number is experienced at 90° azimuth. but the shock wave continues to strengthen and move further aft as Mach number is reduced. The shock wave begins to move forward for azimuth angles above 100° and the maximum shock strength is attained close to 110° of azimuth. Beyond this azimuth angle the shock wave reduces in strength and continues to move towards the leading edge. The shock wave persists until 135° of azimuth by which time it is close to the quarter-chord point.

The importance of dynamic effects on the aerodynamics of the aerofoil can be clearly demonstrated by comparing instantaneous surface pressure coefficients for symmetric azimuth angles, for the present work symmetric azimuth angles are those that share a common instantaneous Mach number. For instance comparing pressure distributions at 60° and 120°, Figure (9.13a), we observe dramatic differences in the character of the flow. At the lower azimuth angle there is no evidence of a shock wave, while at the higher azimuth angle a strong shock wave is present. This comparison is repeated for azimuth angles of 80° and 100° in Figure (9.13b), again there are large differences. Shock waves are present at both azimuth angles, but the shock wave at 100° is substantially stronger and much further aft than that at 80°.

The process of shock formation, motion and disappearance is illustrated more clearly in Figures (9.14) and (9.15) which shows the instantaneous shock strength (ratio of upstream and downstream pressure) and location respectively. Also shown are the corresponding data for the quasi-steady flow.

The initial development of the unsteady transonic flow closely parallels that of the steady flow. As in the steady case the shock wave initially appears in close proximity to the point of maximum thickness on the aerofoil and then moves aft. Significantly, the appearance of the shock wave in the unsteady flow lags about 10° behind that in the steady flow, this phase shift corresponds to an increase in critical Mach number of about 0.025. As the incident Mach number is increased the unsteady shock wave travels aft and grows in strength at about the same rate as the steady shock. During the later stages of the acceleration the unsteady behaviour differs significantly from that observed in the corresponding quasi-steady flow. As Mach number increases from 0.77 to 0.78 in the steady flow the boundary layer separates at the foot of the shock. The position of the shock wave freezes and remains constant up to the maximum Mach number. With the present turbulence model the Mach number attained at 90° azimuth is insufficient to result in a fully separated boundary layer. Large-scale separation was however observed at the maximum Mach number using the Baldwin-Lomax turbulence model and as a consequence the steady shock location at 90° was much further aft than is shown in Figure (9.15).

In the unsteady flow, the shock development proceeds as before. The shock continues to move rearward and grow in strength at about the same rates as observed below the Mach number for incipient separation. As already noted this process continues beyond the point at which the Mach number begins to decrease. The shock wave reaches the furthest point of its travel at 100° azimuth and then begins to move forward. The shock strength lags the shock location by a further 10°. The rate of change of shock position with respect to azimuth is similar during the backward and forward motions up to the point at which the

shock travels forward of the maximum thickness. Forward of the point of maximum thickness the motion is accelerated. The shock wave persists to a much later azimuth angle than observed in the steady flow and the instantaneous Mach number at which it disappears ($M_\infty = 0.699$) is below the critical Mach number for this aerofoil section.

From the calculations we can identify a number of distinct characteristics in the unsteady flow development that cannot be reproduced using a quasi-steady model:

- The shock appears at a Mach number above the critical value while the instantaneous Mach number is increasing
- Separation is delayed/suppressed
- The shock continues to increase in strength and move aft as the Mach number is reduced
- The shock moves forward before the maximum strength is achieved
- The shock persists for Mach numbers below the critical value while the instanataneous Mach number is decreasing

From Figure (9.12) the unsteady shock motion is identified as Type B. This is confirmed by examining the time history of the pressure coefficient ahead of the aerofoil leading edge, Figure (9.16). For azimuth angles upto 130° the pressure coefficient varies in a smooth manner. At 130° there is a rapid rise associated with the passage of a disturbance wave. Also shown in Figure (9.16) is a similar trace for case (2). The maximum Mach number attained by the aerofoil is much higher in this case. Again the pressure varies smoothly for a significant part of the cycle and at 160° there is a sharp rise in pressure coefficient. While the increase in pressure is larger than for case (1) the local Mach number remains sub-critical. Clearly, the existence of such waves is important when determining the acoustical characteristics of the aerofoil section.

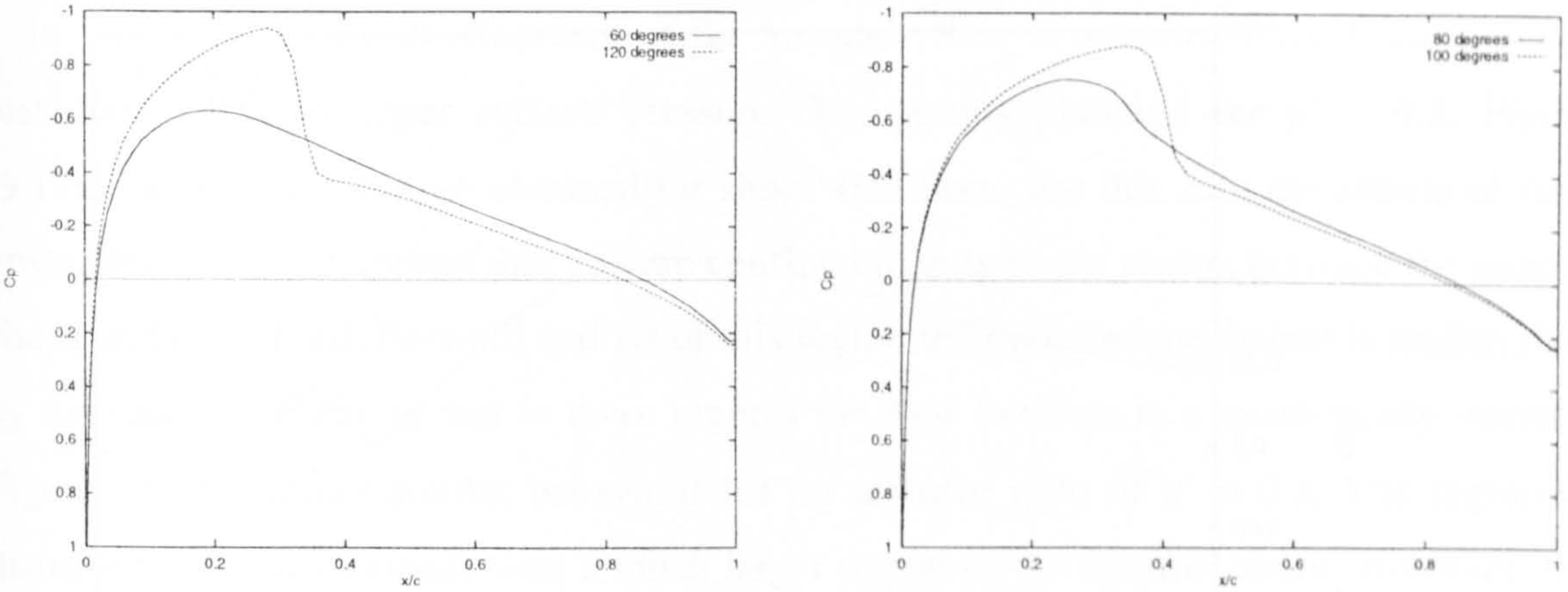

(a) M(t) = 0.744 **(b) M(t) = 0.776**

Figure (9.13) Comparison of pressure distributions for symmetric azimuth angles (Case 1)

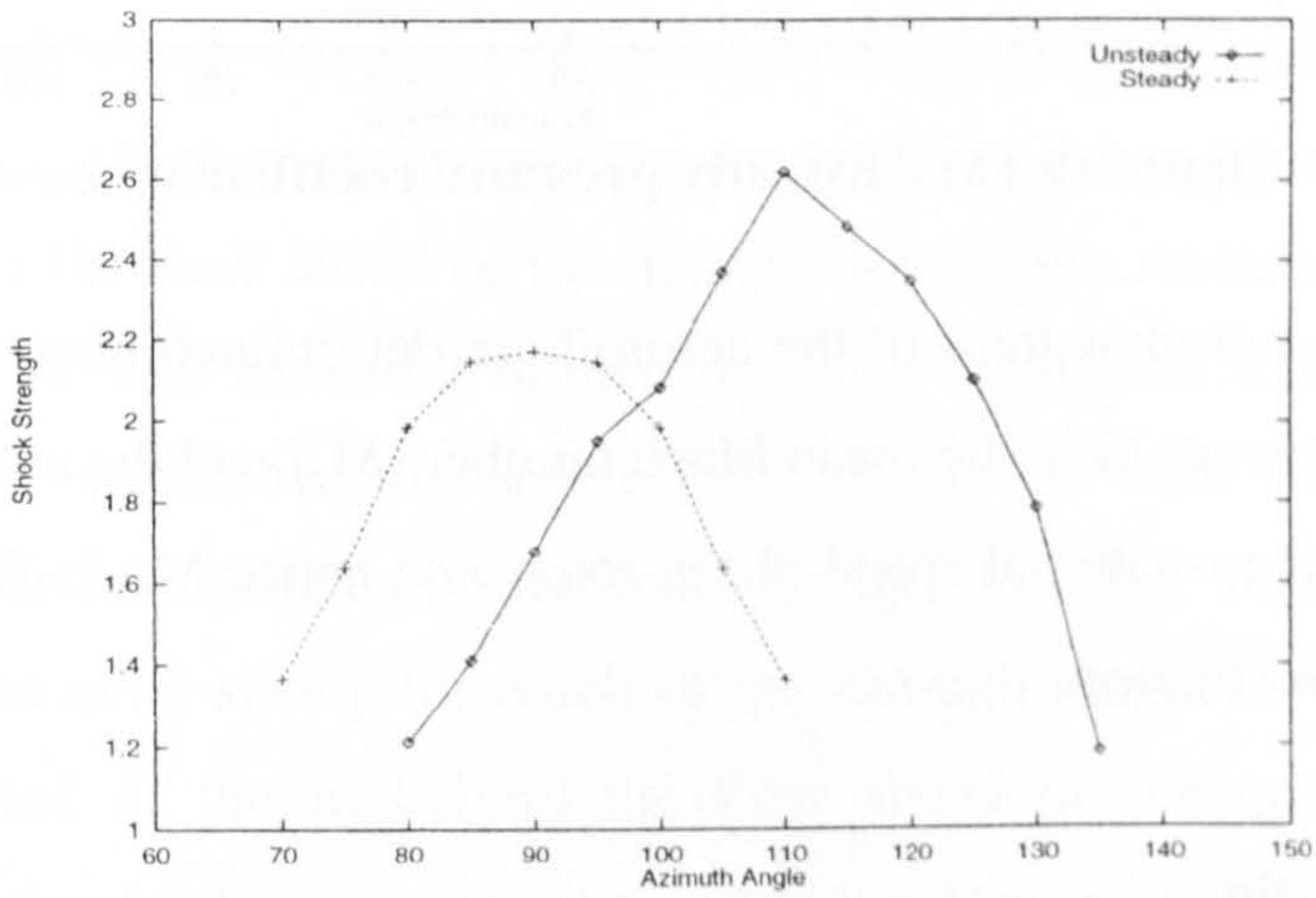

Figure (9.14) Shock strength (Case 1)

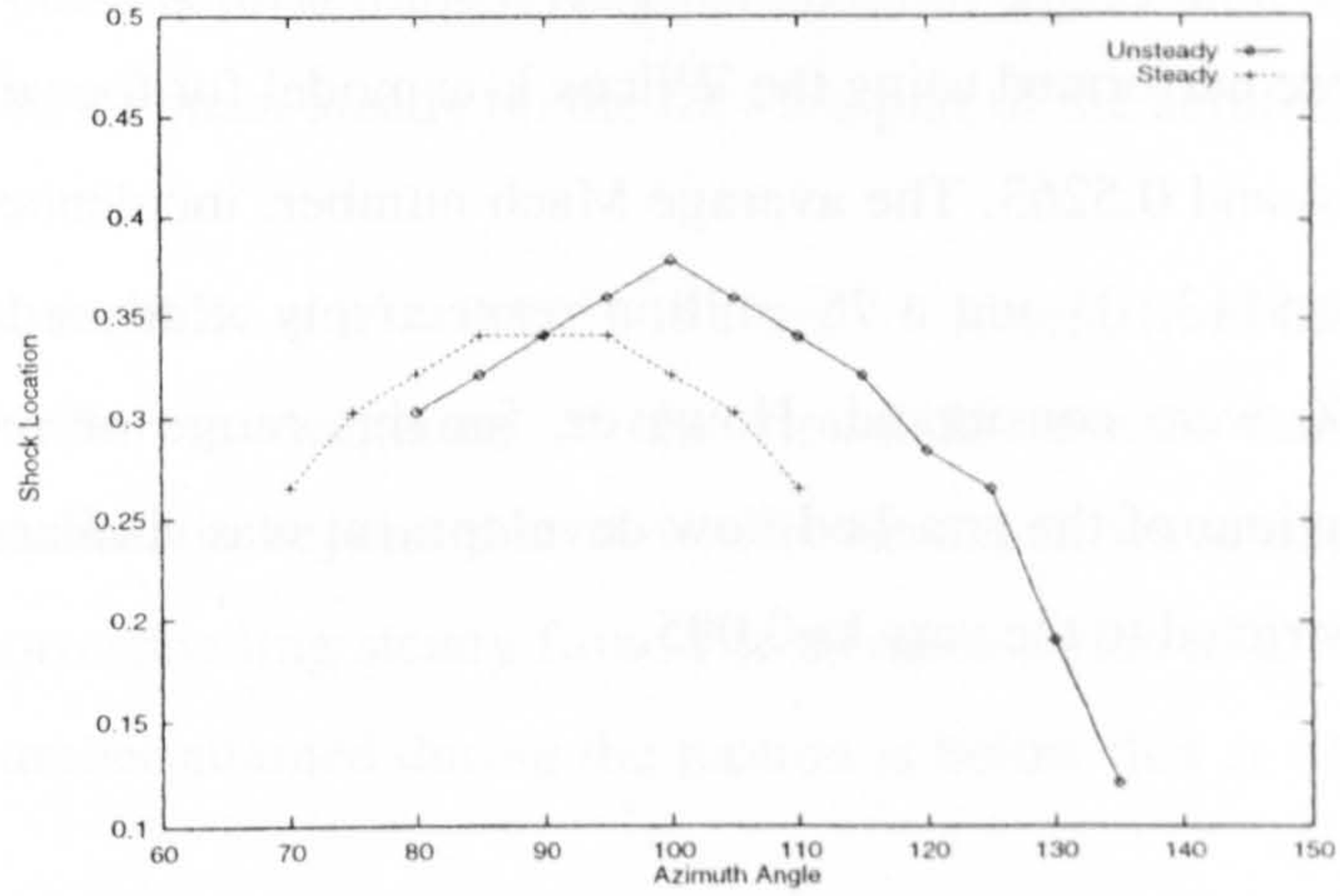

Figure (9.15) Shock location (Case 1)

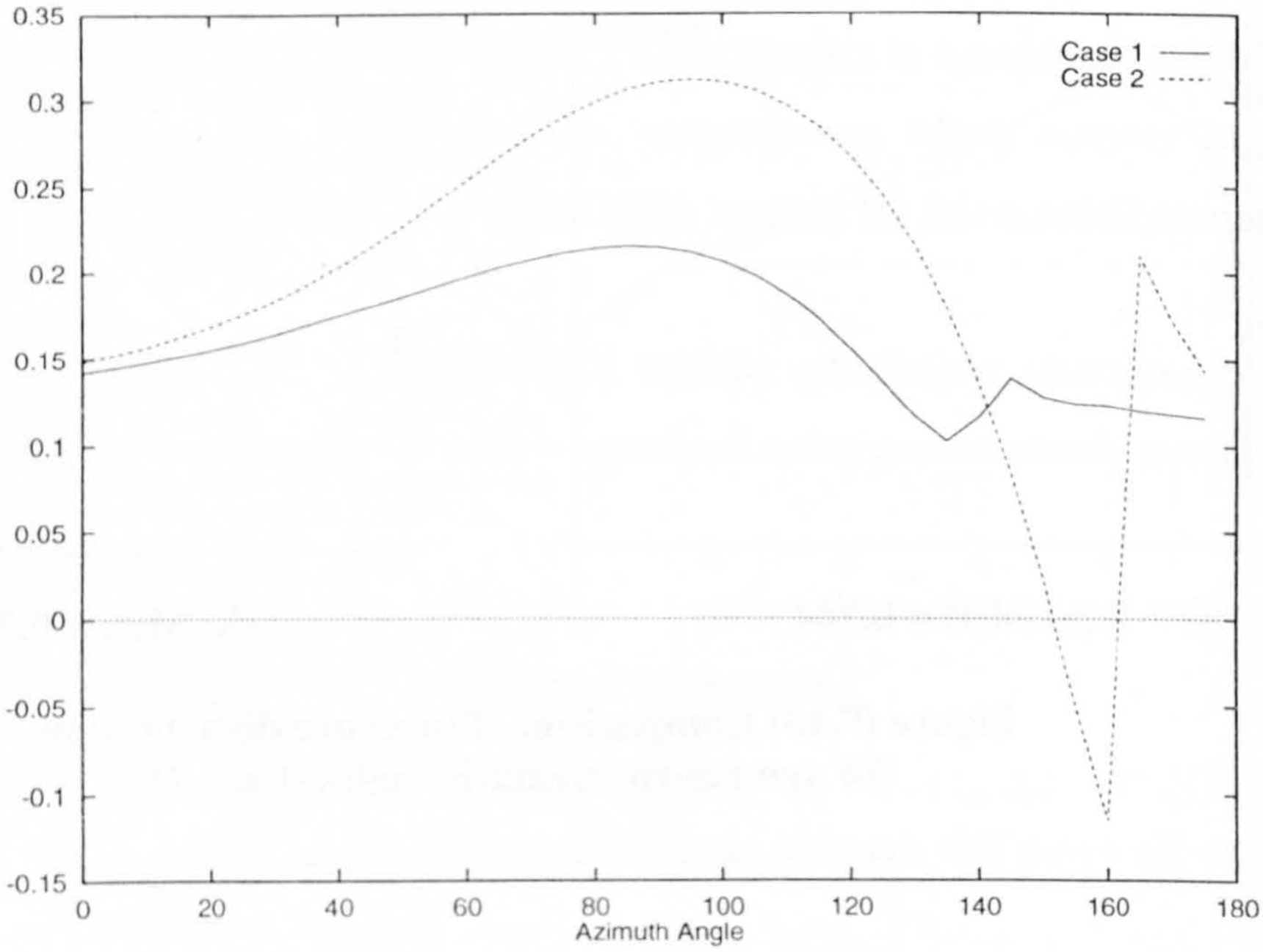

Figure (9.16) Unsteady pressure coefficient, x/c = -0.25

The unsteady aerodynamics of the aerofoil are determined from three main parameters, the reduced frequency (k′), the mean Mach number (M_o) and the amplitude of the variation (μ′). Typically the rotational speed of the rotor, and hence M_o, is fixed and therefore only k′ and μ′ are investigated.

(a) <u>Advance Ratio</u>

The influence of the advance ratio upon the computed flowfield was investigated. Calculations were performed using the Wilcox k-ω model for four different advance ratios, μ′ = 0.2, 0.3, 0.4 and 0.5263. The average Mach number, incidence and Reynolds number were fixed at 0.5113, 0° and 1.75 million respectively. Reduced frequencies of 0.050, 0.095 and 0.150 were considered. However, for this range of reduced frequencies the qualitative behaviour of the attached flow development was similar and for this reason the discussion is restricted to the case k=0.095.

In Figure (9.17) the development of the unsteady flow is revealed through contours of instantaneous local upper surface pressure. The results obtained for $\mu' = 0.2$, Figure (9.17a), are typical of those obtained for shock free flow. For this case the effects of flow unsteadiness are not appreciable and are confined mainly to the region between the quarter chord and mid-chord. Forward and aft of this region the pressure coefficient is undisturbed by the motion indicating that in these regions the flow behaves in a quasi-steady manner. Figure (9.17b) shows similar behaviour for an advance ratio of $\mu' = 0.3$. The region of disturbed flow now extends over a much larger region of the aerofoil chord. However, the pressure contours forward of the quarter-chord point remain parallel to the leading edge indicating that the flow in this region is essentially quasi-steady. For $\mu' = 0.4$ the maximum Mach number experienced during the aerofoil motion exceeds the critical Mach number of the aerofoil and weak shock waves are observed over a narrow azimuth range. The region of the aerofoil over which unsteady effects are significant has again grown in extent, although once more the flow ahead of the quarter-chord point remains essentially steady. When the advance ratio is increased further to 0.5236 strong shock waves appear in the flow and unsteady effects become appreciable, as can be seen from Figure (9.17d). Unsteady effects extend aft almost to the trailing edge. The flow forward of the quarter-chord point remains quasi-steady for much of the azimuth range. However, as the shock front moves forward of the mid-chord the flow ahead of the quarter-chord point is disturbed, this can be clearly seen around $\psi = 125°$ in Figure (9.17d). The unsteady flow ahead of this point persists for a limited range of azimuth angles until by $\psi = 150°$ the flow is once again essentially quasi-steady on the forward part of the aerofoil.

The behaviour of the flow at $\mu' = 0.5236$ is clearly different from that observed at lower advance ratios. Further investigation of the flowfield reveals that for this case the maximum Mach number is beyond that at which the shock wave causes boundary layer separation in the corresponding steady flow. For advance ratios of $\mu' = 0.4$ and below the maximum Mach number attained during the motion is below that at which incipient shock

induced separation is observed in the steady flow, consequently the boundary layer remains attached over the full azimuth range.

The pressure data presented in Figure (9.17) suggest that for attached flow the unsteady effects of changing Mach number can be described by a simple phase lag. This is demonstrated more clearly by Figure (9.18) in which the unsteady behaviour of the peak suction pressure coefficient is plotted against azimuth angle for each of the advance ratios considered. The behaviour of peak suction pressure coefficient with azimuth is regular and for the lower advance ratios the phase lag can be easily obtained. Surprisingly the measured phase lag is, within the uncertainty of the measurement process, constant. For the present data the phase lag is $\phi = 13°$. The magnitude of the peak suction pressure is plotted against advance ratio in Figure (9.19). In order to demonstrate that the unsteady surface pressure coefficients can be described in this way we consider two azimuth angles which are symmetric about $90° + \phi$, $\psi = 80°$ and $\psi = 126°$. Surface pressure distributions are compared in Figure (9.20) for the lower advance ratios. Excellent agreement is observed for $\mu' = 0.2$ and 0.3 while at $\mu' = 0.4$ the correlation is less good.

(b) **Reduced Frequency**

The influence of reduced frequency upon the unsteady flow development was investigated. Calculations were performed for a NACA 0012 aerofoil using the k-ω turbulence model. The calculations employed an average Mach number of 0.5113, an incidence of $\alpha = 0°$ and a Reynolds number of 1.75 million. A range of advance ratios was considered.

The flow development with increasing reduced frequency at $\mu' = 0.5236$ is highlighted in Figure (9.21) which shows contours of surface pressure coefficient plotted against azimuth angle. For the range of reduced frequencies that were considered the flow is super-critical for part of the cycle. As before the flow in the region of the leading and trailing edges is relatively unaffected by the unsteady forcing, while unsteady effects are confined

to the mid-chord region. The most obvious effect of flow unsteadiness here is that the azimuth angle at which the shock first appears increases with increasing reduced frequency. Indeed for k = 0.15 the shock wave develops very late in the acceleration phase, see Figure (9.22b), and at the maximum Mach number, Figure (9.22c), the shock is still very weak. Corresponding behaviour is observed at later azimuth angles, as reduced frequency is increased the shock wave persists until later times in the flow development. At the lower reduced frequency (k=0.05) the shock wave is no longer present for azimuth angles beyond $\psi = 125°$. In contrast at the largest reduced frequency considered the shock wave is present for azimuth angles up to $\psi = 150°$, by which time the instantaneous Mach number has fallen to 0.646, well below the critical Mach number for this aerofoil section.

Calculations were also performed for lower advance ratios. For these cases no shock waves were observed and the unsteadiness of the surface pressure coefficients could be described by a simple phase lag, as described above. It was found that for a given reduced frequency the phase lag remained almost constant over the range of advance ratios considered, however, the phase lag was found to vary with reduced frequency. The behaviour of the phase lag with increasing reduced frequency is plotted in Figure (9.23), note that in this figure it has been assumed that the phase lag for a reduced frequency of k=0 (steady flow) will be 0°. For small reduced frequencies the phase lag is close to zero and increases as the frequency of the forcing motion is increased. It was not possible to correlate the phase lag with reduced frequency.

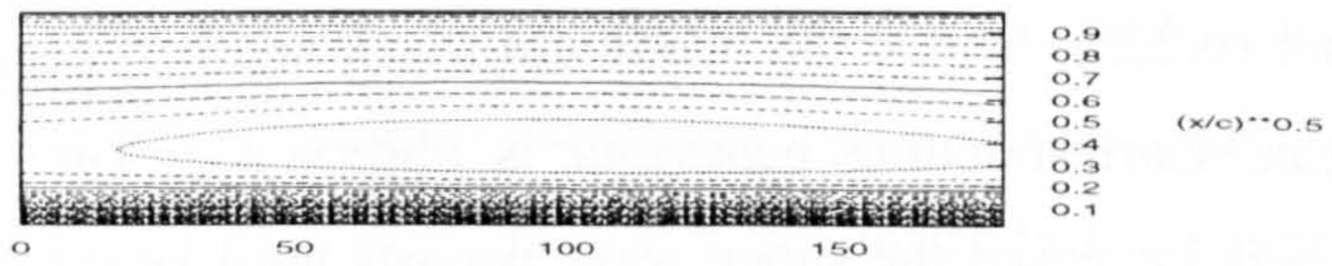

(a) $\mu' = 0.2000$

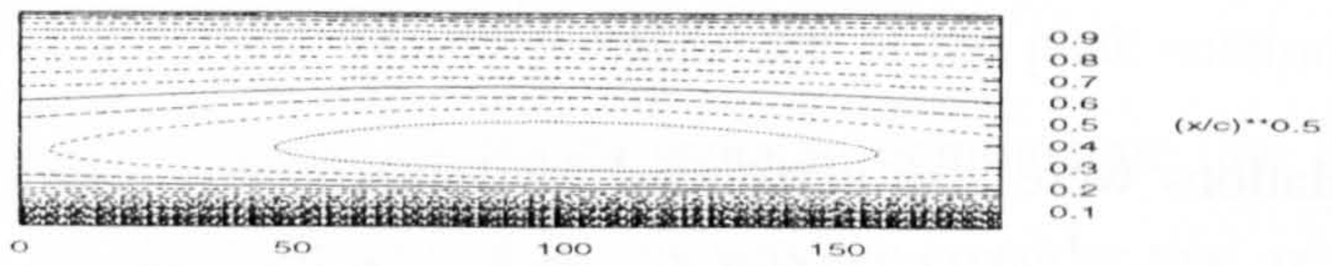

(b) $\mu' = 0.3000$

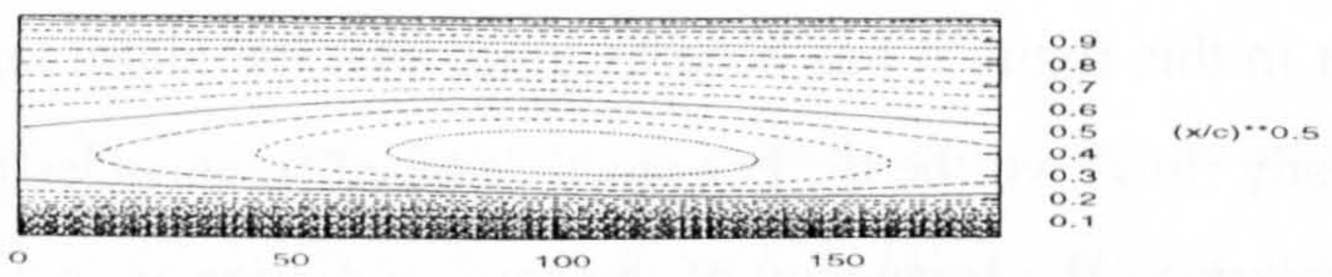

(c) $\mu' = 0.4000$

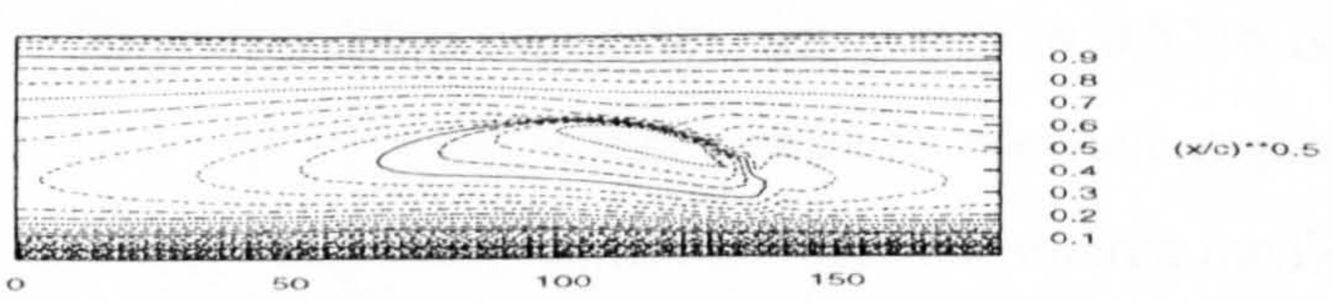

(d) $\mu' = 0.5236$

Figure (9.17) Development of surface pressure contours with advance ratio

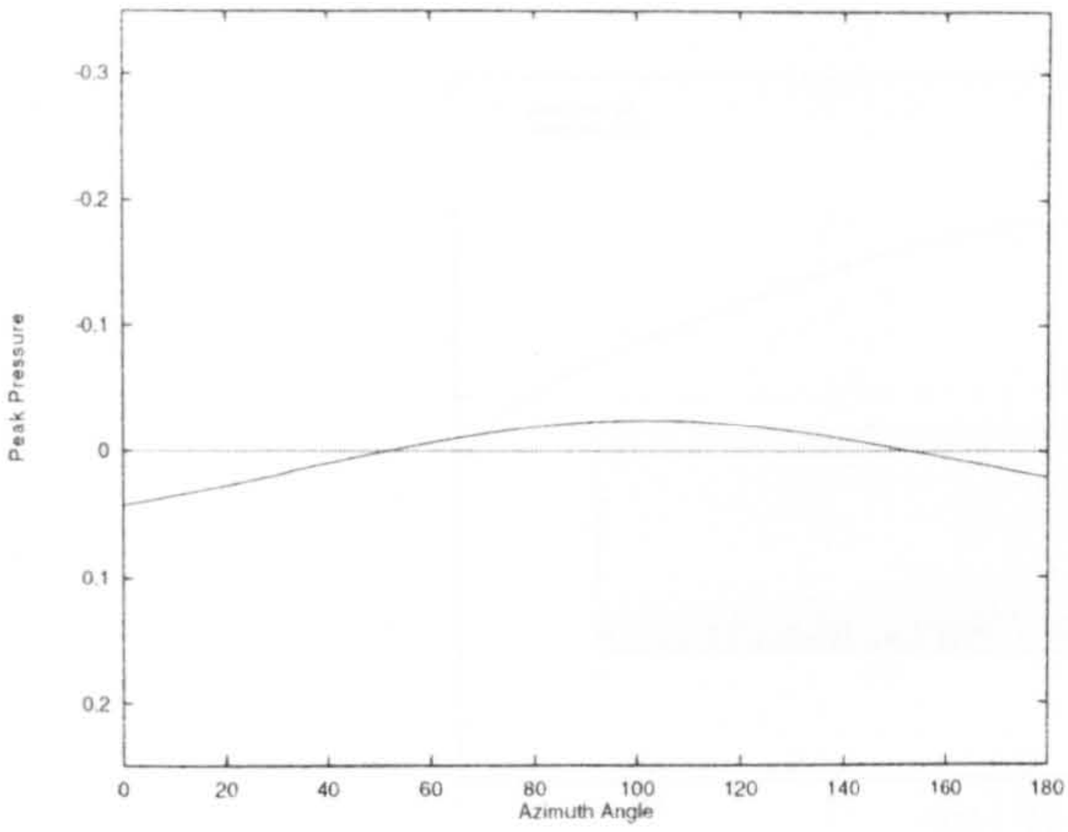

(a) $\mu' = 0.2000$

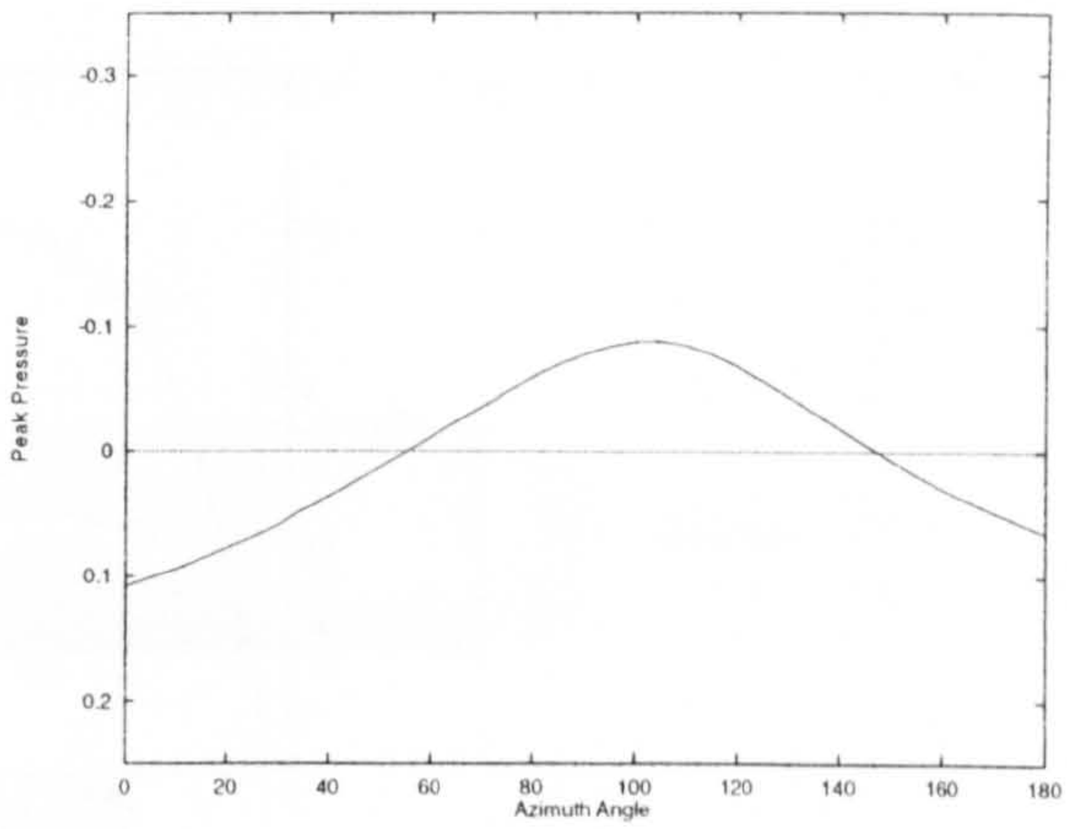

(c) $\mu' = 0.4000$

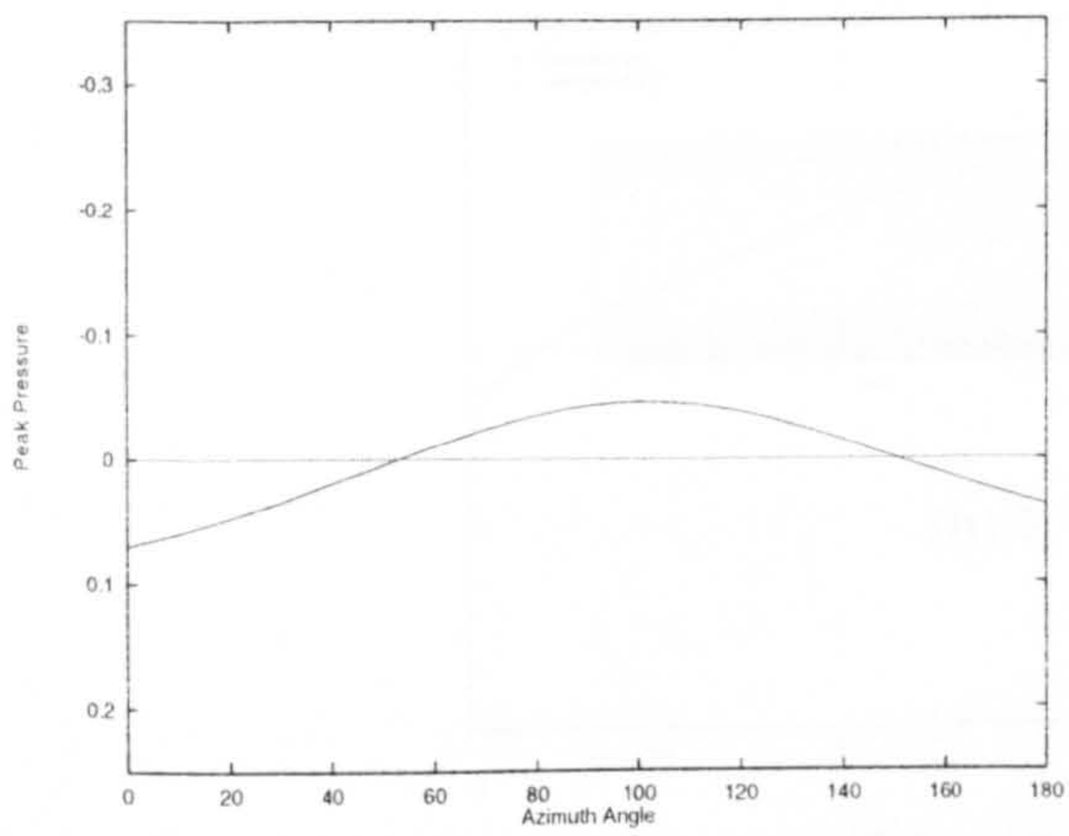

(b) $\mu' = 0.3000$

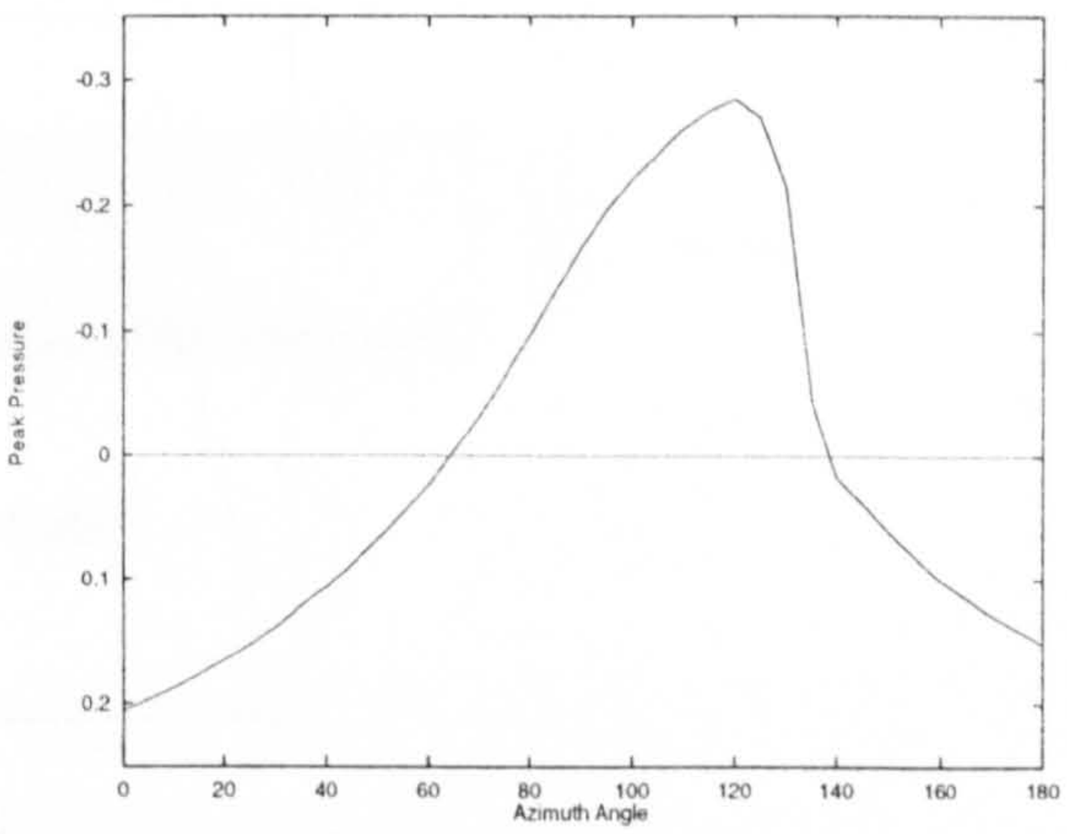

(d) $\mu' = 0.5236$

Figure (9.18) Unsteady development of peak pressure coefficient (k = 0.095)

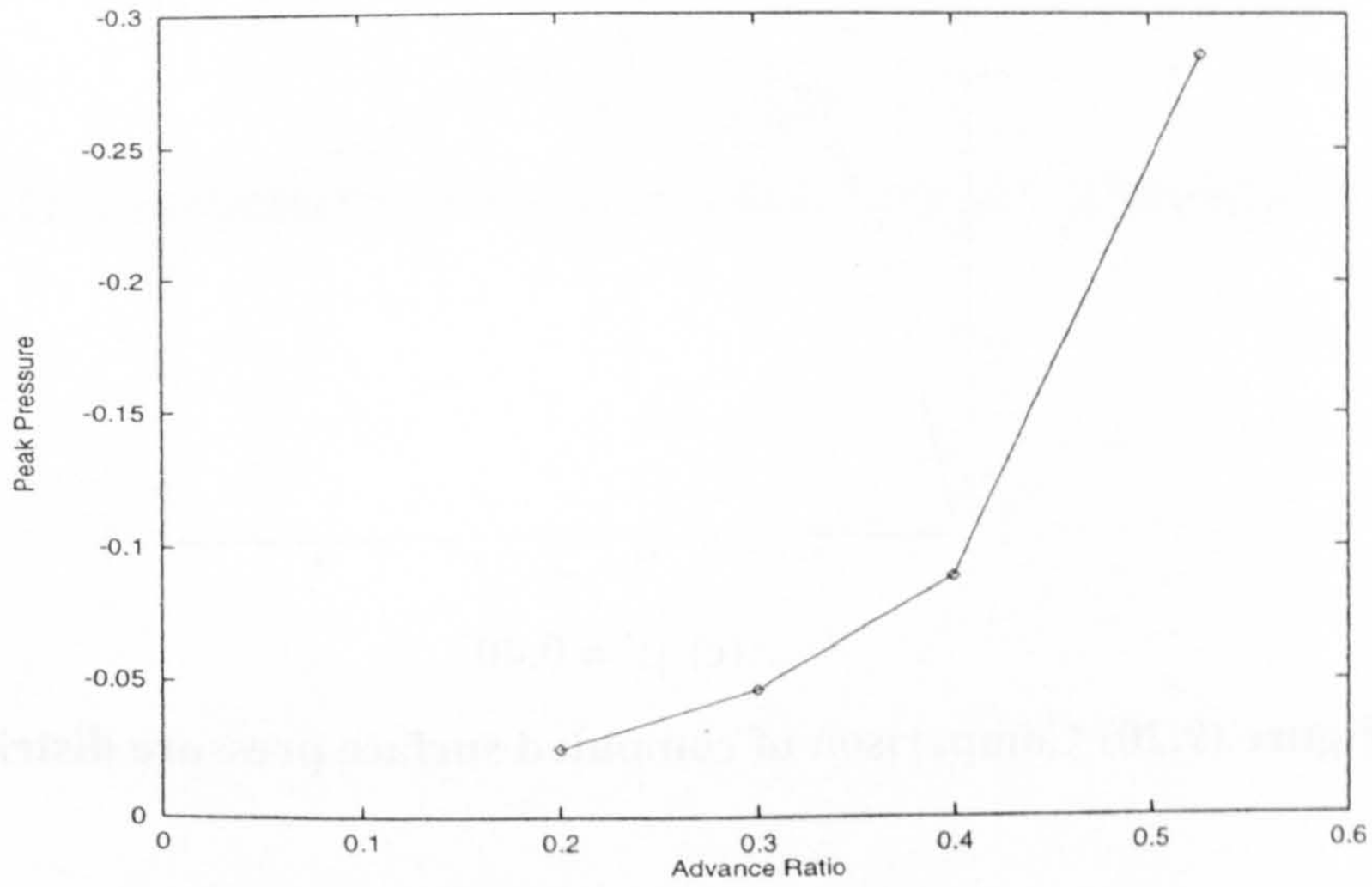

Figure (9.19) Behaviour of maximum peak pressure with advance ratio

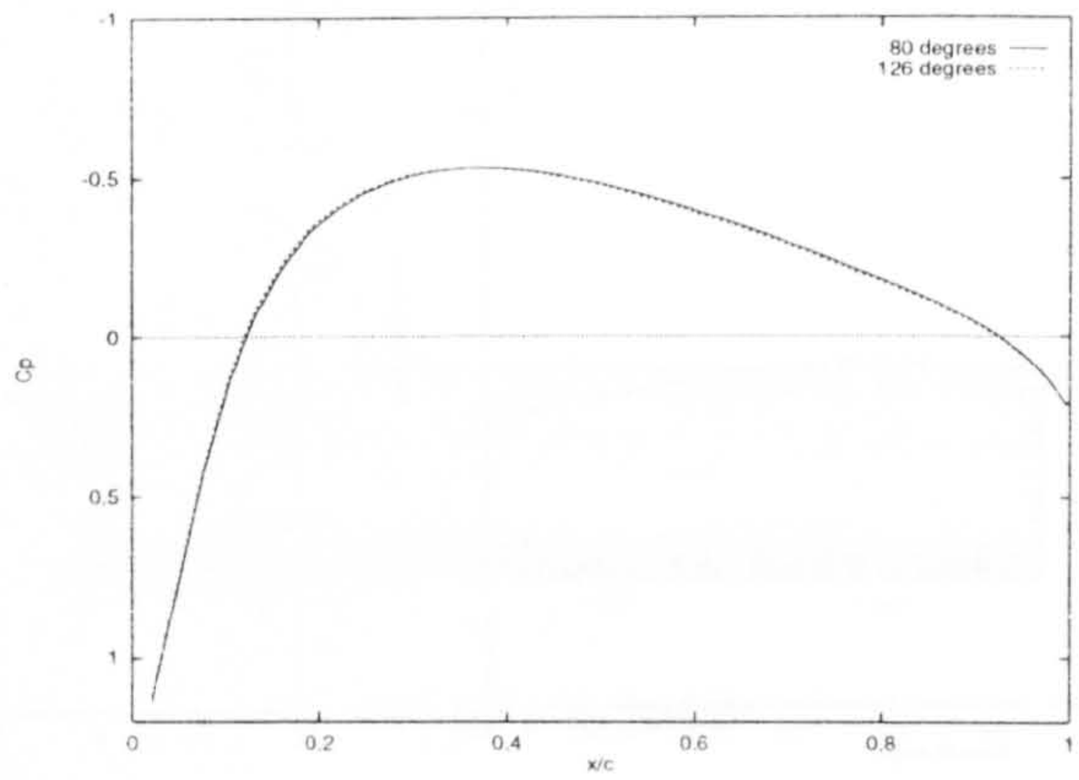

(a) $\mu' = 0.20$

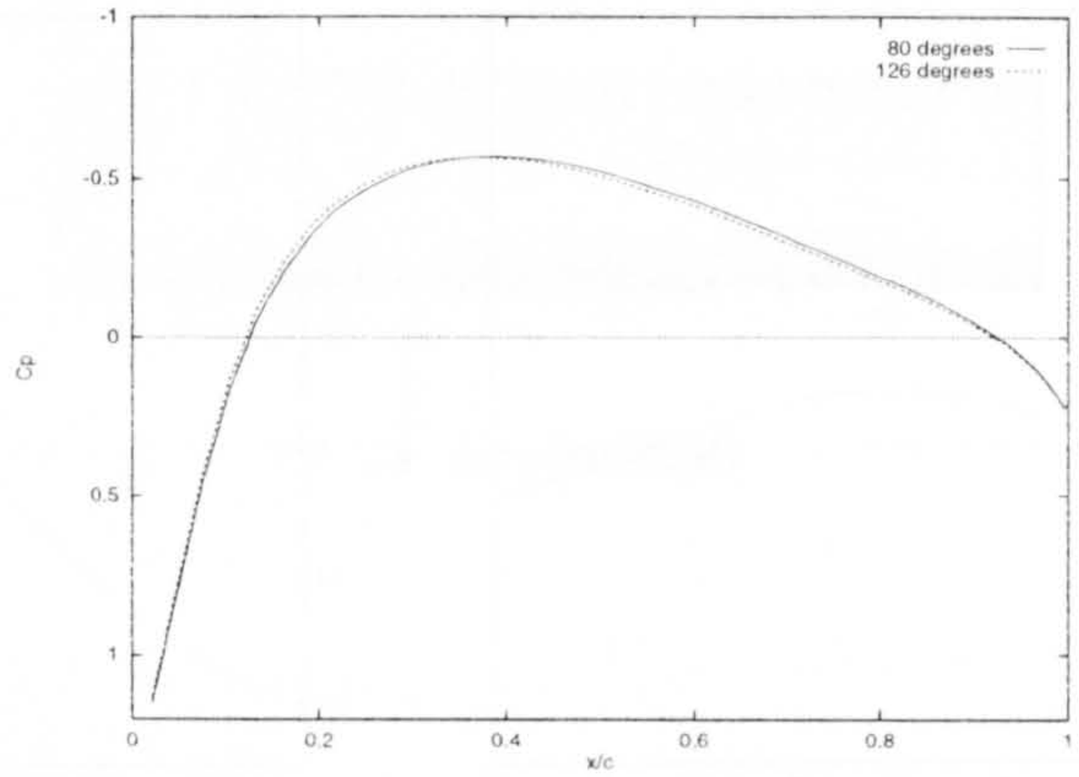

(b) $\mu' = 0.30$

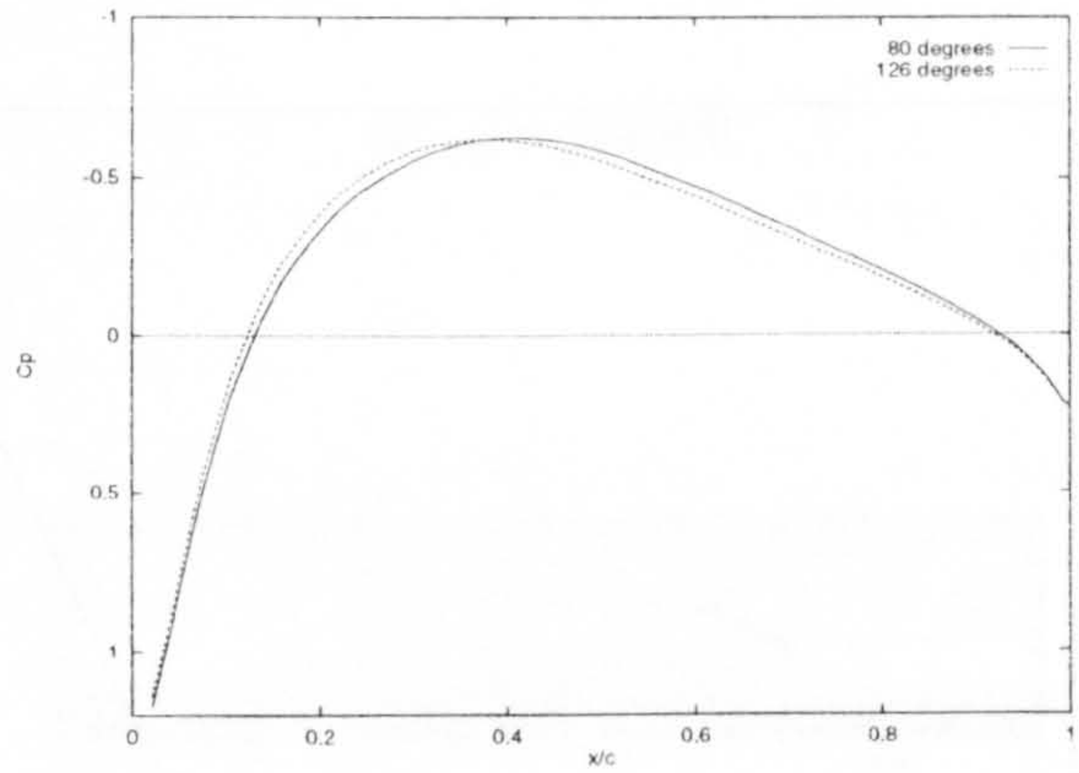

(c) $\mu' = 0.40$

Figure (9.20) Comparison of computed surface pressure distributions

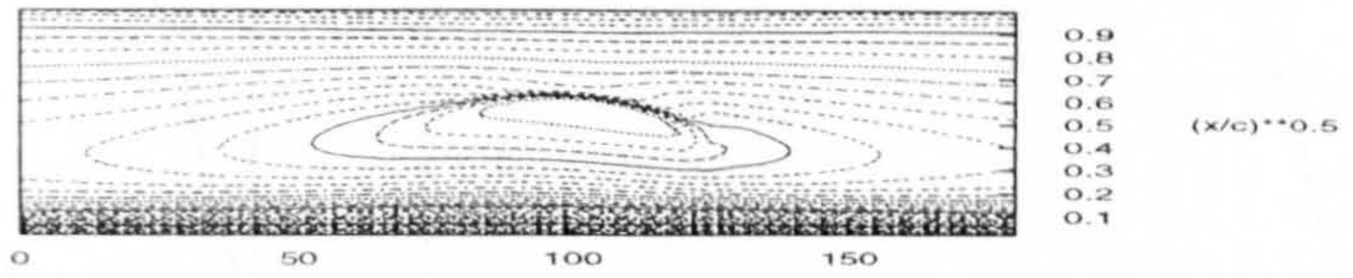

(a) k =0.050

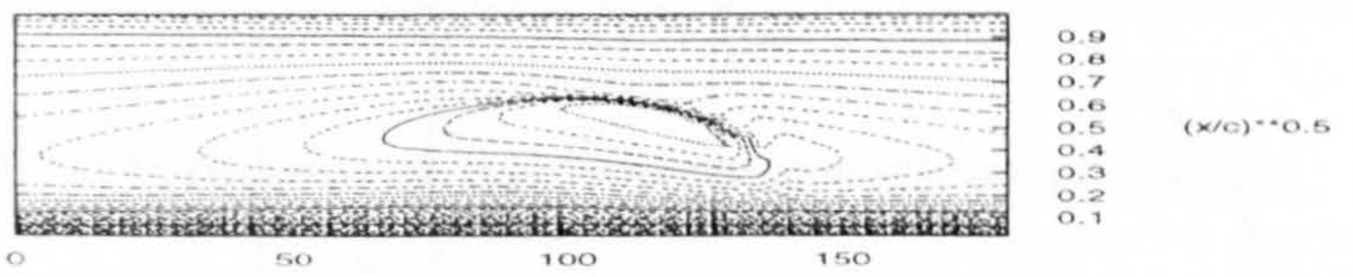

(b) k = 0.095

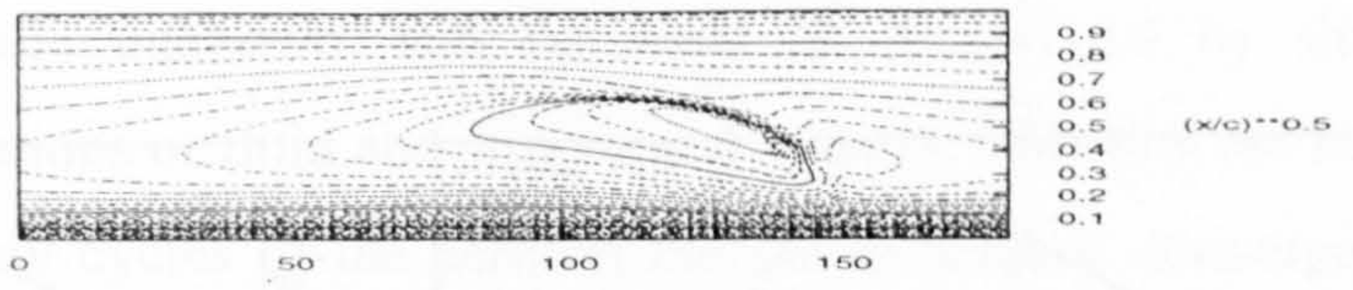

(c) k = 0.150

Figure (9.21) Development of surface pressure contours with reduced frequency

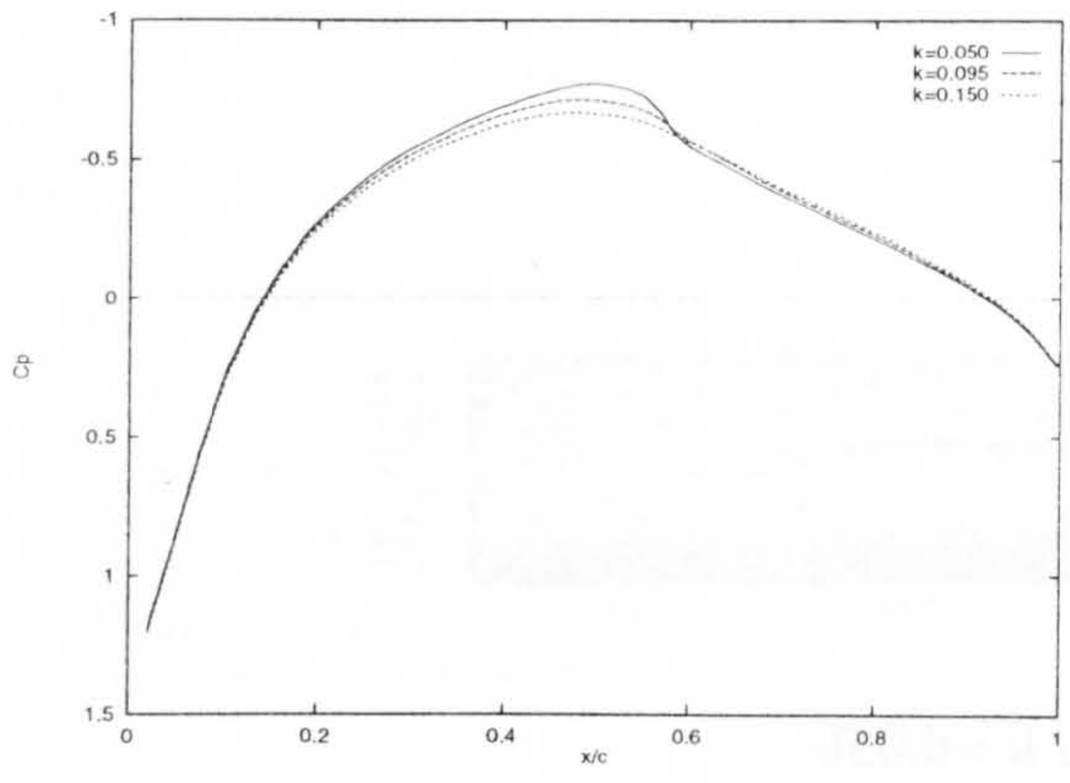

(a) ψ = 75°

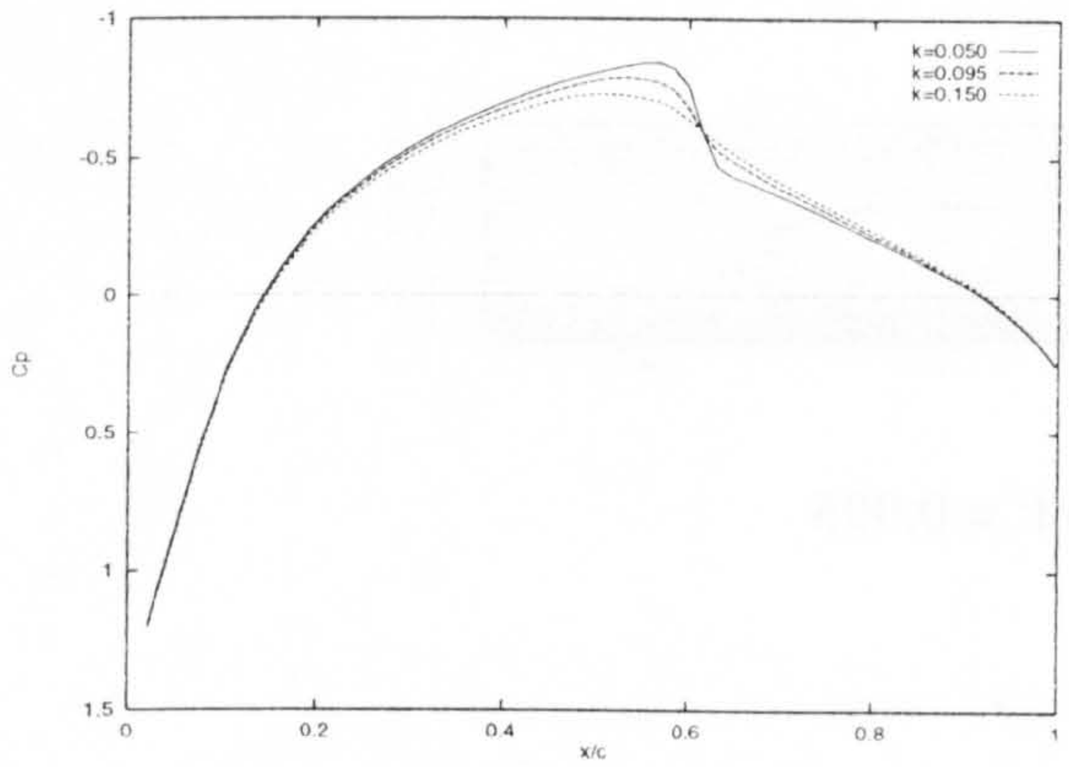

(b) ψ = 85°

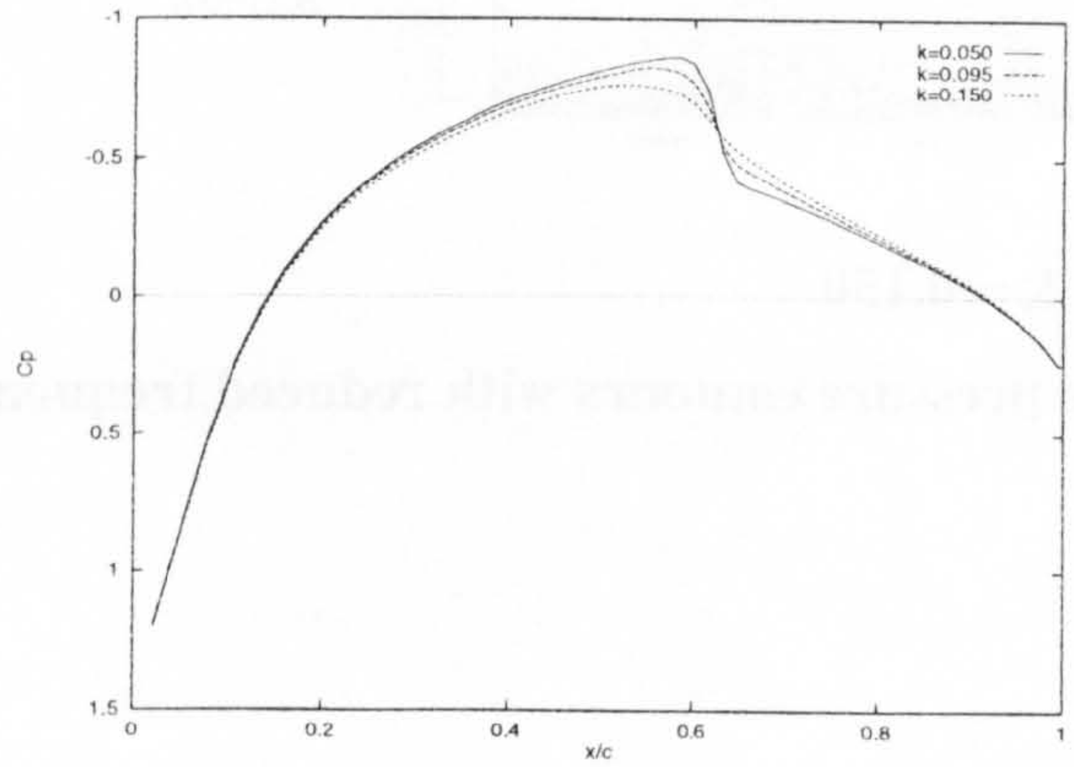

(c) ψ = 90°

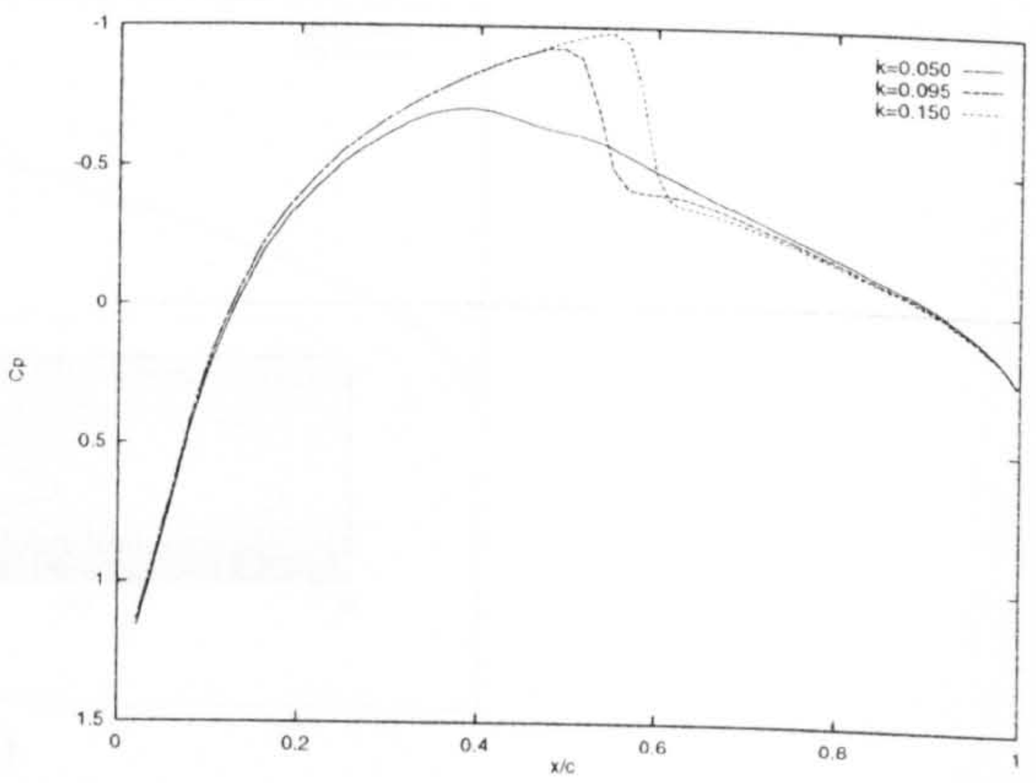

(d) ψ = 125°

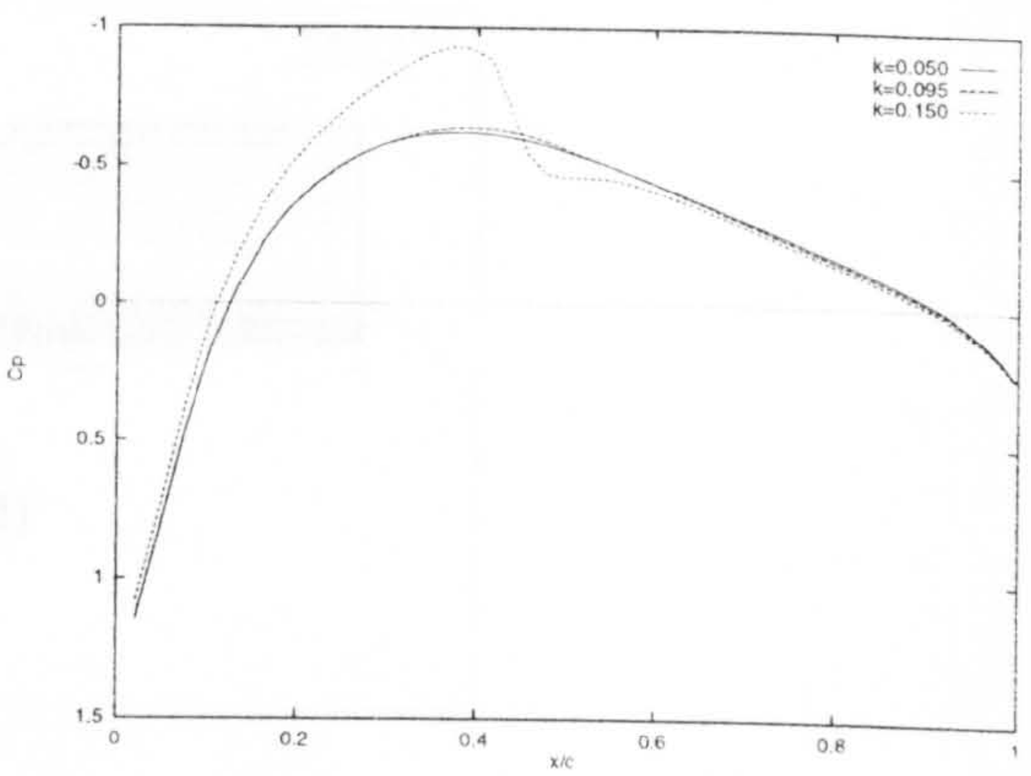

(e) ψ = 140°

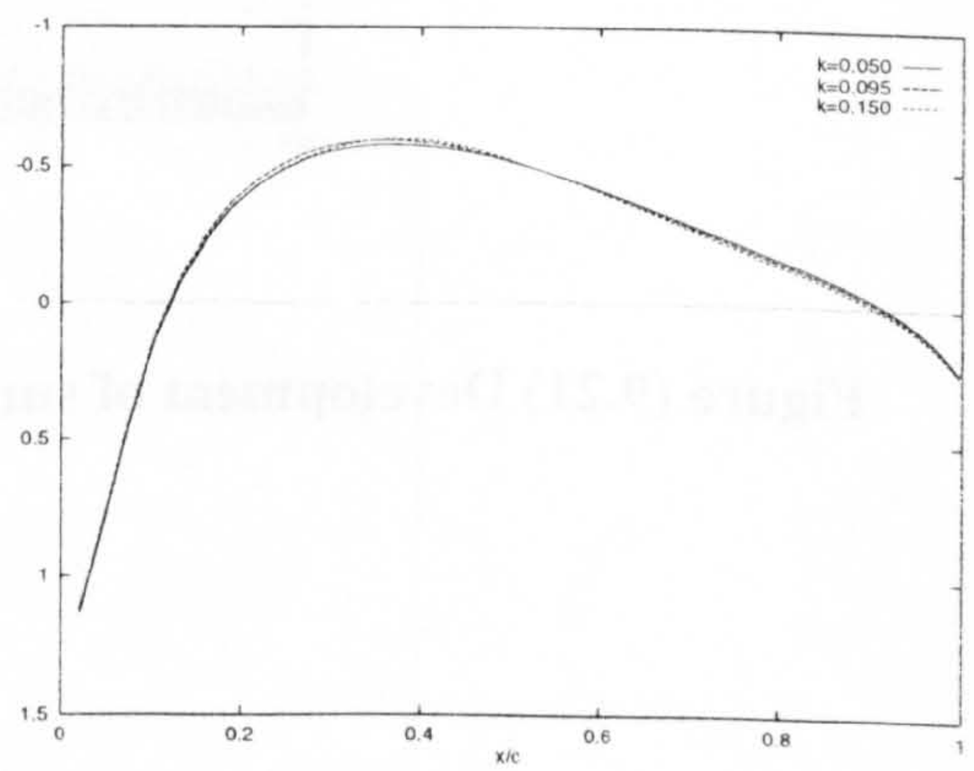

(f) ψ = 150°

Figure (9.22) Comparison of computed instantaneous pressure distributions for increased reduced frequency

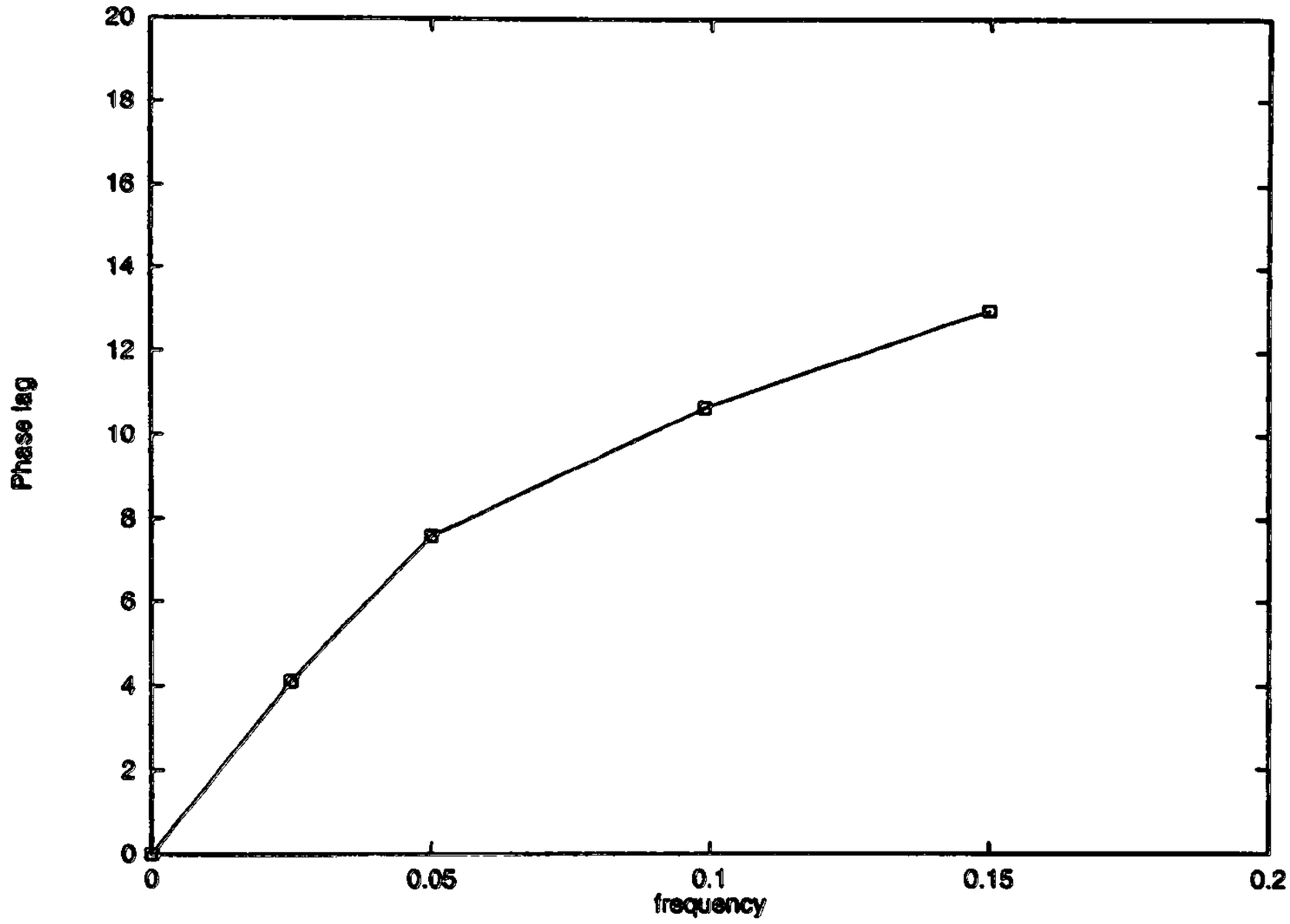

Figure (9.23) Influence of reduced frequency on phase lag

9.4 Aerodynamic Response to Step Increases in Mach Number

The time required for the direct calculation of the unsteady flowfield due to arbitrary motion using CFD techniques remains too long for routine use in the preliminary design process. The problem is further compounded by the fact that the motion of the rotor blade is generally unknown, and can only be determined by simultaneous integration of the equations of fluid and structural dynamics. This process may involve the calculation of many cycles of the aerofoil motion to achieve convergence to the final solution. As a consequence there has been considerable interest in the development of a more general unsteady aerodynamic theory that can be more readily applied to cases involving arbitrary motion of the body. In a series of papers[253-255] Beddoes has developed effective numerical techniques for the calculation of the unsteady aerodynamics of helicopter rotors based upon indicial response theory and careful correlations between theory and experiment. The methodology has been applied to a wide range of problems including dynamically stalling aerofoils[253], blade-vortex interaction[254] and the aero-acoustics of rotor blades[255]. The indicial response is a mathematical concept and represents the response of a system to a step change in one of the degrees of freedom. In the present work the system is the flowfield around the

aerofoil and the degrees of freedom are pitch and translation. Once the indicial response function to some motion, for example pitch, is known then, provided that the response is linear, the integrated forces and moments may be obtained for any schedule of motion with the aid of Duhamel's integral. The indicial response function therefore provides a powerful tool for the determination of unsteady airloads. In Figure (9.24) the normal force coefficient for an aerofoil in pitch, the AGARD CT1 test case discussed in Chapter (7), is compared with experimental measurement, the comparison may be considered excellent and is comparable with the CFD results presented earlier.

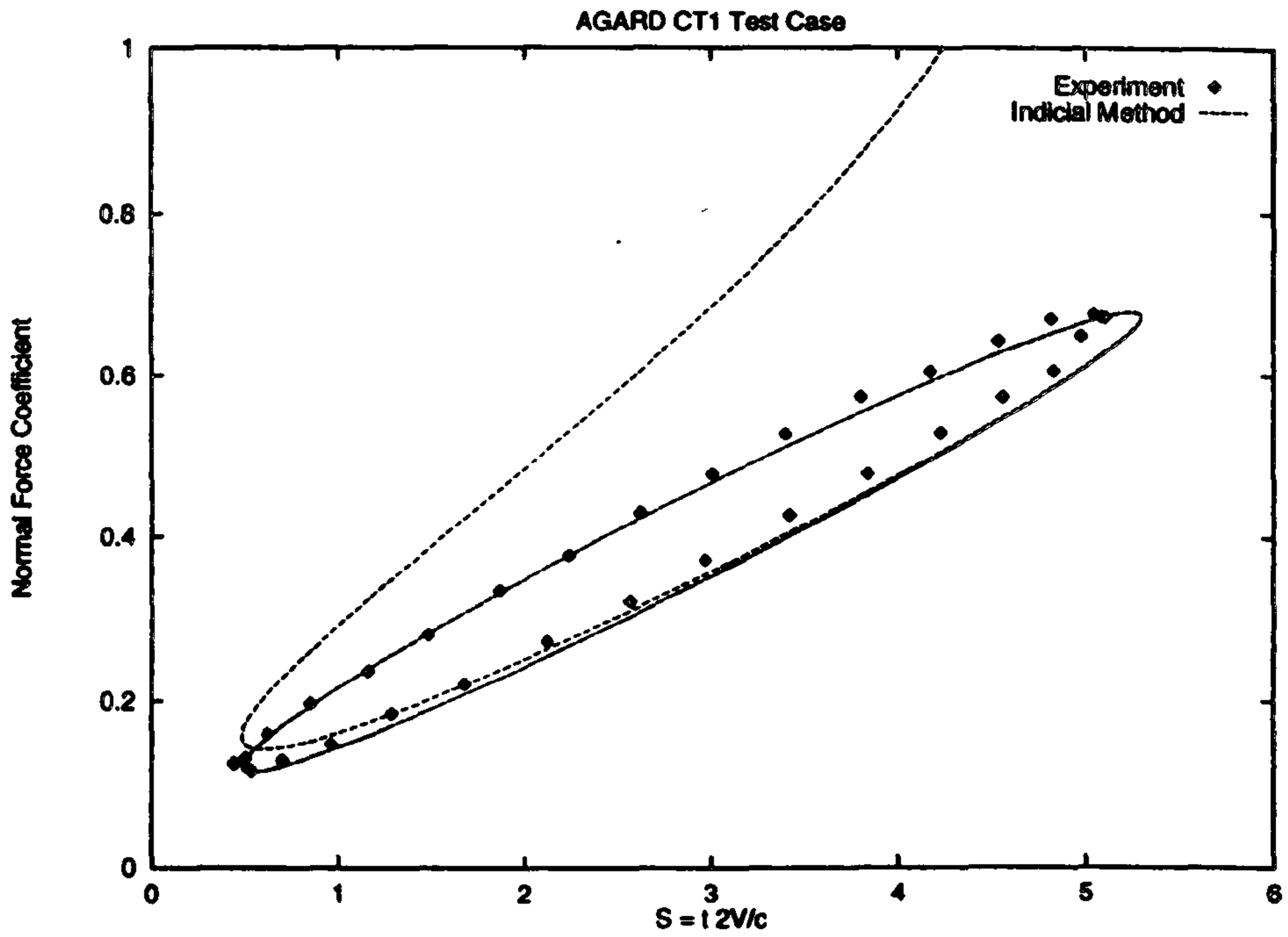

Figure (9.24) Calculation of AGARD CT1 using indicial theory

The determination of generalised indicial response for step changes in Mach number is beyond the scope of the present work, however the computation of response functions for a limited number of cases provides some insight into the physical process involved in more complex motions.

9.4.1 Modelling step changes in Mach number

Indicial response functions can be obtained from numerical solutions of the Euler and Navier-Stokes equations in a number of ways. In the present study the response is calculated directly, the step change in Mach number is incorporated by modifying the

grid velocity terms to reflect the additional velocity produced by the impulsive motion. Thus,

$$\frac{dx}{dt} = \begin{cases} 0 & t < 0 \\ \Delta u & t \geq 0 \end{cases} \tag{9.3}$$

In order to calculate the response function the steady flow at the initial Mach number is computed. In contrast to previous calculations for harmonic forcing it is necessary to obtain a converged steady solution. Once the steady solution is known an unsteady calculation is performed at the initial Mach number but with the grid velocity now given by Equation (9.3).

9.4.2 Calculated response functions

The unsteady response of the flowfield around a NACA 0012 aerofoil set at 2° incidence to the freestream was calculated for a step change in Mach number of $\Delta M = \pm 0.01$ at several Mach numbers. The Reynolds number based upon chord was kept constant with a value of 1 million. The results were obtained from solutions of the unsteady thin-layer Navier-Stokes equations and the Baldwin-Lomax turbulence model. Response functions for normal force and pitching moment coefficient are presented in Figure (9.25) below. Here the forces and moments are non-dimensionalised by their final values and S is a non-dimensional measure of time ($s = t\ U/c$) which can be interpreted as the number of chord lengths travelled.

For low freestream Mach numbers a large initial pulse dominates the aerodynamic loading. This pulse is associated with the system of disturbance waves generated by the instantaneous change in boundary condition. For a step increase in Mach number compression waves are generated at the aerofoil leading edge while at the trailing edge a system of expansion waves is established. The disturbance waves are propagated at the local wave speeds and consequently the initial impulsive loading decays rapidly. By convention this type of loading is termed the non-circulatory loading. From acoustical considerations (piston theory) the impulsive loading is expected to be proportional to the reciprocal of Mach number. Therefore as the freestream Mach number is increased

the magnitude of the initial loading should diminish; this behaviour is observed in the present results.

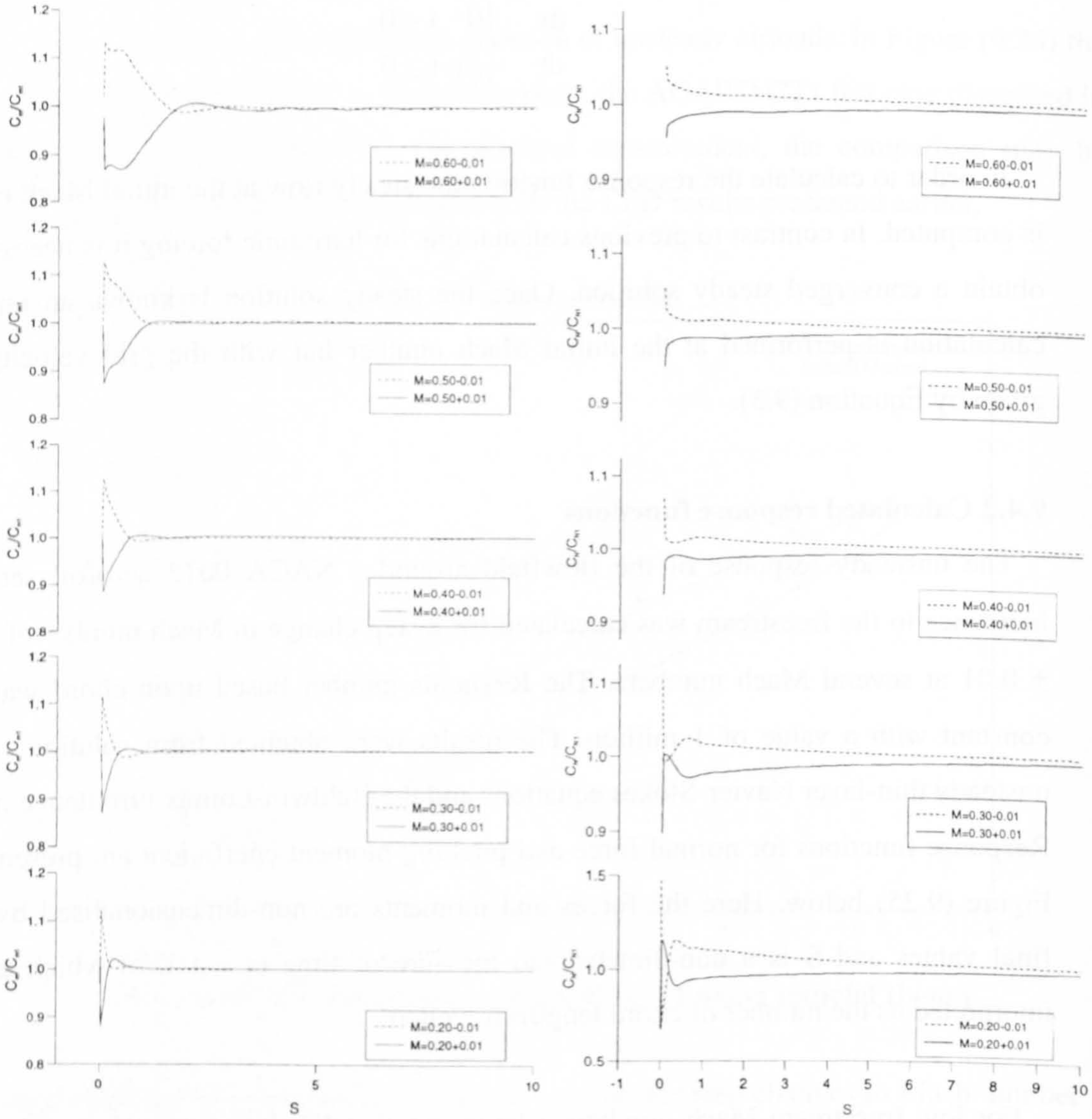

Figure (9.25) Calculated indicial response functions

A second component of the aerodynamic loading arises as a consequence of the creation or destruction of circulation around the aerofoil due to the change in freestream velocity. The change in force due to a small change in Mach number is relatively small when compared to the initial impulsive loading and occurs over a much longer time scale. The build-up of the circulatory loading is shown more clearly in Figure (9.26) in which the indicial responses of normal force coefficient at M = 0.50

are plotted. Finally the influence of Mach number size on the computed response functions is considered. Results are plotted in Figure (9.27) for step sizes of 0.005, 0.010 and 0.020. It is apparent from the initial behaviour that the response is linear with respect to the step size. For later times there is some disagreement between the computed data, however this is due to the different asymptotic states corresponding to the final value of Mach number in each case.

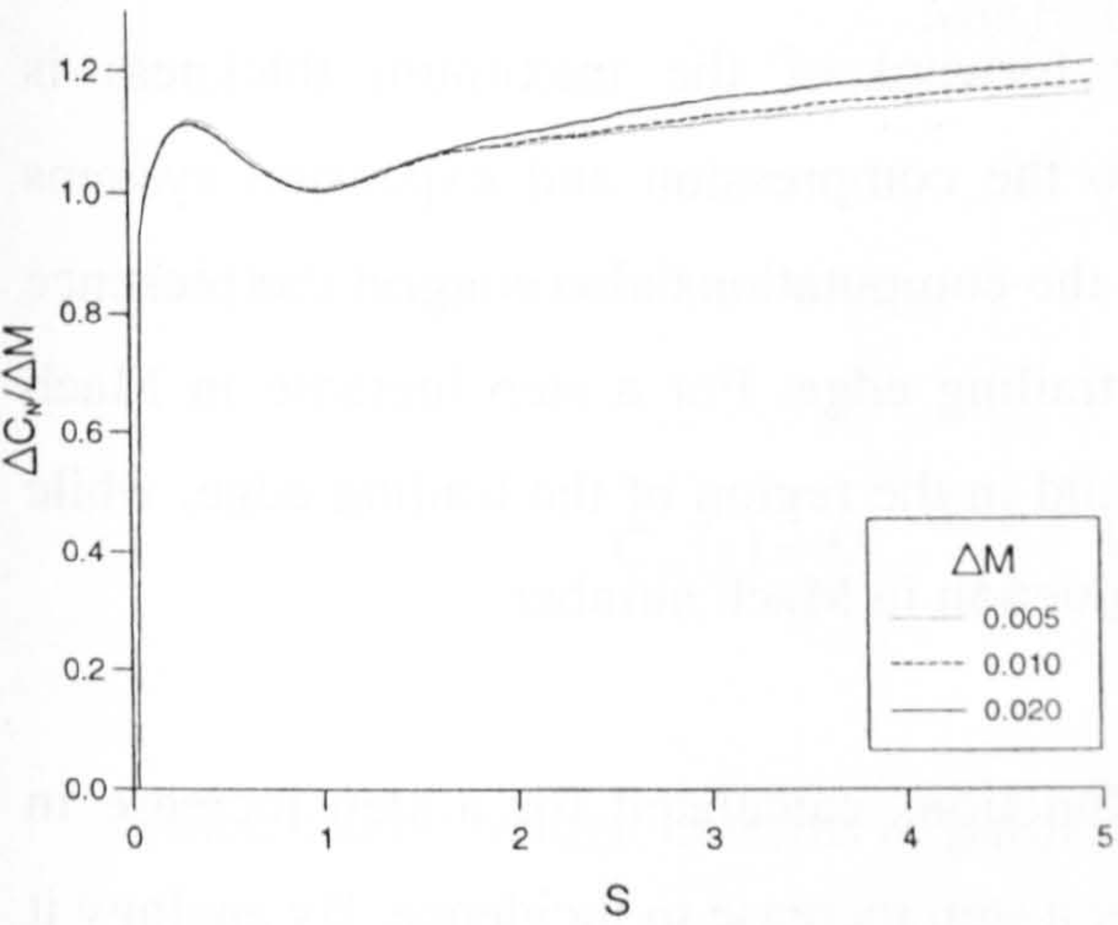

Figure (9.26) Computed normal force response functions at M =0.50

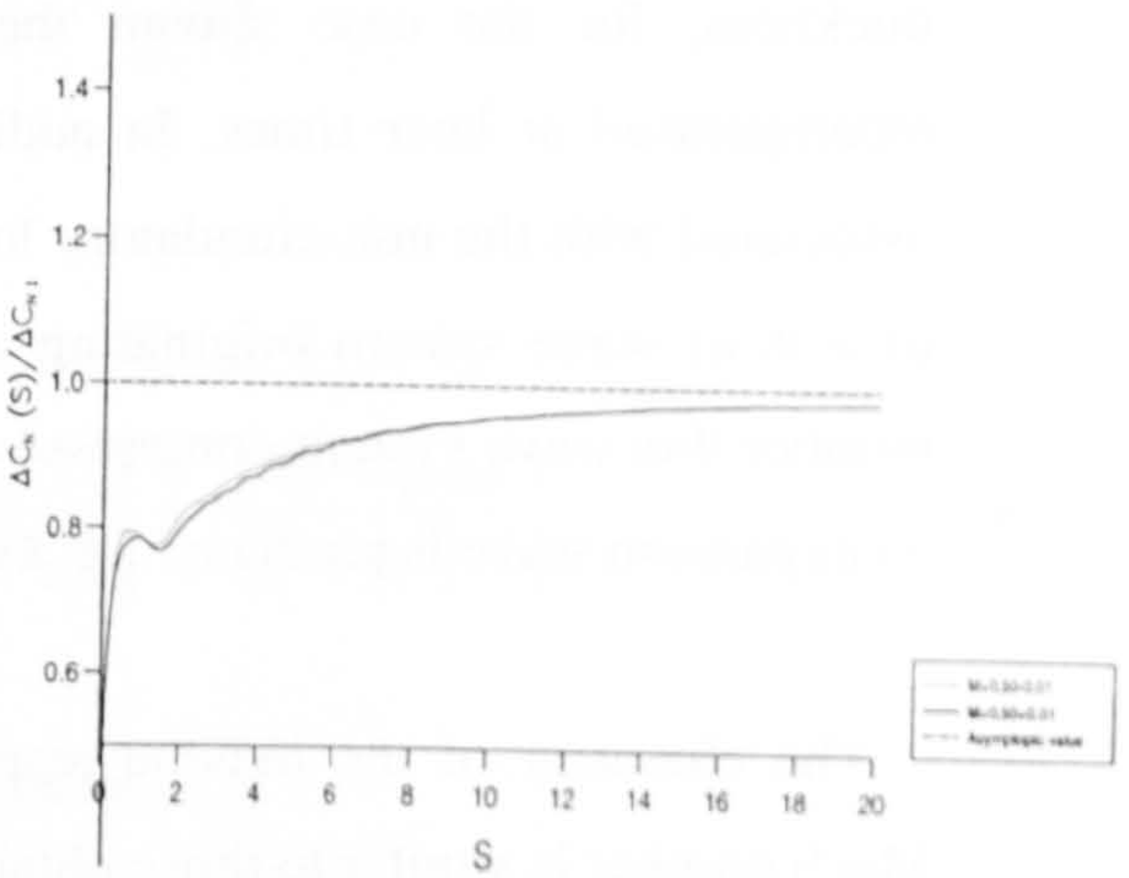

Figure (9.27) Sensitivty of response to step change in Mach number

Further calculations were performed for a NACA 0012 aerofoil set at 0°. The computations were performed at a Mach number of M = 0.51129 with a step change of 0.01. The Reynolds number based upon chord was 1.75 million. The unsteady flow development for this case is illustrated in Figures (9.28a) and (9.28b) which show contours of positive and negative local disturbance pressure coefficient at several instants in time respectively. For the purposes of Figure (9.28) disturbance pressure is defined as the difference between the current pressure and the corresponding pressure in the initial steady flowfield. The development and propagation of disturbance waves can be clearly seen when the data is presented in this manner. Three systems of waves can be inferred from the data. Expansion and compression waves are clearly evident in the early stages of the flow development. Ahead of the point of maximum thickness the

flow is compressed, see Figure (9.28b), while over the aft region of the aerofoil the flow is expanded, Figure (9.28a). The expansion and compression waves responsible for these processes originate at the aerofoil surface and propagate away from the aerofoil for later times. Corresponding calculations for an aerofoil subjected to a step reduction in Mach number show similar behaviour, although the flow is now expanded ahead of the aerofoil maximum thickness and compressed aft. The origin and behaviour of such disturbance waves suggests that they are associated with the discontinuous change in boundary condition at the aerofoil surface. The complex interaction of the wave fronts at later times is clearly visible in the proximity of the aerofoil maximum thickness, for the case shown the flow forward of the maximum thickness is recompressed at later times. In addition to the compression and expansion systems associated with the non-circulatory loading the computations also suggest the presence of a third wave system originating at the trailing edge. For a step increase in Mach number this wave system compresses the fluid in the region of the trailing edge, while an expansion wave is produced for a step reduction in Mach number.

The character of the indicial response functions calculated for a step increase in Mach number is similar to those obtained for a step increase in incidence. By analogy it should therefore be possible to represent the response in the functional form,

$$C_N = \frac{dC_N}{dM}\overline{M}\left(1-\sum_n A_n e^{-t/T_n}\right) \tag{9.4}$$

where $\overline{M}$ is the step change in Mach number and A_n and T_n are constants which must be determined. The constants A_n are subject to the constraint $\sum_n A_n = 1$. Using this assumed form the transfer function can be obtained by transformation to the Laplace domain thus,

$$\frac{C_N(s)}{M(s)} = \frac{dC_N}{dM}\left(1-\sum_n A_n + \sum_n \frac{A_n}{(1+sT_n)}\right) = \frac{dC_N}{dM}\left(\sum_n \frac{A_n}{(1+sT_n)}\right) \tag{9.5}$$

and the normal force for an arbitrary variation of Mach number can be found from,

$$C_N(s)=\frac{C_N(s)}{M(s)}M(s) \tag{9.6}$$

For a sinusoidal variation of Mach number about a mean value M_o the forcing function in the Laplace domain is,

$$M(s)=M_o\left(\frac{1}{s}+\frac{\mu\omega}{s^2+\omega^2}\right) \tag{9.7}$$

and the normal force is given by,

$$C_N(s)=M_o\frac{dC_N}{dM}\left(\sum_n\frac{A_n}{(1+sT_n)}\right)\left(\frac{s^2+\omega^2+\mu\omega s}{s(s^2+\omega^2)}\right) \tag{9.8}$$

which can be written in terms of partial fractions as,

$$C_N(s)=M_o\frac{dC_N}{dM}\left(\sum_n\frac{A_n}{s}+\frac{\pi_{1,n}}{s^2+\omega^2}+\frac{\pi_{2,n}s}{s^2+\omega^2}+\frac{\pi_{3,n}}{1+sT_n}\right) \tag{9.9}$$

Taking the inverse transform and $t\rightarrow\infty$ we obtain the following form for the unsteady normal force due to the prescribed motion,

$$C_N(t)=M_o\frac{dC_N}{dM}\left(1+\sum_n\frac{\pi_{1,n}}{\omega}\sin(\omega t)+\pi_{2,n}\cos(\omega t)\right) \tag{9.10}$$

with,

$$\pi_{1,n}=\frac{1}{T_n}\frac{\mu\omega A_n}{(T_n^2+\omega^2)}\quad\text{and}\quad\pi_{2,n}=-\frac{\mu\omega A_n}{(T_n^2+\omega^2)}$$

Equation (9.10) can be simplified to obtain the following expression for the unsteady normal force coefficient,

$$C_N(t) = M_o \frac{dC_N}{dM}\left(1 + \sum_n B_n \sin(\omega t + \phi_n)\right) \tag{9.11}$$

where the phase angle ϕ_n is obtained from the ratio of the constants $\pi_{1,n}$ $\pi_{2,n}$ using,

$$\tan(\phi_n) = \frac{\pi_{1,n}}{\omega \pi_{2,n}} = -\frac{1}{\omega T_n} \tag{9.12}$$

We observe that the phase angle is a function of only two parameters, the frequency of the prescribed motion and the time constant associated with the exponential representation. This result is in agreement with the behaviour observed in Figure (9.19) which showed that the phase lag between the maximum pressure and the forcing motion was constant for a fixed reduced frequency.

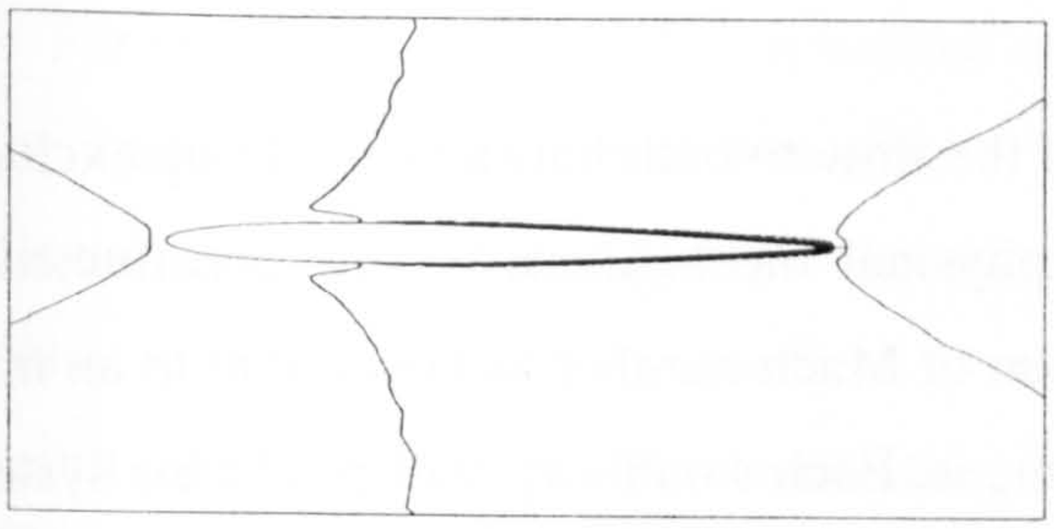

(i) t = 0.0003

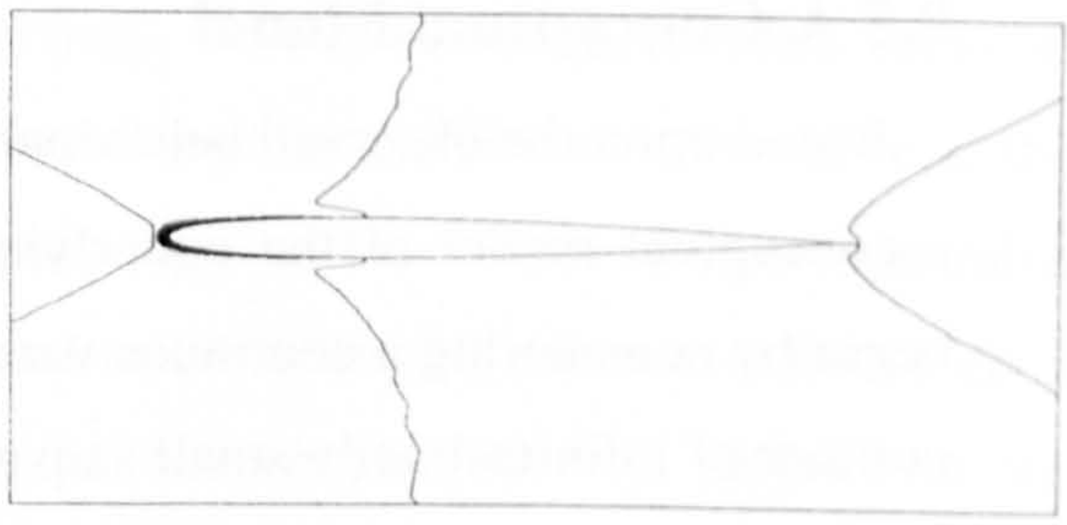

(i) t = 0.0003

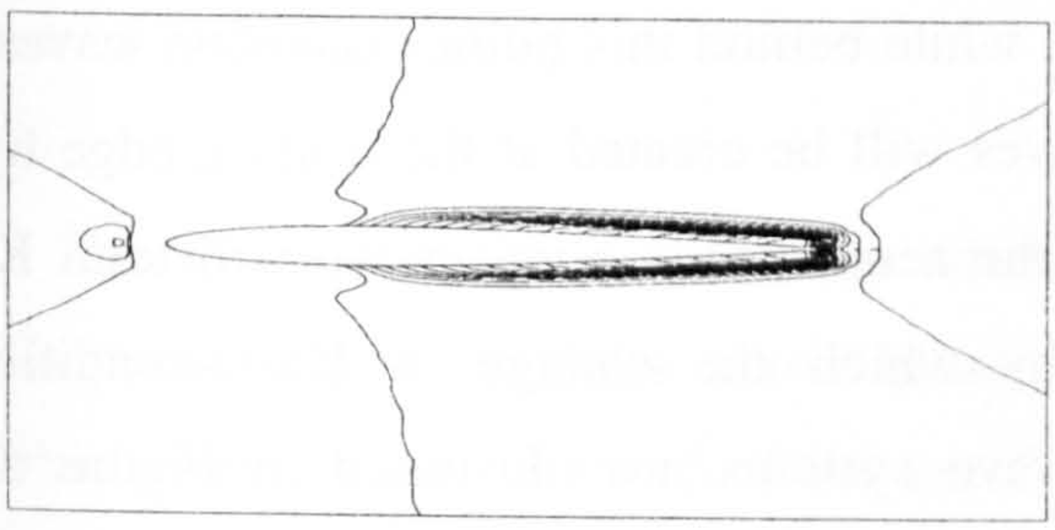

(ii) t = 0.0175

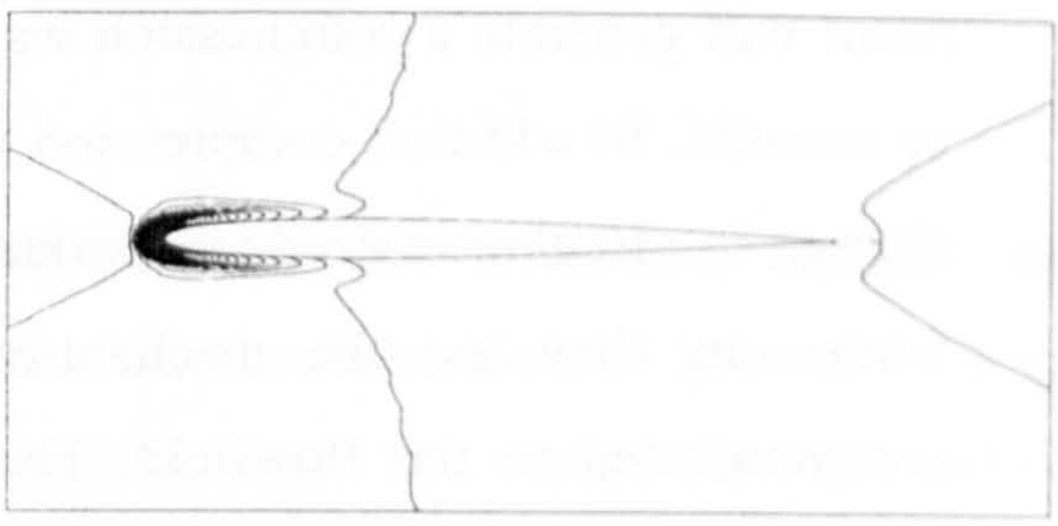

(ii) t = 0.0175

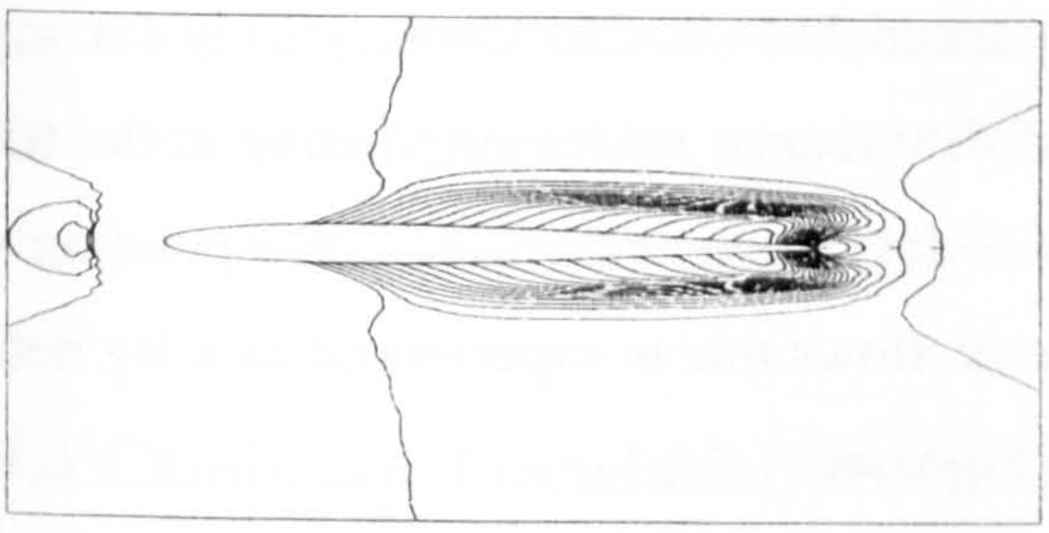

(iii) t = 0.0524

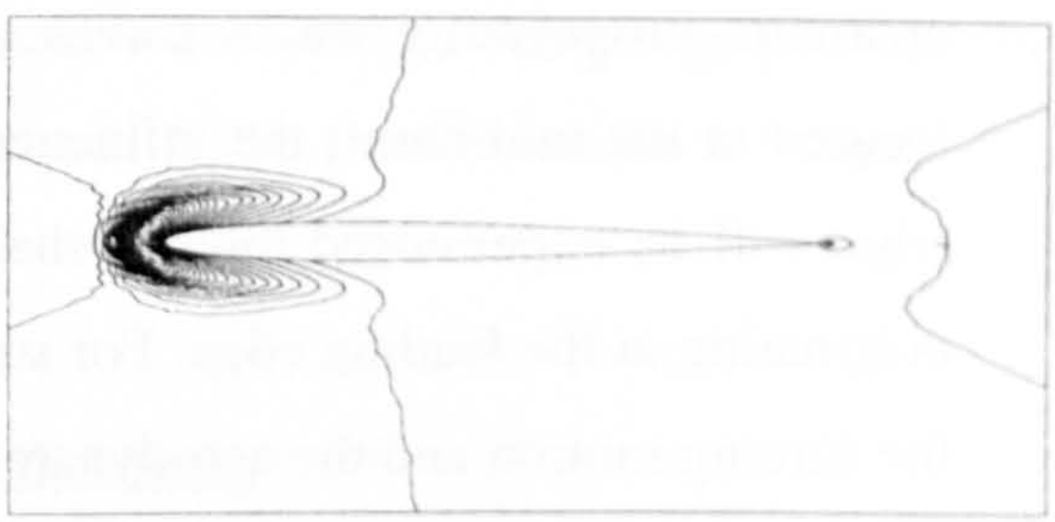

(iii) t = 0.0524

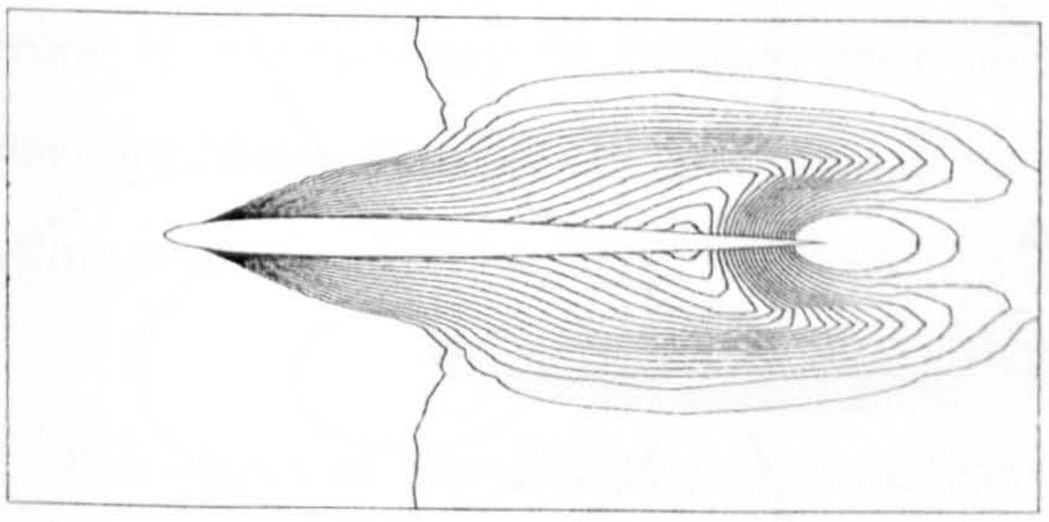

(iv) t = 0.1571

(a) Contours of $\Delta P < 0$

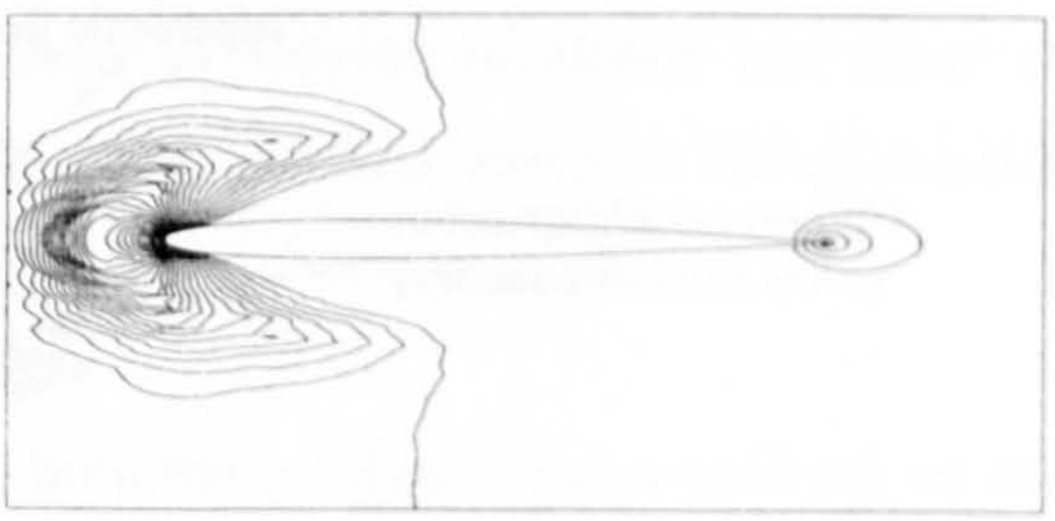

(iv) t = 0.1571

(b) Contours of $\Delta P > 0$

Figure (9.29) Flowfield response to a step increase in Mach number

9.5 A Conceptual Model

Based upon the observed behaviour of the flow to both harmonic and step excitations a conceptual model of the underlying physical mechanisms can be constructed. We begin by considering a continuos variation of Mach number as equivalent to an infinite number of infinitesimally small step changes. Each small step will produce a system of expansion and compression waves due to non-circulatory and circulatory effects. For accelerating flows each point on the aerofoil surface ahead of the maximum thickness point will generate a compression wave, while behind this point expansion waves will be created. In addition compression waves will be created at the trailing edge by the change in circulation produced around the aerofoil, these waves we will term Kutta-waves, as they are the mechanism by which the change in Kutta-condition is communicated to the flowfield. The wave systems are illustrated in Figure (9.30) below. These waves propagate through the fluid around the aerofoil at the local wave speeds. Disturbance waves travel downstream with a velocity U = a + u, while upstream propagating waves travel at a speed U = a – u. Consequently for a point located at the mid-chord the influence of disturbance waves originating at the trailing edge will be experienced later in the flow development than the corresponding wave originating at the leading edge. For subsonic flows this is experienced as a lag between the forcing motion and the aerodynamic response.

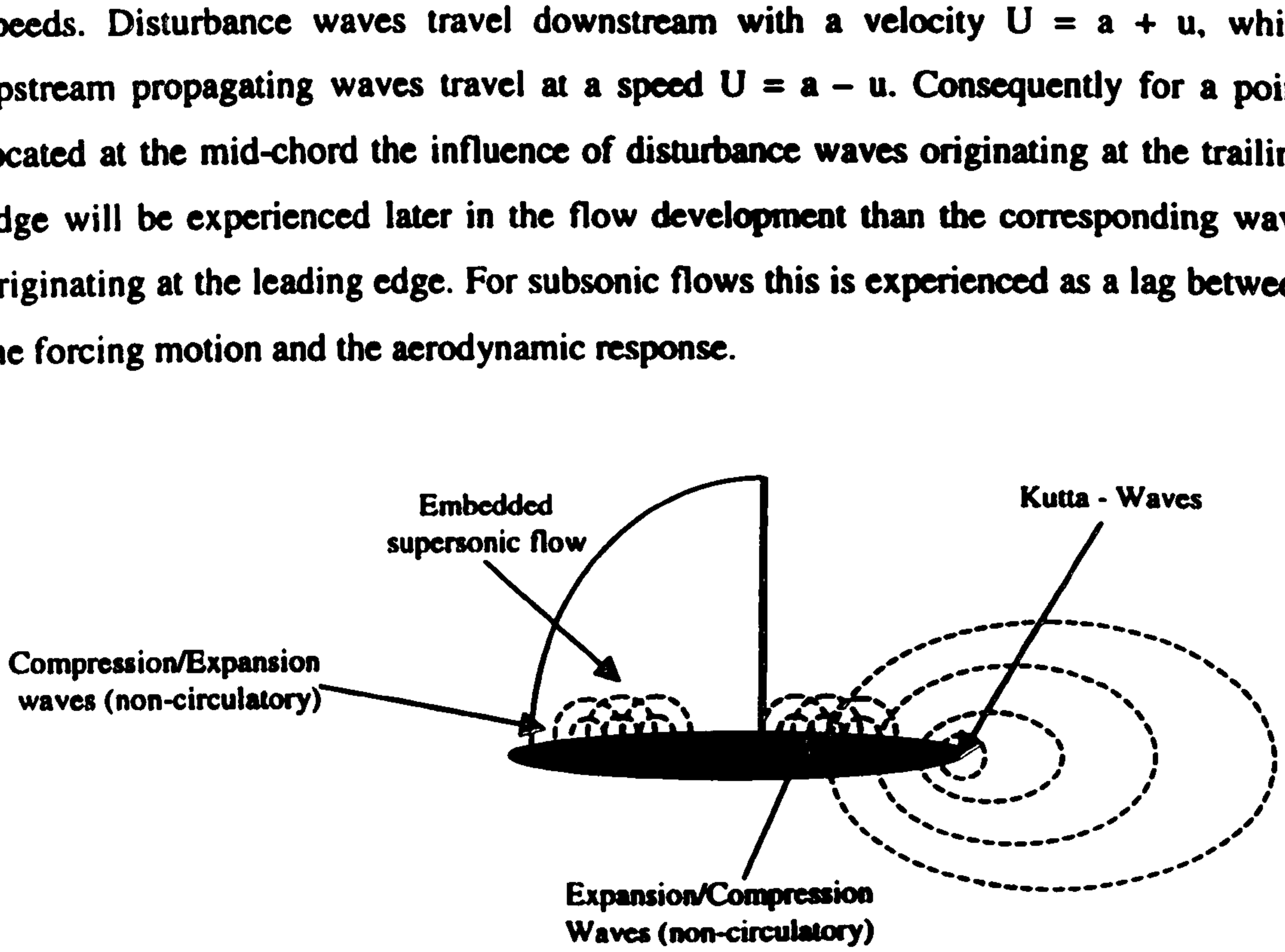

Figure (9.30) Sketch of conceptual model

For supercritical flows the embedded supersonic flow close to the aerofoil prevents the upstream propagation of disturbance waves along the aerofoil surface. Instead the disturbances must travel around the supersonic region. This leads to a considerable delay in the time taken for the flow to respond to the changing Kutta-condition. As a result of these delays the accelerating flow is over expanded with respect to the corresponding steady flow and shock waves form later. Conversely, when the flow is decelerating it is over compressed when compared to the steady flow and the shock waves persist longer.

The model clearly explains the observed delays in the formation, motion and disappearance of the shock wave. In addition it also accounts for the pressure waves which were observed ahead of the aerofoil leading edge. The model can be used to explain the behaviour discussed by Habibie[235] who observed that the flow exhibits little unsteadiness for aerofoils performing small amplitude inplane motion close to the speed of sound. This is clearly because the shock wave at the trailing edge prevents the Kutta-waves from travelling upstream. Consequently the flow is unable to adapt to the change in circulation and no unsteady effect is experienced.

9.6 Combined Translation-Pitch Oscillations

The calculations presented in the preceeding sections were all performed for a symmetric aerofoil at 0° incidence. To approach the more realstic problem of a lifting rotor it is necessary to include both the effects of varying incidence and those of varying Mach number. In this section an example of the flow around a lifting aerofoil using realistic time histories of incidence and Mach number is presented.

The effect of simultaneous fluctuations in both the incidence and magnitude of the freestream velocity vector on the aerodynamic performance of a NACA 0012 aerofoil was investigated by Favier[247-52]. The mechanical system employed produced relatively modest translational velocities. However, the freestream velocities employed in the study were such that advance ratios in the range $0 < \mu < 1$ could be achieved. The main aim of the experiments was to document the influence of velocity fluctuations on the dynamic stall process. The experimental data below stall suggest that for moderate

values of reduced frequency and advance ratio the unsteady flow is dominated by variations of velocity when the motions are in phase, while incidence fluctuations dominate when the motions are out of phase. For higher reduced frequencies and advance ratios the relationship between the unsteady flow and the unsteady motions is more complex. These early experiments have stimulated very little interest from the CFD community. Indeed, the only known numerical solutions for this problem published in the open literature are those presented by Pascazio et al[252]. Pascazio adopts a velocity-vorticity approach that allows the flow computation to be confined to the vortical region of the flow. Results were presented for a NACA 0012 aerofoil that was subjected to the motion,

$$\alpha = 12 - 6\cos(\omega t) \tag{9.13}$$

$$U = U_{\infty}(1 + 0.251\cos(\omega t) \tag{9.14}$$

with a freestream velocity of U_{∞} = 5 m/s, a Reynolds number Re_c = 100,000 and a reduced frequency of 0.188. Discrepancies between the computed and measured flow development are substantial, Pascazio suggests that these differences are largely attributable to the time phase change of flow separation. At a Reynolds number of 100,000 the leading edge flow separation is dominated by transition physics, the turbulence model employed by Pascazio cannot model transition and consequently the flow separates earlier in the numerical solution than is observed experimentally. This has a major impact on the subsequent development of the flow. When this effect is accounted for Pascazio concludes that the salient features of the experimental dynamic stall vortex are modelled accurately by the numerical method.

The above studies have been performed for low Mach numbers and have mainly served to demonstrate the impications of coupling velocity and incidence variations on the dynamic stall process. The motions are not however representative of those experienced on the outboard sections of rotors in high speed forward flight. Previously Shaw and Qin[239] and Qin, Ludlow and Shaw[155] have presented solutions of the thin-layer Navier-Stokes equations together with the Baldwin-Lomax model of turbulence for transonic flows which involve simultaneous variations of both Mach number and

incidence. These calculations were for fictitious schedules of Mach number and incidence but revealed the relative importance of the individual motions it was found that on the advancing side of the rotor disc Mach number variations dominated the calculated flow physics for the motion considered. This conclusion was reached because of evidence for the delay of shock formation and the suppression of separation. At azimuth angles for which the flow was wholly subsonic and attached the development of the unsteady forces was dominated by changing incidence.

9.6.1 Unsteady calculations

In order to understand the physical behaviour of the flow around aerofoils performing combined motions in the transonic regime a number of combined motions were studied. The results presented in (155) and (239) were recomputed using the full Reynolds averaged Navier-Stokes equations and the k-ω model. However, the calculations showed similar behaviour with the previous computations and so will not be discussed further here. Instead the motion studied by Pearcey[7] is investigated. This motion is of more practical concern than the earlier motions and corresponds to the flow conditions experienced by the aerofoil section at r/R = 0.93 on the rotor blade of the Wessex III helicopter. The forward flight velocity is 12 knots above the never exceed speed of the original rotor, this case was selected by Pearcey to demonstrate the effectiveness of a redesigned blade incorporating the RAE 9615 aerofoil in delaying the effects of both dynamic stall and compressibility. The angle of attack and Mach number variations were calculated by GKN Westland Ltd using a comprehensive analysis method. Instantaneous values of Mach number and incidence are tabulated for several azimuth angles in Table (2) of Reference (7). Using this information the time histories of Mach number and incidence can be described by functions of the form,

$$M(t) = M_o(1 + \mu \sin(\omega t)) \tag{9.15}$$

$$\alpha(t) = \alpha_o + \sum \alpha_n \sin(n\omega t) + \sum \beta_n \cos(n\omega t)$$

The locus of instantaneous Mach number and incidence for the motion investigated is presented in Figure (9.31) below.

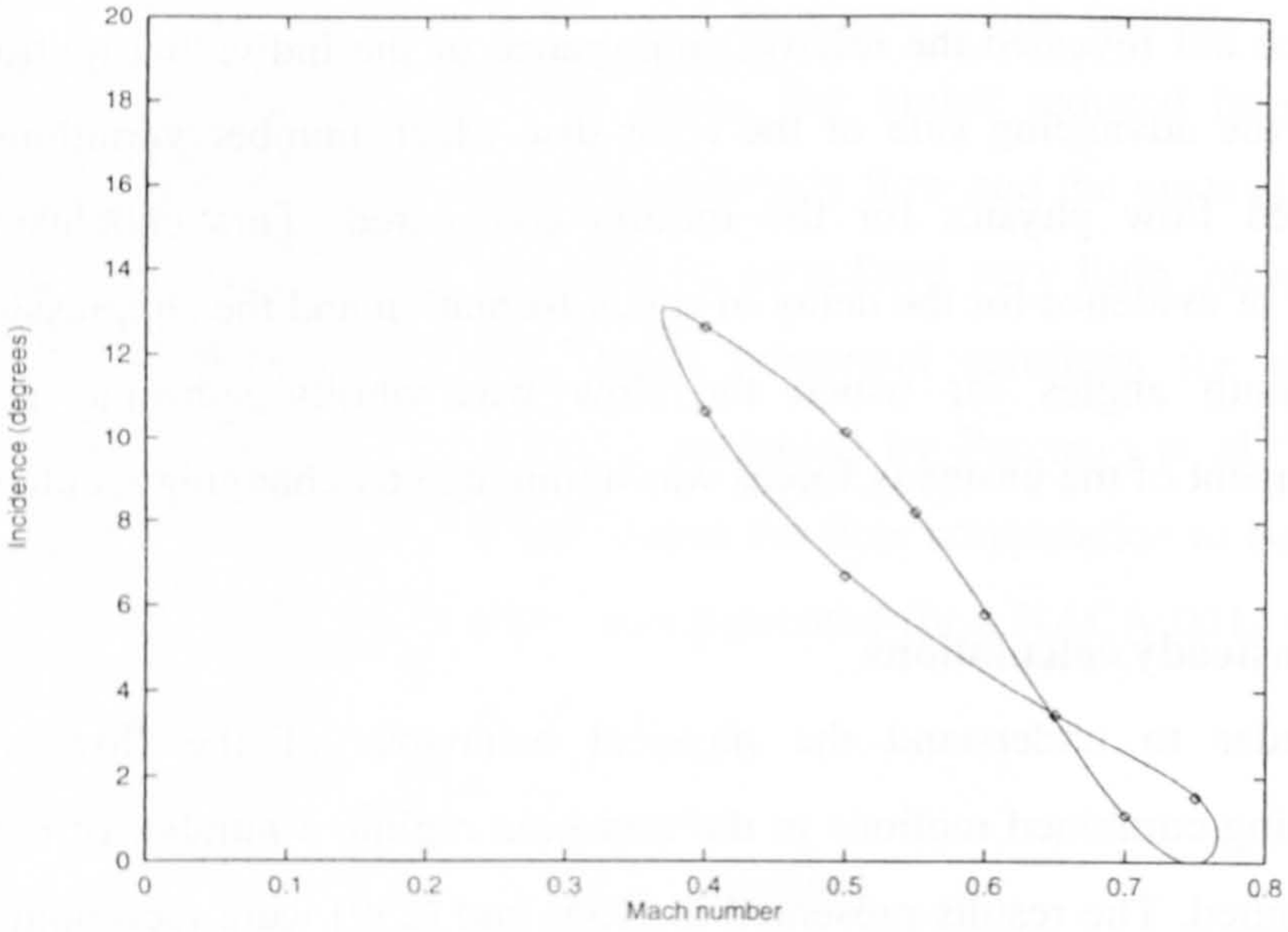

Figure (9.31) Locus of Mach number and incidence (Combined motion)

Like the NACA 0012 aerofoil the RAE 9615 aerofoil has a blunt trailing edge that cannot be treated using the current C-grid topology. In order to overcome this problem it was necessary to modify the geometry to produce a sharp trailing edge. This was acheived by perturbing the trailing edge geometry. The modified geometry is found by summation of the original geometry and the perturbation function thus,

$$y_{mod} = y_{orig} + \phi(x - x_o) \tag{9.16}$$

where x_o is the point beyond which the geometry is modified. In order to ensure that the modification blends smoothly with the original profile we impose the following conditions on the perturbation function,

$$\phi(0) = 0,\ \frac{d\phi(0)}{dx} = 0 \text{ and } \frac{d^2\phi(0)}{dx^2} = 0 \text{ and } \phi(1) = y_1 - y_{te} \tag{9.17}$$

The first three conditions given by (9.17) ensure that the geometry is continous at the modification point and that the gradient and curvature vary smoothly, while the final condition fixes the trailing edge point at the position y_1. These conditions can be

imposed simultaneosuly using a cubic polynomial as the perturbation function. The upper surface of the geometry was modified beyond x/c = 0.95 while the lower surface remained unchanged. The trailing edge postion y_t was chosen to produce a sharp trailing edge. The original and modified geometries are compared in Figure (9.32).

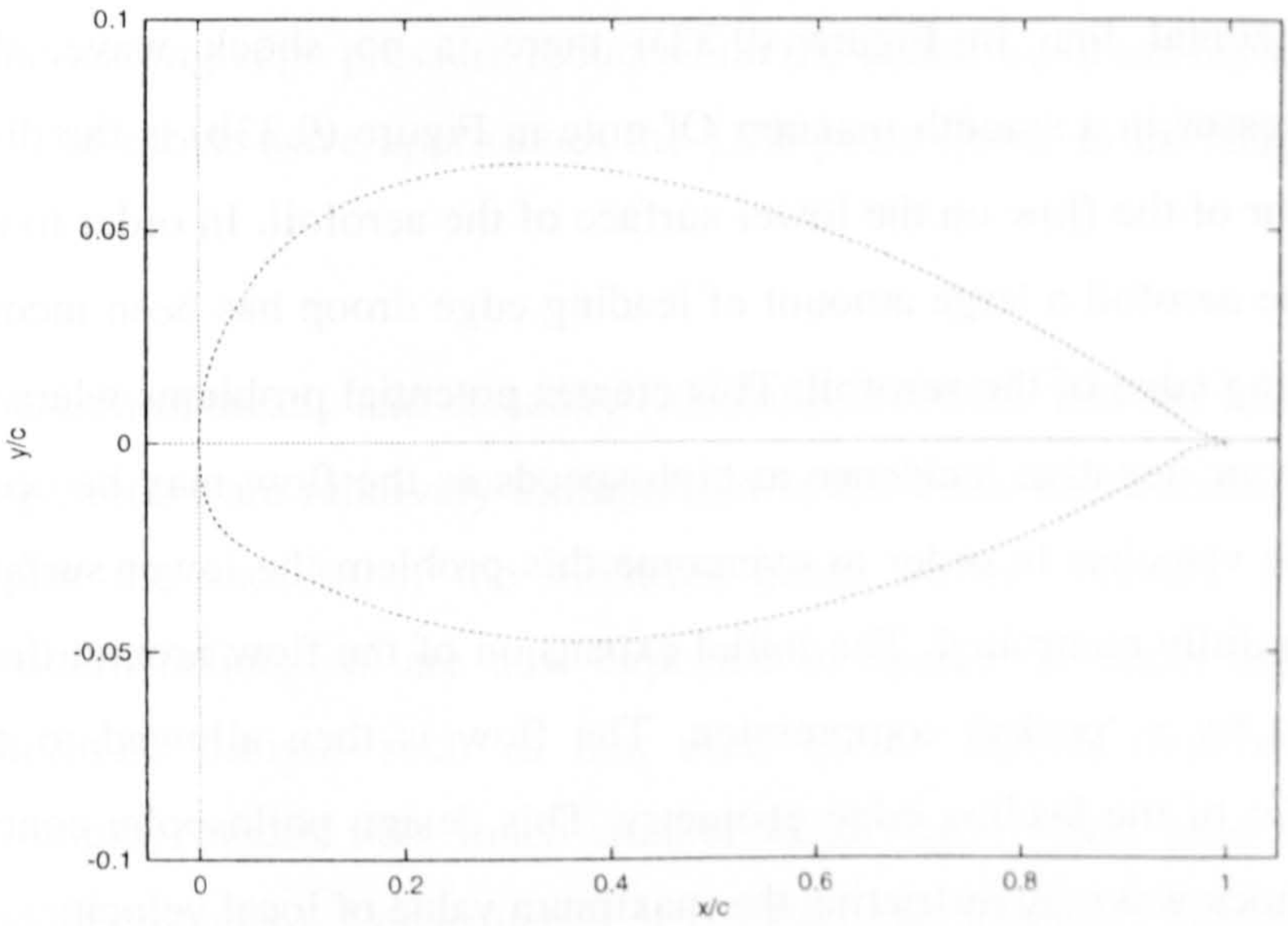

Figure (9.32) The modified RAE 9615 geometry.

Calculations were performed for the modified RAE 9615 aerofoil using a grid having 185 points around the aerofoil and 65 points in the aerofoil normal direction. Steady and unsteady calculations were performed using the k-ω turbulence model. For the unsteady solutions a time step size equivalent to 1/4° of azimuth was employed and the linear system arising at each time step was considered solved when the non-dimensional residual fell below 0.005. This was typically achieved within one step of GMRES (10) once the initial solution transients had been damped.

Calculated pressure distributions are compared for the steady and unsteady calculations in Figure (9.33) and the corresponding instantaneous contours of Mach number are shown in Figure (9.34). The most striking feature of the pressure comparisons is that the unsteady flow behaves in a quasi-steady manner. This is attributed to the combination of a low advance ratio and the low reduced frequency associated with the blade section at r/R = 0.93. However, the development of the flow

is still of interest. At $\psi = 10°$ the combination of modest Mach, M=0.6 number and relatively high incidence, $\alpha = 5.8°$, produce a shock wave at 20% chord. As azimuth is increased ($\psi = 42°$) the Mach number increases to M = 0.7, while the instantaneous value of the incidence is reduced, $\alpha = 1.1°$. While the flow around the leading edge of the aerofoil is accelerated beyond the sonic velocity (the sonic velocity is indicated by the horizontal line in Figure (9.33)) there is no shock wave, the flow instead recompresses in a smooth manner. Of note in Figure (9.33b) is the distinctive 'Peaky' behaviour of the flow on the lower surface of the aerofoil. In order to extend the useful lift of the aerofoil a large amount of leading edge droop has been incorporated close to the leading edge of the aerofoil. This creates potential problems when the aerofoil is at very low or negative incidence at high-speeds as the flow may be accelerated beyond the sonic velocity. In order to overcome this problem the lower surface curvature has been carefully controlled. The initial expansion of the flow around the leading edge is followed by a 'peaky' compression. The flow is then allowed to expand over the remainder of the leading edge geometry. This design philosophy controls the strength of the shock wave by restricting the maximum value of local velocity.

Beyond $\psi = 90°$ the Mach number begins to fall from its maximum value, while the incidence begins to increase. At $\psi = 112°$ values of M = 0.75 and $\alpha = 1.55°$ have been attained for Mach number and incidence respectively. At these conditions there is a strong shock wave evident on the upper surface of the aerofoil. The shock wave moves forward along the aerofoil as azimuth is increased further, By $\psi = 155°$ the shock has reached the 25% chord point. At $\psi = 199°$ the Mach number has fallen to M = 0.5, however ther is still evidence of supersonic flow and a weak shock immediately following the leading edge. For the remaining azimuth angles the effects of increasing incidence outweigh those of decreasing Mach number. This can be clearly seen by the continued increase in local velocity at the leading edge of the aerofoil, Figure (9.33f). The flow remains locally supersonic near the leading edge over the whole of the retreating side despite the fact that the freestream Mach number falls well below the critical value for this aerofoil section. This is due to acceleration of the flow around the aerofoil leading edge at high incidences. Indeed for the original NACA 0012 aerofoils used on the Wessex III blade, Pearcey notes that the retreating blade stall was due to

shock-induced separation (this conclusion was based on the collapse of leading edge pressure prior to stall). Despite the relatively high incidences achieved at the extremes of the present motion, in excess of 12°, the aerofoil does not appear to suffer the adverse consequences of boundary layer separation. For azimuth angles in the final quadrant, $\psi > 270°$ the angle of attack begins to fall while the Mach number increases. As a result the leading edge pressure reduces and the shock wave moves forward along the aerofoil. The shock wave approaches the 15% point chord as the blade begins the next cycle.

The comparison of steady and unsteady calculations reveals that the unsteady effects of the forcing motion are relatively unimportant at the simulated conditions, this may explain in part the success of the modified blade on the Wessex III helicopter. However, modern helicopters are now expected to operate at much higher advance ratios. Furthermore designs such as that used in the British Experimental Rotor Programme employ blades with much smaller local aspect ratios (and hence higher local reduced frequencies). Consequently it is likely that unsteady effects will play a more dominant role in the development of the flow around the blade.

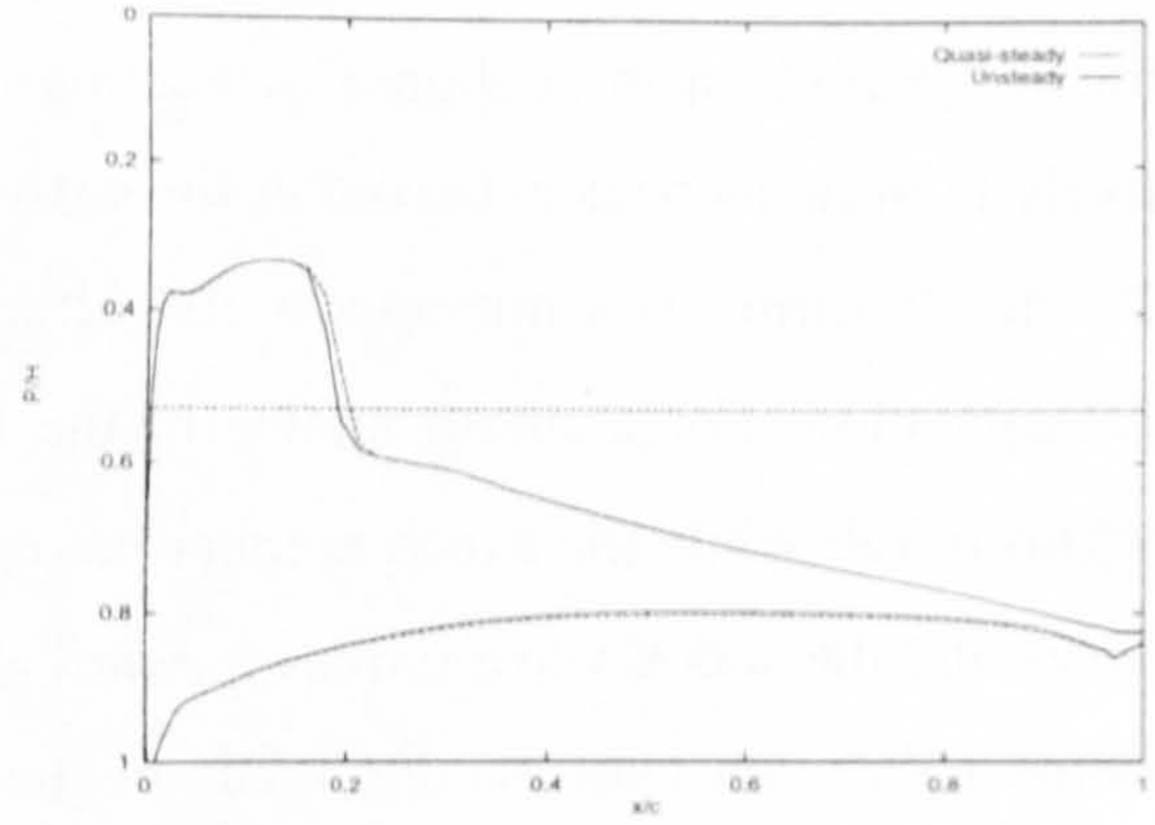

(a) $\psi = 10°$

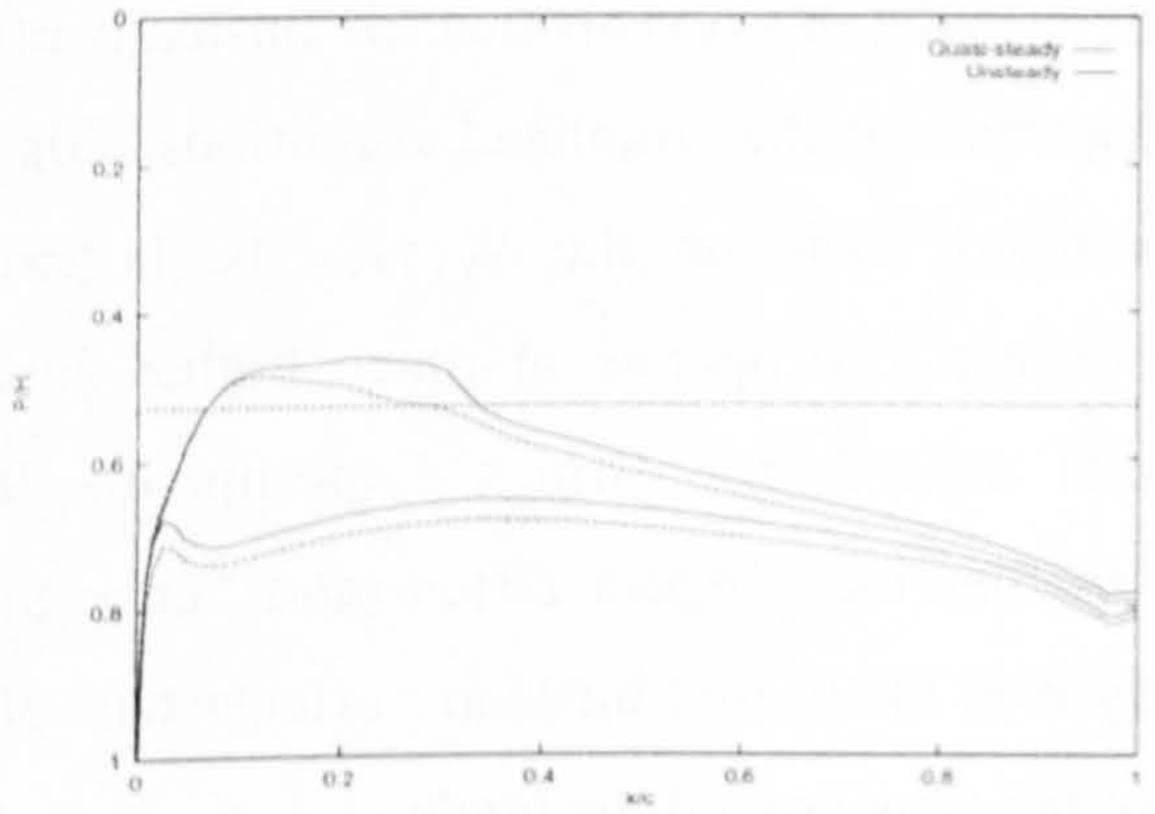

(b) $\psi = 42°$

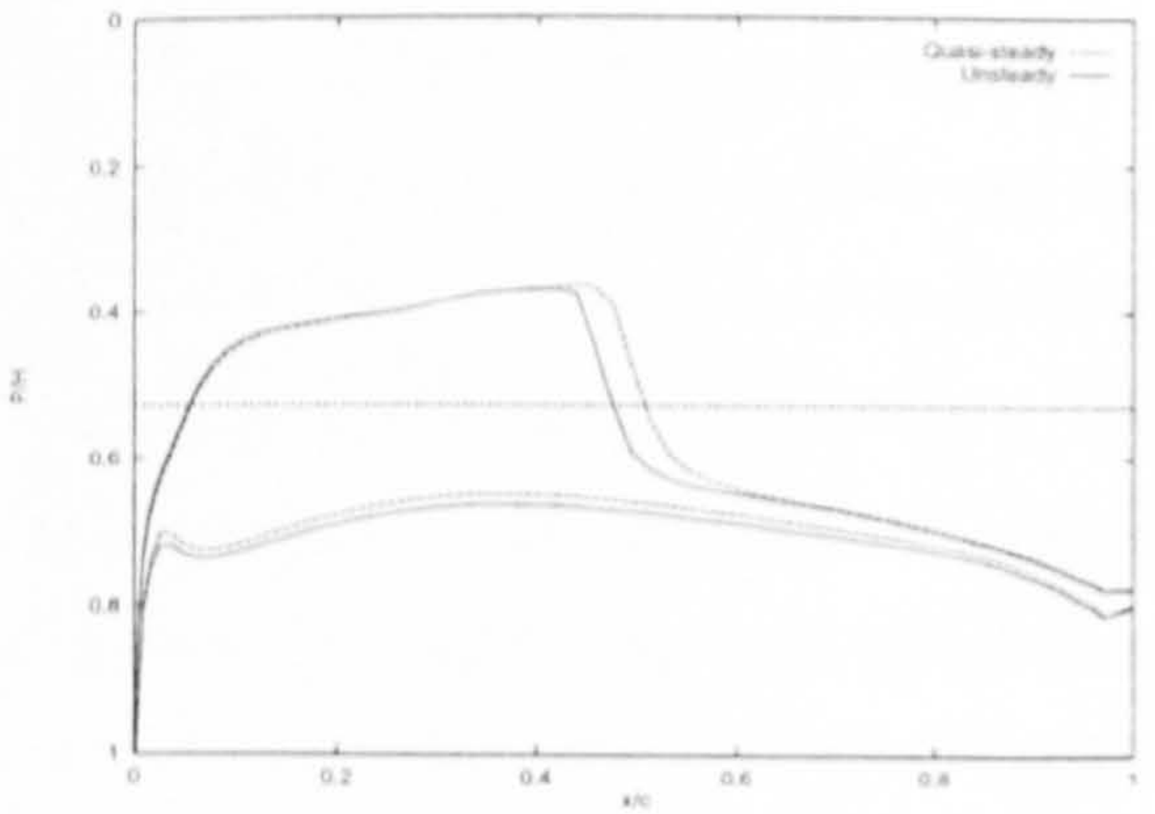

(c) $\psi = 112°$

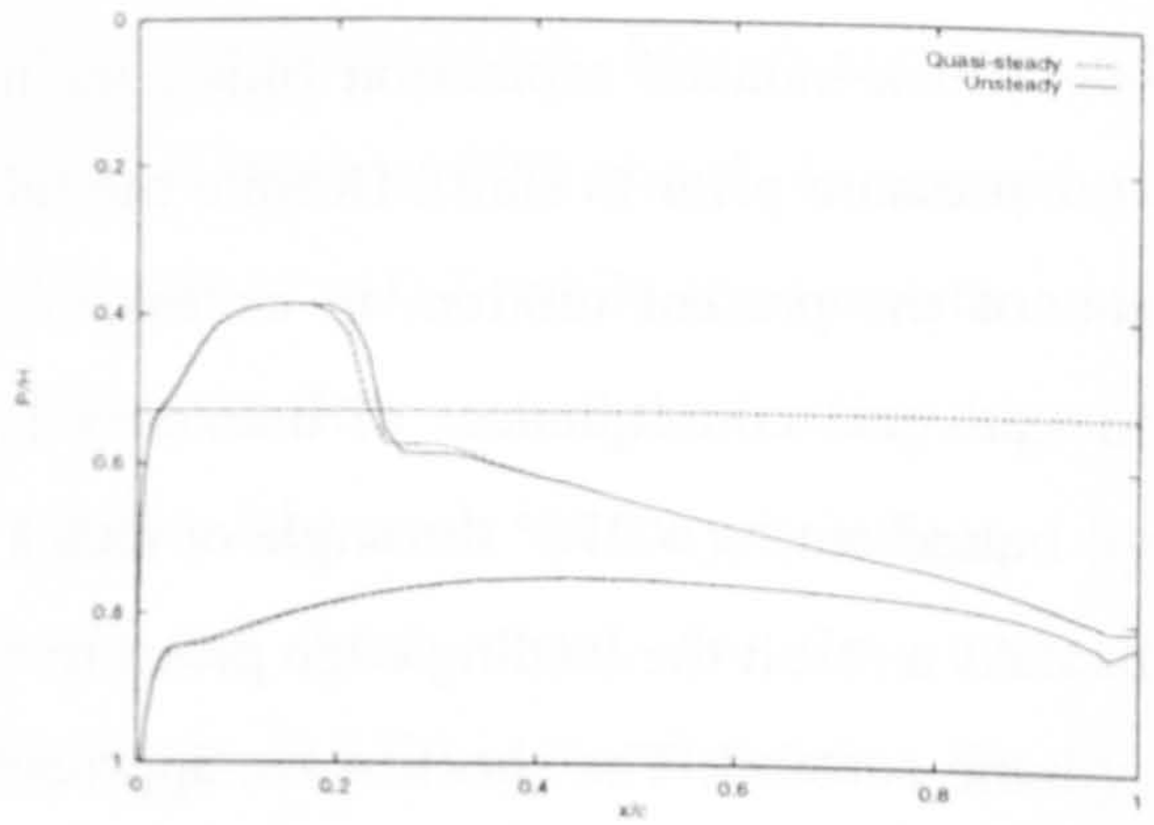

(d) $\psi = 155°$

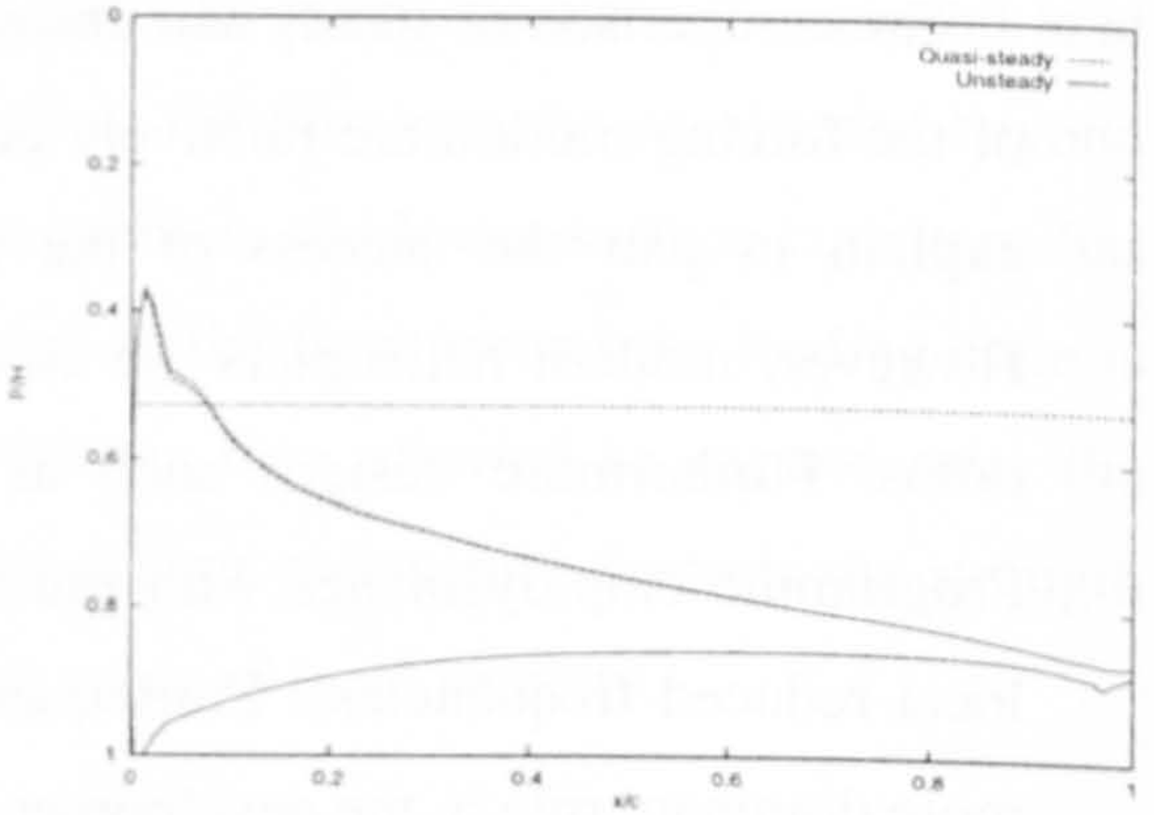

(e) $\psi = 199°$

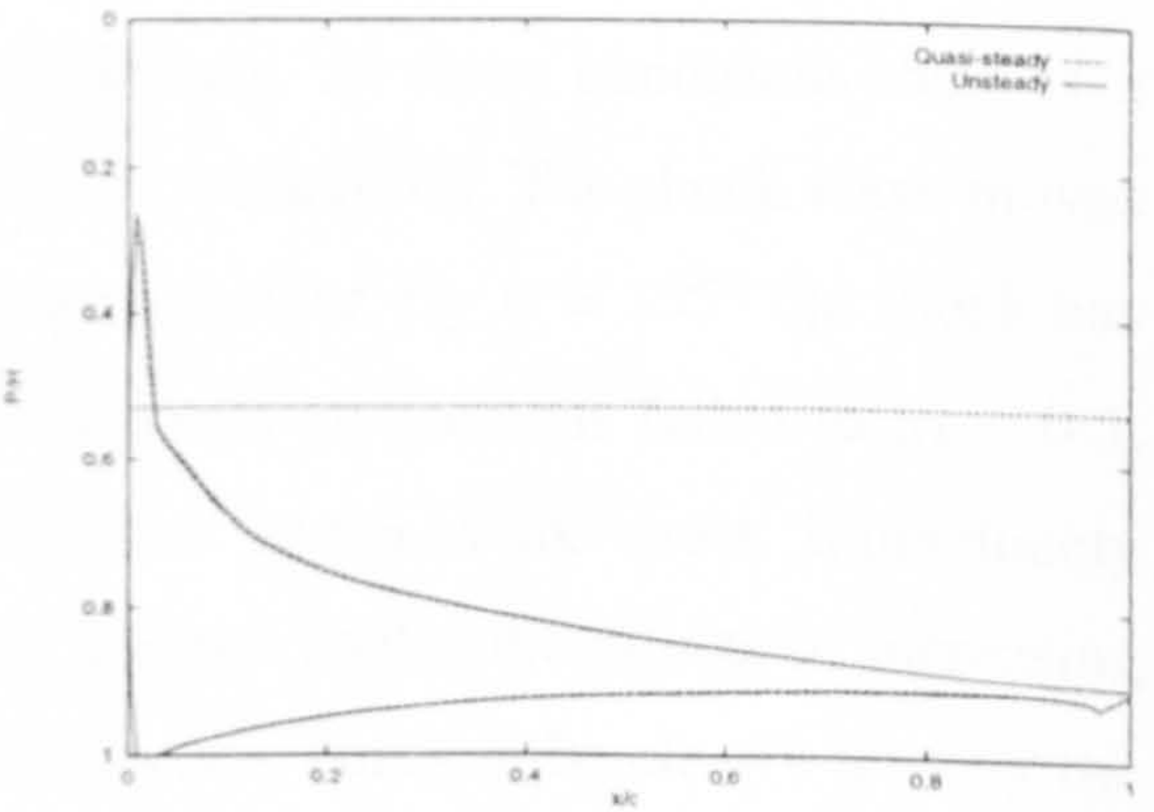

(f) $\psi = 237°$

Figure (9.33) Comparison of steady and unsteady pressure distributions (Combined Motion)

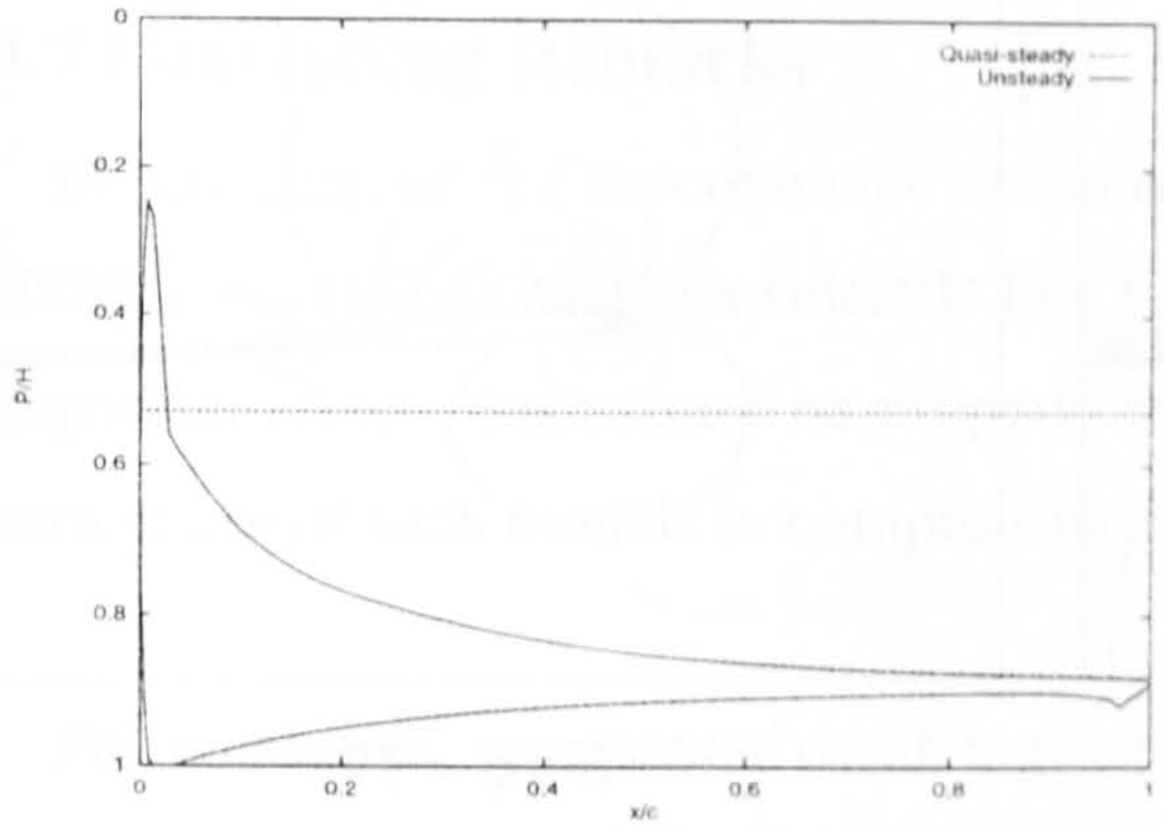

(g) $\psi = 303°$

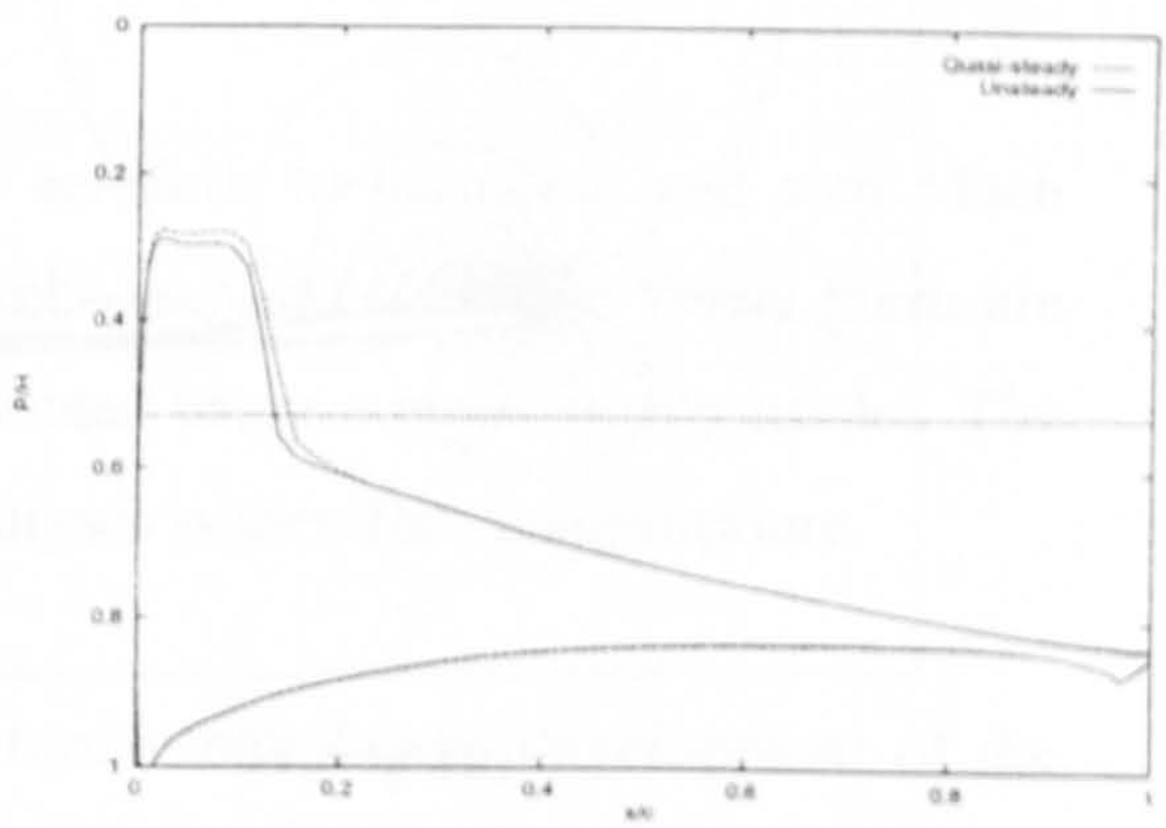

(i) $\psi = 355°$

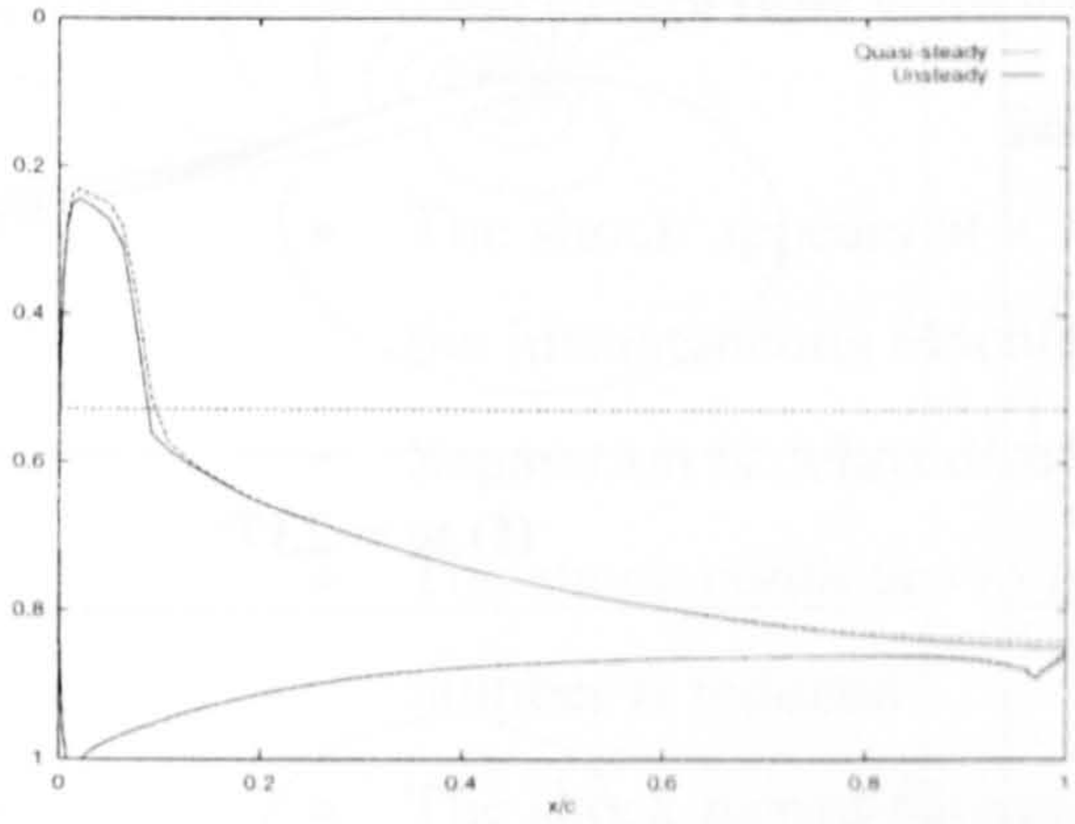

(h) $\psi = 340°$

Figure (9.33) Comparison of steady and unsteady pressure distributions (Combined motion) –concluded.

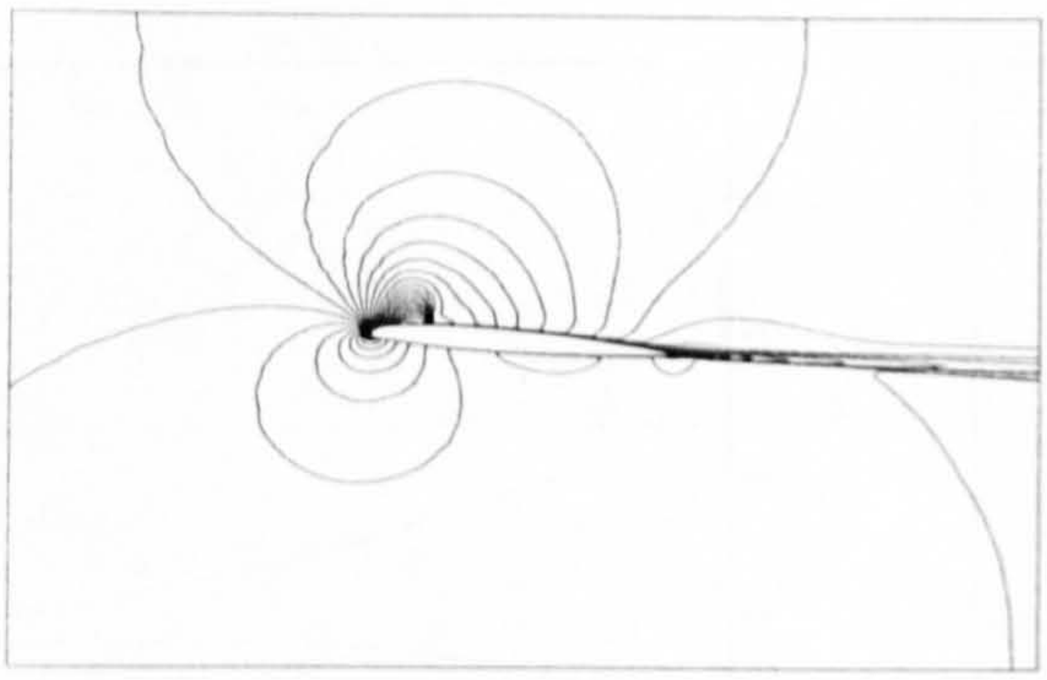

(a) $\psi = 10°$

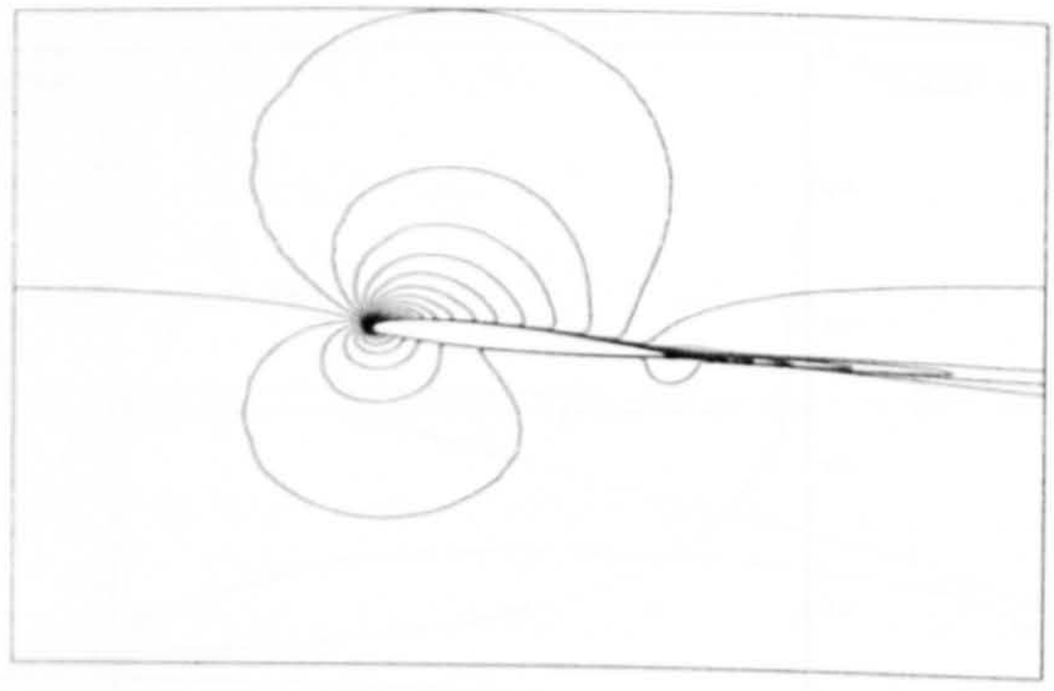

(e) $\psi = 199°$

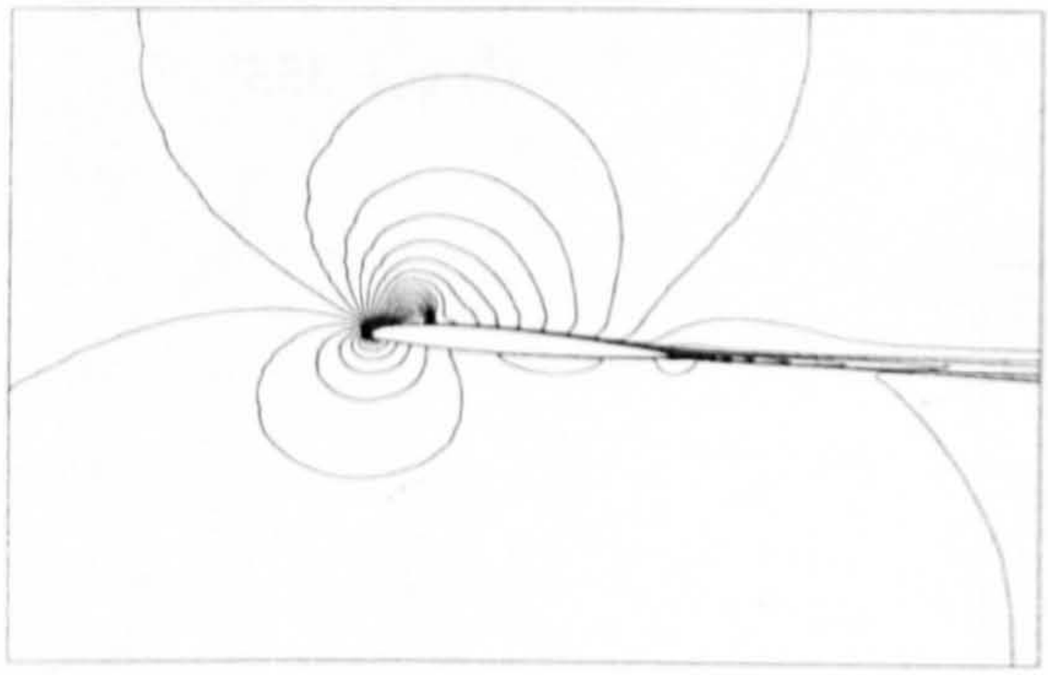

(b) $\psi = 42°$

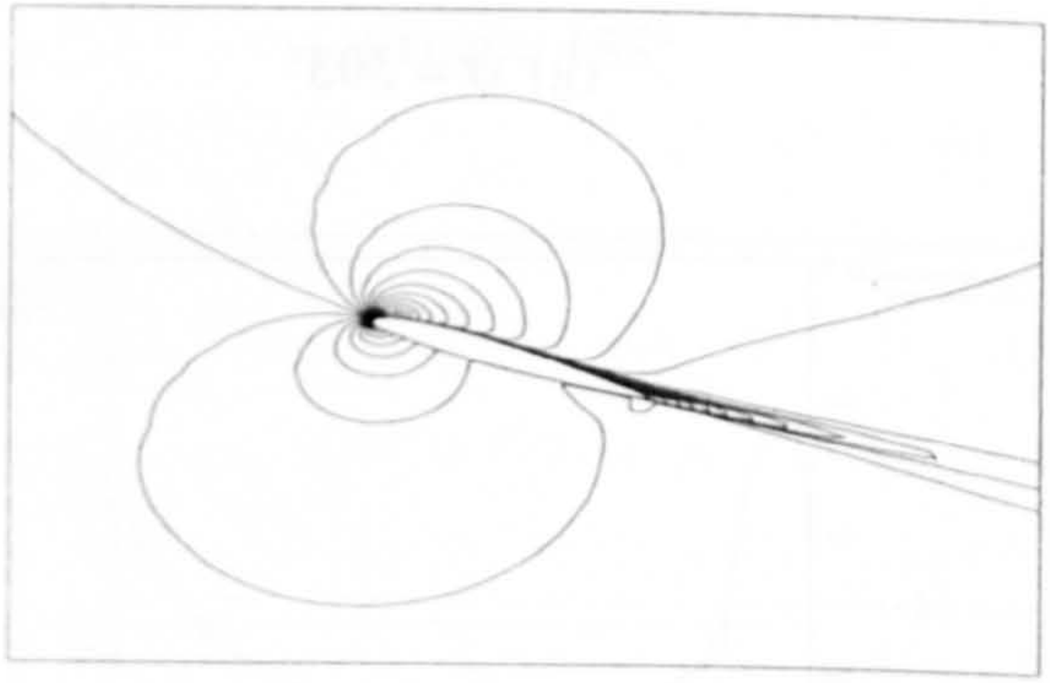

(f) $\psi = 237°$

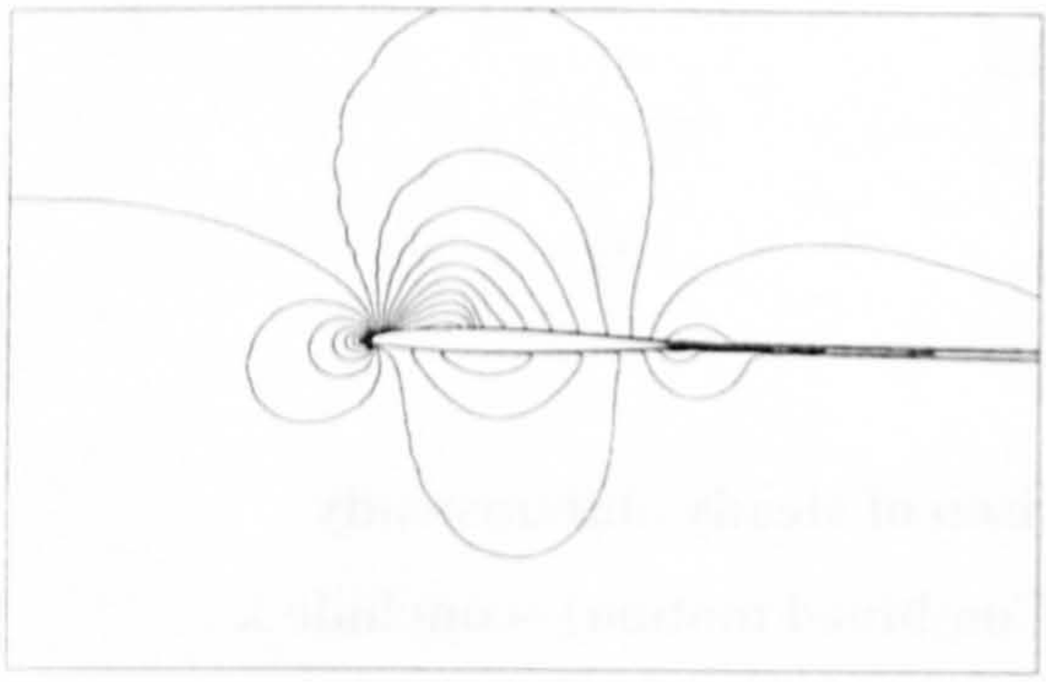

(c) $\psi = 112°$

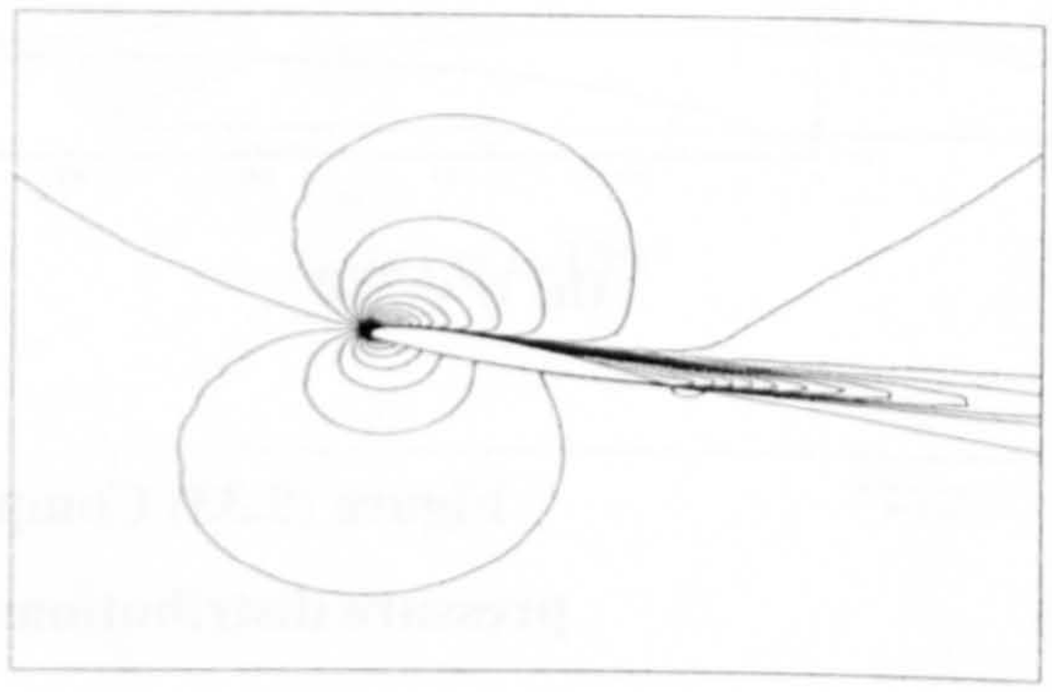

(g) $\psi = 303°$

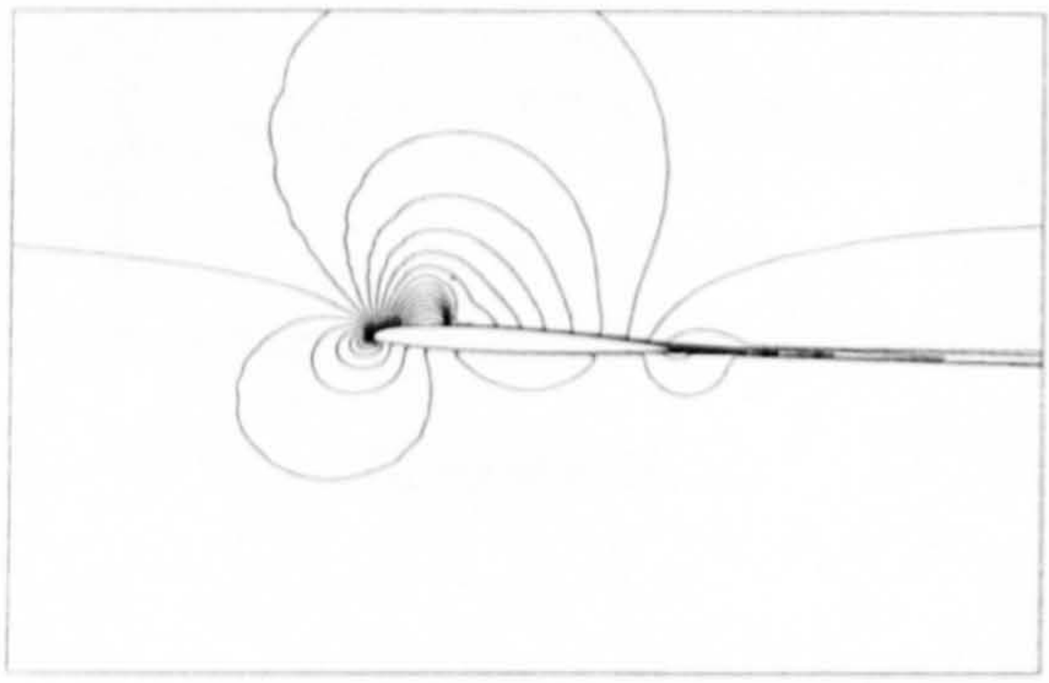

(d) $\psi = 155°$

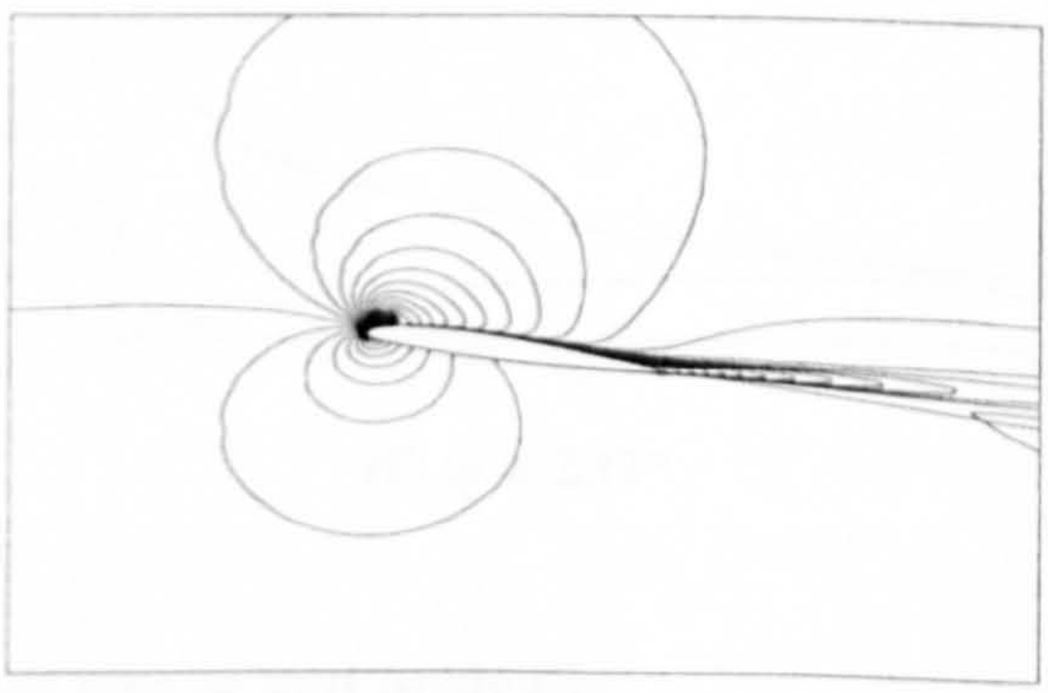

(h) $\psi = 340°$

Figure (9.34) Computed Mach contours (Combined motion)

9.7 Concluding Remarks

In this chapter the aerodynamic response of aerofoils to harmonic and step Mach number excitations was considered. For both subsonic and transonic flows there are important effects that cannot be properly represented using a quasi-steady model. The current use of such models in comprehensive analyses is therefore inappropriate.

For conditions representative of high speed forward flight the development of the shock-wave and its interaction with the boundary layer were found to be significantly influenced by the forcing motion. A number of characteristics that distinguish the unsteady flow from the steady flow were identified:

- The shock appears at a Mach number above the critical value while the instantaneous Mach number is increasing
- Separation is delayed/suppressed
- The shock continues to increase in strength and move aft as he Mach number is reduced
- The shock moves forward before the maximum strength is achieved
- The shock persists for Mach numbers below the critical value while the instanataneous Mach number is decreasing

The parametric effects of reduced frequency and advance ratio were investigated. Based upon the computed response of the peak suction coefficient to harmonic forcing a phase lag, ϕ, was identified. The attached flow at lower advance ratios was shown to be symmetric about $\psi = 90° + \phi$, furthermore, the phase lag was found to be independent of advance ratio. Using an assumed form of the indicial function for Mach number variation a functional form of the response to harmonic forcing was obtained. The response of normal force to harmonic variations of Mach number is itself harmonic with a phase shift. The phase shift was shown to depend only upon the frequency of the motion and the time constants used in the exponential representation of the indicial function. This confirms the results obtained by numerical solution of the Navier-Stokes equations. It was found that the effects of unsteadiness increased with increasing reduced frequency. For subsonic attached flow this is most readily seen by examining

the phase lag. For transonic flows increasing reduced frequency changes the effective critical Mach numbers at which the shock appears and disappears. For k = 0.15 it was observed that the first appearance of the shock wave could be delayed until almost 90° azimuth.

The response of the flowfield to a step change in Mach number was also investigated. The calculated response of normal force for this motion was found to be similar to that obtained for a step increase in incidence. Initially the response is dominated by a rapid increase in normal force resulting from non-circulatory effects associated with the change in surface boundary condition. These effects diminish rapidly. At later times the gradual build up of circulatory effects dominates the response. Three wave systems associated with the non-circulatory (compression and expansion) and circulatory responses (compression) were identified.

A conceptual model based upon the observed flow behaviour was suggested. In the model continuos changes in Mach number produce systems of compression and expansion waves. These waves propagate through the fluid around the aerofoil at the local wave speeds. Consequently disturbance waves originating at the trailing edge due to changing circulation are retarded, and their influence is not felt until later times. For subsonic flows this is experienced as a lag between the forcing motion and the aerodynamic response. For supercritical flows the embedded supersonic flow close to the aerofoil flow prevents the upstream propagation of disturbance waves. Instead the disturbances must travel around the supersonic region. This leads to a considerable delay in the time taken for the flow to respond to the changing Kutta-condition. As a result of these delays the accelerating flow is over expanded with respect to the corresponding steady flow and shock waves form later. Conversely, when the flow is decelerating it is over compressed when compared to the steady flow and the shock waves persist longer. This model accounts for the observed characteristics of the flowfield.

Conclusions

The aim of the work presented in this thesis was to develop an improved understanding of the aerodynamics of the advancing rotor blade in high-speed forward flight. In order to make the problem computationally tractable, a two-dimensional approximation was introduced in which the complex flow around the blade is represented by aerofoils performing inplane and pitching motion.

In order to meet this aim, a numercial scheme was developed for the solution of the Navier-Stokes equations together with a two-equation turbulence model. The development of the unsteady solver makes a number of contributions:

- An extension of Oshers approximate Riemann solver to include both the mean flow and turbulence equations in a strongly coupled fashion.
- Analytical development of the corresponding implicit operator
- Application of the linear solver GMRESR to large scale CFD problems
- Investigation of the utility of Newtons method for unsteady problems

The unsteady solver was validated with both steady and unsteady experimental data. In addition to the standard test cases, the computation of self-excited flow was also considered. The work contributes to our knowledge of such flows in two ways:

- Use of a two-equation turbulence model instead of an algebraic model is shown to improve agreement with experiment.

- Comparisons of steady and unsteady flow calculations reveal that the onset and extent of the periodic region is associated with the physics of shock induced separation and subsequent re-attachment.

The unsteady flow around aerofoils performing unsteady motions representative of rotor blades in forward flight was then investigated. This study represents a significant contribution to the understanding of the flow dynamics on the advancing blades of helicopter rotors. The main findings of the study are:

- Correlation of two-dimensional calculations with experimental data for a model rotor demonstrate that three-dimensional effects may be important over much of the blade tip. However, the low aspect ratio of the model used in the experimental is not representative of realistic main rotor configurations. The usefullness of a two-dimensional approximation therefore warrants further study.
- For shock free flows the effects of flow unsteadiness can be represented by a phase lag that is independent of advance ratio.
- Development of the shock wave and its interaction with the boundary layer is significantly influenced by the forcing motion. The current use of quasi-steady models to represent the aerodynamics of Mach number variation in comprehensive analysis codes is therefore inappropriate.

Results were also presented for combined inplane-pitching motion and for step changes in Mach number. The former, represent the first published attempt to calculate the aerodynamics of rotor blade sections at realistic flight conditions. While the latter pioneering calculations, are usefull in revealing the physical mechanisms responsible for the observed phase delays.

Notation

a	Speed of sound
A	Blade area
	Jacobian matrix
b	Vector
c	Chord
C_d	Drag coefficient
C_f	Skin friction coefficient
C_L	Lift coefficient
C_M	Pitching moment coefficient
C_N	Normal force coefficient
C_p	Pressure coefficient
e	Unit vector
	Internal energy
E	Energy
F	Flux term
H	Source term
k	Reduced frequency
	Turbulent kinetic energy
K	Krylov-subspace
M	Mach number
n	Normal vector
N	Number of iterations
P	Power
	Pressure
Pr	Prandtl number
q	Heat flux
Q	Vector of conserved variables
r	Radial distance from measured from hub
R	Blade radius
	Gas constant
	Empirical constant in (2.10)
	Right Eigenvectors
	Right hand side
Re	Reynolds Number
s	Non-dimensional time
S	Surface area
	Strain rate
t	Time
	Thickness
T	Time period
	Thrust
	Temperature
u,v,w	Components of velocity in Cartesian co-ordinate system
U	Effective freestream velocity
V	Volume
x,y,z	Cartesian co-ordinate system

Symbols

Λ	Vector of Eigenvalues
Ω	Rotor angular velocity
α	Incidence
β	Blade flapping angle
δ	Boundary layer displacement thickness
ε	Small number

PAGE NUMBERING AS ORIGINAL

ϕ	Inflow angle		Left hand state
	Limiter	p	Parallel
γ	Ratio of specific heats (1.4 for air)	r	Local condition at r/R
κ	Constant in MUSCL interpolation	R	Right hand state
λ	Inflow ratio	T	Tangential
	Second coefficient of viscosity		Turbulent
	Eigenvalues	V	Viscous
μ	Advance ratio	x,y,z	Cartesian co-ordinate system
	Viscosity	+	Positive value
θ	Geometric pitch angle	-	Negative value
	Constant in Beam-Warming method	∞	Freestream
ρ	Density	′	Derivative with respect to time
ω	Frequency	–	Contra-variant
	Specific dissipation rate		Time averaged
ξ	Constant in Beam-Warming method		
τ	Non-dimensional time		
	Shear stress		
ψ	Azimuth angle		
	Riemann Invaraints		

Subscripts and Superscripts

0	Average value
1	Upstream of shock
2	Downstream of shock
e	Boundary layer edge
H	Sonic condition
f	Forward flight
i	Induced
	Inviscid
l	Local

References

1. Johnson, W. 'Helicopter theory', Dover, 1980.
2. Buchtala, B, Wehr, D. and Wagner, S. 'Coupling of aerodynamic and dynamic methods for the calculation of helicopter rotors in forward flight', Proceedings of the 23rd European Rotorcraft Forum, September 1997.
3. Wilby, P. 'Shock waves in the rotor world – a personal perspective of 30 years of rotor aerodynamic developments in the UK', Aeronautical Journal Vol. 112 (1013), March 1998, pp. 113-128.
4. Johnson, W. 'Development of a comprehensive analysis for rotorcraft', Vertica Vol. 5(2), 1981, pp. 99-129.
5. Hansford, R.E. and Vorwald, J. 'Dynamics workshop on rotor vibratory loads prediction", J. American Helicopter Society, Vol. 43 (1), January 1998, pp. 76-87.
6. Lau, B., Louie, A.W., Griffiths, N. and Sotiriou, C. 'Performance and rotor load measurements of the Lynx XZ170 helicopter with rectangular blades', NASA TM 104000, May 1993.
7. Pearcey, H.H., Wilby, P.G., Riley, M.J. and Brotherhood, P. 'The derivation and verification of a new rotor profile on the basis of flow phenomena; aerofoil research and flight tests', AGARD CP 111, September 1972.
8. Seddon, J., 'Basic helicopter aerodynamics', BSP Professional Books, 1990.
9. Caradonna, F.X. 'The application of CFD to rotary wing flow problems', NASA TM 102803, March 1992.
10. Newman, S., 'The foundations of helicopter flight', Edward Arnold, 1994.
11. Abbott, I.H. and Von Doenhoff, A.E., 'Theory of wing sections', Dover, 1959.
12. Stepniewski, W.Z. and Keys, C.N., 'Rotary-wing aerodynamics', Dover, 1984.
13. Theodorson, T., 'General theory of aerodynamic instability and the mechanism of flutter', NACA Report 496, 1935.
14. Beddoes, T., 'Practical computation of unsteady lift', Vertica, Vol. 8 (1), 1984, pp. 55-71.
15. Carta, F.O., 'Experimental investigation of the unsteady aerodynamic characteristics of a NACA 0012 airfoil', Research Report M-1283-1, United Aircraft Corporation, July 1960.

16. Carr, L.W., 'Progress in analysis and prediction of dynamic stall', J. Aircraft, Vol. 25 (1), January 1988, pp. 6-17.
17. Isom, M.P. and Caradonna,F.X., 'Subsonic and transonic potential flow over helicopter rotor blades' AIAA Paper 72-0039, 1972
18. Wilby P.G. and Grant, J. 'Transonic aerodynamics of the helicopter rotor', RAe TM (structures) 872, 1975.
19. Fradenburgh, E.A. and Rabbott, J.P., 'High speed helicopter research', Proceedings of the 18th Annual Forum of the American Helicopter Society, May 1962.
20. Lerat, A. and Sides, J., 'Numerical simulation of unsteady transonic flows using the Euler equations in integral form', ONERA, TP 1979-10, 1979.
21. Lock, R.C., 'Introduction to transonic aerodynamics of aerofoils and wings', ESDU TDM – 90008, April 1990.
22. Tidjeman, H. 'Investigation of the transonic flow around oscillating aerofoils', NLR Report TR 77090U, 1977.
23. Erickson, A.L., and Stephenson, J.D., 'A suggested method of analysing for transonic flutter of control surfaces based upon available experimental evidence', NACA RM A7F30, 1947.
24. Lee, B.H.K., Murty, H. and Jiang, H., 'Role of Kutta waves on oscillatory shock motion on an airfoil', AIAA Journal, Vol. 32 (4), April 1994, pp.789-796.
25. Krause, E. and Schweitzer, W.B., 'The effect of an oscillatory free-stream-flow on a NACA-4412 profile at large relative amplitudes and low Reynolds numbers', Experiments in Fluids Vol. 9 (1190), pp. 159-166.
26. McCroskey, W.J., 'Vortex wakes of rotorcraft', AIAA Paper 95-0539, January 1995.
27. Leishman, J.G., Baker, A. and Coyne, A., 'Measurement of rotor tip vortices using three-component laser Doppler velocimetry', J. American Helicopter Society, Vol. 41(4), October 1996, pp. 342-353.
28. Kokkalis, A., 'An experimental investigation of parallel blade-vortex interaction for a NACA 0015 aerofoil', PhD Thesis, University of Glasgow, 1988.
29. Ng, N-L, 'A numerical study of the transonic blade vortex interaction', PhD Thesis, Imperial College, University of London, 1998.

30. Glauert, H., 'A general theory of the autogiro', RAe R&M 1111, 1926.
31. Gessow, A., 'Equations and procedures for numerically calculating the aerodynamic characteristics of lifting rotors', NACA TN 3747, October 1956.
32. Yaggy, P.F. and Statler, I.C., 'Progress in rotor-blade aerodynamics', AGARD CP111, 1972.
33. Caradonna, F.X. and Isom, M.P. 'Subsonic and transonic potential flow over helicopter rotor blades', J. AIAA Vol. 10 (12), 1972, pp. 1606-1612.
34. Caradonna, F.X. and Isom, M.P., 'Numerical calculation of unsteady transonic potential flow over helicopter rotor blades', J. AIAA Vol. 14(4), 1976, pp. 482-488.
35. Tung, C., Caradonna, F.X., Boxwel, D.A. and Johnson, W. 'The prediction of transonic flow on advancing rotors', Proceedings of the 40th Annual Forum of the American Helicopter Society, May 1984.
36. Arieli, R. and Tauber, M.E. 'Computation of subsonic and transonic flow about lifting rotor blades', AIAA Paper 79-1667, 1979.
37. Tauber, M.E. and Hicks, R.M. 'Computerized three dimensional aerodynamic design of a lifting rotor blade', Proceedings of the 36th Annual Forum of the American Helicopter Society, May 1980.
38. Tauber, M.E. 'Computerized aerodynamic design of a transonically quiet blade', Proceedings of the 40th Annual Forum of the American Helicopter Society, May 1984.
39. Caradonna, F.X., 'Application of transonic flow analysis to helicopter rotor problems', Unsteady Transonic Aerodynamics, Edited by Nixon, D., Chapter 6, 1988, pp. 263-285.
40. Ramachandran, Tung, C. and Caradonna, F.X., 'Rotor-hover performance prediction using a free wake, computational fluid dynamics method', J. Aircraft, Vol. 26(12), December 1989, pp. 1105-1110.
41. Roberts, T.W. and Murmann, E.M., 'Solution method for a hovering helicopter rotor using the Euler equations', AIAA Paper 85-0436, 1985.
42. Sankar, N.L., Wake, B.E. and Lekoudis, S.G., 'Solution of the unsteady Euler equations for fixed and rotor wing configurations', J. Aircraft, Vol. 23(4), April 1986, pp. 283-9.

43. Agarwal, R.K. and Deese, J.E., 'Euler calcualtions for flowfield of a helicopter rotor in hover', J. Aircraft, Vol. 24(4), April 1987, pp. 231-238.

44. Chen, C.L., McCroskey, W.J. and Obayashi, S., 'Numercial solutions of forward-flight rotor flow using an upwind method', J. Aircraft Vol. 28(6), June 1991, pp. 374-80.

45. Pahlke, K., 'Grid generation for multi-bladed rotors and calcualtions with a 3-D code for helicopter rotors in hover', DLR-IB 129-91/04, 1991.

46. Boniface, J.C. and Sides, J. 'Numerical simulation of steady and unsteady Euler flows around multi-bladed helicopter rotors', ONERA TP 1993-163.

47. Wake, B.E., Sankar, N.L. and Lekoudis, S.G., 'Computation of rotor blade flows using the Euler equations', J. Aircraft, Vol. 23(7), July 1986, pp. 582-8.

48. Srinivasan, G.R., Raghavan, V., Duque, E.P.N., 'Flowfield analysis of modern helicopter rotors in hover by Navier-Stokes method', International Technical Specialists Meeting on Rotorcraft Acoustics And Rotor Fluid Dynamics, Philadelphia, October 1991.

49. Sankar, L.N. and Tung, C., 'Euler calculations for rotor configurations in unsteady forward flight', Proceedings of the 42nd Annual Forum of the American Helicopter Society, June 1986.

50. Agarwal, R.K. and Deese, J.E., 'An Euler solver for calculating the flowfield of a helicopter rotor in hover and forward flight', AIAA Paper 87-1427, June 1987.

51. Chang, I.C., 'Transonic flow analysis for rotors: Part 3 - Three-dimensional quasi-steady, Euler calculation', NASA TP 2375, June 1990.

52. Lee, D. and Kim, S., 'An efficient method to calculate rotor flow in hover and forward flight', AIAA Paper 93-3336, 1993.

53. Strawn, R.C. and Barth, T.J., 'A finite volume Euler solver for computing rotary-wing aerodynamics on unstructured meshes', J. American Helicopter Society, Vol. 38(2), April 1993, pp. 61-67.

54. Pahlke, K. and Raddatz, J., 'Flexibility of Euler codes for rotor flows by Chimera techniques', Proceedings of the 20th European Rotorcraft Forum, Amsterdam, 1994.

55. Benek, J.A., Buning, P.G., Steger, J.L., 'A 3-D Chimera grid embedding technique', Proceedings of the AIAA 7th CFD Conference, Cincinnati, Ohio, July 1985.

56. Boniface, J.-Ch., Mialon, B., Sides, J., 'Numerical simulation of unsteady Euler flow around multi-bladed rotor in forward flight using a moving grid approach', Proceedings of the 42nd Annual Forum of the American Helicopter Society, Fort Worth, May 1995.

57. Boniface, J.-Ch., Guillen, Ph., Le Pape, M.-C., Darracq, D. and Beaumier, Ph., 'Development of a chimera unsteady method for the numerical simulation of rotorcraft flowfields', AIAA Paper 98-0421, January 1998.

58. Baeder, J.D., Gallman, J.M. and Yu, y.H., 'A computational study of the aeroacoustics of rotors in hover', Proceedings of the 49th Annual Forum of the American Helicopter Society, May 1993.

59. Wake, B.E. and Sankar, L.N., 'Solutions of the Navier-Stokes equations for the flow around a rotor blade', Proceedings of the National Specialists Meeting on Aerodynamics and Aeroacoustics, Arlington, February 1987.

60. Srinivasan, G.R. and McCroskey, W.J., 'Navier-Stokes calculations of hovering rotor flowfields', J. Aircraft, Vol. 25(10), October 1988, pp. 865-75.

61. Srinivasan, G.R., Baeder, J.D., Obayashi, S. and McCroskey, W.J., 'Flowfield of a lifting rotor in hover: A Navier-Stokes simulation', AIAA J., Vol. 30(10), October 1992, pp.2371-8.

62. Srinivasan, G.R., Raghavan, V., Duque, E.P.N. and McCroskey, W.J., 'Flowfield analysis of modern helicopter rotors in hover by Navier-Stokes method', J. American Helicopter Society, Vol. 38(3), July 1993, pp. 3-13.

63. Srinivasan, G.R. and Baeder, J.D., 'TURNS: A free-wake Euler/Navier-Stokes numerical method for helicopter rotors', AIAA J., Vol. 31(5), May 1003, pp.959-62.

64. Duque, E.P.N. and Srinivasan, G.R., 'Numerical simulation of a hovering rotor using embedded grids', Proceedings of the 48th Annual Forum of the American Helicopter Society, Washington, June 1992.

65. Duque, E.P.N., Biswas, R. and Strawn, R. 'A solution adaptive structured/unstructures overset grid solver with applications to helicopter rotor flows', AIAA Paper 95-1766, June 1995.

66. Wake, B.E., Sankar, N.L., Ruo, S.Y. and Malone, J.B., 'Numerical solution of unsteady rotational flow past fixed and rotary wing configurations', NASA CP 3022 Part 2, 1987.

67. Wake, B.E. and Sankar, L.N., 'Solutions of the Navier-Stokes equations for the flow about a rotor blade', J. American Helicopter Society, Vol. 34(2), April 1989, pp. 13-23.

68. Berezin, C.R. and Sankar, L.N., 'An improved Navier-Stokes/Full potential coupled analysis for rotors', AIAA Paper 94-0736, January 1994.

69. Duque, E.P.N., 'A numerical analysis of the British experimental rotor program blade', J. American Helicopter Society, Vol. 37(1), January 1992, pp. 46-54.

70. Scott, M.T. and Narramore, J.C., 'Navier-Stokes correlations of a swept helicopter rotor tip at high alpha', AIAA 91-1752, 1991.

71. Rajagopalan, R. and Keys, C. 'Detailed aerodynamic analysis of the RAH-66 FanTail™ using CFD', J. American Helicopter Society, Volume 42(4), October 1997, pp. 310-320.

72. Poling, D.R., Rosenstein, H. and Rajagopalan, G., 'Use of a Navier-Stokes code in understanding tilt-rotor flowfields in hover', J. American Helicopter Society, Vol. 43(2) April 1998, pp. 103-109.

73. Chaffin, M. and Berry, J., 'Helicopter fuselage aerodynamics under a rotor by Navier-Stokes simulation', J. American Helicopter Society, Vol. 42(3), pp.235-243, July 1997.

74. Serr, C. and Cantillon, M. 'Navier-Stokes calculation: An industrial tool for air intake optimisation', Proceedings of the 22nd European Rotorcraft Forum, Brighton, September 1996.

75. McCroskey, W.J. and Dwyer, H.A. 'Methods of analyzing propellor and rotor boundary layers', J. AIAA Vol. 9(8), 1971.

76. McCroskey, W.J. 'Recent developments in rotor blade stall', AGARD CP 111, 1972.

77. Batchelor, G.K. 'Introduction to Fluid Dynamics', Chapter 5, p. 302 ff Cambridge University Press, 1990.

78. Fogarty, L.E. 'The laminar boundary layer on a rotating blade', J. of the Aeronautical Sciences, Vol. 18(4), 1951.

79. Tanner, W.H. and Yaggy, P.F. 'Experimental boundary layer study on hovering rotors', J. American Helicopter Society, Vol. 11(3) 22-37, 1966.

80. Philippe, J.J. and Chattot, J.J., 'Experimental and theoretical studeis on helicopter blade tips at ONERA', Proceedings of the 6th European Rotorcraft Forum, Bristol, September 1980.

81. Brotherhood, P. and James, C.A., 'Some flight experiments on the XH51N Helicopter', RAe TM (Avionics) 1342, September 1971.

82. Reynolds, O., 'On the dynamical theory of incompressible viscous fluids and the determination of the criterion', Philosophical transactions of the Royal Society of London, Series A, Vol. 186, 1895, p.123

83. Ramm, H.J., 'Fluid dynamics for the study of transonic flow', Oxford University Press, 1990.

84. Pahlke, K., 'Development of a numerical method solving the unsteady Euler Equations for oscillating airfoils', DLR-FB 129-90.35, 1990.

85. Favre, A., 'Equations des gaz turbulents compressibles', J. de Mecanique, Vol. 4(3), 1965, pp. 361-90.

86. Wilcox, D.C., 'Turbulence modelling for CFD',DCW Industries Inc., 1993.

87. Chapman, D.R., 'Computational Aerodynamics: Development and outlook', AIAA J., Vol. 17, 1979, pp. 1293-1313.

88. Boussinesq, J., 'Theorie de l'ecoulement turbillant', Mem. Presentes par Divers Savants Acad. Sci. Inst. Fr., Vol. 23, 1877, pp. 46-59.

89. Speziale, C.G., 'On non-linear k-l and k-e models of turbulence', J. Fluid Mechanics, Vol. 178, 1987, pp.459-475.

90. Prandtl, L., 'Uber ein neues formelsystem fur die ausgebildete turbulenz', Nacr. Akad. Wiss. Gottingen, Math-Phys. Kl., 1945, pp. 6-19.

91. Baldwin, B.S. and Lomax, H., 'Thin layer approximation and algebraic model for separated turbulent flows', AIAA Paper 78-257, 1978.

92. Coakley, T.J., 'Turbulence modelling methods for the compressible Navier-Stokes equations', AIAA Paper 83-1693, 1983.

93. Jones, W.P. and Launder, B.E., 'The prediction of laminarization with a two equation model of turbulence" Int. J. Heat and Mass transfer, Vol. 15, 1972, pp. 301-14.

94. Lindberg, P.A., Weber, C. and Rizzi, A., 'Calculation of the A-airfoil using the k-τ model', Proceedings of the 18th Congress of the International Council for the Aeronautical Sciences, pp. 1046-1052, 1994.

95. Kalitzin, G., Gould, A.R.B. and Benton, J.J., 'Application of two-equation turbulence models in aircraft design', AIAA Paper 96-0327.

96. Kolmogorov, A.N., 'Equations of turbulent motion of an incompressible fluid', Izvestia Academy of Sciences, USSR, Physics, Vol. 6(1), pp.56-58.

97. Saffman, P.G., 'A model for inhomogeneous turbulent flow', Proc, Royal Society, Vol, A317, pp. 417-433, 1970.

98. Launder, B.E. and Spalding, D.B., 'Mathematical models of turbulence', Academic Press, London, 1972.

99. Menter, F.R., 'Influence of freestream values on k-ω turbulence model predictions', AIAA J., Vol. 30(6), pp. 1657-1659, 1992.

100. Menter, F.R., 'Zonal two-equation k-ω turbulence models for aerodynamic flows', AIAA Paper 93-2906, 1993.

101. Richardson, L.F., 'The approximate arithmetical solution by finite differences of physical problems involving differential equations with an application to the stresses in a masonry dam', Philosophical Transactions of the Royal Society, Series A, Vol. 210, 1910, pp. 307-357.

102. Courant, R., Friedrichs, K.O. and Lewy, H., 'On the partial differential equations of mathematical physics', IBM J., Vol. 11, 1967, pp. 215-234.

103. McDonald, P.W., 'The computation of transonic flow through two dimensional gas turbine cascades', ASME Paper 71-GT-89, 1971.

104. MacCormack, R.W. and Paullay, A.J., 'Computational efficiency achieved by time splitting of finite difference operators', AIAA Paper 72-154, 1972.

105. Lax, P.D., 'Weak solutions of non-linear hyperbolic equations and their numerical computation', Comm. Pure and Applied Math., Vol. VII, 1954, pp. 159-193.

106. Steger, J.L. and Warming, R.F., 'Flux vector splitting of the equations of gas dynamics with applications to finite difference methods', J. Comp. Physics, Vol. 40, pp. 263-293, 1981.

107. Van Leer, B., 'Flux vector splitting for the Euler equations' Technical Report ICASE 82-30, 1982.

108. Van Leer, B., 'Flux vector splitting for the Euler equations', Proceedings of the 8th International conference on numerical methods in fluid dynamics, pp. 507-12, 1982.

109. Liou, M.S. and Steffen, C.J., 'A new flux splitting scheme', J. Comp. Physics, Vol. 107, pp. 200-212, 1994.

110. Qin, N., 'A comparative study of two upwind schemes as applied to Navier-Stokes solutions for resolving boundary layers in hypersonic viscous flow', GU Aero Report 9120, Department of Aerospace Engineering, Glasgow University, 1991.

111. Godunov, S.K., 'A finite difference method for the computation of discontinuous solutions of the equations of fluid dynamics', Mat. Sb. Vol. 47, 1959, pp. 357-393.

112. Harten, A., 'High resolution schemes for hyperbolic conservation laws', Vol. 49, 1983, pp. 357-393.

113. Toro, E.F., 'Riemann solvers and numerical methods for fluid dynamics', Springer-Verlag, 1997.

114. Roe, P.L., 'Approximate Reimann solvers, parameter vectors and difference schemes', J. Comp. Physics, Vol. 43, 1981, pp.357-372.

115. Osher, S. and Solomon, F., "Upwind difference schemes for hyperbolic systems of conservation laws", Mathematics of Computation, Volume (38), Number 158, April 1982, pp. 339-374.

116. Qin, N., Ludlow, D.K., Shaw, S.T. and Richardson, G., 'A unified high resolution approach for two equation turbulence modelling', Proceedings of the 3rd Pacific International Conference on Aerospace Science and Technology, p.219, 1997.

117. Goldberg, U.C., Gorski, J.J. and Chakravarthy, S.R., 'Transonic turbulent flow computations for axisymmetric afterbodies', AIAA Paper 85-1639, 1985.

118. Gorski, J.J., Chakravarthy, S.R. and Goldberg, U.C., 'High accuracy TVD schemes and the k-e equations of turbulence', AIAA Paper 85-1665, 1985.

119. Goldberg, U.C., Gorski, J.J. and Chakravarthy, S.R., 'Flowfield computations around nozzle/afterbody configurations at transonic Mach numbers', AIAA Paper 85-4081, 1985.

120. Takakura, Y., 'Turbulence models for 3D transonic viscous flows', AIAA Paper 89-1932, 1989.

121. Lin, H. and Chieg, C.C., 'Comparisons of TVD schemes for turbulent transonic projectile aerodynamics computations with a two-equation model of turbulence', Int. J. Numerical Methods in Fluids, Vol. 16, pp. 365-390, 1993.

122. Liu, F. and Ji, S., 'Unsteady flow calculations with a multigrid Navier-Stokes method', AIAA Paper 95-2205.

123. Sikonen, T., "An application of Roe's flux difference splitting for k-ε turbulence model", Int. J. Numerical Methods in Fluids, Volume (21), pp. 1017-1039, 1995.

124. Yegorov, I., Ivanov, D. and Obabko, A., 'Newton technique in numerical simulation of turbulent flows', Proceedings of the 7th International Symposium on Computational Fluid Dynamics, p.490-95, 1997.

125. Ludlow, D.K., Private communication, 1997.

126. Enquist, B. and Osher, S., 'One sided difference approximations for non-linear conservation laws', Math. Comp. Vol. 36(154), 1981, pp. 321-351.

127. Enquist, B. and Osher, S., 'Stable and entropy satisfying approximations for transonic flow calculations', Math. Comp. Vol. 34, 1980, pp. 45-75.

128. Chakravarthy, S. R. and Osher, S., "Numerical experiments with the Osher upwind scheme for the Euler equations", AIAA J., Volume (21), Number 9, September 1983, pp. 1241-1248.

129. Spekreijse, S.P., 'Multi-grid solution of the steady Euler equations', PhD. Dissertation, Centruum voor Wiskunde en Informatica, Amsterdam, 1988.

130. Van Leer, B., 'Towards the ultimate conservative difference scheme III: Upstream centred finite difference schemes for ideal compressible flow', J. Comp. Physics, Vol. 23, pp. 263-275, 1977.

131. Van Leer, B., 'Towards the ultimate conservative difference scheme IV: A new approach to numerical convection', J. Comp. Physics, Vol. 23, pp. 276-299, 1977.

132. Van Leer, B., 'Towards the ultimate conservative difference scheme V: A second order sequel to Godunovs method', J. Comp. Physics, Vol. 32, pp. 101-136, 1979.

133. Qin, N. and Richards, B.E., 'Sparse quasi-Newton method for Navier-Stokes solution', Notes in Numerical Fluid Dynamics, Vol. 29, pp 474-483, 1990.

134. Qin, N. and Richards, B.E., 'Sparse Newton method for high resolution schemes', Notes in Numerical Fluid Dynamics, Vol. 20, pp. 310-317, 1988.

135. Badcock, K. and Richards, B.E., 'Implicit time stepping methods for the Navier-Stokes equations', AIAA J. 34(3), March 1996.

136. Chakravarthy, S.R. and Rai, M.M., 'An implicit form for the Osher upwind scheme', AIAA J., 24, (5), pp. 735-743, May 1986.

137. Badcock, K., 'A parrallelisable partially implicit method for unsteady viscous aerofoil flows', Glasgow University Aero Report 9312, July 1993.

138. Orkwis, P.D. and Vanden, KJ. , 'On the accuracy of numerical versus analytical Jacobians', AIAA Paper 94-0176, 1994.

139. Gaitonde, A.L. and Fiddes, S.P., 'A dual-time method for the solution of the unsteady Euler equations', Aeronautical Journal, Vol. 98 (978), pp. 283-91, 1994.

140. Briley, W.R. and McDonald, H., 'Solution of the three dimensional compressible Navier-Stokes equations by an implicit technique', Lecture notes in Physics, Vol. 35, 1975.

141. Beam, R.M. and Warming, R.F., 'An implicit factored scheme for the compressible Navier-Stokes equations', AIAA J., Vol. 16, pp. 393-402, 1978.

142. Golub, G.H. and van Loan, C.F., 'Matrix Computations', The Johns Hopkins University Press, 1983.

143. Pulliam, T.H. and Chausee, D.S., 'A diagonal form of an implcit approximate factorisation algorithm', J. Computational Physics, Vol. 39, pp. 347-63, 1981.

144. Shaw, S.T. and Qin, N., 'A Preconditioned Implicit Krylov Subspace Method for the Parabolised Navier-Stokes Equations', AIAA Paper 98-0111, 1998.

145. Sonneveld, P., 'CGS: A fast Lanczos type solver for non-symmetric linear systems', SIAM J. Sci. Stat. Comp., Vol. 10, pp. 36-52, 1989.

146. Saad, Y. and Schultz, M.H., 'GMRES: A genralsised minimal residual algorithm for solving non-symmetric linear systems', SIAM J. Sci. Stat. Comp., Vol. 7(3), pp. 856-869, 1986.

147. Wigton, L.B., Yu, N.J. and Young, D.P., 'GMRES acceleration of computational fluid dynamics codes', AIAA Paper 85-1494, 1985.

148. Venkatikrishnan, V. and Mavriplis, D.J., 'Implicit solvers for unstructured meshes', ICASE Report 91-40, 1991.

149. Hixon, R. and Sankar, L.N., 'Application of generalized minimal residual method to 2d unsteady flows" AIAA Paper 92-0422, 1992.

150. Van der Vorst, H. and Vuik, C., 'GMRESR: A family of nested GMRES methods', Numerical and Linear algebra Vol. 1(1), 1993.

151. Shaw, S.T., 'Comparison of the convergence behaviour of three linear solvers for large, sparse unsymmetric matrices', COA Report 9504, 1995.

152. Choquet, R. and Erhel, J., 'Newton-GMRES algorithm applied to compressible flows', Int. J. Numerical methods in fluids, Vol. 23, pp. 177-190, 1996.

153. Degrez, G. and Issman, E., 'Acceleration of compressible flow solvers by Krylov subspace methods', VKI Preprint 1994-65, 1994.

154. Barth, T. and Linton, S.W., 'An unstructured mesh Newton solver for compressible fluid flow and its parallel implementation', AIAA Paper 95-0221, 1995.

155. Qin, N., Ludlow, D.K. and Shaw, S.T., 'A matrix free Newton GMRES method for steady and unsteady Navier-Stokes solutions', Proceedings of the third ECCOMAS Computational Fluid Dynamics '96 Conference, pp. 784-90, 1996.

156. Venkatakrishnan, V., 'Preconditioned conjugate gradient methods for the compressible Navier-Stokes equations', AIAA J., Vol. 29(7), pp. 1092-1110, 1991.

157. Qin, N., 'Lecture notes on shock capturing methods for compressible flows: part III', Cranfield College of Aeronautics, 1995.

158. Qin, N. and Richards, B.E., 'α-GMRES: A new parallelizable iterative solver for large sparse non-symmetric linear systems arising from CFD', Int. J. Numerical methods in fluids, Vol. 15, pp. 613-23, 1992.

159. Saad, Y., 'Preconditioned Krylov subspace methods for CFD applications', Computational Fluid Dynamics '92..

160. Drela, M., 'Newton solution of coupled viscous/inviscid multielement airfoil flows', AIAA Paper 90-1470.

161. Ajmani, K., Ng, W. and Liou, M., 'Preconditioned conjugate gradient methods for the Navier-Stokes equations, J. Computational Physics, Vol. 110, 1994, pp. 68-81.

162. Dennis, J.E., and Schnabel, R.B., 'Numerical methods for unconstrained optimisation and non-linear equations', Prentice-Hall, 1983.

163. Kim, D.B. and Orkwis, P.D., 'Jacobian update strategies for quadratic and near quadratic convergence of Newton and Newton like schemes', AIAA Paper 93-0878.

164. Ortega, J.M., and Rheinboldt, W.C., 'Iterative solution of non-linear equations in several variables', Academic Press, 1970.

165. Qin, N. And Richards, B.E., 'Sparse quasi-Newton method for high resolution schemes', Notes on Numerical Fluid Mechanics, Vol. 20, 1988, pp. 310-317.

166. Qin, N. And Richards, B.E., 'Newton –like methods for fast high resolution simulation of hypersonic flow', Computing Systems in Engineering, Vol. 3 (1-4), 1992, pp. 429-435.

167. Qin, N., and Richards, B.E., 'Sparse quasi-Newton method for Navier-Stokes solution', Notes on Numerical Fluid Mechanics, Vol. 29, 1990, pp. 474-483.

168. Orkwis, P.D., 'Comparison of Newtons and quasi-Newtons method solvers for the Navier-Stokes equations', AIAA J., Vol. 31(5), 1993.

169. Orkwis, P.D. and McRae, D.S., 'A Newtons method solver for high speed separated flow', AIAA J., Vol. 30(1), pp. 78-85, 1992.

170. Orkwis, P.D. and McRae, D.S., 'Newtons method solver for the axisymmetric Navier-Stokes equations', AIAA J., Vol. 30(6), pp. 1507-1514, 1992.

171. Qin, N., Ludlow, D.K. and Shaw, S.T., 'A matrix free preconditioned Newton/GMRES method for Navier-Stokes solutions', submitted for publication.

172. Holst, T., 'Viscous transonic aerofoil workshop compendium of results', AIAA Paper 87-1460, 1987.

173. Rumsey, C.L., 'Parametric study of grid size, time step and turbulence modeling on Navier-Stokes computations over aerofoils', AGARD, Chapter 5.

174. Harris, C. 'Two-dimensional aerodynamic characteristics of the NACA 0012 airfoil in the Langley 8-foot transonic pressure tunnel', NASA TM-81927, 1981.

175. Cook, P.H., McDonald, M.A. and Firmin, M.C.P., 'Aerofoil RAe 2822 – Pressure distributions, boundary layer and wake measurements', Rae TM Aero 1725, 1977.

176. Johnson, D.A. and King, L.S., 'A mathematically simple turbulence closure model for attached and separated turbulent boundary layers', AIAA J., Vol. 23(11), 1985, pp. 1684-92.

177. Bland, S.R., 'AGARD two-dimensional aeroelastic configurations', AGARD Advisory Report 156, 1979.

178. Lambourne, N.C., 'Compendium of unsteady aerodynamic measurements', AGARD Report 702, 1982.

179. Landon, R.H., 'NACA 0012 oscillatory and transient pitching', Paper 3, AGARD 702, 1982.

180. Wood, M.E., 'Results of oscillatory pitch and ramp tests on the NACA 0012 blade section', ARA memo 220, 1979.

181. Landon, R.H., 'A description of the ARA 2-dimensional pitch and heave rig and some results for the NACA 0012 wing', ARA memo 199, 1977.

182. Edwards, J.W., Bland, S.R. and Seidel, D.A., "Experience with transonic unsteady aerodynamic calculation', NASA TM 86278, 1984.

183. Sankar, V., Hiroshi, I., Gorski, J. and Osher, S., 'A fast time-accurate, unsteady full potential scheme', AIAA Journal 25(2), pp.230-8, 1987.

184. Venkatakrishnan, V. and Jameson, A., 'Computation of unsteady transonic flow by solution of the Euler equations', AIAA Journal 26(8), pp. 974-81, 1988.

185. Kandil, O.A., and Chuang, H.A., 'Unsteady transonic airfoil computation using implicit Euler scheme on body fixed grid', AIAA J., Vol. 27(8), 1989, pp. 1031-7.

186. Borel, C. and Bredif, M., 'High peroformance parallelized implicit Euler solver for the analysis of unsteady aerodynamic flows', CFD '92, Vol. (2), 1992, pp.1069-1076.

187. Gaitonde, A.L. and Fiddes, S.P., 'A three-dimensional moving mesh system for the calculation of unsteady transonic flows', Aeronautical Journal, 99(984), 1995.

188. Gaitonde, A.L. and Fiddes, S.P., 'A moving mesh system for the calculation of unsteady flows" AIAA Paper 93-0641, 1993.

189. Gaitonde, A.L., 'A dual time method for the solution of the 2D unsteady Navier-Stokes equations on structured moving meshes', AIAA Paper 95-1877, 1995.

190. Gaitonde, A.L., Jones, D.P. and Fiddes, S.P., 'A 2D Navier-Stokes method for unsteady compressible flow calculations on moving meshes', Aeronautical Journal, Vol. 102(1012), 1998.

191. Dubuc, L., Badcock, K.J., Richards, B.E. and Woodgate, M., 'Implicit Navier-Stokes simulations of unsteady flows', Paper 11, , RaeS Unsteady Aerodynamics conference, 17-18 July 1996.

192. Badcock, K.J., and Gaitonde, A.L., 'An unfactored implicit moving mesh method for the two-dimensional unsteady N-S equations', Int. J. For numerical methods in fluids, Vol. 23, 1996, pp. 607-31.

193. Badcock, K.J., 'An efficient unfactored implicit method for unsteady aerofoil flows', Glasgow University, Department of Aeronautics Report, GU Aero. Rep. 9313,1993.

194. Badcock, K.J., 'A paralleisable partially implicit method for unsteady viscous aerofoil flows', Glasgow University, Department of Aeronautics Report, GU Aero. Rep. 9314,1993.

195. Thomadakis, M.P., and Tsangaris, S., 'Transonic unsteady inviscid and viscous flows simulation around 2-d moving bodies', AIAA Paper 92-2704, 1992.

196. Thomadakis, M.P. and Tsangaris, S., 'Om the prediction of transonic unsteady flows using second order time accuracy', CFD '92, Vol. (2), 1992, pp. 711-718.

197. Finke, K., "Unsteady shock wave-boundary layer interactions on profiles in transonic flow", AGARD CP 168, 1976.

198. Finke, K., "Shock oscillations in transonic flow and their prevention", Symposium Transonicum II, pp. 57-65, Springer-Verlag, 1975.

199. McDevitt, J.B. Levy, L.L. and Diewert, G.S., "Transonic flows about a circular-arc airfoil", AIAA J. 14(5), May 1976.

200. McDevitt, J.B., "Supercritical flow about a circular-arc airfoil", NASA TM-78549, January 1979.

201. Mabey, D.G., "Oscillatory flows from shock induced separation on bi-convex aerofoils of varying thickness in ventilated wind tunnels", RAe TM 969, 1980.

202. Mabey, D.G., Welsh, N.L. and Cripps, B.E., "Periodic flows on rigid 14% thick bi-convex wings at transonic speeds", RAe TR-81059, May 1981.

203. Mohan, S.R., "Studies in transonic flow", PhD thesis, Cranfield University, 1983.

204. Mohan, S.R., "Periodic flows on rigid aerofoils at transonic speeds", AIAA Paper 91-0598, January 1991.

205. Herzberg, N., "The suppression of shock oscillations on a bi-convex aerofoil", MSc thesis, Cranfield Institute of Technology, 1986.

206. Gibb, J., "The cause and cure of periodic flows at transonic speeds", PhD thesis, Cranfield Institute of Technology, 1988.

207. Mabey, D.G., 'Physical phenomena associated with unsteady transonic flows', Unsteady Transonic Aerodynamics, Edited by Nixon, D., Progress in Aeronautics and Astronautics Volume 120, AIAA, 1989.

208. Levy, L.L., 'An experimental and computational investigation of the steady and unsteady transonic flowfields about an airfoil in a solid wall test channel', AIAA Paper 77-678, June 1977.

209. Yamamoto, K and Tanida, Y., 'Self-excited oscillation of Transonic flow around an airfoil in two-dimensional channels', J. of Turbo-machinery, Vol. 112(4), October 1990, pp. 723-731.

210. Edwards, J.W. and Thomas J.L., "Computational methods for unsteady transonic flows", Unsteady Transonic Aerodynamics, Edited by Nixon, D., Progress in Aeronautics and Astronautics Volume 120, AIAA, 1989, pp. 251-260.

211. Levy, L., "Experimental and computational steady and unsteady transonic flows about a thick airfoil", AIAA J. 16, pp. 564-572, 1978.

212. Levy, L., "Predicted and experimental steady and unsteady flows about a bi-convex airfoil", NASA TM-81262, 1981.

213. Diewert, G.S., "Numerical simulation of high Reynolds number transonic flows", AIAA J. 13(11), pp. 1354-9, 1975.

214. Diewert, G.S., "Computation of separated transonic turbulent flows", AIAA J. 14(6), pp. 735-40, 1976.

215. Steger, J.L., "Implicit finite difference simulation of flow about arbitrary tw dimensional geometry's", AIAA J. 16(7), pp/679-86, 1978.

216. Seegmiller, H.L., Marvin, J.G. and Levy, L.L., "Steady and unsteady transonic flow", AIAA J. Vol.16 (X), 1978, pp. 1262-1270.

217. Le Balleur, J. and Girodroux-Lavigne, "A viscous-inviscid interaction method for computing unsteady transonic separation", ONERA TP 1985-5, 1985.

218. Gillan, M.A., "Computational analysis of buffet alleviation in viscous transonic flow over a porous aerofoil", AIAA J. Vol. 33(4), April 1995, pp. 769-772

219. Edwards, J.W., "Transonic shock oscillations calculated with a new interactive boundary layer coupling method", AIAA Paper 93-0777, 1993.

220. Gillan, M.A., Mitchell, R.D. and Raghunathan, S.R., "Prediction and control of self-excited flow over rigid aerofoils", Paper 18, Royal Aeronautical Society Steady Aerodynamics Conference, July 1996.

221. Rumsey, C.L., Sanetrik, M.D., Biedron, R.T., Melson, N.D. and Parlette, E.B., "Efficiency and accuracy of time-accurate turbulent Navier-Stokes computations", Computers and fluids 25(2), pp. 217-236, 1996.

222. Ji, S. and Liu, F., "Computation of self-excited oscillation of transonic flow around an airfoil in a channel", AIAA Paper 96-0063, January 1996.

223. Badcock, K.J., Cantariti, F., Hawkins, I., Gribben, B., Dubuc, L. and Richards, B.E., "Simulation of unsteady turbulent flows using the pseudo time method", Glasgow University Aerospace Engineering Report 9721, 1997.

224. Pearcey, H.H., Osborne, J. and Haines, A.B., "The interaction between local effects of the shock and rear separation – a source of significant scale effects in wind tunnel tests on aerofoils and wings", AGARD CP-35, 1968.

225. Heinrich, R., Pahlke, K. and Bleecke, H., 'A three-dimensional dual-time stepping method for the solution of the unsteady Navier-Stokes equations', Paper 10, RaeS Unsteady Aerodynamics conference, 17-18 July 1996.

226. Maresca, C., Favier, D. and Rebont, J., 'Experiments on an aerofoil at high angle of incidence in longitudinal oscillations', J. Fluid Mechanics, Vol. 92 (4), 1979.

227. Shi, C. and Ho, C-M., 'Vorticity balance and time scales of a two-dimensional airfoil in an unsteady freestream', Phys. Fluids, Vol. 6(2), 1994, pp. 710-23.

228. Reynolds, W.C. and Carr, W., 'Review of unsteady, driven, separated flows', AIAA Paper 85-0527, 1985.

229. Gursul, I., Lin, H. and Ho, C-M., 'Effects of time scales on lift of airfoils in an unsteady stream', AIAA J., Vol. 32(4), 1994, p.797-801.

230. Gursul, I., Lin, H. and Ho, C-M., 'Parametric effects on lift force of an aerofoil in unsteady freestream', AIAA J. 34(5), 1996, pp.1085-1087.

231. Gursul, I. And Ho, C-M., 'High aerodynamic loads on an airfoil submerged in an unsteady stream', AIAA J., Vol. 30(4), 1992, pp. 1117-1119.

232. Morinishi, K. and Muratu, S., 'Numerical solutions of unsteady oscillating flows past an airfoil', AIAA Paper 92-3212, 1992.

233. Szumowski, A.P., and Meier, G.E.A., 'Forced oscillations of airfoil flows', Experiments in Fluids, Vol. 21, 1996, pp.457-64.

234. Van der Wall, B.G. and Leishman, J.G., 'On the influence of time-varying flow velocity on unsteady aerodynamics', J. American Helicopter Society, Vol. 39(4), 1994, pp. 25-36.

235. Habibie, I.A., Laschka, B. and Weishaupl, C. ,'Analysis of unsteady flows around wing profiles at longitudinal accelerations', Proceedings of the 19th International Congress of the Aeronautical Sciences, pp. 2692-2704, 1994.

236. Lin, C.Q. and Pahlke, K., 'Numerical solution of the Euler equations for aerofoils in arbitrary unsteady motion', Aeronautical Journal, June/July 1994.

237. Pahlke, K., Blazek, J. and Kirchner, A., 'Time accurate Euler computations for rotor flows', RaeS Conference on CFD, Paper 15, 1994.

238. Shaw, S.T. and Qin, N., 'Solution of the Navier-Stokes equations for the flow around an aerofoil in an oscillating freestream', Proceedings of the 20th congress of ICAS, Sorrento, 1996.

239. Shaw, S.T. and Qin, N., 'Solution of the Navier-Stokes equations for aerofoils undergoing combined translation pitch oscillations', 22nd European Rotorcraft Forum, Brighton, September 1996.

240. Shaw, S.T. and Qin, N., 'Unsteady flow around helicopter rotor blade sections in forward flight', Aeronautical Journal, Vol. 103(1019), January 1999.

241. Caradonna, F.X. and Philippe, J.J., 'The flow over a helicopter blade in the transonic regime', Vertica, Vol. 2(1), 1976, pp. 43-61.

242. Philippe, J.J. and Armand, J.J., 'ONERA aerodynamic research work on helicopters', AGARD CP 233, 1977.

243. Philippe, J.J. and Chattot, J.J., 'Experimental and theoretical studies on helicopter blade tips at ONERA', Proceedings of the 6th European Rotorcraft Forum, Bristol, 1980.

244. Pahlke, K., Sides, J. and Wehr, D., 'Two- and Three-bladed ONERA model rotors', Notes on Numerical Fluid Mechanics, Vol. 58, 1997, pp 501-520.

245. Shaw, S.T., 'Solution of the Navier-Stokes equations for aerofoils performing in-plane oscillations', COA Report 9503, Cranfield University, 1995.

246. Shaw, S.T. and Qin, N., 'Numerical prediction of the aerodynamic response of aerofoils subjected to step increases in Mach number', Proceedings of the 23rd European Rotorcraft Forum, Dresden, 1997.

247. Favier, D., Maresca, C. and Rebont, J., 'Dynamic stall due to fluctuations of velocity and incidence', AIAA J. Vol. 20(7), pp. 865-71, July 1982.

248. Favier, D., Agnes, A., Barbi, C. and Maresca, C., 'The combined translation pitch motion: A new airfoil dynamic stall simulation', J. Aircraft, Vol. 25(9), pp. 805-814, September 1988.

249. Favier, D., 'Aerodynamique instationnaire d'un profil d'aile soumis a des variations de vitesse et d'incidence', Ph.D. Dissertation, University od Aix-Marseilles, October 1980.

250. Belleudy, J., 'Influence du couplage des variations de vitesse et d'incidence sur e decrochage dynamique d'un profil: Application au rotor d'Helicoptere', Ph.D. Dissertation, University od Aix-Marseilles, September 1991.

251. Favier, D., Belleudy, J. and Maresca, C., 'Influence of coupling incidence and velocity variations on the airfoil dynamic stall', Annual Forum of the American Helicopter Society, Washington, June 1992, pp. 1385-93.

252. Pascazio, M., Berton, E., Favier, D., Wang, C.M. and Steinhoff, J.S., 'Experimental and numerical investigation of airfoil dynamic stall in combined pitch-translation oscillation', AIAA 95-0310, 1995.

253. Beddoes, T.S and Leishman, J.G., 'A generalised model for airfoil unsteady aerodynamic behaviour and dynamic stall using the indicial method', Annual Forum of the American Helicopter Society, Washington, June 1996.

254. Beddoes, T.S., '2 and 3-D indicial methods for rotor dynamic airloads', AHS/National specialists meeting on rotorcraft dynamics, Arlington, Texas, November 1989.

255. Beddoes, T.S., 'Unsteady Aerodynamics – application to helicopter noise and vibration sources', AGARD CP 386, 1985.